A generalised constitutive model for unsaturated compacted soils considering wetting/drying cycles and environmentally stabilised line within the MPK framework

By

Jayasundara Mudiyanselage

Chathurika Jeewanthi Jayasundara

BSc. Eng. (Hons)

Department of Civil Engineering

Monash University

Australia

March 2020

Copyright notice

DEDICATION

This thesis is dedicated to my parents, my husband, my sister and my brother for their unconditional support to carry out this work

Abstract

The MPK (Monash-Peradeniya-Kodikara) framework is based on the traditional compaction curves, whereby the suction is treated as a dependent variable in the (v, v_w, p) space. By considering the work input to unsaturated soil, the selected variables of the MPK framework are the specific volume (v), mean net stress (p) and specific water volume (v_w) with conjugate consideration of the degree of saturation (S_r) or suction (s) as reflected in soil water retention curve (SWRC). Therefore, the MPK framework is considered a partial theory since it does not couple the SWRC directly. Considering the simplicity and practical application of the MPK framework, the main aim of this research was to develop a generalised model for unsaturated compacted soils by coupling hydraulic and mechanical behaviour incorporating environmental stabilised concepts and strain accumulation upon wet-dry cycles.

As identified in the literature review, phenomenological observations of the volumetric and triaxial response of unsaturated soils have not been fully replicated by most constitutive models. Hence, a generalised constitutive model is proposed in this thesis. The main features of the model are an environmentally-stabilised line representing the states achieved after a sufficient number of wetting/drying cycles and a constant plastic volumetric strain-based LC yield curve and a soil water retention curve. The MPK generalised model has 15 parameters, including 9 parameters for mechanical behaviour. The equations for coupled hydro-mechanical behaviour were developed considering Bishop's effective stress for the wet side of the air transition line and independent stress for the dry side of the air transition line, and the stress/strain conjugates were finally transformed to Bishop's effective stress approach for the overall behaviour. The equations derived for isotropic stress state were validated by reproducing a range of phenomenological observations, and the generalised MPK model is capable of reproducing most observed phenomenological behaviour, at least, qualitatively, in some instances.

A series of loading/unloading experiments were carried out in the isotropic stress state to establish the uniqueness of LWSBS upon drying. It was observed that the volumetric yield surface defined in (v, v_w, p) space is unique for not only wetting but also drying. In addition, several other experiments were carried out to capture the strain accumulation through a minimum of four wet-dry cycles and validation of the model.

The MPK generalised model was then extended to triaxial stress state considering critical stress state concepts. Although the isotropic stress state equations were proposed in the net stress space, final constitutive equations of triaxial stress state were transformed to the Bishop's effective stress space.

The corresponding yield surface of the loading collapse curve is generalised to deviatoric stress state using the concepts of the Modified Cam Clay Model. Only two material parameters are introduced for the extension of the model to triaxial stress state. The performance of the postulated critical state model was then evaluated through a series of experiments, including constant suction, constant water content shearing and shearing on anisotropically loaded shearing tests. The constant suction shearing experiments consisted of isotropic stress paths (loading, unloading, wetting and drying), and model simulations agreed reasonably agreeing with the experiments. Finally, it is envisaged that the model can be used in field applications, especially with smart sensing.

Declaration

This thesis is an original work of my research and contains no material which has been accepted for the award of any other degree or diploma at any university or equivalent institution and that, to the best of my knowledge and belief, this thesis contains no material previously published or written by another person, except where due reference is made in the text of the thesis.

Signature: ………….

Print Name: Jayasundara Mudiyanselage Chathurika Jeewanthi Jayasundara

Date: ……………….

Acknowledgements

This dissertation would not have been possible without the guidance and help of several individuals who in one way or another to the completion of this research.

First and foremost, I would like to express my gratitude to my PhD supervisor, Prof. Jayantha Kodikara, who encouraged me to pursue my PhD study and taught me the art of geotechnical engineering. I am deeply grateful to him for his guidance, inspiration, unconditional support, patience and his time though out my candidature. His ideas and concepts have had remarkable influence on my research work, and he has been always available to advise me. I appreciate the excellent atmosphere he provided to enable me to work effectively and efficiently during my PhD research. I am thankful for my core supervisor, Dr Asadul Hauqe, for his valuable guidance and comments at various stages of my research work. I am also indebted to associate professor Annan Zhou at RMIT University for his mentoring and guidance throughout my candidature. It has been a great privilege to work with him for last three and half years.

Secondly, I am deeply thankful for the presence of Dr Ravin Deo and Dr Ben Shannon at Monash University, for their tremendous support. Dr Ravin Deo was always available for my questions, and his helpful discussions were inevitable. My experiments would never be successful without the support given by Dr Ben Shannon. I am highly appreciate his support throughout my candidature not only for familiarising the apparatus but also through the several breakdown that we had during my candidature.

This acknowledgement would not be complete without thanking to the administrative staff of the Civil Engineering deportment of Monash University, Ms Jenny Manson, Ms Min Major, Mrs Fatin Hasan, and Ms Noi Souvandy for their help and support. I would also like to technical staff, Mr Long Goh, Mr Mike Leach and Zoltan Csaki for their generous support in my experimental works. I also would like to acknowledge Monash University for providing the opportunity to study at Monash and particularly for the financial assistance that I have been offered.

I would never forget the lovely and beautiful moments, including coffee times, dinner outing and planned and unplanned trips and gatherings that I shared with my friends during my candidature at Monash. I am thanful for the great company by Arunodi, Arooran, Darshana, Sameera, Rukshan, Pabasara, Ashani, Tharaka, Ayal, Radhika, Avanthi, Champi, Punthila, Dinesha, Balinee, Dilini, Adehsa, Manoj, Udaya, and Shashika. Their company truly made not only relaxing friendly environment but also enjoyable and unforgettable.

Finally, but most importantly, my deepest appreciation is owed to my beloved parents (Mr Upul Senarath Bandara and Mrs Thamara Kumari Senavirathne), my brother (Madusanka Senarath Bandara), and my sister (Kasunika Jayasundara) for their unconditional support, guidance, loving moments and memories and most importantly trusting me throughout my journey and allowing me to pursue the path that I always wish for. Finally, I would like to acknowledge the practical and moral support, which I received from my loving husband (Rangana Maddumahewa) for being patient and understanding throughout my PhD life.

Table of contents

List of publications

Refereed Journal Articles

- **Jayasundara, C.,** Deo, R. & Kodikara, J. 2019a. An integrated conceptual approach for the monitoring and modelling of geo-structures subjected to climatic loading. *Physics and Chemistry of the Earth, Parts A/B/C,* 114**,** 102798.
- Kodikara, J., **Jayasundara, C.** & Zhou, A. 2020. A generalised constitutive model for unsaturated compacted soils considering wetting/drying cycles and environmentally-stabilised line. *Computers and Geotechnics,* 118**,** 103332.
- **Jayasundara, C.,** Kodikara, J. & Zhou, A. 2020 (under review)-a. Salient phenomenological observations of volumetric behaviour relevant to constitutive modelling of hydro-mechanical behaviour of unsaturated compacted soils. *Canadian geotechnical journal*.
- **Jayasundara, C.,** Kodikara, J. & Zhou, A. 2020 (under preparation). A generalised constitutive model for unsaturated compacted soils considering wetting/drying cycles and environmentally stabilised line: Traxial behaviour.
- Abeyrathne, A., Kodikara, J. & **Jayasundara, C.** 2020 (In preparation). Deviatoric Behaviour of Compacted Unsaturated Soils within (q,v_w,p) Space – An Experimental Study.

Refereed Conference Papers

- **Jayasundara, C.,** Kodikara, J. & Zhou, A. 2019 A volumetric yield surface for compacted soils based on constant water content testing. *7th International Symposium on Deformation Characteristics of Geomaterials.* Glasgow, UK.
- **Jayasundara, C.,** Ravin, N. D. & Kodikara, J. Application of a generalised MPK model with data fusion approaches for landslide risk assessment. 3rd International Conference on Information Technology in Geo-Engineering (ICITG 2019), 2019.
- **Jayasundara, C.** & Kodikara, J. 2020. A generalised constitutive model for modelling of geo infrastructures upon wetting and drying cycles. *3rd International conference on geotechnical engineering.*
- Kodikara, J. & **Jayasundara, C.** A plastic volumetric strain dependent soil water retention curve. 4th European conference on unsaturated soils, 2020 Portugal.

List of Figures

List of Tables

Nomenclature

u_a	Pore air pressure
u_w	Pore water pressure
M	Stress ratio at critical state
v	Specific volume
e	Void ratio
v_w	Specific water volume
e_w	Moisture ratio
p	Mean net stress
s	Suction
G_s	Specific gravity
w	Water content
S_r	Degree of saturation
χ	Effective stress parameter/Material parameter which depends on suction
ε_v	Volumetric strain
p_o	Nominal net stress
p_{op}	Operational net stress
ε_v^p	Volumetric plastic strain
LL	Liquid limit
I_p	Plasticity index
PL	Plastic limit
dW	Incremental work per unit volume of unsaturated soil
q	Shear stress
ε_s	Shear strain
θ	volumetric water content
ϕ	Porosity
p^*	Bishop's effective stress
s^*	Modified suction (ϕs)
v_o	Nominal specific volume at nominal stress p_o
$\lambda(v_w)$	Compression index at constant v_w
v_w^L	Specific moisture volume at nominal stress on ATL
C_1, k_1, C_2 and k_2	Constants for a particular soil
$\lambda(S_r)$	Compression index at constant S_r
S_r^L	Degree of saturation on air transition line (ATL)
λ_L	Compression index for ATL on volumetric yield surface
v_o^L	Specific volume of nominal stress p_o on LC yield stress surface for ATL
k_3 and k_4	Constants for a particular soil

λ_{sat}	Compression index along normally consolidated line (NCL)
$\kappa(v_w)$	Unloading/reloading gradient at constant v_w
α_{ES}	Gradient of environmentally stabilised line (ESL)
$\kappa(S_r)$	Unloading/reloading gradient at constant S_r
κ_{sat}	Unloading/reloading gradient along NCL
s^L	Suction at ATL
p_y^{sat}	Yield pressure at saturation
ε_v^e	Volumetric elastic strain
a, m and n	Parameters related to air entry, asymmetric shape of curve and rate of change of slope of curve
a^L	Modified suction at point of inflexion
v_{sat}	Saturated void ratio
h	General function
α	Wetting/drying hydric gradient
α_o	Initial wetting/drying hydric gradient
β	Rate parameter
$\bar{\eta}$	State parameter
N	Number of wetting/drying cycles for given wetting/drying moisture range
p^*_y	Isotropic yield stress on LC curve
M	Slope of critical state line
X	Distance between wetting path and drying path
u_a	Pore air pressure
u_w	Pore water pressure
G	Shear modulus
T_s	surface tension
R_1 and R_2	principal radii of curvature of the meniscus
p_T	Total cell pressure
S_e	Effective degree of saturation
S_r^{res}	Residual degree of saturation
S_r^o	Degree of saturation at zero suction
p'_x	Intersection point of the MCC ellipse and the p' axis
p'_c	Equivalent saturated yield stress
p_r	Reference stress
$\lambda(S_e)$	compressibility at the degree of saturation S_e
ψ	parameter related to χ
ρ	Dry density
ϕ^b	Contribution of the matric suction to shear strength
p_o	Preconsolidation pressure

p_s	Tensile strength
α	Hydric coefficient
p_o	Nominal net stress
p_c	Reference net stress
p_s	Saturated net stress
$N(x)$	Specific volume (or void ratio) at nominal stress
$\lambda(x)$	Compressibility parameter for changes in mean net stress at constant suction, the degree of saturation or specific water volume virgin loading
$\kappa(x)$	Gradient of unloading/reloading line
$N(s)$	Specific volume (or void ratio) at nominal stress at constant suction loading
$\lambda(s)$	Compressibility parameter for changes in mean net stress at constant suction virgin loading
p_{eff}	Effective stress
$N(v_w)$	Specific volume (or void ratio) at nominal stress at constant specific water volume loading
$\lambda(v_w)$	Compressibility parameter for changes in mean net stress at constant specific water volume virgin loading
κ_s	Wetting drying elastic gradient defined on BBM model
LL	Liquid limit
PL	Plastic limit
I_p	Plasticity index

Abbreviations

MPK	Monash-Peradeniya-Kodikara framework
BBM	Barcelona Basic Model
LOO	Line of optimums
ATL	Air transition line
LC	Loading collapse
NCL	Saturated virgin consolidated line
SWRC	Soil water retention curve
LWSBS	Loading wetting state boundary surface
VEP	Volumetric elastic plane
CSSM	Critical state soil mechanics
ESL	Environmentally-stabilised line
BExM	Barcelona expansive model
MCC	Modified cam clay
2D	Two-dimensional
3D	Three-dimentional
AT	Air transition
IoT	Internet of things
MIP	Mercury intrusion porosimetry
SI	Suction increase
SD	Suction decrease
GCM	Glasgow Coupled Model
PSD	Particle size distribution

CHAPTER 1

Introduction

1 Introduction

1.1 Background

More than 80% of soil near the ground surface of Australia and almost 40% of the earth's surface is considered unsaturated. Hence, the need for the implementation of unsaturated soil mechanics in general geotechnical practice is essential. However, there are still significant advances to be made in unsaturated constitutive modelling to make the modelling applicable in practice (Khalili, 2018). Moreover, the most commonly-used construction material to geotechnical engineering is compacted soils, usually in the range of 75% to 90% of initial saturation (Khalili, 2018). Compacted soils are often used as building materials for earth structures such as foundations, retaining walls, dams, roads, and railway embankments, and almost all geo environment-related structures (Gens, 2010; Fredlund and Rahardjo, 1993). Some of the engineering problems associated with unsaturated soils in field conditions are:

1. collapse and swelling behaviour upon wetting caused by natural events (rain and flooding) and artificial events (sprinklers or pipe bursts);
2. loss of shear strength during rain events as wetting decreases suction and, hence, causes loss of shear strength;
3. heave of earth fills due to wetting or rain events. Many compacted soils, particularly expansive clays, are known to swell upon wetting; and,
4. immediate settlement of compacted fills due to undrained compressibility occurs due to the compressibility of air.

Fuelled by failures in unsaturated soil constructions, attention on the constitutive modelling of unsaturated soils increased significantly in the late 1990s. However, the use of unsaturated soil mechanics principals in the field applications still far from complete for several reasons, including:

- testing unsaturated soil is relatively costly and time-consuming, as the permeability of water may be much smaller under unsaturated conditions. Test results can become unreliable as the difficulties arising due to the measurement of pore pressures and complex systems in comparison to saturated soils;

- unsaturated soils may display complicated behaviour under some conditions, e.g., collapse upon wetting. Phenomenological observations of their behaviour are scattered in various journals and have not been compiled to date for constitutive modelling;
- the diversity of unsaturated soils encountered due to mineralogy, origin and environmental conditions (expansive soils, compacted soils, slurry soils); and
- their mechanical, hydraulic and thermal behaviour is complicated and coupling effects are not very clear. Hence, constitutive modelling has not been developed to complete satisfaction.

A cornerstone of the development of soil mechanics was the introduction of the effective stress concept for saturated soils by Karl von Terzaghi in 1923, who defined effective stress in soil as the difference between the total stress and pore water pressure. Decades later, Bishop (1959) extended the principle of effective stress for unsaturated soils considering the net stress ($p = p_{\mathrm{T}} - u_{\mathrm{a}}$) and suction ($u_{\mathrm{a}} - u_{\mathrm{w}}$) acting on a soil and combining them through a single parameter χ. Subsequently, substantial research was undertaken to validate the modified effective stress concept for unsaturated soils, but with limited success (Bishop and Donald, 1961; Bishop and Blight, 1963; Burland, 1965). Later, Matyas and Radhakrishna (1968) proposed the state surface concept to describe volumetric behaviour using the two independent stress state variables net stress and suction. A subsequent phase of research involved the use of two independent stress variable representations of the volumetric and shear behaviour of unsaturated soils (Fredlund and Rahardjo, 1993; Fredlund and Morgenstern, 1977; Fredlund and Rahardjo, 1988; Fredlund and Morgenstern, 1976; Fredlund, 1979). Most initial models based on this representation assumed non-linear elastic behaviour of soil, ignoring soil plasticity. Later, Alonso et al. (1990) presented a pioneering elastoplastic constitutive model, commonly referred to as the Barcelona Basic Model (BBM). Subsequent research focussed primarily on the improvement of BBM, including for example, the model proposed by Wheeler and Sivakumar (1995) where the volumetric coefficient of compressibility increases with the increase of suction in contrast to the opposite behaviour assumed in BBM. Another phenomenological observation not captured in the original BBM was irreversible plastic strain development during wet/dry cycling. To address this, Gens and Alonso (1992) and Alonso et al. (1999) proposed an extended formulation of BBM known as Barcelona expansive model (BExM) for expansive soils. However, these developments considered that different models are needed for expansive and non-expansive soils, although experimental evidence indicated that both these soil types behave in a similar manner and differ only in degree. In parallel, research effort was also directed to the development of unsaturated constitutive models using the effective stress concept due to the relative simplicity of the resulting formulation, in particular for shear response (Khalili and Khabbaz, 1998; Loret and Khalili, 2002; Nuth and Laloui, 2008). Following Houlsby's (1997) research on work input into unsaturated soils, Wheeler et al. (2003) proposed a model which used Bishop's effective stress to couple hydromechanical behaviour in a water retention model that depended on hydraulic hysteresis and the void ratio. Later, Kodikara (2012) proposed a framework referred to as MPK (Monash – Peradeniya – Kodikara), that emphasised the moisture ratio in place of suction to represent volumetric behaviour, and followed the independent stress state approach. This framework introduced, for the first time, a direct link to the traditional compaction curve in unsaturated soil constitutive modelling, and was validated against experimental data (Kodikara, 2012; Kodikara et al., 2015; Islam and Kodikara, 2015; Abeyrathne, 2017). Parallelly, Sheng and Zhou (2011) introduced a hydro-mechanical model in which the degree of saturation depends on both suction and initial void ratio. Later, Zhou et al. (2012) showed that hydraulic behaviour is caused by suction and volumetric strains due to mechanical loading. Apart from the developments described above, other developments considered hydro mechanical coupling (c.f. Gallipoli et al., 2003a; Gallipoli et al., 2003b; Sheng et al., 2008; Pasha et al., 2019; Pedrotti and Tarantino, 2018; Alonso et al., 2013). Chapter 2 provides a more detailed account of unsaturated soil constitutive models.

However, improvements are still necessary to make these models generally applicable to the modelling of practical problems. Ideally, a suitable model should:

a. incorporate appropriate material parameters that can be determined by relatively simple tests such as constant water content testing in contrast to very time-consuming suction-controlled tests;
b. be able to capture the reported phenomenological observations of isotropic and triaxial behaviour;
c. have a sound theoretical basis and consistent with current knowledge of unsaturated soil mechanics while maintaining the practical applicability, , since the model is based on easily measurable parameters such as water content, in contrast to suction, therefore it is amenable to advent of the internet of things (IoT), data science and sensing technologies.

As in classical mechanics, the constitutive behaviour of saturated soil modelling has been considered in describing the volumetric response and then extending it to incorporate deviatoric loading using a Modified Cam Clay Model in critical state soil mechanics. However, for unsaturated soils, the volumetric response is more complex and requires special effort to capture phenomenological observations. In fact, many other phenomenological features have been observed in various tests undertaken to date under both oedometric (c.f. Islam and Kodikara, 2015; Das and Thyagaraj, 2018) and isotropic/triaxial conditions (c.f. Sivakumar et al., 2010; Kato and Kawai, 2000). In addition, most recent constitutive models of unsaturated soil have not paid attention to these features.

Motivated by practical needs of constitutive modelling of unsaturated soils, Kodikara (2012) proposed the Monash – Kodikara – Peradeniya (MPK) framework. The validation of the framework was carried out using compacted kaolin and natural Merri Creek soil for 1-D stress states (Islam and Kodikara, 2015; Kodikara et al., 2015). Subsequently, the MPK framework was extended to the triaxial stress state by Abeyrathne (2017) and validated for isotropic and triaxial stress states based on the development of a constitutive model. However, it can only be considered a partial model which utilises water content instead of suction, in accordance with the work equation proposed by Houlsby (1997); hence, an extension of the MPK framework coupling soil water retention behaviour is proposed in this thesis.

1.2 Knowledge gaps and objectives of the thesis

On the basis of the review of the literature, the following were identified as key research gaps requiring further research:

- the volumetric and triaxial response of unsaturated soils is complex and requires special effort to capture phenomenological observations. Many other phenomenological features have been observed in various experiments undertaken to date, although recent constitutive models have not paid full attention to these features;
- a constitutive model for use in routine engineering practice should be able to combine with practical approaches such as traditional compaction theory;
- the MPK framework utilises specific moisture ratio instead of suction and can be considered as a partial theory. Nevertheless, incorporation of the soil water retention behaviour in a mechanical model is essential for the model to be considered a more complete theoretical constitutive model, and isothermal conditions;

- most recent constitutive models are based on sophisticated suction-controlled tests that take months to obtain the required material parameters. Hence, material parameters should be linked to simple tests such as constant water content testing instead of sophisticated controlled-suction tests.

Based on the conclusions drawn from a review of the literature, the main aim of this research is to develop a generalised model for unsaturated compacted soils by coupling hydraulic and mechanical behaviour incorporating environmentally stabilised concepts and strain accumulation upon wet/dry cycles.

The following objectives will be achieved by the research program to accomplish the above aim:

1. to identify phenomenological observations of unsaturated soils in the isotropic stress and triaxial stress states and to determine the interpretation of these features in the MPK framework;
2. to develop a generalised model incorporating the environmental stabilisation concept in the MPK framework to capture the plastic strain accumulation and structural stabilisation of wet/dry cycles;
3. to formulate a set of theoretical equations to represent general constitutive isotropic behaviour guided by past phenomenological observations and theory and validation based on the existing data available in the literature;
4. to conduct an experimental program for further verification and refinement of the proposed model at the element level; and,
5. to formulate a set of theoretical equations to represent triaxial behaviour guided by the past phenomenological observations and theory and validation based on existing data available in the literature.

1.3 Thesis outline

The primary aim of this thesis is to develop a generalised model for unsaturated compacted soils by coupling hydraulic and mechanical behaviour incorporating environmental stabilised concepts and strain accumulation upon wet/dry cycles. The thesis is organised into eight chapters and a list of references followed by appendix A, B,C and D. A summary of each chapter is given below.

1.3.1 Chapter 1 – Introduction

A general introduction to the entire research program is presented in this Chapter 1, with a summary of the description of unsaturated soil behaviour and current progress on constitutive modelling. It then outlines the knowledge gaps, followed by the objectives of the study. A summary of the thesis outline concludes Chapter1.

1.3.2 Chapter 2 - Literature review

Chapter 2 includes a brief overview of unsaturated soil mechanics relating to the constitutive modelling of the hydro-mechanical behaviour of unsaturated soils. The literature is reviewed in nine sections: unsaturated soils, constitutive stress/ deformation state variables, mechanical behaviour, hydro-mechanical coupling behaviour (water retention curve), existing constitutive models, the MPK framework, triaxial response, comparison of common selected stress paths in existing models and the MPK framework, phenomenological observations incorporated in past models and additional phenomenological observations that need to be considered.

1.3.3 Chapter 3 – Review of MPK framework and related phenomenological observations

As in classical mechanics, the constitutive behaviour of unsaturated soil modelling has been considered in describing volumetric behaviour and then extending it to incorporate deviatoric loading. However, for unsaturated soils, the volumetric response is more complex and requires special effort to capture phenomenological observations. Many other phenomenological features have been observed in various tests undertaken to date under both oedometric and isotropic/triaxial conditions. However, the reporting of these features is scattered and sometimes not highlighted in multiple publications, and this is not favourable for the advancement of unsaturated soil modelling. In the past, there has not been a concerted effort to compile relevant phenomenological features, highlighting their relative importance while paying due attention to soil type and the initial state used in the tests. As tests take an exceedingly long time for unsaturated soil, especially under suction control, it is essential that the value of past tests is fully utilised. In this regard, the intention of this Chapter 3 is to fill this gap by presenting the observed phenomenological features of volumetric behaviour and the triaxial behaviour of unsaturated soils consistently and providing some theoretical interpretations concerning current constitutive models and the MPK framework.

1.3.4 Chapter 4 - The development of the MPK generalised model: isotropic stress state

Building on the MPK framework, a generalised constitutive model is proposed with emphasis on volumetric behaviour. Key concepts of the model include the constant-moisture-content-testing-based yield surface or volumetric yield surface, the plastic strain-based loading collapse (LC) curve and soil water retention curve (SWRC), the air transition line (ATL) to demarcate the continuity of the air and water phases, the environmentally stabilised line (ESL) to represent the states achieved after wet/dry cycles, and the use of Bishop's effective stress and conjugate strains to describe the hydro-mechanical energetics allowing for transition from unsaturated to saturated behaviour. One of the attractive features of the MPK model is the use of the constant moisture-content-based yield surface on the dry side of the ATL, which can be generated much more quickly than with constant suction loading. The mechanical behaviour of the model has 9 parameters which can be determined by relatively simple testing. The evolution of plastic-strain-based SWRCs involves 6 parameters, some of which require calibration by traditional SWRC testing under constant net stress. The generalised MPK model is capable of capturing the general characteristics of unsaturated behaviour, and typical features of the model are explained at the end of the Chapter 4.

1.3.5 Chapter 5 - Materials, methods, and experimental results

The uniqueness of the yield surface through drying loading stress paths is validated, as previous research on the MPK framework was based on loading/unloading and wetting stress paths only. Based on the results of the experiments, the following observations were made: (1) an increase in yield stress during loading after drying in comparison with loading prior to drying was observed; (2) during yielding, a similar pattern of stress path was found with or without drying. The second aim was to identify the possibility of an environmentally stabilised state though several wet/dry cycles.

1.3.6 Chapter 6 – Validation of the isotropic stress state

The generalised MPK constitutive model for unsaturated soils is proposed in Chapter 4 with the main emphasis on the isotropic stress states. The application of this model to the simulation of volumetric behaviour with a combination of stress paths is discussed in this Chapter 6, with some examples from a series of experiments on kaolin by Abeyrathne (2017); Raveendiraraj (2009) and an expansive kaolin bentonite mixture by Sharma (1998). First, the derived equations are validated against the test series performed in this study, and reasonable agreement is observed in all 10 tests. Next, the ability of the generalised MPK model to reproduce observed phenomenological behaviour is validated through several experimental results.

1.3.7 Chapter 7 - Development of the MPK generalised critical state model: Theory and validation of triaxial stress state

The formulation of the critical state model is carried out following Modified Cam Clay principles. Due to its simplicity and the assumption of associative behaviour, only two parameters (G, M) are introduced. These two parameters can readily be found by experiments. However, it has been found that the M parameter is dependent on either suction or degree of saturation. This has not been incorporated in this thesis, and future extensions need to consider this aspect. A range of experiments on compacted kaolin by Raveendiraraj (2009) and Abeyrathne (2017) is analysed in this Chapter 7, including some isotropic stress paths. Both constant suction and constant water content shearing stress path simulations show reasonable agreement with the experimental results.

1.3.8 Chapter 8 - Conclusions and suggestions for future research

Chapter 8 presents the conclusions and future research directions identified in this study.

Three appendices are attached to this thesis: Appendix A, Appendix B and Appendix C.

Appendix A: Derivation of the elastic surface

Appendix B: Transformation matrices

Appendix C: Matlab codes

Appendix D: An integrated conceptual approach for the monitoring and modelling of geo-structures subjected to climatic loading

The proximal soil sensing techniques were integrated with unsaturated soil mechanics concepts to envision a finite element model capable of studying the behaviour of geo-infrastructures. A systematic workflow was presented, which would provide a robust framework within which soil deformation state analysis can be conducted efficiently. Furthermore, the possibility of integrating data streams from all sensors and measurements onto a cloud-based processing architecture was highlighted. The research work has not included in this thesis; however, the published article is given in the publication list and in Appendix D.

1.4 References

Abeyrathne, W. K. a. P. 2017. *A new modelling approach for compacted clayey soils using specific water volume as a state variable.* Ph.D. thesis, Monash University, Melbourne, Australia.

Alonso, E., Pinyol, N. & Gens, A. 2013. Compacted soil behaviour: initial state, structure and constitutive modelling. *Géotechnique,* 63**,** 463-478.

Alonso, E., Vaunat, J. & Gens, A. 1999. Modelling the mechanical behaviour of expansive clays. *Engineering geology,* 54**,** 173-183.

Alonso , E. E., Gens , A. & Josa, A. 1990. A constitutive model for partially saturated soils. *Géotechnique,* 40(3)**,** pp.405-430.

Bishop, A. & Donald, I. The experimental study of partly saturated soil in the triaxial apparatus. Proceedings of the 5th international conference on soil mechanics and foundation engineering, Paris, 1961. 13-21.

Bishop, A. W. 1959. The principle of effective stress. *Teknisk ukeblad,* 39**,** 859-863.

Bishop, A. W. & Blight, G. 1963. Some aspects of effective stress in saturated and partly saturated soils. *Geotechnique,* 13**,** 177-197.

Burland, J. 1965. Some aspects of the mechanical behaviour of partly saturated soils. *Moisture equilibria and moisture changes in soil beneath covered areas. Butterworths, Sydney***,** 270-278.

Das, A. P. & Thyagaraj, T. 2018. Collapse behaviour of compacted red soil. *International Journal of Geotechnical Engineering,* 12**,** 20-27.

Fredlund, D. 1979. Second Canadian Geotechnical Colloquium: Appropriate concepts and technology for unsaturated soils. *Canadian Geotechnical Journal,* 16**,** 121-139.

Fredlund, D. & Morgenstern, N. 1976. Constitutive relations for volume change in unsaturated soils. *Canadian Geotechnical Journal,* 13**,** 261-276.

Fredlund, D. & Rahardjo, H. 1988. State of development in the measurement of soil suction. *The Emergence of Unsaturated Soil Mechanics***,** 47.

Fredlund, D. G. & Morgenstern, N. R. 1977. Stress state variables for unsaturated soils. *Journal of Geotechnical and Geoenvironmental Engineering,* 103.

Fredlund, D. G. & Rahardjo, H. 1993. *Soil mechanics for unsaturated soils*, John Wiley & Sons.

Gallipoli, D., Gens, A., Sharma, R. & Vaunat, J. 2003a. An elasto-plastic model for unsaturated soil incorporating the effects of suction and degree of saturation on mechanical behaviour. *Géotechnique.,* 53**,** 123-136.

Gallipoli, D., Wheeler, S. & Karstunen, M. 2003b. Modelling the variation of degree of saturation in a deformable unsaturated soil. *Géotechnique.,* 53**,** 105-112.

Gens, A. 2010. Soil–environment interactions in geotechnical engineering. *Géotechnique,* 60**,** 3-74.

Gens, A. & Alonso, E. 1992. A framework for the behaviour of unsaturated expansive clays. *Canadian Geotechnical Journal,* 29**,** 1013-1032.

Houlsby, G. 1997. The work input to an unsaturated granular material. *Géotechnique,* 47**,** 193-196.

Islam, T. & Kodikara, J. 2015. Interpretation of the loading–wetting behaviour of compacted soils within the "MPK" framework. Part I: Static compaction 1. *Canadian Geotechnical Journal,* 53**,** 783-805.

Kato, S. & Kawai, K. 2000. Deformation characteristics of a compacted clay in collapse under isotropic and triaxial stress state. *Soils and Foundations,* 40**,** 75-90.

Khalili, N. 2018. Guidelines for the application of the effective stress principle to shear strength and volume change determination of unsaturated soils. *AGS VICTORIA 2018 Symposium.* Melbourne.

Khalili, N. & Khabbaz, M. 1998. A unique relationship of chi for the determination of the shear strength of unsaturated soils. *Geotechnique,* 48**,** 681-687.

Kodikara, J. 2012. New framework for volumetric constitutive behaviour of compacted unsaturated soils. *Canadian Geotechnical Journal,* 49**,** 1227-1243.

Kodikara, J., Islam, T. & Rajeev, P. 2015. Interpretation of the loading–wetting behaviour of compacted soils within the "MPK" framework. Part II: Dynamic compaction 1. *Canadian Geotechnical Journal,* 53**,** 806-827.

Loret, B. & Khalili, N. 2002. An effective stress elastic–plastic model for unsaturated porous media. *Mechanics of Materials,* 34**,** 97-116.

Matyas, E. L. & Radhakrishna, H. 1968. Volume change characteristics of partially saturated soils. *Géotechnique,* 18**,** 432-448.

Nuth, M. & Laloui, L. 2008. Effective stress concept in unsaturated soils: clarification and validation of a unified framework. *International journal for numerical and analytical methods in Geomechanics,* 32**,** 771-801.

Pasha, A. Y., Khoshghalb, A. & Khalili, N. 2019. Can degree of saturation decrease during constant suction compression of an unsaturated soil? *Computers and Geotechnics,* 106**,** 199-204.

Pedrotti, M. & Tarantino, A. 2018. A conceptual constitutive model unifying slurried (saturated), compacted (unsaturated) and dry states. *Géotechnique***,** 1-17.

Raveendiraraj, A. 2009. *Coupling of mechanical behaviour and water retention behaviour in unsaturated soils.* Ph.D. thesis, University of Glasgow.

Sharma, R. S. 1998. *Mechanical behaviour of unsaturated highly expansive clays.* Ph.D. thesis, University of Oxford.

Sheng, D., Fredlund, D. G. & Gens, A. 2008. A new modelling approach for unsaturated soils using independent stress variables. *Canadian Geotechnical Journal,* 45**,** 511-534.

Sheng, D. & Zhou, A.-N. 2011. Coupling hydraulic with mechanical models for unsaturated soils. *Canadian Geotechnical Journal,* 48**,** 826-840.

Sivakumar, V., Sivakumar, R., Murray, E., Mackinnon, P. & Boyd, J. 2010. Mechanical behaviour of unsaturated kaolin (with isotropic and anisotropic stress history). Part 1: wetting and compression behaviour. *Géotechnique,* 60**,** 581-594.

Wheeler, S., Sharma, R. & Buisson, M. 2003. Coupling of hydraulic hysteresis and stress–strain behaviour in unsaturated soils. *Géotechnique,* 53**,** 41-54.

Wheeler, S. & Sivakumar, V. 1995. An elasto-plastic critical state framework for unsaturated soil. *Géotechnique,* 45**,** 35-53.

Zhou, A.-N., Sheng, D., Sloan, S. W. & Gens, A. 2012. Interpretation of unsaturated soil behaviour in the stress–Saturation space, I: Volume change and water retention behaviour. *Computers and Geotechnics,* 43**,** 178-187.

CHAPTER 2

Literature review

2 Introduction

Over the past few decades, a significant amount of research has been carried out in the field of unsaturated soil mechanics, on the constitutive modelling of unsaturated soils using elastoplastic theories and hydro-mechanical behaviours (Burland, 1965; Matyas and Radhakrishna, 1968; Fredlund and Morgenstern, 1976; Alonso et al., 1990; Gens and Alonso, 1992; Sivakumar, 1993; Wheeler and Sivakumar, 1995; Khalili and Khabbaz, 1998; Alonso et al., 1999; Gallipoli et al., 2003a; Wheeler et al., 2003; Miller et al., 2008; Sanchez et al., 2008; Liu and Muraleetharan, 2011; Casini, 2012; Kodikara, 2012; Zhou et al., 2012a, b; Alonso et al., 2013; Casini et al., 2013; Abeyrathne, 2017; Vaunat and Casini, 2017; Lloret-Cabot and Wheeler, 2018; Pedrotti and Tarantino, 2018; Pasha et al., 2019). Although significant advances have been made, the capabilities of constitutive models to capture phenomenological observations of unsaturated soil are limited. In addition, current models require input parameter determination using sophisticated parameter determination techniques. Kodikara (2012) developed an unsaturated soil constitutive model considering the compaction yield surface that utilises simple constant water content tests. Later, the framework was validated for 1-D (or K_o) stress states by Islam and Kodikara (2015) for statically-compacted soils and Kodikara et al. (2015) for dynamically-compacted soils. Subsequently, Abeyrathne (2017) and Abeyrathne et al. (2019) extended the framework to isotropic and triaxial states on the basis of constant water content isotropic and triaxial loading. However, the water retention behaviour through the soil water retention curve (SWRC) was not coupled with the mechanical model. Hence, the main aim of this thesis is to develop a generalised model which builds on the MPK framework for coupled hydro mechanical behaviour. The primary objective of this chapter is to present a comprehensive literature review of the constitutive modelling of unsaturated soils and to identify the existing research gaps to be addressed in the present study.

This chapter includes a brief overview of unsaturated soil mechanics in relation to the constitutive modelling of the hydro-mechanical behaviour of unsaturated soils. The literature will be reviewed in nine sections: unsaturated soils, constitutive stress/ deformation state variables, mechanical behaviour, hydro-mechanical coupling behaviour (water retention curve), existing constitutive models, the Monash-Peradeniya-Kodikara (MPK) framework, triaxial behaviour, comparison of common selected stress paths in existing models and the MPK framework, phenomenological observations incorporated in current models, and finally, additional phenomenological observations that need to be considered in an improved model.

2.1 Unsaturated soils

Of the various types of soil classifications in soil mechanics, one of the most significant concepts in categorising soil is whether it is saturated or unsaturated. These two categories are sometimes called the primary states of a soil that are transformable from one state to another. Saturated soils have two phases (see Figure 2.1), namely, the solid phase and the water phase, while unsaturated soils have more than two phases (see Figure 2.1). Apart from the solid and water phases, the air phase and a new phase called the air-water interface or contractile skin have been identified as two additional phases of unsaturated soil, adding to the complexity of unsaturated soil behaviour (Fredlund and Rahardjo, 1993). Generally, unsaturated soils can occur as natural soils (above the groundwater table), compacted earthworks (landfills, embankments and dams), beneath foundations and pavements, or as a product of biological processes (organic deposits in wetlands).

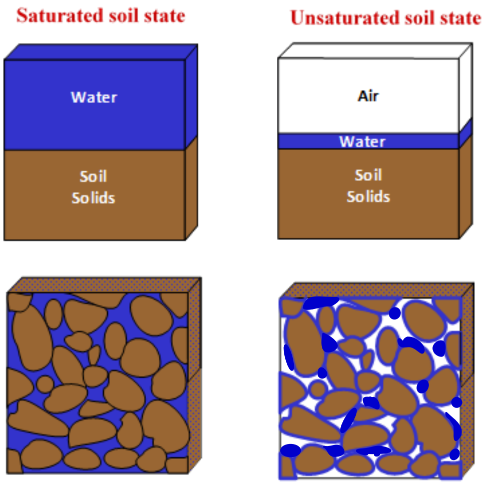

Figure 2.1: Comparison of saturated and unsaturated soil states

The fabric of unsaturated soil, or in other words, the arrangement and packing of the soil particles, depends on various factors including:

1. how the soil is prepared or sampled, for example, whether it is in natural, compacted or reconstituted state. The fabric of sampled natural soil depends on the soil's depositional history and how the soil achieved the unsaturated state, such as through evaporation or wet/dry cycles in nature. The fabric of compacted soil depends predominantly on the initial moisture content and the compaction method (e.g., static versus dynamic) and the energy used. Reconstituted soils are

generally produced by reworking natural or compacted soil to a slurry state and then consolidating it to the required density. During this process, it is possible to lose the original soil fabric or structure or develop fabric that is inherent to the process;

2. size and composition of soil particles. The water retention characteristics are dependent on the pore sizes and their shapes, which are a result of the particle size distribution and how the soil fabric has developed with a particular degree of saturation. For instance, fine-grained soil is capable of sustaining more suction than coarse-grained soil;
3. the degree of saturation (i.e., volume of water pore volume) defining the state of water.

Hence, it is evident that soil sampling plays a critical role in the behaviour of unsaturated soils. Given the significance of compacted soils in civil engineering, this thesis focusses on the study of compacted soils.

2.1.1 Compacted soil behaviour

Compaction is defined as a method of mechanically increasing the density of a soil sample statically or dynamically. Most unsaturated soil constitutive modelling is based on compacted soils. Proctor (1933) developed the original characteristics of compacted soils in the form of Proctor's compaction curve, where a relationship between dry density and moisture content is presented as an inverted parabolic shape for a certain energy input. Subsequently, Proctor's curve was extended to different energy levels representing field compaction equipment and, in some cases, to a family of compaction curves. This concept is routinely used in earthworks in civil engineering, primarily to specify the compaction level required. More detailed accounts of the history of soil compaction and the development of the associated early theories to explain it have been provided by a number of researchers including Kodikara et al. (2018) and Tatsuoka and Correia (2018). Kodikara (2012) provided a direct link to the traditional compaction curve in the development of the MPK framework, highlighting the value of this remarkable phenomenological feature, which is common to most soils and some other particulate systems.

2.1.2 Slurry soil behaviour

Slurry soil is prepared by reworking soil by adding liquid to reach saturation. For example, it is common to add one and a half times the liquid limit of water to a dry soil sample. A sample of soil can then be prepared by consolidating the slurry to the required density or void ratio. Some characteristic differences between consolidated slurry soils and compacted soils are:

1. as evidenced by Mercury Intrusion Porosimetry (MIP) tests, compacted soil has two main categories of pores, named inter-aggregate pores (between aggregates) and intra-aggregate pores (within aggregates) in pore size distribution. These two pore categories can be observed in samples on the dry of optimum side. On the other hand, slurry soil (or reconstituted soil) mostly shows uni-model pore size distribution, i.e., a distribution with one clear peak (Gao et al., 2015;Tarantino, 2010);
2. typically, the air entry value in the soil water retention curve (SWRC) is higher for slurry soil than for compacted soils (Gao et al., 2015; Andriantrehina et al., 2016). However, for both compacted and slurry soils, the SWRC does not affect the method of sample preparation for greater suctions (Gao et al., 2015).;
3. compacted samples normally show less stiffness than slurry soil samples (Gao et al. (2015).

2.1.3 Natural soil behaviour

Natural soils above the water table (or close to the ground surface) can become unsaturated although immediately above the water table, the soil can remain capillary saturated until air entry. Figure 2.2 shows the spatial variation of the layers with respect to unsaturated soil phenomena, indicating the transition from the saturated to the unsaturated state. The unsaturated region can be subdivided into three regions according to the availability of air and water continuity. In the capillary zone, water fills most voids (i.e., capillary saturated) and air is in the occluded or dissolved state; in other words, the free air phase is discontinuous. Further up towards the surface, a three-phase region occurs, where both air and water phases are continuous with the transition of air continuity occurring at some point (referred to as the inflexion point in the SWRC, as explained in Section 2.4). Further up towards the surface, depending on the prevailing weather, soil may be very dry or wet. Generally, these phase variations in these zones occur due to flux boundary conditions at the surface governed by precipitation, evaporation and transpiration, as depicted in Figure 2.2. Experiments on undisturbed natural soil are complicated due to:

- difficulties in measuring the initial condition of the soil (void ratio, water content);
- challenges in predicting the stress history or current state of the soil;
- non-repeatability of initial conditions; and,
- difficulties in the extraction of undisturbed samples and special variation of soil as ground conditions vary.

Therefore, most constitutive unsaturated models are based on compacted soils (Alonso et al., 1990; Wheeler and Sivakumar, 1995; Sharma, 1998; Sivakumar et al., 2010).

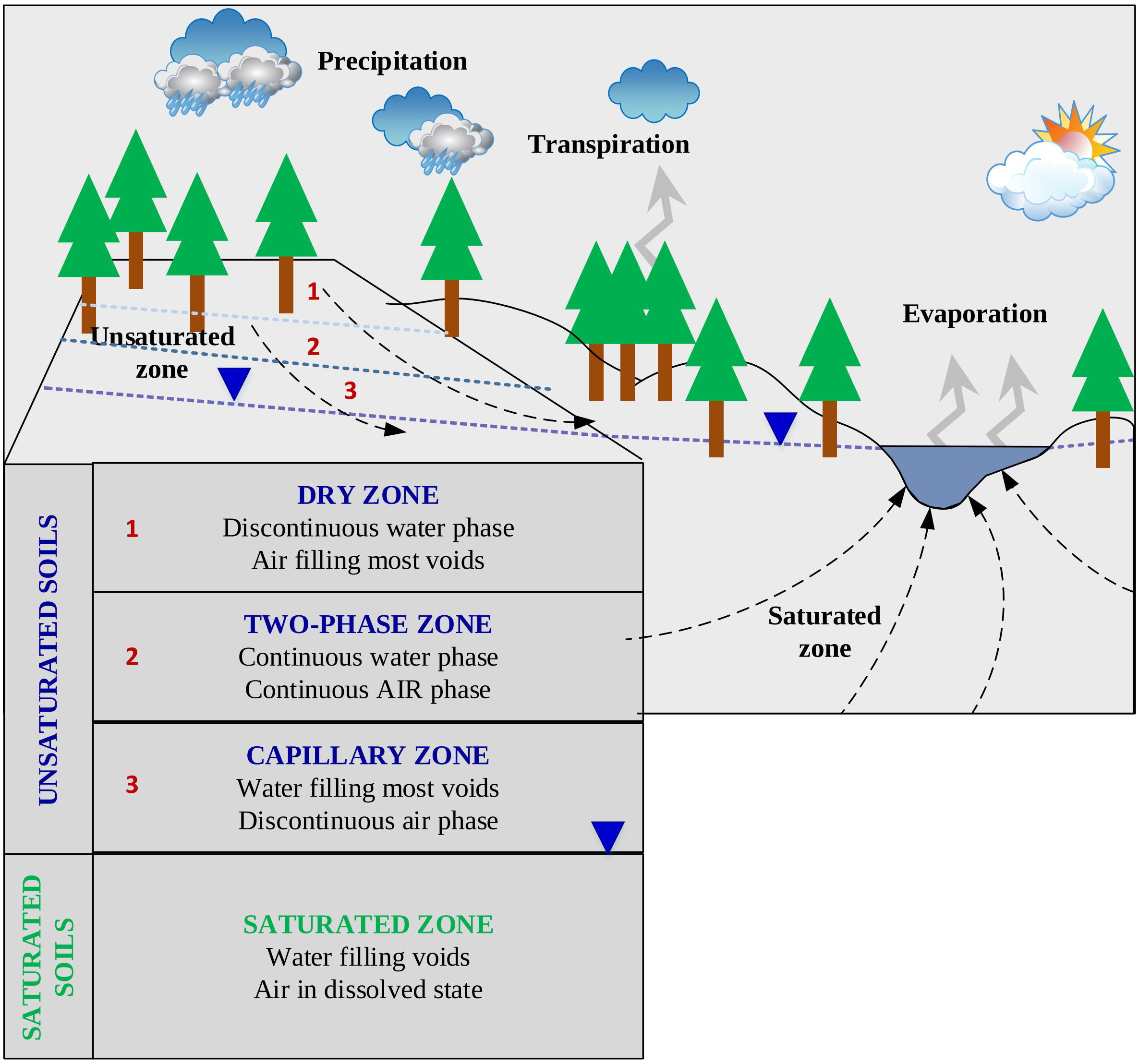

Figure 2.2: Spatial variation of unsaturated soil zone

2.1.4 Suction in unsaturated soils

The presence of air and water creates two pore pressures, namely air pressure and water pressure. The water pressure (u_w) is normally negative (i.e., below atmospheric), and the air pressure (u_a) is positive, causing a positive suction ($u_a - u_w$) in the soil. This is mainly due to surface tension effects causing a stretched meniscus at the pore air and pre-water interface. Generally, the air phase is connected to the atmosphere in the unsaturated zone allowing zero air pressure (u_a = 0), resulting in negative water pressure. This pressure deficit is known as suction (Schofield (1935)), which is normally positive. Suction can be divided into two major categories: matric suction and osmotic suction. Matric suction occurs due to the pressure difference between the air pore pressure and the water pore pressure at the water meniscus, while osmotic suction occurs due to the dissolved ions in the pore fluid. Although the roles of both components are vital on the assumption that the ion (not iron) concertation in the soil is relatively low and the existing concentration remains the same, most laboratory experiments are based only on matric suction measurements (Aitchison, 1961; Tarantino and De Col, 2008), while osmotic suction measurements techniques are still under development (Blatz et al., 2008; Delage et al., 2008).

In this thesis, the term suction refers only to matric suction. At lower suctions the air phase is not continuous, since air is either in the dissolved form in water or isolated bubbles, sometimes referred to as occluded air bubbles. Matric suction occurs due to both capillary and adsorption effects. The capillary effect occurs due to the surface tension of pores and the contact angle between the solid particles and the fluid. The pressure deficit at the water-air interface can be represented by the following equation:

$$(u_a - u_w) = \Delta u = T_s\left(\frac{1}{R_1} + \frac{1}{R_2}\right) \tag{2.1}$$

where, R_1 and R_2 represent the principal radii of curvature of the meniscus in the orthogonal directions, as given in *Figure 2.3* , and T_s denotes the surface tension of the fluid. When R_1 = R_2 , Equation (2.1) transforms to:

$$(u_a - u_w) = \frac{2T_s}{R} \tag{2.2}$$

The adsorption effect due to the water forms a hydration envelope that covers the soil particles. Both capillary and adsorption effects work together, and since it is difficult to separate the capillary and adsorption effects, they are normally considered together.

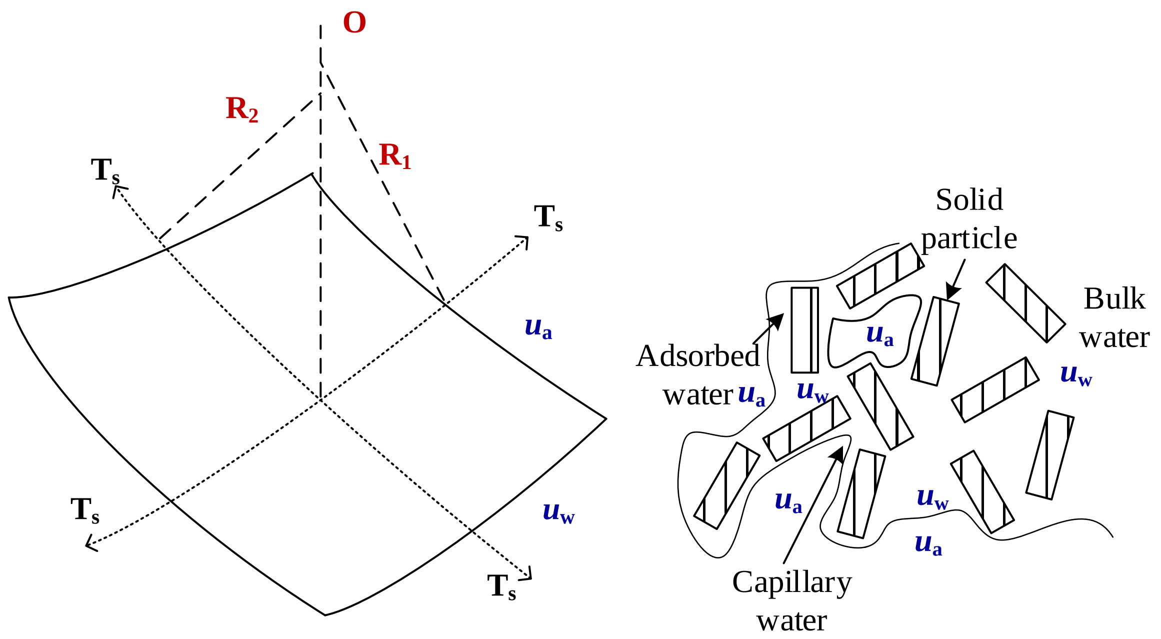

Figure 2.3: (a) surface tension on wrapped membrane; (b) water in unsaturated soil (capillary, absorbed and bulk water)(modified after Fredlund and Rahardjo (1993); Monroy (2006))

Suction is an additional important stress state variable, which comes into consideration when soil changes its state from saturated to unsaturated. Hence, it is common to carry out suction control tests. However, measurement of suction is still a challenging and, time-consuming task. In matric suction, when the air pressure becomes atmospheric, the water pressure becomes negative, and negative pressure can lead to cavitation, causing inaccuracies in suction control and measurement. Axis translation is one of the suction measurement techniques postulated by Hilf (1956), which involves an increase in total cell pressure (p_T), pore pressure (u_w) and air pressure (u_a) by equal amounts to make both air and water pressures positive, while still maintaining a pressure deficit to avoid cavitation. Many experiments related to unsaturated soil have been performed using this technique for oedometric (e.g.,: Alonso et al., 1995), isotropic (Matyas and Radhakrishna, 1968; Raveendiraraj, 2009) and triaxial experiments (e.g.,: Sivakumar, 1993; Raveendiraraj, 2009). Hence, for laboratory experimentation, the axis translation technique is utilised in the present study.

2.2 Constitutive stress/deformation state variables

In order to introduce a discussion of constitutive modelling, a brief discussion of state variables is presented here. For macroscopic continuum modelling, the selection of the state variables is undertaken based on thermodynamic principles. State variables are considered to be the non-material variables required to identify the behaviour of unsaturated soils, and are twofold: (1) stress state variables; (2) deformation state variables (Fredlund and Rahardjo, 1993). The stress state variables define the stress condition, whereas the deformation stress state variables define the deformation condition of the unsaturated soil state. The relationship between these two variables is called a constitutive relationship. Hence, the required stress states are described in the following paragraph before considering existing constitutive relationships. In addition to the stress state variable, material parameters are introduced to define the constitutive relationships between the stress and deformation state variables, which can be considered as constants for a particular type of soil.

Generally, the volumetric behaviour of unsaturated soil can be described by the following four variables: void ratio (e), mean net stress ($p = p_{\mathrm{T}} - u_{\mathrm{a}}$), suction (s), and moisture ratio ($e_{\mathrm{w}} = wG_{\mathrm{s}}$, where, w is the gravimetric water content and G_{s} is the specific gravity, $e_{\mathrm{w}} = S_{\mathrm{r}}e$ where the S_{r} is the degree of saturation). In addition, the triaxial behaviour can be explained by shear stress (q) and shear strain (ε_{s}). As per Houlsby (1997) energy equation (given in Section 2.2.3) which describes the work input into an unsaturated soil (one part of the contribution to the internal energy of soil), p is the net vertical stress for oedometric conditions and net mean stress under triaxial/isotropic conditions. Sometimes, in constitutive modelling, alternative variables such as specific volume v (=1+e), degree of saturation ($S_{\mathrm{r}} = {e}/{e_{\mathrm{w}}}$), Bishop's effective stress ($p^{*} = p + S_{\mathrm{r}}s$), and modified suction (s^{*}) are also used (Wheeler et al., 2003). Here, p, s, q, s^{*} and p^{*} are considered as the stress state variables and e (or v), e_{w} (or v_{w}), S_{r}, ε_{s} are regarded as the deformation state variables. Depending on the modelling approach, the selection of these state variables varies, as discussed in detail later. Temperature can also be considered as a state variable. However, for the purposes of this thesis, the study of the temperature effect is ignored for simplicity by considering isothermal conditions.

2.2.1 Effective stress state approach

The development of theories for unsaturated soil mechanics increased considerably with the introduction of the effective stress concept for saturated soils by Karl von Terzaghi in 1923, where the effective stress (p^*) concept was defined as the difference between total stress (p_T) and pore water pressure (u_w). Later, Bishop (1959) attempted to extend the principle of effective stress for unsaturated soils considering the net stress, ($p = p_T - u_a$) and suction, ($s = u_a - u_w$) acting on soil, as shown in Equation (2.3).

$$p^* = p_T - u_a + \chi(u_a - u_w) \tag{2.3}$$

where, p^*, p_T, u_a and u_w are the effective stress, total stress, pore air pressure and pore water pressure, respectively. χ is considered a material parameter which depends on the degree of saturation and is assumed to vary between 0 and 1. Hence, for simplicity, it was considered that S_r can also be used instead of χ in the effective stress equation, as given in Equation (2.4). This definition is referred to as Bishop's effective stress.

$$p^* = p_T - u_a + S_r(u_a - u_w) = p + S_r s \tag{2.4}$$

Various attempts were made to validate the behaviour of unsaturated soils, although the modified effective stress concept was not capable of accounting for some significant features of unsaturated soil (Bishop and Donald, 1961; Bishop and Blight, 1963; Burland, 1965). Burland (1965) suggested that using the effective stress concept for constitutive modelling on the assumption that the behaviour of air-filled and water-filled voids can be captured by a single parameter representing the degree of saturation is not reliable for the entire region from the dry state to the saturated state. Furthermore, Burland (1965) explained that loading, unloading, wetting and drying occur due to both contact slippage and the shrinkage and swelling of clay packets. In addition, soil usually shows three stages upon wetting. When wetted from a high suction, soil typically shows a small increase in soil volume (swelling), followed at intermediate suctions, by a potential significant reduction in soil volume (collapse) and finally at low suctions, constant volume or a smaller increase in volume. These effects also cannot be explained using the effective stress approach as only one constitutive variable. Hence, the independent stress state approach was introduced as an alternative. However, despite the limitations, many researchers have utilised the effective stress approach as it is capable of handling some other key behaviours, such as shear behaviour (Loret and Khalili, 2002; Wheeler et al., 2003; Nuth and Laloui, 2008a).

2.2.2 Independent stress state approach

Bishop and Blight (1963) were the first researchers to highlight the use of net stress (p) and suction (s) as stress state variables in constitutive modelling. Next, Matyas and Radhakrishna (1968) proposed the concept of state surface to describe volumetric behaviour (as represented by void ratio (v)) using the two stress state variables (p and s) instead of one single state variable, and this approach was named the independent stress state approach. Independent stress state variables do not include any material parameters in contrast to the definition of effective stress. Therefore, the stress space definition is unchanged as the soil deforms or the state of the soil changes. In addition, the two stress variables can be controlled in the laboratory, and raw data can be directly used for analysis. However, constitutive parameters based on two stress variables are complicated and time-consuming to determine. Ensuring the continuity of unsaturated to saturated states is not straightforward, which is limitation.

In the state surface postulated by Matyas and Radhakrishna (1968), the state of a soil element was graphically represented by a point in the 3-D space. The complete stress history of an unsaturated soil element can be represented by a stress path on or below the state surface. However, the state surface is only capable of handling the isotropic stress state, and the triaxial stress state should be treated separately. Later, many models were introduced considering the state surface concept, where a three-dimensional plot is used to explain volumetric behaviour by relating the void ratio, gravimetric water content or degree of saturation with the two state parameters, net stress and suction (Fredlund and Morgenstern, 1976; Fredlund and Morgenstern, 1977; Fredlund, 1979; Fredlund and Rahardjo, 1988; Fredlund and Rahardjo, 1993). Fredlund and Morgenstern (1976) introduced two constitutive relationships to describe the volume change behaviour of partially saturated soil. Those equations are for the soil structure and the change in volume of water in the element level, respectively, and experimental results validated these two constitutive relationships. Later, on the basis of the initial work carried out by Matyas and Radhakrishna (1968), Fredlund and Morgenstern (1976) and colleagues, a significant number of elastic-plastic constitutive models were developed (Alonso et al., 1990; Gallipoli et al., 2003a; Gallipoli et al., 2003b; Wheeler et al., 2003; Sheng et al., 2008).

2.2.3 Houlsby's work equation

On the basis of the energetic analysis performed by Houlsby (1997), the incremental work input ($\mathrm{d}W$) into an unsaturated soil (per unit volume) under volumetric deformational conditions can be given by the following combinations of the above state variables, assuming that the mechanical dissipation associated with fluid flow and air compressibility and the work done by contractile skin are considered to be negligible.

$$\mathrm{d}W = p\,\mathrm{d}\varepsilon_{\mathrm{v}} + \frac{s}{1+e}\mathrm{d}e_{\mathrm{w}} + q\mathrm{d}\varepsilon_{\mathrm{s}} \tag{2.5}$$

$$\mathrm{d}W = (p + S_{\mathrm{r}}s)\,\mathrm{d}\varepsilon_{\mathrm{v}} - \phi s\,\mathrm{d}S_{\mathrm{r}} + q\mathrm{d}\varepsilon_{\mathrm{s}} \tag{2.6}$$

$$\mathrm{d}W = (p + \theta s)\,\mathrm{d}\varepsilon_{\mathrm{v}} + s\,\mathrm{d}\theta + q\mathrm{d}\varepsilon_{\mathrm{s}} \tag{2.7}$$

where, ϕ is the porosity (i.e., $e/(1+e)$), $\mathrm{d}\varepsilon_{\mathrm{v}}$ is the volumetric strain ($-\mathrm{d}e/(1+e)$), θ is the volumetric water content (i.e., $e_{\mathrm{w}}/(1+e)$) and the other variables were explained above. Gens (2010) has indicated that it is possible to choose any corresponding combinations of stress and strain, such as variables from Equations (2.5), (2.6) and (2.7) as work conjugates for constitutive modelling. Buscarnera and Di Prisco (2012) demonstrated that Equations (2.5) and (2.6) are equivalent, and it is possible to formulate constitutive relations from one to the other using transformational matrices. Equation (2.7) is based on previous work by Wei and Muraleetharan (2002b, 2002a). It has the advantage of the simplicity of the second term ($s\mathrm{d}\theta$), but the stress variable (θ) is not as practically desirable. For example, ($p_{\mathrm{net}} + \theta s$) does not readily transform to Terzaghi's effective stress at full saturation.

2.2.4 Bascarnera's transformation concept

Following Buscarnera and Di Prisco (2012), the hydro-mechanical coupled incremental formulation of Equation (2.5) can be given as follows:

$$\begin{Bmatrix} \mathrm{d}p \\ \dfrac{\mathrm{d}s}{1+e} \end{Bmatrix} = \begin{bmatrix} \Delta_{\mathrm{mm}} & \Delta_{\mathrm{mh}} \\ \Delta_{\mathrm{hm}} & \Delta_{\mathrm{hh}} \end{bmatrix} \begin{Bmatrix} \mathrm{d}\varepsilon_{\mathrm{v}} \\ -\mathrm{d}e_{\mathrm{w}} \end{Bmatrix} = \Delta_{\mathrm{HM}} \begin{Bmatrix} \mathrm{d}\varepsilon_{\mathrm{v}} \\ -\mathrm{d}e_{\mathrm{w}} \end{Bmatrix} \tag{2.8}$$

where, the matrix Δ_{HM} represents the coupled hydro-mechanical constitutive relationships, where Δ_{mm} is the mechanical component, Δ_{mh} and Δ_{hm} are the coupling components, and Δ_{hh} is the hydraulic component. Similarly, the transformation of Equation (2.6) can be given by:

$$\begin{Bmatrix} \mathrm{d}p^* \\ \mathrm{d}s^* \end{Bmatrix} = \begin{bmatrix} D_{\mathrm{mm}} & D_{\mathrm{mh}} \\ D_{\mathrm{hm}} & D_{\mathrm{hh}} \end{bmatrix} \begin{Bmatrix} \mathrm{d}\varepsilon_{\mathrm{v}} \\ -\mathrm{d}S_{\mathrm{r}} \end{Bmatrix} = D_{\mathrm{HM}} \begin{Bmatrix} \mathrm{d}\varepsilon_{\mathrm{v}} \\ -\mathrm{d}S_{\mathrm{r}} \end{Bmatrix} \tag{2.9}$$

where, $p^*(=p+S_{\mathrm{r}}s)$ is the Bishop's effective stress and $s^*(=\phi s)$ is the modified suction. The matrix D_{HM} represents the coupled hydro-mechanical constitutive relationships and D_{HM} shows the same corresponding behaviours as in Equation (2.8). The constitutive matrix D_{HM} of Equation (2.8) can be obtained from Δ_{HM} of Equation (2.9) using transformation matrices as follows:

$$D_{\mathrm{HM}} = S_{\mathrm{HM}} \Delta_{\mathrm{HM}} \left[T_{\mathrm{HM}}\right]^{-1} \tag{2.10}$$

where, $S_{\mathrm{HM}} = \begin{bmatrix} s_{\mathrm{mm}} & s_{\mathrm{mh}} \\ s_{\mathrm{hm}} & s_{\mathrm{hh}} \end{bmatrix}$ and $T_{\mathrm{HM}} = \begin{bmatrix} t_{\mathrm{mm}} & t_{\mathrm{mh}} \\ t_{\mathrm{hm}} & t_{\mathrm{hh}} \end{bmatrix}$ define the two transformation matrices given in Equations (2.11), and (2.12) and the derivations of these matrices depend on the theoretical development of the constitutive model.

$$\begin{Bmatrix} \mathrm{d}p^* \\ \mathrm{d}s^* \end{Bmatrix} = \begin{bmatrix} s_{\mathrm{mm}} & s_{\mathrm{mh}} \\ s_{\mathrm{hm}} & s_{\mathrm{hh}} \end{bmatrix} \begin{Bmatrix} \mathrm{d}p \\ \dfrac{\mathrm{d}s}{1+e} \end{Bmatrix} \tag{2.11}$$

$$\begin{Bmatrix} \mathrm{d}\varepsilon_{\mathrm{v}} \\ -\mathrm{d}S_{\mathrm{r}} \end{Bmatrix} = \begin{bmatrix} t_{\mathrm{mm}} & t_{\mathrm{mh}} \\ t_{\mathrm{hm}} & t_{\mathrm{hh}} \end{bmatrix} \begin{Bmatrix} \mathrm{d}\varepsilon_{\mathrm{v}} \\ -\mathrm{d}e_{\mathrm{w}} \end{Bmatrix} \tag{2.12}$$

2.3 Mechanical behaviour

The mechanical behaviour of unsaturated soil is related to both isotropic behaviour and triaxial behaviour, including volume changes and shear strength. Mechanical action can be expressed using a set of constitutive relationships based on the phenomenological observations of unsaturated soils observed in the experiments as well as in the field. In comparison to saturated soil behaviour, unsaturated soil behaviour is relatively complicated due to the two different pore pressures (air pressure and water pressure) and the geometric arrangement of pore fluids (bulk water, capillary water (or meniscus water) and absorbed water, as shown in Figure 2.3). In unsaturated soil, water menisci develop due to the availability of the air phase, and this water menisci effect is broadly discussed by Jennings and Burland, 1962). The normal force at the contact surface enhances the stability of the soil, making bonds to hold soil particles together. In addition, during compression, the menisci offer resistance, and during wetting, particles face slippage and collapse. With the increase of external stress (or loading), if the ratio of tangential to normal force is higher than the inter-particle frictional coefficient, the particle slips, causing plastic strain. On the other hand, with the increase of suction (or drying) additional normal stress develops, leading to an increase in the stability of the particles and reduced slippage (Monroy, 2006). Although several early models could not capture these effects successfully, the first elastoplastic constitutive model by Alonso et al. (1990) was able to capture these effects by incorporating critical state soil mechanics concepts introducing the loading collapse curve (i.e., the Modified Cam Clay model). The model is known as the Barcelona Basic Model (BBM) and has been validated by several experimental pieces of evidence. In the BBM model, the compressibility of unsaturated soils is assumed to decrease with increasing suction, and experiments by Sivakumar (1993) and others showed otherwise for compacted soils. Hence, incorporating increasing compressibility with suction and with other existing features of BBM, Wheeler and Sivakumar (1995) proposed another constitutive model. Later, several other models were developed considering other issues such as hydro-mechanical coupling behaviour (Wheeler et al., 2003; Zhou et al., 2012a).

2.4 Water retention behaviour and hydromechanical coupling

The soil water retention curve (SWRC) provides a conceptual understanding of the mass of water in the soil and the energy state of the water phase, which depends on the soil texture, gradation, initial void ratio, operational stress and several other parameters. In the early stage of unsaturated constitutive modelling, the mechanical response of soil was considered independent of hydraulic action and the elastoplastic models (Matyas and Radhakrishna, 1968; Fredlund and Morgenstern, 1976; Alonso et al., 1990; Wheeler and Sivakumar, 1995). In these models, if all the stresses and suctions are known, the model can be used without considering the water retention behaviour, which is not acceptable in reality. A unique water retention curve for a specific soil was sometimes used to link water content through the suctions used in the model. However, experimental evidence indicates that the mechanical response is affected by the specific moisture content or degree of saturation in addition to net stress and suction variations (Fredlund and Xing, 1994; Vanapalli et al., 1996). Therefore, some constitutive models have been proposed to couple the mechanical and hydraulic behaviour (Gallipoli et al., 2003b; Wheeler et al., 2003; Nuth and Laloui, 2008a; Zhou, 2011; Kodikara, 2012).

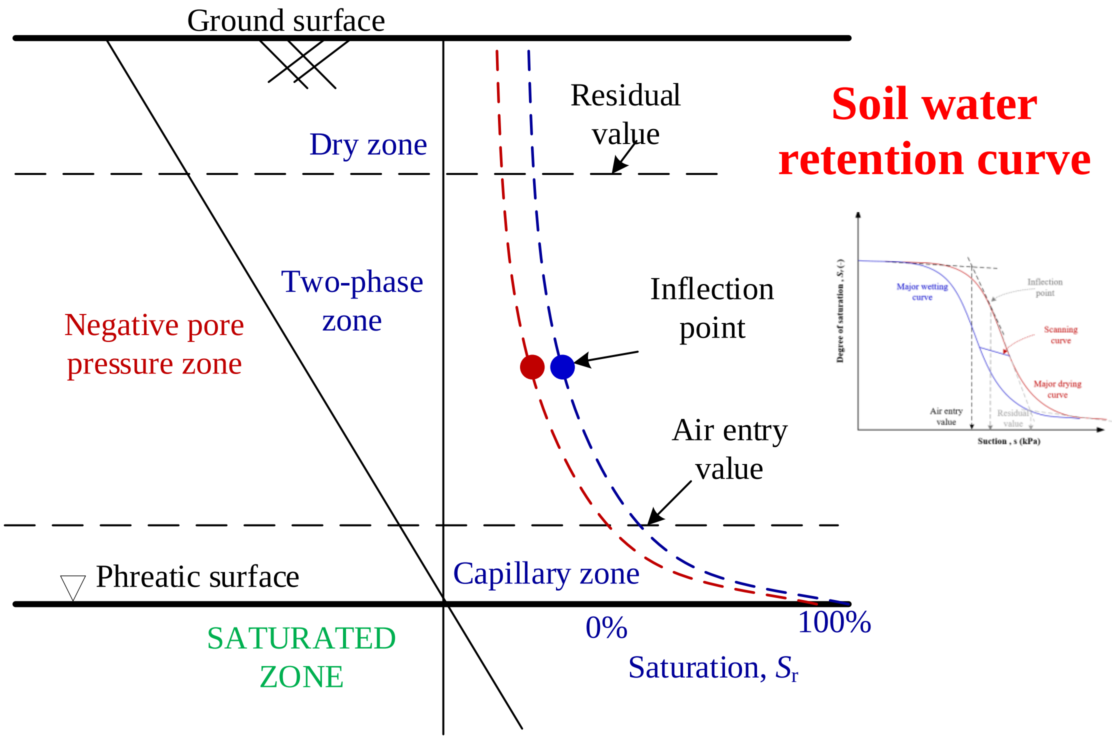

Figure 2.4: Behaviour of SWRC with spatial variation of natural soil

The water retention behaviour of soil can be defined as the relationship between the degree of saturation (or volumetric water content or gravimetric water content) and suction. This response is usually described by the soil-water retention curve (SWRC), which is also known as the water retention curve. The typical responses of soil water retention drying and wetting curves (SWRCs) are shown in Figure 2.4 in linear scale. At the point of equilibrium corresponding to a particular suction, the water potential or suction depends on the water volume, the size and shape of the pores, the chemical composition of the water and its mineralogy. Traditionally, such equilibrium states are measured at nominal stress (or no stress) represented by the SWRC, for instance as the $S_r - \ln(s)$ relationship. The literature commonly refers to two main SWRCs, known as the main drying and main wetting curves (see Figure 2.4). These curves are deemed to be found by drying to high suctions from saturation and then wetting back to saturation. The air entry suction is the suction required for air to enter the soil during the main drying curve, and the residual suction is when S_r diminishes slightly. In addition, the inflexion point (i.e., the maximum gradient point of SWRC in semi-log scale) represents the transition where the air phase becomes continuous and the water phase becomes discontinuous with drying (Dexter, 2004a; Dexter, 2004c; Dexter, 2004b). In addition, if the soil is dried from an intermediate point on the wetting path (or vice versa), it follows a scanning curve. The wetting and drying curves are not the same, signifying the presence of hydraulic hysteresis. The following can be considered as the major reasons for the hysteresis behaviour of unsaturated soils (Raveendiraraj, 2009):

- changes in void passageways during wetting and drying known as the "inkbottle effect". The advancing and receding air-water interface along the void passageways may exhibit different suction for particular volumetric water content, gravimetric water content or degree of saturation;
- the difference of contact angle between the advancing and receding air-water interface. (the advancing angle is higher than the receding angle); and,
- the volume of air may differ during wetting and drying due to the compressibility of air.

The soil hydraulic hysteresis shown by the two separate curves for wetting and drying in Figure 2.4 needs consideration in constitutive modelling. Wheeler et al. (2003) proposed a water retention model that depends on hydraulic hysteresis and void ratio. Later, Sheng and Zhou (2011) proposed a hydro-mechanical model where the degree of saturation depends on both suction and initial void ratio. Later, Zhou et al. (2012a) showed that hydraulic behaviour can be coupled to SWRC by considering volumetric strains due to stresses.

2.5 Existing constitutive models

Houlsby (1997) introduced the thermodynamic work input to the volumetric deformation of unsaturated soils using the macroscopic state variables (e, p, s, e_{w}, S_{r}, q, ε_{s}). This work equation identified three energy components, one associated with stress (p) and volumetric strain $\left(\mathrm{d}\varepsilon_{\mathrm{v}} = -\mathrm{d}e/(1+e)\right)$, one associated with suction (s) and moisture ratio (e_{w}) or the degree of saturation (S_{r}), and the other associated with shear stress (q) and shear strain (ε_{s}), providing the relevant conjugate variables to be used in constitutive modelling. The formulation of current existing constitutive models can be categorised according to the selection of the above state variables. Alonso et al. (1990) (in the Barcelona Basic Model or BBM) and Wheeler and Sivakumar (1995) used the variables specific volume, v $(=1+e)$, p, s, q, ε_{s} without directly coupling the specific moisture volume ($v_{\mathrm{w}} = 1+e_{\mathrm{w}}$) or S_{r}. In the model proposed by Abeyrathne et al. (2019), on the basis of the Monash-Peradeniya-Kodikara (MPK) framework

(Kodikara, 2012), the researchers use v, p, v_w, q, and ε_s to describe unsaturated soil behaviour, that does not couple s directly. On the other hand, effective stress ($p+\chi s$) has been used without considering S_r as a separate variable (e.g., Loret and Khalili, 2002), and χ is proposed as a function of s (Khalili and Khabbaz, 1998). In addition, Bishop's effective stress ($p+S_r s$) has been employed with S_r as a separate variable (e.g., Wheeler et al., 2003), where all six variables (v, p^*, s^*, S_r, q, ε_s) are coupled. Zhou et al. (2012a, 2012b) utilised the same Bishop's effective stress ($p+S_r s$) concept with s instead of s^*.

2.5.1 Barcelona Basic Model (BBM)

Alonso et al. (1990) presented an elastoplastic constitutive model for the first time in unsaturated soil mechanics, which was later named the Barcelona Basic Model (BBM), as shown in Figure 2.5. This was an extension of the Modified Cam Clay (MCC) framework, which is used for saturated soils. The three major stress variables used are mean net stress (p), deviatoric stress (q) and matric suction (s). The main feature of this model is the loading collapse (LC) yield curve in (s, p) plane, which separates the elastic and plastic volumetric behaviour. Volumetric yield occurs due to an increase of p (loading) or decrease in s (wetting); which is the most prominent feature in the BBM model. Furthermore, only recoverable volumetric strains occur in the elastic region, or in other words, inside the LC curve. In addition to the LC curve, a suction increase (SI) line has been incorporated in the BBM model to capture the effects due to yielding in suction, based on the concept that if a soil undergoes suction higher than previously attained, soil undergoes irreversible plastic strains. The maximum suction value that the soil has gained is named the suction increase (SI) by Alonso et al. (1990). Considering the initial yield surface and expanded yield surface, common stress paths of loading (i.e., path AB), drying (i.e., path AC) and shearing (i.e., path AD) are given in Figure 2.5.

Some limitations of the BBM model are: (1) it assumes that unsaturated soil is less compressible than its saturated counterpart. However, compressibility is higher in unsaturated soil than its saturated counterpart; (2) the BBM model ignores the behaviour of the LC curve between saturation to air entry suction, which depicts reduction in net stress with the increase of suction; (3) BBM is more relevant to non-expansive soil behaviours; (4) stress path dependency of compacted soils cannot be explained; and (5) accumulations of stress strains cannot be captured by the model.

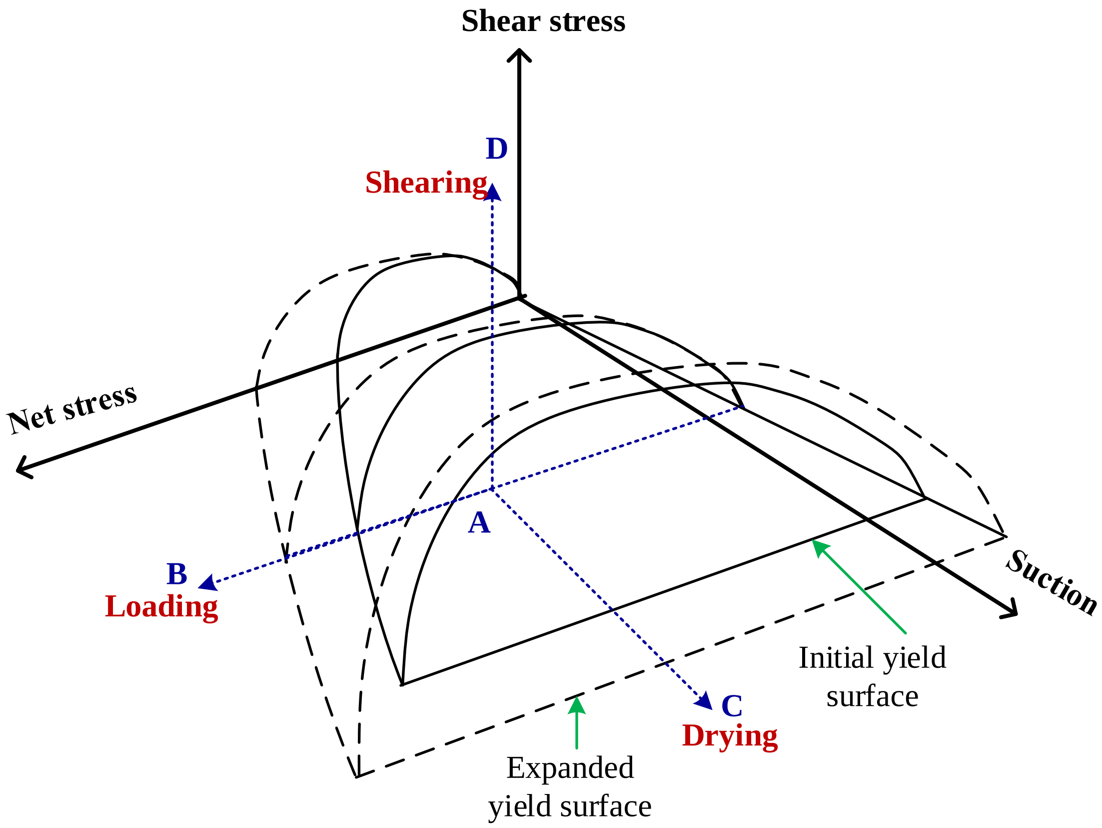

Figure 2.5: Three-dimensional view of yield surfaces (p.q,s) stress space

Later, Wheeler and Sivakumar (1995) proposed a model similar to BBM where the coefficient of compressibility increases with the increase of suction (this will be further discussed in Chapter 3) addressing some limitations of BBM. When expansive soil is subjected to wetting and drying cycles, irreversible swelling occurs, which cannot be explained by the BBM. To address this, Gens and Alonso (1992) and Alonso et al. (1999) proposed a model for expansive soils termed the Barcelona Expansive Model (BExM). This model consists of two levels of soil structure, namely microstructure and macrostructure, and it is assumed that plastic volume change occurs due to the macrostructural effect of soil. In addition, suction decrease (SD) and suction increase (SI) yield lines are used to capture wetting and drying behaviours. The BExM model was developed considering two major structures of soil: macrostructure (aggregated clay particles named "packets" behave as non-expansive clays and capillary effects determine the mechanical behaviour) and microstructure (clay particles and nearby areas and physio-chemical effects dominate the mechanical action). However, packets not only rearrange due to loading but also change volume and shape in contrast to the behaviours of non-expansive soils such as sand and silt. The major limitations of this BExM model are as follows: (1) it includes a great number of material parameters that require time-consuming experimental tests; (2) certain coupling parameters for microstates are hard to quantify; (3) time-dependent effects or thermal effects are not considered.

Meanwhile, Khalili and Khabbaz (1998); Loret and Khalili (2002) and Nuth and Laloui (2008b) formulated unsaturated constitutive models using the effective stress concept. They argued that the use of effective stress is possible when the χ parameter (as in Equation (2.13)) is normalised with respect to air entry suction and its use simplifies the modelling of shear behaviour. Khalili and Khabbaz (1998) introduced a relationship between the material parameter and suction with the use of the air entry value (s_a), which characterises the transition between the saturated and unsaturated state as given in Equation (2.13).

$$\chi = f(x) = \begin{cases} \left(\dfrac{s}{s_a}\right)^{-0.55} & s_a > s \\ 1 & s_a > s \end{cases} \tag{2.13}$$

The constitutive model proposed by Loret and Khalili (2002) was capable of handling most of the key phenomenological features of unsaturated soils. Although the model was capable of predicting prominent behaviours such as drying from the saturated state can lead to initial yielding, and then elastic drying and shear behaviour, the predictions of wetting and drying behaviour deviated slightly from the actual experimental evidence. In addition, this model did not couple hydromechanical behaviour.

2.5.2 Wheeler et al.'s (2003) model

Wheeler et al. (2003) proposed a water retention model that depends on hydraulic hysteresis and void ratio, based on a simplified water retention curve. The model included three yield surfaces for isotropic stress state: The loading collapse (LC) curve, the suction increase (SI) curve and the suction decrease (SD) curve. The model was formulated in terms of two stress state variables, namely Bishop's effective stress ($p^*(=p+S_r s)$) and modified suction ($s^*(=\phi s)$). In this model, it is assumed that air-filled voids and water-filled voids can be considered together by considering the Bishop's effective stress (p^*) as a stress state variable rather than using independent stress state variables (p and s).

Furthermore, yielding on LC produces plastic volumetric strain (mechanical behaviour), which is associated with interparticle or inter-packet slippage, whereas yielding on SI or SD produces a plastic change of the degree of saturation (water retention behaviour) with the emptying and filling of void passageways. With the assumption of a straight LC yield line (i.e., effective yield pressure is constant with respect to suction), it is assumed that the stabilising effect is only dependent on interparticle contacts surrounded by water menisci and it is independent of suction, with no influence on s^* on yielding. Furthermore, the SI and SD lines are horizontal, assuming that Bishop's stress p^* is independent of s^*. This model was later termed the Glasgow Coupled Model (GCM) by Lloret-Cabot et al. (2017) and validated against experimental data. In addition, Lloret-Cabot and Wheeler (2018) explained the double yield curve phenomenon using wetting and drying LC curves.

2.5.3 Zhou et al. (2012)

Sheng and Zhou (2011) introduced a hydro-mechanical model where the degree of saturation depends on both suction and the initial void ratio. Later, Zhou et al. (2012a) showed that hydraulic behaviour is caused by suction and volumetric strains due to stresses. Zhou et al. (2012a) formulated their model in terms of two stress state variables, namely Bishop's effective stress (p^*) and effective degree of saturation (S_{e}), as given in Equation (2.14). The volume change equation ($v - \ln p^*$) is proposed for constant effective degree of saturation, instead of the traditional constant suction curves and compressibility can be found by interpolating saturated and dry state compressibility.

$$S_{\mathrm{e}} = \frac{S_{\mathrm{r}} - S_{\mathrm{r}}^{\mathrm{res}}}{S_{\mathrm{r}}^{\mathrm{o}} - S_{\mathrm{r}}^{\mathrm{res}}} \tag{2.14}$$

$$\text{LC curve: } p'_{\mathrm{x}} = p_{\mathrm{r}} \left(\frac{p'_{\mathrm{c}}}{p_{\mathrm{r}}} \right)^{\beta}, \beta = \frac{\lambda_{\mathrm{o}} - k}{\lambda(S_{\mathrm{e}}) - k} \tag{2.15}$$

$$\text{Hardening law: } \mathrm{d}p'_{\mathrm{c}} = p'_{\mathrm{c}} \left(\frac{1+e}{\lambda_o - k} \right) \mathrm{d}\varepsilon_{\mathrm{v}}^{\mathrm{p}} \tag{2.16}$$

where, S_{r} is the degree of saturation, $S_{\mathrm{r}}^{\mathrm{res}}$ is the residual degree of saturation, $S_{\mathrm{r}}^{\mathrm{o}}$ is the degree of saturation at zero suction, p'_{x} is the intersection point of the MCC ellipse and the p' axis, p'_{c} is the equivalent saturated yield stress, p_{r} is the reference stress and $\lambda(S_{\mathrm{e}})$ is the compressibility at the degree of saturation S_{e}. The model is capable of explaining many primary mechanical responses (drying-induced shrinkage, wetting-induced collapse and loading-induced saturation), the nonlinear compressibility of soil under constant suction and bi-directional hydro-mechanical interaction.

2.5.4 Other recent models

Pedrotti and Tarantino (2018) introduced a novel constitutive conceptual model that incorporates the dry state properties (air-saturated samples) and wet state (reconstituted or water-saturated samples) properties to define the intermediate states (compacted samples) of soil. The model is based on the microstructural properties of unsaturated soil, where the compacted and reconstituted samples exhibit bi-model and mono-model pore size distributions, respectively. Furthermore, the authors have shown that air-saturated samples also show a mono-modal particle size distribution (PSD) for compacted kaolin samples. The model formation based this transition of mono-, bi- and mono- PDSs on water/air saturation according to two assumptions: (1) compacted samples are made of water-saturated and air-saturated pores; (2) air-saturated pores follow the properties of dry powder, and water-saturated pores follow the features of reconstituted soil. Some disadvantages of this model are: (1) it cannot explain the reduction of compressibility towards the drying state prior to a subsequent increase in compressibility; (2) hydro-mechanical coupled behaviour is not defined.

Pasha et al. (2019) proposed a constitutive model to characterise the variation of the degree of saturation upon volumetric deformation. The possibility of the reduction of the degree of saturation during loading is broadly discussed by the authors with evidence of existing experimental evidence of loading after a drying path. In the proposed model, the change in the degree of saturation $\mathrm{d}S_{\mathrm{r}}$ is defined by Equation (2.17):

$$\mathrm{d}S_{\mathrm{r}} = (\psi - S_{\mathrm{r}})\frac{\mathrm{d}e}{e} \tag{2.17}$$

where, e is the void ratio and ψ is a parameter related to χ as given in Khalili et al., 2008. The importance of this model is that it captures the reduction in the degree of saturation upon loading. From phenomenological observations, it is evident that this reduction occurs due to the initial drying stress path. The major limitations of this model are that it has been derived only for constant suction stress paths and the model predictions can only be carried out for known void ratio values.

2.6 MPK framework

Kodikara (2012) proposed a framework whereby suction is treated as a dependent variable in the context of the volumetric behaviour of compacted soils. The framework is based on traditional compaction curves for the first time in constitutive soil modelling, and was developed by considering the volumetric response and validated against experimental data (Kodikara, 2012; Islam and Kodikara, 2015; Kodikara et al., 2015; Abeyrathne, 2017). By considering the work input equation proposed by Houlsby (1997) (given in Equation (2.5)), the selected variables of the MPK framework are the specific volume (v), mean net stress (p) and specific water volume (v_{w}) without coupled consideration of the degree of saturation (S_{r}) or suction (s). In comparison to existing volumetric models, the volumetric yield surface (referred to as the loading wetting state boundary surface, (LWSBS)) is presented in e, e_{w}, p space, as shown in Figure 2.6(a). Figure 2.6(b) shows the same transformed to the compaction ρ, e_{w}, p (ρ = dry density) space. Note that the traditional compaction curve is usually in the unloaded (p = nominal stress) space of the ρ, e_{w} or ρ, w (moisture content) plane.

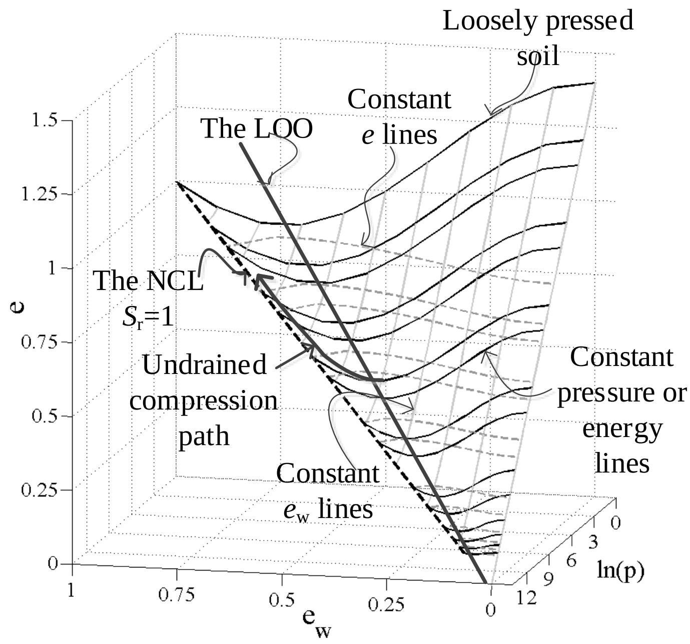

(a)

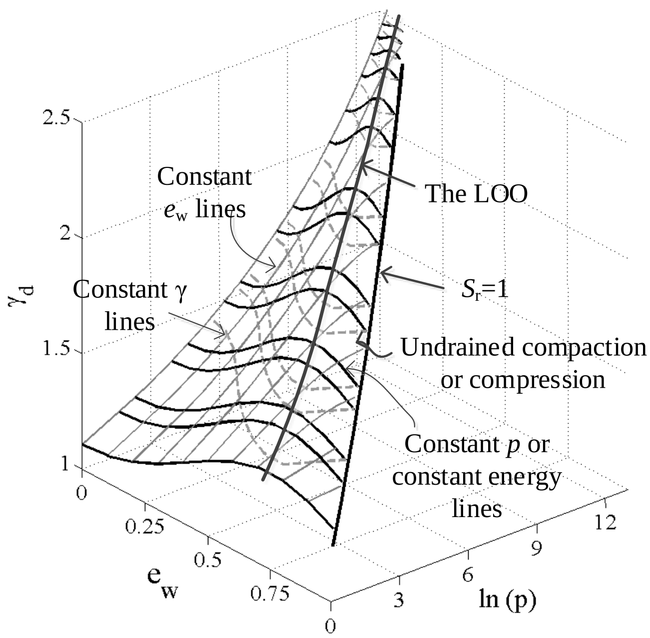

(b)

Figure 2.6: Volumetric yield surface of MPK framework (a) in e, e_w, p space and (b) in compaction ρ, e_w, p space (from Kodikara (2012))

A remarkable feature of the volumetric yield surface is the presence of the line of optimums (LOO, also referred to as the air transition line (ATL) in this thesis), which demarcates the dry side and the wet side of the ATL leading to the saturation line and plane ($e = e_w$). This surface is considered as the extension of the compression line for saturated soils (or the normally consolidated line (NCL)) to unsaturated states featuring the soil's loosest states for different stresses and moisture contents. The MPK framework (Kodikara (2012)) showed how compacted soil behaviour can be explained under various stress paths such as loading, unloading, wetting and drying, or combinations of these stress paths. These explanations were made with respect to net stress and/or moisture content (e_w or S_r) variations without any essential reference to suction (s). Using constant water content tests for compacted kaolin (moderately expansive) and natural Merri Creek soil (highly expansive), the framework was further validated for 1-D (or K_o) stress states by Islam and Kodikara (2015) for statically-compacted soils and by Kodikara et al. (2015) for dynamically-compacted soils. Subsequently, Abeyrathne (2017) and Abeyrathne et al. (2019) extended the framework to isotropic and triaxial states on the basis of constant water content isotropic and triaxial loading. However, these extensions do not incorporate suction as a constitutive variable, in other words there is no hydro-mechanical coupling through a void ratio-dependent SWRC.

2.6.1 Theoretical developments: Isotropic stress state

The volumetric yield surface in the (v, v_w, p) space on the dry side of the ATL is based on the volumetric yield surface developed through constant moisture content tests. Abeyrathne et al. (2019) introduce the volumetric yield surface by a series of constant moisture content (constant v_w) hyperlines given by:

$$v = v_o - \lambda(v_w) \ln(p / p_o) \tag{2.18}$$

where, v_o is the nominal specific volume at the nominal stress p_o and $\lambda(v_w)$ is the compression index at constant v_w, and v_o and $\lambda(v_w)$ are approximated as linear functions of v_w as given by:

$$\lambda(v_w) = C_1 - k_1(v_w - v_w^L) \tag{2.19}$$

$$v_o = C_2 - k_2(v_w - v_w^L) \tag{2.20}$$

In the above equations, $v_{\mathrm{w}}^{\mathrm{L}}$ is the specific moisture volume at the nominal stress on ATL and C_1, k_1, C_2 and k_2 are assumed to be constants for a particular soil, which can be found by fitting experimental data. Similarly, elastic behaviour can be captured by:

$$\mathrm{d}v = -k(v_{\mathrm{w}})\frac{\mathrm{d}p}{p} \tag{2.21}$$

where, $k(v_{\mathrm{w}})$ is the unloading-reloading gradient extracted from constant water content tests. The hardening rule developed from Equations (2.18) and (2.21) is as follows:

$$\mathrm{d}\varepsilon_{\mathrm{v}}^{\mathrm{p}} = \lambda(v_{\mathrm{w}}) - k(v_{\mathrm{w}})\frac{\mathrm{d}p_{\mathrm{y}}}{vp_{\mathrm{y}}} \tag{2.22}$$

Abeyrathne et al. (2019) did not incorporate hydraulic behaviour in the MPK framework, and future research is required to couple the water retention behaviour. In addition, the swelling response of the MPK framework inside the LWSBS is given by Equation (2.23):

$$\mathrm{d}v = \alpha \mathrm{d}v_{\mathrm{w}} \tag{2.23}$$

where, α is the material parameter.

2.7 Triaxial behaviour

The triaxial behaviour of soil is catered by the shear strength (q in critical state soil mechanics and τ in Mohr coulomb approach) and the corresponding deformation state variable shear strain (ε_{s}). The first development of the shear strength equation was defined in term of the effective stress by Bishop (1959) as follows:

$$\tau = c' + ((p_{\mathrm{T}} - u_{\mathrm{a}}) + \chi(u_{\mathrm{a}} - u_{\mathrm{w}}))\tan(\phi') \tag{2.24}$$

where, τ is the shear strength of unsaturated soil, c' is effective cohesion, p_{T} is the total stress, u_{a} is the pore air pressure, u_{w} is the pore water pressure χ is a material parameter and ϕ' is the effective friction angle. With the increase of unsaturated triaxial tests, a reduction in the shear strength with the rise in the suction was observed by Fredlund et al. (1978). This observation resulted in a change to the above shear strength equation proposed by Bishop (1959) as follows:

$$\tau = c' + (p - u_a)\tan(\phi') + (u_a - u_w)\tan(\phi^b) \tag{2.25}$$

where, ϕ^b represents the contribution of the matric suction to shear strength. Alonso et al. (1990) used the critical state soil mechanics concept for constitutive modelling, where the shear behaviour in the BBM model is represented by Equation (2.26), where, the M parameter denotes the slope of the critical state line in the q, p plane, and p_o and p_s are the preconsolidation pressure and the tensile strength, respectively. The tensile strength $p_s (= ks)$ depends on a material parameter (k) and the suction (s):

$$q^2 - M^2(p + p_s)(p_o - p) = 0 \text{ or } q = M(p + p_s) \tag{2.26}$$

Although the material parameter M is assumed to be constant, later Sivakumar (1993) found that the M parameter depends on the suction. Therefore, Equation (2.26) was modified as shown in Equation (2.27).

$$q^2 - M_*{}^2(p + p_o - 2p_x)(p_o - p) = 0 \text{ or } q = M(s)p + \mu(s) \tag{2.27}$$

where, M_* is the aspect ratio of the elliptical yield curve which is assumed to be constant, q is the deviatoric stress, p is the mean net stress, p_o is the intersection point of the MCC ellipse and the p axis, p_x is the critical state value of p, $M(s)$ is the slope of the critical state line and $\mu(s)$ is the intercept of the critical state line in the q, p plot. Zhou et al. (2012b) utilised the critical state soil mechanics Modified Cam Clay theories to extend the isotropic stress state model to the triaxial stress state. In their proposed model, the triaxial stress state was expressed as:

$$q^2 - M^2 p'(p'_x - p') = 0 \tag{2.28}$$

where, M is the material parameter which is assumed to be a constant, q is the deviatoric stress, p' is the effective stress and p'_x is the intersection point of the MCC ellipse and the p' axis. Abeyrathne (2017) extended the proposed isotropic equation to triaxial stress states similar to the theoretical development by Sivakumar (1993).

$$q^2 - M(v_w)^2\left[p + p_t(v_w)\right](p_y - p) = 0 \text{ or } q = M(v_w)(p + p_t(v_w)) \tag{2.29}$$

where, $M(v_w)$ is the slope of the critical state line that depends on v_w, $p_t(v_w)$ is the tensile stress and p_y is the current yield stress. In summary, the derivation of the existing unsaturated triaxial theoretical equations is twofold: (a) an equation developed from saturated Mohr-

Coulomb shear failure; (b) an extension of the isotropic stress formulas similar to the critical stress state concepts for saturated soils (Schofield and Wroth, 1968). Most recent constitutive models tend to be based on the latter while former are not. Hence, in this study, the later concept of the extension of the constitutive model is followed.

2.8 Comparison of stress paths in existing frameworks

For the comparison of current models (Alonso et al., 1990; Wheeler et al., 2003; Kodikara, 2012), a combination of loading, unloading, wetting and drying stress paths was selected. Figure 2.7 interprets these stress paths according to the model proposed by Alonso et al. (1990) in the v, p, s space. A compacted sample with a certain suction value represents state *A*. During compaction, the corresponding LC curve (*GC*) for state *A* can be defined (with a nominal stress value of 10 kPa). During the wetting path *AB*, the soil experiences some elastic swelling, given by the parameter k_s. The stress paths *BC* and *CD* represent elastic reloading (provided by the parameter k) and yielding along the LC curve (provided by the parameter λ_o, compressibility at saturation) in the saturated state. The subsequent unloading results in a slight increase in specific volume and it reaches state *E*. If a drying stress path is performed on the sample at state *E*, it will follow the elastic k_s gradient and will reach state *F*. If the same sample was initially isotopically loaded (given by the parameter k) to state *G* at constant suction prior to the wetting stress path *GH*, sudden collapse behaviour is observed while yielding on the yield surface. In addition, if the reloading stops at state *I* and starts the wetting *IJK* stress path, a swelling (*IJ*, given by the parameter k_s) followed by collapse (*JK*) is observed.

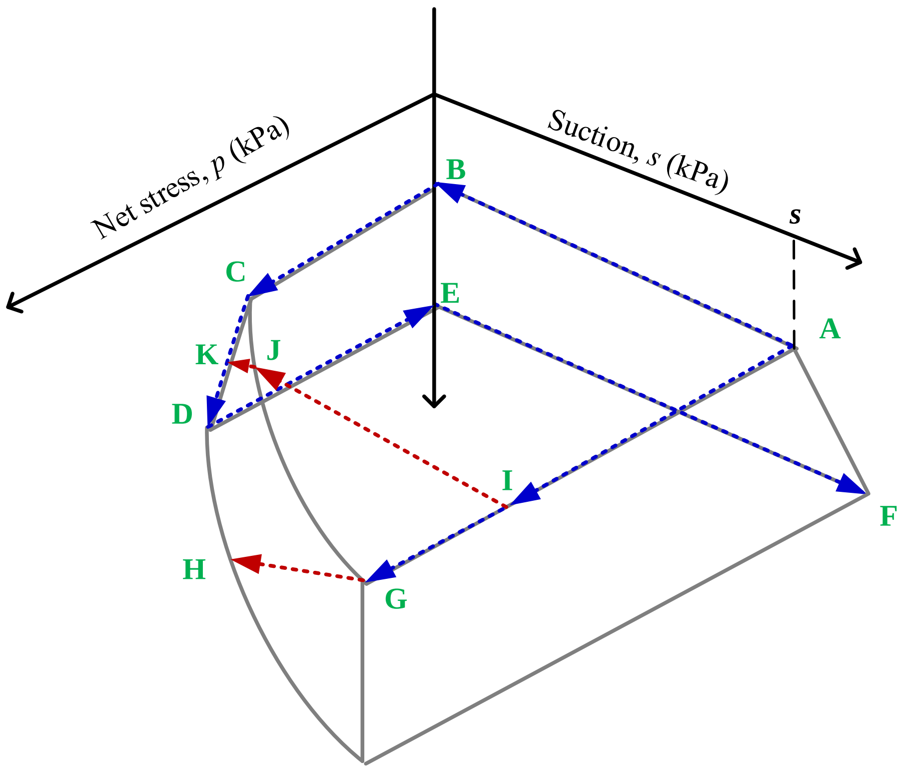

Figure 2.7: Selected stress paths in BBM model

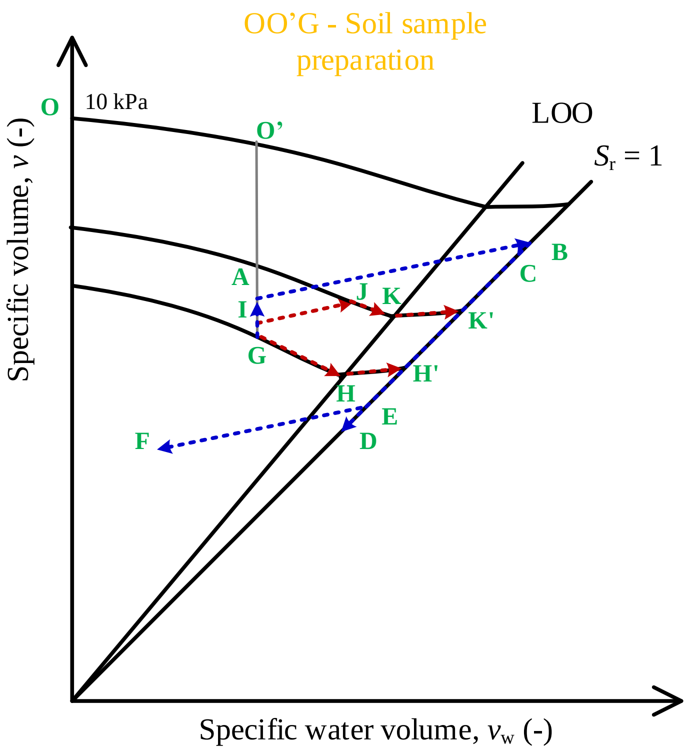

Figure 2.8: Selected stress paths in MPK framework

Figure 2.8 shows the selected stress paths according to the framework proposed by Kodikara (2012) in the v, v_{w}, p space. As stated in Section 2.6, the LWSBS is considered as the loaded compaction surface. If sample preparation starts from dry powder, the state *O* denotes the dry powder. Then, with the addition of water to the dry powder, aggregation occurs, resulting in a reduction in specific volume and reaches state *O'*. The soil is then compacted, and during compaction, the soil follows stress path *O'G* prior to reaching state *A* during unloading. During the subsequent wetting path *AB*, the soil experiences initial swelling, given by the parameter α given in Equation (2.23), known as the hydric coefficient. The stress paths *BC* and *CD* represent the elastic reloading that follows the parameter k and the yielding along the LC curve that follows the parameter λ in the saturated state. The subsequent unloading results in a slight increase in specific volume and it reaches state *E* on the NCL line ,as shown in Figure 2.8. If drying is performed on the sample at state *E*, it will follow an α gradient and will reach state *F*. If the same sample was initially isotopically loaded (given by the parameter k) to state *G* (to be on the LWSBS) at a constant water content prior to wetting path *GH*, sudden collapse behaviour is observed while yielding on the yield surface, resulting a reduction of specific volume. In addition, if the reloading stops at state *I* without reaching the LWSBS and starts wetting following the *IJK* stress path, swelling (*IJ*, given by parameter α) followed by collapse (*JK*) is observed. In addition to collapse behaviour, swelling behaviour is observed with further wetting in both stress paths (*KK'* and *HH'*). Although this phenomenon has been seen in many experiments, the BBM model cannot capture the final swelling that occurs after the collapse.

Figure 2.9 represents the selected stress paths according to the model proposed by Wheeler et al. (2003) in the s^*, p^* and S_{r}, s^* planes. Figure 2.9(a) and Figure 2.9(c) show the same s^*, p^* plane and are used to explain different stress paths. The initial compacted state A and the yield curve configurations are depicted as [1] in the s^*, p^* plane (see Figure 2.9(a)) and as [a] in the S_{r}, s^* plane (see Figure 2.9(b)). During the wetting path *AB*, soil experiences elastic swelling, until it reaches the corresponding SD curve of [1] configuration at state *B'*. During further wetting, the soil reaches state *B* and yield curve configuration [2]. The stress paths *BC* and *CD* represent the elastic reloading that follows the parameter k and the yielding along the LC curve that follows the parameter λ at the saturated state. During yielding, the configuration changes to [3]. The subsequent unloading results in a slight increase in specific volume, and it reaches state *E* on the NCL line, as shown in Figure 2.9(a). Since the states *B*, *C*, *D*, *E* are in the saturation state, $S_r = 1$ and $s^* = 0$. If a drying stress path is performed on the sample at state *E*, it will follow the scanning stress path until it intersects the SI curve (state *E'*) corresponding to [3] prior to yielding on the drying curve until the state *E''* is reached (yield curve configuration [4]). With further drying, state F is achieved ([5] in the s^*, p^* plane and [d] in the S_r, s^* plane).

As Figure 2.9(c) indicates, if the same sample was initially isotopically loaded (provided by the parameter k) to state *G* at constant suction prior to wetting stress path *GH*, sudden collapse behaviour is observed ([6] in the s^*, p^* plane and [c] in the S_r, s^* plane. In addition, if the reloading stops at state *I* and starts the wetting *IJK* stress path, swelling is observed (*IJ*, [7] in the s^*, p^* plane) followed by collapse (*JK*) (([8] in the s^*, p^* plane and [b] in the S_r, s^* plane).

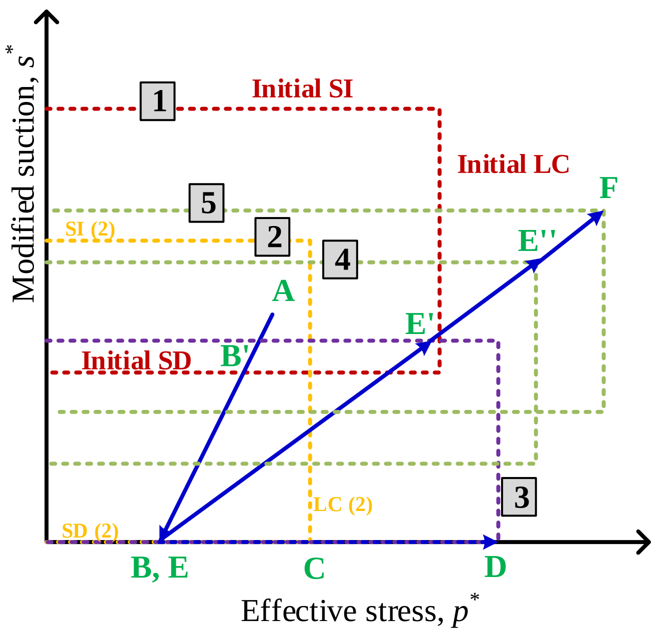

(a)

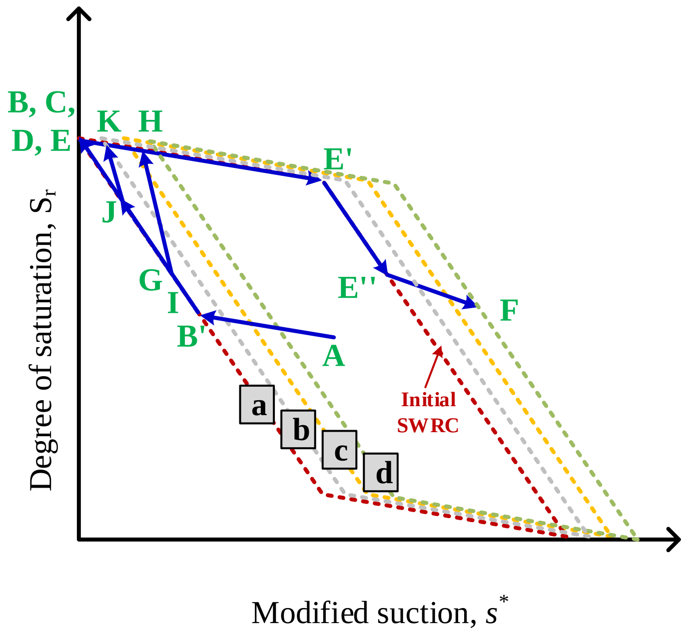

(b)

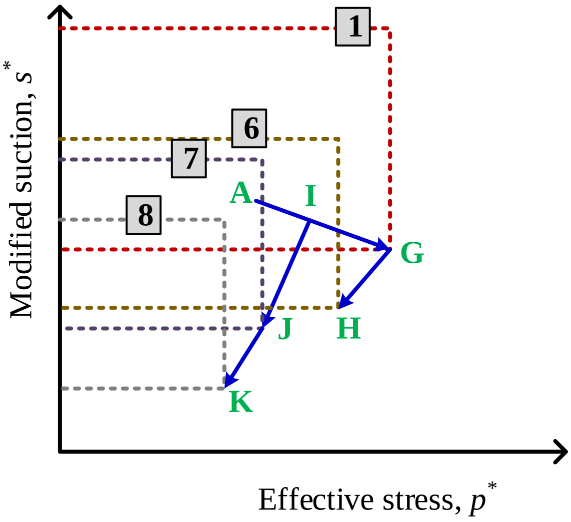

(c)

Figure 2.9: Selected stress paths in Wheeler et al.'s (2003) model

2.9 Current understanding and modelling concepts of unsaturated soils

This section summarises the phenomenological observations identified in the literature and the models which include those characteristics. Although the existing constitutive models are capable of predicting some of the phenomenological features, most of the models have not incorporated all of the following observations (these are discussed in the next Chapter 3).

a) Under isotropic loading for constant suction, the yield stress increases with increasing suction (Alonso et al., 1990; Wheeler and Sivakumar, 1995; Kodikara, 2012; Zhou, 2017).
b) The compressibility of constant suction virgin compression lines increases with increasing suction (Wheeler and Sivakumar, 1995; Kodikara, 2012; Zhou, 2017), and in some cases, the compressibility of constant suction lines decreases with increasing suction (Josa, 1988; Alonso et al., 1990).
c) Prediction of the volumetric response using constant specific water volume or constant degree of saturation hyperlines (Raveendiraraj, 2009; Islam, 2015; Abeyrathne, 2017).
d) During wetting under constant net stress, continued swelling to saturation from an unloaded position (Fleureau et al., 2002); swelling behaviour followed by collapse from an unloaded position higher than the nominal stress (Sharma, 1998; Raveendiraraj, 2009) and subsequent swelling to saturation after collapse (Sivakumar, 1993) or when the soil is on the yield surface, immediate collapse upon wetting (Matyas and Radhakrishna, 1968) and subsequent swelling behaviour to full saturation.
e) The collapse behaviour shows that the collapse potential (at constant net stress wetting) increases with net stress and then decreases. It appears that the peak collapse occurs at pre-consolidation stress and depends on initial microstructure and void ratio (Kato and Kawai, 2000; Sun et al., 2004; Sun et al., 2007; Delage et al., 2015; Das and Thyagaraj, 2018).
f) Constant volume testing for the wet side shows a 1:1 negative gradient line in the s, p plane and a straight line in the effective stress space. However, this gradient may be less than 1 given by $\frac{\mathrm{d}p}{\mathrm{d}s} = -S_\mathrm{r} - s\frac{\mathrm{d}S_\mathrm{r}}{\mathrm{d}s}$ (Sivakumar, 1993; Monroy, 2006).
g) In constrained volume wetting paths, net stress increases before leading to a decrease in net stress. With further wetting, the net stress increases again before achieving the saturation (Romero Morales, 1999; Lloret Morancho et al., 2003; Imbert and Villar, 2006; Raveendiraraj, 2009; Wang and Wei, 2014; Kaufhold et al., 2015; Navarro et al., 2017).

h) The transition from saturated to unsaturated state is demarcated by the air transition line (ATL) (Dexter, 2004a, b; Dexter, 2004c; Li et al., 2017; Azoor et al., 2019).
i) The variation of the degree of saturation between air entry value and saturation in the SWRC (Cunningham et al., 2003; Fredlund et al., 2013).
j) The effect of structural stabilisation on wet/dry cycles and the accumulation of plastic strains during wet/dry cycles (Alonso et al., 1999; Tripathy et al., 2002; Airò Farulla et al., 2010; Nowamooz and Masrouri, 2010; Gould et al., 2011)
k) Initial inelastic swelling experienced by most compacted soils (Gallipoli et al., 2003a; Raveendiraraj, 2009; Airò Farulla et al., 2010)
l) Drying from the saturated state can lead to initial yielding and then elastic drying (Fleureau et al., 2002; Khalili et al., 2004; Gao et al., 2015; Li et al., 2017).
m) Hysteretic behaviour, specific water volume and specific volume with suction for wetting and drying separately (Sharma, 1998; Raveendiraraj, 2009).
n) Distinct behaviour of suction contours in the yield surface and nominal stress plane (Tarantino and De Col, 2008).
o) Wetting/drying and loading/unloading away from the loading yield surface display path-dependency, predominantly due to initial inelastic swelling or drying (Karube, 1988).

2.10 Summary

Many geotechnical structures, such as foundations, pavements, highways and dams, are built with the use of compacted unsaturated soils with 75% to 90% saturation and during operation, the degree of saturation varies as soil moisture equilibrates subject to the influence of climate. Therefore, the performance and safety of structures cannot be predicted without the use of principles of unsaturated soil mechanics. However, unsaturated soil mechanics is still not commonly used similar to saturated soil mechanics. For instance, many design problems and analyses of geotechnical structures are still based on the fully saturated state, which leads to over-design for most cases, since suction in the unsaturated state provides additional strength. However, under-design may occur in some cases, such as when collapse settlements take place during major wetting events and under complex loading conditions. Unsaturated soil mechanics mainly developed considering saturated soil conditions starting from the 1950s due to complexities arising mainly due to the compressibility of air. Hence, little attention was given to unsaturated soil mechanics over subsequent years. Consequently, there was little necessity for knowledge of unsaturated soil behaviour. However, numerous geotechnical problems are associated with unsaturated soil behaviour and little consideration is not sufficient.

Due to the importance of unsaturated soil behaviour, as discussed in the literature review, researchers have focused on unsaturated soil mechanics during the last four decades. The existing elastoplastic constitutive models are summarised in Figure 2.10 where the elastoplastic unsaturated models are divided into three major divisions based on the selection of constitutive variables: the effective stress approach, the independent stress state approach and the Monash-Peradeniya-Kodikara (MPK) framework. A detailed description of these models is given in the above sections. However, the constitutive modelling of unsaturated soils is far from entirely satisfactory.

On the basis of the review of the literature, the following research gaps were identified as requiring further research. The volumetric and triaxial responses of unsaturated soils are complex and require special efforts to capture phenomenological observations. In fact, many other phenomenological features have been observed in various experiments undertaken to date, although recent constitutive models have not paid attention to these features. In addition, a constitutive model suitable for use in routine engineering practice should be able to be coupled with practical approaches such as traditional compaction curve. The MPK framework utilises specific moisture ratio instead of suction. However, incorporation of the soil water retention behaviour in a mechanical model is essential if it is to be considered a complete theoretical constitutive model. Most recent constitutive models are based on sophisticated suction-controlled tests which take months to obtain the required material parameters. Hence, material parameters should be linked to relatively simple tests such as constant water content tests instead of more complex controlled suction tests. This will also allow unsaturated soil models to be amenable to linking with data-driven models, since the moisture content is more easily measured in the field than measuring the suction.

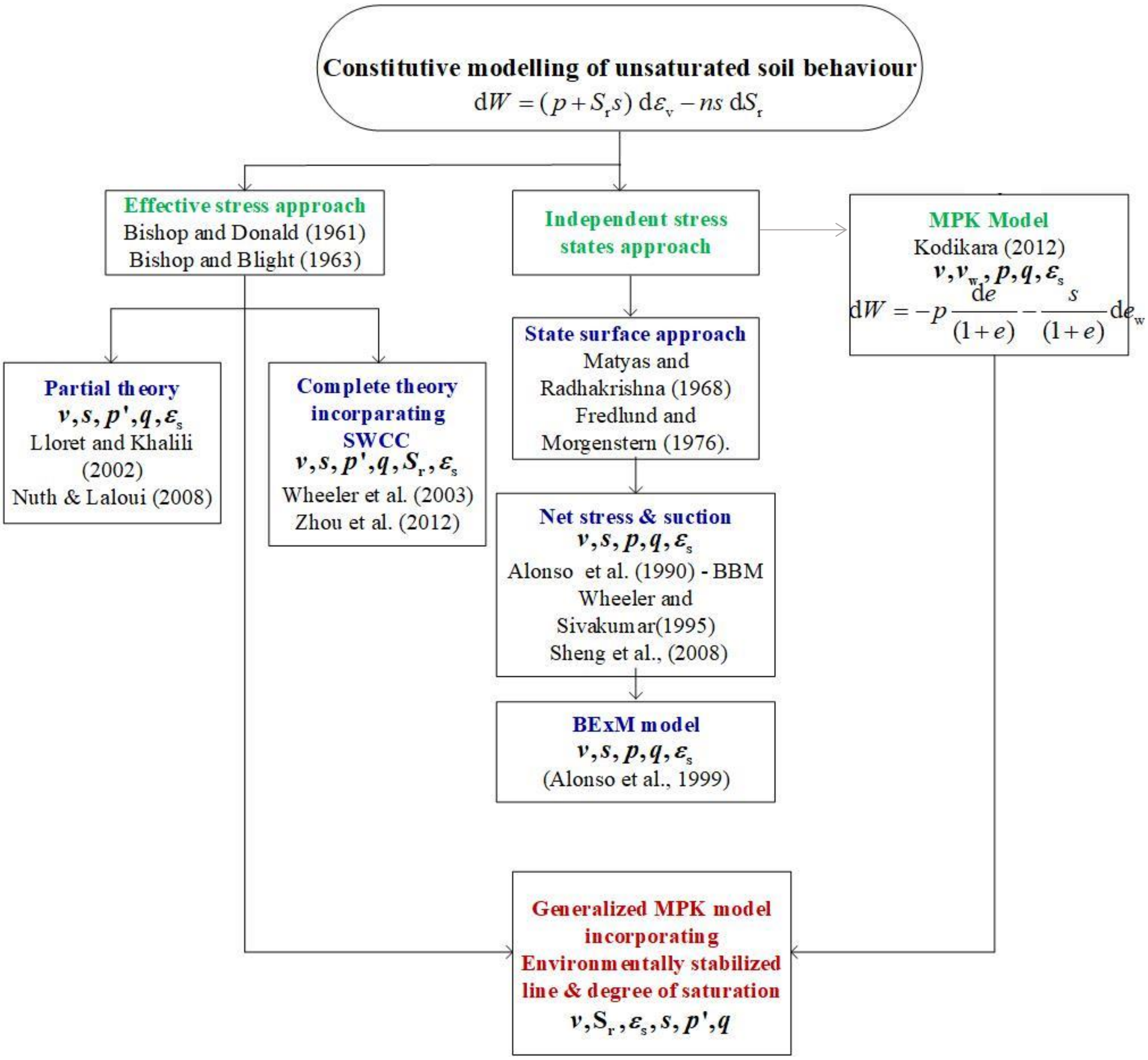

Figure 2.10: Summary of constitutive modelling

Considering the simplicity and practical application of the MPK framework, it is recommended that a generalised constitutive model incorporating hydro coupling with plasticity-based SWRC be derived satisfying phenomenological observations following the steps in Figure 2.11. Based on the environmentally stabilised concept (which is discussed in the next Chapter 3) and the accumulation of plastic strains on wet-dry cycles, a generalised MPK model is proposed in this thesis.

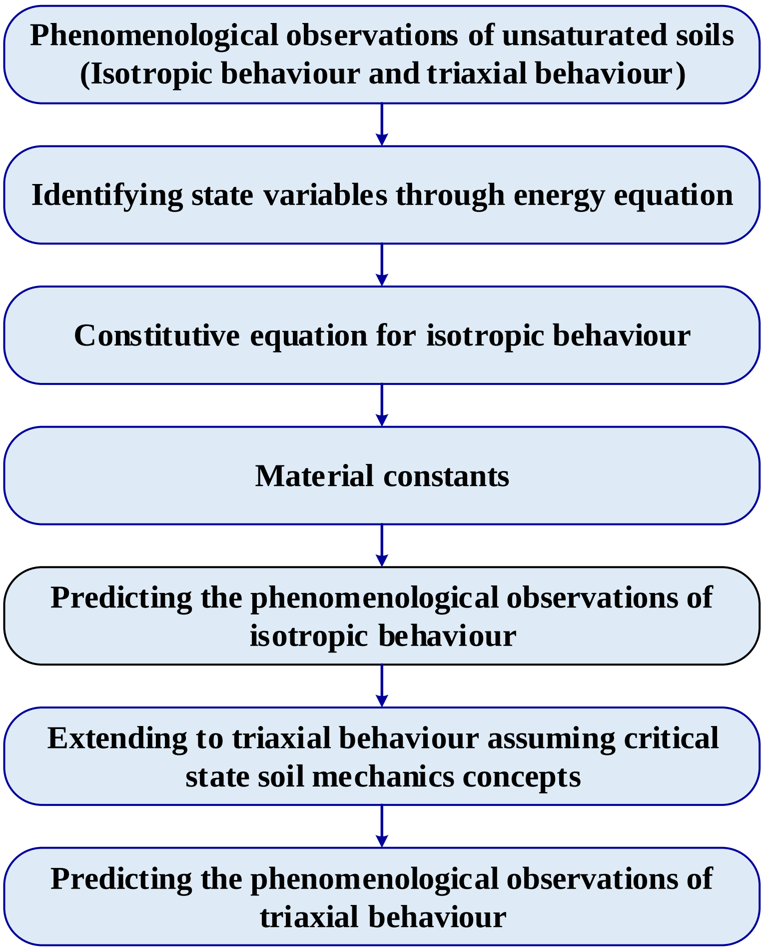

Figure 2.11: Flow chart of constitutive modelling at element level

2.11 Reference

Abeyrathne, A., Sivakumar, V. & Kodikara, J. 2019. Isotropic Volumetric Behaviour of Compacted Unsaturated Soils within (v, v w, p) Space. *Canadian Geotechnical Journal*, 56(12)**,** pp.1756-1778.

Abeyrathne, W. K. a. P. 2017. *A new modelling approach for compacted clayey soils using specific water volume as a state variable.* Ph.D. thesis, Monash University, Melbourne, Australia.

Airò Farulla, C., Ferrari, A. & Romero, E. 2010. Volume change behaviour of a compacted scaly clay during cyclic suction changes. *Canadian Geotechnical Journal*, 47**,** 688-703.

Aitchison, G. 1961. Relationships of moisture stress and effective stress functions in unsaturated soils. *Pore pressure and suction in soils: conference organised by the British National Society of the International Society of Soil Mechanics and Foundation Engineering.* London: Butterworths, procite:ac76b4f1-a1ca-4273-a44b-aa2d64205cf7.

Alonso, E., Lloret, A., Gens, A. & Yang, D. Experimental behaviour of highly expansive double-structure clay. Proceedings of the first international conference on unsaturated soils, 1995 Paris,France.

Alonso, E., Pinyol, N. & Gens, A. 2013. Compacted soil behaviour: initial state, structure and constitutive modelling. *Géotechnique,* 63**,** 463-478.

Alonso, E., Vaunat, J. & Gens, A. 1999. Modelling the mechanical behaviour of expansive clays. *Engineering geology,* 54**,** 173-183.

Alonso , E. E., Gens , A. & Josa, A. 1990. A constitutive model for partially saturated soils. *Géotechnique,* 40(3)**,** pp.405-430.

Andriantrehina, S. R., Mahmutovic, D., Taibi, S., Boutonnier, L. & Fleureau, J.-M. Hydromechanical behavior of a quasi-saturated compacted soils on drying-wetting paths-experimental and numerical approaches. E3S Web of Conferences, 2016. EDP Sciences, 14013.

Azoor, R. M., Deo, R. N., Shannon, B. M. & Kodikara, J. K. 2019. Using soil moisture retention curves and corrosimetry to characterise the role of soil moisture in underground corrosion. Perth.

Bishop, A. & Donald, I. The experimental study of partly saturated soil in the triaxial apparatus. Proceedings of the 5th international conference on soil mechanics and foundation engineering, Paris, 1961. 13-21.

Bishop, A. W. 1959. The principle of effective stress. *Teknisk ukeblad,* 39**,** 859-863.

Bishop, A. W. & Blight, G. 1963. Some aspects of effective stress in saturated and partly saturated soils. *Geotechnique,* 13**,** 177-197.

Blatz, J. A., Cui, Y.-J. & Oldecop, L. 2008. Vapour equilibrium and osmotic technique for suction control. *Geotechnical and Geological Engineering,* 26**,** 661.

Burland, J. 1965. Some aspects of the mechanical behaviour of partly saturated soils. *Moisture equilibria and moisture changes in soil beneath covered areas. Butterworths, Sydney***,** 270-278.

Buscarnera, G. & Di Prisco, C. 2012. Discussing the definition of the second‐order work for unsaturated soils. *International journal for numerical and analytical methods in geomechanics,* 36**,** 36-49.

Casini, F. 2012. Deformation induced by wetting: a simple model. *Canadian Geotechnical Journal,* 49**,** 954-960.

Casini, F., Serri, V. & Springman, S. M. 2013. Hydromechanical behaviour of a silty sand from a steep slope triggered by artificial rainfall: from unsaturated to saturated conditions. *Canadian Geotechnical Journal,* 50**,** 28-40.

Cunningham, M., Ridley, A., Dineen, K. & Burland, J. 2003. The mechanical behaviour of a reconstituted unsaturated silty clay. *Géotechnique,* 53**,** 183-194.

Das, A. P. & Thyagaraj, T. 2018. Collapse behaviour of compacted red soil. *International Journal of Geotechnical Engineering,* 12**,** 20-27.

Delage, P., Pereira, J. & Cui, Y. 2015. Collapse behaviour of a natural loess from Northern France. *Bioinspired Photonics: Optical Structures and Systems Inspired by Nature***,** 315.

Delage, P., Romero, E. & Tarantino, A. Recent developments in the techniques of controlling and measuring suction in unsaturated soils. Keynote Lecture, Proc. 1st Eur. Conf. on Unsaturated Soils, 2008. 33-52.

Dexter, A. 2004a. Soil physical quality: Part II. Friability, tillage, tilth and hard-setting. *Geoderma,* 120**,** 215-225.

Dexter, A. 2004b. Soil physical quality: Part III: Unsaturated hydraulic conductivity and general conclusions about S-theory. *Geoderma,* 120**,** 227-239.

Dexter, A. R. 2004c. Soil physical quality: Part I. Theory, effects of soil texture, density, and organic matter, and effects on root growth. *Geoderma,* 120**,** 201-214.

Fleureau, J.-M., Verbrugge, J.-C., Huergo, P. J., Correia, A. G. & Kheirbek-Saoud, S. 2002. Aspects of the behaviour of compacted clayey soils on drying and wetting paths. *Canadian geotechnical journal,* 39**,** 1341-1357.

Fredlund, D. 1979. Second Canadian Geotechnical Colloquium: Appropriate concepts and technology for unsaturated soils. *Canadian Geotechnical Journal,* 16**,** 121-139.

Fredlund, D., Houston, S. & Caicedo, B. 2013. Interpretation of soil-water characteristic curves when volume change occurs as soil suction is changed. *Advances in unsaturated soils,* 1**,** 15.

Fredlund, D. & Morgenstern, N. 1976. Constitutive relations for volume change in unsaturated soils. *Canadian Geotechnical Journal,* 13**,** 261-276.

Fredlund, D., Morgenstern, N. R. & Widger, R. 1978. The shear strength of unsaturated soils. *Canadian geotechnical journal,* 15**,** 313-321.

Fredlund, D. & Rahardjo, H. 1988. State of development in the measurement of soil suction. *The Emergence of Unsaturated Soil Mechanics***,** 47.

Fredlund, D. G. & Morgenstern, N. R. 1977. Stress state variables for unsaturated soils. *Journal of Geotechnical and Geoenvironmental Engineering,* 103.

Fredlund, D. G. & Rahardjo, H. 1993. *Soil mechanics for unsaturated soils*, John Wiley & Sons.

Fredlund, D. G. & Xing, A. 1994. Equations for the soil-water characteristic curve. *Canadian geotechnical journal,* 31**,** 521-532.

Gallipoli, D., Gens, A., Sharma, R. & Vaunat, J. 2003a. An elasto-plastic model for unsaturated soil incorporating the effects of suction and degree of saturation on mechanical behaviour. *Géotechnique.,* 53**,** 123-136.

Gallipoli, D., Wheeler, S. & Karstunen, M. 2003b. Modelling the variation of degree of saturation in a deformable unsaturated soil. *Géotechnique.,* 53**,** 105-112.

Gao, Y., Sun, D. A. & Zhou, A. 2015. Hydromechanical behaviour of unsaturated soil with different specimen preparations. *Canadian Geotechnical Journal,* 53**,** 909-917.

Gens, A. 2010. Soil–environment interactions in geotechnical engineering. *Géotechnique,* 60**,** 3-74.

Gens, A. & Alonso, E. 1992. A framework for the behaviour of unsaturated expansive clays. *Canadian Geotechnical Journal,* 29**,** 1013-1032.

Gould, S. J., Kodikara, J., Rajeev, P., Zhao, X.-L. & Burn, S. 2011. A void ratio–water content–net stress model for environmentally stabilized expansive soils. *Canadian Geotechnical Journal,* 48**,** 867-877.

Hilf, J. W. 1956. An investigation of pore water pressure in compacted cohesive soils.

Houlsby, G. 1997. The work input to an unsaturated granular material. *Géotechnique,* 47**,** 193-196.

Imbert, C. & Villar, M. V. 2006. Hydro-mechanical response of a bentonite pellets/powder mixture upon infiltration. *Applied Clay Science,* 32**,** 197-209.

Islam, M. 2015. *A study of volumetric behaviour of compacted clayey soils in the void ratio, moisture ratio and net stress space.* Monash University. Faculty of Engineering. Department of Civil Engineering.

Islam, T. & Kodikara, J. 2015. Interpretation of the loading–wetting behaviour of compacted soils within the "MPK" framework. Part I: Static compaction 1. *Canadian Geotechnical Journal,* 53**,** 783-805.

Jennings, J. & Burland, J. 1962. Limitations to the Use of Effective Stresses.

Josa, A. 1988. *Un modelo eslastoplirstico para suelos no saturados.* Tesis Doctoral. Universitat PoWcnica de Catalunya, Barcelona.

Karube, D. 1988. New concept of effective stress in unsaturated soil and its proving test. *In:* DONAGHE, R., CHANEY, R., AND SILVER, M. (ed.) *Advanced triaxial testing of soil and rock.* West Conshohocken, PA: ASTM International, 539-552.

Kato, S. & Kawai, K. 2000. Deformation characteristics of a compacted clay in collapse under isotropic and triaxial stress state. *Soils and Foundations,* 40**,** 75-90.

Kaufhold, S., Baille, W., Schanz, T. & Dohrmann, R. 2015. About differences of swelling pressure—dry density relations of compacted bentonites. *Applied Clay Science,* 107**,** 52-61.

Khalili, N., Geiser, F. & Blight, G. 2004. Effective stress in unsaturated soils: review with new evidence. *International Journal of Geomechanics,* 4**,** 115-126.

Khalili, N., Habte, M. & Zargarbashi, S. 2008. A fully coupled flow deformation model for cyclic analysis of unsaturated soils including hydraulic and mechanical hystereses. *Computers and Geotechnics,* 35**,** 872-889.

Khalili, N. & Khabbaz, M. 1998. A unique relationship of chi for the determination of the shear strength of unsaturated soils. *Geotechnique,* 48**,** 681-687.

Kodikara, J. 2012. New framework for volumetric constitutive behaviour of compacted unsaturated soils. *Canadian Geotechnical Journal,* 49**,** 1227-1243.

Kodikara, J., Islam, T. & Rajeev, P. 2015. Interpretation of the loading–wetting behaviour of compacted soils within the "MPK" framework. Part II: Dynamic compaction 1. *Canadian Geotechnical Journal,* 53**,** 806-827.

Kodikara, J., Islam, T. & Shounthrarajah, A. 2018. Review of Soil Compaction: History and Recent Developments. *Transportation Geotechnics,* 17**,** 24-34.

Li, Z.-S., Fleureau, J.-M. & Tang, L.-S. 2017. Aspects of compaction and drying–wetting curves of a subgrade clayey soil. *Géotechnique***,** 1-7.

Liu, C. & Muraleetharan, K. K. 2011. Coupled hydro-mechanical elastoplastic constitutive model for unsaturated sands and silts. I: Formulation. *International Journal of Geomechanics,* 12**,** 239-247.

Lloret-Cabot, M. & Wheeler, S. J. 2018. The Mechanical Yield Stress in Unsaturated and Saturated Soils. *The 7th International Conference on Unsaturated Soils (UNSAT2018).* Hong Kong, China.

Lloret-Cabot, M., Wheeler, S. J., Pineda, J. A., Romero, E. & Sheng, D. 2017. From saturated to unsaturated conditions and vice versa. *Acta Geotechnica***,** 1-23.

Lloret Morancho, A., Villar, M. V., Sanchez, M., Gens Solé, A., Pintado Llurba, X. & Alonso Pérez De Agreda, E. 2003. Mechanical behaviour of heavily compacted bentonite under high suction changes.

Loret, B. & Khalili, N. 2002. An effective stress elastic–plastic model for unsaturated porous media. *Mechanics of Materials,* 34**,** 97-116.

Matyas, E. L. & Radhakrishna, H. 1968. Volume change characteristics of partially saturated soils. *Géotechnique,* 18**,** 432-448.

Miller, G. A., Khoury, C. N., Muraleetharan, K. K., Liu, C. & Kibbey, T. C. 2008. Effects of soil skeleton deformations on hysteretic soil water characteristic curves: Experiments and simulations. *Water Resources Research,* 44.

Monroy, R. 2006. *The influence of load and suction changes on the volumetric behaviour of compacted London Clay*. Ph.D. thesis, Imperial College London (University of London).

Navarro, V., De La Morena, G., Yustres, Á., González-Arteaga, J. & Asensio, L. 2017. Predicting the swelling pressure of MX-80 bentonite. *Applied Clay Science,* 149**,** 51-58.

Nowamooz, H. & Masrouri, F. 2010. Influence of suction cycles on the soil fabric of compacted swelling soil. *Comptes Rendus Geoscience,* 342**,** 901-910.

Nuth, M. & Laloui, L. Advanced hydro-mechanical coupling for unified constitutive modelling of unsaturated soils. Unsaturated Soils: Advances In Geo-Engineering, 2008a. Crc Press-Taylor & Francis Group, 6000 Broken Sound Parkway Nw, Ste 300, Boca Raton, Fl 33487-2742 Usa, 559-565.

Nuth, M. & Laloui, L. 2008b. Effective stress concept in unsaturated soils: clarification and validation of a unified framework. *International journal for numerical and analytical methods in Geomechanics,* 32**,** 771-801.

Pasha, A. Y., Khoshghalb, A. & Khalili, N. 2019. Can degree of saturation decrease during constant suction compression of an unsaturated soil? *Computers and Geotechnics,* 106**,** 199-204.

Pedrotti, M. & Tarantino, A. 2018. A conceptual constitutive model unifying slurried (saturated), compacted (unsaturated) and dry states. *Géotechnique***,** 1-17.

Proctor, R. 1933. Fundamental principles of soil compaction. *Engineering news-record,* 111**,** 245-248.

Raveendiraraj, A. 2009. *Coupling of mechanical behaviour and water retention behaviour in unsaturated soils.* Ph.D. thesis, University of Glasgow.

Romero Morales, E. E. 1999. *Characterisation and thermo-hydro-mechanical behaviour of unsaturated Boom clay: an experimental study*, Universitat Politècnica de Catalunya.

Sanchez, M., Lloret, M., Wheeler, S. & Karstunen, M. Generalised Elasto-Plastic Stress-Strain Relations of a Fully Coupled Hydro-Mechanical Model. 1st European Conference on Unsaturated Soils, 2008. Taylor and Francis, 567-573.

Schofield, A. & Wroth, P. 1968. *Critical state soil mechanics*, McGraw-Hill London.

Schofield, R. The pF of water in soil. Trans. of the Third International Congress on Soil Science, 2, Plenary Session Papers, 30 July-7 August, 1935 Oxford, UK, 1935. 37-48.

Sharma, R. S. 1998. *Mechanical behaviour of unsaturated highly expansive clays.* Ph.D. thesis, University of Oxford.

Sheng, D., Fredlund, D. G. & Gens, A. 2008. A new modelling approach for unsaturated soils using independent stress variables. *Canadian Geotechnical Journal*, 45**,** 511-534.

Sheng, D. & Zhou, A.-N. 2011. Coupling hydraulic with mechanical models for unsaturated soils. *Canadian Geotechnical Journal,* 48**,** 826-840.

Sivakumar, V. 1993. *A critical state framework for unsaturated soil.* Ph.D. thesis, University of Sheffield.

Sivakumar, V., Sivakumar, R., Murray, E., Mackinnon, P. & Boyd, J. 2010. Mechanical behaviour of unsaturated kaolin (with isotropic and anisotropic stress history). Part 1: wetting and compression behaviour. *Géotechnique,* 60**,** 581-594.

Sun, D., Matsuoka, H. & Xu, Y. 2004. Collapse behavior of compacted clays in suction-controlled triaxial tests.

Sun, D. A., Sheng, D. & Xu, Y. 2007. Collapse behaviour of unsaturated compacted soil with different initial densities. *Canadian Geotechnical Journal,* 44**,** 673-686.

Tarantino, A. Unsaturated soils: compacted versus reconstituted states. 5th International Conference on Unsaturated Soil, 2010. 113-136.

Tarantino, A. & De Col, E. 2008. Compaction behaviour of clay. *Géotechnique,* 58**,** 199-213.

Tatsuoka, F. & Correia, A. G. 2018. Importance of Controlling the Degree of Saturation in Soil Compaction linked to Soil Structure Design. *Transportation Geotechnics,* 143**,** 556-565.

Tripathy, S., Rao, K. S. & Fredlund, D. 2002. Water content-void ratio swell-shrink paths of compacted expansive soils. *Canadian geotechnical journal,* 39**,** 938-959.

Vanapalli, S. K., Fredlund, D. G. & Pufahl, D. E. 1996. The relationship between the soil-water characteristic curve and the unsaturated shear strength of a compacted glacial till. *Geotechnical Testing Journal,* 19**,** 259-268.

Vaunat, J. & Casini, F. 2017. A procedure for the direct determination of Bishop's χ parameter from changes in pore size distribution. *Géotechnique,* 67**,** 631-636.

Wang, G. & Wei, X. 2014. Modeling swelling–shrinkage behavior of compacted expansive soils during wetting–drying cycles. *Canadian Geotechnical Journal,* 52**,** 783-794.

Wei, C. & Muraleetharan, K. K. 2002a. A continuum theory of porous media saturated by multiple immiscible fluids: I. Linear poroelasticity. *International Journal of Engineering Science,* 40**,** 1807-1833.

Wei, C. & Muraleetharan, K. K. 2002b. A continuum theory of porous media saturated by multiple immiscible fluids: II. Lagrangian description and variational structure. *International Journal of Engineering Science,* 40**,** 1835-1854.

Wheeler, S., Sharma, R. & Buisson, M. 2003. Coupling of hydraulic hysteresis and stress–strain behaviour in unsaturated soils. *Géotechnique,* 53**,** 41-54.

Wheeler, S. & Sivakumar, V. 1995. An elasto-plastic critical state framework for unsaturated soil. *Géotechnique,* 45**,** 35-53.

Zhou, A.-N., Sheng, D., Sloan, S. W. & Gens, A. 2012a. Interpretation of unsaturated soil behaviour in the stress–Saturation space, I: Volume change and water retention behaviour. *Computers and Geotechnics,* 43**,** 178-187.

Zhou, A.-N., Sheng, D., Sloan, S. W. & Gens, A. 2012b. Interpretation of unsaturated soil behaviour in the stress–saturation space: II: constitutive relationships and validations. *Computers and Geotechnics,* 43**,** 111-123.

Zhou, A. 2011. Constitutive modelling of hydromechanical behaviour of unsaturated soils| NOVA. The University of Newcastle's Digital Repository.

Zhou, A. 2017. Modelling hydro-mechanical behavior for unsaturated soils. *Japanese Geotechnical Society Special Publication*, 5**,** 79-94.

CHAPTER 3

Review of MPK framework and related phenomenological observations

3 Introduction

Since the pioneering work at Imperial College led by Professor Bishop in the early 1960s, the modelling of unsaturated soils has been a major research focus of the global geotechnical research community (Bishop, 1959; Bishop et al., 1960; Bishop and Donald, 1961; Bishop and Blight, 1963). Significant advances to date have been primarily based on phenomenological observations sourced from a large number of experiments conducted on various soils. Some significant phenomenological observations inherent to unsaturated soils include the dependency of soil compressibility with respect to suction or moisture content (e.g.,: Alonso et al., 1990; Sivakumar, 1993; Sharma, 1998), the possibility of expansion (e.g.,: Sharma, 1998; Raveendiraraj, 2009), or collapse (Jennings and Burland, 1962; Maswoswe, 1985; Delage et al., 2015), or collapse followed by expansion (e.g.,: Raveendiraraj, 2009) upon wetting or swelling pressure development during constrained wetting (e.g.,: Lloret Morancho et al., 2003; Imbert and Villar, 2006), increase of tensile strength with unconstrained drying or cracking with constrained drying and apparent stabilisation of soil structure during wet/dry cycles (e.g.,: Tripathy et al., 2002; Gould et al., 2011). However, not all these phenomenological features are manifest for every unsaturated soil, since these manifestations depend on the soil type and the initial state from which the tests have been undertaken, and the stress paths followed. In general, soil can be categorised as fine-grained (e.g., silts and clays) and coarse-grained (e.g., sands, gravels) and their mixtures. When an unsaturated soil test is performed, the soil specimen is brought to an initial state based on which the test results are explained. Typical initial states used in testing include: (a) soils compacted either statically or dynamically at a particular moisture content and then wetted and/or dried to a certain suction (e.g.,: Josa, 1988; Sivakumar, 1993) (b) compacted soils with particular moisture contents (e.g.,: Islam, 2015; Abeyrathne, 2017) (c) soils made to slurries or high water content remoulded soils, and then consolidated and subsequently dried to a particular suction (e.g.,: Fleureau et al., 2002) and (d) soils obtained from ground in the natural state (e.g.,: Delage et al., 2015). Because of the different behaviours observed due to varying initial states, it is very important to consider this factor in assessing phenomenological features for the constitutive modelling of unsaturated soils. Nonetheless, they are features of overall unsaturated soil behaviour.

As in classical mechanics, the constitutive behaviour of unsaturated soil modelling has been considered in describing volumetric behaviour and then extending it to incorporate deviatoric loading. However, for unsaturated soils, the volumetric response is more complex and requires special effort in capturing phenomenological observations. In fact, many other phenomenological features have been observed in various tests undertaken to date under both oedometric (e.g.,: Islam and Kodikara, 2015; Das and Thyagaraj, 2018) and isotropic/triaxial conditions (e.g.,: Kato and Kawai, 2000; Sivakumar et al., 2010b).

However, the reporting of these features is scattered and sometimes not highlighted in various publications, and this is not favourable for the advancement of unsaturated soil modelling. In the past, there has not been a concerted effort to compile relevant phenomenological features highlighting their relative importance while paying due attention to soil type and the initial state used in the tests. As tests take an exceedingly long time for unsaturated soil (especially under suction control), it is important that we fully utilise the value of the tests undertaken in the past. Therefore, the intention of this chapter is to fill this gap by presenting the observed phenomenological features of the volumetric behaviour and triaxial behaviour of unsaturated soils consistently and providing some theoretical interpretations concerning current constitutive models and the MPK framework.

3.1 Initial states

The four initial states: (a), (b), (c), and (d) defined in the Introduction can be elucidated using the four state variables (void ratio (e), net stress (p), suction (s), and moisture ratio (e_{w})), and may be illustrated using the v, v_{w} plane or e, e_{w} plane with the applied p shown as contours (Kodikara, 2012) in Figure 3.1(a). Here, the specific volume ($v = 1 + e$) and specific water volume ($v_{\mathrm{w}} = 1 + e_{\mathrm{w}}$) are utilised instead of the typical shrinkage curve on the e, e_{w} plane, as the general behaviour of unsaturated soils can well be interpreted in the v, v_{w} plane. The description of these stress states is presented with respect to three yield contours, namely nominal stress (the lowest stress to which the soil is subjected to achieve consistent results), compaction stress (the stress to which the soil has been compacted) and the operational stress (the stress to which the soil is loaded in operation after unloading from compaction and subsequent wetting and drying take place).

The initial state of the dry powder form of soil at the nominal stress can be depicted by State 1, where the designation of suction is debatable. For example, suction is zero (soil particles are discrete) or may be a high value like 10^6 kPa (soil potential corresponding to approximately 0% relative humidity), if individual particle adsorption potential is considered. Following the addition of water and mixing at the nominal stress, the particles aggregate with the build-up of overall soil structure, resulting in an increase of the specific volume (State 2) (Alonso et al., 2013). With the further addition of water, the soil starts to develop softer aggregates at State 3 and undergoes progressive slippage and compaction of the aggregated particles, reaching a minimum void ratio in State 4 (see the particle pictures in Figure 3.1 (a)). This phenomenon is considered to occur predominantly due to a decrease in effective stress between the soil aggregates with the reduction of suction and the induction of slippage during the mixing process under nominal stress. After soil reaches the air transition line (ATL), where air can be trapped against movement (or becomes occluded), swelling is observed until full saturation (State 5) due to a further reduction in effective stress but without any slippage.

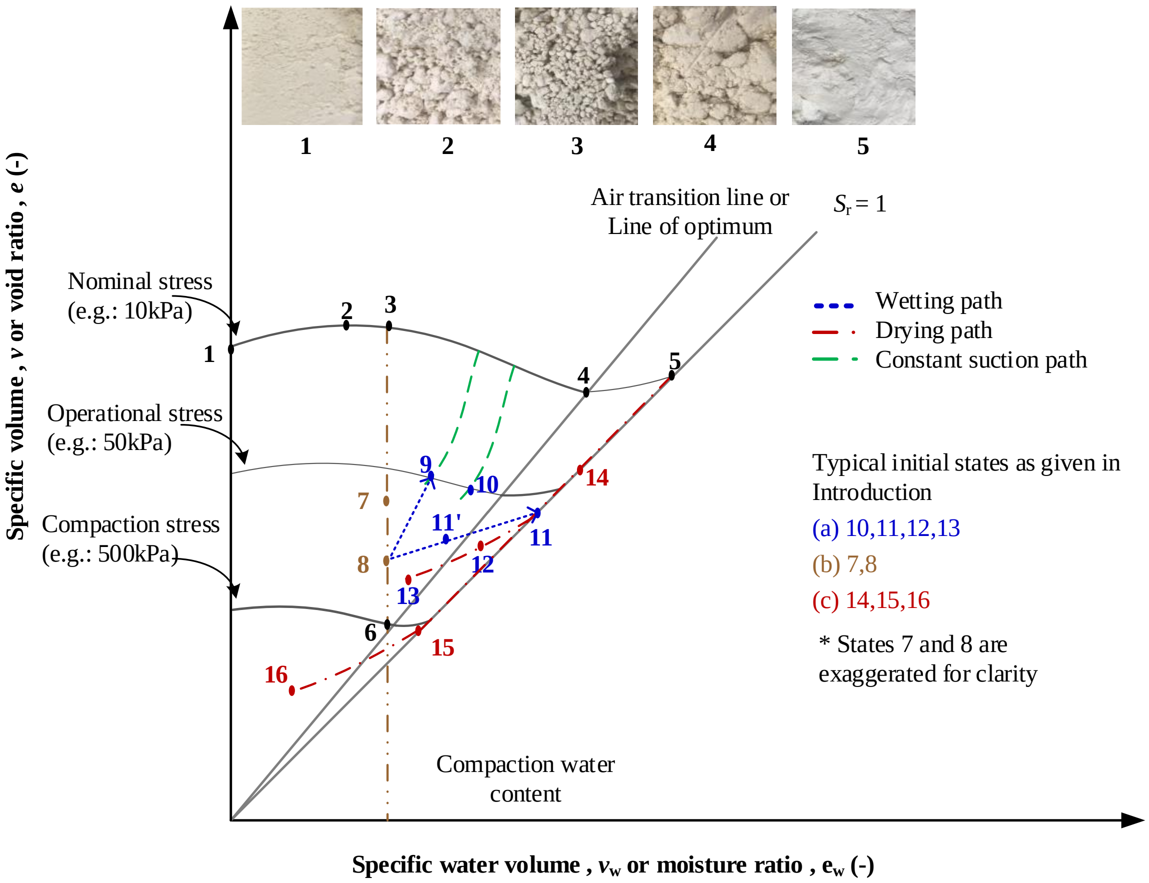

(a)

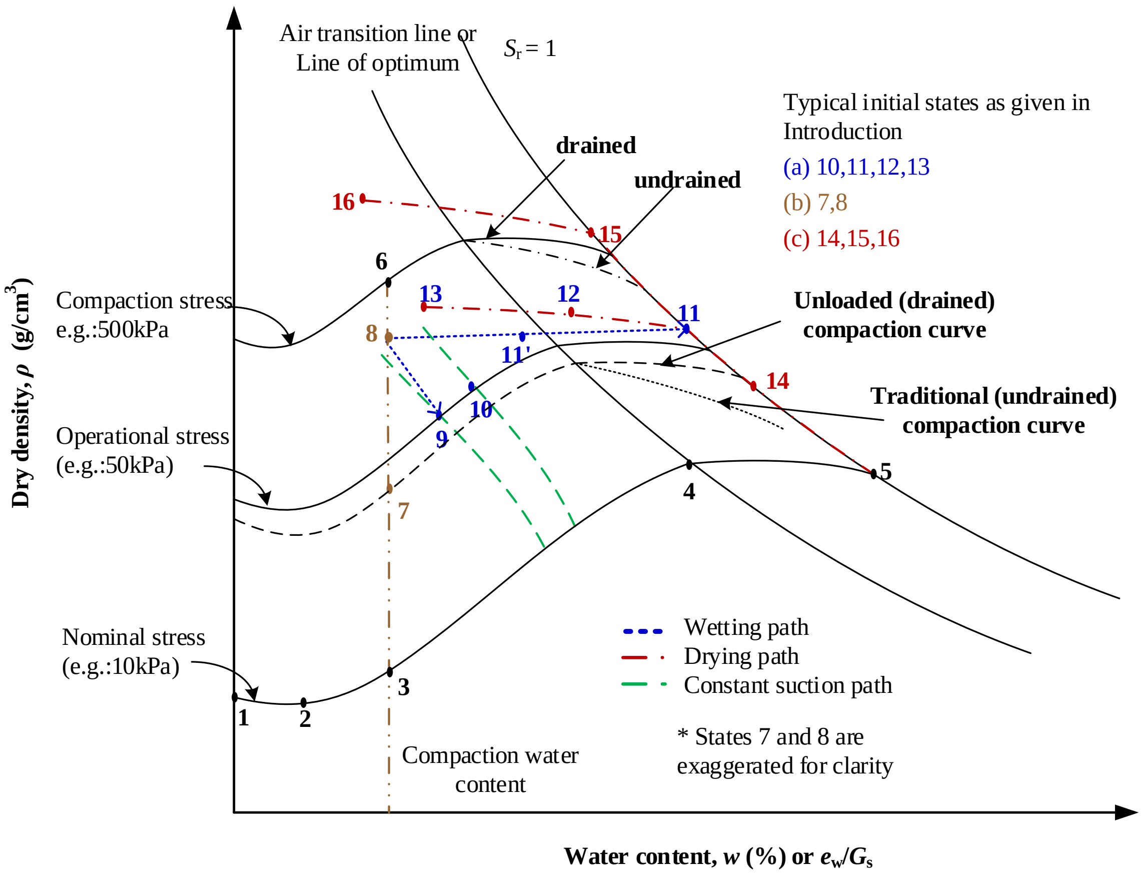

(b)

Figure 3.1: Initial states of soil (The photographs were captured by compacting Speswhite kaolin samples to 10kPa nominal stress for different moisture contents - 4cm x 4cm area) (The compaction lines and unloading have been exaggerated for clarity)

During the compaction process, a soil prepared to a certain moisture content (State 3), with the increase of static or dynamic loading (usually under constant water content loading), achieves State 6, and the soil rebounds to State 7 during unloading at constant water content (the likely amount of rebound is exaggerated for clarity). State 7 is the as-compacted initial state after unloading to nominal stress (see Initial state (b) noted in the Introduction). Then soils may be loaded again to an operational stress of, for example, 50kPa (State 8) before the soil is subjected to other stress paths. For instance, during wetting at constant operational stress, the soil achieves States 9 and 10 (State 9 is reached after swelling to the yield contour for the operational stress, and State 10 is reached after further wetting featuring some collapse on the same yield contour). Alternatively, the soil can swell to State 11' or 11 during wetting without intercepting the operational yield curve and undergoing any collapse. The likelihood of following these alternative stress paths depends on the swelling gradient (or hydric coefficient $\alpha = \left(\frac{\partial e}{\partial e_{w}}\right)_{p}$, and the shrinkage and swelling gradient (see Kodikara, 2012)). If the soil is dried from State 11, it may follow a stress path to States 12 (on the wet side of ATL) and 13 (on the dry side of ATL). States 10 and 11 (11') can be defined as the initial states achieved after loading/ unloading/ wetting, whereas States 12 and 13 can be defined as the initial states obtained after loading/ unloading/ wetting/ drying (see Initial state (a) in the Introduction). Slurry soil is considered to start from State 5 and during saturated consolidation may reach States 14 and 15 and will reach State 16 with further drying (see Initial state (c) in the Introduction).

Following Kodikara (2012), the above initial states can also be elucidated using the well-known traditional compaction curve given in the compaction plane of the dry density and water content (ρ, w), where the dry density ρ can be given as $\rho = \frac{G_{s}\rho_{w}}{e+1} = \frac{G_{s}\rho_{w}}{v}$ (or the inverse of v or e) and w can be given as $w = \frac{e_{w}}{G_{s}} = \frac{v_{w}-1}{G_{s}}$, where ρ_{w} is the density of water and other variables are as defined earlier. Figure 3.1(b) shows Figure 3.1(a) transformed into the ρ, w plane. It should be highlighted that the conventional compaction curves are defined for the unloaded state (as shown by the dashed contour in Figure 3.1(b) for the operational stress), whereas Figure 3.1(b) shows loaded compaction curves (at nominal stress, operational stress, and compaction stress – loaded from States 7 to 6, for example), representing the yield contours. Note that on the wet side of the LOO or ATL, the traditional compaction curve has a markedly downward limb due to air and water pressure build-up during compaction under undrained conditions, as shown in Figure 3.1(b) (see Kodikara (2012) for more details). For constitutive modelling purposes, v, v_{w} (or e, e_{w}) is preferred, but the same interpretation can be given in the compaction plane using this transformation as follows.

Similar to Figure 3.1(a), Figure 3.1(b) also depicts the initial state of the dry powder form of soil at the nominal stress as State 1. Following mixing with the addition of water and subjecting it to the nominal stress, the dry density follows States 2, 3 and 4, and the density is maximum at State 4. Further addition of water decreases the density due to swelling to saturation at State 5. As previously noted, if the soil is compacted from State 3 to the compaction stress, it increases in dry density and reaches State 6. Subsequently, the soil rebounds to State 7 during unloading to the nominal stress. If the soil is reloaded from State 7 to an operational stress of 50kPa, State 8 is reached and the applicable loaded compaction curve is that which corresponds to the 50 kPa stress. Subsequent stress paths shown in Figure 3.1(a) can also be depicted in the ρ,w plane, as shown in Figure 3.1(b).

3.2 Deformation under compression

The deformation (i.e., the variation in the void ratio) is measured keeping one of the variables in the second half of Equations (2.5) and (2.6) constant during loading by increasing the net stress. Most measurements have been made with constant s loading (e.g.,: Sivakumar, 1993; Sharma, 1998), although some measurements have been made keeping e_w or v_w (e.g.,: Islam, 2015; Kodikara et al., 2015; Abeyrathne, 2017) and S_r constant (e.g.,: Raveendiraraj, 2009). Alternatively, keeping v_w or S_r constant is consistent for v-$\ln(p)$ representation, since the complementary representation for the soil water retention curve (SWRC) (as in the second half of Equations (2.5) and (2.6), e.g., e_w or S_r-$\ln(s)$) is considered at constant v . These deformation curves are characterised by three main responses: elastic deformation, yield pressure, and deformation after yielding (i.e., yield lines). When soil specimens with a range of initial states are used, a series of v-$\ln(p)$ yield lines may be generated, commonly referred to as yield hyperlines. Figure 3.2 shows yield hyperlines commonly used in constitutive modelling for unsaturated soil. The yield lines are commonly characterised by the mathematical relationship given by Equation (3.1), where $N(x)$ is the specific volume at nominal stress, and are functions of the variable that is kept constant during loading (either s, v_w or S_r which are generally represented by x) and $\lambda(x)$ represents the compressibility of the soil, which normally depends on the variable that is kept constant. The gradient ($\kappa(x)$) of the unload/reload line (URL) is commonly approximated as constant on the basis of experimental evidence.

$$v(x) = N(x) - \lambda(x)\ln(p) \tag{3.1}$$

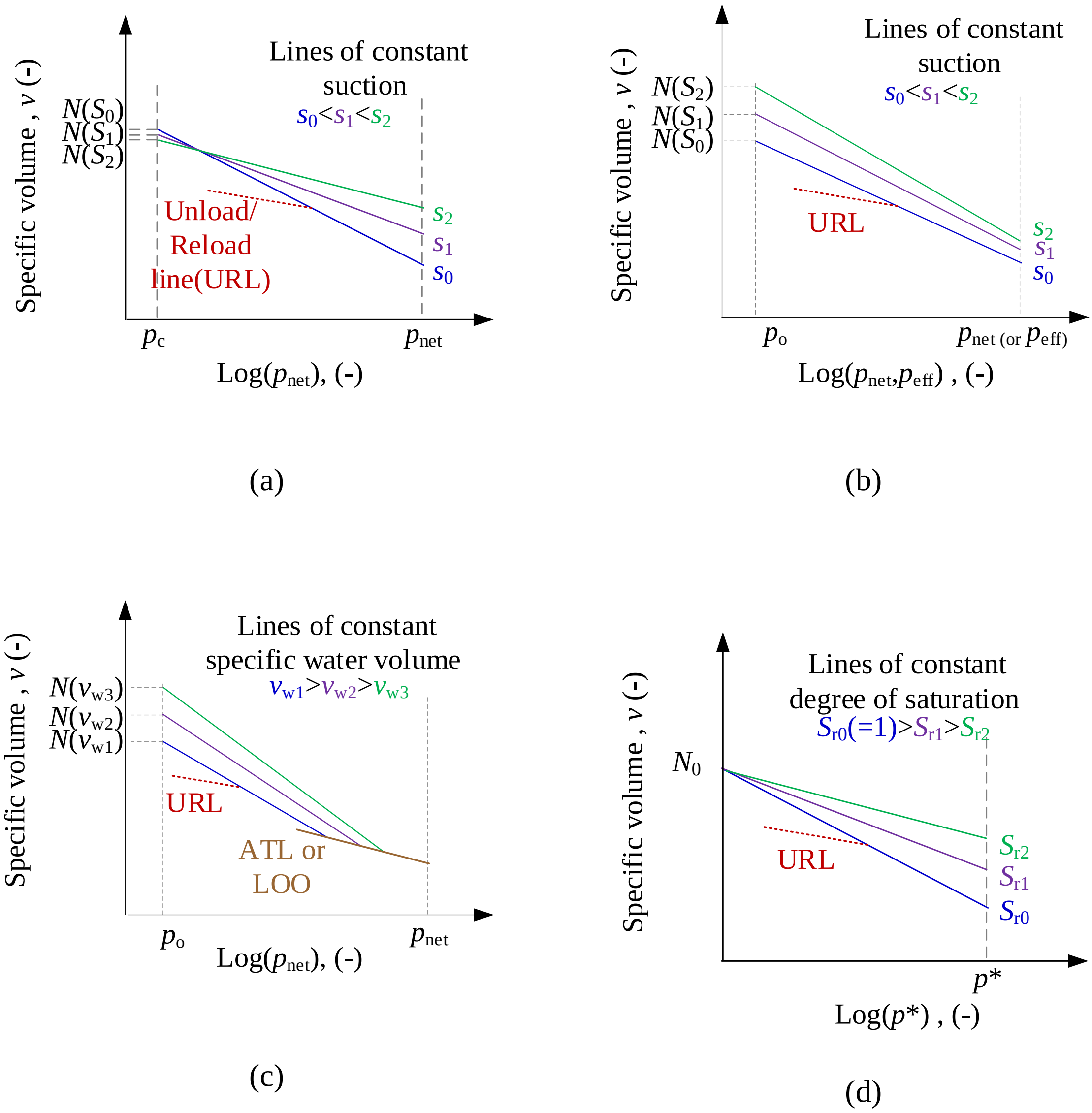

Figure 3.2 : Compression curves suggested by (a) Alonso et al. (1990) (b) Wheeler and Sivakumar (1995) (c) Kodikara (2012) (d) Zhou et al. (2012a); 2012b)

The four major commonly observed phenomenological features used for yield hyperline configurations described above are: Phenomenological feature P1: constant suction hyperlines with increasing (Figure 3.2(a)) or decreasing (Figure 3.2(b)) compressibility (gradient) with the increase of suction; P2: constant specific water volume (or moisture ratio) hyperlines (Figure3.2 (c)); P3: constant degree of saturation hyperlines (Figure 3.2(d)). The hyperline configuration given in Figure 3.2(a) was proposed by Alonso et al. (1990). The two major phenomenological observations which can be seen in the v-$\ln(p)$ representation of the BBM are the decrease in compressibility $\lambda(s)$ and the decrease of the initial specific volume($N(s)$) with the increase of s . The BBM model validation in 1990 is based on experiments carried out on compacted kaolin (LL=38.7%, PL=26.9%) by Josa (1988), a low plasticity sandy clay (lower chrome till) (LL=25%, PL=12%) by Maswoswe (1985), and compacted kaolin (LL=37%, PL=28%) by Karube (1988). The experimental results by Maswoswe (1985) mainly focused on collapse behaviour on wetting, while the data from Karube (1988) were used for the validation of stress path dependency. The experimental results by Josa (1988) were used for validation of the loading paths. The initial states (such as States 12 and 13 in Figure 3.1) of Josa (1988) experiments were achieved by drying after wetting stress paths. These states obtained after drying paths appear to be responsible for the compressibility and initial specific volume characteristics embodied in Figure 3.2(a).

In addition, Sheng et al. (2008) developed a constitutive model, referred to as the Sheng-Fredlund-Gens (SFG) model, for unsaturated slurry soils considering the decrease in compressibility $\lambda(s)$ and the decrease in the initial void ratio ($N(s)$) with the increase of suction. The corresponding initial states can be identified as States 14, 15 and 16 (see Figure 3.1), which are also after drying paths and result in lower compressibility and lower initial specific volumes with an increase of suction. The loading hyperlines of the SFG model were corroborated by the experimental results of Lloret Morancho et al. (2003) for a bentonite clay obtained from Spain (LL=102%, PL=53%). The initial states of these samples were obtained by significant compaction (preconsolidation pressure =700kPa) before wetting and, therefore, were similar to those in the experiments by Josa (1988). However, it is possible that the compacted soil may not have exhibited yield during loading to the relatively low stresses applied.

The hyperline configuration shown in Figure 3.2 (b), where $\lambda(s)$ and $N(s)$ increase with the increase of suction, is the most commonly reported with respect to net stress (e.g.,: Sivakumar, 1993; Zakaria, 1994; Sharma, 1998; Sivakumar and Wheeler, 2000; Monroy, 2006; Sivakumar et al., 2006; Raveendiraraj, 2009) or effective stress ($p+\chi s$) (e.g.,: Khalili and Khabbaz, 1998; Loret and Khalili, 2002), where χ is the effective stress parameter commonly represented as a function of s . Most of the experiments reported here are based on compacted soil samples with initial states (e.g., States 9,10 and 11) through wetting by an equalisation stage prior to suction-controlled loading.

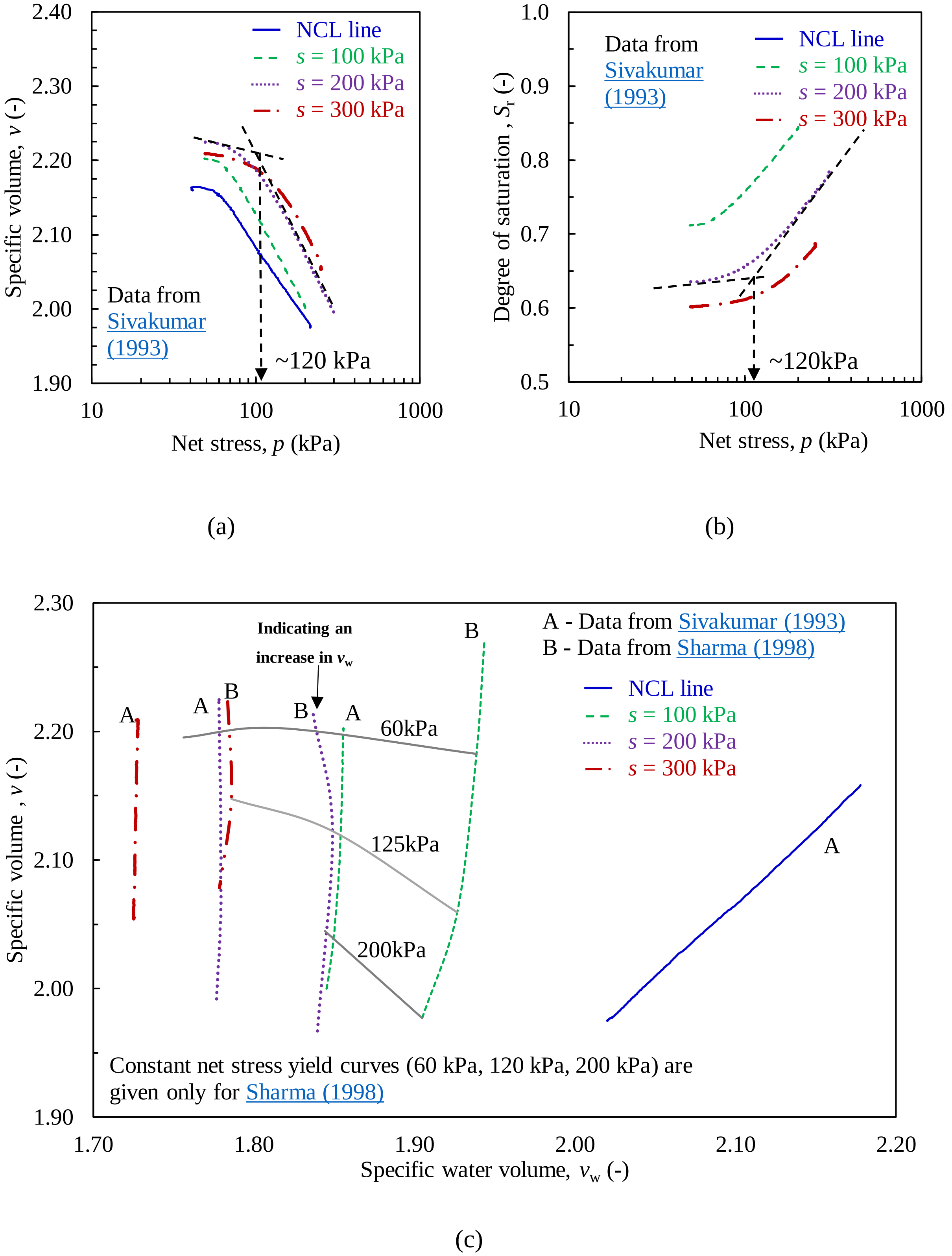

Figure 3.3: Yield hyperlines for compacted kaolin in terms of (a) specific volume (b) degree of saturation (c) MPK framework

Figure 3.3 describes typical phenomenological features associated with this configuration with respect to the data for kaolin by Sivakumar (1993) and Sharma (1998). In addition to the typical compression behaviour discussed above (Figure 3.3(b)), S_r increases with the increase of net stress but the rate of increase diminishes at higher suction levels. Figure 3.3(a) and Figure 3.3(b) clearly indicate another phenomenological feature (P4) of yield stress during suction-controlled loading: the yield stresses for both v and S_r responses are approximately the same (as indicated in Figure 3.3(a)_and Figure 3.3(b), the yield stress for the 200 kPa constant suction loading stress path is 120 kPa). The virgin loading stress paths of Sharma (1998) given in Figure 3.3(c) exhibit an increase of v_w at the beginning of loading, and then v_w eventually decreases with further loading. The increase of v_w during loading was also observed by Buenfil et al. (2005) for clayey silt based on10kPa suction loading tests.

Figure 3.2(c) illustrates the constant water volume yield hyperlines presented by Kodikara (2012) and verified by Abeyrathne (2017) based on constant water content testing, where the initial specific volume ($N(v_w)$) and compressibility ($\lambda(v_w)$) are based on the specific water volume. The advantages of using constant water constant hyperlines include: (a) a direct relationship between traditional compaction curves and the yield surface (i.e., the compaction curve corresponding to a certain stress is a line of compacted states joining the points, such as state 7 in Figure 3.1); (b) the incorporation of a hydraulic coupling according to Equation (2.5); (c) the significant relative ease of obtaining experimental data through constant moisture content testing.

The degree of saturation is also used to define the yield hyperlines, as shown in Figure 3.2(d) (Zhou, 2011; Zhou et al., 2012a, b; Zhou and Sheng, 2015; Lloret-Cabot et al., 2017b; Zhou et al., 2018), and this is consistent with the work equation given in Equation (2.6) with Bishop's stress ($p+S_r s$). However, the initial specific volume (N_o) is assumed to be a constant, and this assumption simplifies the equations and reduces the number of parameters. With this designation, the yield hyperlines can be easily generated using the LWSBS developed through constant water-content testing.

With constant water-content loading, the work equation becomes $\mathrm{d}W = p\mathrm{d}\varepsilon_v$, meaning that the compressive work can be fully defined by v-$\ln(p)$ hyperlines with suction not contributing to internal volumetric work. In contrast, the hyperlines of constant suction testing need to be explained by Equation (3.1), where $v\text{-}\ln(p)$ (see Figure 3.2 (a) and (b)) would only encompass part of the work and another part described by the SWRC is needed to fully explain volumetric work. However, hyperlines at constant S_r, (see Figure 3.2(d)) fully encompass the volumetric work in $v\text{-}\ln(p+S_\mathrm{r}s)$ representation as per Equation (2.6), since $\mathrm{d}S_\mathrm{r}=0$. Nonetheless, they are all part of a yield surface (e.g., LWSBS) as discussed below.

In contrast to saturated soils, where the volumetric yield is represented by a single $v\text{-}\ln(p^*)$, the virgin consolidated line (NCL) and virgin compression hyperlines for unsaturated soils give rise to a yield surface in volumetric space (Matyas and Radhakrishna, 1968; Fredlund and Morgenstern, 1976; Kodikara, 2012). When constructing this yield surface from loading-based hyperlines, it is assumed that 'cross-validity' exists (Islam and Kodikara, 2015), which means that crossing these hyperlines through stress paths like wetting collapse under constant p is catered for. The model proposed by Kodikara (2012) is based on static compaction curves and creates a surface for the volumetric behaviour of the compacted soils by incorporating the hyperlines in Figure 3.2(c) . It should be noted that, here, the compaction curves are loaded to yield states from traditional unloaded states. The unloading and reloading (URL) after reaching the yield surface, the soil is assumed to follow the URL, as shown in Figure 3.2. Normally, the gradient of URL is assumed to be constant for all hyperline configurations (see Figure 3.2) as a reasonable approximation. However, refinement of this assumption requires further testing and research (Delage, 2008).

3.2.1 Loading Collapse (LC) curve

When the soil is loaded from an unloaded position, it yields after reaching the yield surface. Alonso et al. (1990) argued that this yield pressure increases with increased suction, indicating the stiffening effect of suction. They presented this phenomenological feature (P5) as a LC curve in the plane, which corresponds to a certain level of plasticity the soil achieves when compressed at saturation or zero suction. In other words, along the LC curve the soil has the same level of plasticity. The volumetric plasticity content has been captured either as a component of specific volume (Alonso et al., 1990; Abeyrathne, 2017) or plastic volumetric strain (Sheng et al., 2008).

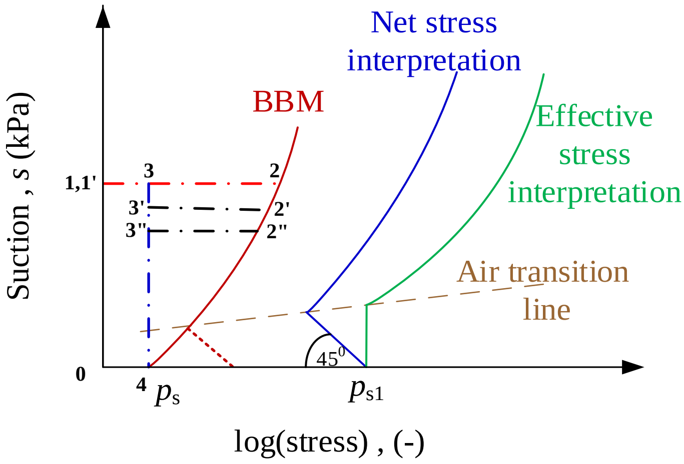

(a)

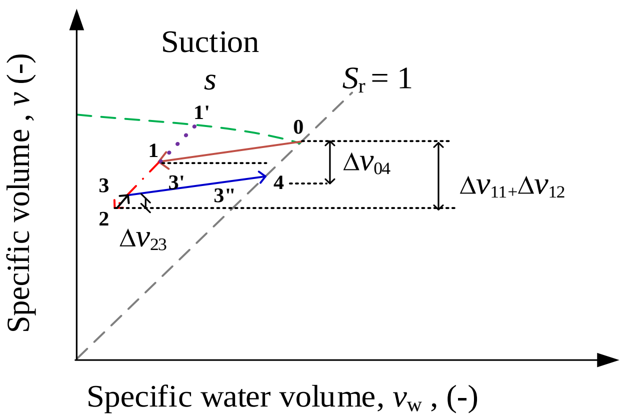

(b)

Figure 3.4: (a) Shape of loading collapse yield curve net stress (b) BBM model volume interpretation

Assuming elastic behaviour within the volumetric yield surface (with reference to Figure 3.4(a)), Alonso et al. (1990) derived an equation for the LC curve given as:

$$\left(\frac{p_o}{p^c}\right) = \left(\frac{p_o^*}{p^c}\right)^{\lambda(0)-k \big/ \lambda(s)-k} \tag{3.2}$$

where, p_o is the yield stress at suction s, p^c is the reference stress, p_o^* is the yield stress at saturation, $\lambda(0)$ is the stiffness parameter for saturation, $\lambda(s)$ is the stiffness parameter at suction s, and k is the elastic stiffness parameter (i.e., URL gradient). With reference to

Figure 3.4(a), the derivation of Equation (3.2) can be explained by considering the overall change of volume change from States 0 → 1 (elastic drying), 1 → 2 (elasto-plastic loading), 2 → 3 (elastic unloading) and 3 → 4 (elastic wetting) to volume change from 0 → 4 under saturated conditions. The change in specific volume can be expressed as $\Delta v_{04} = \Delta v_{01} + \Delta v_{12} - \Delta v_{23} - \Delta v_{34}$, and is illustrated in Figure 3.4(b) in the $e - e_{\mathrm{w}}$ space. In these state paths, plasticity is assumed to occur only in 1 → 2 and 0 → 4, whereas the other two paths, namely 0 → 1 and 3 → 4, are considered elastic (defined by the k_{s} in the $v - \ln(s)$ representation). In addition, the LC curve definition requires the plasticity on the LC to be the same, i.e., $\Delta v_{12}^{\mathrm{p}} = \Delta v_{04}^{\mathrm{p}}$. However, there is experimental evidence that wetting, predominantly initial wetting, from State 3 → 4 may not be elastic, causing the LC curve to shift inwards during the wetting process (Sivakumar et al., 2006; Sivakumar et al., 2010b). Similarly, the initial drying path from State 0 → 1 may also not be elastic. If the soil was mixed to suction s from a dry state, State 1 would be located in a position such as 1', located at one position on the s, p plane (Figure 3.4(a)) and at two distinct positions on the e, e_{w} plane (Figure 3.4(b)). Wheeler and Sivakumar (1995) derived a LC curve from a set of stress paths (3'→2' and 3"→2", after wetting to different suctions from State 3 and then loading to yield) in addition to loading from 3→2, as shown in Figure 3.4(a). Here, it is considered that such wetting prior to loading does not incur plastic strains, as assumed in the BBM. Therefore, it is assumed that all yield points fall on one specific LC curve. However, the shift in the LC curve has been identified in subsequent experiments (e.g.,: Sivakumar et al., 2006; Sivakumar et al., 2010b).

The yield curve can be divided into two major portions by using the air transition value, as shown in Figure 3.4(a). The associated phenomenological feature (P6) for the wet side can be given as follows. In the net stress space, the LC curve is depicted as a 1:1 (negative) gradient line, whereas in the s, p' effective stress space a vertical straight line for the wet side is depicted (where the effective stress is applicable). However, this gradient is obtained by assuming $p + s$ constant and S_{r} is 1. More appropriately, it should be $\frac{\mathrm{d}p}{\mathrm{d}s} = -S_{\mathrm{r}} - s\frac{\mathrm{d}S_{\mathrm{r}}}{\mathrm{d}s}$ since $\mathrm{d}p' = \mathrm{d}(p + S_{\mathrm{r}}s) = 0$. The stress path was derived for the wet side of ATL by Lloret-Cabot et al. (2017a) based on constant volume experiments carried out on compacted London clay (LL=83%, PL=29%) by Monroy (2006). Similarly, Nuth and Laloui (2008b) developed the LC yield curves by using data provided by Sivakumar (1993) for compacted kaolin, where the LC curve was derived for the wet and dry sides separately, as discussed previously.

3.2.2 Suction increase (SI) and suction decrease (SD) curves

In the BBM, Alonso et al. (1990) introduced the suction increase yield curve (SI) to capture the irreversible strains that may occur when the soil is dried past a previously experienced suction. In addition, with particular reference to expansive soils, Gens and Alonso (1992) and Alonso et al. (1999) introduced the suction decrease yield curve (SD) to consider similar irreversibility due to wetting. The SI and SD curves invoke the change in yield pressure during a wet/dry cycle at operational stress within the LC yield surface. The phenomenological observations supporting these suggestions were obtained from a number of different experiments reported in the literature, including:

(1) the suction increase beyond past suction experienced by soil causes irreversible strains (existence of SI curve) (Yong et al., 1971);
(2) the increase/decrease in apparent pre-consolidation pressure with drying/wetting (Josa, 1988; Sivakumar et al., 2006; Chen and Ng, 2013);
(3) swelling pressure behaviour (decreases with increasing void ratio and reduction in swelling pressure after hitting the yield surface) (Brackley, 1973);
(4) reversible and irreversible components of swelling deformation (Chu and Mou, 1973);
(5) higher swelling pressure for higher suction (Kassiff and Shalom, 1971);
(6) stress path dependency (Justo et al., 1984; Brackley, 1975b.);
(7) stress-strain accumulation during wet/dry cycles (Dif and Bluemel, 1991); and
(8) the existence of the microstructure in natural soils and compacted soils (Delage et al., 1982; Delage and Lefebvre, 1984).

However, Sharma (1998) and Raveendiraraj (2009) questioned the existence of SI and SD curves on the basis of experimental results performed on kaolin (lightly expansive) and a mixture of bentonite/kaolin (expansive). Here, we discuss some of their test results. Figure 3.5 shows a test carried out on a bentonite/kaolin mixture by Sharma (1998), where the soil specimen was subjected to a wet/dry/wet cycle after compacting and unloading to the operational net stress of 10 kPa. Since the specimen was prepared from soil in the dry state, during the first wetting cycle (*ab*), the soil should continue to yield on SD curve, shifting it progressively down. During the subsequent drying cycle (*bc*), the soil should have behaved elastically, since it was previously at a much drier state with the SI curve corresponding to high suction. This is reflected in the S_r, s curve (see Figure 3.5(a)), indicating that S_r has apparently changed on what seems to be a scanning curve. However, it is difficult to highlight perceived elastic behaviour from the v, s curve (see Figure 3.5(a)) because there is significantly more deformation during drying (*bc*) than during wetting (*ab*). According to the SD concept, during the next wetting cycle (*cd*), the soil should behave elastically up to the previous suction at b (shown as *d*') and then continue to yield. This behaviour is reflected in the S_r, s response but not in the v, s response. Figure 3.5(b) also shows the state paths drawn in v, v_w space. It is evident that the perceived elastic type response reflecting the curve is clearly shown in paths *bc* and *cd*' (on the scanning curve), and the subsequent wetting path *d'd* has deviated from this response.

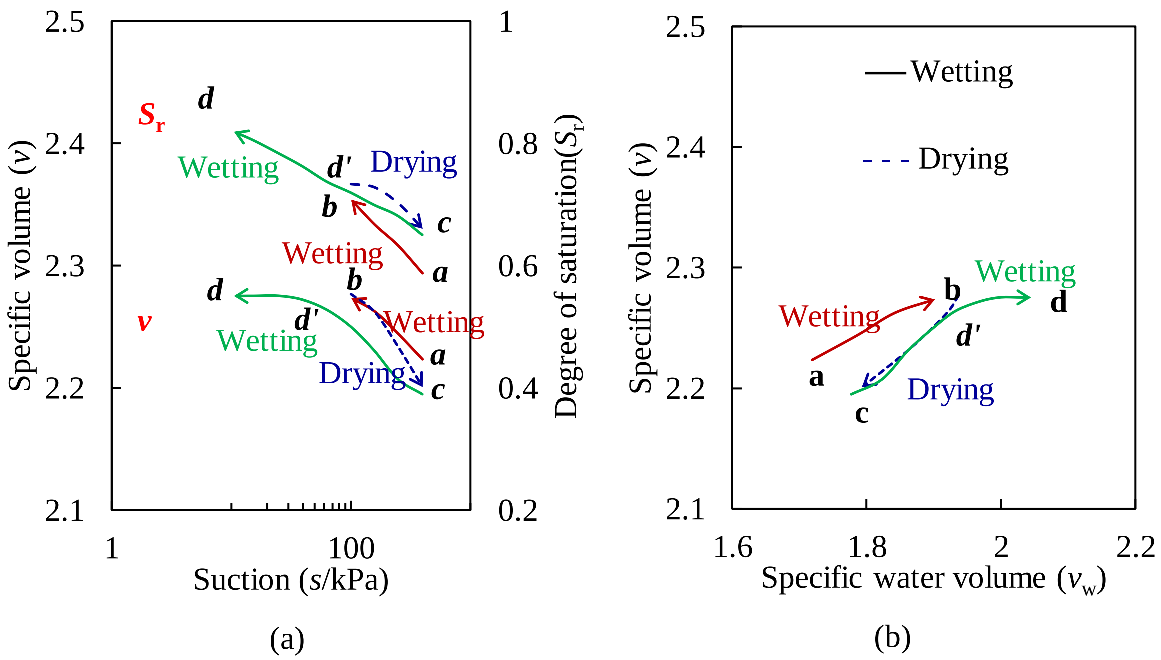

Figure 3.5: Wet/dry testing on compacted bentonite/kaolin mixture

Figure 3.6 shows a test carried out by Sharma (1998) on the same expansive soil mixture, which involved loading (*ab*), unloading (*bc*), wetting (*cd*), drying (*de*), reloading (*ef*) and unloading (*fg*) paths. Five phenomenological features are highlighted with respect to this result: P4: similar to Figure 3.2(b), yielding of v (Figure 3.6(a)) and S_r (the corresponding graph is not shown) occurs at the same net stress; P7: during the wetting path *cd*, continual yielding of v (Figure 3.6(b)) and S_r (Figure 3.6(c)) is observed as virgin wetting is experienced (or lowering of the SD curve); P8 The subsequent drying path *de* shows some apparent elastic behaviour followed by yielding in both v (Figure 3.6(b)) and S_r (Figure 3.6(c)) at similar suction values (≈53 kPa). Since the soil had experienced higher suction previously, yielding at this lower suction indicates a shift in the SI curve, as argued by Wheeler et al. (2003); P9 (as given in Chapter 2): at states *c* and *e* before after a wet/dry cycle, the variables (v, p, s) are almost the same, but the yield stresses differ significantly (100 kPa at *c* and 70 kPa at *e* in Figure 3.6(a)). This cannot be explained by the BBM, since it predicts unique yield stress when v, p, s are the same. Therefore, this highlights the importance of having hydraulic coupling, as reflected by the S_r response. It should be noted that this phenomenon cannot be captured by the effective stress ($p + \chi s$) (Khalili and Khabbaz, 1998; Loret and Khalili, 2002), where the material parameter χ depends only on the suction, hence giving the same effective stress as net stress. However, Bishop's stress ($p + S_r s$) is capable of handling this effect due to the difference in S_r at the two states. Figure 3.6(d) shows the v, v_w plot of the stress paths. All paths are very clearly evident in this diagram. The wetting (*cd*) and drying (*de*) paths are quite distinct, showing the difference in S_r (or v_w) at States *c* and *e* and the resulting yield stresses are also different when the LWSBS is intersected during loading.

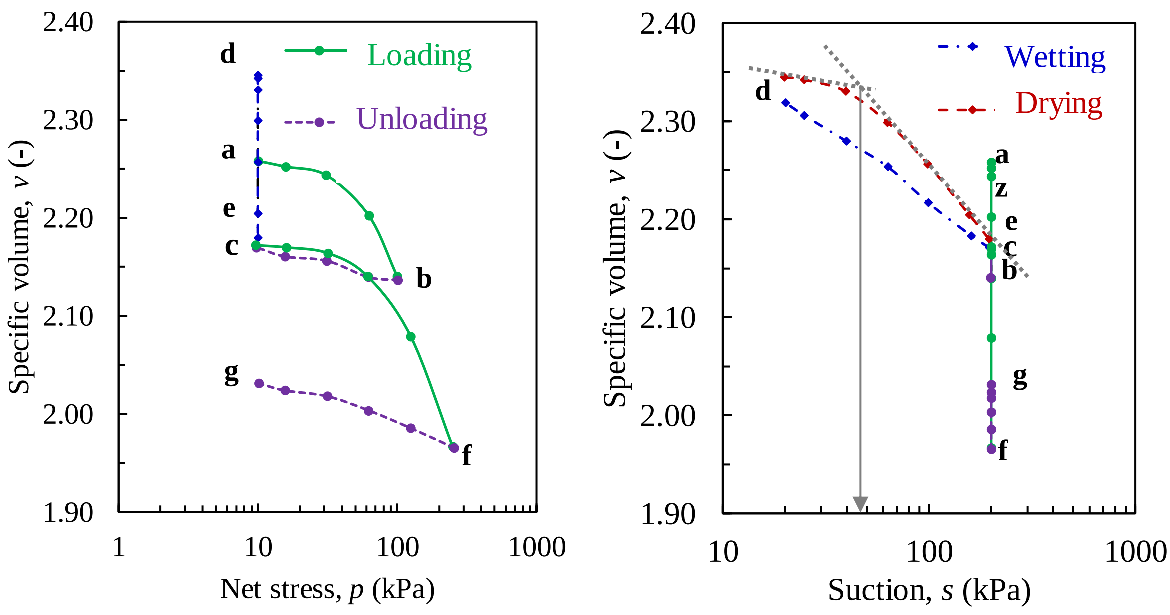

(a) (b)

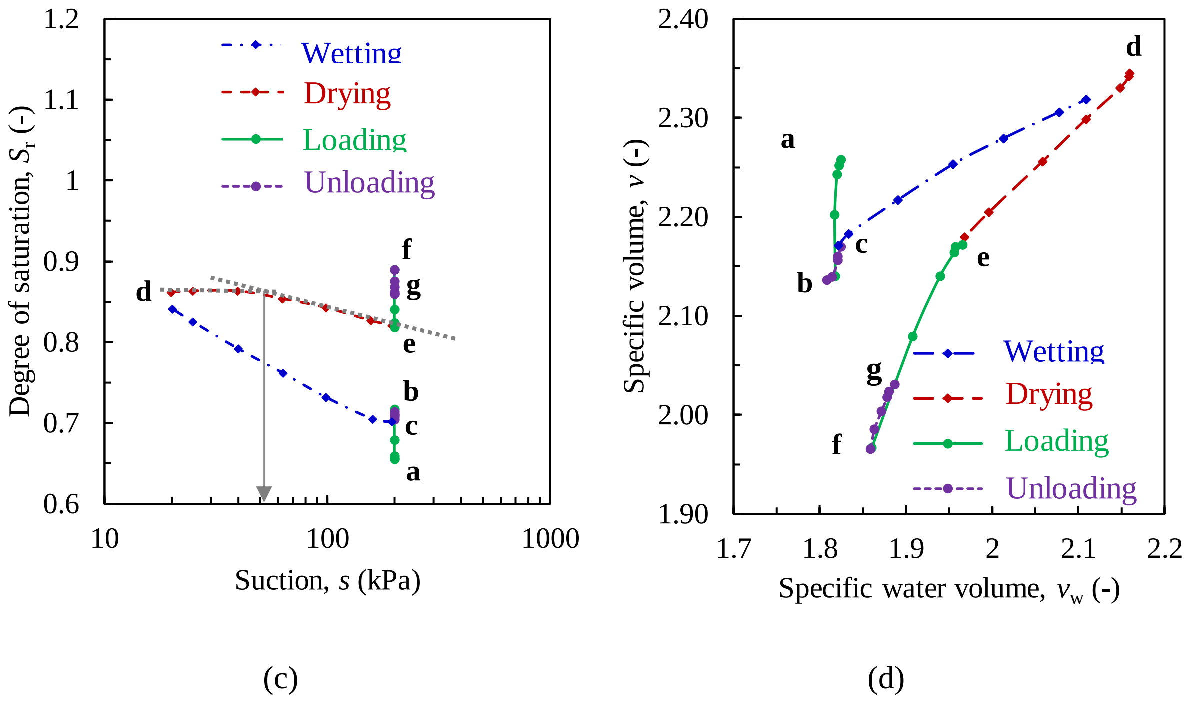

Figure 3.6: Combinations of stress path testing on compacted bentonite/kaolin mixture by Sharma (1998)

3.3 Wetting behaviour

Wetting behaviour is commonly considered under two main stress paths, namely, wetting under constant net stress and wetting under constant volume. On the basis of a large number of experiments undertaken by various researchers, the main observed phenomenological behaviours are summarised here, and Figure 3.7 shows the respective stress paths. Figure 3.7 indicates the constant suction loading (stress path *AB* from p_0 to p_1 and *BC* from p_1 to p_2) and unloading (stress path *CD* from p_2 to p_1 and *DE* from p_1 to p_0) prior to the constant net stress wetting stress paths *CJK* (constant net stress p_2), *DGHI* (constant net stress p_1) and *EF* (constant net stress p_0). In addition, the soil is loaded to p_3 (stress path *CL*) to capture the collapse behaviour. During wetting under constant net stress, the main phenomenological observations can be expressed as P10(as given in Chapter 2): continued swelling to saturation from an unloaded position (at nominal stress p_o on stress path *EF*) (Fleureau et al., 2002); swelling behaviour (stress path *DG*) followed by collapse (stress path *GH*) from an unloaded position(p_1) higher than the nominal stress(p_o) (Sharma, 1998; Raveendiraraj, 2009) and subsequent swelling to saturation after collapse (Sivakumar, 1993), whose results were interpreted by Nuth and Laloui (2008b) and Kodikara (2012)); when the soil is on the yield surface, immediate collapse (stress path *CJ*) upon wetting (Matyas and Radhakrishna, 1968) and with subsequent swelling behaviour to full saturation (stress path *JK*). P11: increase in collapse potential until the pre-consolidation pressure (Sun et al., 2004) and further increase in load results in a reduction in collapse (Sun et al., 2007; Delage et al., 2015; Das and Thyagaraj, 2018). In other words, the collapse volume changes in stress paths *GH* and *LM* are lower than those on *CJ*, as shown in Figure 3.7(a) and Figure 3.7(b).

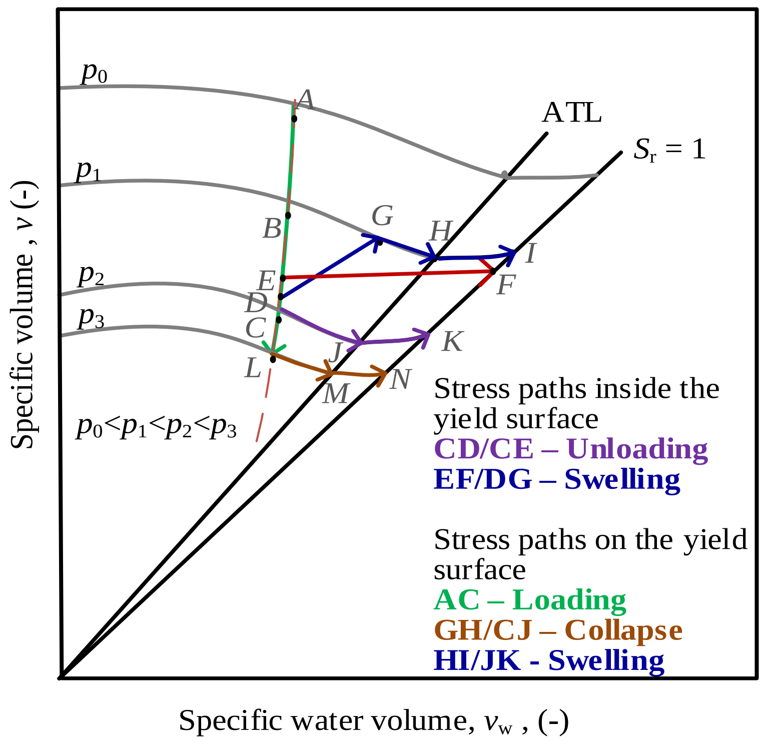

(a)

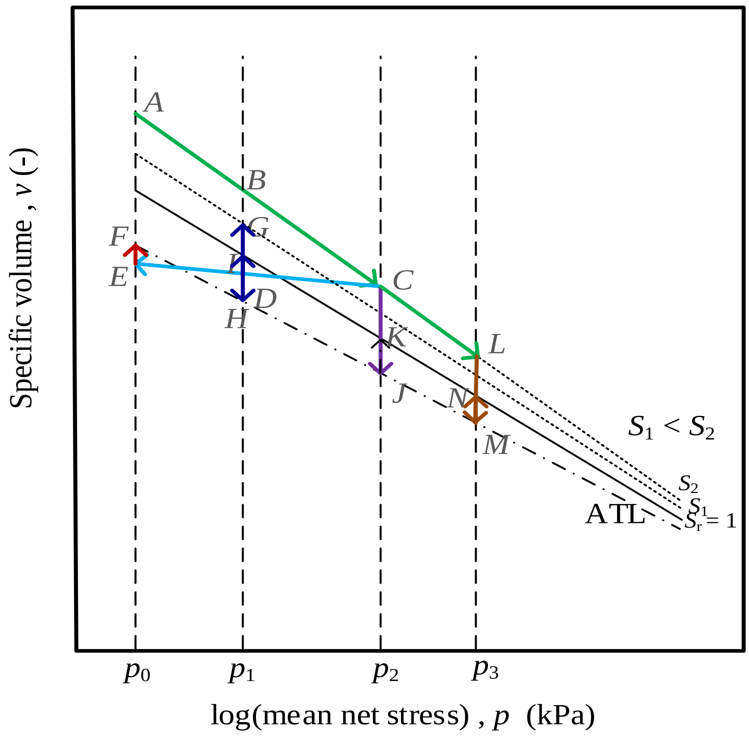

(b)

Figure 3.7: Constant net stress wetting behaviour

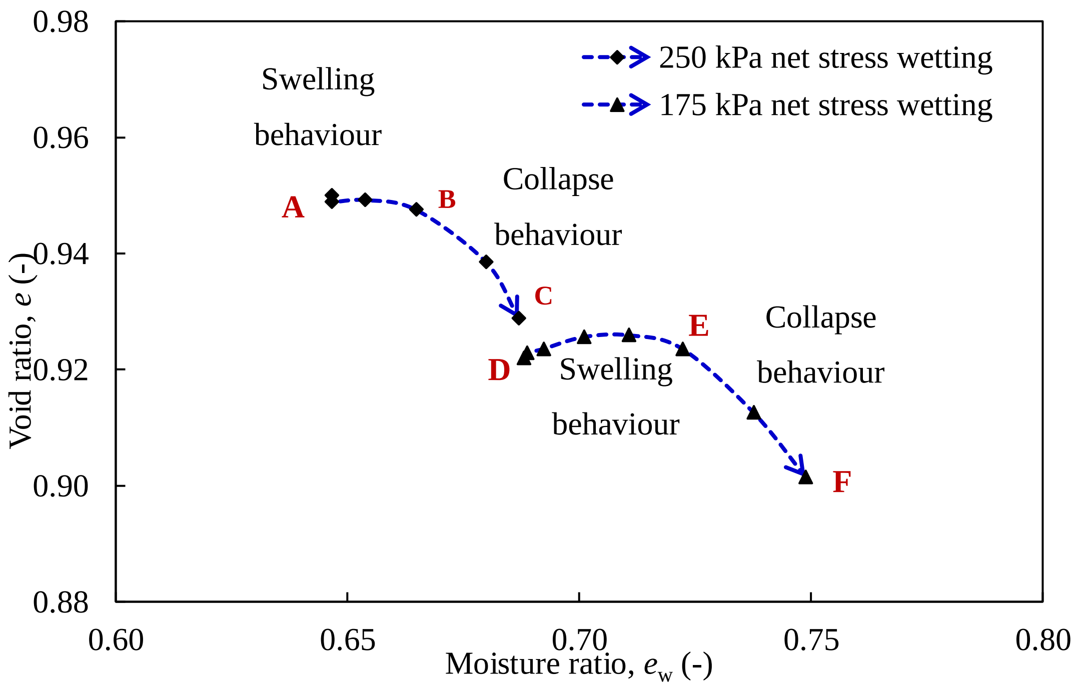

Figure 3.8: Swelling collapse behaviour under constant net stress modified after [Raveendiraraj (2009)](#)

The deformation of unsaturated soil upon wetting has been studied for decades, and a recent experiment performed by Raveendiraraj (2009) on Speswhite kaolin is used as shown in Figure 3.8. The sample was initially equalised at suction of 350 kPa and net stress of 20 kPa prior to constant suction loading to 325 kPa. Subsequently, the sample was dried to 370 kPa and simultaneously unloaded to 250 kPa. During the wetting stress path A – B – C at constant net stress of 250 kPa, swelling followed by collapse behaviour is observed. In the next stress path, the sample was dried to suction of 185 kPa and unloaded to net stress of 175 kPa prior to wetting stress path D – E – F. As explained by Kodikara (2012), the collapse occurs due to yielding on the corresponding mean net stress contour in the e, e_w plane. It should be noted that the collapse can observed only until it reaches ATL, where with further wetting, the soil mostly feature swelling behaviour (Wheeler et al., 2003; Kodikara, 2012).

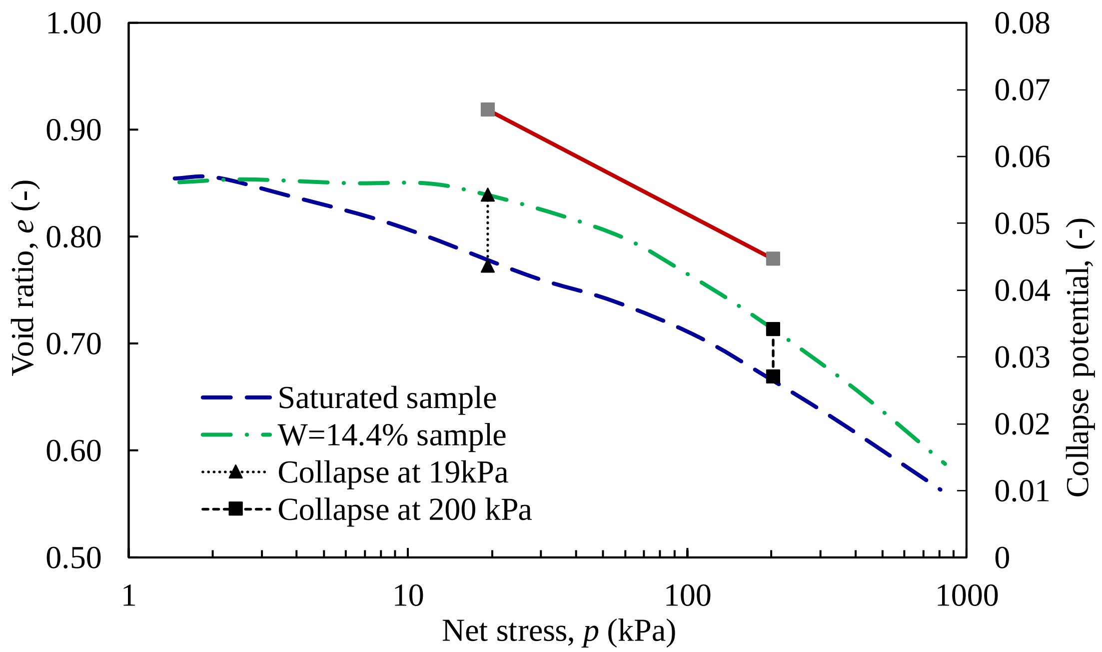

Figure 3.9: Collapse behaviour of natural loess modified after Delage et al. (2015)

The term 'collapse' refers to a sudden decrease of volume due to decrease in suction or water content where the yielding of soil is observed. Collapse behaviour is affected by various factors, namely net stress, suction, the initial condition of the sample (water content), the sample preparation method and the dry density. The collapse potential increases with net stress and then decreases after preconsolidation stress with constant net stress wetting. Although collapse has been studied using oedometer tests from the early stages, (Jennings and Burland, 1962; Matyas and Radhakrishna, 1968; Barden et al., 1969; Maswoswe, 1985) later, many researchers were able to model collapse behaviour of compacted soils using controlled suction isotropic equipment and 1-D oedometer compression equipment (Kato and Kawai, 2000; Sun et al., 2004; Sun et al., 2007; Delage et al., 2015; Das and Thyagaraj, 2018). Figure 3.9 shows a recent data set of collapse experiments carried out on Bapaume loess (ρ_d =1.45Mg/m^3, LL=28, I_p=9) by Delage et al. (2015). The results clearly indicate that the collapse potential decreases with the increase of net stress after a preconsolidation pressure of 16 kPa.

The main phenomenological features identified during constrained volume wetting (swelling pressure testing) can be categorised into two primary stress paths: where the stress path starts (1) on the yield surface or (2) inside the yield surface. The phenomenological observation (P12) associated with constant volume wetting behaviour is a pattern of increased/ decreased/increased swelling pressure. The identified phenomenological observations are: (1) during constrained wetting, on the yield surface the soil shows a reduction in net stress (Matyas and Radhakrishna, 1968; Sharma, 1998); (2) in addition, inside the yield surface, it shows an increase in net stress until it reaches the yield surface and subsequently the stress decreases followed by a further increase in net stress (Romero Morales, 1999; Lloret Morancho et al., 2003; Imbert and Villar, 2006; Raveendiraraj, 2009; Wang et al., 2014; Kaufhold et al., 2015; Navarro et al., 2017). Kodikara (2012) interpreted these phenomenological features using the concepts of the LWSBS and the line of optimum (LOO), which may be considered as the ATL.

3.4 Drying behaviour

Similar to wetting behaviour, drying behaviour has been observed in two major categories, i.e., constant net stress testing and constrained volume testing. In constant net stress drying, soil exhibits a reduction in volume upon drying. Depending on the sample preparation method, soil can be categorised into compacted samples or slurry samples. As noted in Section 3.2.2 on SI/SD curves, the response on the v, s plane (Figure 3.6(b) stress path *de*) and the S_r, s plane (Figure 3.6(c) stress path *de*) of compacted soils upon drying after a wetting stress path shows a response on the scanning curve followed by a response on the major drying curves (yielding behaviour). This behaviour is identified by the phenomenological feature P8. On the other hand, a straight line can be observed in the v, v_w plane (Figure 3.6(d) stress path *de*). The same behaviour is observed in the drying stress paths, which starts after a loading stress path or unloading stress path.

In constant, net stress testing, soil exhibits a reduction in volume upon drying, which can be categorised into two groups, depending on the sample preparation method: compacted samples or reconstituted samples. For compacted samples, depending on the yield conditions, soil displays elastic or elasto-plastic behaviour. In other words, if the soil sample is on wetting curve prior to drying, the sample exhibits elastic behaviour (i.e. on scanning curve) followed by yielding elasto-plastic behaviour (i.e. crossing major drying curves). If the soil is on a scanning curve, the sample follows the scanning drying path prior to crossing major drying curves. For slurry soils, drying at constant net stress from the saturated state leads to initial shrinkage and then a reduction in shrinkage after air transition (Fleureau et al., 2002; Cunningham et al., 2003; Fredlund and Zhang, 2017). Some researchers have also performed wetting after drying and found that the path after air transition behaves predominantly in an elastic manner (Fleureau et al., 1993; Fleureau et al., 2002) (P13). Figure 3.10 shows a typical set of drying experiments carried out on a mix of 20% Speswhite kaolin, 10% London clay and 70% HPF4 silica silt (G_s=2.64, LL=28%, I_p=18%) by Cunningham et al. (2003) and a sample of Jossigny silt (G_s=2.74, LL=37%, I_p=21%) by Fleureau et al. (2002). The experimental data indicate the behaviour outlined above (the wetting path is given only for the data by Fleureau et al. (2002)) and air transition occurs when S_r equals 97.8% and 92% for a mixture of clay silt and Jossigny silt, respectively. Loret and Khalili (2002) explained this phenomenon using the effective stress concept, where the soil yields up to the air transition and subsequently the effective stress increases at a lower rate and falls behind the corresponding yield stress, indicating a partial elastic response, as evident from the subsequent wetting response.

A limited number of test results have been reported for testing under constant specific volume drying. The corresponding phenomenological observation for these tests is that the net stress reduces with the increase of suction during drying (P14) (e.g.,: Raveendiraraj, 2009).

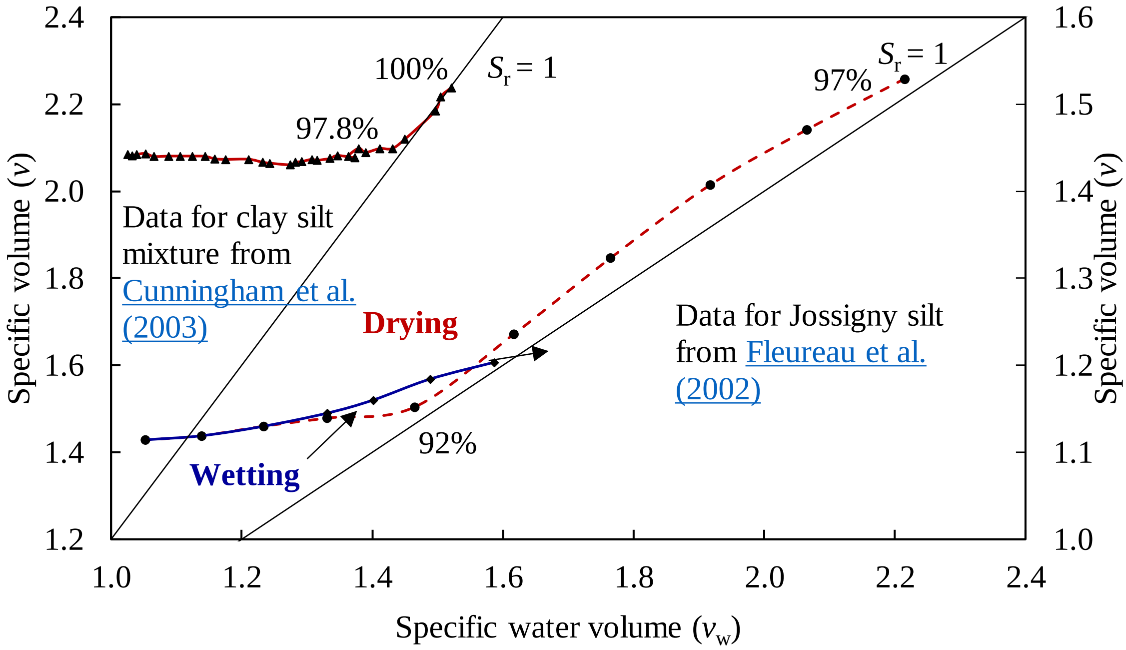

Figure 3.10: Virgin drying behaviour of slurry soil

3.5 Air transition line (ATL) and saturation line

On the basis of available experimental evidence (Dexter, 2004b, a; Dexter, 2004c; Reynolds et al., 2009), it is considered that the inflexion point of the SWRC better represents the ATL, which features the transition of the continuity of the water and air phases. It is normally considered that the air entry occurs close to saturation ($S_r \simeq 1$), whereas at ATL S_r is lower, but depends on the soil type. Typically, S_r^L is between 0.85 and 0.95 for clayey soils, 0.80 and 0.85 for silt, and 0.65 and 0.80 for sand, depending on its particle size uniformity (Thiam et al., 2019). This is consistent with the direct validity of Bishop's effective stress on the wet side of the ATL, where the water phase is continuous. Furthermore, the available evidence indicates that the ATL coincides closely with the line of optimums (LOO) in a family of compaction curves (Azoor et al., 2019; Azoor, 2020).

As shown in Figure 3.1, the ATL represents the line demarcating the continuous air phase (dry of ATL) and the discontinuous air phase (wet of ATL) in the v, v_w, p space. For compacted soils, Kodikara (2012) represented this as the line of optimums (LOO). The behaviour of the ATL can be identified as an important phenomenological observation (P15) during constitutive modelling in the v, v_w, p space. As shown in Figure 3.1, the soil features a significant aggregated structure dry of ATL, where the aggregates are close to full saturation, while the bulk soil can be significantly unsaturated (e.g.,: Delage and Lefebvre, 1984; Rondet et al., 2009). Therefore, the behaviour of aggregates can be better described by effective stress (i.e., Bishop's effective stress) while the bulk soil behaviour is better captured by net stress, as encapsulated in BExM by Gens and Alonso (1992) and Alonso et al. (1999). In contrast, since this aggregated structure is not significantly present wet of ATL, the bulk soil behaviour is better described by the effective stress principle, as represented by Bishop's effective stress.

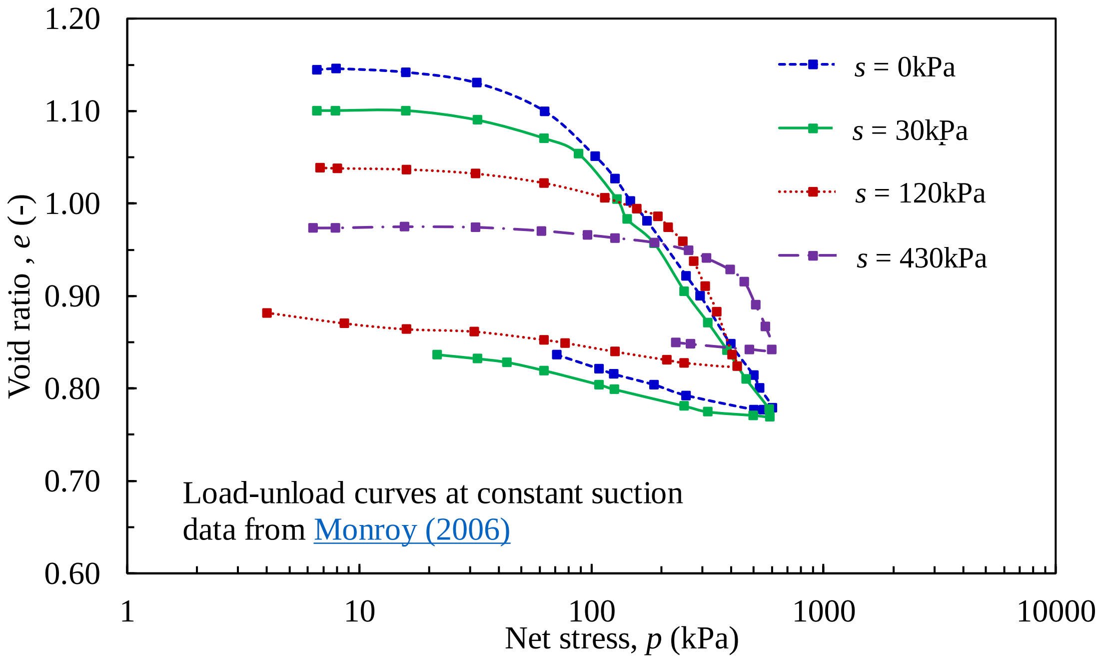

Figure 3.11: Constant suction virgin loading curves

For constant net stress paths, the specific volume at the ATL is lower than that at saturation due to the suction prevailing at the ATL. Therefore, the v-$\ln(p)$ paths may fall below the corresponding saturation compression line as the suction is increased within the ATL (Kodikara, 2012). As shown in Figure 3.11(a), the experimental data produced by Monroy (2006) for constant suction paths provide evidence for this phenomenological feature (P16). The compression line corresponding to 30 kPa suction falls below the saturation line, whereas compression lines corresponding to higher suctions fall above the saturation line with increasing compressibility.

3.6 The environmentally stabilised line and accumulation of plastic strains

When a compacted soil is subject to a sufficient number of wet/dry cycles at a particular net stress, the soil from its as-compacted state tends to achieve a structurally stabilised state, where soil behaves predominantly elastically for subsequent wet/dry cycling (Kodikara et al., 2014; Kodikara et al. (2018)). In this state, the soil can be considered to be an environmentally-stabilised soil that exhibits reversible volume changes with a constant amount of plastic strain (P17). Kodikara (2012) highlighted this concept utilising the data of Tripathy et al. (2002), and Gould et al. (2011), along with its dependence on the net stress.

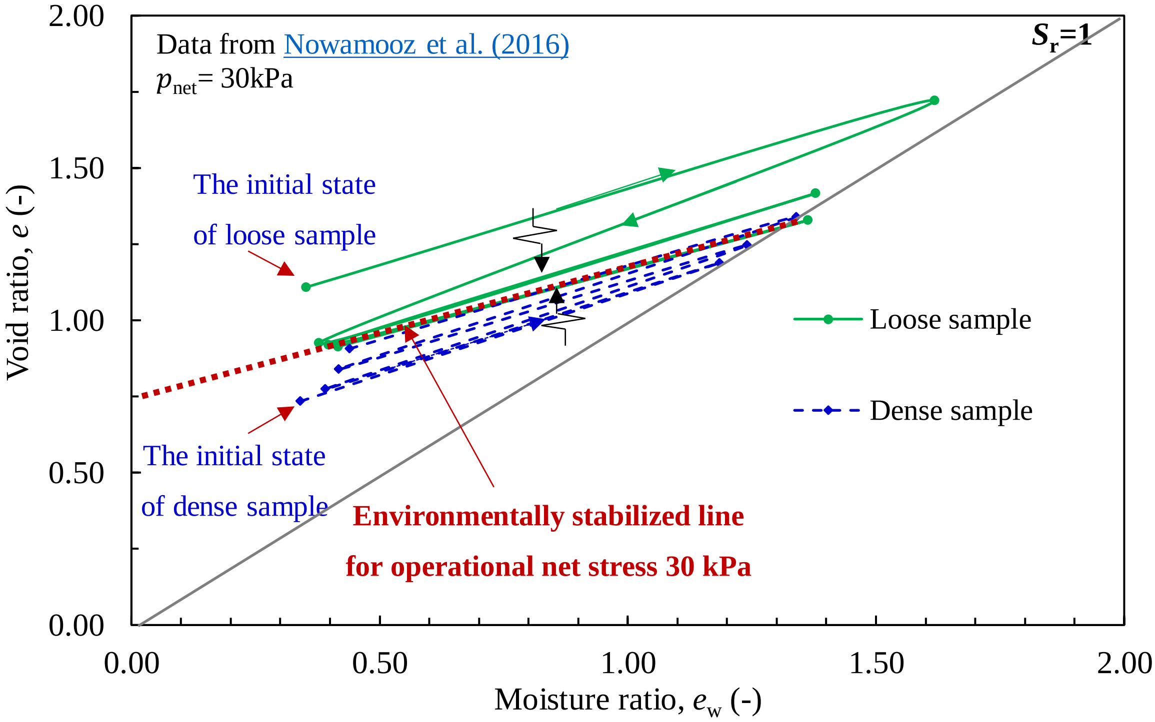

Figure 3.12: Effect of wet/dry cycles

Figure 3.12 shows the data of Nowamooz et al. (2016), who conducted wet/dry experiments on a mixture of compacted silt and bentonite (G_s=2.67%, LL=87%, I_p=22%), and found that the soil achieved an environmentally-stabilised state after four wet/dry cycles. Stabilisation has also been reported by Dif and Bluemel (1991), Alonso et al. (1995), Alonso et al. (1999) and Estabragh et al. (2018). In addition, all the compacted samples mentioned above displayed a substantial irreversible component of swelling in the first wet/dry cycle, which was highlighted earlier as a phenomenological feature of unsaturated soils (P18). Inelastic swelling during the first wetting cycle is apparent in Figure 3.12. Most current models are not capable of handling inelastic behaviour during the initial swelling path due to wetting. For example, in the BBM, it is assumed that the wetting/drying inside the LC curve is elastic, whereas, according to the model by Wheeler et al. (2003) only elastic swelling can take place except when collapse occurs due to the interception of the yield surface or the corresponding LC curve. Furthermore, models using effective stress such as that by Loret and Khalili (2002) also predict swelling to be elastic (except when collapse takes place), since the effective stress reduces during swelling.

Moreover, Figure 3.12 also shows that the wet/dry paths of a loose sample progressively move downwards, whereas those of a dense sample move upwards to meet the environmentally-stabilised path. This behaviour (P19) has also been elaborated on the basis of other experimental evidence by Kodikara et al. (2014).

3.7 Hysteretic behaviour of specific volume and specific water volume with suction

Constitutive modelling of unsaturated soils at present is based only on the hysteresis effect of wetting and drying on the SWRC. However, it appears that suction shows hysteresis effects with e and e_w during wetting and drying (Sharma, 1998; Sivakumar et al., 2006; Raveendiraraj, 2009; Airò Farulla et al., 2010). For instance, Raveendiraraj (2009) carried out isotropic wet/dry testing of compacted kaolin samples, where the samples were dried to 30 kPa from 300 kPa suction (*AB*), wetted to 40 kPa from 300 kPa (*BC*) and again dried to 200 kPa (*CD*). As shown in Figure 3.13(a), only minor hysteresis is visible on the plane, while significant hysteresis is seen (refer to Figure 3.13(b)) on the e, s plane and the e_w, s plane (P20). It may be considered that although not much plasticity occurs on paths *AB*, *BC* and *CD*, significant hysteresis is evident, especially when the variables are plotted with suction.

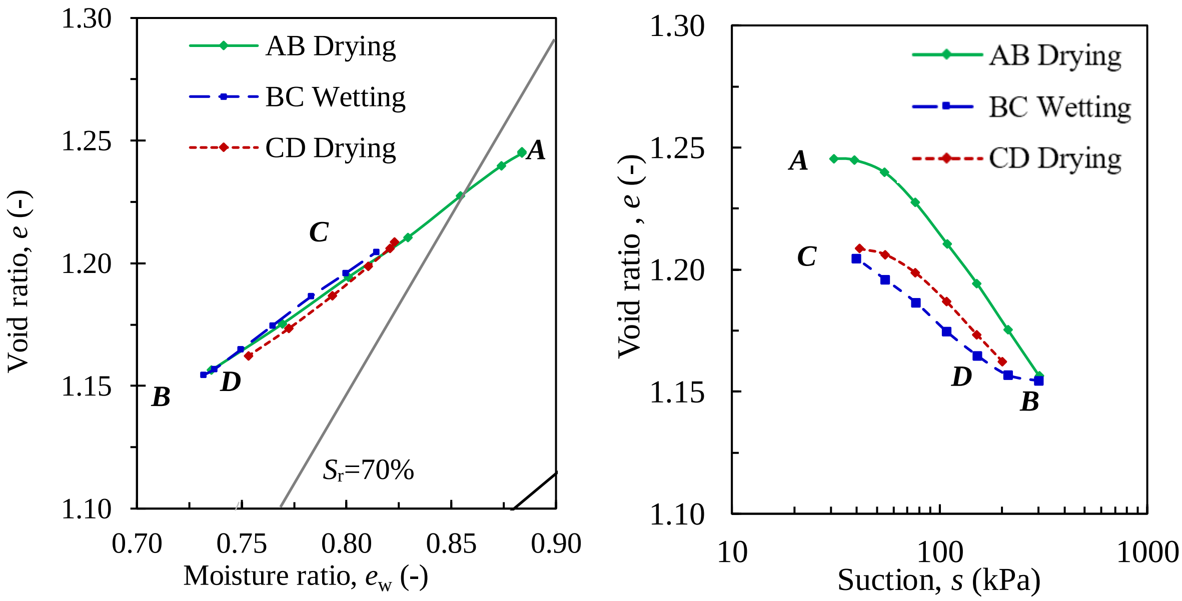

(a) (b)

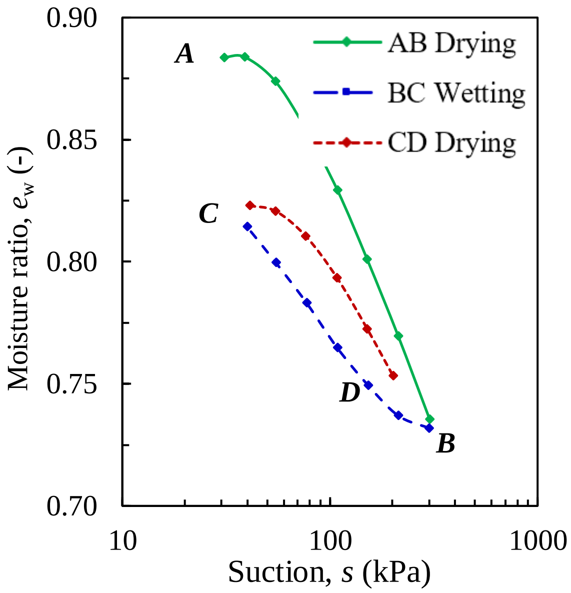

(c)

Figure 3.13: Stress paths for wetting and drying data from Raveendiraraj (2009)

Sivakumar et al. (2006) performed isotropic wetting drying tests on compacted kaolin samples, where the samples were wetted from a suction of 800 kPa and mean net stress of 50 kPa to saturation. Upon wetting to saturation the first test was stopped at 300 kPa (i.e., stress path AB) and the second test at 200 kPa (i.e., stress path BC) for isotropic loading testing to 250 kPa, as shown in Figure 3.14. In addition, one saturated sample (i.e., 3rd test) was loaded to a mean net stress of 250 kPa (i.e., stress path DE). Two saturated samples were dried (DIH) to 200 kPa and 300 kPa suctions (i.e., 4th and 5th test), respectively. These two samples were also loaded to net stress of 250 kPa as given in the stress paths by IK and HJ, respectively. From these experiments it is evident that the moisture ratio for drying suction is higher than that for wetting suction, as given in State B and H for 300 kPa suction and State C and I for 200 kPa suction. The same behaviour was observed in experiments by Chen and Ng (2013).

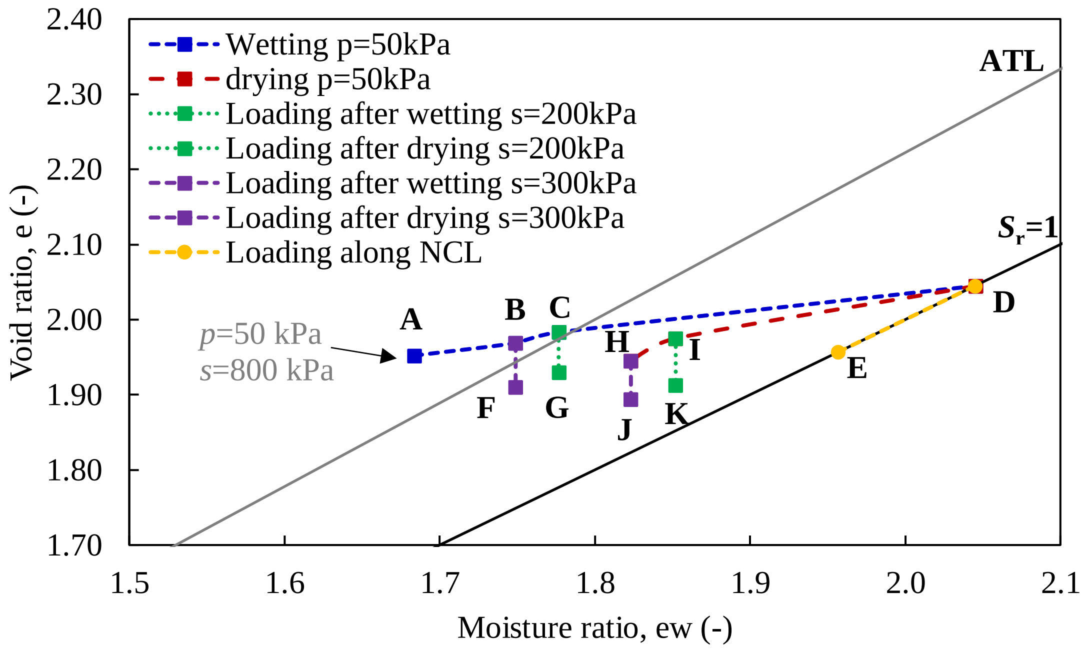

Figure 3.14: The hysteretic behaviour of suction (modified after Sivakumar et al. (2006))

3.8 Soil water retention curve (SWRC)

The non-uniqueness characteristic of unsaturated soils during wetting and drying, known as hysteresis, has been taken into account in many constitutive models. (e.g.,: Gallipoli et al., 2003; Wheeler et al., 2003; Casini et al., 2008; Nuth and Laloui, 2008a; Mašín, 2010; Zhou, 2011; Kodikara, 2012). The water retention behaviour of soil can be defined as the relationship between the degree of saturation (or volumetric water content or gravimetric water content) with suction. This response is usually described by soil water retention curves (SWRCs).

At a point of equilibrium corresponding to a particular suction, the water potential depends on the water volume, the size and shape of the pores, the chemical composition of the water, and its mineralogy. Typically, such equilibrium states measured at nominal stress (or no stress) can be represented by the SWRC, for instance as the $S_r - \ln(s)$ relationship. More recently, however, the influence or shift of SWRC due to mechanical deformation or stress has been highlighted. For instance, Wheeler et al. (2003) proposed a simplified water retention model which depends on the volumetric plastic strain. Sheng and Zhou (2011) introduced a hydro-mechanical model where the degree of saturation depends on both suction and volumetric strain change due to net stress change for isotropic conditions.

According to experimental evidence, the following two points were identified by Sheng and Zhou (2011):

- S_r measured at constant net stress depends on the net stress level.

$$dS_r = f(s, p)ds, dp = 0 \tag{3.3}$$

- S_r measured at constant suction depends on the net stress level.

$$dS_r = h(s, p)dp, ds = 0 \tag{3.4}$$

However, most of the experimental evidence reveals that changes in S_r upon virgin loading are the most significant, whereas during unloading/reloading S_r does not change appreciably, as shown in Figure 3.15 (Sivakumar, 1993; Zakaria, 1994; Sharma, 1998; Gallipoli et al., 2003; Raveendiraraj, 2009). Hence, it can be concluded that change in the plastic volumetric stain is the major factor affecting the shift of SWRC, which is reflected by changes in the deformation, net stress or initial void ratio given in P21. This dependence is depicted in Equation (3.5). This relationship is supported by the work of Tamagnini (2004) and Lloret-Cabot et al. (2017a), who used this approach to modify the model developed by Wheeler et al. (2003).

$$dS_r = f(s^*, \varepsilon_v^p)ds^* + f(s^*, \varepsilon_v^p)d\varepsilon_v^p \tag{3.5}$$

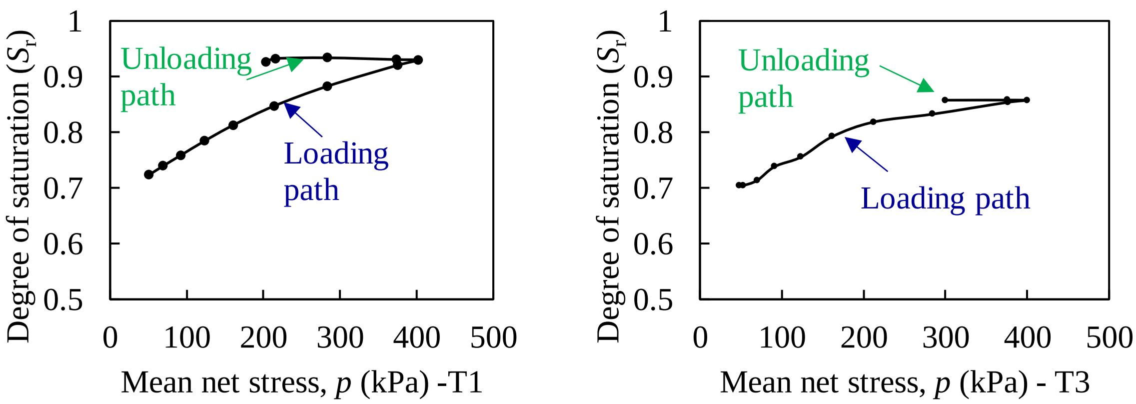

Figure 3.15: Isotropic loading-unloading test at constant suction on compacted Speswhite kaolin (data from Zakaria (1994))

Although most current models simplify that S_r does not vary from unity to saturation up to the air transition suction (AEV), there is significant experimental evidence that saturation progressively decreases (or increases) towards the ATL (Tessier and Pédro, 1984; Marinho and Stuermer, 2000; Cunningham et al., 2003; Fredlund et al. (2013)). In fact, Khalili (2017) has shown this by highlighting a more appropriate way of determining ATL suction and the associated S_r. The phenomenological observation corresponding to these experiments is that a S_r value lower than unity is applicable at the air transition (P22). Theoretically, such a gradual reduction of S_r is expected, since the pore sizes are distributed over a range of pore sizes rather than featuring an abrupt pore air transition size, as needed for the above simplification.

3.9 Suction contours on the unloaded v,v_w planes (P23)

Phenomenological observations have been made of suction contours on the v,v_w planes (corresponding to different net stresses), where the suction is typically measured on compacted soils in an unloaded state. The experimental evidence indicates that for soils that are well into the dry side of the ATL, the suction contours are predominantly vertical in the nominal (unloaded) stress plane, independent of the specific volume or dry density. For example, Figure 3.16 shows the suction contours for unloaded compacted Chataignier clay (Li et al. (2017) (G_s=2.83, LL=705%, I_p=33.5%) corresponding to 8.2 MPa, 3.6 MPa and 3.2 MPa suctions. When the specific volume is less than 1.8 (or S_r < 70%), the suction contours on the nominal stress plane are mostly vertical. As the specific water volume increases close to the LOO, the suction contours slant towards the saturation line. These phenomenological observations are also evident from the results of Romero Morales (1999); Estabragh et al. (2004); Tarantino and Tombolato (2005); Tarantino and De Col (2008) and Nowamooz and Masrouri (2010). When v_w is lower, there is little menisci water in the aggregated soil. Hence, during compaction, aggregates predominantly compress elastically, and the suction is recovered during unloading, as shown in Figure 3.17(a) corresponding to a water constant compression. On the 2.2 MPa contour, it is evident that v_w increases before it becomes almost constant and some other researchers have observed this behaviour (Romero Morales, 1999; Tarantino and De Col, 2008). As shown in Figure 3.17(b), how the suction increases during unloading after compaction explains the shape of this contour. As v_w approaches the ATL, the suction contours become slanted towards the S_r=1 line, as explained in Figure 3.17(c) for the 1 MPa contour.

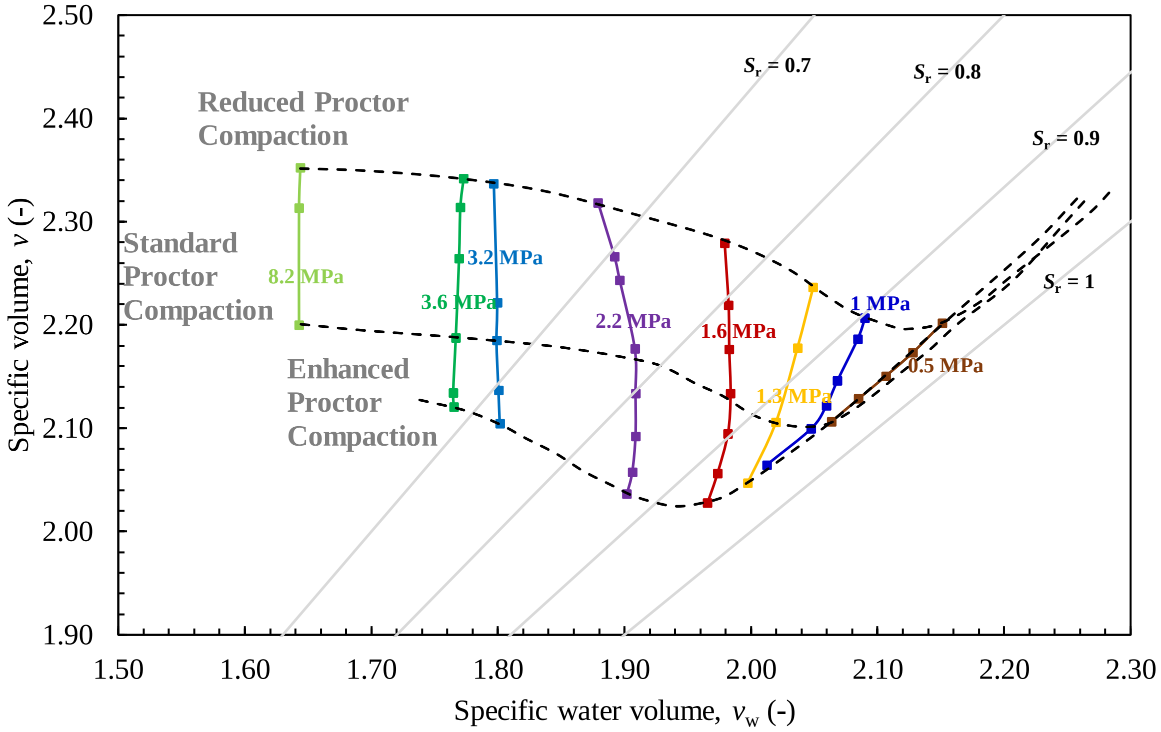

Figure 3.16: Behaviour of suction contours in the v, v_w plane

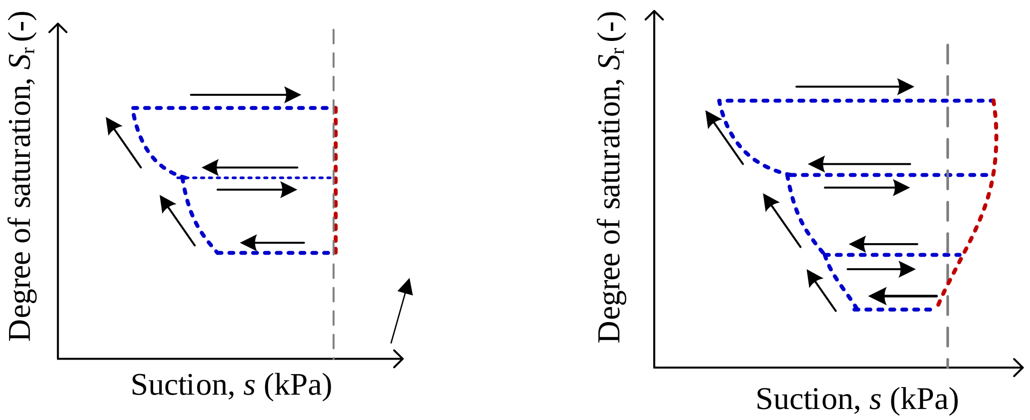

(a) s = 3.2 MPa

(b) s = 2.2 MPa

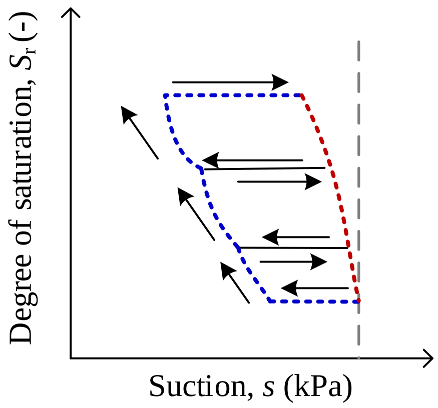

(c) s = 1 MPa

Figure 3.17: Change in S_r during v_w loading as applicable to compaction

3.10 Stress path dependency within loaded space (P24)

If the soil behaves elastically within the unloaded space away from the yield surface, any state path (defined in v, v_w, s, p) should show path independence. This point has been discussed among researchers since the experimental data do not always support it. To highlight this point, consider the BBM model, where unloaded space is considered to be purely elastic. In the BBM, a change in v can be written as in Equation (3.6)), where k_s is the wetting/drying gradient on the constant net stress (p) planes and unloading/reloading gradient k .

$$\mathrm{d}v = \left(\frac{k_s}{s + p_{sat}}\right)\mathrm{d}s + \left(\frac{k}{p}\right)\mathrm{d}p \tag{3.6}$$

For Equation (3.6), the applicability of path independence can be proved using Green's theorem, as: $\left(\frac{\partial\left(\frac{k}{p}\right)}{\partial s} = \frac{\partial\left(\frac{k_s}{s+p_{sat}}\right)}{\partial p} = 0\right)$, in accordance with the BBM assumptions of constant drying/wetting gradient of k_s and k . However, the experimental data do not support this for light and heavy clays. For instance, the state path dependency experiments carried out by Karube (1988) on compacted kaolin are illustrated in Figure 3.18, where the state paths ABCDA and ADCBA are followed, reaching the initial state in both cases. As shown in the e, e_w plot in 2-D, Figure 3.18(b) and Figure 3.18(c) show that the state does not return to the original state in any of the paths undertaken. As identified in phenomenological observation P18, a major reason is the initial inelastic swelling during wetting, and initial inelastic drying may also contribute to this dependency. The slight collapse in Figure 3.18(b) in the stress path CD does not count in the stress path analysis.

In the above manner, stress path dependency can be evaluated using Green's theorem. For instance, Zhang and Lytton (2008) showed that the SFG model is not stress-path independent in the unloaded space, even with its assumptions of elastic wetting/drying and elastic loading/unloading. For the effective stress models, Equation (3.6) simplifies to $\mathrm{d}v = k\mathrm{d}p^*$ for all state paths in the loaded space and, therefore, can be considered path independent. However, a problem exists with their applicability due to the initial inelastic wetting/drying observed commonly, regardless of soil reactivity.

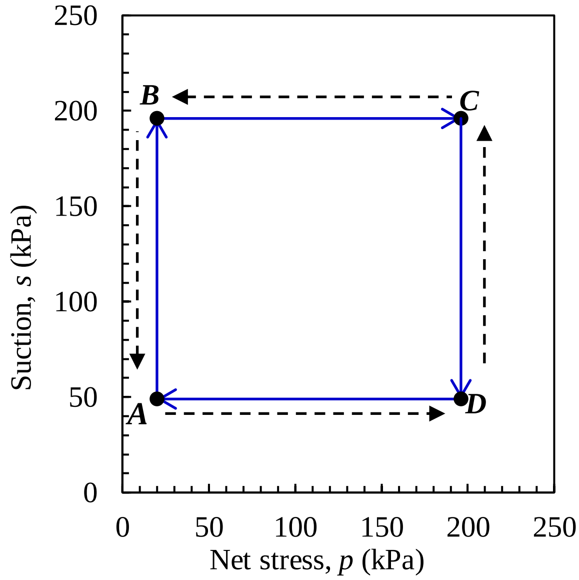

(a)

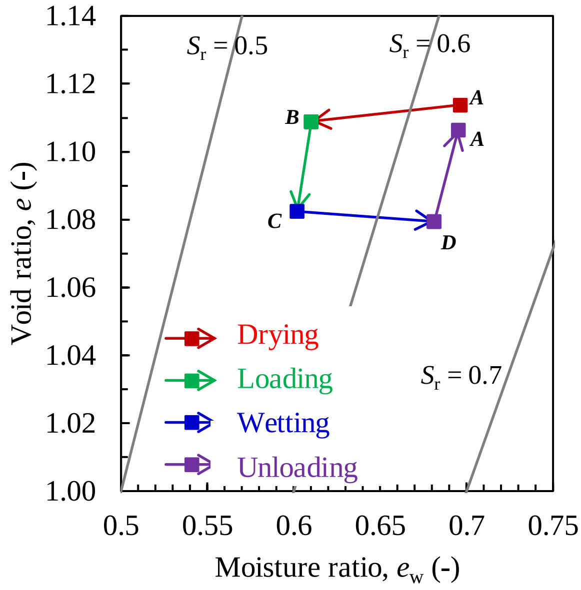

(b)

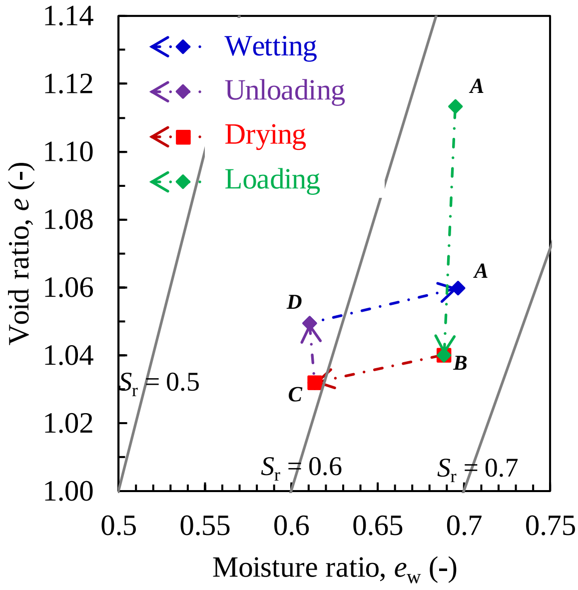

(c)

Figure 3.18: Stress path dependency elastic behaviour for kaolin data from Karube (1988)

3.11 The compaction curve and relationship to Line of Optimums (LOO)(P25)

As shown in Figure 3.1, the ATL represents the line demarcating the continuous air phase (dry of ATL) and the discontinuous air phase (wet of ATL) in the v, v_w, p space. For compacted soils, Kodikara (2012) represented this as the line of optimums (LOO). For many soils, the ATL can be considered to be associated with a constant degree of saturation ($S_{r,ATL}$) based on the phenomenological observations of compaction curves obtained from both laboratory and field tests (e.g., Tatsuoka and Correia (2018)).

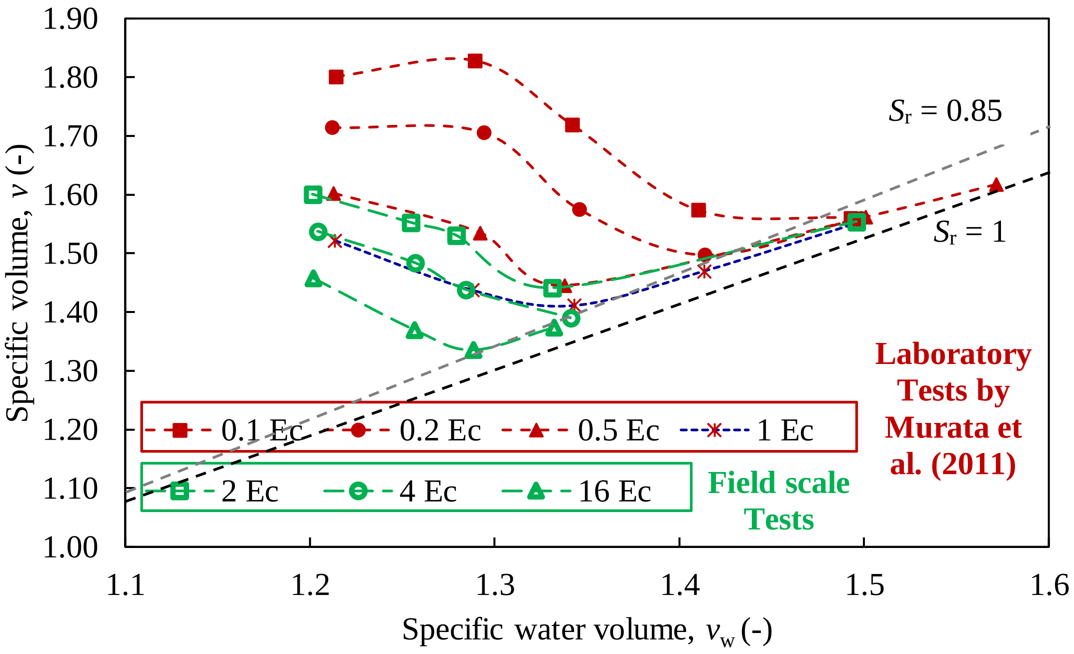

(a)

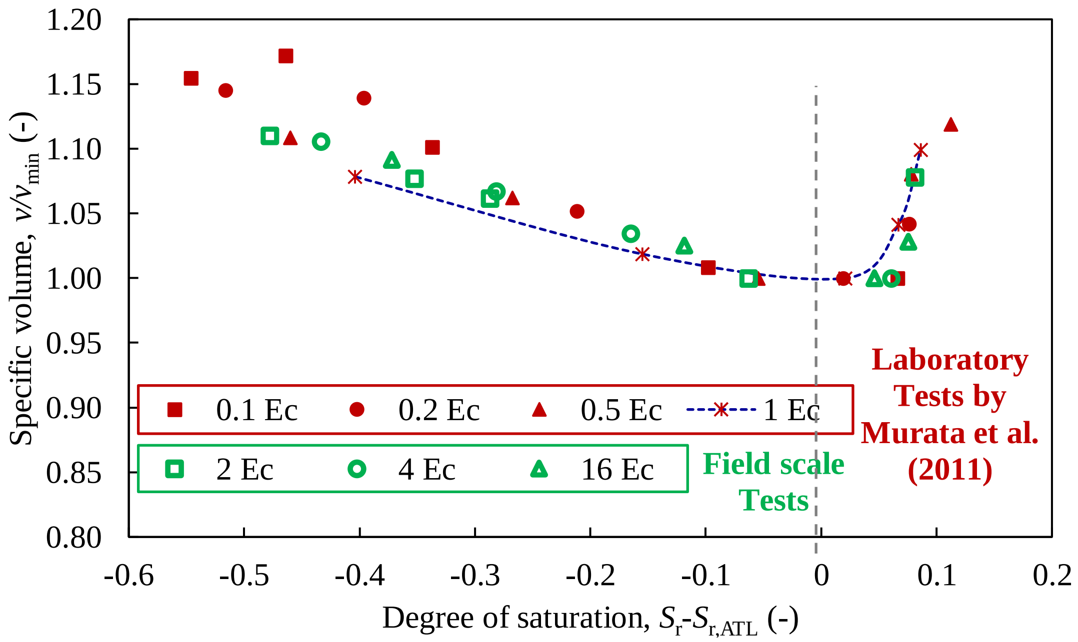

(b)

Figure 3.19: Compaction curves on (a) v, v_w *plane (b)* $v/v_{min}, S_r - S_{r,ATL}$ *relations modified after Tatsuoka and Correia (2018)*

For instance, as shown in Figure 3.19(a) in the v, v_w plane, Tatsuoka and Correia (2018) analysed a series of compaction tests performed at a range of compaction energy levels in both the laboratory and the field. The field studies in Figure 3.19 were carried out in a large concrete pit for the period from 1965 to 1990 using a wide range of compaction equipment including rollers (only the energy levels of 2Ec, 4Ec,16Ec are given here; 1Ec represents Standard Proctor with 596kJ/m^3). In addition, Figure 3.19 also shows another set of laboratory experiments by Murata et al. (2011) carried out at lower energy levels for the same soil type. It is evident that the ATL or the LOO can be designated by a constant $S_{\mathrm{r,ATL}}$ of 0.85 for this soil. In addition, these researchers showed a normalised form of the compaction curves, as shown in Figure 3.19(b), where $v / v_{\min}$ is plotted against $S_{\mathrm{r}} - S_{\mathrm{r,ATL}}$, where $v_{\min}$ is the specific volume at ATL, following the MPK representation. It is clear from these normalised curves that $S_{\mathrm{r,ATL}}$ can be reasonably assumed unique for this soil, regardless of the energy level and compaction equipment used.

3.12 Discussion of Isotropic behaviour

Salient phenomenological observations of the volumetric behaviour relevant to constitutive modelling of the hydro-mechanical behaviour of unsaturated compacted soils are summarised below.

P1	The compressibility of constant suction hyperlines decreases with increasing suction and the corresponding initial specific volume decreases with increasing suction (Figure 3.2(a)). In contrast, compressibility may increase along with the initial specific volume as the suction is increased (Figure 3.2(b)). The former appears to arise when the soil initial states are after drying and the latter appears to arise when the initial states are after wetting.	Josa (1988); Lloret Morancho et al. (2003); Sivakumar (1993); Sharma (1998)
P2	The compressibility of constant water content virgin compression lines increases with decreasing water content.	Islam and Kodikara (2015); Abeyrathne (2017)
P3	The compressibility of the constant degree of saturation of virgin compression lines increases with decreasing degree of saturation.	Raveendiraraj (2009)

P4	During loading, the yield stress is similar for both v and S_r.	Sivakumar (1993); Sharma (1998)
P5	For isotropic loading at constant suction, the yield stress increases with increasing suction for all types of soils.	Wheeler and Sivakumar (1995)
P6	Constant volume testing for the wet side shows a 1:1 negative gradient line in the s, p plane and a straight line in the effective stress space. However, this gradient may be less than 1 given by $\frac{dp}{ds} = -S_r - s\frac{dS_r}{ds}$	Sivakumar (1993); Monroy (2006)
P7	During a wetting path, continual yielding of v and S_r is observed as virgin wetting is experienced.	Sivakumar et al. (2006)
P8	Starting from a loading, unloading or wetting path, subsequent drying causes some apparent elastic behaviour before any yielding in both v and S_r occurs.	Sharma (1998); Raveendiraraj (2009)
P9	During wetting and drying, there can be two different yield stresses, even when the v, p, s values are the same, indicating the importance of whether soils are on a wetting path or a drying path.	Sharma (1998); Raveendiraraj (2009); Sivakumar et al. (2006)
P10	Under constant net stress wetting, swelling leads to collapse, which is turn leads to swelling.	Matyas and Radhakrishna (1968); Sivakumar (1993)
P11	The collapse behaviour shows that the collapse potential (at constant net stress wetting) increases with net stress and then decreases. It appears that the peak collapse occurs at pre-consolidation stress	Kato and Kawai (2000); Sun et al. (2004); Sun et al. (2007); Delage et al. (2015); Das and Thyagaraj (2018)

P12	In constrained volume wetting paths, net stress increases before leading to a decrease in net stress. With further wetting, the net stress increases again before achieving saturation.	Romero Morales (1999); Lloret Morancho et al. (2003); Imbert and Villar (2006); Raveendiraraj (2009); Wang et al. (2014); Kaufhold et al. (2015); Navarro et al. (2017)
P13	Drying from the saturated state leads to initial yielding and then predominantly reversible drying.	Fleureau et al. (2002); Khalili et al. (2004); Gao et al. (2015); Li et al. (2017)
P14	Constrained volume drying testing on compacted kaolin sample shows a decrease in net stress with the increase of suction.	Raveendiraraj (2009)
P15	The transition from the saturated state to an unsaturated state is demarcated by the air transition line (ATL).	Li et al. (2017)
P16	With the increase of suction, the compressibility of the soil initially reduces before the increase of compressibility starts.	Monroy (2006)
P17	During wet/dry cycles, plastic strains accumulate and eventually stabilise.	Dif and Bluemel (1991); Gould et al. (2011); Kodikara (2012)
P18	Initial inelastic swelling is experienced by compacted clay soils regardless of their shrinkage/swelling potential.	Chu and Mou (1973)
P19	Loosely compacted soils tend to densify, whereas dense soil specimens tend to loosen to achieve an environmentally-stabilised plane (at a particular moisture ratio)	Nowamooz and Masrouri (2010); Nowamooz et al. (2016)
P20	Hysteretic behaviour of specific volume and specific water volume with suction is observed based on experimental evidence.	Raveendiraraj (2009)

P21	The water retention curve appears to be dependent on the volumetric plastic strain.	Zakaria (1994); Tamagnini (2004); Lloret-Cabot et al. (2017a)
P22	The degree of saturation gradually decreases towards the ATL from saturation.	Fredlund et al. (2013) Cunningham et al. (2003)
P23	The emergence of suction contours on the v, v_w plane on compacted soils in an unloaded state	Romero Morales (1999); Estabragh et al. (2004); Tarantino and Tombolato (2005); Tarantino and De Col (2008);Nowamooz and Masrouri (2010)
P24	Wetting/drying and loading/unloading away from the loading yield surface display path dependency, predominantly due to initial inelastic swelling.	Karube (1988)
P25	The compaction curve and relationship to Line of Optimums	Tatsuoka and Correia (2018)

3.13 Phenomenological observations of triaxial behaviour

The discussion thus far has been limited to triaxial behaviour and isotropic behaviour has been studied broadly due to its importance. This thesis utilises critical state soil mechanics concepts to extend the isotropic model to triaxial stress state. In order to identify phenomenological observations of the triaxial behaviour of unsaturated soil, first, the triaxial behaviour of saturated soils was studied. The features of saturated soils in the triaxial stress state can be summarised as follows:

1. The two main types of tests carried out on saturated soils are drained tests and undrained tests. Since saturated samples do not have an air phase, during drained tests the water is drained out. During undrained shear tests, the total volume change is constant;
2. One of the phenomenological observations of saturated drained tests is that higher shear strength and lower change in specific volume occur with the increase of confining stress

for normally consolidated soils. Similarly, shear strength is higher with the rise in confining stress for undrained shear tests; and,

3. For heavily overconsolidated soils, the specific volume increases (dialation) during drained tests while a peak followed by a plateau is observed in the shear strength.

Unsaturated triaxial behaviour has been studied considering either controlled suction (Sivakumar, 1993; Raveendiraraj, 2009) or controlled water content (Abeyrathne, 2017) tests and the former has been used by most constitutive models. Hence, the phenomenological observations of unsaturated soils are studied under three categories, namely phenomenological observations of constant suction shearing paths, phenomenological observations of constant water content shearing paths, and the features of critical state hyperlines.

3.13.1 Phenomenological observations of constant suction shearing tests

A comprehensive study of the triaxial behaviour of unsaturated soils for constant suction shearing reveals that:

1) Shear strength increases with increasing suction and with the further increase of suction shear strength reduces (PT1), as given in Figure 3.20(a) (Alonso et al., 1990; Sivakumar, 1993; Colmenares Montanez, 2002). This observation is associated with the increase in tensile strength prior to the reduction of tensile strength with suction (PT2), as shown in Figure 3.20(b) (Fredlund et al., 1996; Sheng et al., 2013). The behaviour of shear strength in the q,s plane and v,s plane can also be interpreted in the s,p plane, as depicted in Figure 3.20(c) (Shannon, 2013);
2) During the constant suction shearing stress path (i.e., the drained stress path), S_r increases and v decreases for normally consolidated or lightly consolidated samples (PT3) (Raveendiraraj, 2009). However, when the soil is highly over-consolidated, the S_r decreases and v increases (PT4) (Casini, 2008; Zhou and Sheng, 2015; Wu, 2018; Wu et al., 2018). Wu (2018) carried out constant suction shearing experiments for different over-consolidation ratios (OCR=1, 2, 4, 8), where high over-consolidation is clearly visible at OCR=8;

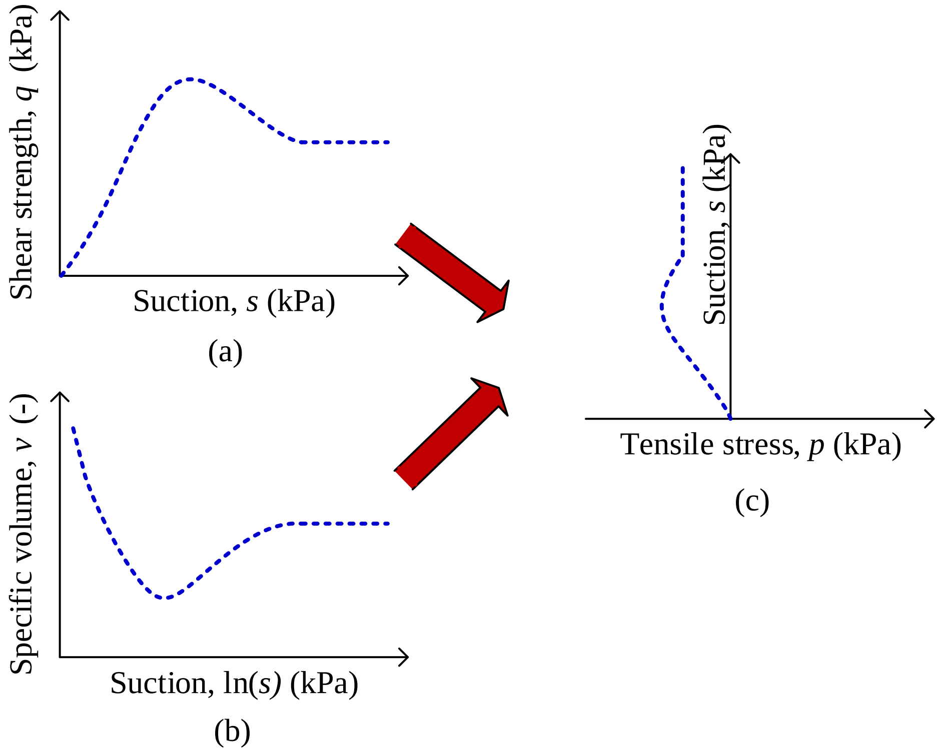

Figure 3.20: The behaviour of shear strength in (a) q,s plane; (b) v,s plane; (c) s,p plane

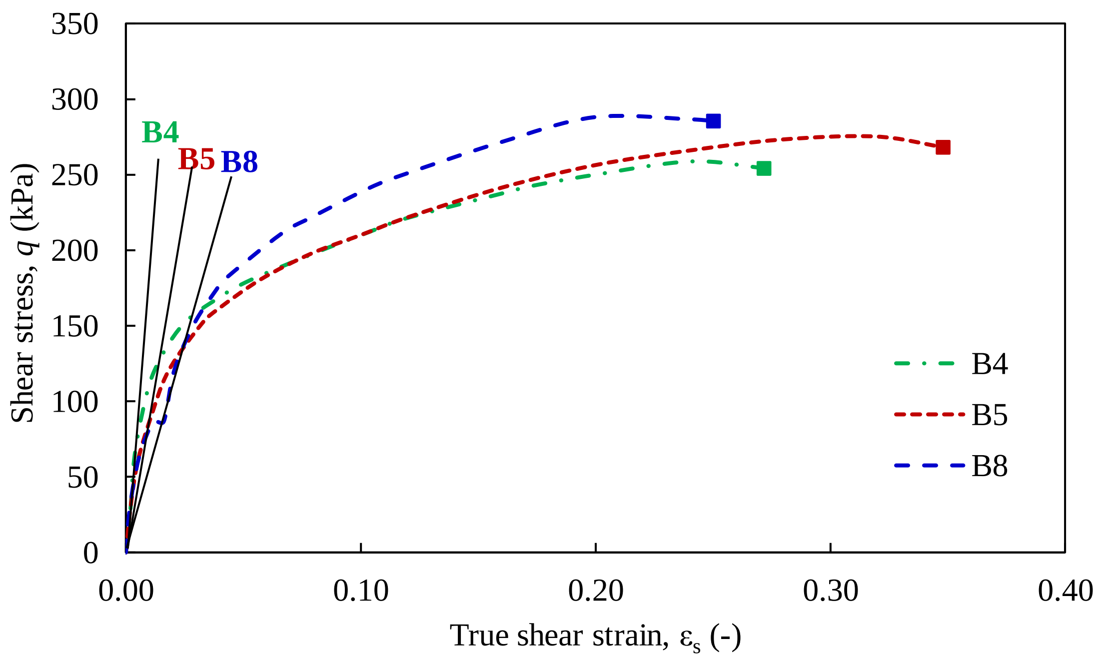

Figure 3.21: Deviatoric stress against shear strain for experiments by Raveendiraraj (2009)

3) For the same suction, higher confining stress (or higher cell pressure) results in higher shear strength (PT5) (Rahardjo et al., 2004; Vanapalli, 2009; Sheng, 2011). In addition, Sheng (2011) argued that a greater increase in shear strength can be achieved by increasing the

confining stress than by increasing the suction. The change of specific volume during shearing after isotropic compaction showed a reduction and increased with increasing confining stress (PT6) (Sivakumar et al., 2010a); and

4) Raveendiraraj (2009) performed a series of triaxial tests on Spacewhite kaolin to capture the phenomenological observations of unsaturated soils associated with isotropic stress paths. Figure 3.21 includes three constant suction shearing experiments and all the three tests sheared at a suction of 300 kPa. Tests T4 and T5 were performed after loading to mean net stress of 75 kPa. However, Test T9 was carried out after a wetting (through equalisation to suction of 30 kPa) drying stress path (i.e., drying to suction of 300 kPa). It is evident from Figure 3.21 that the initial elastic stiffness for Tests T4 and T5 is higher than that for Test T9, resulting in a higher deviatoric stress. In addition, Melinda et al. (2004) experimentally proved that the ultimate shear strength and friction angle are higher for shearing stress paths performed after drying compared to wetting (PT7).

3.13.2 Phenomenological observations of constant water content loading tests

Over the last few decades, two main testing approaches have been used to study the triaxial behaviour of unsaturated soil mechanics, namely, constant suction shearing tests where suction plays a significant role and constant water content shearing tests where the water content plays a significant role. However, suction is difficult to measure as an independent parameter as it is very complicated and time-consuming. The advantages of constant water constant tests are:

- The traditional suction loading test requires at least 10 days initial equilibrium for clay-type soils (Sivakumar, 1993; Sharma, 1998; Raveendiraraj, 2009), whereas constant water content loading tests can be carried out within one day after preparation (Abeyrathne, 2017);
- Due to the complexities of suction testing, sophisticated equipment and procedures are needed for long-term testing;
- In the geotechnical industry, constant moisture content testing is more common than constant suction testing; and,
- Measurements of suction under field conditions are more complicated than water content measurements and in many field senarios constant water content condition appled, for example soil compaction. In contrast, constant suction loading is not comman in field.

Abeyrathne (2017) experimentally validated the triaxial behaviour of loosely-compacted Speswhite kaolin considering different moisture contents including saturation. Figure 3.22 includes the constant water content shearing stress paths for saturation and water contents of 36.9% and 29.9% at 200 kPa confining stress. It is clear that the shear strength increases with decreasing moisture content at constant confining stress (PT8). In a similar manner, it is observed that the shear strength increases with increasing confining stress at constant water content (PT9) (Tarantino and Tombolato, 2005; Sheng et al., 2013; Abeyrathne, 2017). For both of these approaches, a reduction in v and increase in S_r are observed. In addition, similar to the highly over consolidation behaviour of suction-controlled triaxial tests, there was no indication of the highly over-consolidation behaviour of water-content controlled triaxial tests.

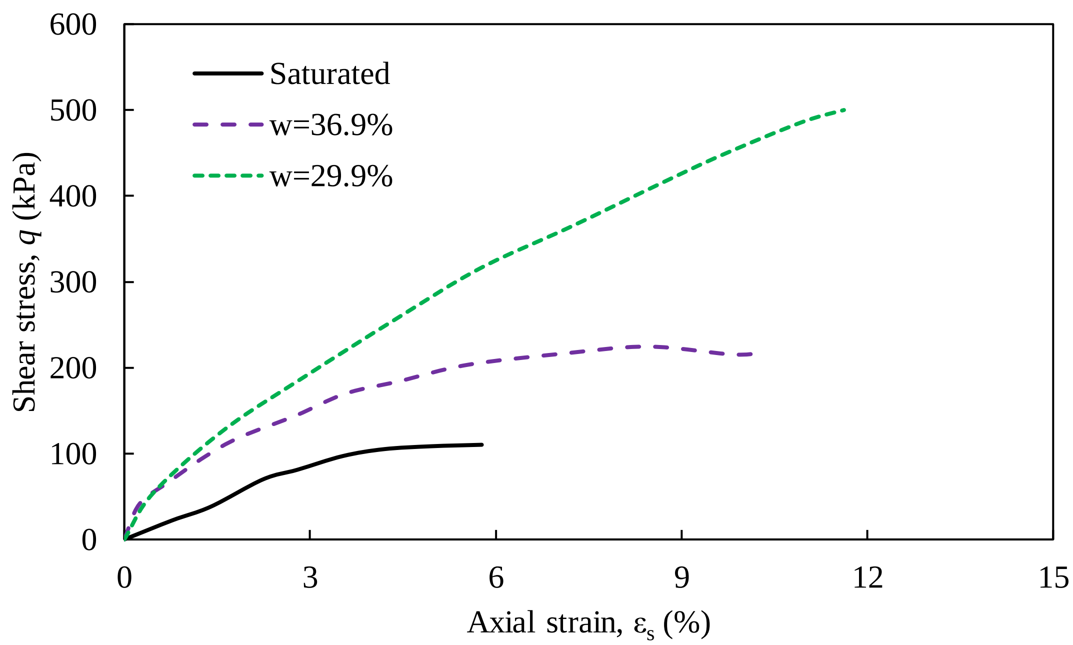

Figure 3.22: Constant water content shearing stress paths

3.13.3 Features of critical state hyperlines

In saturated soils, the volumetric yield is normally represented by the virgin or normally consolidated line (NCL) given by a straight line $v - \ln(p')$. This represents the loosest states in which soil can exist under different effective stress conditions, and unloading from yield will reach a lower v (or a denser state) at the same effective stress. For unsaturated soils, however, volumetric yield v needs to be considered as a function of p and s or e_w or S_r. This consideration can give rise to a yield surface (in contrast to a single line) representing the loosest states of unsaturated soil (e.g., Matyas and Radhakrishna, 1968; Fredlund and Morgenstern, 1976; Kodikara, 2012). In a similar manner, the critical state line for saturated soils is also given by a single straight line $v - \ln(p^*)$. Nevertheless, for unsaturated soils the variation due to s or e_w or S_r gives rise to a critical surface (in contrast to a single line).

Lloret-Cabot (2011) developed the volumetric yield surface and critical state surface as a function of p and s for the experimental data of Sivakumar (1993). It is evident from these experiments that for a certain net stress contour, v drops with decreasing s. In a similar manner, Abeyrathne (2017) developed the volumetric yield surface and critical state surface as a function of p and v_w, where the v drops with increasing v_w for a certain net stress contour (PT10). However, thorough experimental investigation of the critical state behaviour at the wet side of ATL has not been undertaken to date (see Figure 3.23).

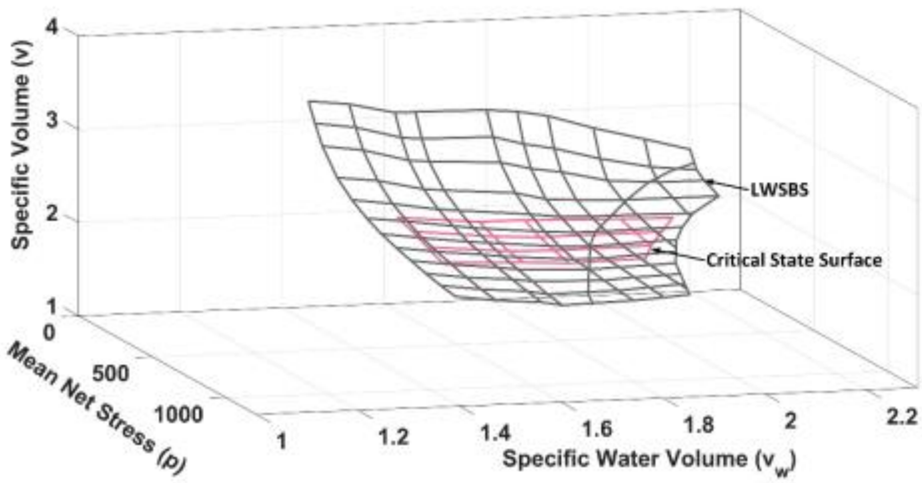

Figure 3.23: Comparison of LWSBS with the critical state surface for kaolin (extracted from Abeyrathne (2017))

As stated in Section 3.5, the compressibility contour for ATL lies below the saturation line, and the same behaviour is apparent in the triaxial experiments (PT11) reported by Sivakumar (1993), as shown in Figure 3.24.

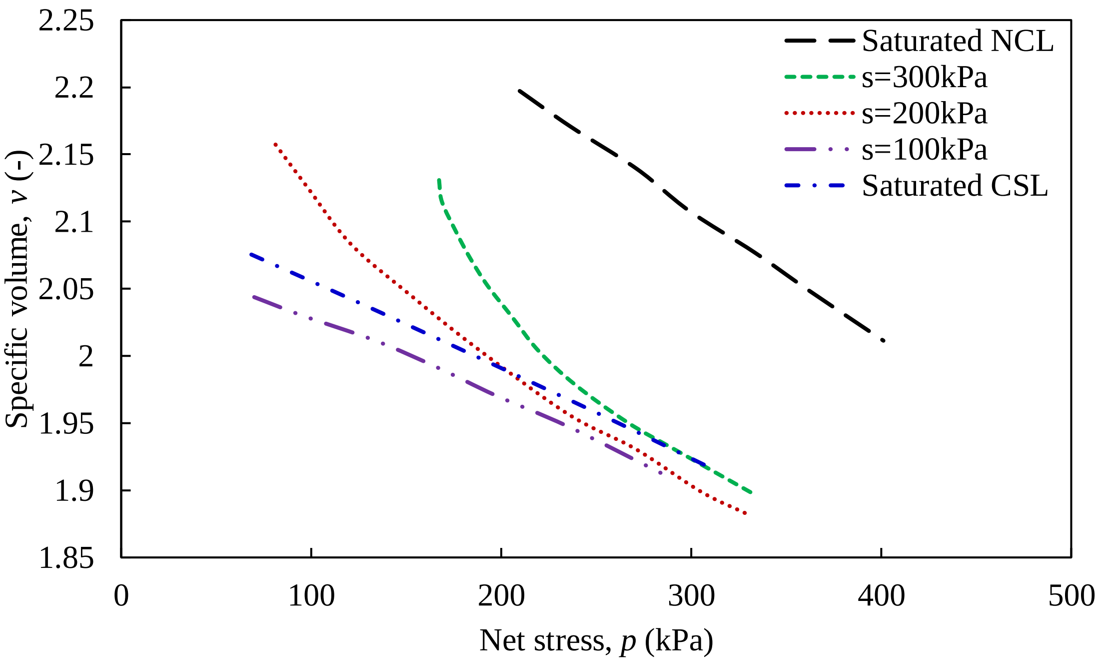

Figure 3.24: Constant suction critical state contours (Extracted from Sivakumar (1993))

3.14 Discussion of triaxial behaviour

Salient phenomenological observations of the triaxial behaviour relevant to constitutive modelling of the hydro-mechanical behaviour of unsaturated compacted soils are summarised below.

PT1	Shear strength increases with increasing suction and with the further increase of suction shear strength reduces.	Alonso et al. (1990); Sivakumar (1993); Colmenares Montanez (2002)
PT2	The associated with what needs to spell out behaviour of tensile strength with the increase of suction.	Fredlund et al. (1996); Shannon (2013); Sheng et al. (2013)
PT3	During the constant suction shearing stress path (i.e., drained stress path), S_r increases and v decreases for normally-consolidated and lightly-consolidated samples.	Raveendiraraj (2009); Li et al. (2017)
PT4	When the soil is highly over-consolidated, S_r decreases and v increases.	Casini et al. (2008); Zhou and Sheng (2015); Wu (2018); Wu et al. (2018)

PT5	For the same suction, higher confining stress (or higher cell pressure) results in higher shear strength.	Rahardjo et al. (2004); Vanapalli (2009); Sheng et al. (2011)
PT6	The change of specific volume during shearing after isotropic compaction shows a reduction and increases with increasing confining stress.	Sivakumar et al. (2010a)
PT7	The initial elastic stiffness for tests with initial wet dry cycles is lower compared to shear stress paths without wetting drying stress paths. In addition, the ultimate shear strength and friction angle are higher for shearing stress paths performed after drying compared to wetting.	Melinda et al. (2004); Raveendiraraj (2009)
PT8	For constant water content shearing tests, the shear strength increases with decreasing moisture content at constant confining stress. In addition, a reduction in v and an increase in S_r are observed.	Tarantino and Tombolato (2005); Sheng et al. (2013); Abeyrathne (2017)
PT9	For constant water content shearing tests, shear strength increases with increasing confining stress at constant water content. In addition, a reduction in v and an increase in S_r are observed.	Tarantino and Tombolato (2005); Sheng et al. (2013); Abeyrathne (2017)
PT10	For a certain net stress contour, v drops with decreasing s creating the critical state surface below the yield surface. In a similar manner, the volumetric yield surface and critical state surface can be developed as a function of p	Toll (1990); Sivakumar (1993); Abeyrathne (2017);Lloret - Cabot (2011)

	and v_w, where the v drops with increasing v_w for a certain net stress contour.	
PT11	For isotropic experiments, the compressibility contour for ATL lies below the saturation line, and the same behaviour is apparent in triaxial experiments.	Sivakumar (1993)

3.15 Conclusion

Based on reviews of published papers and theses, salient phenomenological features of the volumetric and triaxial behaviour of unsaturated soils have been compiled in this chapter. Special attention was given to relating these phenomenological features to the type of soil, initial soil state and the stress path followed. The ability to capture these phenomenological features by various constitutive modelling approaches was also examined. One specific aspect examined was coupling the soil water retention curve to soil deformation. It was identified that plastic volumetric strain is a suitable parameter to couple the shift of the water retention curve with soil deformation. A total of 25 phenomenological observations were identified for isotropic behaviour, whereas 11 phenomenological observations were identified for triaxial behaviour, which can be considered as advances in unsaturated soil constitutive modelling and will be taken into account in the development of the MPK model in the following chapters.

3.16 References

Abeyrathne, W. K. a. P. 2017. *A new modelling approach for compacted clayey soils using specific water volume as a state variable.* Ph.D. thesis, Monash University, Melbourne, Australia.

Airò Farulla, C., Ferrari, A. & Romero, E. 2010. Volume change behaviour of a compacted scaly clay during cyclic suction changes. *Canadian Geotechnical Journal,* 47**,** 688-703.

Alonso, E., Lloret, A., Gens, A. & Yang, D. Experimental behaviour of highly expansive double-structure clay. Proceedings of the first international conference on unsaturated soils, 1995 Paris,France.

Alonso, E., Pinyol, N. & Gens, A. 2013. Compacted soil behaviour: initial state, structure and constitutive modelling. *Géotechnique,* 63**,** 463-478.

Alonso, E., Vaunat, J. & Gens, A. 1999. Modelling the mechanical behaviour of expansive clays. *Engineering geology,* 54**,** 173-183.

Alonso , E. E., Gens , A. & Josa, A. 1990. A constitutive model for partially saturated soils. *Géotechnique,* 40(3)**,** pp.405-430.

Azoor, R. 2020. *Evaluation of soil aeration as applicable to underground metal corrosion.* PhD, Monash University.

Azoor, R., Deo, R., Birbilis, N. & Kodikara, J. 2019. On the optimum soil moisture for underground corrosion in different soil types. *Corrosion Science,* 159**,** 108116.

Barden, L., Madedor, A. O. & Sides, G. R. 1969. Volume change characteristics of unsaturated clay. *Journal of Soil Mechanics & Foundations Div*.

Bishop, A. & Donald, I. The experimental study of partly saturated soil in the triaxial apparatus. Proceedings of the 5th international conference on soil mechanics and foundation engineering, Paris, 1961. 13-21.

Bishop, A. W. 1959. The principle of effective stress. *Teknisk ukeblad,* 39**,** 859-863.

Bishop, A. W., Alpan, I., Blight, G. & Donald, I. 1960. Factors controlling the strength of partly saturated cohesive soils.

Bishop, A. W. & Blight, G. 1963. Some aspects of effective stress in saturated and partly saturated soils. *Geotechnique,* 13**,** 177-197.

Brackley, I. 1973. *Swell pressure and free swell in compacted clay*, National Building Research Institute, Council for Scientific and Industrial Research.

Brackley, I. J. 1975b. . A model for unsaturated clay structure and its application to swell behaviour. *Proceedings, 6th Regional Conference for Africa on Soil Mechanics and Foundation Engineering*

Buenfil, C., Romero, E., Lloret, A. & Gens, A. 2005. Hydro-mechanical behaviour of a clayey silt under isotropic compression. *Unsaturated Soils: Experimental Studies.* Springer.

Casini, F. 2008. Effetti del grado di saturazione sul comportamento meccanico di un limo. *Dottorato di Ricerca in Ingegneria Geotecnica.“Sapienza” Universit’a degli Studi di Roma*.

Casini, F., Vassallo, R., Mancuso, C. & Desideri, A. Application to a compacted soil of a Cam Clay model extended to unsaturated conditions. 1st European Conference on unsaturated soils, E-UNSAT 2008, 2008. Taylor & Francis Group, 609-615.

Chen, R. & Ng, C. W. 2013. Impact of wetting–drying cycles on hydro-mechanical behavior of an unsaturated compacted clay. *Applied clay science,* 86**,** 38-46.

Chu, T. & Mou, C. Volume change characteristics of expansive soils determined by controlled suction tests. proc. 3rd int. conf. on expansive soils. Haifa, 1973. 177-185.

Colmenares Montanez, J. E. 2002. *Suction and volume changes of compacted sand-bentonite mixtures.* Imperial College London (University of London).

Cunningham, M., Ridley, A., Dineen, K. & Burland, J. 2003. The mechanical behaviour of a reconstituted unsaturated silty clay. *Géotechnique,* 53**,** 183-194.

Das, A. P. & Thyagaraj, T. 2018. Collapse behaviour of compacted red soil. *International Journal of Geotechnical Engineering,* 12**,** 20-27.

Delage, P. 2008. Experimental unsaturated soil mechanics. *arXiv preprint arXiv:0803.1434*.

Delage, P. & Lefebvre, G. 1984. Study of the structure of a sensitive Champlain clay and of its evolution during consolidation. *Canadian Geotechnical Journal,* 21**,** 21-35.

Delage, P., Pereira, J. & Cui, Y. 2015. Collapse behaviour of a natural loess from Northern France. *Bioinspired Photonics: Optical Structures and Systems Inspired by Nature***,** 315.

Delage, P., Tessier, D. & Marcel-Audiguier, M. 1982. Use of the Cryoscan apparatus for observation of freeze-fractured planes of a sensitive Quebec clay in scanning electron microscopy. *Canadian Geotechnical Journal,* 19**,** 111-114.

Dexter, A. 2004a. Soil physical quality: Part II. Friability, tillage, tilth and hard-setting. *Geoderma,* 120**,** 215-225.

Dexter, A. 2004b. Soil physical quality: Part III: Unsaturated hydraulic conductivity and general conclusions about S-theory. *Geoderma,* 120**,** 227-239.

Dexter, A. R. 2004c. Soil physical quality: Part I. Theory, effects of soil texture, density, and organic matter, and effects on root growth. *Geoderma,* 120**,** 201-214.

Dif, A. & Bluemel, W. 1991. Expansive soils under cyclic drying and wetting. *Geotechnical Testing Journal,* 14(1)**,** pp.96-102.

Estabragh, A., Javadi, A. A. & Boot, J. C. 2004. Effect of compaction pressure on consolidation behaviour of unsaturated silty soil. *Canadian Geotechnical Journal,* 41**,** 540-550.

Estabragh, A., Soltani, A. & Javadi, A. 2018. Effect of pore water chemistry on the behaviour of a kaolin–bentonite mixture during drying and wetting cycles. *European Journal of Environmental and Civil Engineering*, 1-20.

Fleureau, J.-M., Kheirbek-Saoud, S., Soemitro, R. & Taibi, S. 1993. Behavior of clayey soils on drying–wetting paths. *Canadian geotechnical journal,* 30, 287-296.

Fleureau, J.-M., Verbrugge, J.-C., Huergo, P. J., Correia, A. G. & Kheirbek-Saoud, S. 2002. Aspects of the behaviour of compacted clayey soils on drying and wetting paths. *Canadian geotechnical journal,* 39, 1341-1357.

Fredlund, D., Houston, S. & Caicedo, B. 2013. Interpretation of soil-water characteristic curves when volume change occurs as soil suction is changed. *Advances in unsaturated soils,* 1, 15.

Fredlund, D. & Morgenstern, N. 1976. Constitutive relations for volume change in unsaturated soils. *Canadian Geotechnical Journal,* 13, 261-276.

Fredlund, D. G., Xing, A., Fredlund, M. D. & Barbour, S. 1996. The relationship of the unsaturated soil shear to the soil-water characteristic curve. *Canadian Geotechnical Journal,* 33, 440-448.

Fredlund, D. G. & Zhang, F. 2017. Effect of Initial Conditions on the Interpretation of Soil-Water Characteristic Curves (SWCCs) in Geotechnical Engineering. *PanAm Unsaturated Soils 2017.*

Gallipoli, D., Wheeler, S. & Karstunen, M. 2003. Modelling the variation of degree of saturation in a deformable unsaturated soil. *Géotechnique.,* 53, 105-112.

Gao, Y., Sun, D. A. & Zhou, A. 2015. Hydromechanical behaviour of unsaturated soil with different specimen preparations. *Canadian Geotechnical Journal,* 53, 909-917.

Gens, A. & Alonso, E. 1992. A framework for the behaviour of unsaturated expansive clays. *Canadian Geotechnical Journal,* 29, 1013-1032.

Gould, S. J., Kodikara, J., Rajeev, P., Zhao, X.-L. & Burn, S. 2011. A void ratio–water content–net stress model for environmentally stabilized expansive soils. *Canadian Geotechnical Journal,* 48, 867-877.

Imbert, C. & Villar, M. V. 2006. Hydro-mechanical response of a bentonite pellets/powder mixture upon infiltration. *Applied Clay Science,* 32, 197-209.

Islam, M. 2015. *A study of volumetric behaviour of compacted clayey soils in the void ratio, moisture ratio and net stress space.* Monash University. Faculty of Engineering. Department of Civil Engineering.

Islam, T. & Kodikara, J. 2015. Interpretation of the loading–wetting behaviour of compacted soils within the "MPK" framework. Part I: Static compaction 1. *Canadian Geotechnical Journal,* 53**,** 783-805.

Jennings, J. & Burland, J. 1962. Limitations to the Use of Effective Stresses.

Josa, A. 1988. *Un modelo eslastoplirstico para suelos no saturados.* Tesis Doctoral. Universitat PoWcnica de Catalunya, Barcelona.

Justo, J., Delgado, A. & Ruiz, J. The influence of stress-path in the collapse-swelling of soils at the laboratory. Fifth International Conference on Expansive Soils 1984: Preprints of Papers, 1984. Institution of Engineers, Australia, 67.

Karube, D. 1988. New concept of effective stress in unsaturated soil and its proving test. *In:* DONAGHE, R., CHANEY, R., AND SILVER, M. (ed.) *Advanced triaxial testing of soil and rock.* West Conshohocken, PA: ASTM International, 539-552.

Kassiff, G. & Shalom, A. B. 1971. Experimental relationship between swell pressure and suction. *Géotechnique,* 21**,** 245-255.

Kato, S. & Kawai, K. 2000. Deformation characteristics of a compacted clay in collapse under isotropic and triaxial stress state. *Soils and Foundations,* 40**,** 75-90.

Kaufhold, S., Baille, W., Schanz, T. & Dohrmann, R. 2015. About differences of swelling pressure—dry density relations of compacted bentonites. *Applied Clay Science,* 107**,** 52-61.

Khalili, N. 2017. Guidelines for the application of the effective stress principle to shear strength and volume change determination of unsaturated soils. *AGS VICTORIA 2017 Symposium.* Melbourne.

Khalili, N., Geiser, F. & Blight, G. 2004. Effective stress in unsaturated soils: review with new evidence. *International Journal of Geomechanics,* 4**,** 115-126.

Khalili, N. & Khabbaz, M. 1998. A unique relationship of chi for the determination of the shear strength of unsaturated soils. *Geotechnique,* 48**,** 681-687.

Kodikara, J. 2012. New framework for volumetric constitutive behaviour of compacted unsaturated soils. *Canadian Geotechnical Journal,* 49**,** 1227-1243.

Kodikara, J., Islam, T. & Rajeev, P. 2015. Interpretation of the loading–wetting behaviour of compacted soils within the "MPK" framework. Part II: Dynamic compaction 1. *Canadian Geotechnical Journal,* 53**,** 806-827.

Kodikara, J., Islam, T. & Shounthrarajah, A. 2018. Review of soil compaction: History and recent developments. *Transportation Geotechnics*.

Kodikara, J., Islam, T., Wijesooriya, S., Bui, H. & Burman, B. On controlling influence of the line of optimums on the compacted clayey soil behavior. Proceedings of the Sixth International Conference on Unsaturated Soils, UNSAT2014. Edited by N. Khalili, AR Russell, and A. Khoshghalb. Sydney, Australia, 2014. 219-225.

Li, Z.-S., Fleureau, J.-M. & Tang, L.-S. 2017. Aspects of compaction and drying–wetting curves of a subgrade clayey soil. *Géotechnique***,** 1-7.

Lloret-Cabot, M., Wheeler, S. J., Pineda, J. A., Romero, E. & Sheng, D. 2017a. From saturated to unsaturated conditions and vice versa. *Acta Geotechnica***,** 1-23.

Lloret-Cabot, M., Wheeler, S. J. & Sánchez, M. 2017b. A unified mechanical and retention model for saturated and unsaturated soil behaviour. *Acta Geotechnica,* 12**,** 1-21.

Lloret - Cabot, M. 2011. *Numerical modelling of coupled behaviour in unsaturated soils.* University of Strathclyde.

Lloret Morancho, A., Villar, M. V., Sanchez, M., Gens Solé, A., Pintado Llurba, X. & Alonso Pérez De Agreda, E. 2003. Mechanical behaviour of heavily compacted bentonite under high suction changes.

Loret, B. & Khalili, N. 2002. An effective stress elastic–plastic model for unsaturated porous media. *Mechanics of Materials,* 34**,** 97-116.

Marinho, F. A. & Stuermer, M. M. 2000. The influence of the compaction energy on the SWCC of a residual soil. *Advances in unsaturated geotechnics.*

Mašín, D. 2010. Predicting the dependency of a degree of saturation on void ratio and suction using effective stress principle for unsaturated soils. *International Journal for Numerical and Analytical Methods in Geomechanics,* 34**,** 73-90.

Maswoswe, J. 1985. *Stress paths for compacted soil during collapse due to wetting.* Imperial College London (University of London).

Matyas, E. L. & Radhakrishna, H. 1968. Volume change characteristics of partially saturated soils. *Géotechnique,* 18**,** 432-448.

Melinda, F., Rahardjo, H., Han, K. & Leong, E. C. 2004. Shear strength of compacted soil under infiltration condition. *Journal of Geotechnical and Geoenvironmental Engineering,* 130**,** 807-817.

Monroy, R. 2006. *The influence of load and suction changes on the volumetric behaviour of compacted London Clay.* Ph.D. thesis, Imperial College London (University of London).

Murata, T., Tateyama, K., Yamamoto, T., Yoshida, T. & Kawano, K. 2011. Experimental method of predicting the compaction effect in fill work practice. *Geotechnical Engineering Journal, JGS,* 5**,** 589-601.

Navarro, V., De La Morena, G., Yustres, Á., González-Arteaga, J. & Asensio, L. 2017. Predicting the swelling pressure of MX-80 bentonite. *Applied Clay Science,* 149**,** 51-58.

Nowamooz, H., Jahangir, E., Masrouri, F. & Tisot, J.-P. 2016. Effective stress in swelling soils during wetting drying cycles. *Engineering Geology,* 210**,** 33-44.

Nowamooz, H. & Masrouri, F. 2010. Influence of suction cycles on the soil fabric of compacted swelling soil. *Comptes Rendus Geoscience,* 342**,** 901-910.

Nuth, M. & Laloui, L. Advanced hydro-mechanical coupling for unified constitutive modelling of unsaturated soils. Unsaturated Soils: Advances In Geo-Engineering, 2008a. Crc Press-Taylor & Francis Group, 6000 Broken Sound Parkway Nw, Ste 300, Boca Raton, Fl 33487-2742 Usa, 559-565.

Nuth, M. & Laloui, L. 2008b. Effective stress concept in unsaturated soils: clarification and validation of a unified framework. *International journal for numerical and analytical methods in Geomechanics,* 32**,** 771-801.

Rahardjo, H., Heng, O. B. & Choon, L. E. 2004. Shear strength of a compacted residual soil from consolidated drained and constant water content triaxial tests. *Canadian Geotechnical Journal,* 41**,** 421-436.

Raveendiraraj, A. 2009. *Coupling of mechanical behaviour and water retention behaviour in unsaturated soils.* Ph.D. thesis, University of Glasgow.

Reynolds, W., Drury, C., Tan, C., Fox, C. & Yang, X. 2009. Use of indicators and pore volume-function characteristics to quantify soil physical quality. *Geoderma,* 152**,** 252-263.

Romero Morales, E. E. 1999. *Characterisation and thermo-hydro-mechanical behaviour of unsaturated Boom clay: an experimental study*, Universitat Politècnica de Catalunya.

Rondet, E., Delalonde, M., Ruiz, T. & Desfours, J. 2009. Identification of granular compactness during the kneading of a humidified cohesive powder. *Powder Technology,* 191**,** 7-12.

Shannon, B. 2013. *Fracture propagation of cohesive soils under tensile loading and desiccation.* PhD thesis, Monash University, Australia.

Sharma, R. S. 1998. *Mechanical behaviour of unsaturated highly expansive clays.* Ph.D. thesis, University of Oxford.

Sheng, D. 2011. Review of fundamental principles in modelling unsaturated soil behaviour. *Computers and Geotechnics,* 38**,** 757-776.

Sheng, D., Fredlund, D. G. & Gens, A. 2008. A new modelling approach for unsaturated soils using independent stress variables. *Canadian Geotechnical Journal,* 45**,** 511-534.

Sheng, D., Zhang, S. & Yu, Z. 2013. Unanswered questions in unsaturated soil mechanics. *Science China Technological Sciences,* 56**,** 1257-1272.

Sheng, D. & Zhou, A.-N. 2011. Coupling hydraulic with mechanical models for unsaturated soils. *Canadian Geotechnical Journal,* 48**,** 826-840.

Sheng, D., Zhou, A. & Fredlund, D. G. 2011. Shear strength criteria for unsaturated soils. *Geotechnical and Geological Engineering,* 29**,** 145-159.

Sivakumar, V. 1993. *A critical state framework for unsaturated soil.* Ph.D. thesis, University of Sheffield.

Sivakumar, V., Sivakumar, R., Boyd, J. & Mackinnon, P. 2010a. Mechanical behaviour of unsaturated kaolin (with isotropic and anisotropic stress history). Part 2: performance under shear loading. *Géotechnique,* 60**,** 595.

Sivakumar, V., Sivakumar, R., Murray, E., Mackinnon, P. & Boyd, J. 2010b. Mechanical behaviour of unsaturated kaolin (with isotropic and anisotropic stress history). Part 1: wetting and compression behaviour. *Géotechnique,* 60**,** 581-594.

Sivakumar, V., Tan, W., Murray, E. & Mckinley, J. 2006. Wetting, drying and compression characteristics of compacted clay. *Géotechnique,* 56.

Sivakumar, V. & Wheeler, S. 2000. Influence of compaction procedure on the mechanical behaviour of an unsaturated compacted clay. Part 1: Wetting and isotropic compression. *Géotechnique,* 50**,** 359-368.

Sun, D., Matsuoka, H. & Xu, Y. 2004. Collapse behavior of compacted clays in suction-controlled triaxial tests.

Sun, D. A., Sheng, D. & Xu, Y. 2007. Collapse behaviour of unsaturated compacted soil with different initial densities. *Canadian Geotechnical Journal,* 44**,** 673-686.

Tamagnini, R. 2004. An extended Cam-clay model for unsaturated soils with hydraulic hysteresis. *Géotechnique,* 54**,** 223-228.

Tarantino, A. & De Col, E. 2008. Compaction behaviour of clay. *Géotechnique,* 58**,** 199-213.

Tarantino, A. & Tombolato, S. 2005. Coupling of hydraulic and mechanical behaviour in unsaturated compacted clay. *Géotechnique,* 55**,** 307-317.

Tatsuoka, F. & Correia, A. G. 2018. Importance of Controlling the Degree of Saturation in Soil Compaction linked to Soil Structure Design. *Transportation Geotechnics,* 143**,** 556-565.

Tessier, D. & Pédro, G. 1984. Recherches sur le rôle des minéraux argileux dans l'organisation et le comportement des sols. *AFES, Livre Jubilaire***,** 223-234.

Thiam, M., Thuyet, D. Q., Saito, H. & Kohgo, Y. 2019. Performance of the tangential model of soil water retention curves for various soil texture classes. *Geoderma,* 337**,** 514-523.

Toll, D. 1990. A framework for unsaturated soil behaviour. *Géotechnique,* 40**,** 31-44.

Tripathy, S., Rao, K. S. & Fredlund, D. 2002. Water content-void ratio swell-shrink paths of compacted expansive soils. *Canadian geotechnical journal,* 39**,** 938-959.

Vanapalli, S. Shear strength of unsaturated soils and its applications in geotechnical engineering practice. Keynote Address. Proc. 4th Asia-Pacific Conf. on Unsaturated Soils. New Castle, Australia, 2009. 579-598.

Wang, Q., Cui, Y.-J., Tang, A. M., Delage, P., Gatmiri, B. & Ye, W.-M. 2014. Long-term effect of water chemistry on the swelling pressure of a bentonite-based material. *Applied Clay Science,* 87**,** 157-162.

Wheeler, S., Sharma, R. & Buisson, M. 2003. Coupling of hydraulic hysteresis and stress–strain behaviour in unsaturated soils. *Géotechnique,* 53**,** 41-54.

Wheeler, S. & Sivakumar, V. 1995. An elasto-plastic critical state framework for unsaturated soil. *Géotechnique,* 45**,** 35-53.

Wu, S. 2018. Rate dependent behaviour of unsaturated soil with different overconsolidation ratios and its constitutive modelling.

Wu, S., Zhou, A., Li, J., Kodikara, J. & Cheng, W.-C. 2018. Hydromechanical behaviour of overconsolidated unsaturated soil in undrained conditions. *Canadian Geotechnical Journal*.

Yong, R. N., Japp, R. D. & How, G. 1971. shear strength of partly saturated clays. *4th Asian Regional Conference on Soil Mechanics and Foundations Engineering.* Bangkok.

Zakaria, I. 1994. *Yielding of unsaturated soil.* Ph.D. thesis, University of Sheffield.

Zhang, X. & Lytton, R. L. 2008. Discussion of “A new modelling approach for unsaturated soils using independent stress variables”. *Canadian Geotechnical Journal,* 45**,** 1784-1787.

Zhou, A.-N., Sheng, D., Sloan, S. W. & Gens, A. 2012a. Interpretation of unsaturated soil behaviour in the stress–Saturation space, I: Volume change and water retention behaviour. *Computers and Geotechnics,* 43**,** 178-187.

Zhou, A.-N., Sheng, D., Sloan, S. W. & Gens, A. 2012b. Interpretation of unsaturated soil behaviour in the stress–saturation space: II: constitutive relationships and validations. *Computers and Geotechnics,* 43**,** 111-123.

Zhou, A. 2011. Constitutive modelling of hydromechanical behaviour of unsaturated soils| NOVA. The University of Newcastle's Digital Repository.

Zhou, A. & Sheng, D. 2015. An advanced hydro-mechanical constitutive model for unsaturated soils with different initial densities. *Computers and Geotechnics,* 63**,** 46-66.

Zhou, A., Wu, S. & Li, J. A Constitutive Model for Unsaturated Soils Using Degree of Capillary Saturation and Effective Interparticle Stress as Constitutive Variables. GeoShanghai International Conference, 2018. Springer, 79-86.

CHAPTER 4

The development of the MPK generalised model: Isotropic stress state

The majority of the work reported in this chapter has been published in the Computers and Geotechnics Journal: KODIKARA, J., JAYASUNDARA, C. & ZHOU, A. 2020. A generalised constitutive model for unsaturated compacted soils considering wetting/drying cycles and environmentally-stabilised line. *Computers and Geotechnics*, 118**,** 103332.

4 Introduction

The primary advantage of MPK approach is that the MPK framework revealed for the first time the direct relevance of the traditional compaction curves to constitutive soil modelling. In addition, much simpler and faster constant water content loading can be used to produce the experimental data required as input. However, the MPK framework does not incorporate suction as a constitutive variable, and no reference to the water retention curve is made. Hence, a new generalised MPK model is proposed considering the accumulation of plastic strains upon wet/dry cycles and environmental stabilisation. The development to isotropic stress state is presented in this Chapter.

As exemplified by Kodikara (2012), the transition from the air phase being continuous to the air phase being discontinuous (or vice-versa in relation to the continuity of the water phase) can be demarcated by the line of optimums (LOO) applicable to the traditional compaction curves. To capture this important phenomenological feature, this line is termed the air transition line (ATL) hereafter. Due to the respective continuity (or discontinuity) of the phases, it is argued that the net stress approach is valid only for the dry side of the ATL, whereas the effective stress approach is valid only for the wet side of the ATL. In fact, both these approaches have shown that they can reproduce phenomenological observations predominantly in these respective regions. Therefore, it follows that a generalised constitutive model that combines the relative merits of these approaches would be attractive and more comprehensive.

The present chapter introduces a generalised model following the above approach, and the general concepts are described as follows. Kodikara and co-workers (Kodikara, 2012; Islam and Kodikara, 2015; Kodikara et al., 2015; Abeyrathne et al., 2019) have demonstrated that the isotropic (or 1-D) compression yield surface, especially on the dry side of ATL, can be very easily developed through constant moisture content testing in contrast to suction-controlled testing, which can be exceedingly time-consuming. They have demonstrated that the volumetric yield surface developed in (p, v, v_w) space is a transformed view of the compression yield surface traditionally given in (p, v, s) through a series of constant suction p, v hyperlines. On the hand, the loading collapse (LC) curve (as in the BBM) can be considered as an intersection of any of these two surfaces corresponding to a certain level of soil plasticity. If Bishop's effective stress (which assumes the continuity of the water phase for the averaging of the influence of suction through the degree of saturation) is used, the yield surface on the wet side of ATL is uniquely described by a single line given by the normal consolidation line (NCL) for saturated soils. The required hydro-mechanical linkages to suction could then be captured by a void ratio-dependent soil water retention curve (SWRC). The dependence of the SWRC has been examined with respect to various governing parameters, including void ratio by Gallipoli et al. (2003),Pasha et al. (2017); net stress (Zhou et al., 2012); total volumetric strain (Khalili et al., 2008); and plastic volumetric strain (Wheeler et al., 2003; Lloret-Cabot et al., 2014; Lloret-Cabot et al., 2017). The relevance of these concepts in defining the SWRC is discussed in this chapter. Buscarnera and Di Prisco (2012) showed that the constitutive equations are written both the net stress and Bishop's stress approaches and can be transformed from one to the other considering the conjugate variable sets presented by Houlsby (1997). In the current model, this approach is used to transform the net stress-based constitutive equations developed through much easier constant moisture content testing to Bishop's effective stress-based equations, so that a smooth transition from unsaturated to saturated state can be maintained.

4.1 A description of the conceptual basis of the proposed model

Figure 4.1 shows an idealised volumetric yield surface or LWSBS (loading wetting state boundary surface) (marked by *ONML*) in the (p, v, v_{w}) space with linear idealisation using $\log(p)$. In Figure 4.1, the initial state of the dry soil grains at a nominal stress level of p_{o} is shown as state *L*, where the suction may be a high value like the 10^6 kPa applicable to an adsorbed moisture layer (Fredlund and Xing, 1994). With the addition of water at the nominal stress and subsequent mixing, the soil particles aggregate and undergo slippage, resulting in a decrease of volume until they reach a minimum value at state *M*, at which the soil air phase becomes discontinuous (or trapped) and can be considered to have reached the air transition line or ATL. With the further addition of water, swelling takes place with the reduction of suction and decreasing effective stress as the soil structure is relatively homogenised without much slippage, ideally reaching full saturation at state *N*. If the saturated soil from state *N* is normally consolidated to a state *X* with an operational stress of p ($p^* = p$ when $s = 0$) on the NCL, it undergoes some compressive plastic volumetric strain $\varepsilon^{\mathrm{p}}_{\mathrm{v,x}}$, and, in consistent with saturated soil mechanics, this strain is computed by assuming that the plastic strain at the nominal state *N* is zero. It is possible to identify the constant mean net stress contour for stress p_{op} on the volumetric yield surface, as shown by *ABC*. This contour also represents the loaded compaction curve corresponding to this stress, and when unloaded to the nominal stress plane represents the traditional compaction curve on the dry side of LOO or ATL.

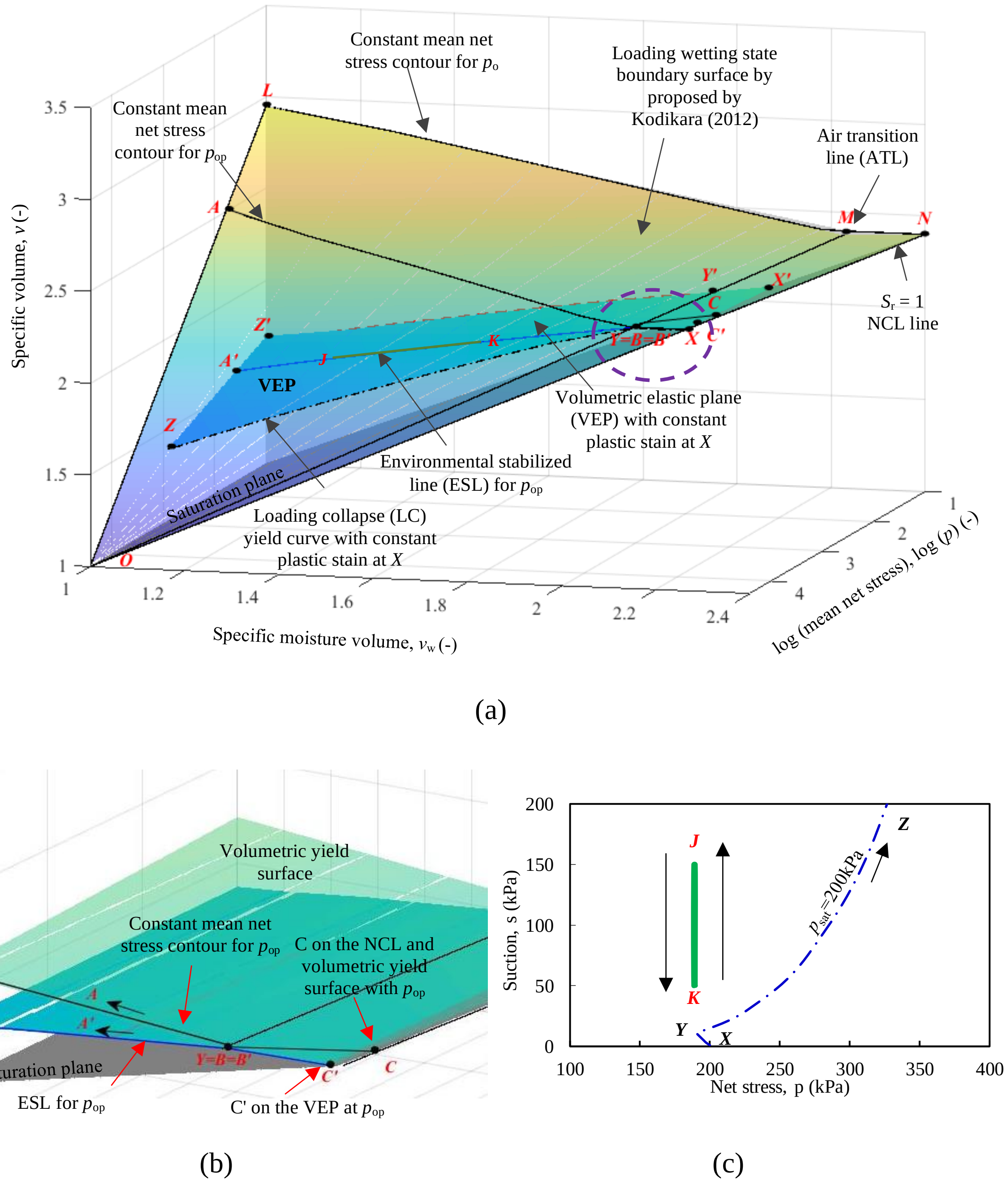

Figure 4.1(a) Generalised MPK model in (v, v_w, p) space (b) Exaggerated view of wet side of generalised model in (v, v_w, p) space (c) Behaviour of environmentally stabilised soil in (s, p) plane

Similarly, it is possible to identify a line on the volumetric yield surface with constant plastic strain pinned at *X* given by (*XYZ*), which is the LC curve corresponding to that plastic strain.

Here, *XY* represents the part corresponding to the wet side of the ATL with constant Bishop's effective stress, whereas *YZ* represents the part on the dry side of the ATL on the volumetric yield surface. This curve in the traditional (s, p) plane is shown in Figure 4.1(c). When the mean net stresses on the LC curve are unloaded to the nominal stress level p_{o}, a volumetric elastic plane (VEP) given by *XX'Z'Z* is generated, which is an elastic plane corresponding to the plastic strain $\varepsilon^{\mathrm{p}}_{\mathrm{v,x}}$. One can view this elastic plane as analogous to the "elastic wall" used in critical state soil mechanics (CSSM) (Schofield and Wroth, 1968). One of the auxiliary 2-D figures of Figure 4.1(a) is Figure 4.8, which includes the constant net stress and suction contours, which are discussed in the section on the general characteristics of the model. In addition, later, in Figures 4.9 and 4.11, further elaboration of Figure 4.1 is given in the (s^*, p), (S_{r}, p) and (S_{r}, s^*) planes.

A clarification of the enivironmentally stabilised line (ESL) with respect to Figure 4.1 is presented here. In Figure 4.1, it is also possible to identify the line *A'B'C'* on the volumetric elastic plane corresponding to the operational stress (p_{op}) (the intersection line of the above elastic plane and the vertical plane passing through p_{op}). This line is referred to as ESL (*A'B'C'*), and the *Y* coincides with *B* and *B'* at the ATL. The gradient of the ESL is given by $\left(\dfrac{\partial e_{\mathrm{w}}}{\partial e}\right)_{p_{\mathrm{op}}}$ designated as α_{ES}, a material property (also referred to as the hydric coefficient). This ESL corresponds to the environmentally-stabilised wetting/drying paths of soil depicting elastic behaviour following a large number of wet/dry cycles at stress p_{op}. Therefore, when the soil is wetting or drying on the ESL (as shown by paths *JK*), the LC yield curve does not change or shift inward or outward on the (s, p) plane (Figure 4.1(c)). However, when wetting or drying paths starting from other initial states at p_{op} deviate from the ESL, the LC curve shifts, incurring additional plastic strains and either softening (inward) or hardening (outward) depending on the initial α or $\left(\dfrac{\partial e_{\mathrm{w}}}{\partial e}\right)_{p_{\mathrm{op}}}$ and eventually approaching that corresponding to the ESL.

4.2 Choice of conjugate constitutive variables and their relationships

It was noted earlier that the current model utilises both the net stress and Bishop's effective stress approaches, exploiting the relative merits of the two approaches in the domains of the dry and wet sides of ATL. A brief explanation is given below of how this can be achieved. Following Houlsby (1997), the incremental work per unit volume of unsaturated soil ($\mathrm{d}W$) can be written as in Equations (4.1) and (4.2), ignoring the mechanical dissipation associated with fluid flow and air compressibility along with the influence of the contractile skin. In addition, the work equations developed by Houlsby (1997) are approximate, primarily due to lack of consideration of the contractile skin effects and the differentiation of bounded water. Researchers such as Lu and Likos (2004) and Cho and Santamarina (2001) have carried out pioneering work explaining the influence of these effects, especially in relation to particulate materials. However, for the present research, these effects are assumed to be negligible, as is the case in the other leading unsaturated constitutive models (Alonso et al., 1990; Alonso et al., 1999; Wheeler et al., 2003; Sheng et al., 2008; Zhou et al., 2012; Pasha et al., 2019). Both volumetric and deviatoric components are shown here, but emphasis is placed on the volumetric component, since the deviatoric component is the same in both approaches, and it is possible to use either approach to capture it.

$$\mathrm{d}W = p\,\mathrm{d}\varepsilon_{\mathrm{v}} + \frac{s}{1+e}\mathrm{d}e_{\mathrm{w}} + q\mathrm{d}\varepsilon_{\mathrm{s}} \tag{4.1}$$

$$\mathrm{d}W = (p + S_{\mathrm{r}}s)\,\mathrm{d}\varepsilon_{\mathrm{v}} - \phi s\,\mathrm{d}S_{\mathrm{r}} + q\mathrm{d}\varepsilon_{\mathrm{s}} \tag{4.2}$$

where, p is the mean net stress, $\mathrm{d}\varepsilon_{\mathrm{v}} = \left(\frac{\text{-de}}{1+e}\right)$ is the change in volumetric strain, s is the suction, e is the void ratio, $e_{\mathrm{w}}(=eS_{\mathrm{r}})$ is the moisture ratio, q is the shear stress, $\mathrm{d}\varepsilon_{\mathrm{s}}$ is the change in shear strain, S_{r} is the degree of saturation and ϕ is the porosity. In Equations (4.1) and (4.2), the respective work conjugates for external energy input based on stress and the hydromechanical internal work based on suction are shown, highlighting the possible combinations of constitutive relationships that can be developed (Gens, 2010). It is noteworthy that in Equation (4.1), the constitutive relationship between p and $\mathrm{d}\varepsilon_{\mathrm{v}}$ can be better captured (as the compression yield lines or compression yield surface) keeping $\mathrm{d}e_{\mathrm{w}} = 0$ (with constant moisture content testing), whereas the hydromechanical work (through SWRC) is better captured as a constitutive relationship between $\left(\frac{s}{1+e}\right)$ and $\mathrm{d}e_{\mathrm{w}}$ keeping $\mathrm{d}\varepsilon_{\mathrm{v}}$ =0, $\mathrm{d}e$ =0 with constant void ratio testing, which is practically difficult, but has been advocated by several researchers (c.f., Vanapafli et al., 1999; Karube and Kawai, 2001; Gallipoli et al., 2003; Pasha et al., 2017). This aspect is addressed later in this chapter. Similarly, in Equation (4.2), the constitutive relationship between $p^{*}(=p+S_{\mathrm{r}}s)$ and $\mathrm{d}\varepsilon_{\mathrm{v}}$ can be better captured by keeping $\mathrm{d}S_{\mathrm{r}}$ =0 (with constant S_{r} testing) (Zhou et al., 2012; Zhou et al., 2018), whereas the hydromechanical work is better captured as a constitutive relationship between $s^{*}(=\phi s)$ and $\mathrm{d}S_{\mathrm{r}}$ keeping $\mathrm{d}\varepsilon_{\mathrm{v}}$ =0, $\mathrm{d}e$ =0 with constant void ratio testing, as noted above. As was highlighted earlier, the former is more suitable for the dry side of the ATL (as in the BBM), and the latter is more suitable for the wet side of the ATL, which provides a direct transition to saturated states (as in other models, such as that of Wheeler et al. (2003)). Therefore, the relative merits of these relationships are exploited through the transformation of these relationships as follows.

Following Buscarnera and Di Prisco (2012), the hydro-mechanical coupled incremental formulation of Equation (4.1) can be given as follows:

$$\begin{Bmatrix} \mathrm{d}p \\ \dfrac{\mathrm{d}s}{1+e} \end{Bmatrix} = \begin{bmatrix} \Delta_{\mathrm{mm}} & \Delta_{\mathrm{mh}} \\ \Delta_{\mathrm{hm}} & \Delta_{\mathrm{hh}} \end{bmatrix} \begin{Bmatrix} \mathrm{d}\varepsilon_{\mathrm{v}} \\ -\mathrm{d}e_{\mathrm{w}} \end{Bmatrix} = \Delta_{\mathrm{HM}} \begin{Bmatrix} \mathrm{d}\varepsilon_{\mathrm{v}} \\ -\mathrm{d}e_{\mathrm{w}} \end{Bmatrix} \tag{4.3}$$

where, the matrix Δ_{HM} represents the coupled hydro-mechanical constitutive relationships, where Δ_{mm} is the mechanical component, Δ_{mh} and Δ_{hm} are the coupling components, and Δ_{hh} is the hydraulic component. Similarly, the transformation of Equation (4.2) can be given by Equation (4.4):

$$\begin{Bmatrix} \mathrm{d}p^{*} \\ \mathrm{d}s^{*} \end{Bmatrix} = \begin{bmatrix} D_{\mathrm{mm}} & D_{\mathrm{mh}} \\ D_{\mathrm{hm}} & D_{\mathrm{hh}} \end{bmatrix} \begin{Bmatrix} \mathrm{d}\varepsilon_{\mathrm{v}} \\ -\mathrm{d}S_{\mathrm{r}} \end{Bmatrix} = D_{\mathrm{HM}} \begin{Bmatrix} \mathrm{d}\varepsilon_{\mathrm{v}} \\ -\mathrm{d}S_{\mathrm{r}} \end{Bmatrix} \tag{4.4}$$

where, $p^{*}(=p+S_{\mathrm{r}}s)$ the Bishop's effective stress and $s^{*}(=\phi s)$ is the modified suction. The matrix D_{HM} represents the coupled hydro-mechanical constitutive relationships, and D_{HM} shows the same corresponding behaviours as in Equation (4.3). The constitutive matrix D_{HM} of

Equation (4.3) can be obtained from Δ_{HM} of Equation (4.4) through transformation matrices as follows:

$$D_{\mathrm{HM}} = S_{\mathrm{HM}} \Delta_{\mathrm{HM}} \left[T_{\mathrm{HM}}\right]^{-1} \tag{4.5}$$

where, $S_{\mathrm{HM}} = \begin{bmatrix} s_{\mathrm{mm}} & s_{\mathrm{mh}} \\ s_{\mathrm{hm}} & s_{\mathrm{hh}} \end{bmatrix}$ and $T_{\mathrm{HM}} = \begin{bmatrix} t_{\mathrm{mm}} & t_{\mathrm{mh}} \\ t_{\mathrm{hm}} & t_{\mathrm{hh}} \end{bmatrix}$ which define the two transformation matrices given in Equations (4.6) and (4.7) and detailed derivations of both matrices are presented in Appendix B for the isotropic stress states.

$$\begin{Bmatrix} \mathrm{d}p^* \\ \mathrm{d}s^* \end{Bmatrix} = \begin{bmatrix} s_{\mathrm{mm}} & s_{\mathrm{mh}} \\ s_{\mathrm{hm}} & s_{\mathrm{hh}} \end{bmatrix} \begin{Bmatrix} \mathrm{d}p \\ \dfrac{\mathrm{d}s}{1+e} \end{Bmatrix} \tag{4.6}$$

$$\begin{Bmatrix} \mathrm{d}\varepsilon_{\mathrm{v}} \\ -\mathrm{d}S_{\mathrm{r}} \end{Bmatrix} = \begin{bmatrix} t_{\mathrm{mm}} & t_{\mathrm{mh}} \\ t_{\mathrm{hm}} & t_{\mathrm{hh}} \end{bmatrix} \begin{Bmatrix} \mathrm{d}\varepsilon_{\mathrm{v}} \\ -\mathrm{d}e_{\mathrm{w}} \end{Bmatrix} \tag{4.7}$$

Owing to the double structural behaviour of unsaturated soils (Alonso et al., 2013), the proposed generalised model is based on both approaches: the Bishop's stress controls the wet side of the ATL, and the mean net stress controls the dry side of the ATL. Hence, the derivation of the dry side is based on Equation (4.1), and the derivations of the wet side are based on Equation (4.2). However, the final equations are based on Equation (4.2), and the stress transformation is carried out, as shown above. After the transformations, the final work conjugates in the proposed model are used as $p^*\mathrm{d}\varepsilon_{\mathrm{v}}$ and $s^*\mathrm{d}S_{\mathrm{r}}$, where the p^*, s^* are stresses and $\mathrm{d}\varepsilon_{\mathrm{v}}$ and $\mathrm{d}S_{\mathrm{r}}$ are strains within the constitutive relationships. A detailed derivation of the transformation matrices (which requires the introduction of the constitutive relations in the following sections) is given in Appendix B.

4.3 Formulation of theoretical equations for the proposed model

4.3.1 Normal compression yield surface in the (v, v_{w}, p) space

The volumetric yield surface in the (v, v_{w}, p) space on the dry side of the ATL is based on the volumetric yield surface developed through constant moisture content testing, as discussed earlier. The uniqueness of the volumetric yield surface for wetting and loading/unloading paths has been demonstrated for 1-D stress states by Islam and Kodikara (2015), and Kodikara et al.

(2015), and for isotropic stress states by Abeyrathne (2017) for both less reactive compacted kaolin and highly reactive Merri Creek soil. More recently, the uniqueness of the volumetric yield surface for paths involving drying has also been demonstrated by Jayasundara et al. (2019). Abeyrathne et al. (2019) introduced the volumetric yield surface by a series of constant moisture content (constant v_{w}) hyperlines given by Equation (4.8).

$$v = v_{\mathrm{o}} - \lambda(v_{\mathrm{w}}) \ln(p / p_{\mathrm{o}}) \tag{4.8}$$

where, v_{o} is the nominal specific volume at the nominal stress p_{o} and $\lambda(v_{\mathrm{w}})$ is the compression index at constant v_{w} , and v_{o} and $\lambda(v_{\mathrm{w}})$ are approximated as linear functions of v_{w} as given by Equations (4.9) and (4.10).

$$\lambda(v_{\mathrm{w}}) = C_1 - k_1(v_{\mathrm{w}} - v_{\mathrm{w}}^{\mathrm{L}}) \tag{4.9}$$

$$v_{\mathrm{o}} = C_2 - k_2(v_{\mathrm{w}} - v_{\mathrm{w}}^{\mathrm{L}}) \tag{4.10}$$

In Equations (4.9) and (4.10), $v_{\mathrm{w}}^{\mathrm{L}}$ is the specific moisture volumes at the nominal stress on ATL and C_1 , k_1 , C_2 and k_2 are assumed to be constants for a particular soil, which can be found by fitting experimental data. However, the intention of the current model is to transform this surface into (v, S_{r}, p) space so that it will be compatible with Equation (4.2). Therefore, the compressibility gradient ($\lambda(S_{\mathrm{r}})$) and nominal specific volume (v_{o}) are defined in terms of S_{r} as given by Equations (4.11) and (4.12):

$$\lambda(S_{\mathrm{r}}) = \lambda_{\mathrm{L}} - k_3(S_{\mathrm{r}} - S_{\mathrm{r}}^{\mathrm{L}}) \tag{4.11}$$

$$v_{\mathrm{o}} = v_{\mathrm{o}}^{\mathrm{L}} - k_4(S_{\mathrm{r}} - S_{\mathrm{r}}^{\mathrm{L}}) \tag{4.12}$$

where, $\lambda(S_{\mathrm{r}})$ is the compression index at constant S_{r} and $S_{\mathrm{r}}^{\mathrm{L}}$ is the degree of saturation on ATL. In particular, λ_{L} and $v_{\mathrm{o}}^{\mathrm{L}}$ arise from the definition of ATL, which can be depicted as:

$$v = v_{\mathrm{o}}^{\mathrm{L}} - \lambda_{\mathrm{L}} \ln(p / p_{\mathrm{o}}) \tag{4.13}$$

Further, k_3 and k_4 are determined from the rate of change in compressibility ($\lambda(S_{\mathrm{r}})$) and change in specific volume (v_{o}) with the change of S_{r} . The specific volume (v) on the volumetric yield surface can be written as:

$$v = v_o - \lambda(S_r)\ln(p / p_o) \tag{4.14}$$

Equation (4.14) is not valid for some soil types, especially for those with lower S_r. In addition, as noted earlier, this volumetric yield surface is valid for the dry side of the ATL, i.e., $S_r \le S_r^L$. For the wet side of the ATL, i.e., $S_r > S_r^L$, the compression index $\lambda(S_r)$ is assumed to be constant with the value of the saturated soils λ_{sat}, since Bishop's effective stress is considered valid. It should also be noted that for some soils, Equation (4.12) may not be valid (or line *LM* may not be a single straight line in Figure 4.1(a)) all the way to $S_r = 0$ (c.f.,Islam and Kodikara, 2015). In such cases, the practical validity of this equation is limited to S_r greater than 30 or 40%. This behaviour may also be reflected in soil compaction curves which show an upward trend (or downward trend in the v, v_w plane) towards $S_r = 0$.

4.3.2 Loading – unloading elastic behaviour

Associated with constant plastic strain ε_v^p, elastic loading/unloading and wetting/drying (after environmental stabilisation) take place on a volumetric elastic plane, as depicted in Figure 4.1. The gradients of this plane are defined by two orthogonal gradients $\kappa(v_w)$ ($\left(\partial v / \partial p\right)_{v_w}$ loading/unloading) and α_{ES} (constant net stress wetting/drying, $\left(\partial v / \partial v_w\right)_p$), giving $dv = \alpha_{ES}\, dv_w + \left(\frac{\kappa(v_w)}{p}\right) dp$. This equation has a resemblance to the equation in BBM for soil's elastic response, except that it is based on suction and all wetting/drying behaviour is assumed to be elastic. To be compatible with the energetics in Equation (4.2), dv^e can be written as (see Appendix A for full derivation):

$$dv^e = -\kappa(S_r)\frac{dp}{p} \tag{4.15}$$

$$\kappa(S_r) = -\frac{\kappa(v_w)}{1 - \alpha_{ES} S_r} \tag{4.16}$$

Similar to the yield curves, the above equations are valid only for the dry side, i.e., $S_r \le S_r^L$. For the wet side of the ATL, i.e., $S_r > S_r^L$, the compression index $\kappa(S_r)$ for the constant degree of saturation is assumed to be a constant κ_{sat}, since Bishop's effective stress is considered to be valid.

4.3.3 Loading- collapse (LC) yield curve

In the current model, the LC yield curve is defined for a certain plastic volumetric plastic strain ε_v^p and is derived from the volumetric yield surface developed through constant moisture content testing. In Figure 4.2, *ADEH* shows a typical LC curve, with plastic strain corresponding to the value at the NCL (at *A*) with the assumption of zero plastic strain at *N*.

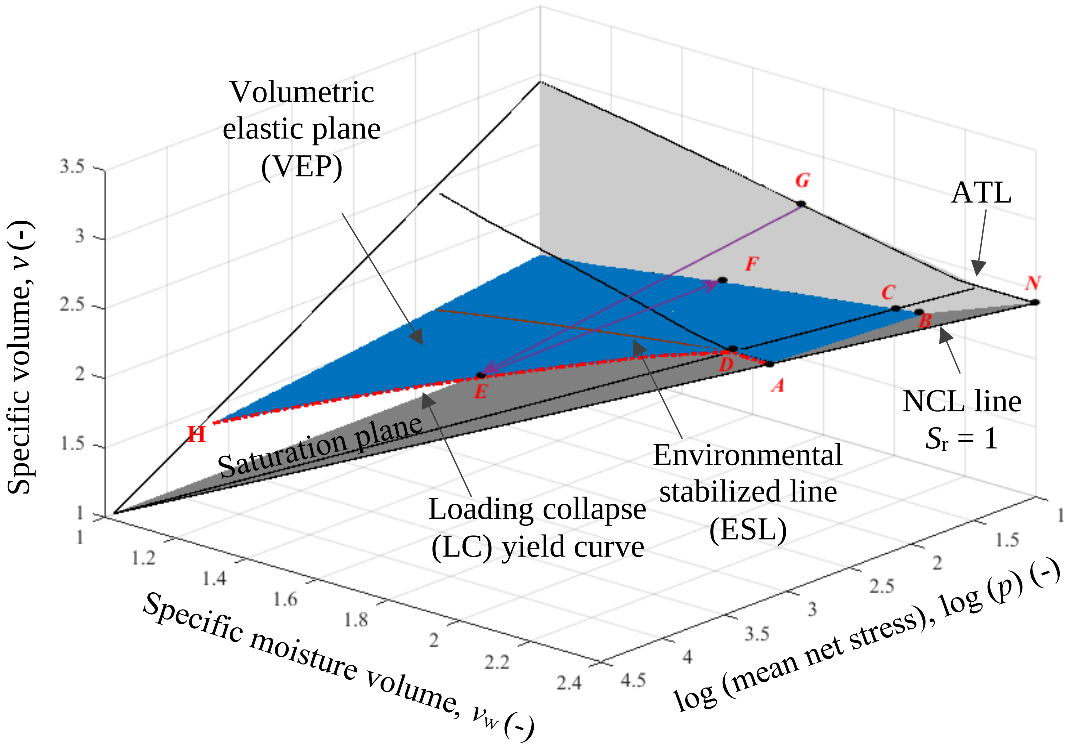

Figure 4.2: Loading – collapse yield curve

Table 4.1: Descriptions of states of the LC curve in Figure 4.2

Position	Specific volume and volumetric strain	Remarks

A	$v_A, (\varepsilon_v)_A$, $(\varepsilon_v^p)_A$	$(\varepsilon_v^p)_A$ is the plastic volumetric strain at position *A*, which is the hinging point of the volumetric elastic plane to the saturation line
B	$v_B, (\varepsilon_v)_B$, $(\varepsilon_v^p)_B$	$(\varepsilon_v^p)_A = (\varepsilon_v^p)_B$ (on the same volumetric elastic plane), the state achieved after unloading from state *A*. B is on the saturated plane
C	$v_C, (\varepsilon_v)_C$, $(\varepsilon_v^p)_C$	$(\varepsilon_v^p)_A = (\varepsilon_v^p)_C$ (on the same volumetric elastic plane), the state achieved after elastic drying from state *B*
D	$v_D, (\varepsilon_v)_D$, $(\varepsilon_v^p)_D$	Since Bishop's effective stress controls the wet side, $v_A = v_D$ and since both are in one volumetric elastic plane: $(\varepsilon_v^p)_A = (\varepsilon_v^p)_D$. D is on the ATL.
E	$v_E, (\varepsilon_v)_E$, $(\varepsilon_v^p)_E$	$(\varepsilon_v^p)_A = (\varepsilon_v^p)_E$ (on the same volumetric elastic plane), the state achieved after drying from state *C* on the nominal stress plane with a gradient of α_{ES}
F	$v_F, (\varepsilon_v)_F$, $(\varepsilon_v^p)_F$	$(\varepsilon_v^p)_A = (\varepsilon_v^p)_F$ (on the same volumetric elastic plane), the state achieved after loading from state E to the volumetric yield surface
G	$v_G, (\varepsilon_v)_G$, $(\varepsilon_v^p)_G$	G corresponds to the state on the volumetric yield surface at nominal stress, from which soil can be loaded at constant S_r to reach *F*. At G, $(\varepsilon_v^p)_G < 0 = N\ (\varepsilon_v^p)_N$

4.3.3.1 LC curve and associated unloading behaviour for the wet side ($S_r > S_r^L$)

For this region, *AD* represents the part of the LC curve as a constant specific volume line ($v_A = v_D$) since the effective stress is constant (Nuth and Laloui, 2008; Alonso et al., 2013; Lloret-Cabot and Wheeler, 2018). The specific volume at *A* (v_A) can be found from NCL as given in Equation (4.17). The stress paths *AB* (saturated unloading to p_o), *BC* (elastic drying at p_o)

and *CD* (elastic reloading along constant $S_{\mathrm{r}}^{\mathrm{L}}$) are based on the gradient of κ_{sat} in the effective stress space, as given by Equations (4.17), (4.18), (4.19) and, (4.20).

$$v_{\mathrm{A}} = v_{\mathrm{N}} - \lambda_{\mathrm{sat}} \ln(p_{\mathrm{A}} / p_{\mathrm{o}}) \tag{4.17}$$

$$v_{\mathrm{A}} = v_{\mathrm{B}} - \kappa_{\mathrm{sat}} \ln(p_{\mathrm{A}} / p_{\mathrm{o}}) \tag{4.18}$$

$$v_{\mathrm{C}} = v_{\mathrm{B}} - \kappa_{\mathrm{sat}} \ln\left(\frac{p_{\mathrm{o}} + S_{\mathrm{r}}^{\mathrm{L}} s^{L}}{p_{\mathrm{o}}}\right) \tag{4.19}$$

$$v_{\mathrm{D}} = v_{\mathrm{C}} - \kappa_{\mathrm{sat}} \ln\left(\frac{p_{\mathrm{D}} + S_{\mathrm{r}}^{\mathrm{L}} s^{L}}{p_{\mathrm{o}} + S_{\mathrm{r}}^{\mathrm{L}} s^{L}}\right) = v_{\mathrm{A}} \tag{4.20}$$

where, s^{L} is the suction at the ATL, which depends on the net stress. In addition, since Bishop's effective stress at *A* is equal to Bishop's effective stress at *D* ($p^*_{\mathrm{A}} = p^*_{\mathrm{D}}$), $S_{\mathrm{r}}^{\mathrm{L}} < 1$, and $s^{\mathrm{L}} > 0$, the net stress at state *A* is higher than that at state *D* ($p_{\mathrm{A}} > p_{\mathrm{D}}$). In the above equations, p_{D} and s^{L} are still unknown. Using the $v - p$ relationships for NCL and ATL, Section 4.3.5 gives s^{L} as given by:

$$s^{\mathrm{L}} = \frac{p_{\mathrm{o}}}{S_{\mathrm{r}}^{\mathrm{L}}}\left[e^{\left(\frac{N_{\mathrm{sat}} - v_{\mathrm{A}}}{\lambda_{\mathrm{sat}}}\right)} - e^{\left(\frac{v_{\mathrm{o}}^{\mathrm{L}} - v_{\mathrm{A}}}{\lambda_{\mathrm{L}}}\right)}\right] \tag{4.21}$$

where, $v_{\mathrm{o}}^{\mathrm{L}}$ is the specific volume of nominal stress p_{o} on the LC yield stress surface for ATL and λ_{L} is the compression index for the ATL on the volumetric yield surface , which is lower than λ_{sat} . Hence, the yield stress p_{D} for the ATL can be written as:

$$p_{\mathrm{D}} = p_{\mathrm{A}} - s^{\mathrm{L}} S_{\mathrm{r}}^{\mathrm{L}} \tag{4.22}$$

4.3.3.2 LC curve and associated unloading behaviour for the dry side ($S_{\mathrm{r}} \le S_{\mathrm{r}}^{\mathrm{L}}$)

The dry side of the LC curve for a specific $\varepsilon_{\mathrm{v}}^{\mathrm{p}}$ is based on the yielding response on the volumetric yield surface (stress path *GF*, Figure 4.2) and the elastic response on the VEP (stress path *CE* and *EF*). Considering the stress path *GF* and *EF* given in Figure 4.2, the specific volume at the soil states *E*, *F*, *G* for particular yield stress (p_{y}) can be written as:

$$v_{\mathrm{F}} = v_{\mathrm{G}} - \lambda(S_{\mathrm{r}})\ln(p_{\mathrm{y}} / p_{\mathrm{o}}) \tag{4.23}$$

$$v_{\mathrm{F}} = v_{\mathrm{E}} - \kappa(S_{\mathrm{r}})\ln(p_{\mathrm{y}} / p_{\mathrm{o}}) \tag{4.24}$$

$$v_{\mathrm{E}} = \frac{v_{\mathrm{C}}(1-\alpha_{\mathrm{ES}}S_{\mathrm{r}}^{\mathrm{L}}) - \alpha_{\mathrm{ES}}(S_{\mathrm{r}} - S_{\mathrm{r}}^{\mathrm{L}})}{(1-\alpha_{\mathrm{ES}}S_{\mathrm{r}})} \tag{4.25}$$

$$v_{\mathrm{G}} = v_{\mathrm{o}}^{\mathrm{L}} - k_4(S_{\mathrm{r}} - S_{\mathrm{r}}^{\mathrm{L}}) \tag{4.26}$$

In Equations (4.25) and (4.26), v_{E} is obtained considering the gradient of ESL and v_{G} is obtained from Equation A4. Equating v_{F} from Equations (4.23) and (4.24), the LC yield curve can be given as:

$$p_{\mathrm{y}} = p_{\mathrm{o}} e^{\left(\frac{v_{\mathrm{G}} - v_{\mathrm{E}}}{\lambda(S_{\mathrm{r}}) - k(S_{\mathrm{r}})}\right)} = p_{\mathrm{o}} e^{\left(\frac{\left[v_{\mathrm{o}}^{\mathrm{L}} - k_4(S_{\mathrm{r}} - S_{\mathrm{r}}^{\mathrm{L}})\right] - \frac{v_{\mathrm{C}}(1-\alpha_{\mathrm{ES}}S_{\mathrm{r}}^{\mathrm{L}}) - \alpha_{\mathrm{ES}}(S_{\mathrm{r}} - S_{\mathrm{r}}^{\mathrm{L}})}{(1-\alpha_{\mathrm{ES}}S_{\mathrm{r}})}}{\lambda(S_{\mathrm{r}}) - k(S_{\mathrm{r}})}\right)} \tag{4.27}$$

Here, the specific volume of state C (v_{C}) is indirectly related to the parameters of the saturation state A. Hence, p_{y} becomes a function of S_{r} and yield pressure at saturation, $p_{\mathrm{y}}^{\mathrm{sat}}$.

4.3.3.3 Hardening rules

The plastic volumetric strain, $\varepsilon_{\mathrm{v}}^{\mathrm{p}}$ is considered as the hardening parameter associated with the hardening rule (Alonso et al., 1990). In the current model, an isotropic hardening rule is derived concerning saturation similar to the Modified Cam Clay Model (MCCM) and the BBM (Sheng et al., 2004). The total ($\mathrm{d}\varepsilon_{\mathrm{v}}$) and elastic ($\mathrm{d}\varepsilon_{\mathrm{v}}^{\mathrm{e}}$) volumetric strain of the current model can be calculated using Equations (4.28) and (4.29) as:

$$\mathrm{d}\varepsilon_{\mathrm{v}} = \frac{-\mathrm{d}v}{v} = \lambda(S_{\mathrm{r}})\frac{\mathrm{d}p}{vp} \tag{4.28}$$

$$\mathrm{d}\varepsilon_{\mathrm{v}}^{\mathrm{e}} = \frac{-\mathrm{d}v^{\mathrm{e}}}{v} = \kappa(S_{\mathrm{r}})\frac{\mathrm{d}p}{vp} \tag{4.29}$$

Therefore, the plastic component of the volumetric strain ($\mathrm{d}\varepsilon_{\mathrm{v}}^{\mathrm{p}}$) can be given as:

$$\mathrm{d}\varepsilon_{\mathrm{v}}^{\mathrm{p}} = \mathrm{d}\varepsilon_{\mathrm{v}} - \mathrm{d}\varepsilon_{\mathrm{v}}^{\mathrm{e}} = (\lambda(S_{\mathrm{r}}) - \kappa(S_{\mathrm{r}}))\frac{\mathrm{d}p}{vp} \tag{4.30}$$

On the saturation line ($\mathrm{d}S_{\mathrm{r}}$ =0 and S_{r} =1), $\mathrm{d}\varepsilon_{\mathrm{v}}^{\mathrm{p}}$ becomes:

$$d\varepsilon_{\mathrm{v}}^{\mathrm{p}} = \left(\frac{\lambda_{\mathrm{sat}} - \kappa_{\mathrm{sat}}}{v_{\mathrm{sat}}} \right) \frac{dp_{\mathrm{sat}}}{p_{\mathrm{sat}}} \tag{4.31}$$

which is the same as for the saturated soil.

4.3.4 Hydromechanical_coupling and soil water retention curve (SWRC)

To this point, the coupling of moisture content to suction has not been considered. This coupling is achieved by introducing a SWRC which evolves with the plastic strain (Lloret-Cabot et al., 2014; Lloret-Cabot et al., 2017; Lloret-Cabot and Wheeler, 2018). In other words, the SWRC is defined for a certain $\varepsilon_{\mathrm{v}}^{\mathrm{p}}$, which means it is directly associated with a particular LC curve. Following Equations (4.1) and (4.2), two options are possible: (a) a relationship of moisture ratio (e_{w}) and void ratio-related suction parameter $\left(\frac{s}{1+e} \right)$ (Equation (4.1)) (b); a relationship of degree of saturation (S_{r}) and modified suction ($s^{*} (= \phi s)$) (Equation (4.2)). The latter, which was also used by Wheeler et al. (2003), is adopted for the current model, which is based on Equation (4.2).

Following Van Genuchten (1980), a closed-form equation for an entire range of modified suction is proposed as:

$$S_{\mathrm{r}} = \frac{1}{\left(1 + \left(\frac{s^{*}}{a} \right)^{\mathrm{n}} \right)^{\mathrm{m}}} \tag{4.32}$$

where, a, m and n are commonly referred to as parameters related to the air entry, the asymmetric shape of the curve and the rate of change of the slope of the curve, respectively. As suggested by Fredlund and Xing (1994), m and n are treated as two separate independent parameters. In the current model, it is considered that the inflexion point of the SWRC better represents the ATL, which features the transition of the continuity of the water and air phases. Moreover, the available evidence indicates that the ATL coincides closely with the line of optimums (LOO) in a family of compaction curves. Typically, $S_{\mathrm{r}}^{\mathrm{L}}$ is between 0.85 and 0.95 for clayey soils, 0.80 and 0.85 for silt, and 0.65 and 0.80 for sand, depending on its particle size uniformity (Thiam et al., 2019). Unfortunately, none of the above parameters directly represent the inflexion point. Hence, the following modification is proposed.

By differentiating Equation (4.32) twice, the point of inflexion of the SWRC (the point with the maximum slope) can be obtained as:

$$\frac{\mathrm{d}^2 S_\mathrm{r}}{\mathrm{d}(\ln s^*)^2} = \frac{-mns^{*\mathrm{n}-1}}{a^\mathrm{n}}\left(1+\left(\frac{s^*}{a}\right)^\mathrm{n}\right)^{-\mathrm{m}-2}\left\{n\left(1+\left(\frac{s^*}{a}\right)^\mathrm{n}\right)-\frac{(m+1)ns^{*\mathrm{n}}}{a^\mathrm{n}}\right\} \tag{4.33}$$

The modified suction and the degree of saturation of point of inflexion can then be found as $a^\mathrm{L} = am^{-1/\mathrm{n}}$ and $S_\mathrm{r}^\mathrm{L} = \left(\frac{m}{1+m}\right)^\mathrm{m}$. Hence, the adapted SWRC with the point of inflexion given as (S_r^L , a^L) can be rewritten as:

$$S_\mathrm{r} = \frac{1}{\left(1+\frac{1}{m}\left(\frac{s^*}{a^\mathrm{L}}\right)^\mathrm{n}\right)^\mathrm{m}} \tag{4.34}$$

Like the original Van Genuchten equation (1980), the above model still has three parameters, S_r^L (which defines m) and a^L and n . The hysteretic behaviour of SWRC is captured by two curves, namely the wetting curve and the drying curve. As evidenced by experiments, the degree of saturation along the ATL, S_r^L (or in other words at the inflexion point) can be considered constant for a certain soil (Tarantino and Tombolato, 2005; Tatsuoka and Correia, 2018). Therefore, for wetting and drying, m is a constant, whereas the n parameter and a^L are twofold for wetting and drying ($n_\mathrm{w}, n_\mathrm{d}, a_\mathrm{w}^\mathrm{L}$ and a_d^L). Hence, the equations for the wetting and drying branches are:

$$S_\mathrm{r} = \frac{1}{\left(1+\frac{1}{m}\left(\frac{s^*}{a_\mathrm{w}^\mathrm{L}}\right)^{\mathrm{n_w}}\right)^\mathrm{m}} \text{ and } S_\mathrm{r} = \frac{1}{\left(1+\frac{1}{m}\left(\frac{s^*}{a_\mathrm{d}^\mathrm{L}}\right)^{\mathrm{n_d}}\right)^\mathrm{m}} \tag{4.35}$$

Therefore, the change in the degree of saturation (S_r) along the wetting and drying paths (w/d) can be expressed as:

$$\mathrm{d}S_\mathrm{r} = C_\mathrm{w}\mathrm{d}s^* + D_\mathrm{w}\mathrm{d}a_\mathrm{w}^\mathrm{L} \text{ and } \mathrm{d}S_\mathrm{r} = C_\mathrm{d}\mathrm{d}s^* + D_\mathrm{d}\mathrm{d}a_\mathrm{d}^\mathrm{L} \tag{4.36}$$

where, $C_{\mathrm{w/d}}\left(=\dfrac{\partial S_{\mathrm{r}}}{\partial s^{*}}\right)_{a^{\mathrm{L}}_{\mathrm{w/d}}}$ and $D_{\mathrm{w/d}}\left(=\dfrac{\partial S_{\mathrm{r}}}{\partial a^{\mathrm{L}}_{\mathrm{w/d}}}\right)_{s^{*}}$ can be represented using hydraulic parameters ($a^{\mathrm{L}}_{\mathrm{w/d}}, s^{*}$) and material parameters ($m, n_{\mathrm{w/d}}$) as:

$$C\left(=\frac{\partial S_{\mathrm{r}}}{\partial s^{*}}\right)_{a^{\mathrm{L}}_{\mathrm{w/d}}}=\frac{-n_{\mathrm{w/d}}\left(s^{*}\right)^{\mathrm{n_{w/d}}\text{-}1}}{\left(a^{\mathrm{L}}_{\mathrm{w/d}}\right)^{\mathrm{n_{w/d}}}}\frac{1}{\left(1+\dfrac{1}{m}\left(\dfrac{s^{*}}{a^{\mathrm{L}}_{\mathrm{w/d}}}\right)^{\mathrm{n_{w/d}}}\right)^{\mathrm{m+1}}} \tag{4.37}$$

$$D\left(=\frac{\partial S_{\mathrm{r}}}{\partial a^{\mathrm{L}}_{\mathrm{w/d}}}\right)_{s^{*}}=\frac{n_{\mathrm{w/d}}\left(s^{*}\right)^{\mathrm{n_{w/d}}}}{\left(a^{\mathrm{L}}_{\mathrm{w/d}}\right)^{\mathrm{n_{w/d}}+1}}\frac{1}{\left(1+\dfrac{1}{m}\left(\dfrac{s^{*}}{a^{\mathrm{L}}_{\mathrm{w/d}}}\right)^{\mathrm{n_{w/d}}}\right)^{\mathrm{m+1}}} \tag{4.38}$$

The discussion thus far has been limited to only wetting and drying curves applicable to a certain $\varepsilon^{\mathrm{p}}_{\mathrm{v}}$, and the scanning behaviours of the wetting and drying paths are captured by Equations (4.39) and (4.40) proposed by Zhou et al. (2012) considering that scanning behaviour is bounded by the respective SWRCs.

$$\left(\frac{\partial S_{\mathrm{r}}}{\partial s^{*}}\right)_{\mathrm{w}}=\left(\frac{s^{*}_{\mathrm{w}}}{s^{*}}\right)^{\mathrm{b}}\left(\frac{\partial S_{\mathrm{r}}}{\partial s^{*}}\right)\quad\text{with}\quad s^{*}_{\mathrm{w}}=a^{\mathrm{L}}_{\mathrm{w}}\left[m(S_{\mathrm{r}}^{\text{-1/m}}-1)\right]^{1/\mathrm{n_w}} \tag{4.39}$$

$$\left(\frac{\partial S_{\mathrm{r}}}{\partial s^{*}}\right)_{\mathrm{d}}=\left(\frac{s^{*}_{\mathrm{d}}}{s^{*}}\right)^{\text{-b}}\left(\frac{\partial S_{\mathrm{r}}}{\partial s^{*}}\right)\quad\text{with}\quad s^{*}_{\mathrm{d}}=a^{\mathrm{L}}_{\mathrm{d}}\left[m(S_{\mathrm{r}}^{\text{-1/m}}-1)\right]^{1/\mathrm{n_d}} \tag{4.40}$$

4.3.5 The air transition value ($a^{\mathrm{L}}_{\mathrm{w}}$)

As shown in Figure 4.3, The specific volume at state A along the ATL and saturation line can be written as given in Equations (4.41) and (4.42), and the p_{L} and p_{sat} can therefore be written as Equation (4.43). Since on the wet side of the LC, the curve is considered to follow the effective stress approach, and the effective stress is assumed to be equivalent to p_{sat} and is equal to $p_{\mathrm{L}}+S^{\mathrm{L}}_{\mathrm{r}}s^{\mathrm{L}}$, $a^{\mathrm{L}}_{\mathrm{w}}$ can be found using Equation (4.44):

$$v_{\mathrm{A}}=C_{4}-\lambda_{\mathrm{L}}\ln(p_{\mathrm{L}}/p_{o}) \tag{4.41}$$

$$v_{\mathrm{A}}=N_{\mathrm{sat}}-\lambda_{\mathrm{sat}}\ln(p_{\mathrm{sat}}/p_{\mathrm{o}}) \tag{4.42}$$

$$p_{\mathrm{L}} = p_{\mathrm{o}} e^{\left(\frac{C_4 - v_{\mathrm{A}}}{\lambda_{\mathrm{L}}}\right)} \text{ and } p_{\mathrm{sat}} = p_{\mathrm{o}} e^{\left(\frac{N_{\mathrm{sat}} - v_{\mathrm{A}}}{\lambda_{\mathrm{sat}}}\right)} \tag{4.43}$$

$$s^{\mathrm{L}} = \frac{p_{\mathrm{o}}}{S_{\mathrm{r}}^{\mathrm{L}}}\left[e^{\left(\frac{N_{\mathrm{sat}} - v_{\mathrm{A}}}{\lambda_{\mathrm{sat}}}\right)} - e^{\left(\frac{C_4 - v_{\mathrm{A}}}{\lambda_{\mathrm{L}}}\right)}\right] \tag{4.44}$$

$$a_{\mathrm{w}}^{\mathrm{L}} = \phi s^{\mathrm{L}} = \left(\frac{v_{\mathrm{A}} - 1}{v_{\mathrm{A}}}\right)\frac{p_{\mathrm{o}}}{S_{\mathrm{r}}^{\mathrm{L}}}\left[e^{\left(\frac{N_{\mathrm{sat}} - v_{\mathrm{A}}}{\lambda_{\mathrm{sat}}}\right)} - e^{\left(\frac{C_4 - v_{\mathrm{A}}}{\lambda_{\mathrm{L}}}\right)}\right] \tag{4.45}$$

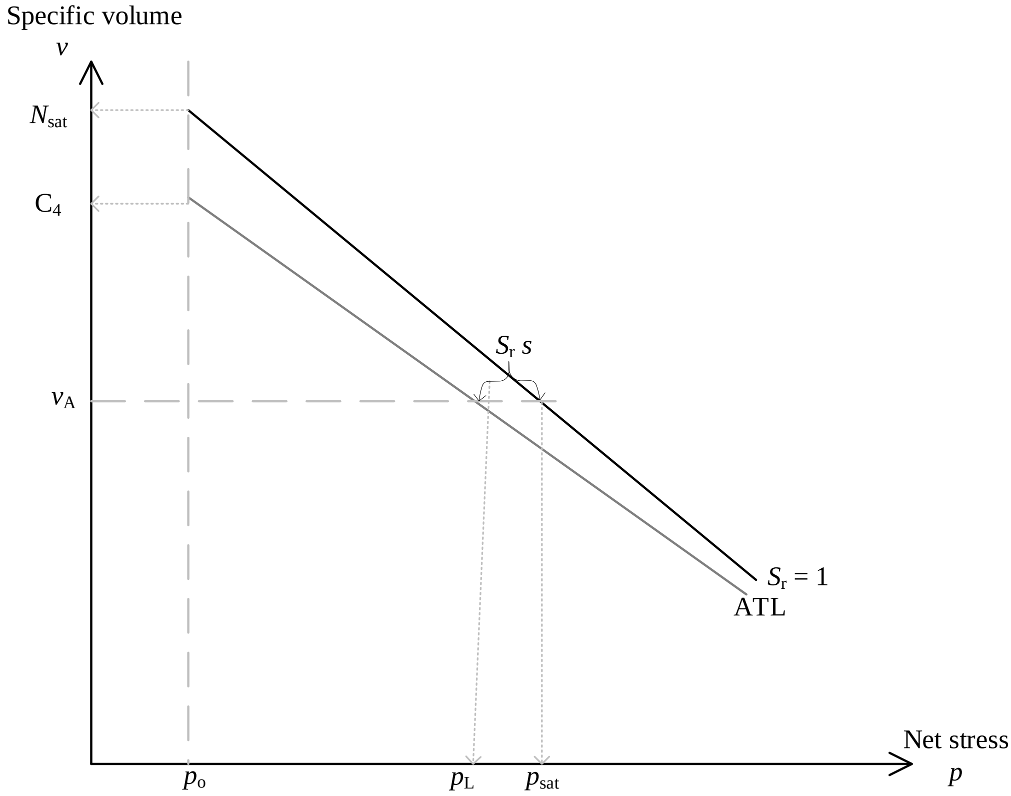

Figure 4.3: Behaviour of ATL and saturation line

According to Equation (4.45), the air transition value ($a_{\mathrm{w}}^{\mathrm{L}}$) is a function of the specific volume at saturation (v_{sat}). Therefore, $\mathrm{d}a_{\mathrm{w}}^{\mathrm{L}} = h\,\mathrm{d}v_{\mathrm{sat}}$, where $h = \dfrac{\partial a_{\mathrm{w}}^{\mathrm{L}}}{\partial v_{\mathrm{sat}}}$ can be derived as follows:

$$h = \frac{da_{\mathrm{w}}^{\mathrm{L}}}{dv_{\mathrm{sat}}} = \frac{p_{\mathrm{o}}}{S_{\mathrm{r}}^{\mathrm{L}}}\left(\frac{1}{v_{\mathrm{sat}}}\right)^2\left[e^{\left(\frac{N_{\mathrm{sat}} - v_{\mathrm{sat}}}{\lambda_{\mathrm{sat}}}\right)} - e^{\left(\frac{C_4 - v_{\mathrm{sat}}}{\lambda_{\mathrm{L}}}\right)}\right] - \frac{p_{\mathrm{o}}}{S_{\mathrm{r}}^{\mathrm{L}}}\left[\frac{1}{\lambda_{\mathrm{sat}}}e^{\left(\frac{N_{\mathrm{sat}} - v_{\mathrm{sat}}}{\lambda_{\mathrm{sat}}}\right)} - \frac{1}{\lambda_{\mathrm{L}}}e^{\left(\frac{C_4 - v_{\mathrm{sat}}}{\lambda_{\mathrm{L}}}\right)}\right] \tag{4.46}$$

It is also worth noting that the $a_{\mathrm{w}}^{\mathrm{L}}$ depends on the saturated void ratio (v_{sat}), which is, in turn, associated with the plastic volumetric strain $\varepsilon_{\mathrm{v}}^{\mathrm{p}}$. Therefore, substituting $\mathrm{d}a_{\mathrm{w}}^{\mathrm{L}} = h\,\mathrm{d}v_{\mathrm{sat}}$ into Equation (4.36), the change in the degree of saturation ($\mathrm{d}S_{\mathrm{r}}$) can be depicted as:

$$\mathrm{d}S_{\mathrm{r}} = C_{\mathrm{w}}\mathrm{d}s^{*} + D_{\mathrm{w}}h\,\mathrm{d}v_{\mathrm{sat}} \tag{4.47}$$

where, h is a general function defined in Equation (4.46).

4.3.6 The environmentally-stabilised line (ESL)

As noted earlier, the ESL is defined as the path which soil follows during wetting and drying after a large number of wet/dry cycles subject to a given operational net stress p_{op}. Such a path in idealised form is shown in Figure 4.4 as *KYC'* for 100 kPa (or log (p_{op}) =2). The gradient of this line on the dry side of ATL is given as α_{ES}. When a soil is compacted to achieve a certain state above this line, say state *A*, it undergoes downward movement during wet/dry cycles towards the ESL (Sharma, 1998). In contrast, when a soil is compacted to achieve a certain state below this line, say state *B*, it undergoes upward movement during wet/dry cycles towards the ESL (Kodikara et al., 2014; Kodikara et al., 2018). Based on this concept, the soil undergoes an accumulation of plastic strains until it reaches the ESL. To capture this phenomenological feature in idealised form, the following equation for the wetting/drying hydric gradient (α) is proposed:

$$\alpha = \alpha_{\mathrm{ES}} + (\alpha_{\mathrm{o}} - \alpha_{\mathrm{ES}})e^{\frac{-\beta(N-1)}{abs(\bar{\eta})}} \tag{4.48}$$

where, α_{o} is the initial wetting/drying hydric gradient, β is a rate parameter, $\bar{\eta}$ is a state parameter and N is the number of wet/dry cycles for a given wetting/drying moisture range. The state parameter $\bar{\eta}$ is the specific volume difference between the initial soil state (*A* or *B* in Figure 4.4) and the ESL for a constant specific moisture volume. Hence, it is $\bar{\eta}$ > 0 for state *A* and $\bar{\eta}$ < 0 for state *B*. The initial gradient α_{o} can also have two values: α_1 ($>\alpha_{\mathrm{ES}}$) for initial drying when $\bar{\eta}$ > 0 and initial wetting when $\bar{\eta}$ < 0; and α_2 ($< \alpha_{\mathrm{ES}}$) for initial wetting when $\bar{\eta}$ > 0 and initial drying when $\bar{\eta}$ < 0. Figure 4.5 shows an illustrative example of the evolution of α according to Equation (4.48) along with the associated parameters. The parameter β

governs the rate of environmental stabilisation with wet/dry cycling. For a general α, the change in specific volume (dv) upon wetting and drying on the v, v_w plane is given as follows:

$$dv = \frac{\alpha(v-1)}{1-\alpha S_r} dS_r \tag{4.49}$$

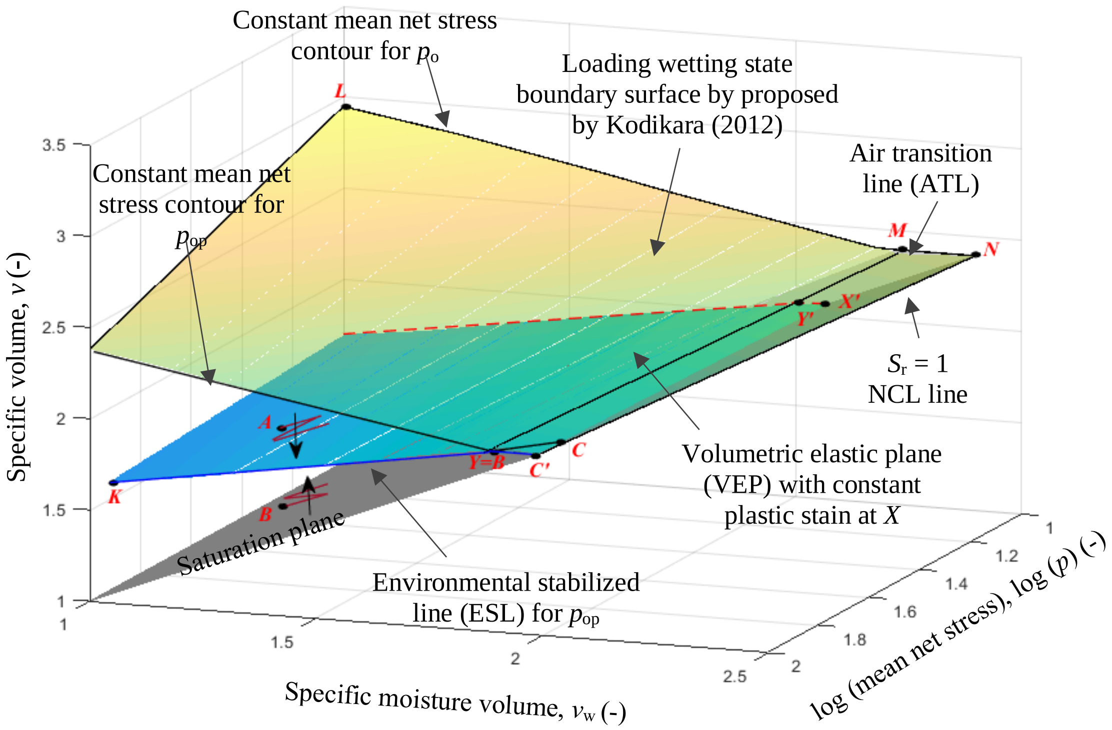

Figure 4.4: The behaviour of a soil on the operational stress level

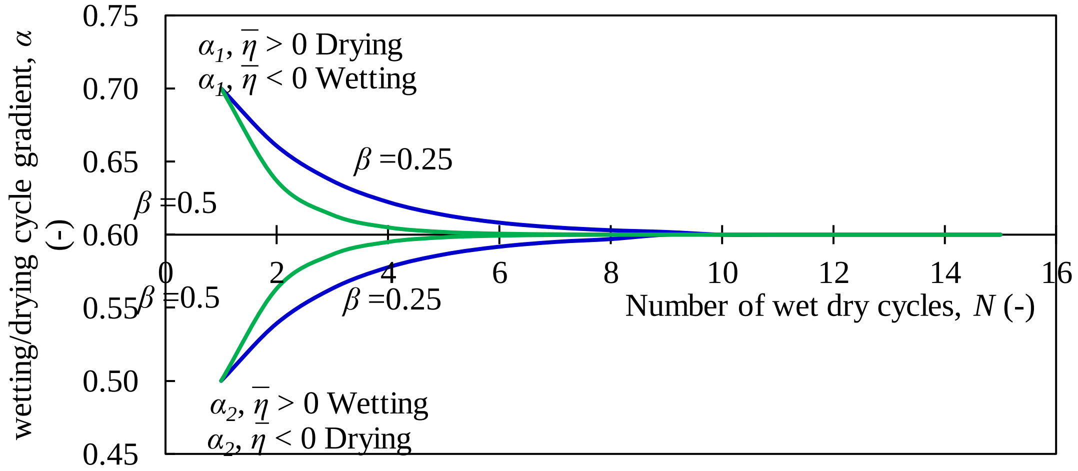

Figure 4.5: Definition of $\bar{\eta}$, β and α_o with respect to the number of wet/dry cycles

4.3.7 The constitutive equations for volumetric behaviour

The incremental stresses $\mathrm{d}p^*$ and $\mathrm{d}s^*$ are related to the incremental strains $\mathrm{d}\varepsilon_\mathrm{v}, \mathrm{d}S_\mathrm{r}$ as given in Equation (4.4) by the matrix D_HM, which represents the coupled hydro-mechanical constitutive relationships, where D_mm is th e mechanical component, D_mh and D_hm are the coupling components, and D_hh is the hydraulic component of the matrix. Since the current model comprises the wet and dry side, the D_HM matrix is twofold.

The D_HM matrix for the dry side ($S_r \le S_\mathrm{r}^\mathrm{L}$) is as follows:

$$D_\mathrm{HM} = \begin{bmatrix} D_\mathrm{mm} & D_\mathrm{mh} \\ D_\mathrm{hm} & D_\mathrm{hh} \end{bmatrix} = \begin{bmatrix} \left(\dfrac{pv}{\lambda(S_\mathrm{r})} + \dfrac{S_\mathrm{r} D_\mathrm{w} hgv}{\phi C_\mathrm{w}} + \dfrac{sS_\mathrm{r}}{v\phi} \right) & \left\{ \left(\dfrac{S_\mathrm{r}}{C_\mathrm{w}\phi} \right) + s \right\} \\ \dfrac{D_\mathrm{w} hgv}{C_\mathrm{w}} & \dfrac{1}{C_\mathrm{w}} \end{bmatrix} \tag{4.50}$$

The D_HM matrix for the wet side ($S_r > S_\mathrm{r}^\mathrm{L}$) is as follows:

$$D_\mathrm{HM} = \begin{bmatrix} D_\mathrm{mm} & D_\mathrm{mh} \\ D_\mathrm{hm} & D_\mathrm{hh} \end{bmatrix} = \begin{bmatrix} \dfrac{vp^*}{\lambda_\mathrm{sat}} & 0 \\ \dfrac{D_\mathrm{w} hgv}{C_\mathrm{w}} & \dfrac{1}{C_\mathrm{w}} \end{bmatrix} \tag{4.51}$$

The full derivation of the transformation matrices is given in Appendix B. Both matrices (in Equation (4.50) and (4.51)) coincide to the same, displaying the continuity at ATL when $S_r = S_\mathrm{r}^\mathrm{L}$.

4.4 Model predictions and comparison with experimental results

4.4.1 Selection of model parameters

The total number of model parameters for the current model (for volumetric behaviour only) is 15, with nine parameters ($\lambda_\mathrm{L}, k_3, v_\mathrm{o}^\mathrm{L}, k_4, \kappa_\mathrm{w}, v_\mathrm{sat}^0, \lambda_\mathrm{sat}, \kappa_\mathrm{sat}$, and S_r^L) being used to predict the mechanical behaviour, while the other six (n, X, b, $\alpha_\mathrm{ES}, \alpha_\mathrm{o}$, and β) are used to predict the coupled hydraulic behaviour (see Table 4.2 and Table 4.3). Of the 9 parameters for the mechanical response, five parameters $\lambda_{\mathrm{L}}, k_3, v_{\mathrm{o}}^{\mathrm{L}}, k_4$ and κ_{w} can be determined using a number of isotropic constant moisture content compression loading/unloading tests undertaken to reach the ATL (Abeyrathne et al., 2019). It is not essential to measure the suction during these tests, which makes the testing much simpler. The parameters λ_{L} and $v_{\mathrm{o}}^{\mathrm{L}}$ can be determined as the compressibility gradient and the specific volume at the nominal stress plane (p_{o} = 10 kPa) of the ATL (given by $v = v_{\mathrm{o}}^{\mathrm{L}} - \lambda_{\mathrm{L}} \ln(p / p_{\mathrm{o}})$). The parameter k_3 represents the change in the compressibility with the change of the degree of saturation (given by $\lambda(S_{\mathrm{r}}) = \lambda_{\mathrm{L}} - k_3(S_{\mathrm{r}} - S_{\mathrm{r}}^{\mathrm{L}})$) while the parameter k_4 denotes the gradient of the constant p_{o} net stress line in the (v, v_{w}) plane (provided by $v_{\mathrm{o}} = v_{\mathrm{o}}^{\mathrm{L}} - k_4(S_{\mathrm{r}} - S_{\mathrm{r}}^{\mathrm{L}})$). The fifth parameter κ_{w} is the unloading/reloading gradient of the constant moisture content tests.

Of the other four parameters (v_{sat}^{0} , λ_{sat} , κ_{sat} and $S_{\mathrm{r}}^{\mathrm{L}}$),the parameters v_{sat}^{0} , k_{sat} and λ_{sat} can be found through saturated loading/unloading (isotropic consolidation test) experiments. The $S_{\mathrm{r}}^{\mathrm{L}}$ is the degree of saturation at the ATL (this is approximately the LOO of the unloaded compaction curves, as noted earlier) and is at the inflexion point of the SWRCs. This parameter can also be easily estimated or determined from the above constant moisture compression tests (typical values of $S_{\mathrm{r}}^{\mathrm{L}}$ were presented earlier).

The six other parameters used for coupled hydraulic behaviour are n , X , b , α_{ES}, α_{o} , and β . Of these, n , X , b are related to the SWRC measured at constant plastic volumetric strains $\varepsilon_{\mathrm{v}}^{\mathrm{p}}$. However, controlling $\varepsilon_{\mathrm{v}}^{\mathrm{p}}$ is not very practical, since, during traditional wetting/ drying/ wetting measurements, the plastic strains can accumulate at varying degrees, depending on the soil type (Fleureau et al., 2002; Cunningham et al., 2003; Fredlund and Zhang, 2017). Therefore, by applying the model recursively, the parameter n (given by n_{w} , and n_{d}) can be back-calculated or calibrated from a traditional wetting-drying stress path experiment, including a traditional SWRC at constant net stress. In addition, the parameter n_{w} can be estimated through constant moisture content testing where the suction is measured; c.f. the compression experiments carried out by Tarantino and De Col (2008). It is worth highlighting that the SWRC (including the so-called main wetting or main drying curves) depends on the stress path followed during testing (constant p , e_{w} , e etc.,), but the SWRC based on $\varepsilon_{\mathrm{v}}^{\mathrm{p}}$ could be considered as unique for a certain soil on the basis of the definition presented in the present research. To simply capture the distance between the wetting path and drying path, the parameter X is introduced, which in turn gives the modified suction at the inflexion point on the drying path as $a_{\mathrm{d}}^{\mathrm{L}} = 10^{(\mathrm{X}+\log(a_{\mathrm{w}}^{\mathrm{L}}))}$. Pham et al. (2005) evaluated the parameter X for different soil types, where X is assumed to be a constant for a particular soil type. If this parameter can be assessed through direct testing, the above approximation is not necessary. The parameter b which captures the scanning behaviour of the SWRC can be back-calculated from a wetting-drying stress path experiment. Another parameter related to the SWRC is m, which can be obtained from $S_{\mathrm{r}}^{\mathrm{L}}$.

The gradient of the ESL, α_{ES}, can be obtained from wet/dry cycle testing on the (v, v_{w}) plane undertaken at constant net stress. Generally, α_{ES} decreases as the soil moisture reactivity decreases, as the soil type changes from clay and silt to sand. According to the experiments carried out by Tripathy et al. (2002) on two highly reactive expansive clays obtained from the northern Karnataka state in India, Soil A ($G_{\mathrm{s}} = 2.68$, $I_{\mathrm{p}} = 58$, LL =100) and Soil B ($G_{\mathrm{s}} = 2.73$, $I_{\mathrm{p}} = 42$, LL =74) showed an average α_{ES} value of 0.96 for both these soil types. For moderately reactive compacted kaolin, a value of about 0.6 is appropriate, according to the experiments undertaken by Raveendiraraj, 2009). It can be inferred that a small value such as 0.1 may be appropriate for sands. A detailed summary of typical hydric coefficients may be found in Wijesooriya (2012). In addition, these wetting/drying experiments can also be used to estimate the α_{o} parameter (see experiments by Raveendiraraj (2009) in Appendix 5), which is twofold: α_1 and α_2. From the same set of tests, the rate parameter β may be estimated.

Table 4.2: Definition of mechanical model parameters

MECHANICAL CONSTITUTIVE MODEL	
λ_{L}	The compressibility gradient of the ATL (given by $v = v_{\mathrm{o}}^{\mathrm{L}} - \lambda_{\mathrm{L}} \ln(p/p_{\mathrm{o}})$)
k_3	The change in the compressibility with the change of the degree of saturation (given by $\lambda(S_{\mathrm{r}}) = \lambda_{\mathrm{L}} - k_3(S_{\mathrm{r}} - S_{\mathrm{r}}^{\mathrm{L}})$)
$v_{\mathrm{o}}^{\mathrm{L}}$	The specific volume at the nominal stress plane (p_{o} = 10 kPa) of the ATL (given by $v = v_{\mathrm{o}}^{\mathrm{L}} - \lambda_{\mathrm{L}} \ln(p/p_{\mathrm{o}})$)

k_4	The gradient of the constant p_o net stress line in the (v, v_w) plane (given by $v_o = v_o^L - k_4(S_r - S_r^L)$)
κ_w	The unloading/reloading gradient of the constant moisture content tests
v_{sat}^0	The specific volume at the nominal stress plane (p_o = 10 kPa) of the NCL
λ_{sat}	The compressibility gradient of the NCL
κ_{sat}	The unloading/reloading gradient of the NCL
S_r^L	The degree of saturation at the ATL

Table 4.3: Definition of hydraulic model parameters

WATER RETENTION CONSTITUTIVE MODEL	
n	A parameter related to the SWRC measured at constant plastic volumetric strains ε_v^p, which changes the gradient of the wetting and drying paths
X	A parameter related to the SWRC measured at constant plastic volumetric strains ε_v^p, which changes the distance between wetting drying paths
b	A parameter related to the SWRC measured at constant plastic volumetric strains ε_v^p, which defines the scanning behaviour
α_{ES}	The gradient of the environmentally-stabilised line
α_o	Initial swelling gradient of loose/dense soil

β	A rate parameter, which controls the wetting/drying gradient

4.4.2 Experimental data

For the validation of the isotropic stress state, the model predictions of a selected number of experimental results for compacted kaolin, Abeyrathne et al. (2019), Raveendiraraj (2009) and Sharma (1998) are presented. The first three datasets are for less reactive kaolin, whereas the last is for a reactive soil mixture comprising bentonite and kaolin. Using isotropic constant moisture content tests by Abeyrathne et al. (2019), the mechanical parameters λ_{L} (=0.167; intercept) , k_3 (=0.424; gradient), $v_{\mathrm{o}}^{\mathrm{L}}$ (=2.714; intercept), and k_4 (=1.522; gradient) were found, as shown in Figure 4.6, through hyperlines with a constant degree of saturation. The other five mechanical parameters (κ_{w} (=0.0005), v_{sat}^0 (=2.83), λ_{sat} (=0.17), κ_{sat} (0.0012) , and $S_{\mathrm{r}}^{\mathrm{L}}$ (=0.85)) for nominal stress (p_{o} =10 kPa) were adopted directly from the paper by Abeyrathne et al. (2019) for the current model predictions given in Table 4.4. The parameter, κ_{w} ,the unloading/reloading gradient was determined from constant water content tests. Based on the test undertaken on saturated soil, the parameters v_{sat}^0 , λ_{sat} , κ_{sat} were determined. The $S_{\mathrm{r}}^{\mathrm{L}}$ was taken as 0.85. Unfortunately, suction was not measured in the experiments, and therefore, the parameters for the coupled hydraulic behaviour were not determined and validation was also not carried out (n_{w} , n_{d} , X , b , α_{ES} , and α_{o}).

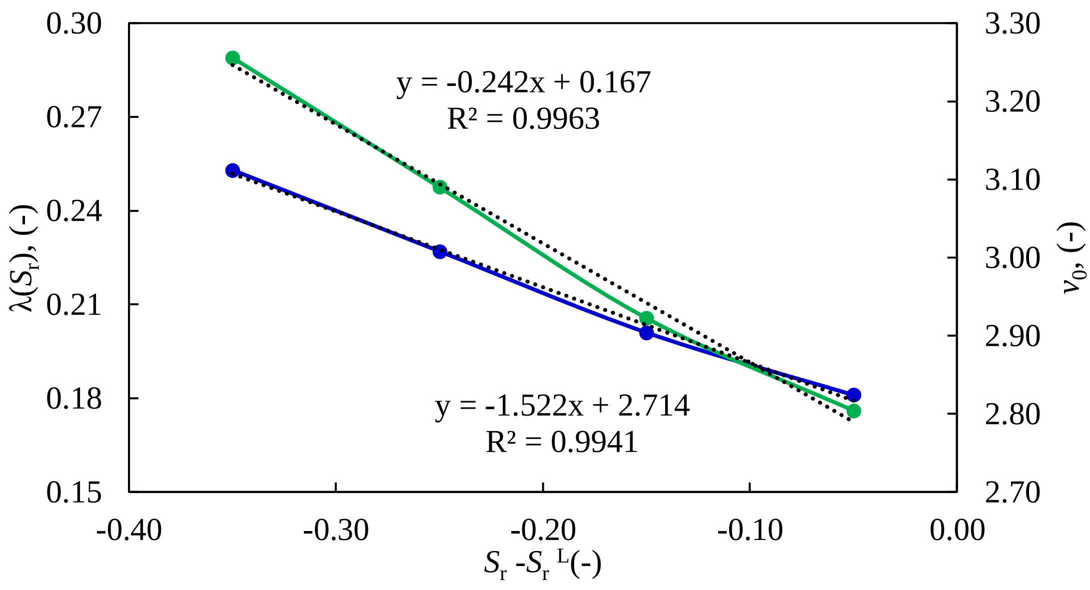

Figure 4.6: $\lambda_L, k_3, v_o^L, k_4$ *parameter estimation through constant water content loading tests by Abeyrathne (2017)*

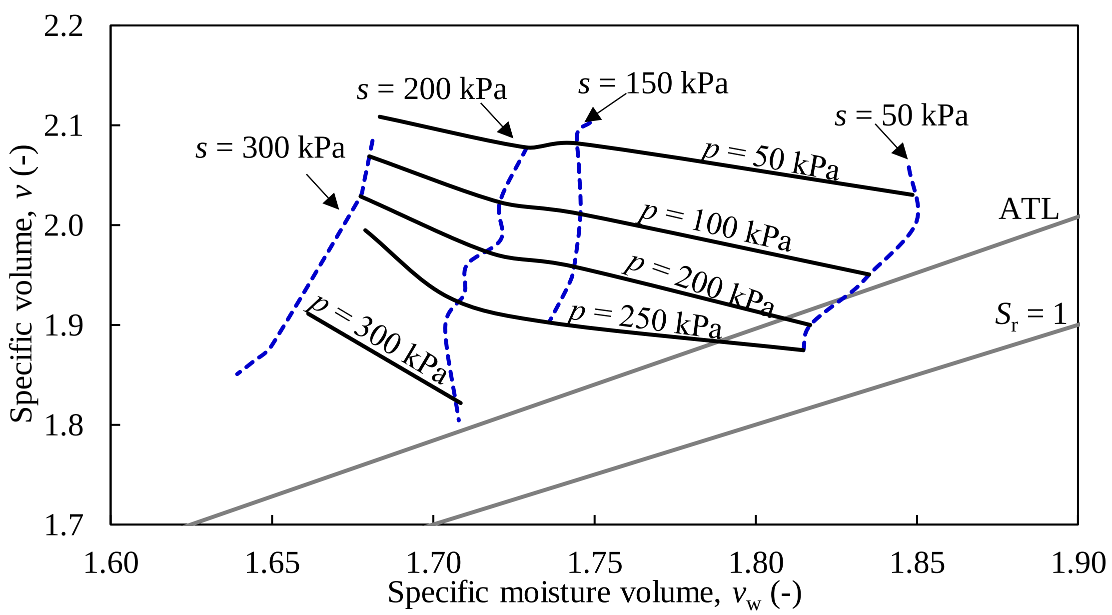

Figure 4.7 : The volumetric yield surface created using experimental data from Raveendiraraj (2009)

The second set of selected experimental data (by Raveendiraraj (2009)) includes constant suction loading tests instead of constant moisture content tests. Therefore, the volumetric yield surface was created using suction-controlled loading stress paths to estimate the nine mechanical parameters, as shown in Figure 4.7. The S_r^L was taken to be 0.85. Since the nominal stress contour (p_o =10 kPa) was not captured by the experiments, the volumetric yield surface was extended to obtain the parameters $\lambda_L, k_3, v_o^L, k_4$, in which v_o^L was taken as the specific volume at the intersection of ATL and nominal stress contour and k_4 was the gradient of the nominal stress contour. Subsequently, the parameters κ_w, v_{sat}^0, λ_{sat}, and κ_{sat} were obtained, being 0.0005, 2.4, 0.0012 and 0.181, respectively. In addition, the hydraulic parameters were determined from a wet/dry cyclic stress path test (Test A10), including n_w (=1.45), n_d (=1.35), X (=0.5), b (=5), α_{ES} (=0.6), and α_o (=0.63 and 0.57). The parameter X was estimated as indicated previously using the approach suggested by Pham et al. (2005). The determination of the parameters for the data of Sharma (1998) was performed in a similar way to that of Raveendiraraj (2009).

Table 4.4: Model parameters

	Parameter	Compacted kaolin Abeyrathne (2017)	Raveendiraraj (2009)	Sharma (1998)
Mechanical behaviour	λ_L	0.167	0.175	0.117
	k_3	0.242	0.23	0.2
	v_o^L	2.714	2.38	2.3
	k_4	1.522	1.3	0.9
	κ_w	0.0005	0.0005	0.0005
	v_{sat}^0	2.83	2.4	2.36
	κ_{sat}	0.0012	0.0012	0.0012
	λ_{sat}	0.170	0.181	0.120
	S_r^L	0.85	0.85	0.89
Water retention behaviour	n_w and n_d		1.45 and 1.35	1.2 and 1.1
	b		5	5
	α_{ES}		0.6	0.7
	α_1 and α_2		0.63 and 0.57	0.8 and 0.6
	β		0.1	0.2

	X		0.5	0.7

4.4.3 General characteristics of the model

To illustrate some general aspects of the model, the parameters determined from the data of Raveendiraraj (2009) were used in the application of the model. To develop the general characteristics, Figure 4.8, Figure 4.9, Figure 4.10, and Figure 4.11, and the full form of the mathematical equations were used. First, a set of saturation stresses, p_{sat} (50 kPa, 100 kPa, 200 kPa, 300 kPa, 500 kPa and 1000 kPa) including the nominal stress 10 kPa was selected prior to the calculation of v_{sat} (from Equation (4.42) for known values of N_{sat}, λ_{sat} and p_o), ε_v^p (from hardening rule Equation (4.31) for known values of κ_{sat}, λ_{sat}, v_{sat} and p_{sat}), a_w^L (from Equation (4.45) for known values of λ_{sat}, v_{sat}, N_{sat}, p_{sat}, λ_L, v_o^L, S_r^L and p_o), s^L (from Equation (4.44)), p_L (from Equation (4.22) for known values of S_r^L and s^L) and v_L (from Equation (4.41) for known values of v_o^L, λ_L and p_o), respectively. Subsequently, the parameters of the LC curves were developed by fixing the p_{sat} for changing S_r. >The parameters $\lambda(S_r)$, $k(S_r)$, p_y and, s^* were found from Equation (4.11), (4.16) (4.27) and (4.32) respectively. The suction contours, s (50 kPa, 100 kPa, 200 kPa, 300 kPa, 500 kPa, 1000 kPa) were developed from the suction values extracted from LC curve data. For the values on the nominal stress contour, p_o, the extrapolated a_w^L values were used. In addition, the constant net stress contours were developed from $\lambda(S_r)$ (from Equation (4.11)) for changing S_r.

Figure 4.8 shows a 2-D representation of the volumetric yield surface in the form of a series of constant net stress lines in the (v, v_w, p) space. A common feature of these contours is that the specific volume reduces with the increase of the specific moisture volume until the ATL, and there is then a slight increase in the specific volume with a further increase of specific moisture volume (phenomenological observation P2, P3, and P16), as originally predicted by Kodikara (2012). In fact, the constant net stress lines are equivalent to the "loaded" compaction curves brought to the yield state. Figure 4.8 shows the constant suction lines on the volumetric yield surface (phenomenological observation P23). It is worth noting that the theoretical constant suction curves in Figure 4.8 are similar to those developed from the experimental results by

Tarantino and De Col (2008), Jotisankasa (2005), Sharma (1998) and others. In particular, Sharma's data show a negative gradient $\left(\frac{\partial e_w}{\partial e}\right)_s$ at low stresses.

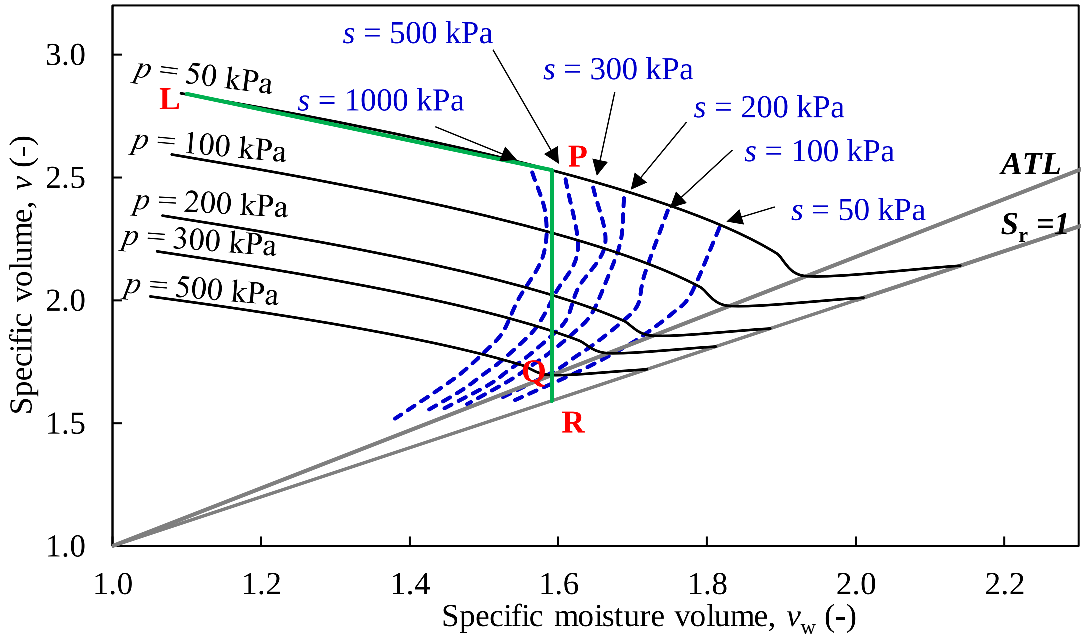

Figure 4.8: Predicted constant net stress lines and suction contours on the volumetric yield surface

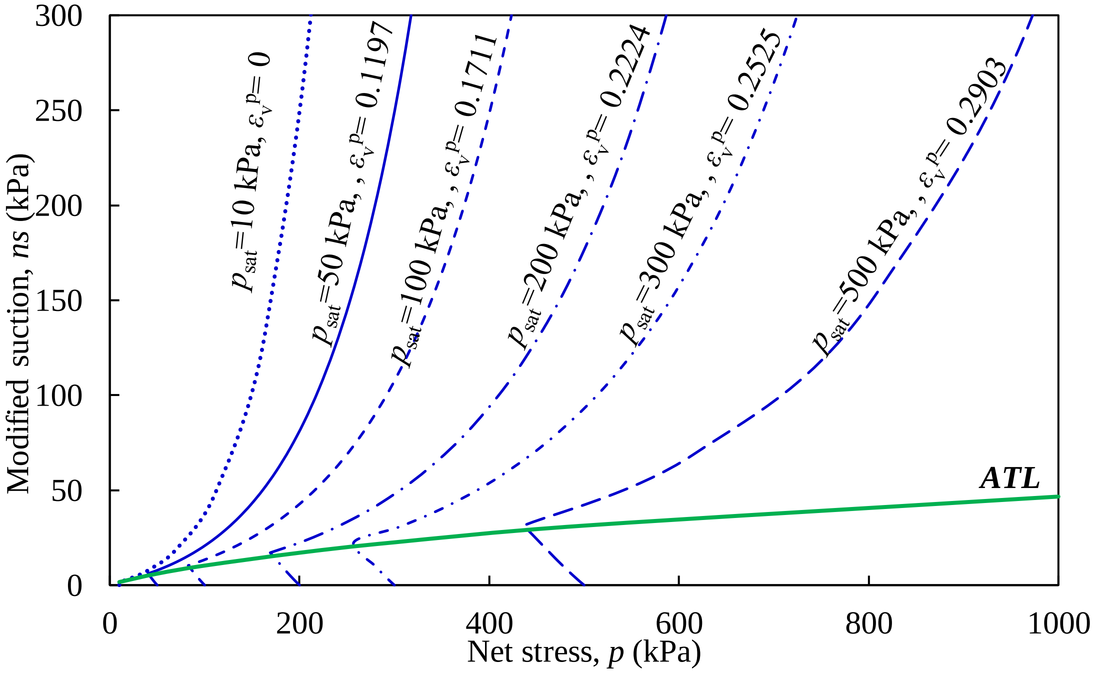

(a)

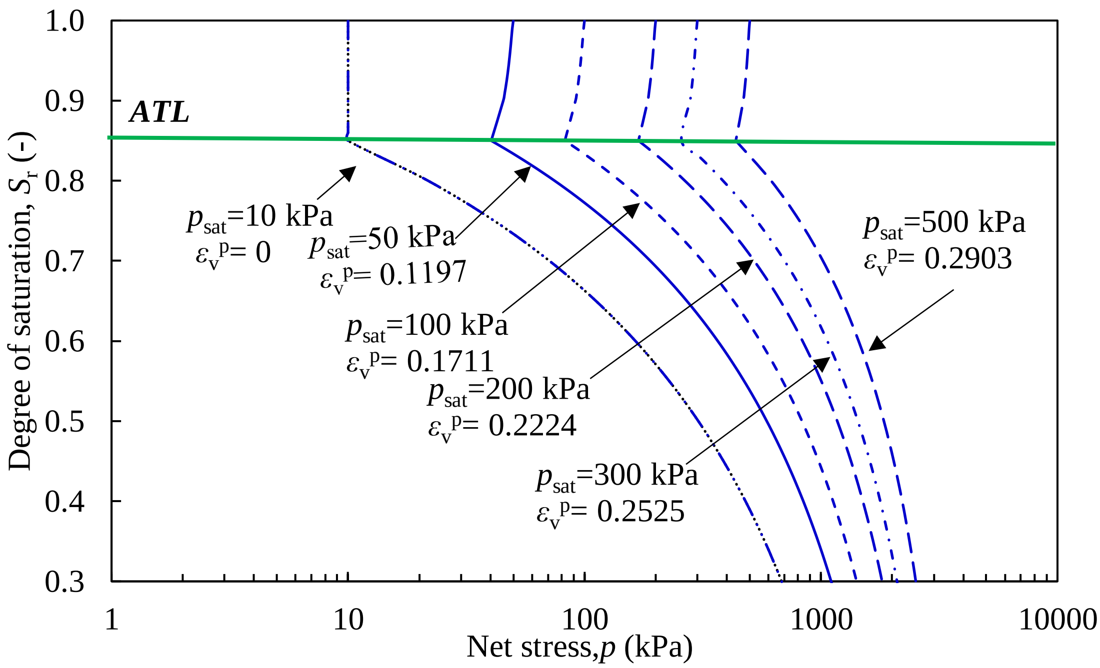

(b)

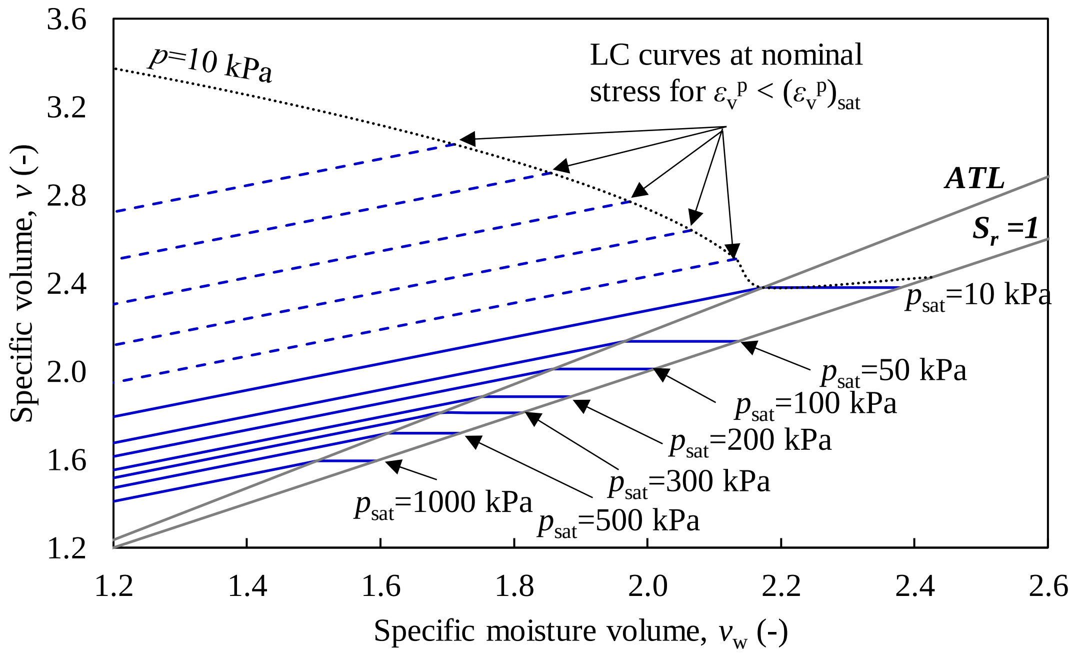

(c)

Figure 4.9: Behaviour of loading collapse curves

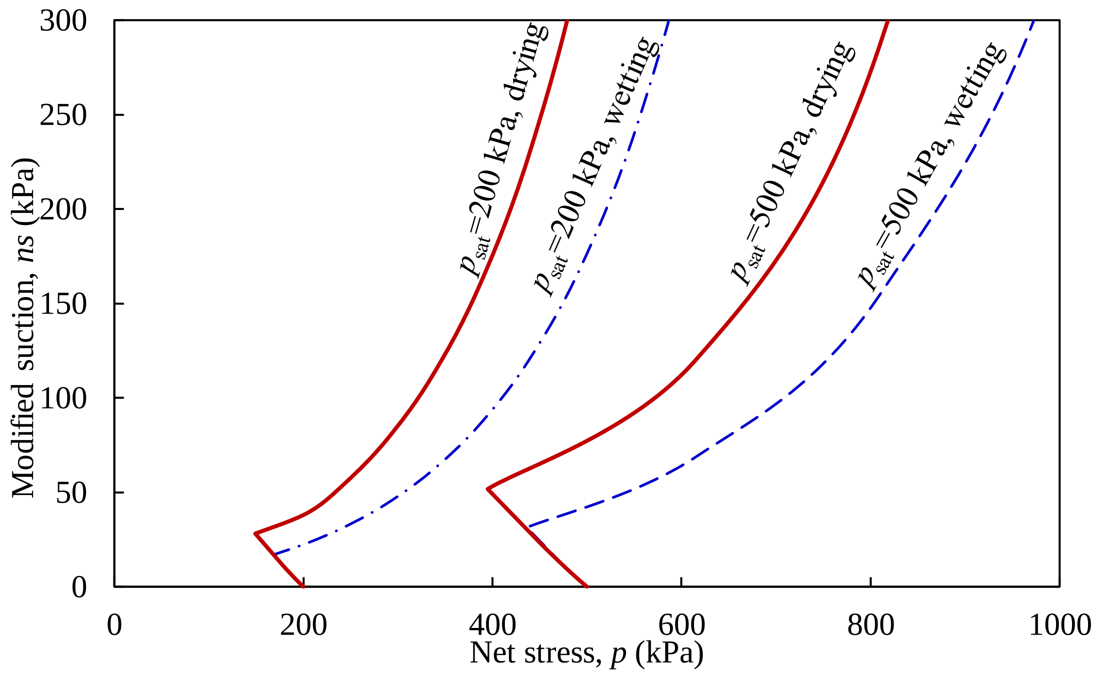

Figure 4.10: The double yield curve behaviour of loading collapse curves

Figure 4.9 depicts the mapping of the LC curves in the traditional (s^*, p) plane (Figure 4.9(a): phenomenological observation P5), in the (S_r, p) plane (Figure 4.9(b)) and in the (v, v_w) plane (Figure 4.9(c)). The LC curves in Figure 4.9(a) show similar characteristics to those reported by others (Monroy (2006) Lloret-Cabot et al. (2017)), and it displays an approximately 1:1 gradient in the (s, p) plane up to the ATL and then an increase in yield stress with the increase of suction (phenomenological observation P6). Figure 4.9(b) shows the same LC curves in the (S_r, p) plane, and the line is vertical down to the ATL. It should be noted that these LC curves correspond to suctions when the state prior to loading was on a wetting SWRC for a particular ε_v^p. It is also possible to develop a complementary LC curve when the state prior to loading was on a corresponding drying curve for the same ε_v^p. A further explanation of this aspect is given in the discussion of Test A5 by Raveendiraraj (2009). Figure 4.9(b) shows the same LC curves in the (v, v_w) plane, for a fixed saturation mean net stress (10 kPa, 50 kPa, 100 kPa, 200 kPa, 300 kPa, 500 kPa and 1000 kPa). In addition, some LC curves that have ε_v^p below ε_v^p saturation nominal stress is also depicted. As explained above, for a certain LC curve there is a wetting curve and a dry curve, resulting in hysteric yield curve behaviour in the (s^*, p) plane, as illustrated in Figure 4.10.

Figure 4.11 exhibits the SWRCs for several plastic strains ($\varepsilon_{\rm v}^{\rm p}$ = 0, 0.1197, 0.2903) and corresponding to some LC curves in Figure 4.9 (Phenomenological observation P21). The drying air transition (AT) value ($a_{\rm d}^{\rm L} = 10^{({\rm X}+\log(a_{\rm w}^{\rm L}))}$) is a function of the wetting AT value and the distance between the two curves is assumed to be constant for a particular soil, as noted earlier. It should also be noted that the SWRC in the current model shows a smaller gradient than the conventional SWRC. This occurs due to the possible accumulation of $\varepsilon_{\rm v}^{\rm p}$ during the wetting and subsequent drying applicable to so-called major wetting and drying curves. As shown in Figure 4.9 and Figure 4.11, the initial state of the dry powder can be identified as state *L* with an approximate suction value of 10^6 kPa. With the addition of water to dry power, state *P* is achieved, as shown in Figure 4.8 in the $(v, v_{\rm w})$ plane and Figure 4.11 in the $(S_{\rm r}, s^*)$ plane. During virgin compaction, the $\varepsilon_{\rm v}^{\rm p}$ increases crossing several SWRCs and reaches state *Q* at the ATL where the soil reaches state *R* with further loading.

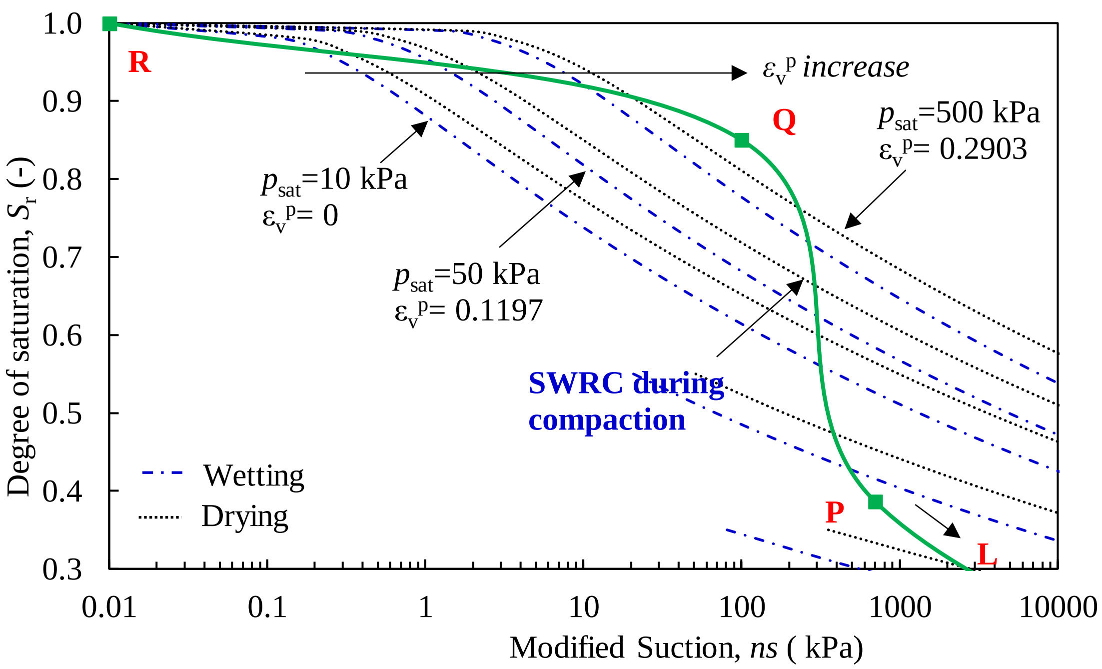

Figure 4.11: Evolution of SWRC curves with increase of plastic volumetric strain

4.4.4 Behaviour of soil water retention curves with $a_{\rm w}^{\rm L}$

Figure 4.12(a) exhibits the SWRCs for several plastic strains ($\varepsilon_{\rm v}^{\rm p}$ = 0 ($a_{\rm w}^{\rm L}$ =1.64 kPa), 0.1197 ($a_{\rm w}^{\rm L}$ =6.06 kPa), 0.2903 ($a_{\rm w}^{\rm L}$ =31.34 kPa)) corresponding to some LC curves in Figure 4.12(b) for a constant m (0.055), and $n_{w/d}$ (1.45 and 1.35). The drying air transition (AT) value ($a_d^L = 10^{(X+\log(a_w^L))}$) is a function of the wetting AT value, and the distance between the two curves is assumed to be constant for a particular soil, as noted earlier. It should also be noted that the SWRC in the current model manifests a smaller gradient than the conventional SWRC. This occurs due to the possible accumulation of ε_v^p during wetting and subsequent drying as applicable to the so-called major wetting and drying curves.

Another set of partial SWRCs can be defined considering the LC curves derived on the nominal stress contour, as shown in Figure 4.13. Considering the initial degree of saturation (i.e., $(S_r)_{\text{Initial}}$ = 0.75, 0.65, 0.55, 0.45 and 0.35), a set of loading collapse yield curves can be defined by hinging on the nominal stress contour instead of hinging on NCL. The required air transition a_w^L can be found by extrapolating the a_w^L (i.e., 1.64 kPa) associated with the complete SWRC at p =10 kPa. For one LC curve in Figure 4.13(b), a partial wetting curve and a drying curve can be obtained, as shown in Figure 4.13(a). These partial SWRC curves occur because we considered them up to the S_r corresponding nominal stress, as shown in Figure 4.13.

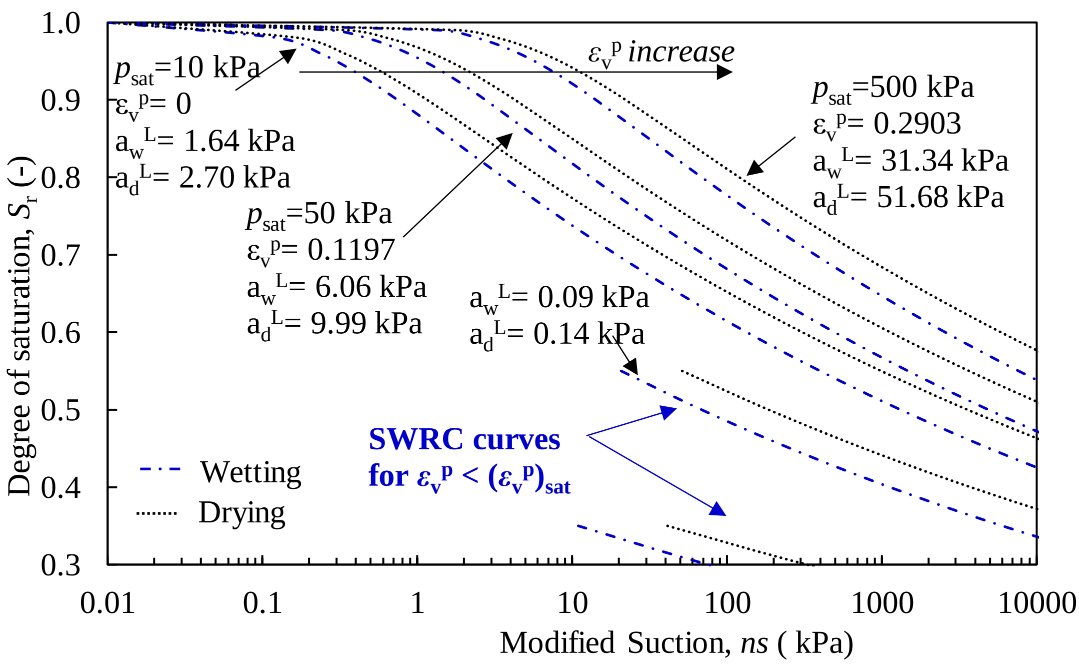

(a)

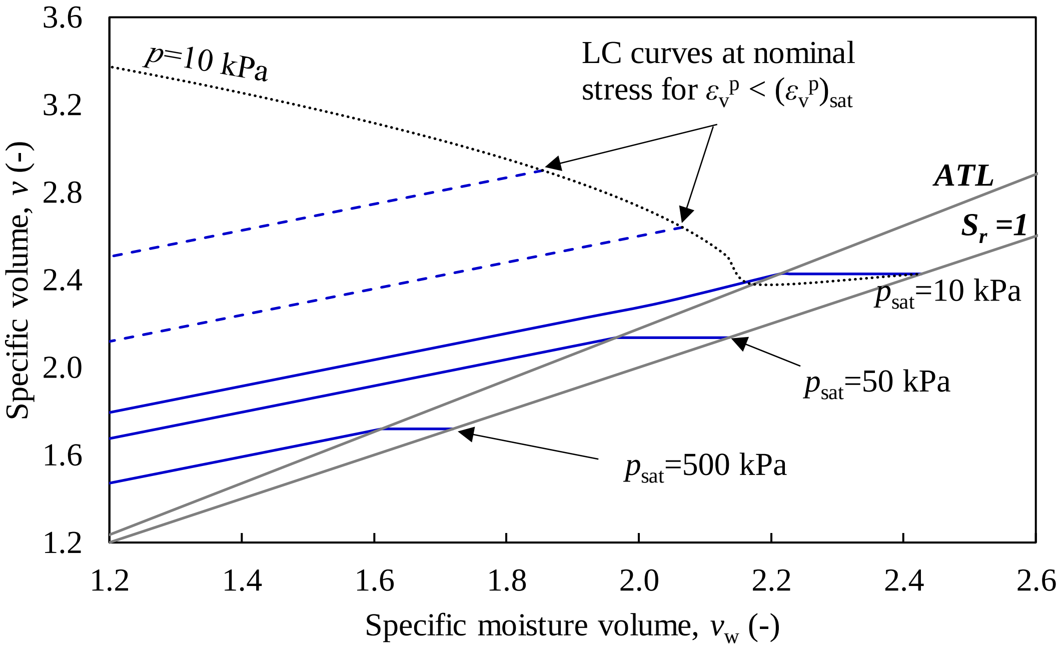

(b)

Figure 4.12: Loading collapse yield curves of the model

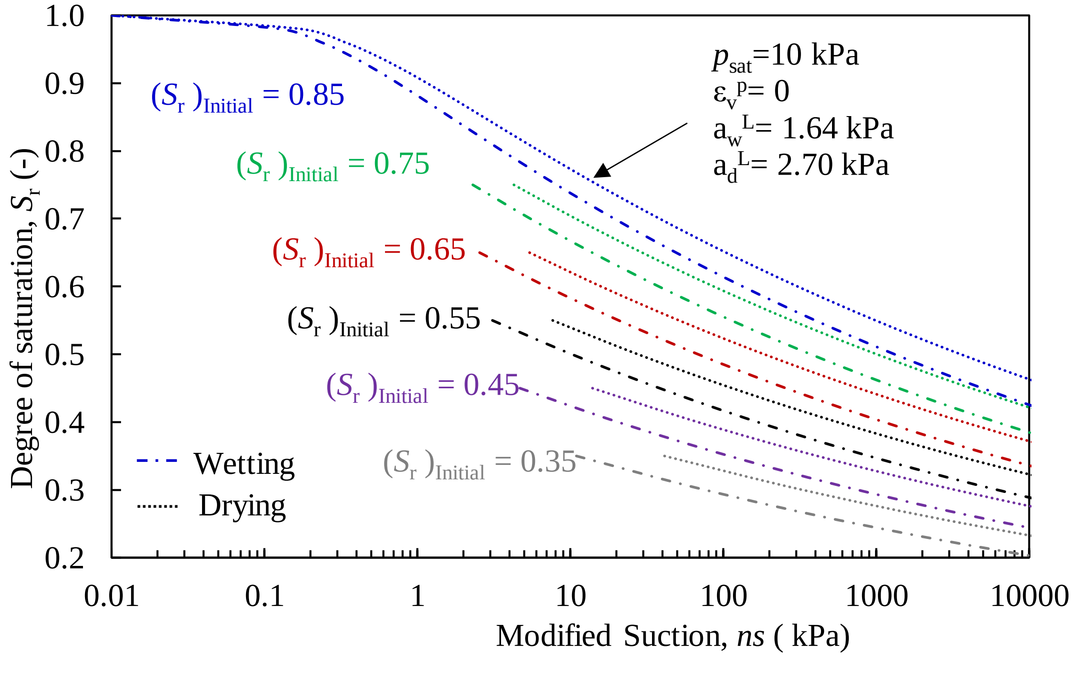

(a)

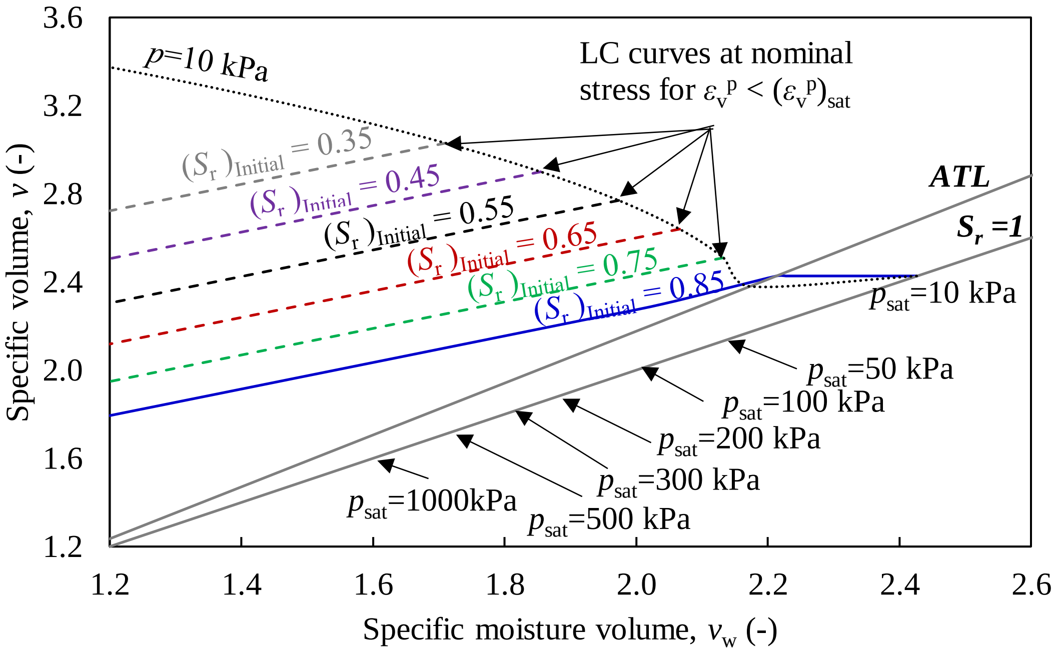

(b)

Figure 4.13: Loading collapse yield curves of the model

4.4.4.1 Major drying and wetting curves

As indicated earlier, the common practice for developing major drying and wetting curves is to saturate the specimen from the compacted state and then dry it to high suctions. The drying process defines the major drying curve. When the specimen is wetted from a dried state, major wetting is obtained. Here we highlight that the so-called major drying and wetting curves can cross a number of SWRCs defined based on the constant plastic strains due to changes in plastic strain with drying and wetting. Of course, the plastic strain change depends on the soil reactivity (more clayey or sandy), as reflected by the material parameters of the model.

In Figure 4.14, we simulate the development of major drying and wetting curves corresponding to 10 kPa mean net stress using the data for kaolin. State C refers to the unloaded state after compaction to State B from the initial state A. The soil is then wetted to full saturation, as shown in path CD, signifying the saturation process. Subsequently, the soil is dried to high suction, as shown path DEF, which can be considered as a major drying curve. As this simulation shows, the plastic volumetric strain increases along the major drying path, highlighting that plastic hardening takes place during first drying. When the soil is wetted from this position, it follows the path FGH, which can be considered as a major wetting curve, and softening again takes place with reduction of ε_v^p. This also means that the LC curve shifts rightwards as ε_v^p increases with drying and leftwards as ε_v^p decreases with wetting.

In addition, it is also clear that during initial saturation (path CD), soil undergoes plastic softening (or reduction in ε_v^p). Similarly, the common initialisation process in suction control tests (where the soil is wetted to achieve a target suction) can also induce plastic strain changes. Furthermore, during subsequent dry/wet cycles the measured SWRC can shift with plastic strain changes until they stabilise to constant plastic strain SWRCs where the soil is considered environmentally stabilised, as defined in the model. This aspect is simulated considering 4 dry/wet cycles as shown in Figure 4.14, where SWRC at the 4th cycle approaches close to the environmentally-stabilised state with a constant ε_v^p. This process of SWRC development can also occur differently when the operating mean net is changed. Under these circumstances, the definitions of major drying and wetting curves need to considered, taking these factors into account. This behaviour has also been experimentally observed by Zeng et al. (2020).

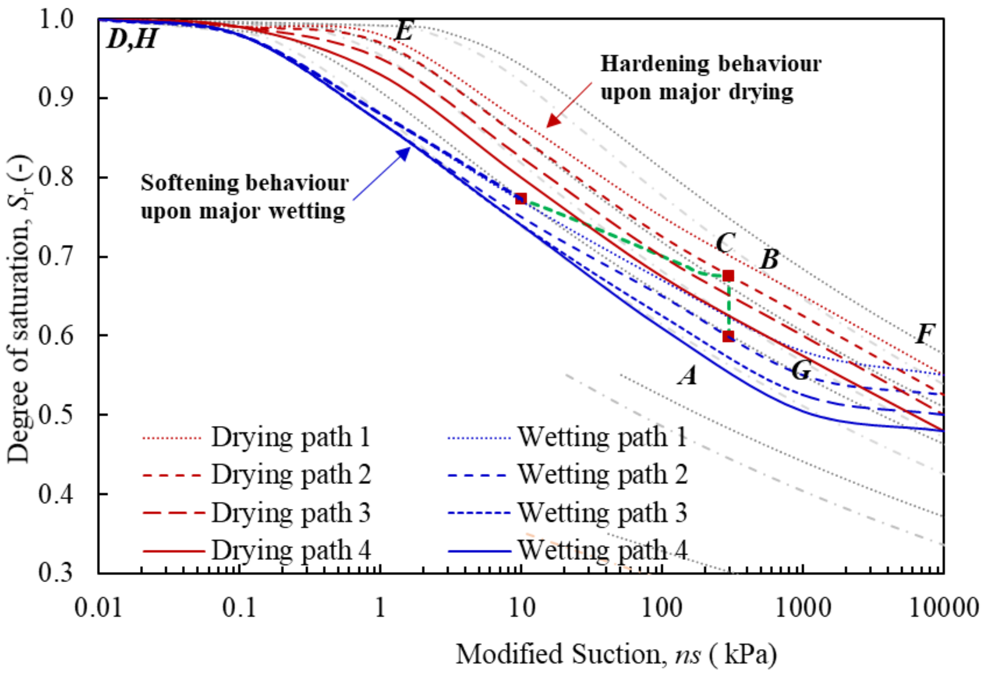

Figure 4.14: Model simulations of major wetting and major drying paths

4.5 Conclusion

Building on the MPK framework, a generalised constitutive model was proposed with emphasis on volumetric behaviour. Key concepts of the model include the constant-moisture-content-testing-based yield surface or volumetric yield surface, the plastic strain-based LC curve and SWRC, the air transition line (ATL) to demarcate the continuity of the air and water phases, the environmentally-stabilised line (ESL) to represent states achieved after the wet/dry cycles, and the use of Bishop's effective stress and conjugate strains to represent the hydro-mechanical energetics allowing for transition from unsaturated to saturated behaviour.

One of the attractive features of the model is the use of the constant moisture-content-based yield surface on the dry side of the ATL, which can be generated much more easily than with constant suction loading. It represents the loosest state of soil, embodying macroscopically the double structure that naturally emerges in compacted unsaturated soils. The mechanical behaviour of the model has 9 parameters which can be determined by relatively simple testing. The evolution of the plastic-strain-based SWRCs involves 6 parameters, some of which require calibration through traditional SWRC testing under constant net stress.The generalised MPK model is capable of capturing the general characteristics of unsaturated behaviour, and typical features of the model were explained.

4.6 References

Abeyrathne, A., Sivakumar, V. & Kodikara, J. 2019. Isotropic Volumetric Behaviour of Compacted Unsaturated Soils within (v, v w, p) Space. *Canadian Geotechnical Journal,* 56(12)**,** pp.1756-1778.

Abeyrathne, W. K. a. P. 2017. *A new modelling approach for compacted clayey soils using specific water volume as a state variable.* Ph.D. thesis, Monash University, Melbourne, Australia.

Alonso, E., Pinyol, N. & Gens, A. 2013. Compacted soil behaviour: initial state, structure and constitutive modelling. *Géotechnique,* 63**,** 463-478.

Alonso, E., Vaunat, J. & Gens, A. 1999. Modelling the mechanical behaviour of expansive clays. *Engineering geology,* 54**,** 173-183.

Alonso , E. E., Gens , A. & Josa, A. 1990. A constitutive model for partially saturated soils. *Géotechnique,* 40(3)**,** pp.405-430.

Buscarnera, G. & Di Prisco, C. 2012. Discussing the definition of the second-order work for unsaturated soils. *International journal for numerical and analytical methods in geomechanics,* 36**,** 36-49.

Cho, G. C. & Santamarina, J. C. 2001. Unsaturated particulate materials—particle-level studies. *Journal of geotechnical and geoenvironmental engineering,* 127**,** 84-96.

Cunningham, M., Ridley, A., Dineen, K. & Burland, J. 2003. The mechanical behaviour of a reconstituted unsaturated silty clay. *Géotechnique,* 53**,** 183-194.

Fleureau, J.-M., Verbrugge, J.-C., Huergo, P. J., Correia, A. G. & Kheirbek-Saoud, S. 2002. Aspects of the behaviour of compacted clayey soils on drying and wetting paths. *Canadian geotechnical journal,* 39**,** 1341-1357.

Fredlund, D. G. & Xing, A. 1994. Equations for the soil-water characteristic curve. *Canadian geotechnical journal,* 31**,** 521-532.

Fredlund, D. G. & Zhang, F. 2017. Effect of Initial Conditions on the Interpretation of Soil-Water Characteristic Curves (SWCCs) in Geotechnical Engineering. *PanAm Unsaturated Soils 2017.*

Gallipoli, D., Wheeler, S. & Karstunen, M. 2003. Modelling the variation of degree of saturation in a deformable unsaturated soil. *Géotechnique.,* 53**,** 105-112.

Gens, A. 2010. Soil–environment interactions in geotechnical engineering. *Géotechnique,* 60**,** 3-74.

Houlsby, G. 1997. The work input to an unsaturated granular material. *Géotechnique,* 47**,** 193-196.

Islam, T. & Kodikara, J. 2015. Interpretation of the loading–wetting behaviour of compacted soils within the “MPK” framework. Part I: Static compaction 1. *Canadian Geotechnical Journal,* 53**,** 783-805.

Jayasundara, C., Kodikara, J. & Zhou, A. 2019 A volumetric yield surface for compacted soils based on constant water content testing. *7th International Symposium on Deformation Characteristics of Geomaterials.* Glasgow, UK.

Jotisankasa, A. 2005. *Collapse behaviour of a compacted silty clay.* Ph.D. thesis, University of London.

Karube, D. & Kawai, K. 2001. The role of pore water in the mechanical behavior of unsaturated soils. *Geotechnical & Geological Engineering,* 19**,** 211-241.

Khalili, N., Habte, M. & Zargarbashi, S. 2008. A fully coupled flow deformation model for cyclic analysis of unsaturated soils including hydraulic and mechanical hystereses. *Computers and Geotechnics,* 35**,** 872-889.

Kodikara, J. 2012. New framework for volumetric constitutive behaviour of compacted unsaturated soils. *Canadian Geotechnical Journal,* 49**,** 1227-1243.

Kodikara, J., Islam, T. & Rajeev, P. 2015. Interpretation of the loading–wetting behaviour of compacted soils within the "MPK" framework. Part II: Dynamic compaction 1. *Canadian Geotechnical Journal,* 53**,** 806-827.

Kodikara, J., Islam, T. & Shounthrarajah, A. 2018. Review of Soil Compaction: History and Recent Developments. *Transportation Geotechnics,* 17**,** 24-34.

Kodikara, J., Islam, T., Wijesooriya, S., Bui, H. & Burman, B. On controlling influence of the line of optimums on the compacted clayey soil behavior. Proceedings of the Sixth International Conference on Unsaturated Soils, UNSAT2014. Edited by N. Khalili, AR Russell, and A. Khoshghalb. Sydney, Australia, 2014. 219-225.

Lloret-Cabot, M. & Wheeler, S. J. 2018. The Mechanical Yield Stress in Unsaturated and Saturated Soils. *The 7th International Conference on Unsaturated Soils (UNSAT2018).* Hong Kong, China.

Lloret-Cabot, M., Wheeler, S. J., Pineda, J. A., Romero, E. & Sheng, D. 2017. From saturated to unsaturated conditions and vice versa. *Acta Geotechnica***,** 1-23.

Lloret-Cabot, M., Wheeler, S. J., Pineda, J. A., Sheng, D. & Gens, A. 2014. Relative performance of two unsaturated soil models using different constitutive variables. *Canadian geotechnical journal*, 51**,** 1423-1437.

Lu, N. & Likos, W. J. 2004. *Unsaturated soil mechanics*, Wiley.

Monroy, R. 2006. *The influence of load and suction changes on the volumetric behaviour of compacted London Clay.* Ph.D. thesis, Imperial College London (University of London).

Nuth, M. & Laloui, L. 2008. Effective stress concept in unsaturated soils: clarification and validation of a unified framework. *International journal for numerical and analytical methods in Geomechanics,* 32**,** 771-801.

Pasha, A. Y., Khoshghalb, A. & Khalili, N. 2017. Hysteretic model for the evolution of water retention curve with void ratio. *Journal of Engineering Mechanics,* 143**,** 04017030.

Pasha, A. Y., Khoshghalb, A. & Khalili, N. 2019. Can degree of saturation decrease during constant suction compression of an unsaturated soil? *Computers and Geotechnics,* 106**,** 199-204.

Pham, H. Q., Fredlund, D. G. & Barbour, S. L. 2005. A study of hysteresis models for soil-water characteristic curves. *Canadian Geotechnical Journal,* 42**,** 1548-1568.

Raveendiraraj, A. 2009. *Coupling of mechanical behaviour and water retention behaviour in unsaturated soils.* Ph.D. thesis, University of Glasgow.

Schofield, A. & Wroth, P. 1968. *Critical state soil mechanics,* McGraw-Hill London.

Sharma, R. S. 1998. *Mechanical behaviour of unsaturated highly expansive clays.* Ph.D. thesis, University of Oxford.

Sheng, D., Fredlund, D. G. & Gens, A. 2008. A new modelling approach for unsaturated soils using independent stress variables. *Canadian Geotechnical Journal,* 45**,** 511-534.

Sheng, D., Sloan, S. & Gens, A. 2004. A constitutive model for unsaturated soils: thermomechanical and computational aspects. *Computational Mechanics,* 33**,** 453-465.

Tarantino, A. & De Col, E. 2008. Compaction behaviour of clay. *Géotechnique,* 58**,** 199-213.

Tarantino, A. & Tombolato, S. 2005. Coupling of hydraulic and mechanical behaviour in unsaturated compacted clay. *Géotechnique,* 55**,** 307-317.

Tatsuoka, F. & Correia, A. G. 2018. Importance of Controlling the Degree of Saturation in Soil Compaction linked to Soil Structure Design. *Transportation Geotechnics,* 143**,** 556-565.

Thiam, M., Thuyet, D. Q., Saito, H. & Kohgo, Y. 2019. Performance of the tangential model of soil water retention curves for various soil texture classes. *Geoderma,* 337**,** 514-523.

Tripathy, S., Rao, K. S. & Fredlund, D. 2002. Water content-void ratio swell-shrink paths of compacted expansive soils. *Canadian geotechnical journal,* 39**,** 938-959.

Van Genuchten, M. T. 1980. A closed-form equation for predicting the hydraulic conductivity of unsaturated soils. *Soil science society of America journal,* 44**,** 892-898.

Vanapafli, S., Fredlund, D. & Pufahl, D. 1999. The influence of soil structure and stress history on the soil-water characteristics of a compacted till. *Geotechnique,* 49**,** 143-159.

Wheeler, S., Sharma, R. & Buisson, M. 2003. Coupling of hydraulic hysteresis and stress–strain behaviour in unsaturated soils. *Géotechnique,* 53**,** 41-54.

Wijesooriya, R. 2012. *Modelling of desiccation crack depths in clay soils.* Ph.D. thesis, Monash University Australia.

Zeng, L., Li, F., Liu, J., Gao, Q.-F. & Bian, H.-B. 2020. Effect of initial gravimetric water content and cyclic wetting-drying on soil-water characteristic curves of disintegrated carbonaceous mudstone. *Transportation Safety and Environment*.

Zhou, A.-N., Sheng, D., Sloan, S. W. & Gens, A. 2012. Interpretation of unsaturated soil behaviour in the stress–Saturation space, I: Volume change and water retention behaviour. *Computers and Geotechnics,* 43**,** 178-187.

Zhou, A., Wu, S., Li, J. & Sheng, D. 2018. Including degree of capillary saturation into constitutive modelling of unsaturated soils. *Computers and Geotechnics*, 95**,** 82-98.

CHAPTER 5

Materials, Methods, and Experimental results

5 Introduction

The MPK framework has two surfaces, namely the loading wetting state boundary surface (LWSBS or the volumetric yield surface) and the tensile failure surface with two primary lines: the air transition line (ATL) and the saturation line (the $v = v_w$ line or NCL). The LWSBS comprises a family of loaded compaction curves for various net stress levels, and is considered to represent the loosest states of compacted soil, in the same way that the NCL represents the loosest states of saturated soil. To establish the uniqueness and concept validation of the LWSBS upon wetting, loading/unloading combinations in an extensive number of experiments were carried out in the 1-D stress state by Islam and Kodikara (2015) and Kodikara et al. (2015) in the isotropic stress state by Abeyrathne (2017) for less reactive compacted kaolin and highly reactive Merri Creek soil. However, the present research considered only paths containing loading/unloading and wetting stress paths, and its applicability to paths containing drying was not examined. Hence, in this chapter, this aspect of the model is examined experimentally using the stress paths including drying.

The GCTS (GCTS, 1994) unsaturated triaxial apparatus was used for the isotropic testing of compacted kaolin, for which the material selection, sample preparation, experimental set-up and recalibration of the experimental apparatus are outlined in Sections 5.1 to 5.7. Only a selected number of tests were carried out due to time limitations, and the experimental results are described in Sections 5.8, 5.9 and 5.10. The primary objective of the experiments was to validate the proposed constitutive model through experimental studies for certain specific aspects, which have not been undertaken previously. Therefore, two series of tests were designed in order to examine the drying behaviour and the concept of environmental stabilisation of soil.

5.1 Material selection

The three major types of samples generally available are: (1) undisturbed natural samples (2) reconstituted samples and (3) compacted samples. As discussed in Chapter 2, the research undertaken in this study focusses on compacted soils. As a control material, commercially-available powdered kaolin (Kaolin Ecalite 1) was used for the experimental program. Some desirable features of using kaolin include:

1. Kaolin is a homogeneous uniform material, which is readily available;

2. The research is an extension of the MPK framework, and several previous researchers have been used Kaolin Ecalite 1 for the validation of the MPK framework for the I-D stress state (Islam and Kodikara, 2015; Kodikara et al., 2015) and isotropic stress state (Abeyrathne et al., 2016). In addition, significant experimental evidence is available on kaolin (e.g., Sivakumar, 1993; Sharma, 1998; Raveendiraraj, 2009).
3. The duration of the test can be minimised due to the significant increase in the rate of consolidation. If the rate of consolidation is lower, the equilibrium at each pressure increase requires a longer time, which ultimately leads to a longer experimental duration.
4. Kaolin falls into the fine-grained soil clay category, and has a 75% fraction of clay, making the research undertaken relevant to clayey soils. The specific gravity, liquid limit and plastic limit of the studied kaolin is 2.65, 60.5% and 27.9%, respectively. A detailed summary of the properties of kaolin is provided in Islam and Kodikara (2015).

5.2 Preparation of kaolin aggregates and samples

The isotropic compression tests in the research reported here required samples with different moisture contents. The moisture contents of series one T1, T2 and T3 were 25%, and the other three samples were prepared according to the required moisture contents. The dry powder kaolin was hand-mixed in a consistent fashion with the distilled water required for different moisture contents. The samples were then placed in sealed plastic bags for 24 hrs for equalisation. The moisture content was checked by taking three small samples and measuring the water contents. Since static compaction produces replicable results compared to dynamically compacted soils (Sivakumar, 1993), the static compaction procedure was utilised in the present research. The sample preparation was identical to that employed by Abeyrathne (2017), where the soil samples were statically compacted to 50 kPa using a compression frame in five similar layers to achieve the loosest state of compacted soils. A rubber membrane was placed using O-rings on the cylindrical compression mould and a fixed axial displacement rate of 1.5mm/min was applied during compaction. Figure 5.1 shows a compacted sample before, during and after a test.

5.3 Experimental set-up

The designed experimental program was carried out using the GCTS unsaturated triaxial apparatus, which is shown in Figure 5.2. The equipment consists of a double-walled triaxial cell, three pressure chambers (cell pressure, back pressure and air pressure), a diffused air flushing device, a volume change device, four pressure transducers, a loading frame, a controller and a data acquisition system. A schematic diagram of the set-up is given in Figure 5.3. A detailed description of the apparatus is provided in the following sections. A simple modification was made to the conventional triaxial GCTS equipment, as it was not capable of holding air pressures more than 200 kPa during refilling of the air chamber.

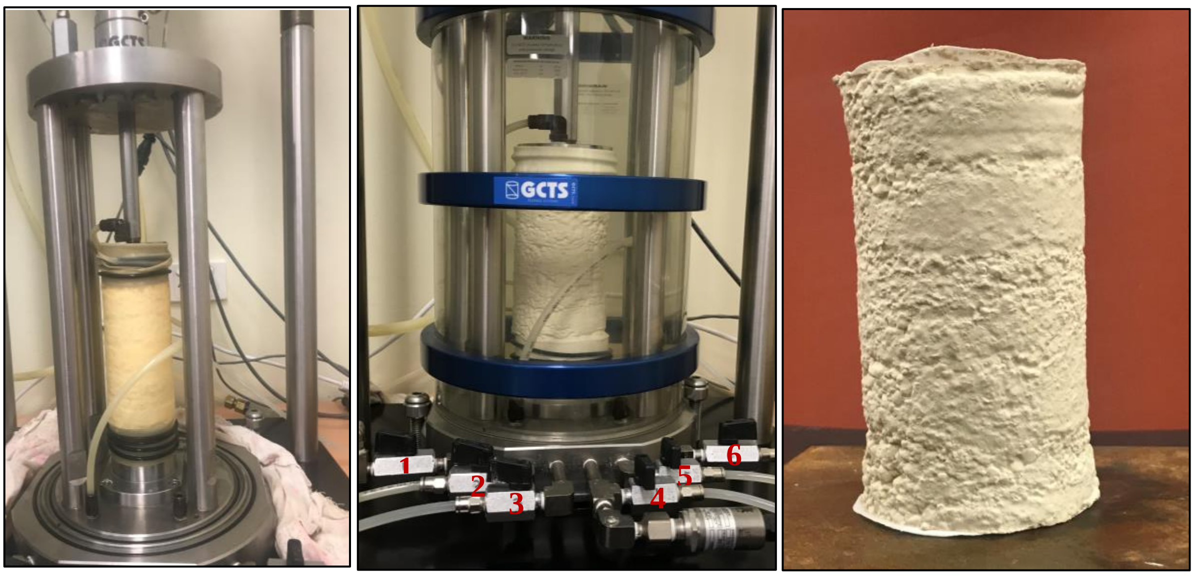

(a) (b) (c)

Figure 5.1: Sample (a)before test; (b) during test (c)after test

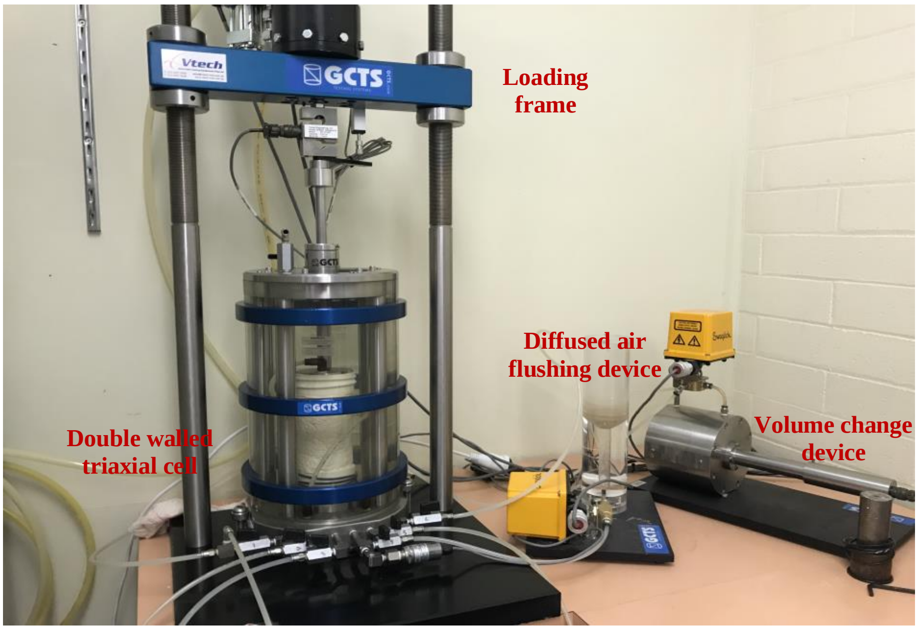

Figure 5.2: GCTS triaxial apparatus

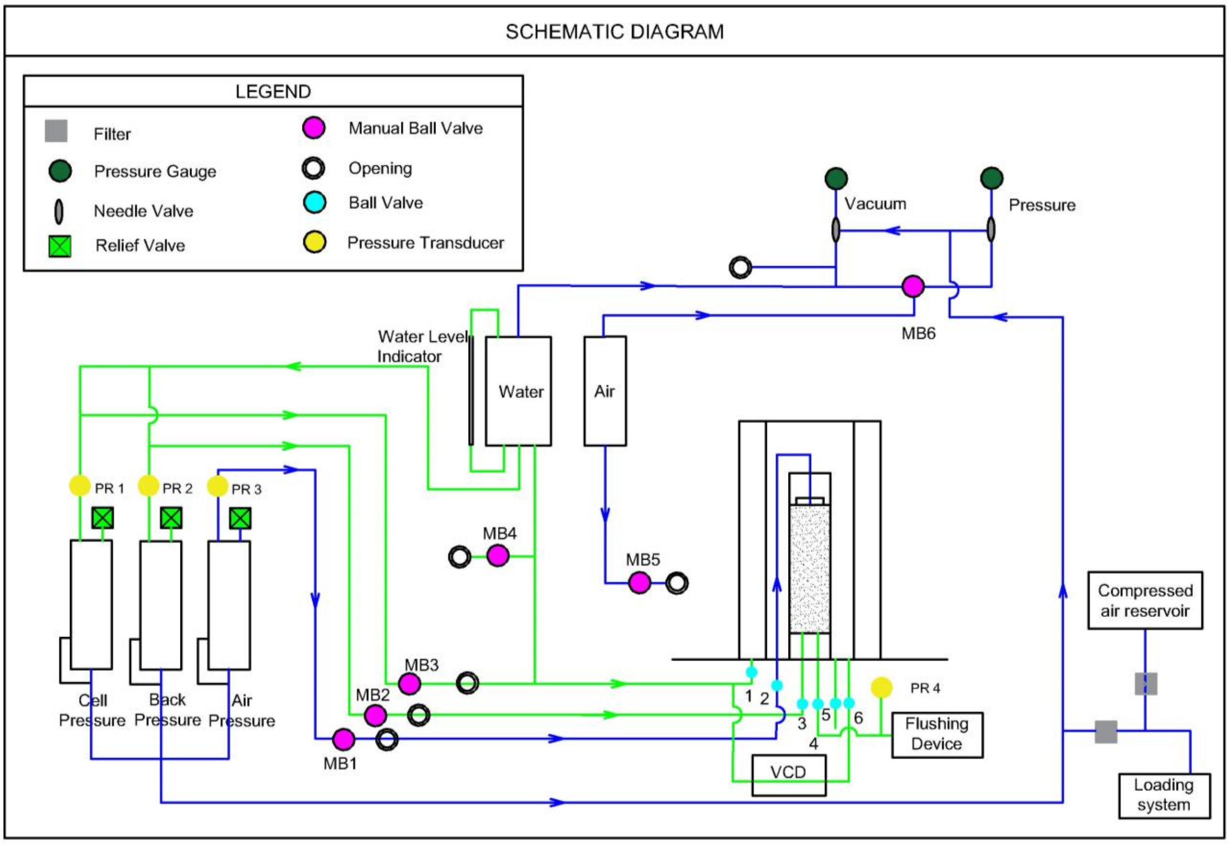

Figure 5.3: Overall system layout

5.3.1 Double-walled triaxial cell (DWTC)

A single triaxial cell was used in testing unsaturated soils while it was in the developmental stage. Later, the use of a double-walled triaxial cell (DWTC) was identified (Bishop and Donald, 1961; Wheeler, 1986) and it significantly reduced the compliance, creep, and leakage errors associated with the measurement of the total volume change. Therefore, the GCTS unsaturated triaxial configuration uses a DWTC. The air pressure is applied at the top of the sample and the back pressure (pore water pressure) from the bottom of the pedestal. One of the drawbacks of the GCTS system is that the pore drainage is based on the sample length, and it takes a long time to reach equilibrium (more than 15 days). Sharma (1998) and Raveendiraraj (2009) utilised the two-way drainage concept for the back pressure line and a one-way drainage path for the air pressure line, which resulted in less time than for the experiments carried out using the GCTS apparatus. The base pedestal and the top cap of the isotropic cell are made of steel, and transparent Perspex is used for the triaxial cell. O-rings were used to fix the sample to the top cap and to the bottom pedestal. Six drainage paths were utilised in the experiments (see Figure 5.1(b) and Figure 5.3) as follows. Two drainage lines (i.e., the 1st and 6th) were used for the double-walled triaxial cell, one for filling/removing water and the other for refilling. The 2nd drainage line was used to apply air pressure to the sample from the top pedestal, whereas the 3rd drainage path was used as the back pressure line. The 4th drainage line was fixed to the flushing device. In addition, the 5th drainage linewas used for removing and refilling water from and to the inner cell. A porous stone and an air entry disk of 1500 kPa suction were used for the top and bottom pedestals, respectively.

5.3.2 Volume change device

The measurement of the volume change of the unsaturated specimen was performed by measuring the volume of fluid entering or leaving the inner confining pressure cell. Therefore, a volume change device (VCD) was used in the system, and other researchers (Sharma, 1998; Raveendiraraj, 2009) have used the same technique in their experiments. Figure 5.4 includes the GCTS volume change device equipped with an internal linear variable differential transformer (LVDT), a smooth guided piston stroke, a frictionless rolling diaphragm, and stainless steel housing to avoid hysteretic behaviour (no pressure differential), resulting in reduced compliance errors. The rolling diaphragm eliminates the sliding friction of the device. Another main feature of VCD is the 4-way crossover value that has an finite volume capacity with an accuracy of 0.01cm^3. If the VCD is filled with water, the water used to fill the DWTC is sent through the VCD before filling the DWTC.

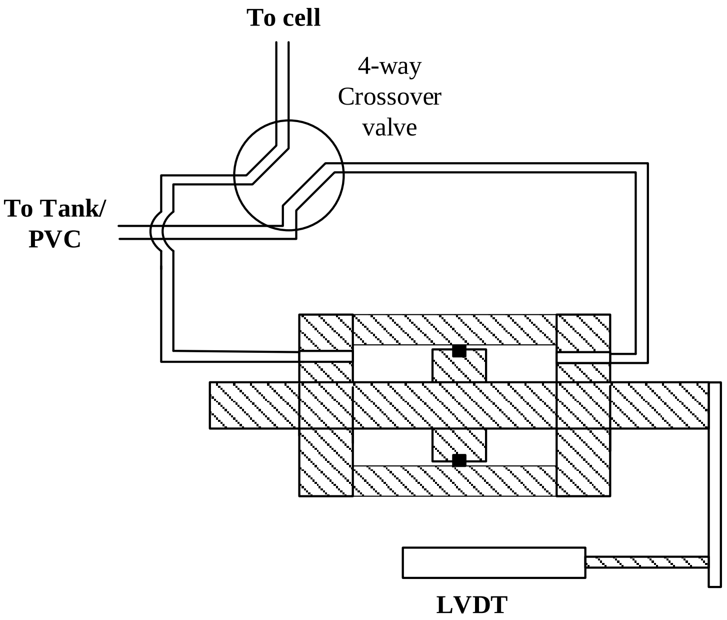

Figure 5.4: Schematic diagram of volume change device

5.3.3 Air flushing device

The diffused air beneath the air entry disc can introduce errors in the system, although the applied suction of the test is less than the capacity of the air entry disc and the disk is fully saturated prior to each test. For example, during equalisation for drained experiments, a significant time delay can be observed due to the diffused air. This occurs due to de-saturation caused by menisci formation, leading to lower hydraulic conductivity. Therefore, flushing the diffused air from the pore water line was identified as essential. Figure 5.5 includes the flushing device used for the GCTS set-up; this process corrects the pore-water volume change measurements while maintaining the saturation of the air entry disk. The flushing device consists of three components, namely, a differential pressure transducer, a computer-controlled ball valve and a water reservoir. The total capacity of the flushing device is 400cm^3 with an accuracy of 0.06cm^3. The pore pressure controller is used along with the flushing device to remove the diffused air underneath the air entry disk. The detailed flushing procedure is as follows: (1) set the pore pressure controller to volume control and open valves 3 and 4 in Figure 5.1; (2) open the flushing system allowing the water to enter the flushing device and water is then pumped to the pore pressure controller. This step should be repeated at least three times; (3) close valve 4 prior to the test.

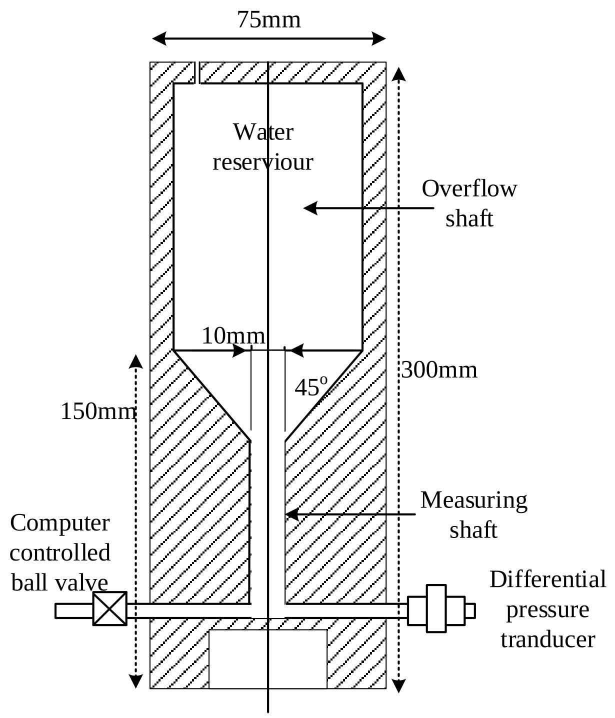

Figure 5.5: Schematic diagram of diffused air flushing device

5.3.4 Logging and control system

Since an automatic control system was used in GCTS apparatus, the same system was used for the experimental program in this study as the control system captures continuous measurements of pressure changes and volume changes over a long period of time (around 6 months). Furtthermore, the test program included a combination of stress paths of loading, unloading, wetting, and drying, and manual control was not incorporated due to the associated difficulties. Moreover, the combination of stress paths could be automated using the controller to avoid discontinuation of the tests. Apart from all the above advantages, the controller provided the final logged data for post-processing using the standard software Microsoft Excel, which made the experimentation convenient.

In the GCTS software, one test can be performed in several stages, such that each stage represented a particular part of the stress path, such as loading, unloading, wetting, and drying. For example, Figure 5.6 shows the defined back pressure variation for a wetting test. The intention is to reduce back pressure from 220 kPa to 20 kPa at a rate of 0.5 kPa/hr. The total time duration of the defined stress path can also be set.

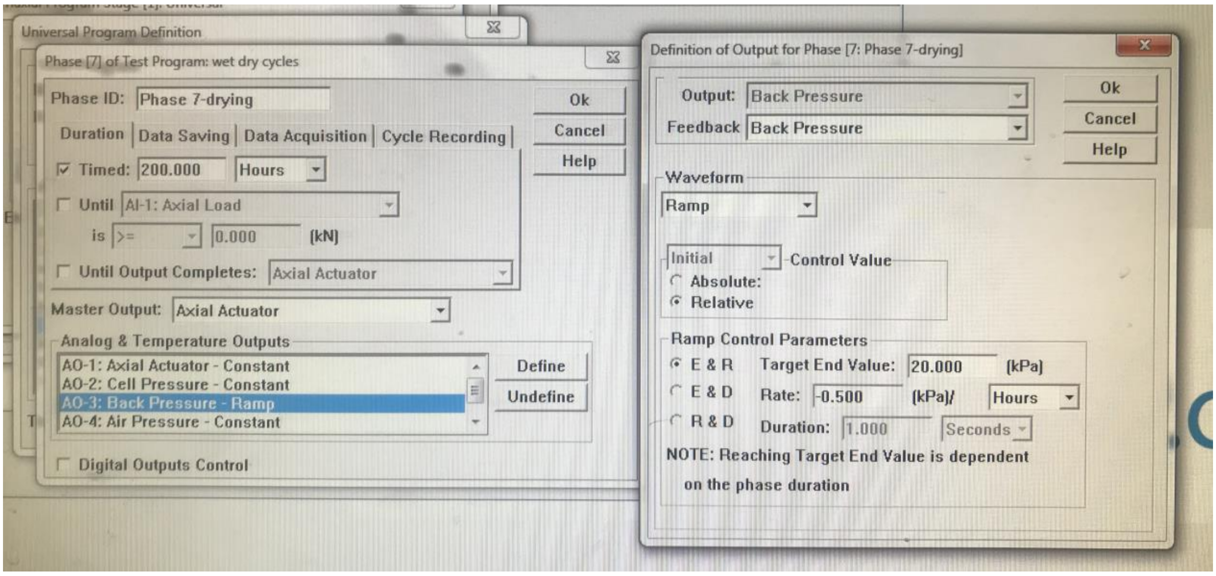

Figure 5.6: Example of back pressure variation for drying test

5.4 Recalibration of the apparatus

The GCTS apparatus at Monash University was originally installed in 2012, and a complete calibration of transducers, VCD, load cell, and displacement gauges was carried out prior to the experiments reported by Abeyrathne (2017). However, for the new experimental series, the set-up was recalibrated using the previous calibration as a reference. In addition, a quality experimental series requires careful calibration of the pressure transducers and LVDTs. Therefore, the GCTS apparatus transducers and all the LVDTs were recalibrated using appropriate approaches, as explained in the following sections. In addition to errors in the transducers, the VCD, the load cell, and the displacement gauges, errors can occur due to temperature variations. Therefore, the GCTS apparatus was housed in a temperature-controlled room.

5.4.1 Recalibration of pressure transducers

In the GCTS system, there are four main transducers, namely, an air pressure transducer, a water pressure transducer, a cell pressure transducer on the pressure control panel and a pore pressure transducer positioned close to the bottom pedestal of the DWTC. In order to convert the transducer voltages to engineering units of kPa, the transducers were calibrated using an appropriate reference. As the appropriate reference for the calibration of the pressure transducers, a pressure gauge connected to the compressed air line was selected. Three main types of calibration methods are available in the GCTS controller system as follows:

a. Set-up and gain which is used for a completely new sensor or when the system is installed, as the base parameters are required;
b. Two-point calibration. For this approach, 0 kPa pressure is selected for the first point and higher pressure for the second point; and,
c. Multi-point calibration is used to check the errors of the previous calibration. This process can be considered as validation rather than calibration.

5.4.1.1 Pressure transducers

Of the three main calibration processes, multi-point calibration with 11 points was selected (zero and another 10), starting from 0 kPa air pressure and ending at 600 kPa. Since the maximum compressed air line was slightly higher than 600 kPa in the laboratory, the calibration was carried out only up to 600 kPa, and most of the experiments were based on net pressures less than 600 kPa. However, the transducers are capable of capturing pressures up to 2000kPa. The values used were 0kPa, 40 kPa, 80 kPa, 100 kPa, 140 kPa, 200 kPa, 300 kPa, 360 kPa, 400 kPa, 500 kPa, and 580 kPa. The pressure gauge was set at the above values and the transducer sensor voltages were recorded, and the results are given in Figure 5.7(a) for the air pressure transducer, Figure 5.7(b) for the water pressure transducer, Figure 5.7(c) for the cell pressure transducer, and Figure 5.7(d) for the pore pressure transducer. Subsequently, the calibration files were exported to the system, and a number of pressure values were then rechecked with known pressure references for each transducer separately.

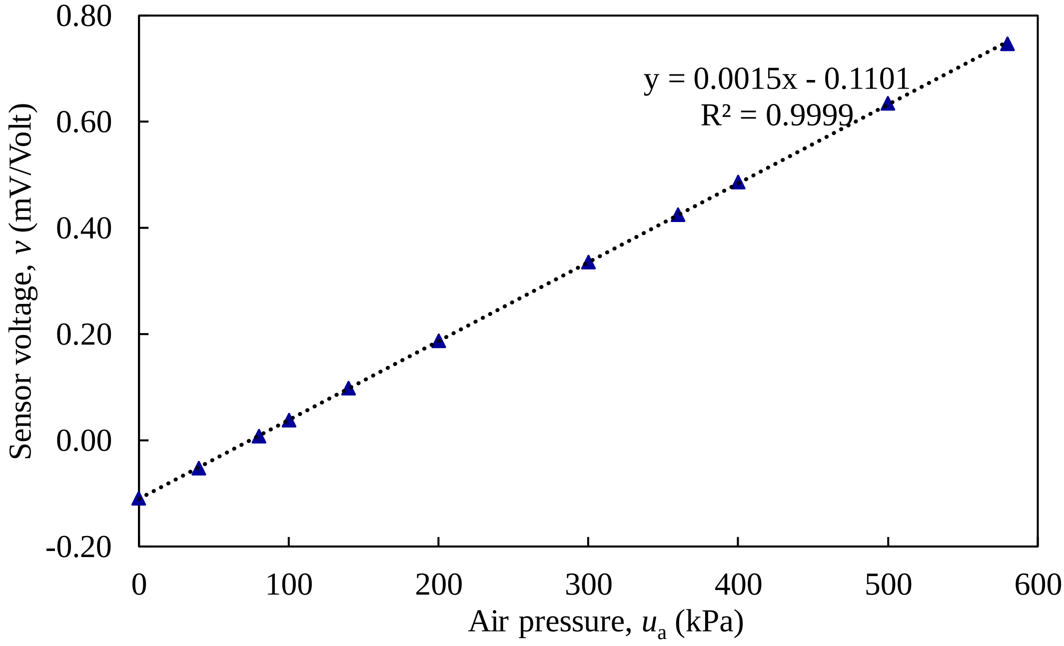

(a)

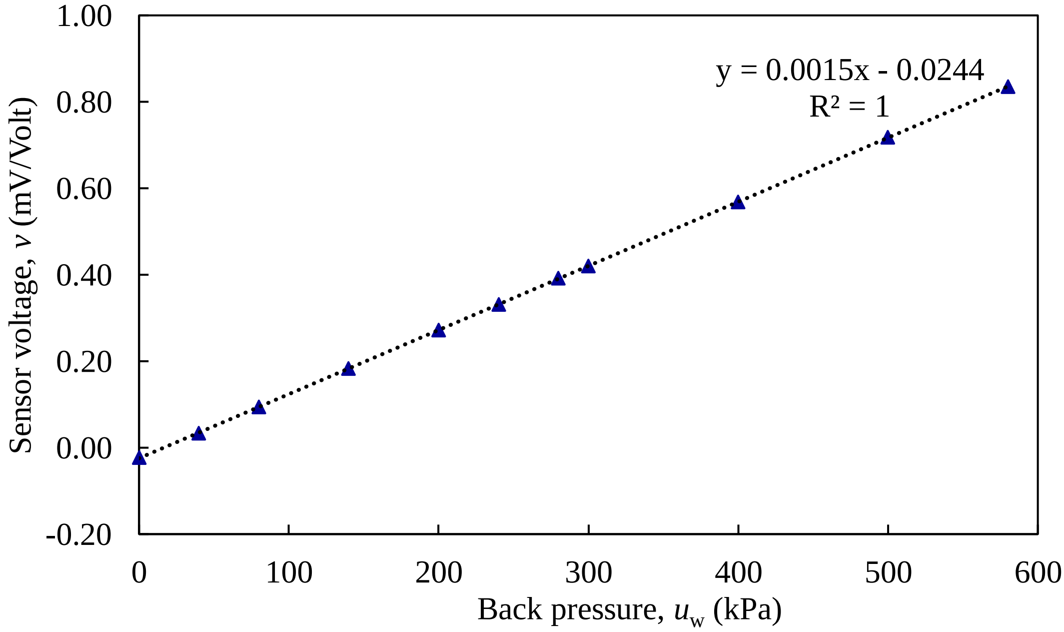

(b)

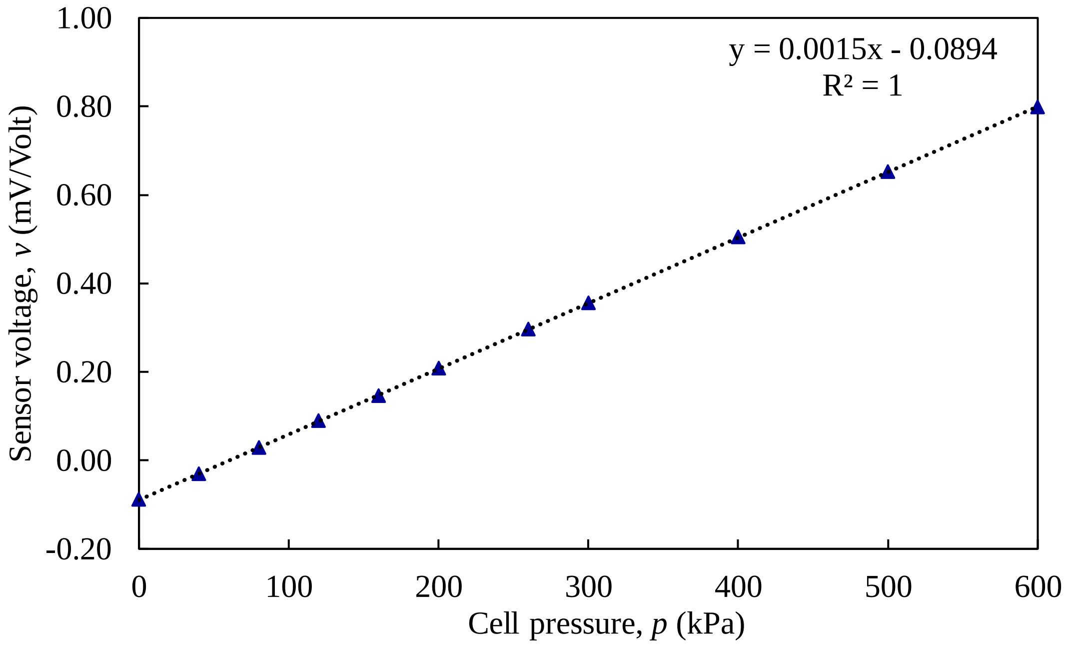

(c)

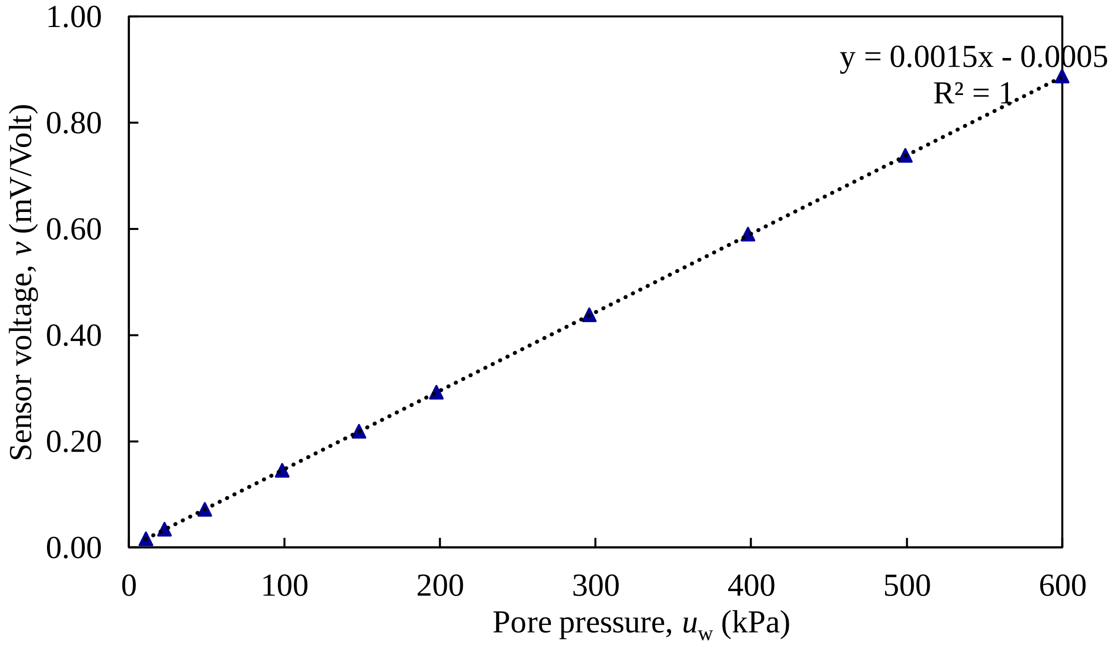

(d)

Figure 5.7: Calibration curves for (a) air pressure; (b) back pressure; (c) cell pressure (d) pore pressure transducers

5.4.2 Calibration of VCD

The calibration of the VCD was carried out by correlating the actual volume of water expelled from the VCD to the LVDT reading. The following steps were followed for the calibration of the LVDT of VCD

1. A pressure of 5 kPa was applied to the water coming into the VCD. Prior to calibration, the VCD system was de-aired by opening the shut-off valve and flowing water through the system until no water bubbles were visible in the water tubes.
2. The corresponding zero volume was taken when the VCD was at the extreme end.
3. Then the shut-off valve was slowly opened, and all of the water which escaped from the VCD was captured in a container
4. The mass of the expelled water was measured, and the expelled water volume was calculated (1g water = 1 cm^3). The results are given in Table 5.1.
5. Finally, the area of the VCD (old area 69mm^2) was adjusted to 62.79mm^2.

Table 5.1: Variation of expelled water mass and VCD reading

Mass (g)	VCD volume measured (cm^3)
11.06	12.6
20.85	23.4
38.93	43.1
60	66.4

5.4.3 Calibration of load cell

To calibrate the load cell, a proving ring was used, and the results are provided in Table 5.2. The proving ring coefficient obtained was 5.88N/div.

Table 5.2: Variation of applied load and proving ring reading

Load applied (kN)	Proving ring reading
0.1	16
0.2	32.5
0.3	49.5
0.5	83.5

1	170
1.5	256
2.0	341

5.5 Set-up procedure

After the recalibration of all the transducers, the VCD, the load cell and the displacement gauges, a number of trial tests were performed prior to the experimental program. The GCTS set-up procedure for constant suction loading was as follows:

1. The experimental sample was placed inside the double-walled triaxial cell (DWTC), as shown in Figure 5.1(a).
2. The DWTC cell was placed around the sample as Figure 5.1(b) prior to filling the cell with water. The water was supplied to the inner chamber using valve 5 and stopped when the chamber was almost full. The remaining water was to remove any air inside the volume-changing device (VCD). After filling the cell halfway through valve 5, the valve was closed, and valves 1 and 6 opened. Hence, the water coming through the reservoir went through valve 1 and through VCD to valve 6, as shown in Figure 5.3.
3. Subsequently, the loading frame was attached to the system, and 5 kPa pressure was applied as a sealing stress.
4. Using the diffused air-flushing device, the air underneath the air entry disk was removed using valves 3 and 4.
5. Before commencing the test, the input offsets of the VCD, cell pressure chamber (CPC), back pressure chamber (BPC), and air pressure chamber (APC) were set at zero.
6. The corresponding program was defined using the GCTS software to assign the required equalisation times and pressure increment or final pressure.
7. 20 kPa cell pressure (through valve 1), air pressure of 10 kPa (through value 2) and 5 kPa of back pressure (through valve 3) were applied before commencing the test.
8. Next, the initial stresses were applied and kept for equilibrium until the pore water discharge became 0.05cm^3/day.
9. Finally, the experiment was performed, and periodically, the variations of total volume change and water volume change were monitored. Finally, as explained earlier, all the data were exported as an Excel file.

5.6 Stress path stages

A typical test performed in this study included several stages, and in each stage, a selected variable varied with time. All the experiments commenced with an initial equalisation stage, with the relevant initial net stress and suction values. The equalisation period ranged from 10 days to 15 days, or in some cases more, due to the single drainage path. The initial states of the experiments varied depending on the requirement. However, generally the net stress varied from 10 kPa to 20 kPa whereas the suction varied from 200 kPa to 300 kPa. In all cases, water drainage was monitored, and equalisation was assumed to be complete when the pore water change reached 0.05cm^3/day. During equalisation, sudden collapse was observed, due to the initial 50 kPa 1-D compaction stage. Since the effect of 1-D compaction is less than that of isotropic compaction, 50 kPa isotropic stress state was achieved upon collapse from the 1-D stress state.

Isotropic loading and unloading tests were carried out for constant suction or constant water content stress paths, depending on the requirement of the test. A rate of 2 kPa/hr for mean net stress was found to be adequate, and the same rate was applied by Raveendiraraj (2009). After each stress stage, a 24hr equalisation stage was performed in all the tests to acquire reasonable equalisation. For the wetting and drying stress paths a rate of 1 kPa/hr was selected, which was a lower rate than that for loading and unloading. In some stress paths, a rate of 0.5 kPa/hr was applied, when sample was close to saturation. No shear tests or controlled volume tests were employed due to time limitations.

5.7 Data processing

The data files extracted from the GCTS software were analysed to obtain the specific volume (v) and degree of saturation (S_r) for the loading, unloading, wetting and drying stress paths. The v and S_r can be obtained from:

$$v = \frac{\rho_w G_s (V_o - \Delta V)}{M_s} \qquad (1)$$

$$S_r = \frac{\frac{(M_o - M_s)}{\rho_w} - \Delta V_w}{(V_o - \Delta V) - \left(\frac{M_s}{\rho_w G_s}\right)} \quad (2)$$

where, M_o is the mass of the sample at the start of the test, M_s is the mass of the solids (measured after oven-drying the sample at the end of the test), ρ_w is the density of the water, V_o is the sample volume at the start of the stage, ΔV is the reduction of the sample volume from the beginning of the test, ΔV_w is the reduction of the water volume from the start of the test, and G_s is the specific gravity.

5.8 Validation of uniqueness of MPK framework in v, v_w, p plane

To establish the uniqueness and validate to concept of the LWSBS upon wetting, loading/unloading combinations in an extensive number of experiments have been carried out in the 1-D stress state by Islam and Kodikara (2015); Kodikara et al. (2015) and in the isotropic stress state by Abeyrathne (2017) for less reactive compacted kaolin and highly reactive Merri Creek soil. However, the present study considered only paths containing loading/unloading and wetting stress paths, and its applicability to paths containing drying was examined. Hence, an experimental series was designed to examine the general validity of the LWSBS and mathematical equations were developed based on constant water content testing. Soil samples were prepared and compacted to 50 kPa to achieve the loosest state of compacted soil.

Trial isotropic testing was initially carried out using the unsaturated soil triaxial apparatus. From the trail observations, a rate of 2 kPa/hr for loading and 1 kPa/hr for wetting and drying stress paths with subsequent equilibrium time of 24 hours was selected for future testing. In total, six experiments were carried out in the drying/loading series of tests. The main aims of these six experiments were:

(a) to examine the yield stress upon loading starting from two different states: (1) loading after drying stress path; and (2) loading from as-compacted state with the same initial v_w, p states and;

(b) to verify whether both stress paths coincide during yield or, in other words, to determine if the same LWSBS applies to both tests during yield.

Therefore, the first three stress paths (T1, T2 and T3) were designed considering constant suction loading-unloading-drying–constant water content loading paths (ABCDE), as shown Figure 5.8(a) in the v,v_w plane and Figure 5.8(b) in the v,p plane. These three tests were carried out for three suction ranges: 100 kPa-200 kPa (T1), 200 kPa-300 kPa (T2) and 300 kPa-400 kPa (T3). The other three independent constant water content tests which started from the as-compacted state (GH, T4, T5 and T6) were carried out for the water contents arrived at by the drying stress path tests. It should be noted that, although the MPK framework is in the v,v_w,p space, suction was used to bring the soil to a drier state.

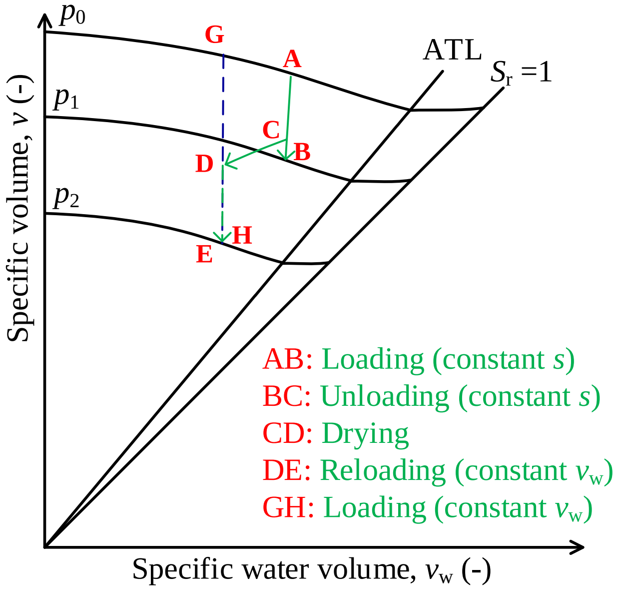

(a)

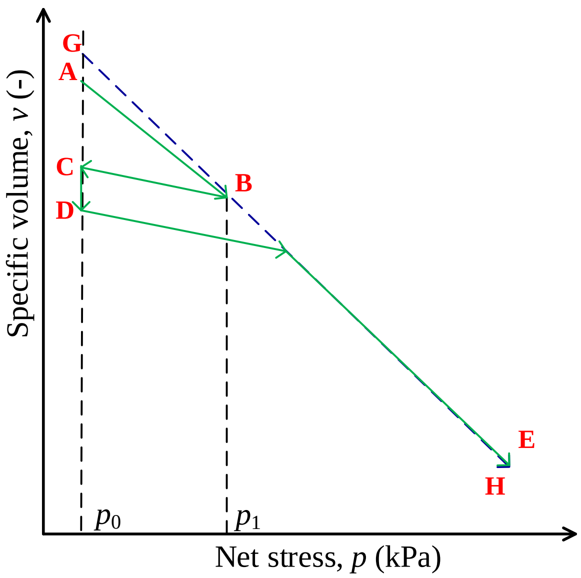

(b)

Figure 5.8: Stress paths designed for validation of uniqueness of MPK framework in (a) v,v_w plane; and (b) v,p plane (for uniqueness E and H must be the same)

5.8.1 Test T1

Test T1 was designed for the lower suctions (100 kPa to 200 kPa) which can be achieved using the experimental set-up. Table 5.3 and Figure 5.9 show the stress paths followed in test T1. The sample was first equalised (AA') to the mean net stress of 10 kPa and suction of 100 kPa. The duration of the equalisation was 14 days. Constant suction loading and unloading cycles (A'BB'C) were then performed on the soil sample over a net stress change to 50 kPa, and the sample was then dried to 200 kPa suction under the net stress of 10 kPa. Finally, constant water content loading was performed on the sample to mean net stress of 250 kPa. The B', C', D', and E' states are not marked in Figure 5.9, as no significant change occurred during the 24 hr equalisation.

During initial equalisation, collapse behaviour is observed where the soil yields volumetrically during the initial equalisation wetting due to the lower initial stress compaction of the sample. The subsequent loading path A'B also depicts some yielding behaviour, suggesting that the reduction of the specific volume of I-D compaction is lower than that of isotropic compaction. The yield stress of Figure 5.9(b) is almost 15 kPa. Then during the unloading stress path B'C, the soil behaves elastically. Figure 5.9(c) shows the behaviour of the sample during the drying stress path on the v,s plane. One of the phenomenological observations highlighted during test T1 is the increase in yield stress with constant suction after drying (to approximately 60 kPa), as shown in Figure 5.9(b). Similarly, T2 and T3 were carried out for higher suction ranges of 200 kPa to 300 kPa and 300 kPa to 400 kPa, respectively. The constant water content loading was carried out for the specific moisture ratio of 1.95 for test T1. Test T4 was carried out with the same moisture ratio (v_w =1.95).

Table 5.3: Stress path for T1

Stage			Net stress (kPa)	suction(kPa)
From	To	Description		
A	A’	Initial equalisation	10	100
A’	B	Isotropic loading	10→50	100
B	B’	Equalisation	50	100
B’	C	Isotropic unloading	50→10	100
C	C’	Equalisation	10	100
C’	D	Drying	10	100→200
D	D’	Equalisation	10	200
D’	E	Constant water content loading	10→250	200→190
E	E’	Equalisation	250	190

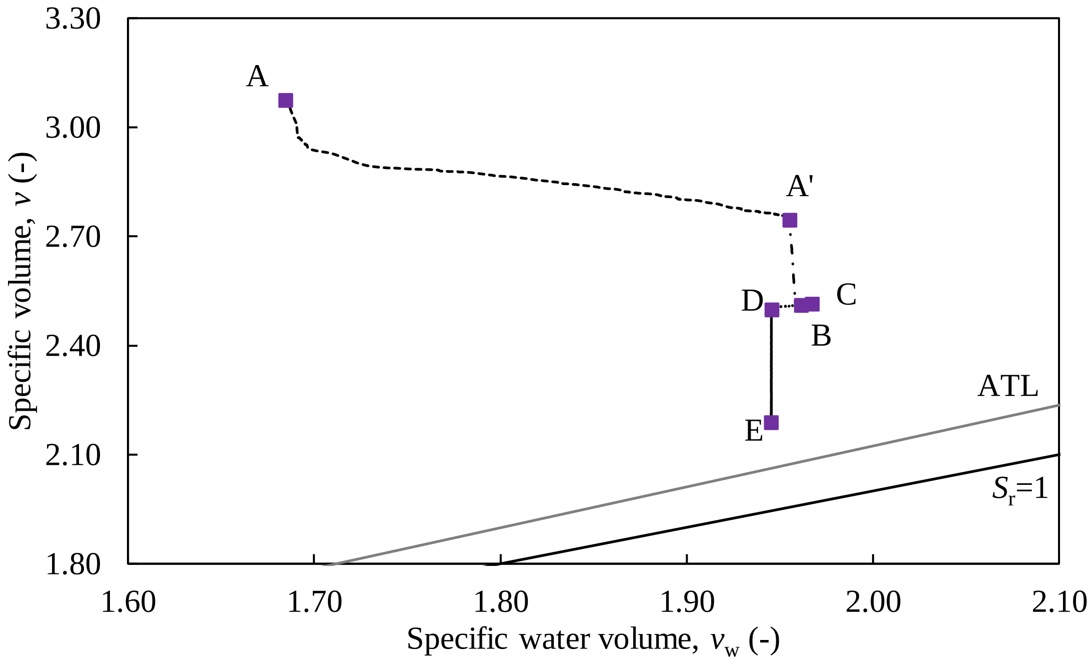

3.30
3.00
2.70
2.40
2.10
1.80
1.60
1.70
1.80
1.90
2.00
2.10
Specific volume, *v* (-)
Specific water volume, v_w (-)
A
A'
B
C
D
E
ATL
S_r=1

(a)

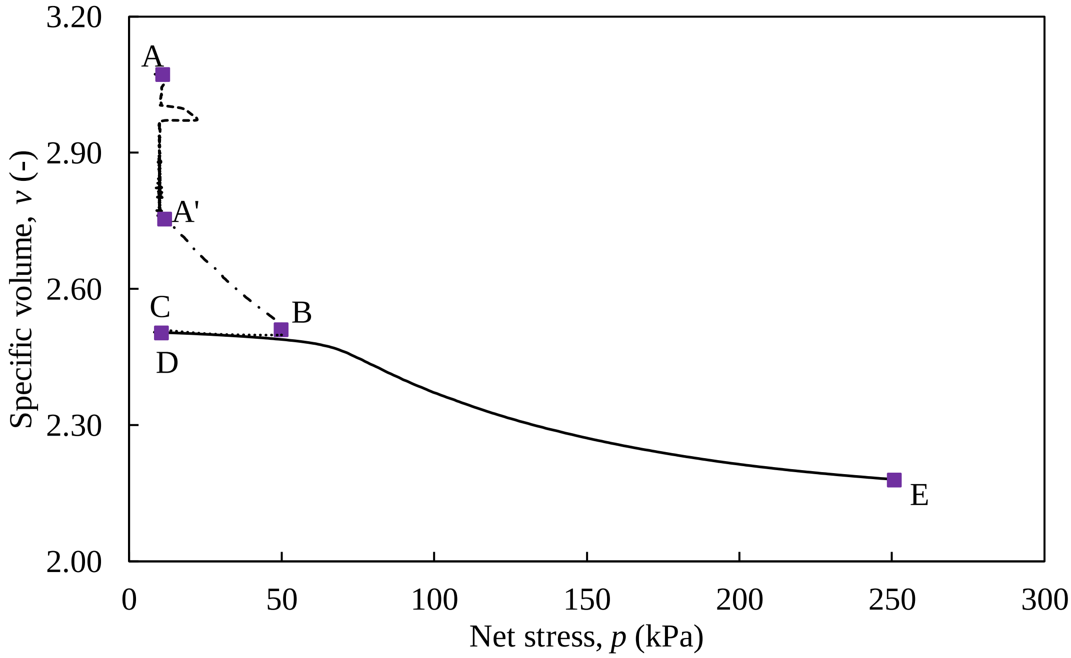

3.20
2.90
2.60
2.30
2.00
0
50
100
150
200
250
300
Specific volume, *v* (-)
Net stress, *p* (kPa)
A
A'
B
C
D
E

(b)

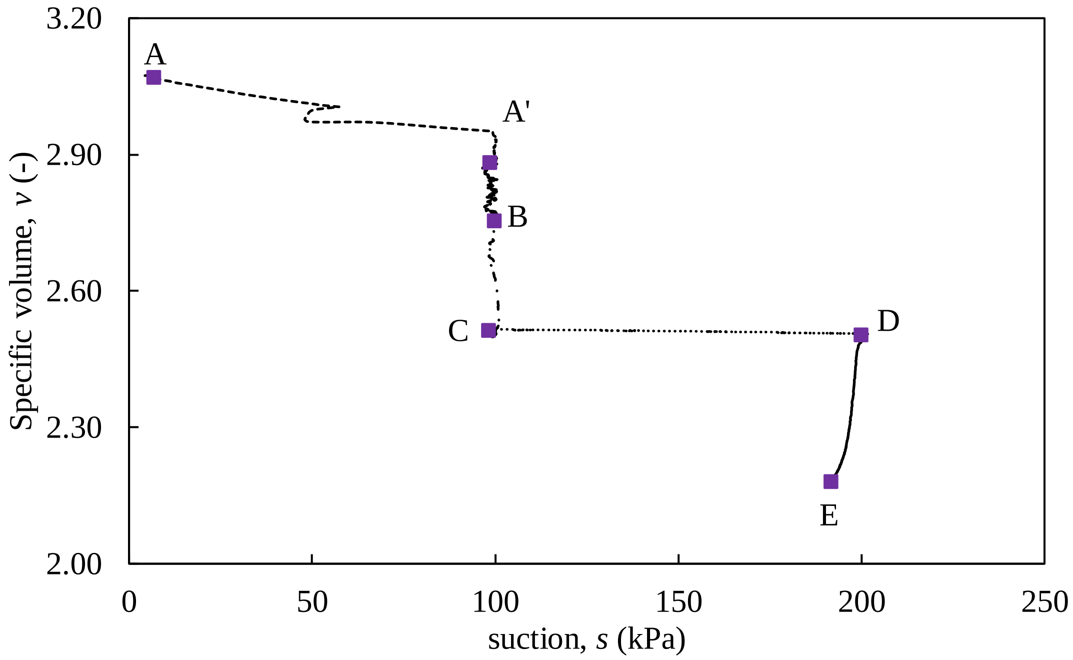

(c)

Figure 5.9: Experimental results of T1 (a) v,v_w *plane;(b)* v,p *plane;(c)* v,s *plane*

5.8.2 Test T2

Test T2 was designed for the suction values of 200 kPa to 300 kPa, and the results are shown in Table 5.4 and Figure 5.10(a) in the v,v_w plane, Figure 5.10(b) in the v,p plane, and Figure 5.10(c) in the v,s plane. The sample was first equalised (AA') at mean net stress of 10 kPa and suction of 200 kPa. The duration of the equalisation was 16 days. Constant suction loading and unloading cycles (A'BB'C) were then performed on the soil sample over a net stress change to 50 kPa, and the sample was then dried to 300 kPa suction under the net stress of 10 kPa. Subsequently, constant water content loading was performed on the sample to a mean net stress of 320 kPa. The loading path A'B depicts some yielding behaviour, suggesting that the reduction of the specific volume of I-D compaction is lower than that of isotropic compaction. Similar to test T1, the yield stress of Figure 5.9(b) is almost 15 kPa. Then during the subsequent unloading stress path B'C the soil behaves elastically. Figure 5.9(c) shows the behaviour of the sample during the drying stress path on the v,s plane. One of the phenomenological observations during test T2 is that the increase in yield stress after drying (to approximately 70 kPa) where the drying results in yielding of soil can be observed during stress path DE in Figure 5.9(b).

The constant water content loading was carried out under a specific moisture ratio of 1.85 for test T2, and it was planned to carry out test T5 with the same moisture ratio.

Table 5.4: Stress path for T2

Stage			Net stress (kPa)	suction(kPa)
From	To	Description		
A	A’	Initial equalisation	10	200
A’	B	Isotropic loading	10→50	200
B	B’	Equalisation	50	200
B’	C	Isotropic unloading	50→10	200
C	C’	Equalisation	10	200
C’	D	Drying	10	200→300
D	D’	Equalisation	10	300
D’	E	Constant water content loading	10→320	300→282
E	E’	Equalisation	320	282

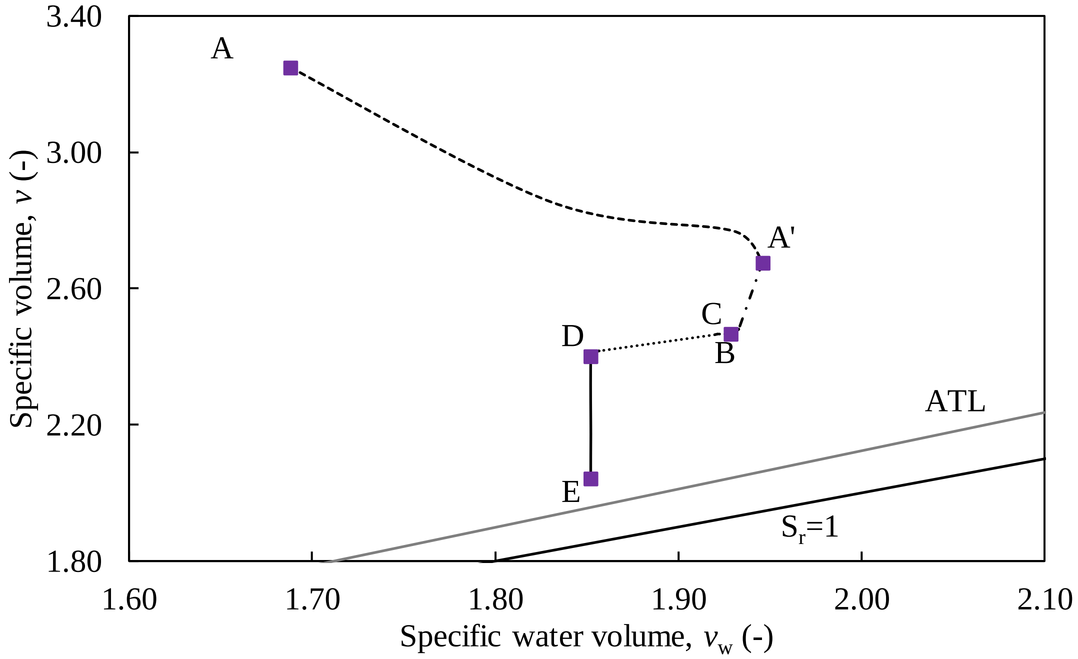

(a)

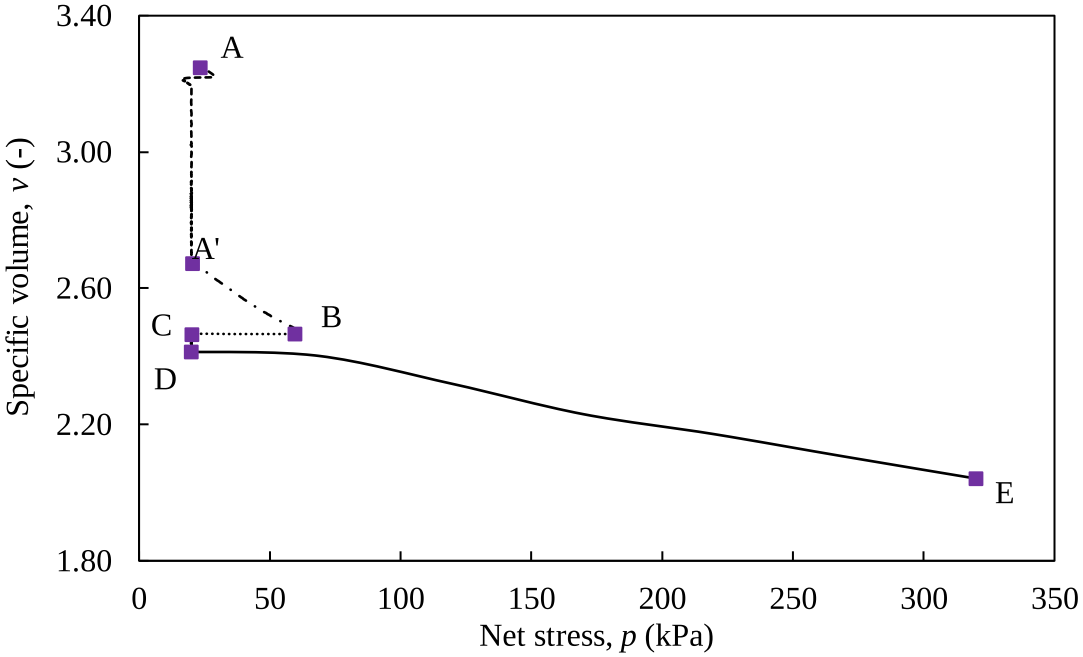

(b)

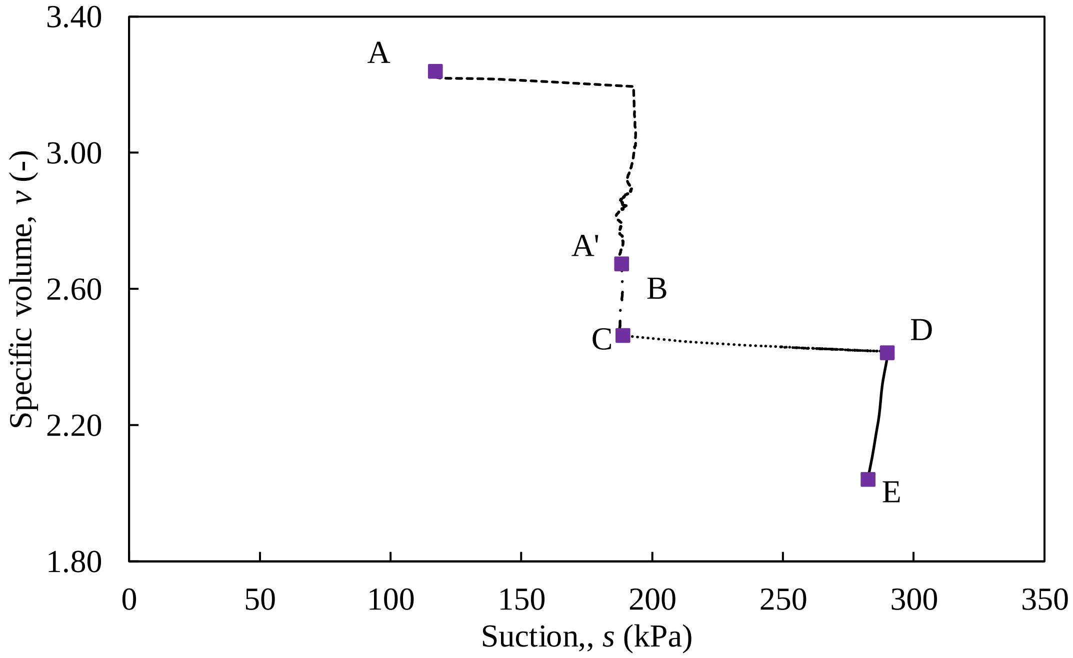

(c)

Figure 5.10: Experimental results of T2 (a) v, v_w *plane;(b)* v, p *plane;(c)* v, s *plane*

5.8.3 Test T3

Test T3 was designed for the suction values of 300 kPa to 400 kPa and the results are presented in Table 5.5 and Figure 5.11(a) in the v,v_w plane, Figure 5.11(b) in the v,p plane, and Figure 5.11(c) in the v,s plane. The sample was first equalised (AA') to mean net stress of 10 kPa and suction of 300 kPa. Constant suction loading and unloading cycles (A'BB'C) were then performed on the soil sample over a net stress change to 50 kPa, and the sample was then dried to 400 kPa suction under the net stress of 10kPa. Finally, constant water content loading was performed on the sample to mean net stress of 400 kPa. Test T3 exhibits similar behaviours to tests T1 and T2. The purpose of repeating the same stress paths for different suctions was to validate the uniqueness of the MPK model in relation to yield stress after major wetting and drying for a given v,v_w state. Constant water content loading was carried out for a specific moisture ratio of 1.83 for the test T3 stress path DE. It was planned to carry out test T6 with the same moisture ratio.

Table 5.5: Stress path for T3

Stage			Net stress (kPa)	suction(kPa)
From	To	Description		
A	A’	Initial equalisation	10	300
A’	B	Isotropic loading	10→50	300
B	B’	Equalisation	50	300
B’	C	Isotropic unloading	50→10	300
C	C’	Equalisation	10	300
C’	D	Drying	10	300→400
D	D’	Equalisation	10	400
D’	E	Constant water content loading	10→400	400→395
E	E’	Equalisation	400	395

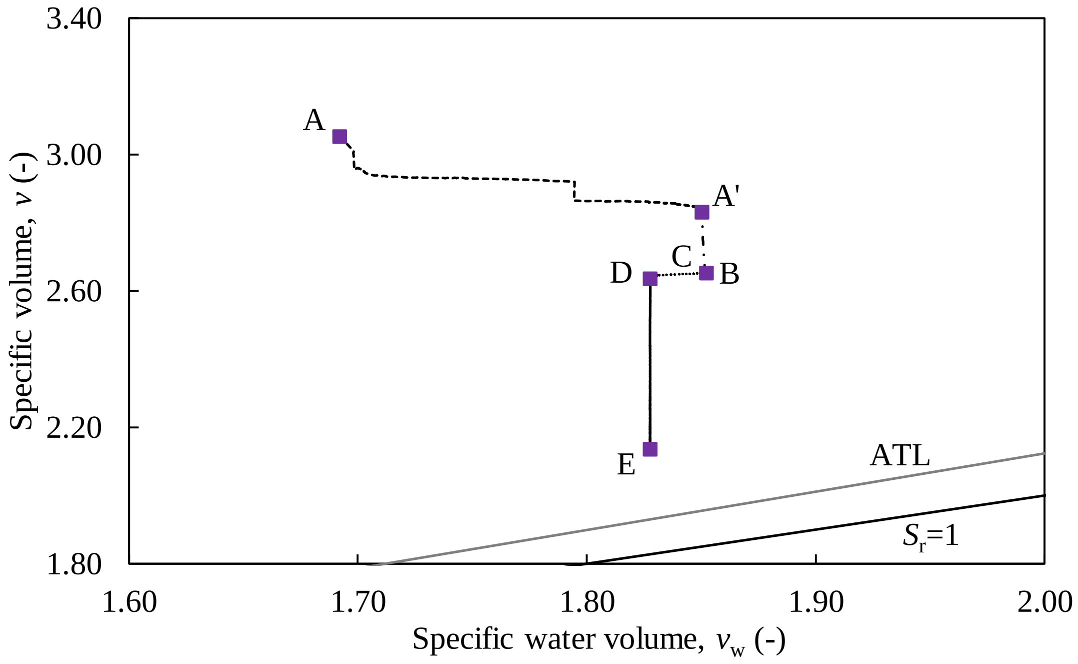
3.40
3.00
2.60
2.20
1.80
1.60
1.70
1.80
1.90
2.00
Specific volume, v (-)
Specific water volume, v_w (-)
A
A'
B
C
D
E
ATL
S_r=1

(a)

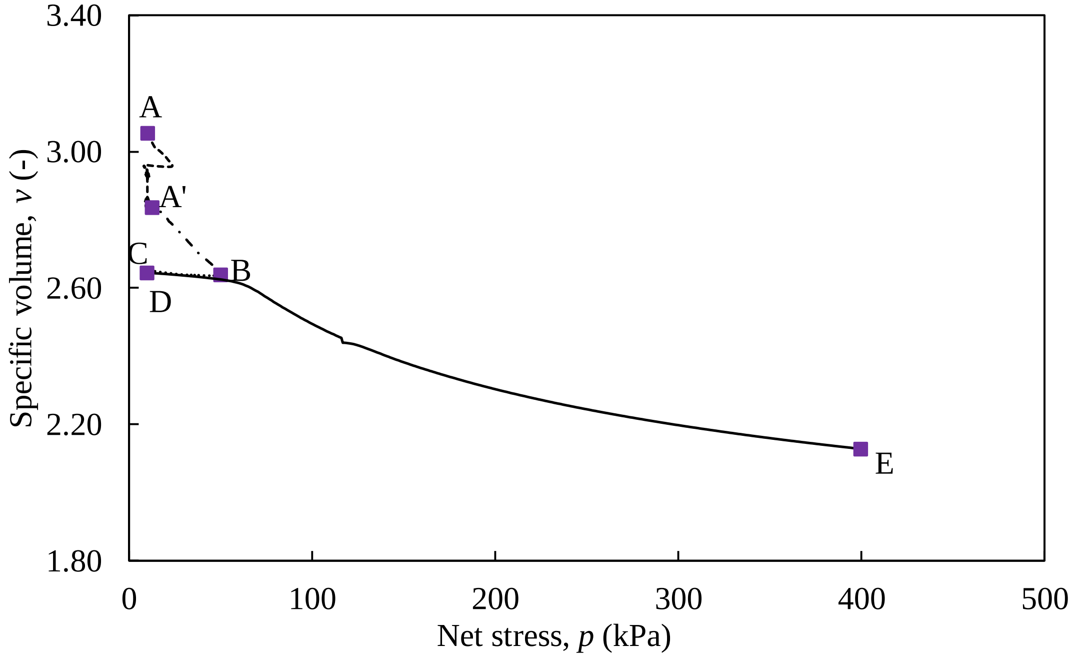
3.40
3.00
2.60
2.20
1.80
0
100
200
300
400
500
Specific volume, v (-)
Net stress, p (kPa)
A
A'
B
C
D
E

(b)

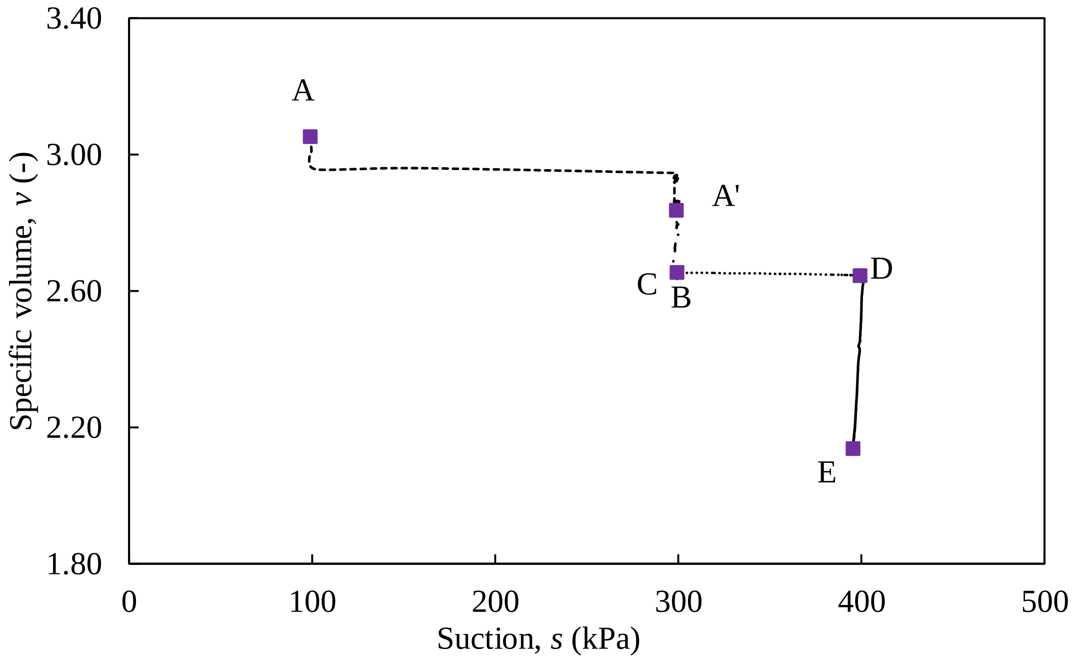

(c)

Figure 5.11: Experimental results of T3 (a) v,v_w plane;(b) v,p plane;(c) v,s plane

5.8.4 Tests T4, T5, T6

Three constant water content tests were carried out (v_w = 1.93 (T4), 1.85 (T5), 1.82 (T6)) using the GCTS triaxial software and no suction measurements were performed. Similar to tests T1, T2 and T3, yielding prior to compaction stress (50 kPa) was apparent in tests T4, T5 and T6. As stated in the previous section, tests T4, T5 and T6 included only constant water content loading stress paths. These three tests were used for comparison with the loading stress paths of tests T1, T2 and T3. For instance, if tests T1 and T4 have the same yield stress at a particular specific volume, the uniqueness of the LWSBS can be established. Furthermore, after achieving the same yield stress, both stress paths should be coincided during continual loading. This is further elaborated in Section 5.8.5.

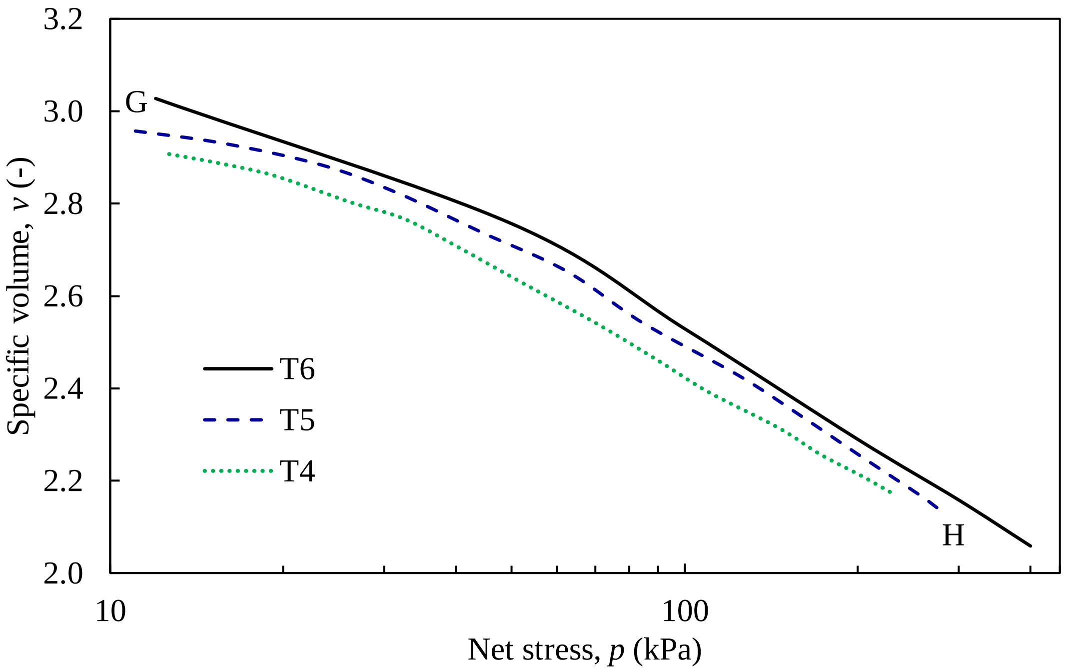

Figure 5.12: Experimental results of T4, T5, T6

5.8.5 Comparison of test results

As the primary objective of the testing series was to clarify the uniqueness of the LWSBS during drying, the constant water content loading stress paths were compared with the drying loading stress paths. Figure 5.13 summarises the comparison of the six tests (T1, T2, T3, T4, T5 and T6), and gives the corresponding variation of the specific volume with loading with or without drying where both stress paths tend to follow similar stress paths after yielding. Figure 5.13(a), (b) and (c) give a comparison of these loading paths for water contents of 1.93, 1.85 and 1.82, respectively.

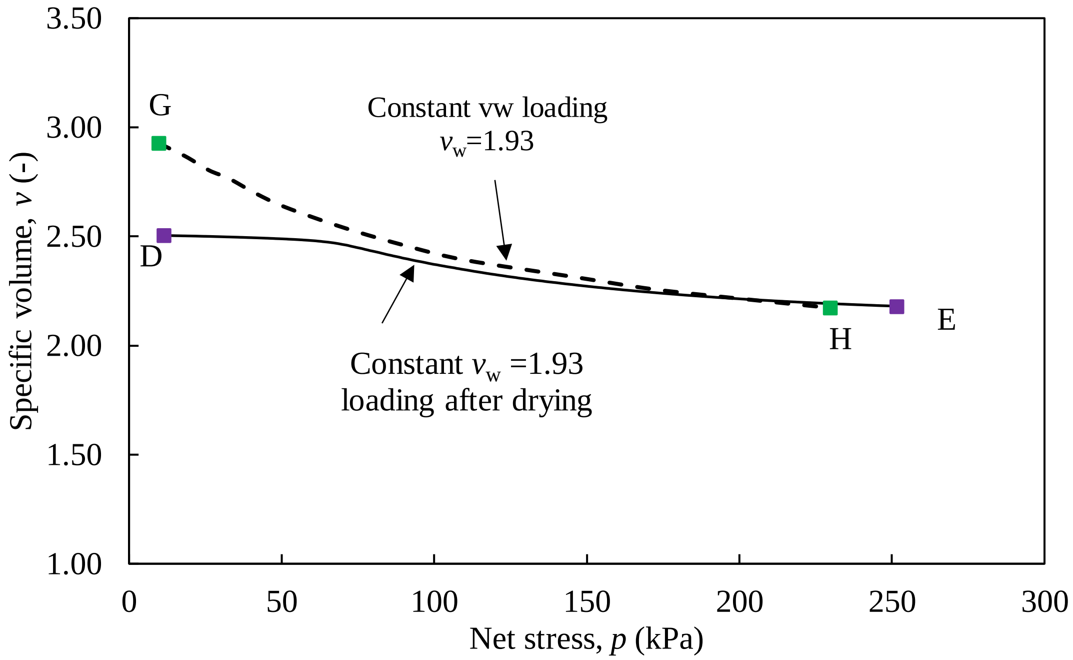

3.50
3.00
2.50
2.00
1.50
1.00
0
50
100
150
200
250
300
Specific volume, v (-)
Net stress, p (kPa)
G
D
H
E
Constant vw loading
vw=1.93
Constant vw =1.93
loading after drying

(a)

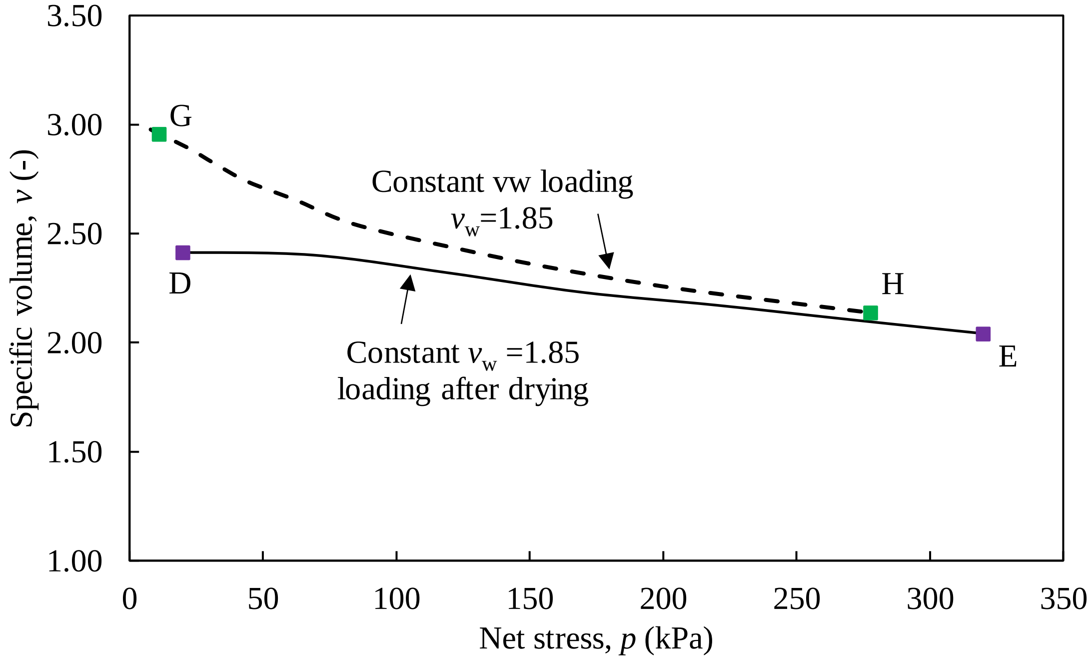

3.50
3.00
2.50
2.00
1.50
1.00
0
50
100
150
200
250
300
350
Specific volume, v (-)
Net stress, p (kPa)
G
D
H
E
Constant vw loading
vw=1.85
Constant vw =1.85
loading after drying

(b)

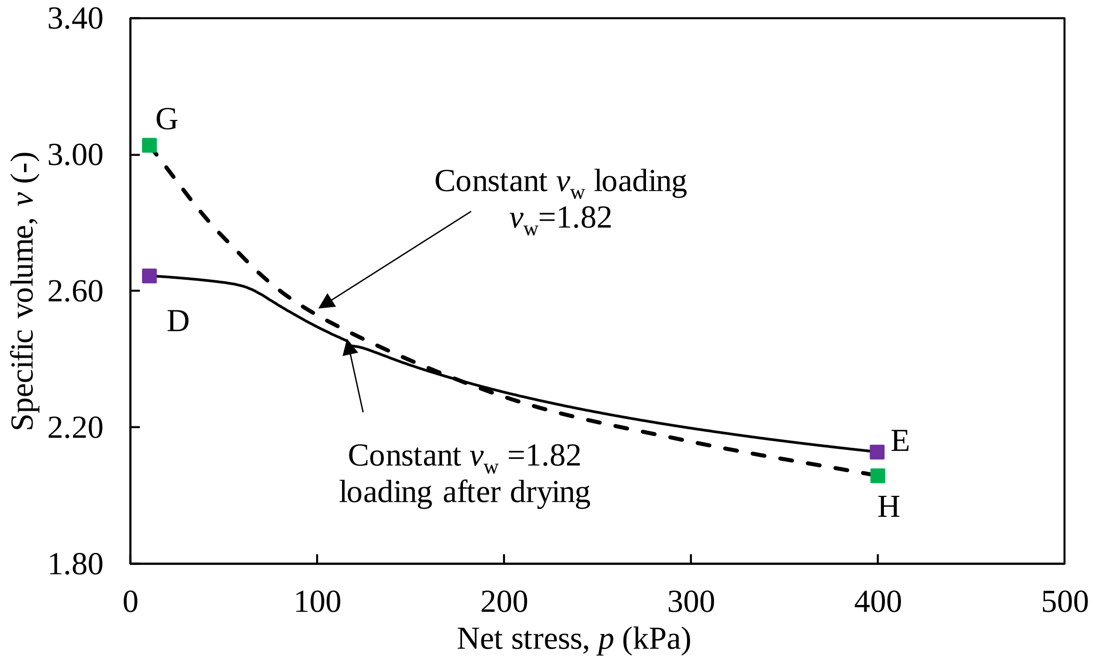

(c)

Figure 5.13: Comparison of (a) T1 and T4; (b) T2 and T5; (c) T3 and T6

On the basis of the observations in Figure 5.13 on loading with drying and without drying, the experimental results follow a similar compression line for the change in specific volume. For example, as Figure 5.13(a) shows, after yielding at 60 kPa, stress path DE follows the T4 constant water content loading (v_w =1.95) stress path. The values of v_w in both T1 and T4 loading paths were made almost equal for the comparison, although the T1 v_w is 1.95 and the T4 v_w is 1.93. It is apparent that the yield stress of 60 kPa is higher than the initial yield stress of 50 kPa, due to the drying of the sample. Similarly, the results of T2 and T5, given in Figure 5.13(b) for v_w =1.85 and the results of T3 and T6, presented in Figure 5.13(c) for v_w =1.82 follow similar behaviour upon loading. In addition, the yield stresses achieved after drying to the suctions of 300 kPa in T2 and 400 kPa in T3 are 70 kPa and 80 kPa, respectively. It should be noted that before drying the yield stress of the samples was 50 kPa and after drying an increase in yield stress was apparent in the experiments. In addition, the test T1 yield stress was close to the T4 loading stress path, and the stress paths coincide reasonably well after yielding, confirming the uniqueness of the LWSBS. In other words, there are similar patterns in the drying loading stress paths (DE in T1, T2, T3) and loading stress paths (i.e., T4, T5, T6). Hence, it can be concluded that the LWSBS is unique for loading/unloading, wetting and drying stress states. In summary, the experimental results show:

(1) the yield stress due to loading after drying increases in comparison to that prior to drying;

(2) the yield stress is the same upon loading from two different states: (1) loading after drying stress path; and (2) loading from as-compacted state with the same initial v_{w}, p states, and;

(3) both stress paths coincide with further loading.

5.9 Validation of hydro-mechanical coupling behaviour and environmental stabilisation (T7 and T8)

The response of hydro-mechanical coupling was observed in two major long-term experimental programs in which the soil was initially subjected to four wet/dry cycles prior to loading under constant water content, and the results are shown in Figure 5.14. The main aim of these tests was to identify the possibility of an environmentally-stabilised state of kaolin for a particular operational stress level after the sample was subjected to a large number of wet/dry cycles. For the first test (T7 in Figure 5.14(a)), it was planned to carry out four wet/dry cycles prior to loading. However, the test stopped in the middle of the experiment due to a power outage. Hence, test T7 could not be completed, and is therefore not reported in this thesis. In the second test (T8 in Figure 5.14(a)), it was also planned to perform four wet/dry cycles and another further drying stress path prior to loading stress path *LM*. A complete analysis of T8 is given in Figure 5.15 and Table 5.6.

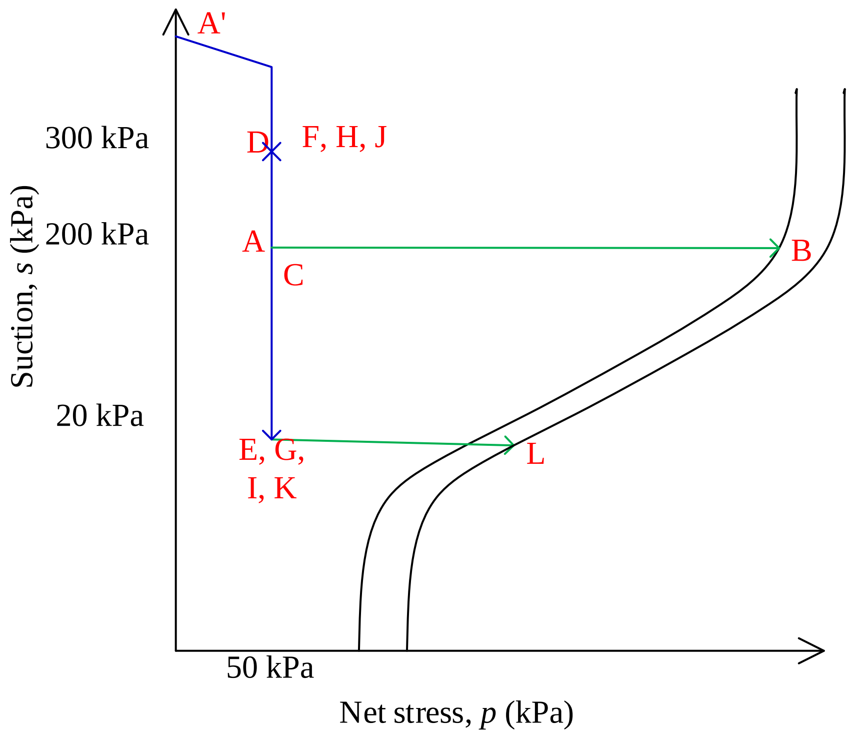

(a)

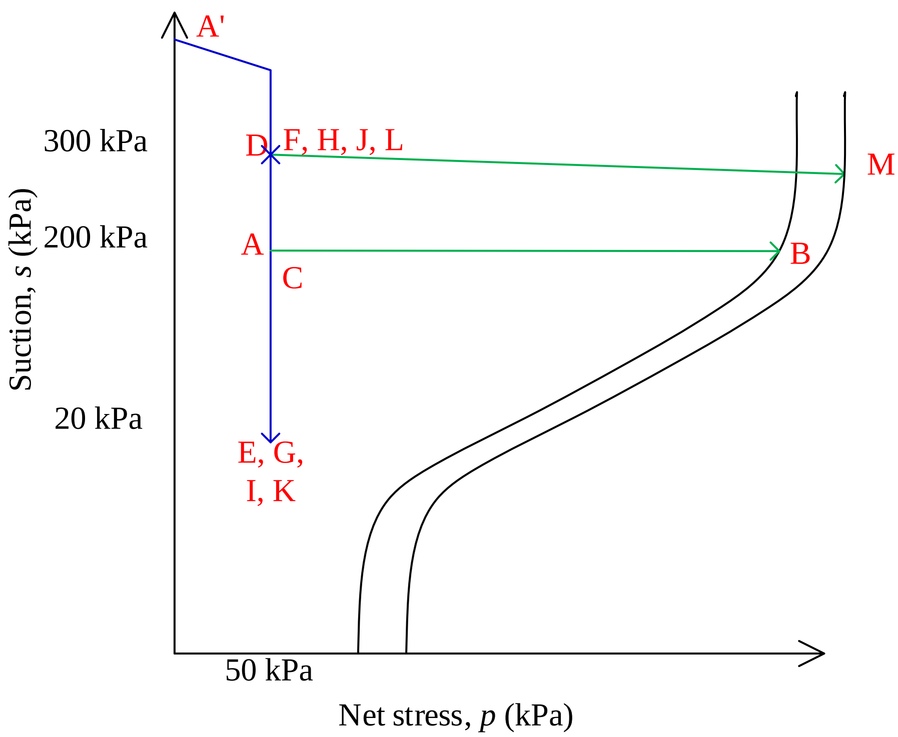

(b)

Figure 5.14: Stress path for test (a) T7 and (b)T8

5.9.1 Test T8

Test T8 was designed for the suction values of 20 kPa to 300 kPa, and the results are shown in Table 5.6 and Figure 5.15(a) in the v,v_{w} plane, Figure 5.15(b) in the v,p plane, and Figure 5.15(c) in the S_{r},s plane. The sample was first equalised (AA') to the mean net stress of 10 kPa and suction of 200 kPa. The duration of equalisation was 16 days. Constant suction loading and unloading cycles (A'BB'C) were then performed on the soil sample over a net stress change to 50 kPa, and the sample was then dried to 300 kPa suction under the net stress of 10 kPa. BB' is the equilibrium stress path and B' was close to B. Hence, B' is not included in Figure 5.15 and the same symbol configuration was used for the following stress paths. Four wet/dry cycles (i.e., wetting (D'E, F'G, H'I and J'K) and drying (E'F, G'H, I'J and K'L)) were performed in the suction range 300 kPa to 20 kPa. Constant water content loading was finally performed on the sample to mean net stress of 278 kPa. Loading path A'B depicts some yielding behaviour, suggesting that the reduction of the specific volume with I-D compaction is lower than that of isotropic compaction and the yield stress of Figure 5.15(b) is almost 20 kPa. Then during the subsequent unloading stress path B'C the soil behaves elastically. Figure 5.15(c) shows the behaviour of the sample during the wetting drying stress paths on the S_{r},s plane.

Table 5.6: Stress path for test T8

Stage			Net stress (kPa)	Suction (kPa)
From	To	Description		
A	A'	Initial equalisation	10	200
A'	B	Isotropic loading	10→50	200
B	B'	Equalisation	50	200
B'	C	Isotropic unloading	50→10	200
C	C'	Equalisation	10	200
C'	D	Drying	10	200→300
D	D'	Equalisation	10	300
D'	E	Wetting	10	300→20
E	E'	Equalisation	10	20
E'	F	Drying	10	20→300

F	F'	Equalisation	10	300
F'	G	Wetting	10	300→20
G	G'	Equalisation	10	20
G'	H	Drying	10	20→300
H	H'	Equalisation	10	300
H'	I	Wetting	10	300→20
I	I'	Equalisation	10	20
I'	J	Drying	10	20→300
J	J'	Equalisation	10	300
J'	K	Wetting	10	300→20
K	K'	Equalisation	10	20
K'	L	Drying	10	20→300
L	L'	Equalisation	10	300
L'	M	Constant moisture content loading	10→278	300→267

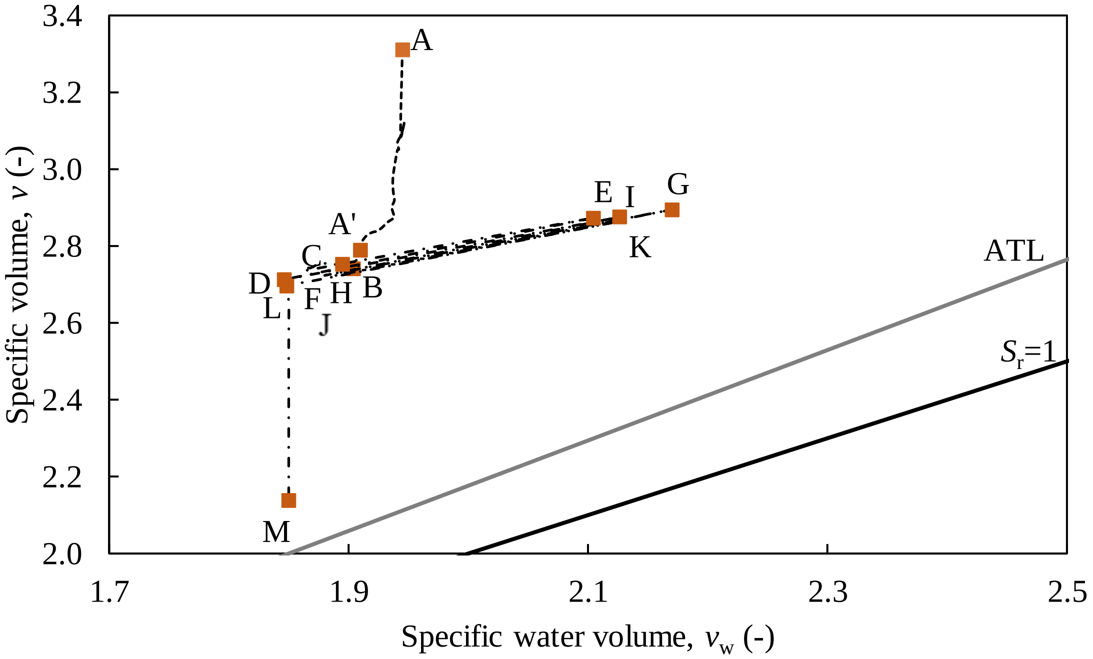

(a)

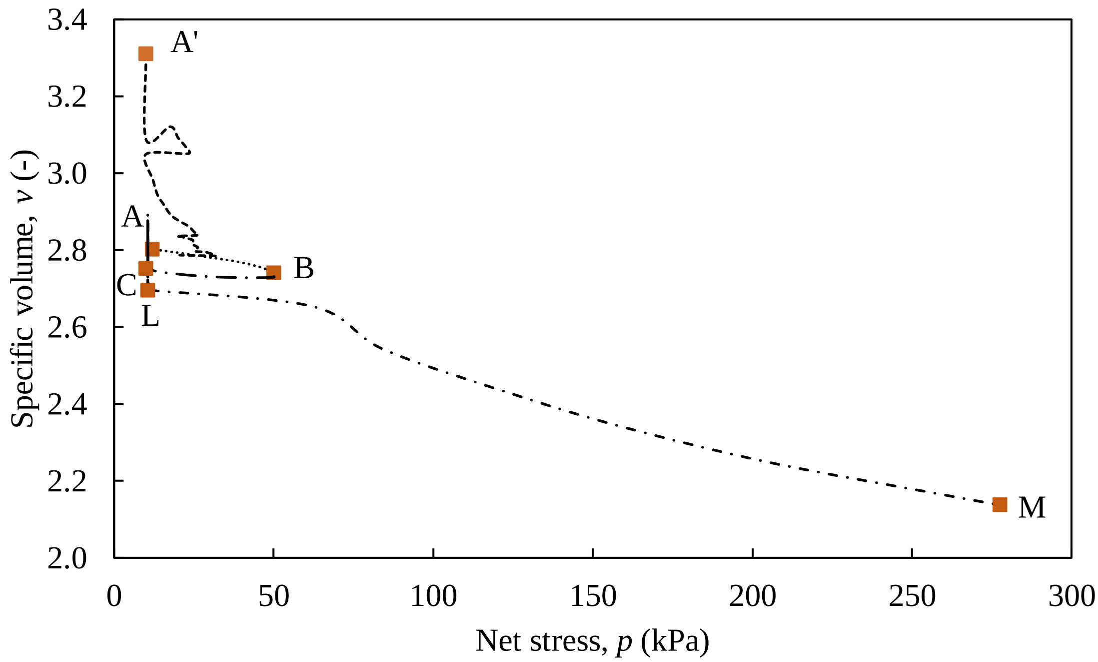

(b)

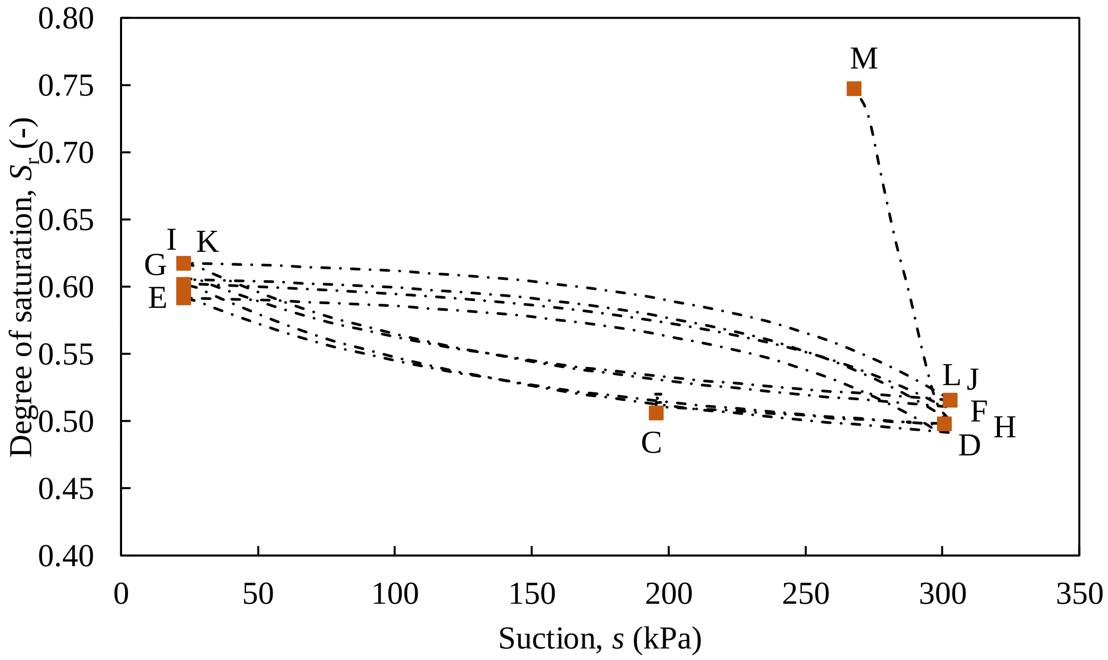

(c)

Figure 5.15: T8 in (a) v, v_w plane; (b) v, p plane; (c) S_{r}, s plane

5.10 Some additional suction-controlled tests

In addition to the above tests, another three tests (T9, T10 and T11) were performed on the same compacted kaolin, and the results are presented in Figure 5.16(a) in the v,v_w plane, and Figure 5.16(b) in the v, p plane. The main aim of these tests was to validate the applicability of the LWSBS through a combination of isotropic stress paths. In test T9, the stress path ABCDE (constant suction loading (AB) → constant suction unloading (BC) →Drying (CD) → Reloading (DE)) was followed. For test T10, a loading/ unloading/ reloading controlled suction stress path was performed. The final test T11 was similar to test T9 with the associated stress paths of GHIKL (constant suction loading (GH) → constant suction unloading (HI) →Drying (IK) → Reloading (KL)).

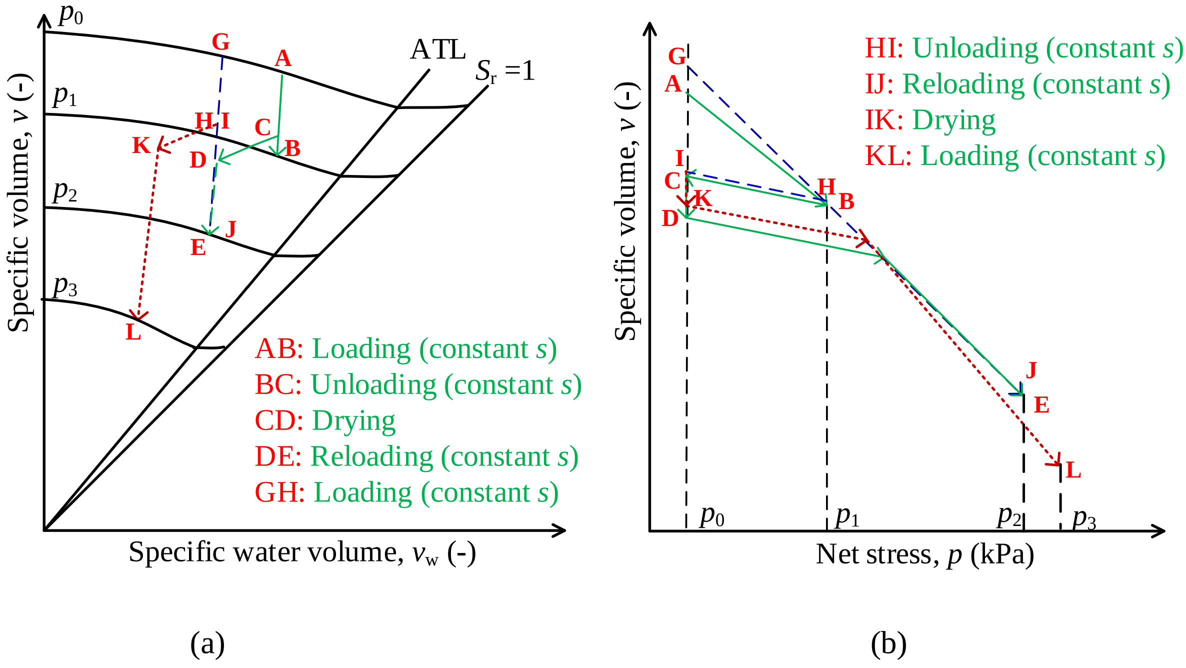

Figure 5.16: Stress paths designed for validation of uniqueness of MPK framework in (a) *v,v_w plane, and (b) v, p plane*

5.10.1 Test T9

Test T9 involved the suctions of 200 kPa to 300 kPa which can be achieved using the experimental set-up. As Table 5.7 and Figure 5.17 show, the sample was first equalised (AA') to the mean net stress of 10 kPa and suction of 200 kPa. The duration of equalisation was 16 days. Constant suction loading and unloading cycles (A'BB'C) were then performed on the soil sample over a net stress change to 50 kPa, and the sample was then dried to 300 kPa suction under the net stress of 10 kPa. Finally, constant suction loading at 300 kPa was performed on the sample to mean net stress of 240 kPa. The B', C', D', and E' states are not marked in Figure 5.17 as no significant change occurred during the 24-hr equalisation.

The loading path A'B also depicts some yielding behaviour, suggesting that the reduction of the specific volume with I-D compaction is lower than that of isotropic compaction. The yield stress in Figure 5.17(b) is nearly 40 kPa. During the subsequent unloading stress path B'C the soil behaves elastically. Figure 5.17(c) shows the behaviour of the sample during the drying stress path on the v,s plane. One of the phenomenological observations during test T10 is that the increase in yield stress after drying where the drying results in yielding of soil can be observed during stress path DE in Figure 5.17(b). Similarly, T11 was performed for a higher suction range of 300 kPa to 400 kPa. The constant suction loading-unloading test was carried out under the suction of 300 kPa for test T9, stress path DE. It was planned to carry out test T10 with the same suction.

Table 5.7: Stress path for T9

Stage			Net stress (kPa)	Suction (kPa)
From	To	Description		
A	A’	Initial equalisation	10	200
A’	B	Isotropic loading	10→50	200
B	B’	Equalisation	50	200
B’	C	Isotropic unloading	50→10	200
C	C’	Equalisation	10	200
C’	D	Drying	10	200→300
D	D’	Equalisation	10	300
D’	E	Constant suction loading	10→240	300
E	E’	Equalisation	240	300

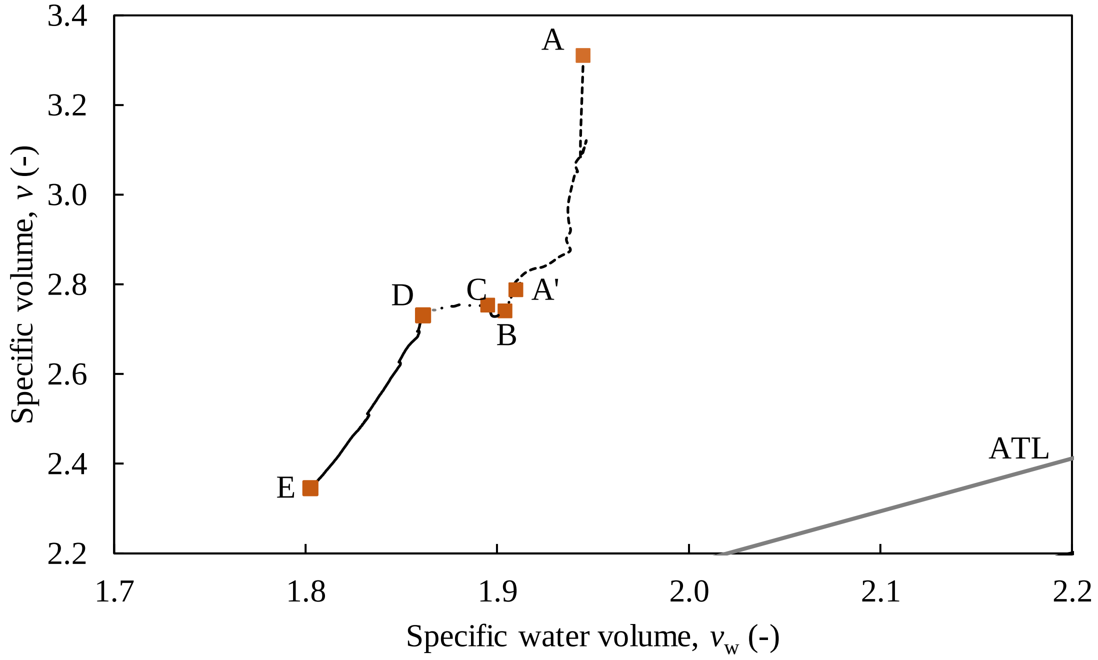

3.4
3.2
3.0
2.8
2.6
2.4
2.2
1.7
1.8
1.9
2.0
2.1
2.2
Specific volume, v (-)
Specific water volume, v_w (-)
A
A'
B
C
D
E
ATL

(a)

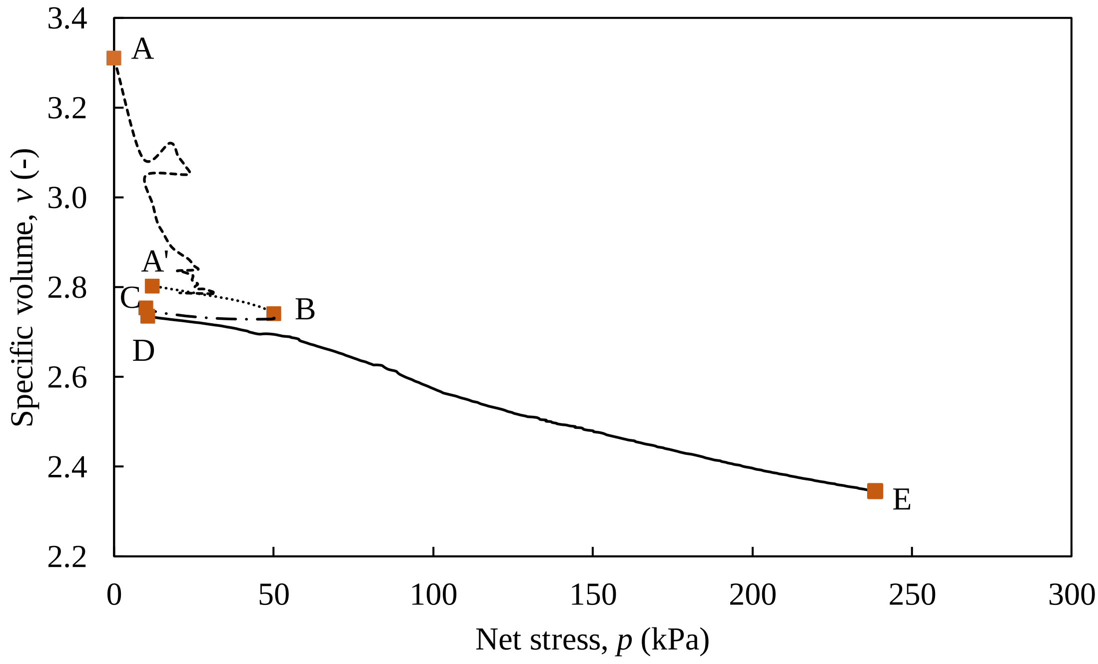

3.4
3.2
3.0
2.8
2.6
2.4
2.2
0
50
100
150
200
250
300
Specific volume, v (-)
Net stress, p (kPa)
A
A'
B
C
D
E

(b)

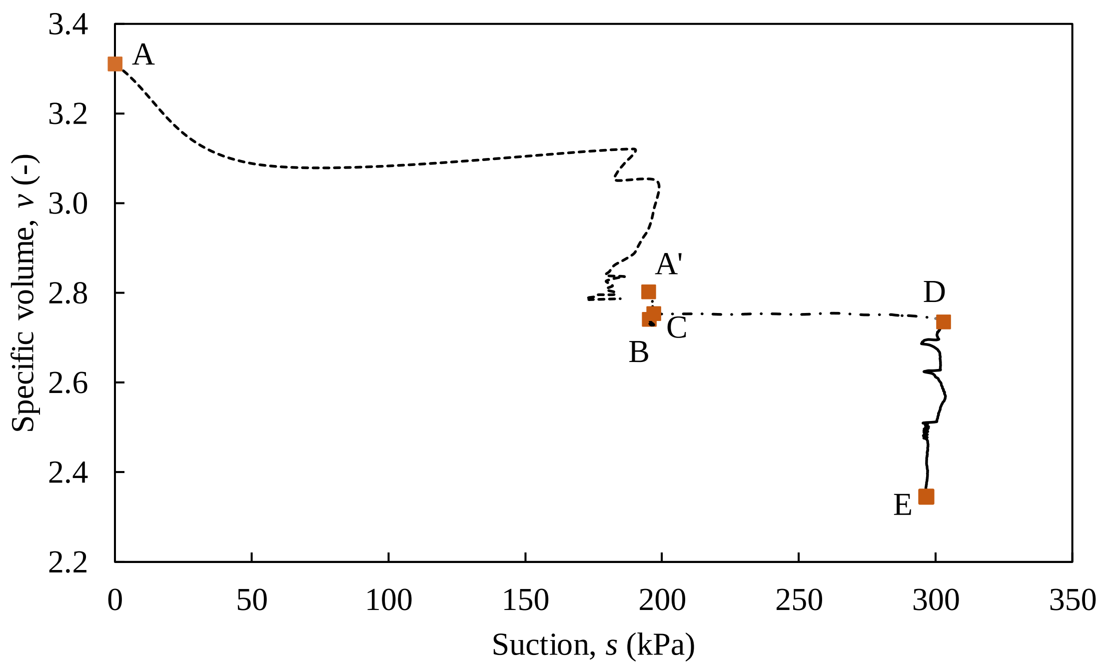

c)

Figure 5.17: Test T9 in (a) v, v_w plane; (b) v, p plane; (c) v, s plane

5.10.2 Test T10

As stated in the previous section, T10 included only constant suction loading/unloading/ reloading stress paths. A constant suction content test of 300 kPa was performed using the GCTS triaxial software. Similar to all the above experiments, T10 was started after equalising at mean net stress of 10 kPa and suction of 300 kPa as shown in Table 5.8 and Figure 5.18, in the (a) v, v_w plane; (b) v, p plane; and (c) S_r, p plane. Constant suction loading and unloading cycles (G'HH'I) were then performed on the soil sample over a net stress change to 50 kPa, and the sample was then unloaded to net stress of 10 kPa prior to reloading to 240 kPa. The H', I', J', and E' states are not marked in Figure 5.18 as no significant change occurred during the 24-hr equalisation.

Table 5.8: Stress path for T10

Stage			Net stress (kPa)	Suction (kPa)
From	To	Description		

G	G’	Initial equalisation	10	300
G’	H	Isotropic loading	10→50	300
H	H’	Equalisation	50	300
H’	I	Isotropic unloading	50→10	300
I	I’	Equalisation	10	300
I’	J	Constant suction loading	10→280	300
J	J’	Equalisation	240	300

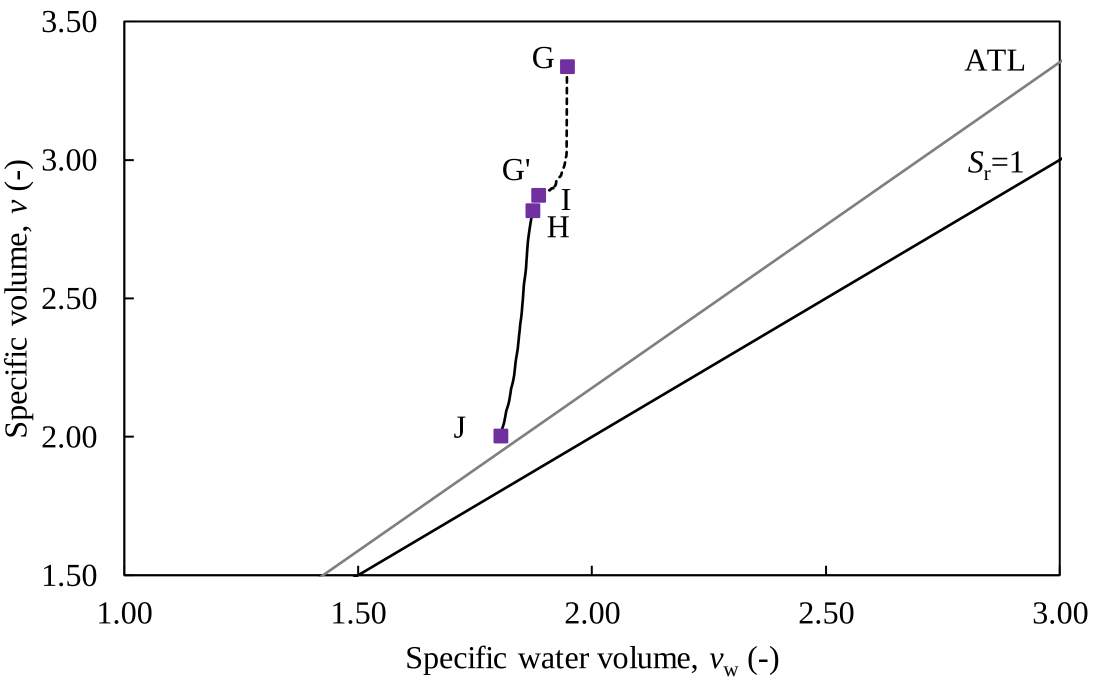

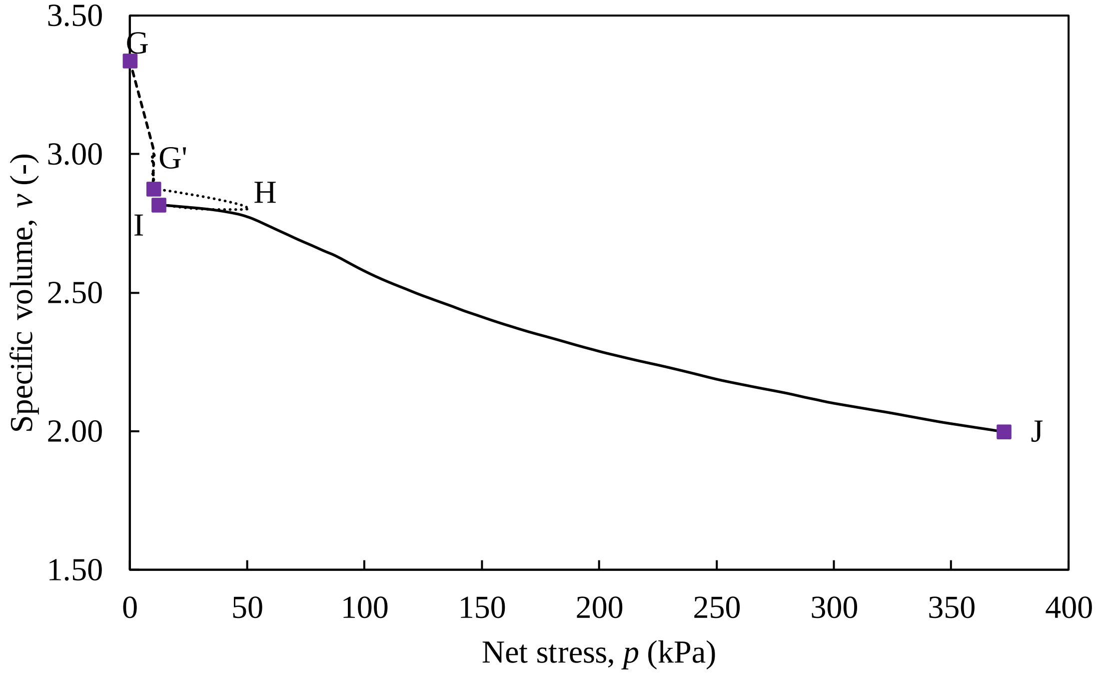

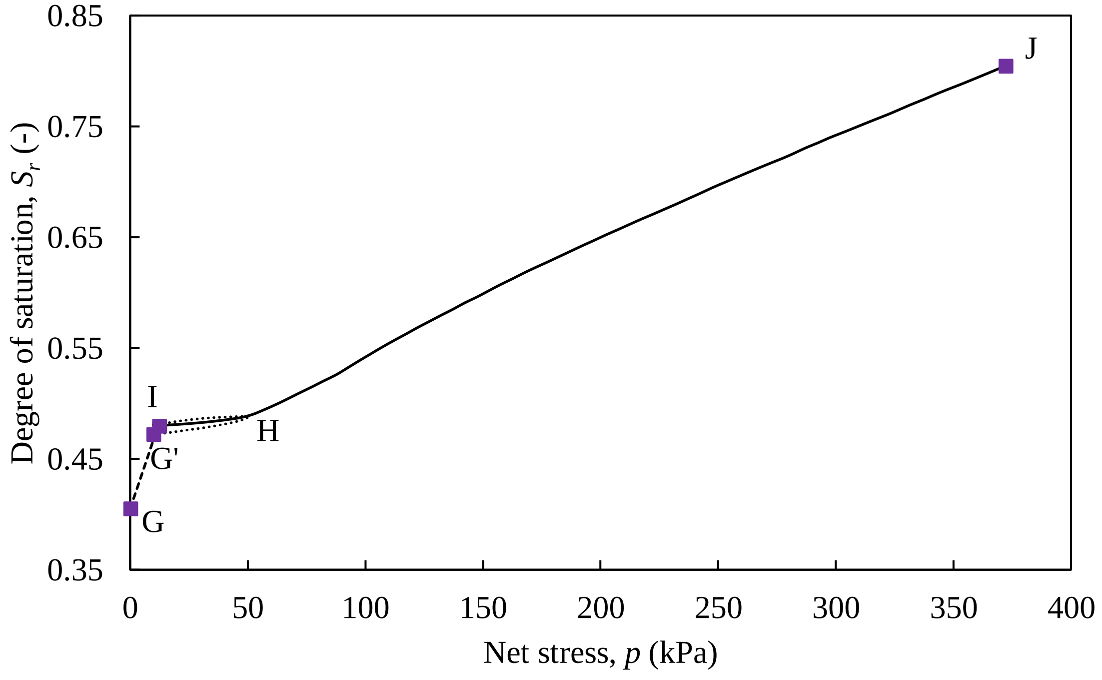

Figure 5.18: Test T10 in (a) v, v_w plane; (b) v, p plane; (c) S_r, p plane

5.10.3 Test T11

Test T10 was performed for suctions of 300 kPa to 400 kPa. As Table 5.9 and Figure 5.19 show, the sample was first equalised (GG') at the mean net stress of 10 kPa and suction of 300 kPa.

Constant suction loading and unloading cycles (G'HH'I) were then performed on the soil sample over a net stress change to 50 kPa, and the sample was then dried to 400 kPa suction under the net stress of 10 kPa. Finally, constant suction loading at 400 kPa was performed on the sample to mean net stress of 270 kPa. The H', I', J', and K' states are not marked in Figure 5.19.

The loading path G'H also depicts some yielding behaviour, suggesting that the reduction of the specific volume with I-D compaction is lower than that of isotropic compaction. The yield stress of Figure 5.19(b) is nearly 25 kPa. During the subsequent unloading stress path B'C the soil behaves elastically. Figure 5.19(c) shows the behaviour of the sample during the drying stress path on the v,s plane. One of the phenomenological observations in test T11 is that the increase in yield stress where the drying results in yielding of soil can be observed during stress path IK in Figure 5.19(b).

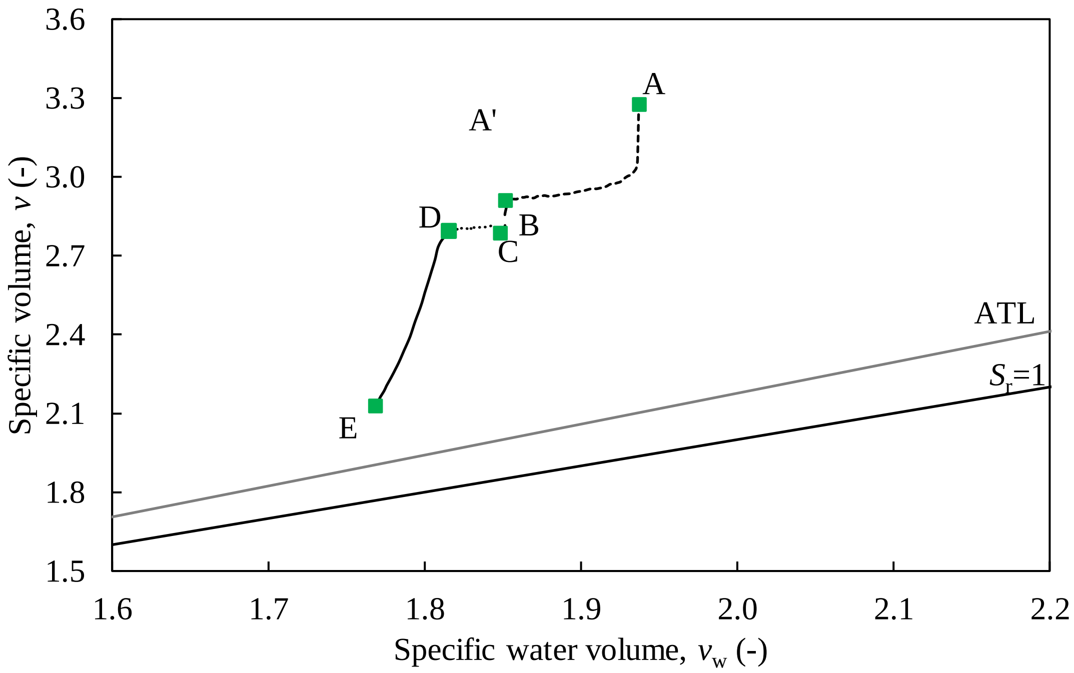

(a)

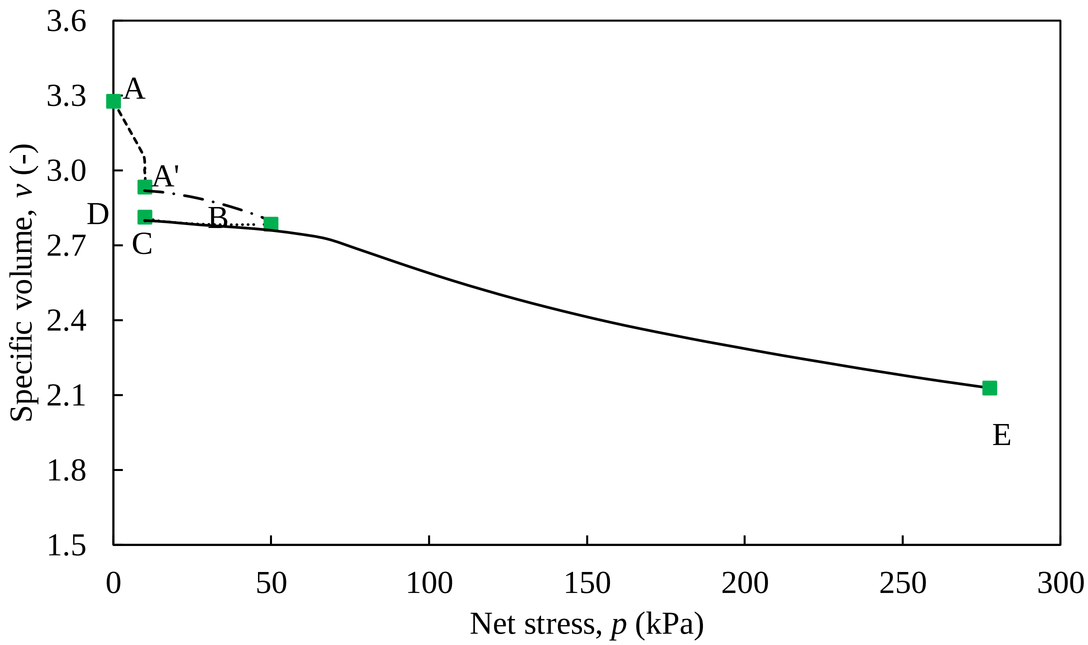

(b)

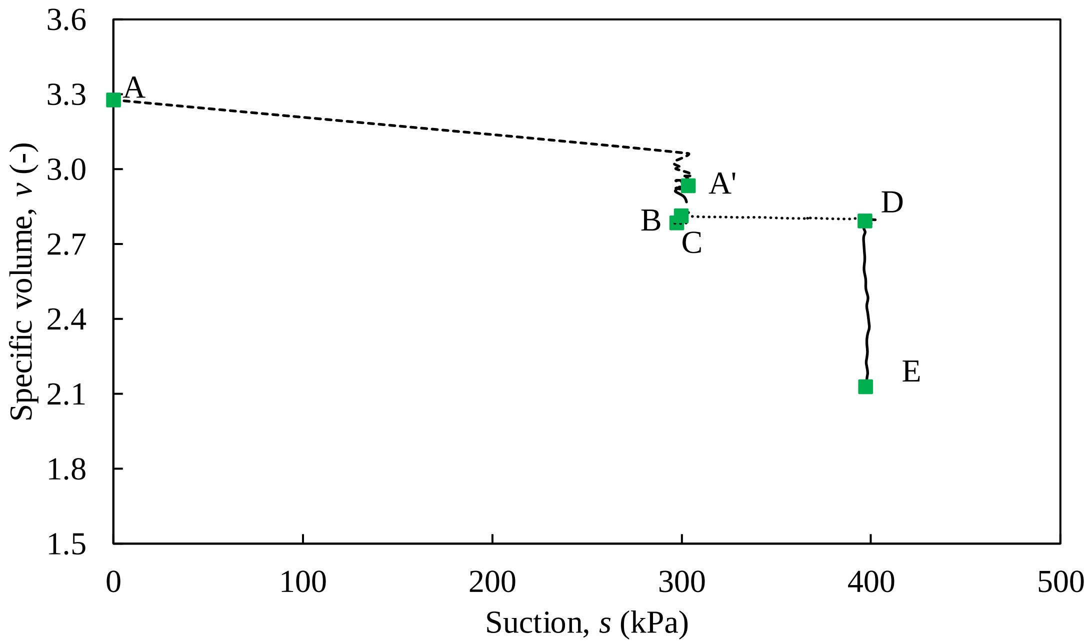

(c)

Figure 5.19: Test T11 in (a) (a) v, v_w plane; (b) v, p plane; (c) v, s plane

Table 5.9: Stress path for T11

Stage			Net stress (kPa)	Suction (kPa)
From	To	Description		

G	G'	Initial equalisation	10	300
G'	H	Isotropic loading	10→50	300
H	H'	Equalisation	50	300
H'	I	Isotropic unloading	50→10	300
I	I'	Equalisation	10	300
I'	K	Drying	10	300→400
K	K'	Equalisation	10	400
K'	L	Constant suction loading	10→270	400
L	L'	Equalisation	270	400

5.11 Conclusion

The GCTS unsaturated triaxial apparatus was utilised for the isotropic testing of compacted kaolin. The material selection, sample preparation, experimental set-up and recalibration of the experimental set-up have been discussed. Complete recalibrations of the transducers, the VCD, the load cell, and the displacement gauges were carried out prior to the experiments using the previous calibrations as references. The primary objective of the experiments was to validate the uniqueness of the LWSBS and to provide a data set for the validation of the proposed constitutive model for certain specific aspects, which have not been examined previously. For this reason, two series of tests were designed in order to examine drying behaviour, as previous research on the MPK framework was based on loading/unloading and wetting stress paths, and the concept of environmental stabilisation of soil.

Based on the results of the experiments, the following conclusions can be drawn:

(1) an increase in yield stress during loading after drying in comparison to loading prior to drying was observed;

(2) during yielding, a similar pattern of stress path was found with or without drying with the same initial v_w, p states; and the possibility of the environmentally stabilised state was observed.

In summary, first, the experimental results highlighted the uniqueness of the LWSBS, not only for wetting but also for drying. which was developed through constant water content tests apply to loading /unloading and wetting/drying stress paths. Second, the environmentally stabilised state through several wet/dry cycles was identified. However, only one test was able to complete during the period of this thesis, and further experiments are required.

5.12 References

Abeyrathne, A., Kodikara, J. & Bui, H. Prediction of wetting-induced volume change behaviour of compacted unsaturated soils in the context of the MPK framework. E3S Web of Conferences, 2016. EDP Sciences, 17011.

Abeyrathne, W. K. a. P. 2017. *A new modelling approach for compacted clayey soils using specific water volume as a state variable.* Ph.D. thesis, Monash University, Melbourne, Australia.

Bishop, A. & Donald, I. The experimental study of partly saturated soil in the triaxial apparatus. Proceedings of the 5th international conference on soil mechanics and foundation engineering, Paris, 1961. 13-21.

Gcts. 1994. *GCTS traxial apparatus* [Online]. https://gcts.com/?s=products&p=products. [Accessed 2020].

Islam, T. & Kodikara, J. 2015. Interpretation of the loading–wetting behaviour of compacted soils within the "MPK" framework. Part I: Static compaction 1. *Canadian Geotechnical Journal*, 53**,** 783-805.

Kodikara, J., Islam, T. & Rajeev, P. 2015. Interpretation of the loading–wetting behaviour of compacted soils within the "MPK" framework. Part II: Dynamic compaction 1. *Canadian Geotechnical Journal*, 53**,** 806-827.

Raveendiraraj, A. 2009. *Coupling of mechanical behaviour and water retention behaviour in unsaturated soils.* Ph.D. thesis, University of Glasgow.

Sharma, R. S. 1998. *Mechanical behaviour of unsaturated highly expansive clays.* Ph.D. thesis, University of Oxford.

Sivakumar, V. 1993. *A critical state framework for unsaturated soil.* Ph.D. thesis, University of Sheffield.

Wheeler, S. J. 1986. *The stress-strain behaviour of soils containing gas bubbles.* University of Oxford.

CHAPTER 6

Validation of the MPK model for isotropic stress state

6 Introduction

The generalised MPK constitutive model for unsaturated soils was developed in Chapter 4, with the main emphasis on the isotropic stress state. The main features of the model include the constant-moisture-content testing-based LWSBS or volumetric yield surface, the plastic strain-based LC curve and the SWRC, the air transition line (ATL) to demarcate the continuity of the air and water phases, the environmentally-stabilised line (ESL) to represent states achieved after a large number of wet/dry cycles, and the use of Bishop's effective stress and conjugate strains to represent the hydro-mechanical energetics allowing for transition from unsaturated to saturated behaviour. The mechanical behaviour of the model has 9 parameters which can be determined by relatively simple constant moisture content testing. The evolution of the plastic-strain-based SWRCs involves 6 parameters, some of which require calibration through traditional SWRC testing under constant net stress. In Chapter 4, parameter extraction is discussed, and some typical features of the model are explained.

The governing equations developed were programmed for the simulation of different stress paths at element level (e.g., loading, unloading, drying, wetting and their combinations). The accuracy of the simulations was validated with more straightforward spreadsheet calculations, as explained in Chapter 4. In Chapter 4, the extraction of material parameters and the general characteristics of the model are illustrated with some references to previous models. Subsequently, the application of this model to the simulation of volumetric behaviour with a combination of stress paths was discussed in the following sections, with some examples. Nevertheless, a comprehensive validation of past experiments on unsaturated soil including the tests in the thesis is required. Hence, Chapter 6 includes an extensive validation of the proposed generalised MPK model with a series of experiments on kaolin by Abeyrathne (2017), Raveendiraraj (2009) and an expansive kaolin bentonite mixture by Sharma (1998). Furthermore, since the test series conducted in the present study for compacted kaolin (as presented in Chapter 5) followed the same procedure as that used by Abeyrathne (2017), the same parameters were used for the simulations.

6.1 Incremental quantiles for simulations

The incremental quantiles for the simulations were based on the explicit stress-driven approach and the stress increments were used to find the strain increments. Once the initial stress states of the soil are defined considering the full forms of the theoretical equations as explained in Section 4.4.3, simulations can be carried out using the explicit partial derivatives of these equations. In this section, the selection of those constitutive equations is explained in detail considering the loading/unloading stress path, the wetting stress path and the drying stress path.

A computational flow chart of the isotropic suction-controlled loading/unloading process is given in Figure 6.1. If the initial stress states (v, S_r, p, s) are known, considering the S_r, the state of the soil, whether it is on the dry side or wet side should be determined. If the sample is on the dry side, yield stress (p_y) is obtained from Equation (6.1) to characterise the elastic ($p < p_y$) and elastoplastic ($p \geq p_y$) behaviour.

$$p_y = p_o e^{\left(\frac{v_G - v_E}{\lambda(S_r) - \kappa(S_r)}\right)} = p_o e^{\left(\frac{\left[v_o^L - k_4(S_r - S_r^L)\right] - \frac{v_C(1-\alpha_{ES} S_r^L) - \alpha_{ES}(S_r - S_r^L)}{(1-\alpha_{ES} S_r)}}{\lambda(S_r) - \kappa(S_r)}\right)} \tag{6.1}$$

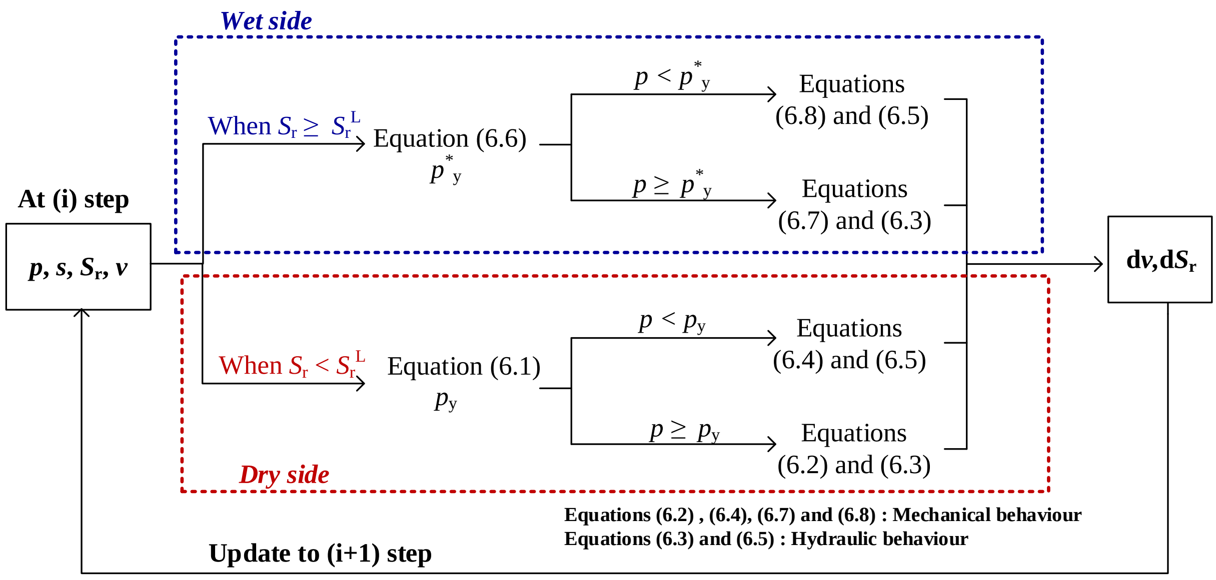

Figure 6.1: Computational flow chart for suction-controlled isotropic loading/unloading/reloading test

From the yield equation proposed in Equation (4.14), the constant suction stress paths, or the elastoplastic behaviour (or yield behaviour), were determined considering the change in specific volume (dv) as given in Equation (6.2).

$$\mathrm{d}v = -\lambda(S_\mathrm{r})\frac{\mathrm{d}p}{p} \tag{6.2}$$

Then, using Equation (6.3), $\mathrm{d}S_\mathrm{r}$ can be found once the C_w, D_w, g and h parameters are known (see Chapter 4 and Equation (B10) in Appendix C). The derivations of C_w, D_w and h can be found in Chapter 4 (Equations (4.37), (4.38) and (4.46)) and the derivation of g can be found in Appendix C (Equation (B9)), which is a general function which depends on material parameters.

$$\mathrm{d}S_\mathrm{r} = C_\mathrm{w}\phi\mathrm{d}s + \left(C_\mathrm{w}\frac{s}{v^2} + D_\mathrm{w}hg\right)\mathrm{d}v \tag{6.3}$$

In elastic behaviour (or unloading/reloading behaviour), the change in specific volume ($\mathrm{d}v$) can be found from Equation (6.4) (see Equation (4.15) of Chapter 4 for derivations). The hydraulic counterpart is then obtained from Equation (6.3), assuming the elastic behaviour (no plastic stain change) given in Equation (6.5).

$$\mathrm{d}v = -\kappa(S_\mathrm{r})\frac{\mathrm{d}p}{p} \tag{6.4}$$

$$\mathrm{d}S_\mathrm{r} = \left(C_\mathrm{w}\frac{s}{v^2}\right)\mathrm{d}v \tag{6.5}$$

If the sample is on the wet side, the yield effective stress (p^*_y) is obtained from Equation (6.6) to characterise the elastic ($p^* < p^*_\mathrm{y}$) and elastoplastic ($p^* \geq p^*_\mathrm{y}$) behaviour.

$$p^*_{\ \mathrm{y}} = p_\mathrm{o}e^{\left(\frac{v^\mathrm{o}_\mathrm{sat} - v_1}{\lambda_\mathrm{sat}}\right)} \tag{6.6}$$

$$\mathrm{d}v = -\lambda_\mathrm{sat}\frac{\mathrm{d}p^*}{p^*} \tag{6.7}$$

$$\mathrm{d}v = -\kappa_\mathrm{sat}\frac{\mathrm{d}p^*}{p^*} \tag{6.8}$$

Once the equations relevant to the elastic and elastoplastic behaviours are differentiated, the mechanical counterpart for elastoplastic behaviour can be found using Equation (6.7), and the hydraulic counterpart can be found using Equation (6.3). For the elastic response, Equations (6.5) (for hydraulic behaviour) and (6.8) (for mechanical behaviour) should be solved simultaneously.

During wetting, the calculations are carried out in three stages (swelling, collapse, and swelling) at operational stress level (p_{op}) as shown in Figure 6.2. The three stress paths can be differentiated by identifying the specific water volume values ($v_{\mathrm{w}}^{\mathrm{F}}$ and $v_{\mathrm{w}}^{\mathrm{L}}$) for the corresponding p_{op}. These three stress paths can be distinguished as follows:

1. $v_{\mathrm{w}} < v_{\mathrm{w}}^{\mathrm{F}}$ is recognised as swelling behaviour on the dry side of ATL;
2. $v_{\mathrm{w}}^{\mathrm{F}} \leq v_{\mathrm{w}} \leq v_{\mathrm{w}}^{\mathrm{L}}$ is recognised as collapse behaviour; and,
3. $v_{\mathrm{w}}^{\mathrm{L}} \leq v_{\mathrm{w}}$ is recognised as swelling behaviour on the wet side of ATL.

The normal compression yield equation in the (v, v_{w}, p) space can be written as:

$$v = v_{\mathrm{o}}^{\mathrm{L}} - k_4(S_{\mathrm{r}} - S_{\mathrm{r}}^{\mathrm{L}}) - \left[\lambda_{\mathrm{L}} - k_3(S_{\mathrm{r}} - S_{\mathrm{r}}^{\mathrm{L}})\right]\ln(p / p_{\mathrm{o}}) \tag{6.9}$$

The $v_{\mathrm{w}}^{\mathrm{F}}$ can be found by simultaneously solving Equations (6.9) and (6.10). The $v_{\mathrm{w}}^{\mathrm{L}}$ can be found from Equation (6.11) derived from the theoretical equations given in Chapter 4.

$$v_{\mathrm{w}}^{\mathrm{F}} = \frac{v^{\mathrm{F}} - v}{\alpha} + v_{\mathrm{w}} \tag{6.10}$$

$$v_{\mathrm{w}}^{\mathrm{L}} = S_{\mathrm{r}}^{\mathrm{L}}\left[v_{\mathrm{o}}^{\mathrm{L}} - \lambda_{\mathrm{L}} \ln\left({p_{\mathrm{op}}}/{p_{\mathrm{o}}} \right)\right] + 1 \tag{6.11}$$

where, $S_{\mathrm{r}}^{\mathrm{L}}, v_{\mathrm{o}}^{\mathrm{L}}, \lambda_{\mathrm{L}}$, and p_{o} are the material parameters and p_{op} is the operational stress of the stress path.

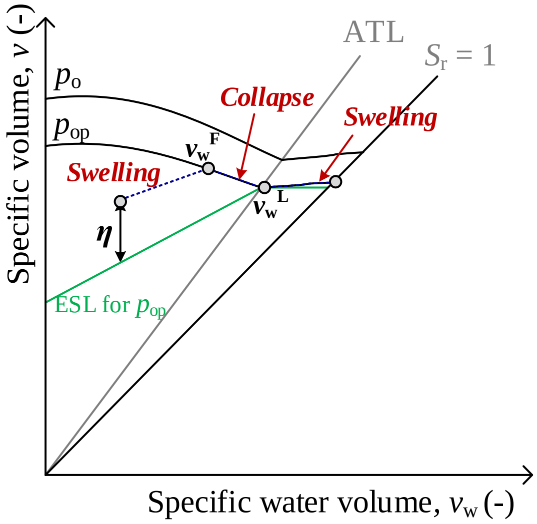

Figure 6.2: Three stages of wetting behaviour

For the swelling response (see Figure 6.3), the stress path initially follows the scanning stress path before yielding on major wetting curves. The yielding suction (s_{y}), where the scanning behaviour finishes can be found determined using Equation (6.12).

$$s_{\mathrm{y}} = \frac{v a_{\mathrm{w}}^{\mathrm{L}}}{(v-1)} \left[m\left((S_{\mathrm{r}})^{-(1/m)} - 1 \right) \right]^{1/n} \tag{6.12}$$

where, m and n are material parameters and v and S_{r} are initial state parameters and $a_{\mathrm{w}}^{\mathrm{L}}$ can be found from Equation (4.45) in Chapter 4. To find the $a_{\mathrm{w}}^{\mathrm{L}}$, the saturation-specific volume, v_{sat} is required, and it can be found considering the ESL gradient and finding the corresponding unloading specific volume at ATL $v_{\mathrm{L}}^{\mathrm{ul}}$. For the scanning behaviour, Equation (6.13) should be solved simultaneously with Equation (6.14).

$$\mathrm{d}S_{\mathrm{r}} = \left(\frac{s_{\mathrm{y}}}{s} \right)^{\mathrm{b}} C_{\mathrm{w}} \phi \mathrm{d}s + \left(C_{\mathrm{w}} \frac{s}{v^2} \right) \mathrm{d}v \tag{6.13}$$

Once the yielding on wetting curve starts, Equation (6.13) should be solved simultaneously with Equation (6.14). The parameter α can be found from Equation (4.48) in Chapter 4, where α_{ES}, and α_{o} are material parameters and η is the state parameter. To determine the α_{o}, the state of the soil should be identified. For example, the state of the soil on the (v, v_{w}) plane should be determined corresponding to the ESL for the relevant p for which the wetting is carried out. If the initial state is above the ESL (as shown in Figure 6.2), the soil is looser than ESL, for which wetting results in soil hardening or densifying, hence a lower α_{o} parameter results. On the other hand, if the initial state is below the ESL, the soil is denser than the ESL, for which wetting results in softening or de-densification, giving a higher α_{o} parameter. The state parameter η should then be determined as the vertical distance ($\mathrm{d}v$) between the initial state and the ESL for the initial v_{w} as given in Figure 6.2. It should be noted that, for the above example, if the initial state is below the ESL, the α is lower than α_{ES} and hence, overall hardening is observed upon wetting. On the other hand, if the initial state is below the ESL, overall softning behaviour can be seen, due to the fact that α is higher than α_{ES}. In addition, upon collapse, a hardening is always observed.

$$dv = \frac{\alpha(v-1)}{1-\alpha S_r} dS_r \tag{6.14}$$

By differentiating Equation (6.9) with respect to S_r, the collapse behaviour can be obtained on the constant net stress contour. Once the collapse starts, Equation (6.3) should be solved simultaneously with Equation (6.15).

$$dv = \left(k_3 \ln(p/p_o) - k_4\right) dS_r \tag{6.15}$$

For the final swelling behaviour (*i.e.* on the wet side), Equation (6.3) should be solved simultaneously with Equation (6.16).

$$dv = -\kappa \frac{dp^*}{p^*} \tag{6.16}$$

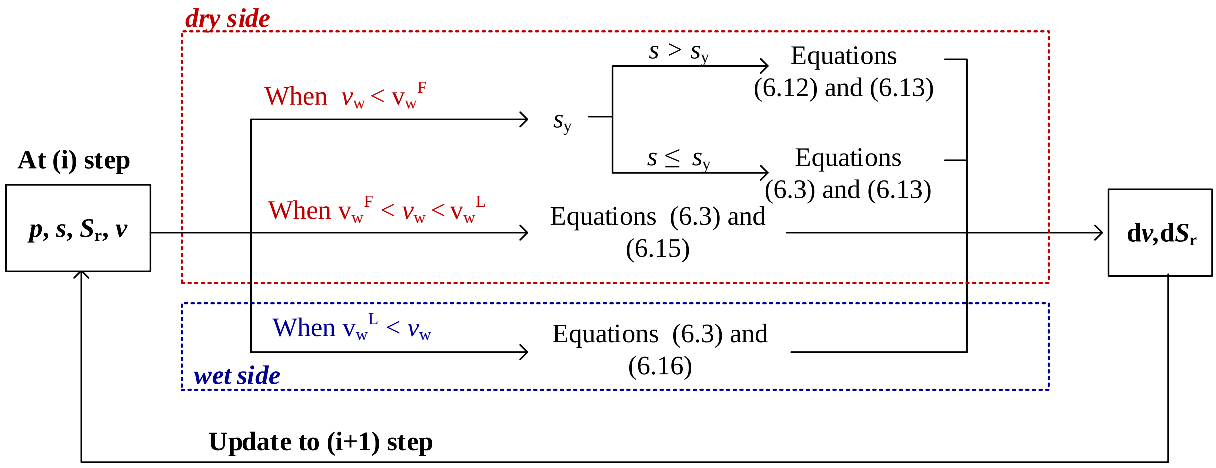

Figure 6.3: Computational flow chart for wetting test at constant net stress

Similar to wetting behaviour, drying behaviour (see Figure 6.4) depends on the initial state of the soil. If the sample is on a major wetting curve and above the ESL, initially a scanning behaviour is observed followed by major drying (soil sample may not yield if the plastic volumetric strain is the same) on drying curves. When the parameter α is higher than α_{ES}, the yield suction s_y should be obtained from Equation (6.17).

$$s_y = \frac{v a_d^L}{(v-1)} \left[m\left((S_r)^{-(1/m)} - 1 \right) \right]^{1/n_d} \tag{6.17}$$

where, m and n are material parameters, v and S_r are initial state parameters, and a_d^L can be found from $a_d^L = 10^{(X+\log(a_w^L))}$ once a_w^L is known. For scanning behaviour, Equation (6.13) should be solved simultaneously with Equation (6.18). Similarly, for yielding behaviour, Equation (6.13) should be solved simultaneously with Equation (6.19). In addition, the drying behaviour can be obtained by solving Equations (6.16) and (6.19) simultaneously.

$$\mathrm{d}S_\mathrm{r} = \left(\frac{s_\mathrm{y}}{s}\right)^{-\mathrm{b}} C_\mathrm{d}\phi \mathrm{d}s + \left(C_\mathrm{d}\frac{s}{v^2}\right)\mathrm{d}v \tag{6.18}$$

$$\mathrm{d}S_\mathrm{r} = C_\mathrm{d}\phi \mathrm{d}s + \left(C_\mathrm{d}\frac{s}{v^2} + D_\mathrm{d}hg\right)\mathrm{d}v \tag{6.19}$$

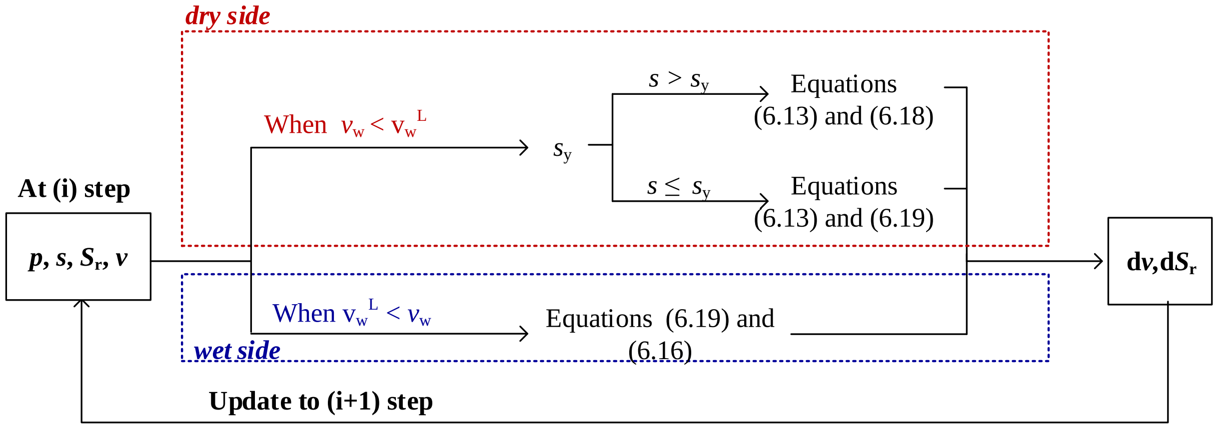

Figure 6.4: Computational flow chart for drying test at constant net stress

6.2 Experimental data in Chapter 5

The experiments in Chapter 5 were performed using GCTS based on constant suction isotropic loading, unloading and isotropic wetting, drying and constant water content loading tests on compacted kaolin. These tests were used to demonstrate how the uniqueness of the volumetric yield surface is obtained through drying loading stress paths and to establish the environmentally stabilised state.

6.2.1 T1: Constant suction loading → Constant suction unloading → Drying → Constant water content loading

Test T1 was designed for the lowest suction (100 kPa to 200 kPa) that can be achieved using the experimental set-up. As shown in Figure 6.5, the simulation follows the experimental results and indicates a reasonable agreement with the experimental results. The loading path AB also depicts some yielding behaviour, suggesting that the reduction of the specific volume of I-D compaction is lower than that of isotropic compaction. The yielding stress of Figure 6.5(a) is almost 15 kPa for experiments and 20 kPa for simulations. The sample was dried to 200 kPa suction under the net stress of 10 kPa prior to constant water content loading being performed on the sample to a mean net stress of 250 kPa. During the sample drying path to the suction of 200 kPa (path *CD*) and α_1 is determined as 0.63 ($\bar{\eta}$= 0.1768). It is apparent that this current state is above the ESL, and during drying, the state slowly approaches ESL (refer to phenomenological observation P17 in Chapter 3). Although the simulations of the drying path over-estimate the changes in v and S_r, the subsequent loading path simulations follow the experimental results, acquiring a higher yield stress (70 kPa for simulations) than the previously-obtained yield stress of 50 kPa. One of the phenomenological observations highlighted during test T1 was the increase in yield stress after drying (see phenomenological observation P5 in Chapter 3). In other words, the drying resulting in yielding of soil can be observed during stress path DE in Figure 6.5(a) on the (v, p) plane and Figure 6.5(b) on the (S_r, p) plane. Overall, it is clear that the model simulations are able to replicate the variations of v and S_r reasonably accurately throughout test T1.

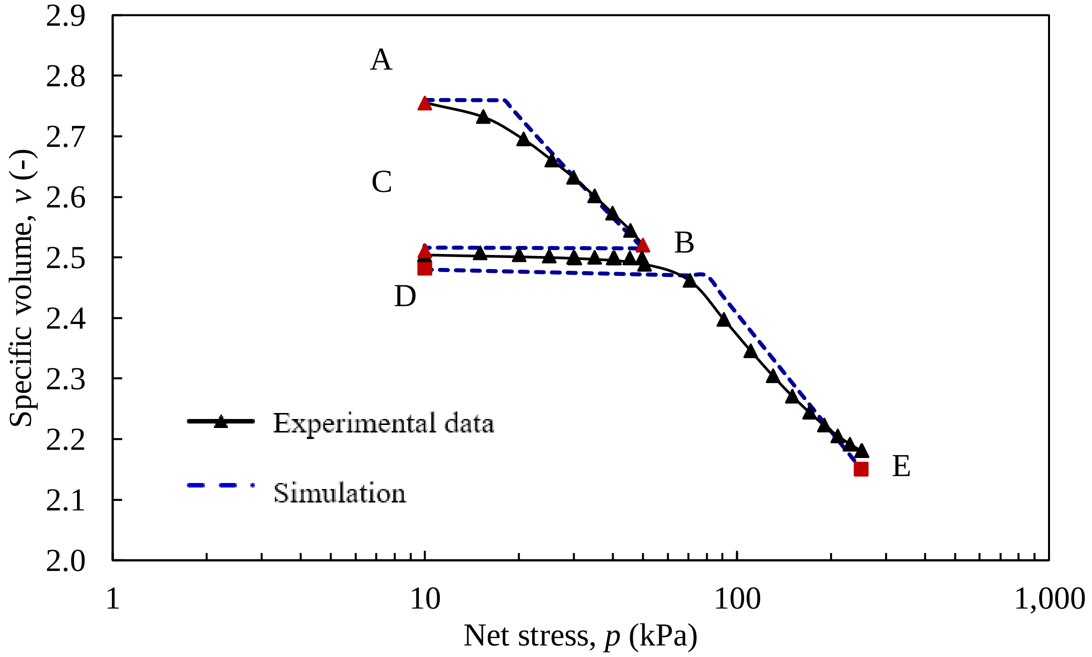

(a)

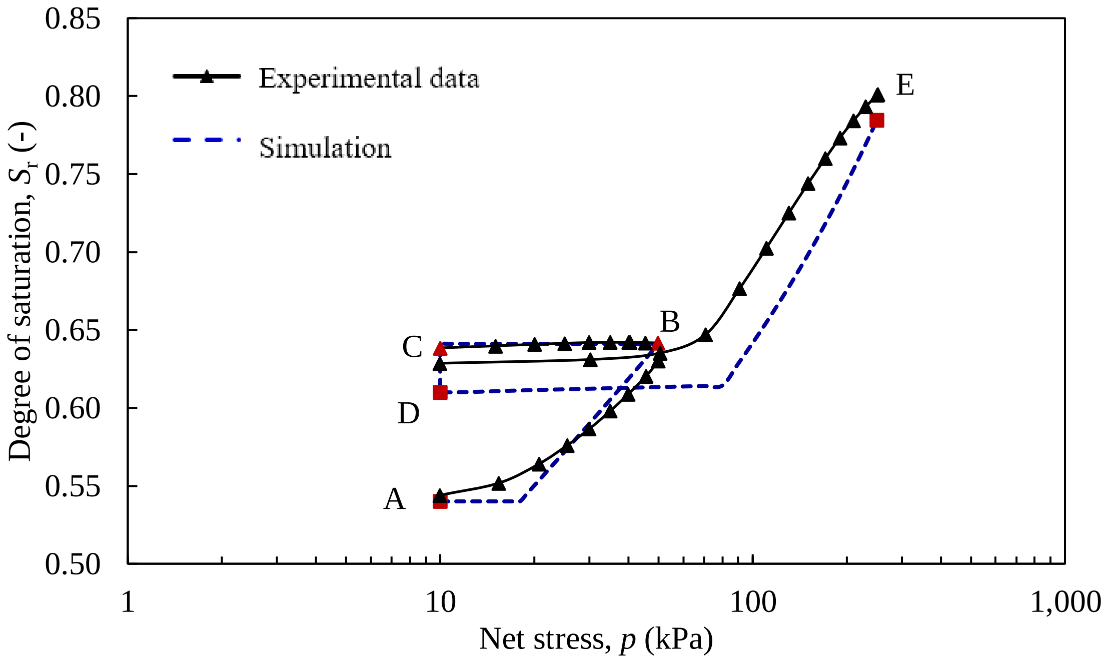

(b)

Figure 6.5: Experimental validation of test T1 on: (a) (v, p) plane; (b) (S_r, p) plane

6.2.2 T2: Constant suction loading → Constant suction unloading → Drying → Constant water content loading

Test T2 was designed for the suction values of 200 kPa to 300 kPa, as shown in Figure 6.6(a) on the (v, p) plane, and Figure 6.6(b) on the (S_r, p) plane. The sample was first equalised to the mean net stress of 10 kPa and suction of 200 kPa. Constant suction loading and unloading cycles (ABBC) were then performed on the soil sample over a net stress change to 50 kPa, and the sample was then dried to 300 kPa suction under the net stress of 10 kPa. As shown in Figure 6.6, the loading-unloading simulation follows the experimental results and indicates a reasonable agreement with the experimental results. The yielding stress of Figure 6.6(a) is nearly 15 kPa for experiments and 25 kPa for simulations. During the sample drying path to the suction of 300 kPa (path *CD*) and α_1 is to 0.63 ($\bar{\eta}$ = 0.186). It is apparent that the present state is above the ESL, and during drying, the state slowly approaches the ESL (see phenomenological observation P17 in Chapter 3). Nonetheless, the simulations of the drying path estimate the changes in v and S_r close to the experimental results. The subsequent constant water content loading (with a specific moisture ratio of 1.85) experiment path follows the model simulations, achieving a higher yield stress (80 kPa for simulations) than the previously-obtained yield stress of 50 kPa (refer to phenomenological observation P5 in Chapter 3).

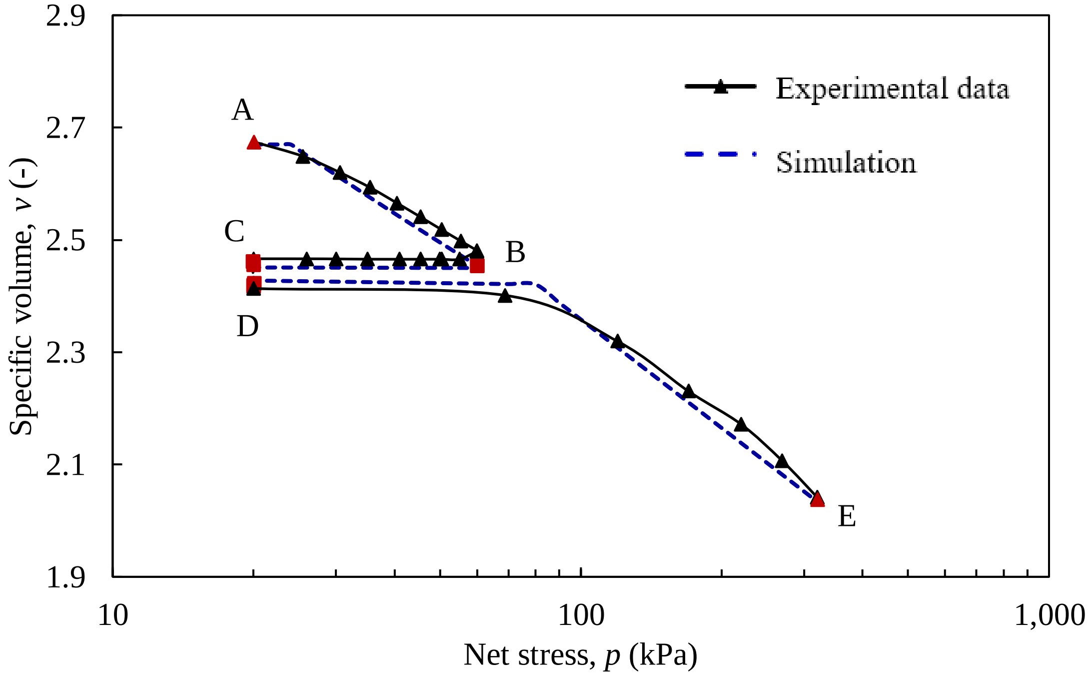

(a)

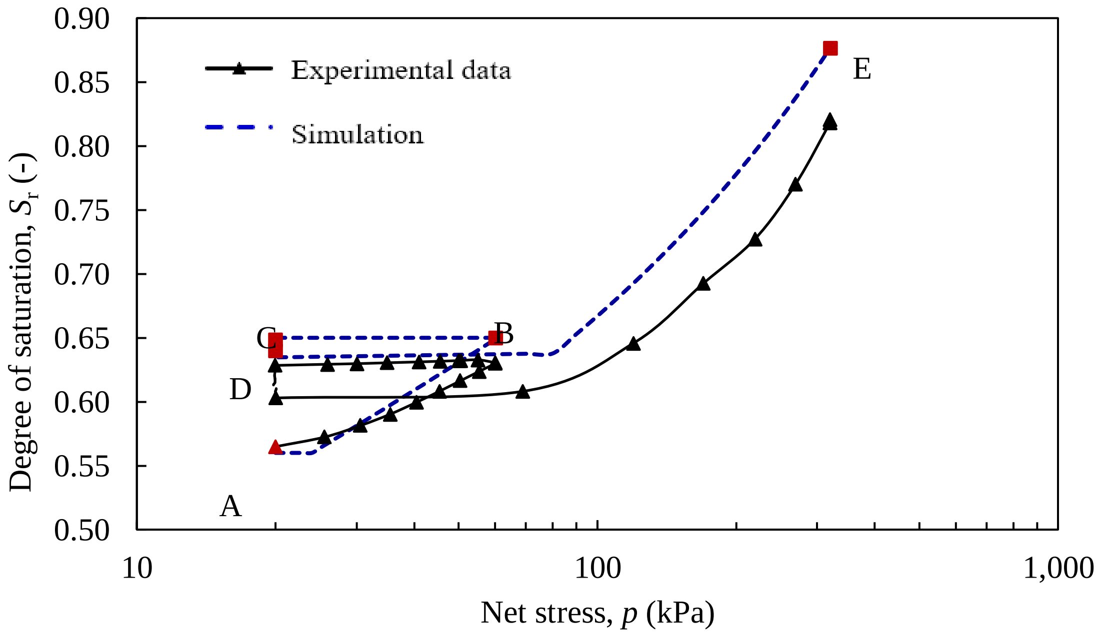

(b)

Figure 6.6: Experimental validation of test T2 on: (a) (v, p) plane; (b) (S_r, p) plane

6.2.3 T3: Constant suction loading → Constant suction unloading → Drying → Constant water content loading

Test T3 was designed for the suction values of 300 kPa to 400 kPa, as shown in Figure 6.7(a) on the (v, p) plane, and Figure 6.7(b) on the (S_r, p) plane . Constant suction loading and unloading cycles (*ABBC*) were then performed on the soil sample over a net stress change to 50 kPa, which was first equalised at the mean net stress of 10 kPa and suction of 300 kPa. The yielding stress of the *AB* stress path of Figure 6.7(a) is nearly 15 kPa for experiments and 20 kPa for simulations, indicating a reasonable agreement. During the subsequent drying path to the suction of 400 kPa (path *CD*) and α_1 is to 0.63 ($\bar{\eta}$ = 0.2924). It is apparent that the present state is above the ESL, and during drying, the state slowly approaches the ESL (see phenomenological observation P17 in Chapter 3). The subsequent constant water content loading (with a specific moisture ratio of 1.83) experiment path follows the model simulations, achieving a higher yield stress (85 kPa for simulations) than the previously-obtained yield stress of 50 kPa (see phenomenological observation P5 in Chapter 3).

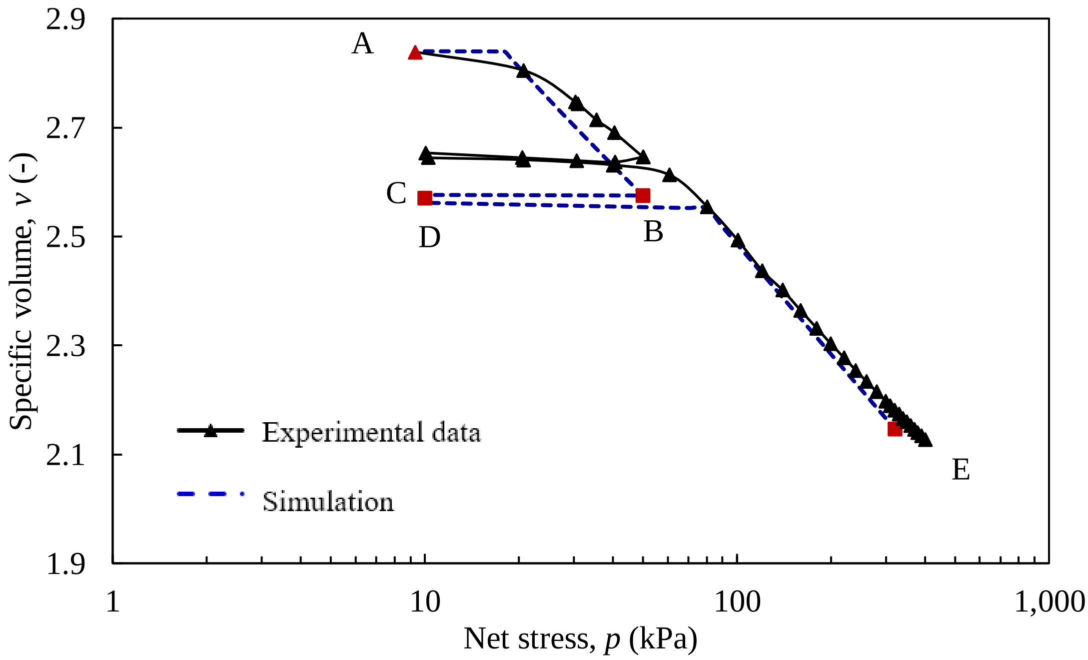

(a)

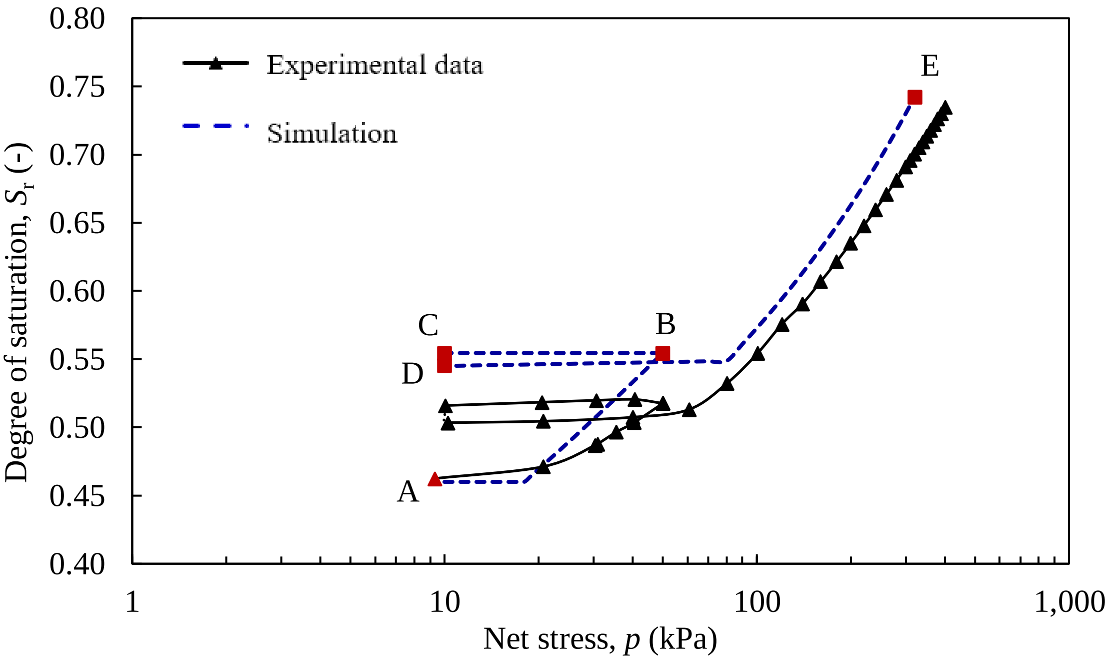

(b)

Figure 6.7: Experimental validation of test T3 on: (a) (v, p) plane; (b) (S_r, p) plane

6.2.4 T4, T5 and T6: Constant water content loading

As noted in Chapter 5, tests T4, T5 and T6 included only constant water content loading stress paths. These three tests were used for comparison with the drying loading stress paths and to validate the uniqueness of the LWSBS. Three constant water content tests were carried out (v_w = 1.93 (T4), 1.85 (T5), 1.82 (T6)) using the GCTS triaxial software and no suction measurements were performed. Similar to tests T1, T2 and T3, the yielding of tests T4, T5 and T6 started prior to 50 kPa compaction stress. Figure 6.8 includes the loading stress paths on the (v, p) plane and (S_r, p) plane. The simulation follows the experimental results and exhibits reasonable agreement between experimental and simulated results (refer to phenomenological observation P2 in Chapter 3).

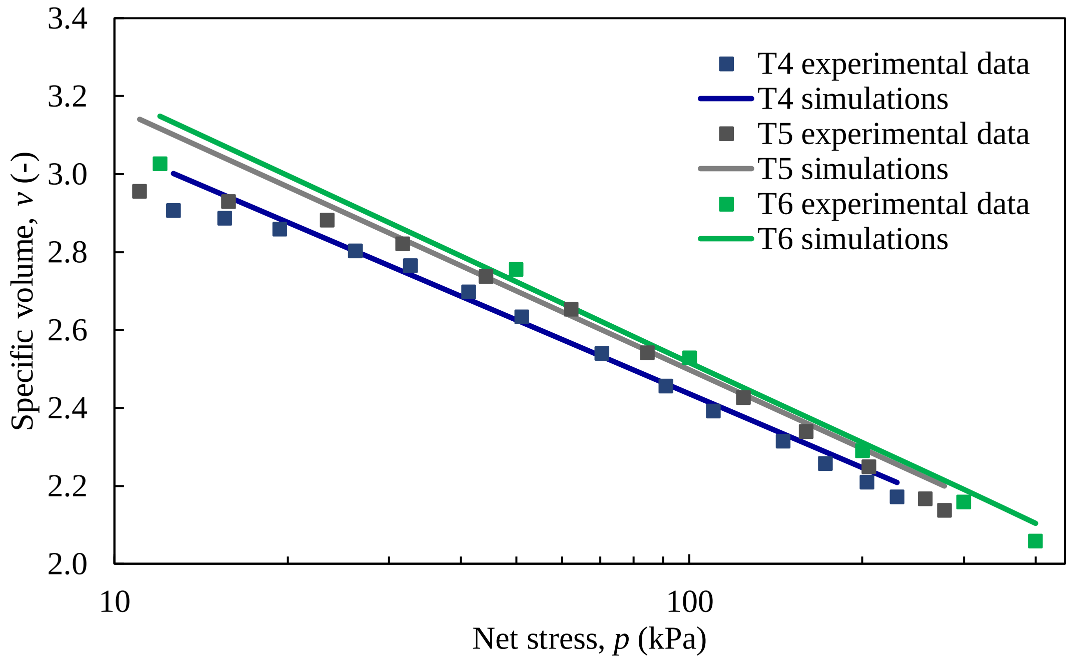

(a)

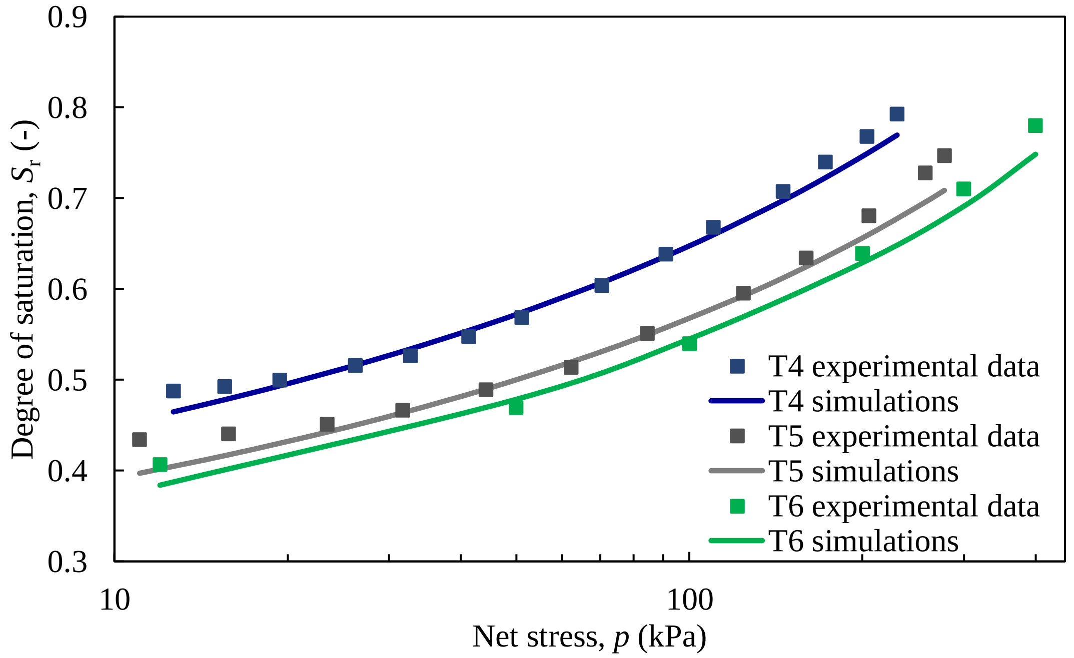

(b)

Figure 6.8: Experimental validation of tests T4, T5 and T6 on: (a) (v, p) plane; (b) (S_r, p) plane

6.2.5 T8: Wet-dry cycles

Test T8 was designed to capture the stress-strain accumulation phenomenon upon wet/dry cycles (see phenomenological observation P17 in Chapter 3), as shown in Figure 6.9(a) on the (v, p) plane, Figure 6.9(b) on the (S_r, p) plane, Figure 6.9(c) on the (v,s) plane, and Figure 6.9(d) on the (S_r, s) plane. The sample was first equalised to the mean net stress of 10 kPa and suction of 200 kPa. Constant suction loading and unloading cycles (ABBC) were then performed on the soil sample over a net stress change to 50 kPa, and the sample was then dried to 300 kPa suction under the net stress of 10 kPa. As shown in Figure 6.9, the loading-unloading simulation follows the experimental results and indicates a reasonable agreement with the experimental results. The yielding stress of Figure 6.9(a) is almost 35 kPa for experiments and 40 kPa for simulations. During the sample drying path to the suction of 300 kPa (path *CD*) and α_1 is to 0.63 ($\bar{\eta}$ = 0.1863). It is apparent that the present state is above the ESL, and during drying, the state slowly approaches ESL.

Subsequently, four wet/dry cycles (i.e., wetting (DE, FG, HI and JK) and drying (EF, GH, IJ and KL)) were performed in the suction range 300 kPa to 20 kPa. The η and wetting gradients of these stress paths are DE: $\bar{\eta}$=0.4239, α =0.57; FG: $\bar{\eta}$=0.4182, α =0.5764; HI : $\bar{\eta}$ =0.4115, α = 0.5815 and JK: $\bar{\eta}$=0.4069, α =0.5856 and the $\bar{\eta}$ and drying gradients of these stress paths are drying EF: $\bar{\eta}$=0.42, α =0.6236; GH: $\bar{\eta}$=0.4149, α =0.6185; IJ : $\bar{\eta}$ =0.4089, α =0.6144 and KL: $\bar{\eta}$=0.4048, α =0.6112 . As shown in Figure 6.9, the drying wetting simulation follows the experimental results and indicates a reasonable agreement with the experimental results. The subsequent constant water content loading experiment path to mean net stress 280 kPa follows the model simulations, achieving a higher yield stress (65 kPa for simulations) than the previously-obtained yield stress of 50 kPa. The simulations of v and S_r with s are not consistent with the experimental results, primarily due to the selection of the constant n parameter during the shift of SWRC.

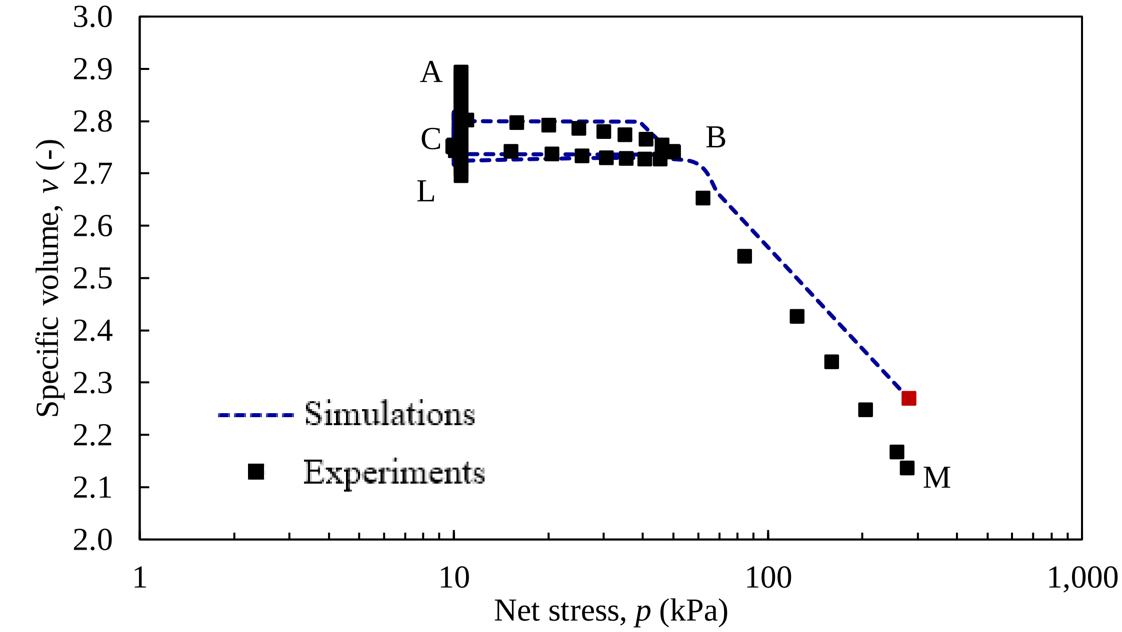
3.0
2.9
2.8
2.7
2.6
2.5
2.4
2.3
2.2
2.1
2.0
Specific volume, v (-)
A
C
L
B
M
Simulations
Experiments
1
10
100
1,000
Net stress, p (kPa)

(a)

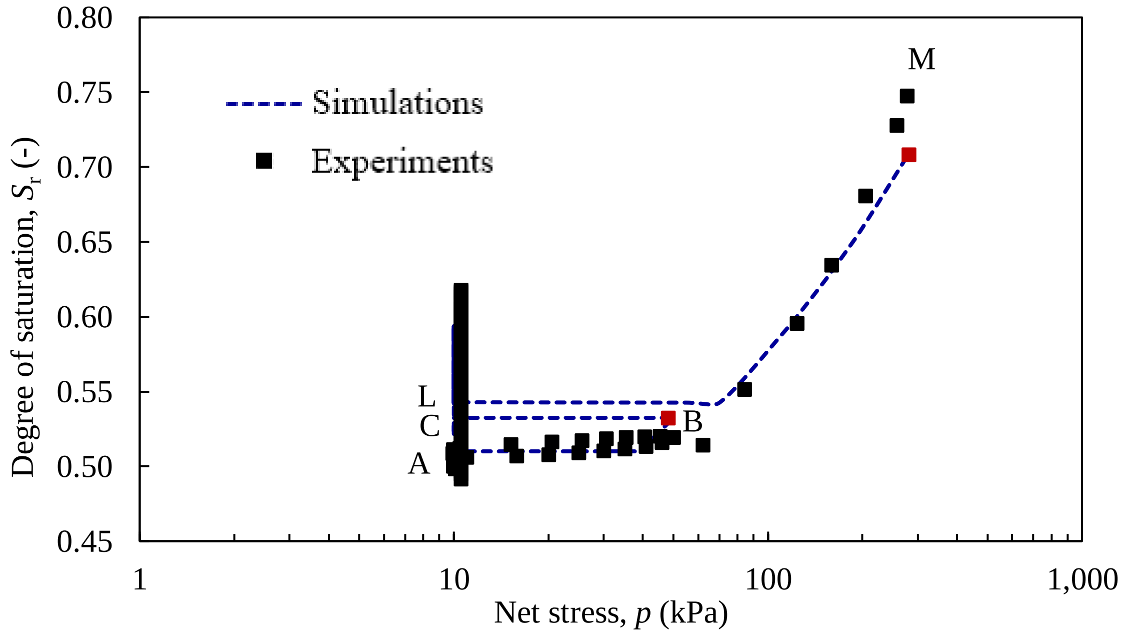
0.80
0.75
0.70
0.65
0.60
0.55
0.50
0.45
Degree of saturation, Sr (-)
M
L
C
B
A
Simulations
Experiments
1
10
100
1,000
Net stress, p (kPa)

(b)

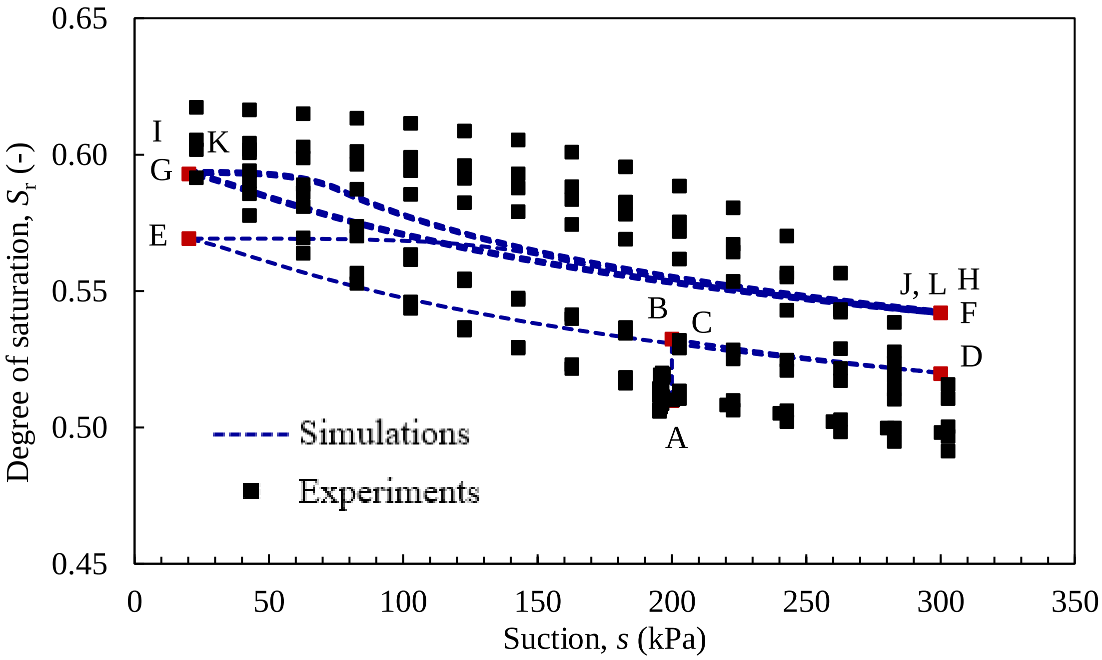

(c)

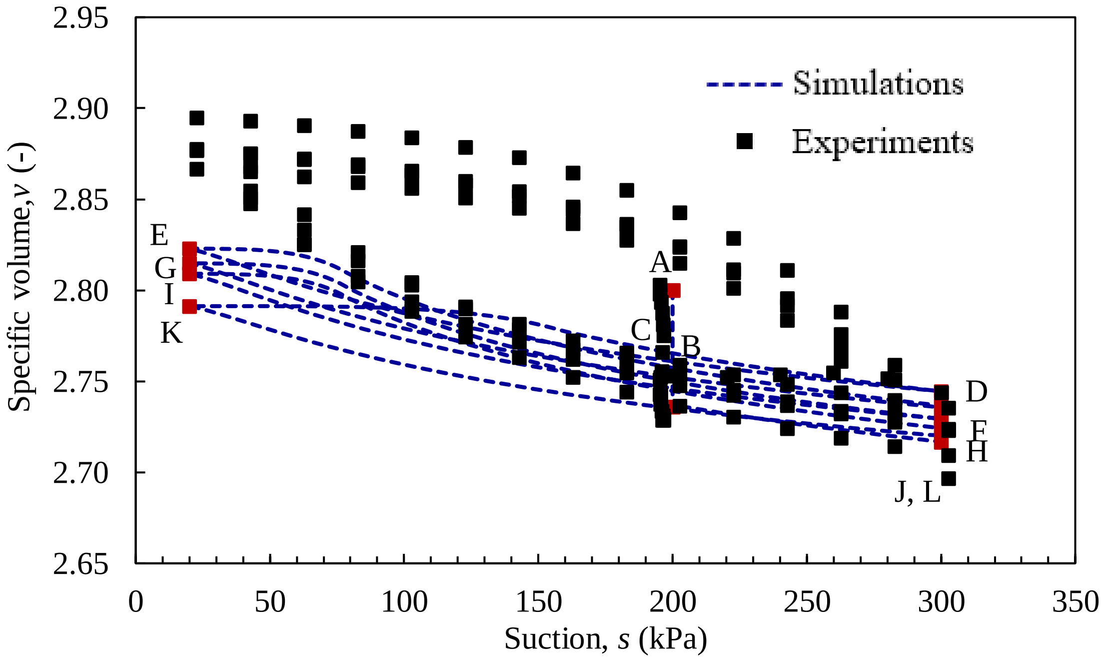

(d)

Figure 6.9: Experimental validation of test T8 on: (a) (v, p) plane; (b) (S_r, p) plane; (c) (S_r, s) plane (d) (v, s) plane;

6.2.6 T9: Constant suction loading → Constant suction unloading → Drying → Constant suction reloading

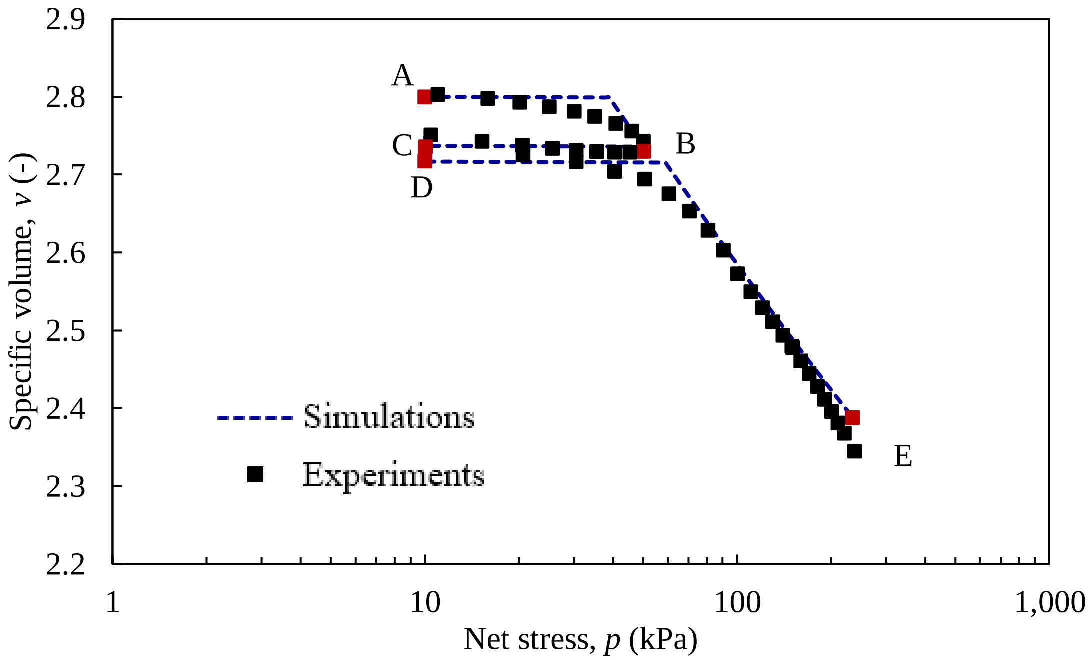

(a)

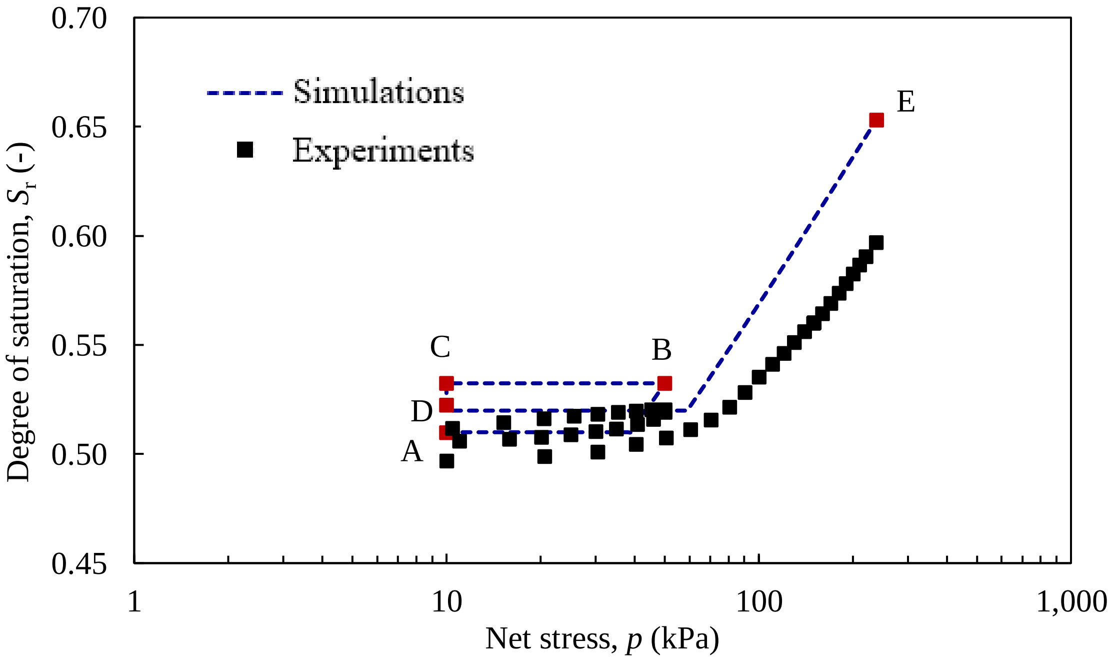

(b)

Figure 6.10: Experimental validation of test T9 on: (a) (v, p) plane; (b) (S_r, p) plane

Test T9 included controlled suction loading, unloading, drying and constant suction reloading stress paths. The sample was first loaded to 50 kPa mean net stress under the constant suction of 200 kPa and subsequently unloaded to 10 kPa. As shown in Figure 6.10, the simulation follows the experimental results and indicates a reasonable agreement with the experimental results. The loading path AB also depicts some yielding behaviour, suggesting that the reduction of the specific volume of I-D compaction is lower than that of isotropic compaction. The yielding stress of Figure 6.10(a) is almost 35 kPa for experiments and 40 kPa for simulations. The sample was dried to 300 kPa suction under the net stress of 10 kPa prior to constant suction loading being performed on the sample to the mean net stress of 240 kPa. During the sample drying path to the suction of 300 kPa (path *CD*) and α_1 is to 0.63 ($\bar{\eta}$ = 0.4227). It is apparent that the current state is above the ESL, and during drying, the state slowly approaches ESL (refer to phenomenological observations P8, P17 and P19 in Chapter 3). Nonetheless, the simulations of the drying path over-estimate the changes in v and S_r, primarily due to the assumption that the '*n*' parameter is constant during the shift of SWRC with the volumetric strain (see phenomenological observation P21 in Chapter 3). However, subsequent loading path simulations of specific volumes follow the experimental results more closely, achieving a higher yield stress (60 kPa for simulations) than the previously-obtained yield stress of 50 kPa (see phenomenological observation P5 in Chapter 3).

6.2.7 T10: Constant suction loading → Constant suction unloading → Constant suction reloading

As stated in the previous section, T10 included only constant suction loading/unloading/reloading stress paths. Similar to the above experiments, T10 was started after equalisation at a mean net stress of 10 kPa and suction of 300 kPa. Constant suction loading and unloading cycles (G'HH'I) were then performed on the soil sample over a net stress change to 50 kPa, and the sample was then unloaded to the net stress of 10 kPa prior to reloading to 240 kPa. As shown in Figure 6.11, on the (a) (v, p) plane and the (b) (S_r, p) plane, the simulation follows the experimental results and indicates a reasonable agreement with the experimental results (refer to phenomenological observations P1 and P4 in Chapter 3).

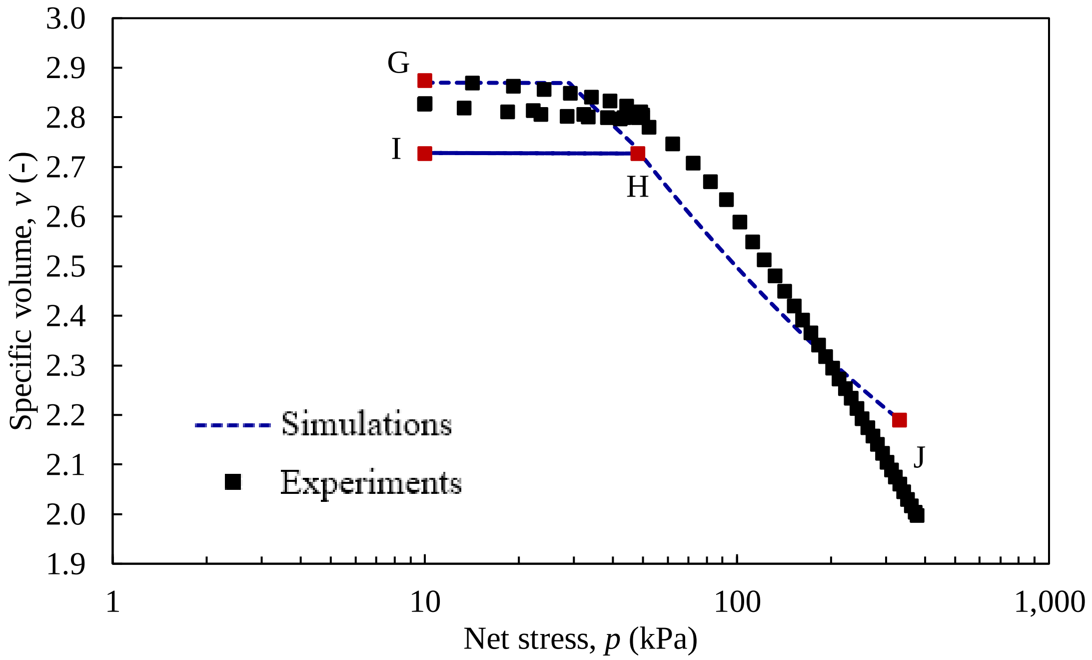

(a)

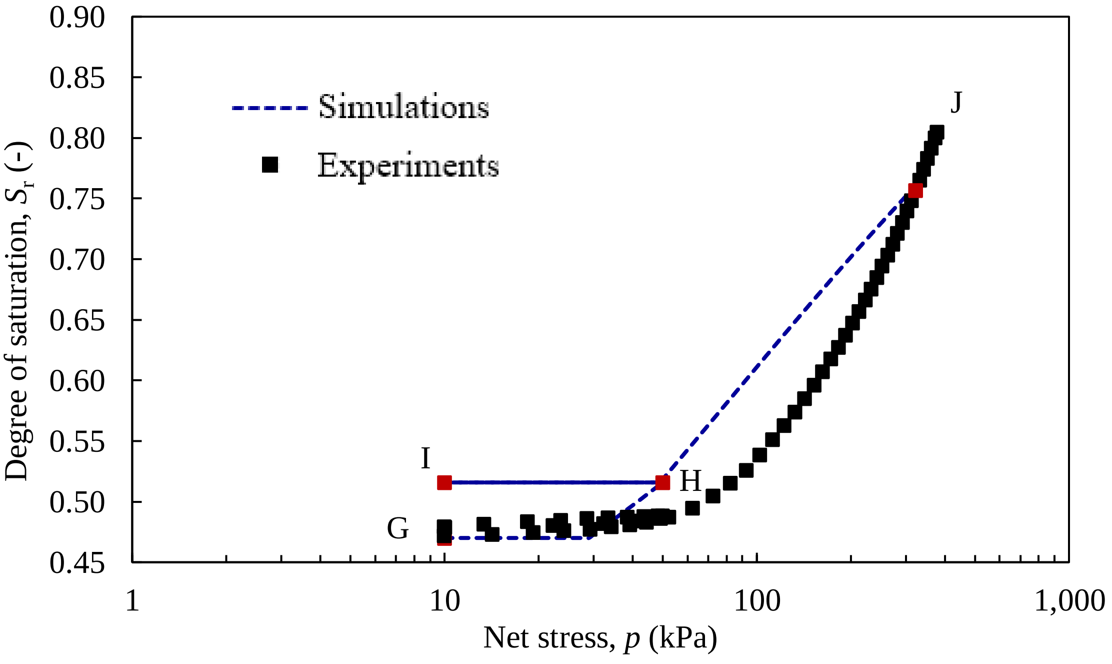

(b)

Figure 6.11: Experimental validation of test T10 on: (a) (v, p) plane; (b) (S_r, p) plane

6.2.8 T11: Constant suction loading → Constant suction unloading → Drying → Constant suction reloading

As shown in Figure 6.12, the sample was first equalised to the mean net stress of 10 kPa and suction of 300 kPa. Constant suction loading and unloading cycles (G'HH'I) were then performed on the soil sample over a net stress change to 50 kPa, and the sample was then dried to 400 kPa suction under the net stress of 10 kPa. Finally, constant suction loading at 400 kPa was performed on the sample to the mean net stress of 270 kPa. The yielding stress of the initial loading reloading cycle stress path in Figure 6.12(a) is almost 45 kPa for the experiments and 40 kPa for the simulations, indicating reasonable agreement with the experimental results. During the subsequent drying path to the suction of 400 kPa (path *CD*) and α_1 was estimated as 0.63 (explained in Chapter 5) ($\bar{\eta}$ = 0.5812). It is apparent that the current state is above the ESL, and during drying, the state slowly approaches ESL (see phenomenological observations P8, P17, and P19 in Chapter 3). The subsequent constant suction loading experiment path follows the model simulations reasonably closely, achieving a higher yield stress (70 kPa for simulations) than the previously-obtained yield stress of 50 kPa (refer to phenomenological observation P5 in Chapter 3).

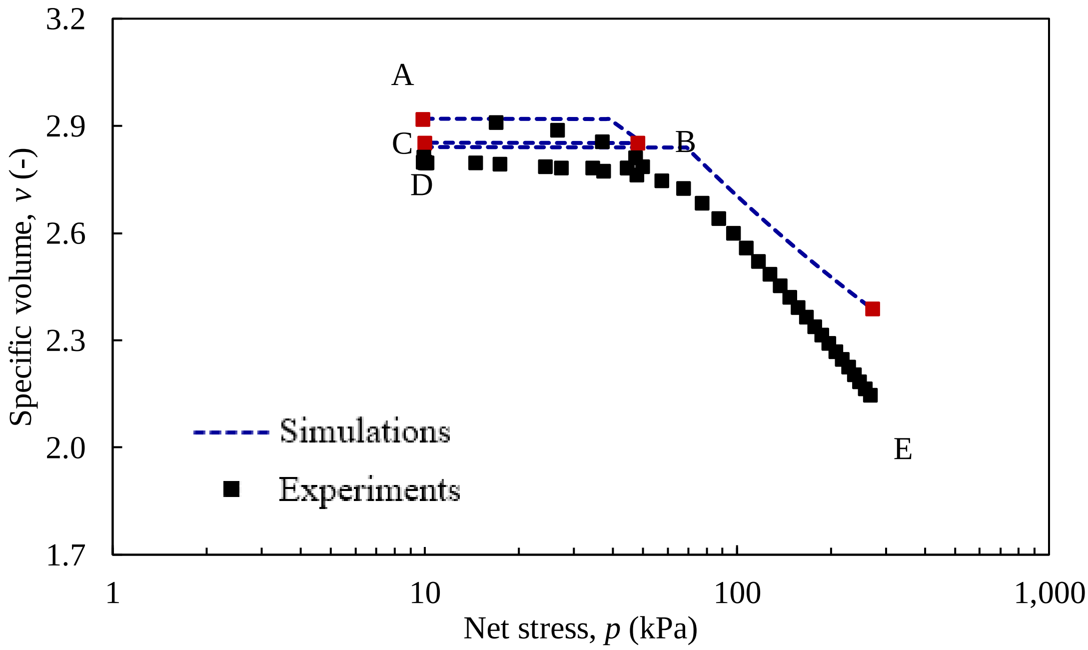

(a)

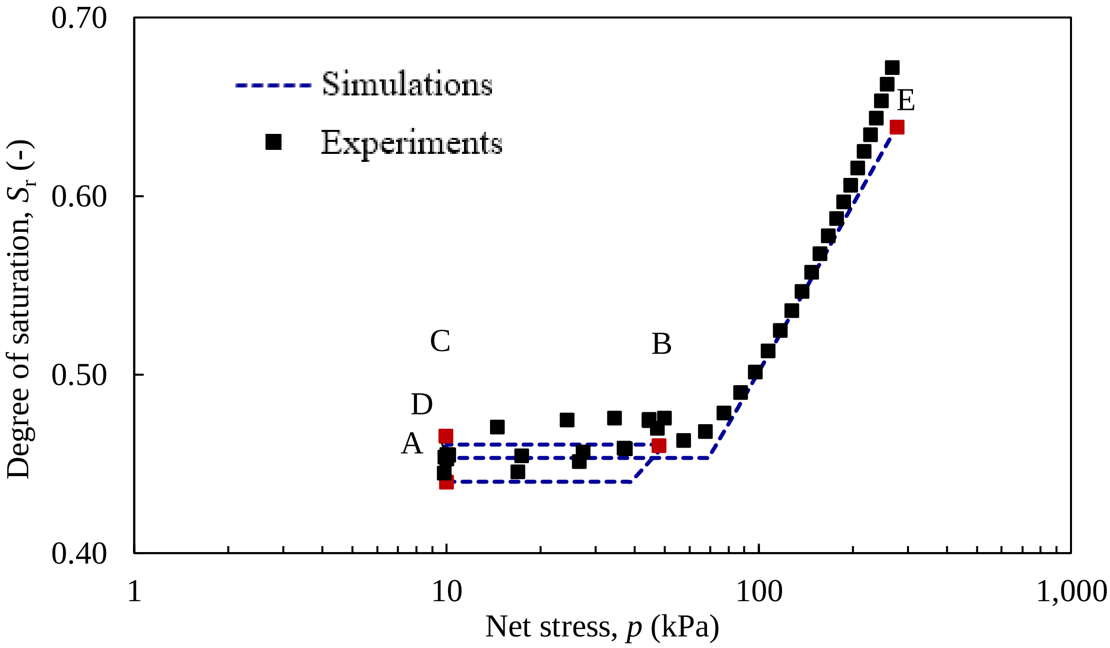

(b)

Figure 6.12: Experimental validation of test T11 on: (a) (v, p) plane; (b) (S_r, p) plane

6.3 Tests reported by Abeyrathne et al. (2019)

Abeyrathne et al. (2019) performed constant moisture content isotropic loading, unloading and isotropic wetting tests on compacted kaolin (LL=60.5%, PL=27.9%) with the brand name Eckalite 1. These tests were used to demonstrate how the volumetric yield surface-related parameters of the model (listed in Chapter 4) can be obtained through constant water content testing. The dry kaolin was hand-mixed with distilled water to produce different moisture contents for the tests. The soil was statically compacted in 1-D to the 50 kPa stress, prior to placing it in the triaxial cell for isotropic loading. Suction was not measured during testing, which made the tests relatively easy, and the results were used to determine the suitability of the equations derived for the volumetric yield surface.

The predictions of the suction behaviour were not simulated due to to the unavailability of suction measurements. However, if the SWRC is measured by conventional experiments, the required coupled hydraulic parameters of the model can be captured, and the variation in suction can be simulated, but this simulation is not reported here.

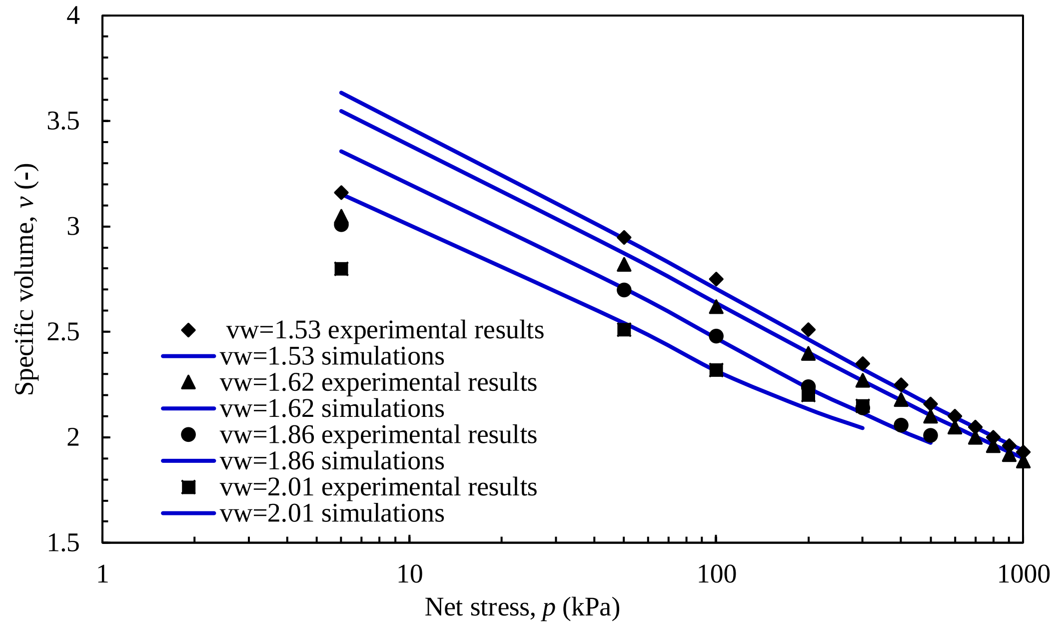

(a)

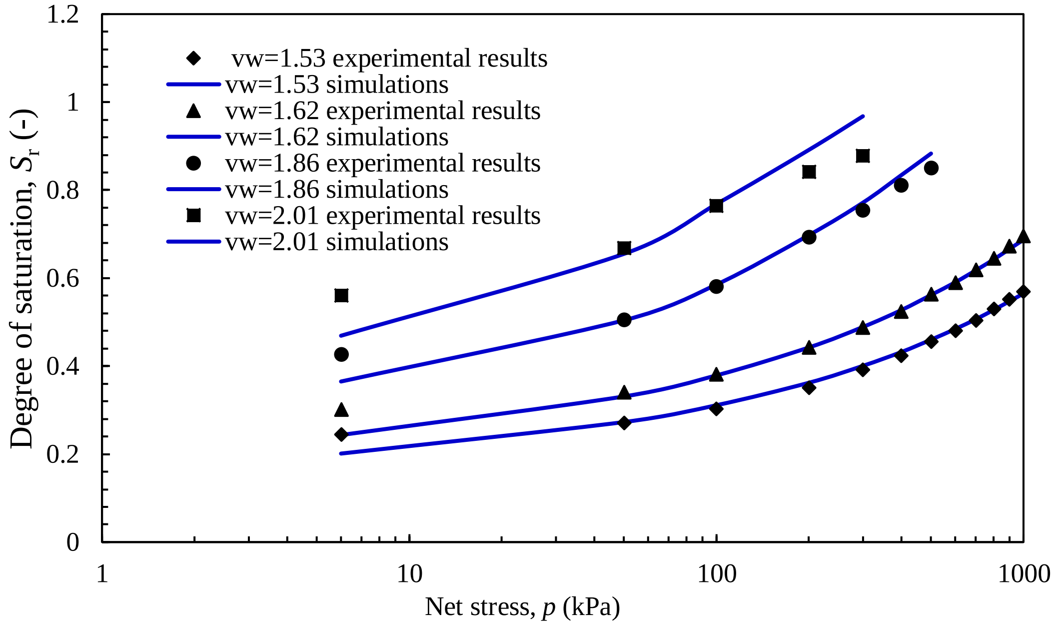

(b)

Figure 6.13: Comparison of simulated and experimental results on: (a) (ν, p) plane (b) (S_r, p) plane

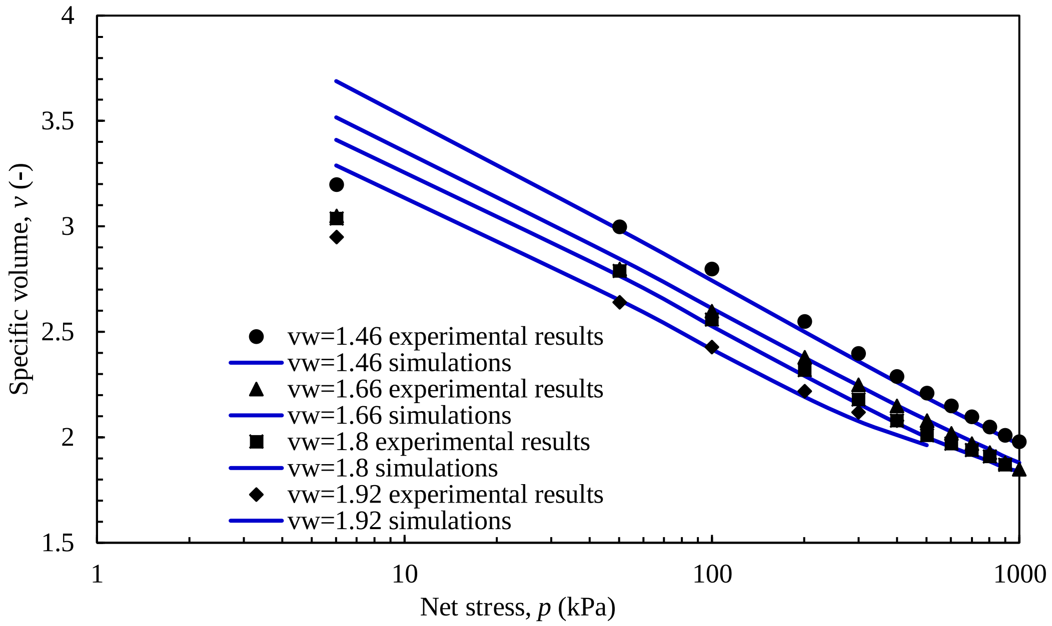

(a)

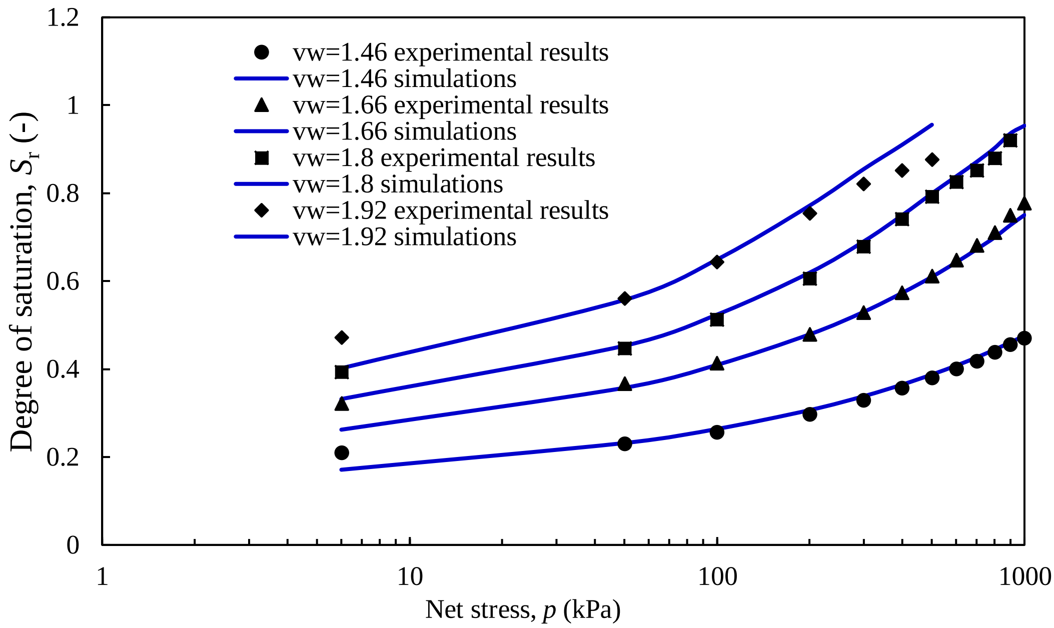

(b)

Figure 6.14: Comparison of simulated and experimental results on: (a) v, p plane (b) S_r, p plane

Due to the large number of constant moisture content compression experiments performed by Abeyrathne et al. (2019), the validation of the experimental results is given for Figure 6.13 and

Figure 6.14. As shown in Figure 6.13, model simulations were also carried out for different constant moisture content loadings (v_w = 1.53, 1.62, 1.86 and 2.01), and the results showed reasonable agreement with the simulations (see phenomenological observation P2 in Chapter 3). Figure 6.13(b) shows the change in S_r with the increase of p . In a similar manner, Figure 6.14 shows model simulations for v_w = 1.46, 1.66, 1.8 and 1.92, and the results show reasonable agreement with the simulations.

In addition to virgin constant moisture content loading stress paths, the proposed equation for the elastic behaviour of the specific volume was validated against the results of the constant specific moisture unloading experiments. The experimental data and the simulation are given in Figure 6.15 for specific moisture volumes (v_w =1.55, 1.64 and 1.91). During the unloading simulation, the v increases slightly, whereas S_r reduces slightly, showing better agreement with the experimental results (refer to phenomenological observation P2 in Chapter 3).

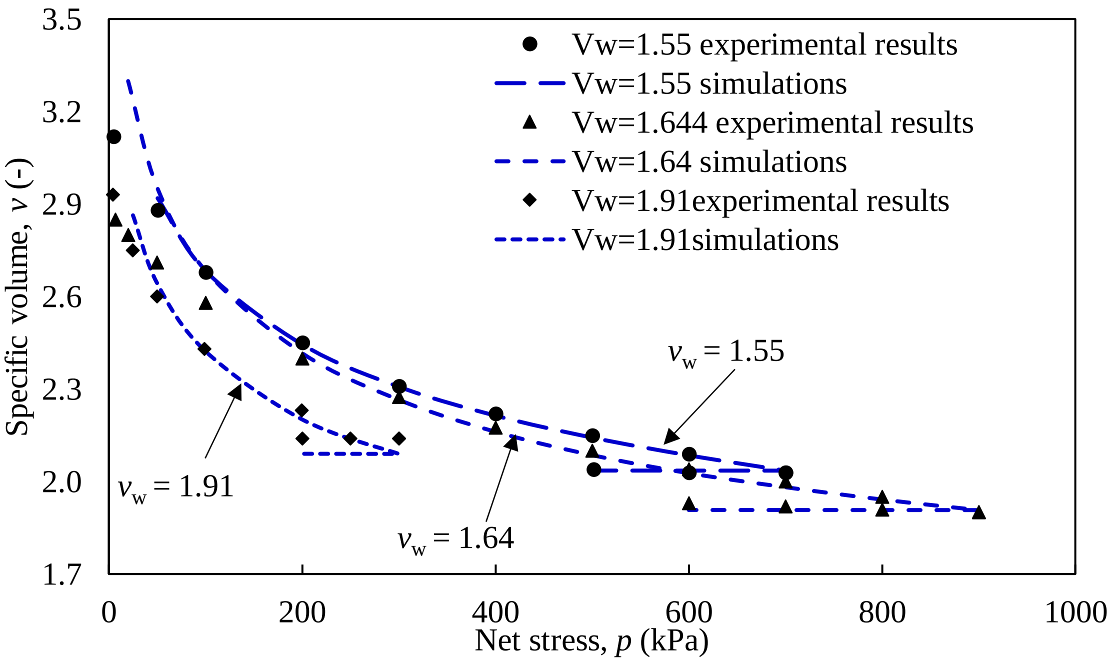

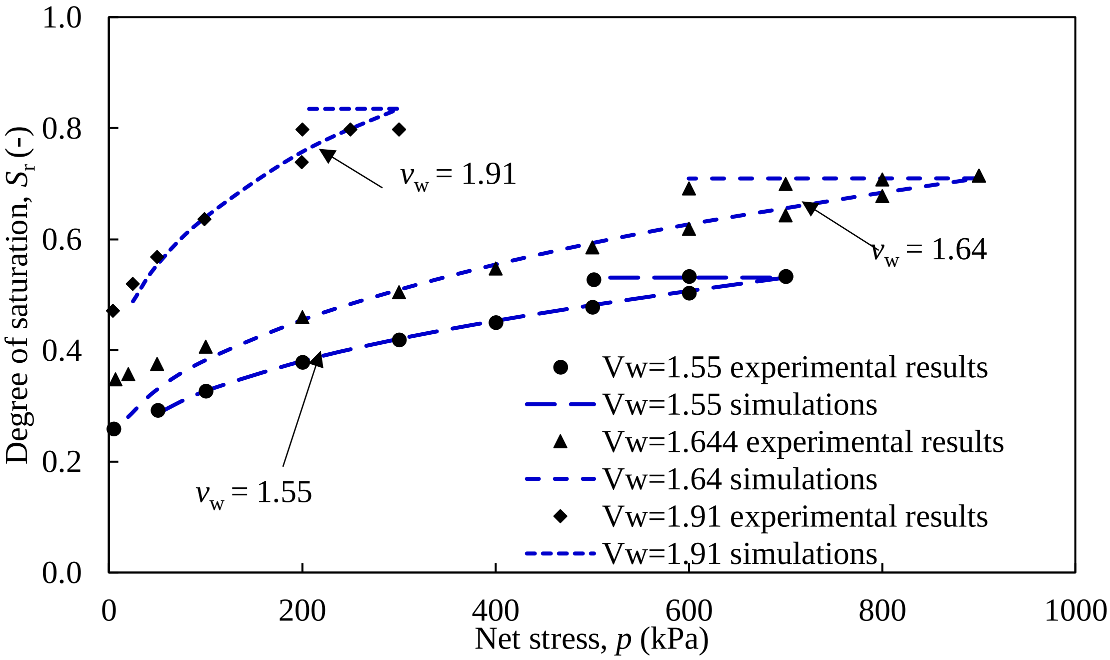

Figure 6.15: Comparison of simulated and experimental results on: (a) (v, p) plane (b) (S_r, p) plane

The current model for constant degree of saturation loading was compared with the data for S_r = 0.5, 0.6, 0.7 and 0.8 from Abeyrathne et al. (2019) A reasonable agreement was obtained (see phenomenological observation P3 in Chapter 3), as shown in Figure 6.16(a) on the (v, p) plane and Figure 6.16(b) on the (v_w, p) plane.

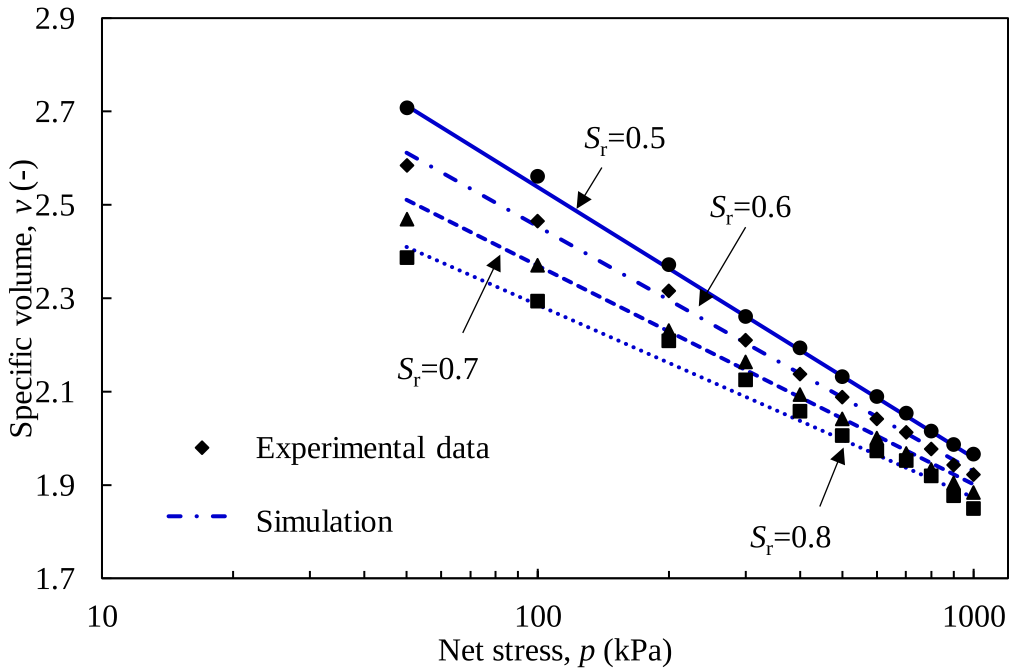

(a)

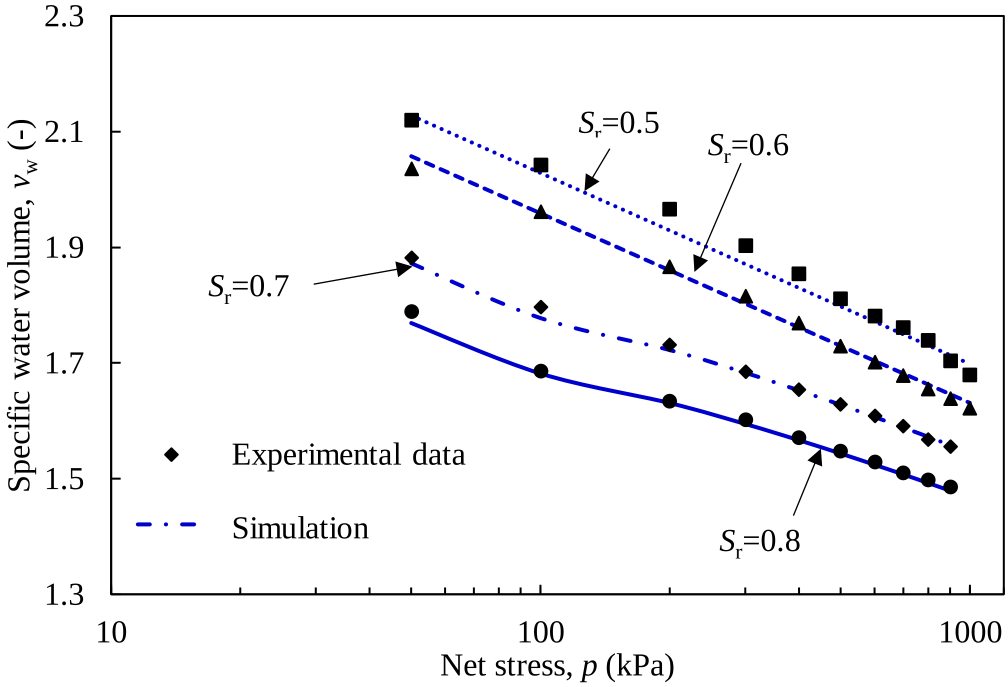

(b)

Figure 6.16: Constant degree of saturation model simulations with data extracted from Abeyrathne et al. (2019) on: (a) (v, p) plane (b) (v_w, p) plane

6.4 Tests reported by Raveendiraraj (2009)

Raveendiraraj (2009) published a series of sophisticated experimental results for various combinations of isotropic loading, unloading, wetting and drying performed on compacted kaolin. For the validation of the MPK generalised model, tests A1, A3, A4, A5, A9, A10, A11 are used in this chapter. Samples 50 mm in diameter and 50mm high were statically compacted at 25% moisture content. The initial v and S_r of the compacted samples were 2.14 ± 0.02 and 55.5 ± 2.5%. Initial equalisation was performed to reach the targeted initial stress values, and the test stress paths were completed after equalisation and were mostly wetting paths. Unfortunately, however, despite their importance, no measurements were taken during this phase, and hence, predictions start after initialisation. In the following sections, MPK model predictions for three tests are compared with the respective experimental results. Raveendiraraj (2009) presented comparisons with the predictions of the BBM and the model by Wheeler et al. (2003)

6.4.1 Test A1: Loading → Unloading → Drying → Loading → Wetting

The sample was equalised to the mean net stress of 10 kPa and suction of 150 kPa (State *A* in Figure 6.17) prior to the loading, unloading, drying (elastic), loading, and wetting (elastic) stress paths. The sample was loaded to a mean net stress of 250 kPa under suction of 150 kPa (i.e., stress path *AB*) whereas the model predicted yielding after 90 kPa. The sample was subsequently unloaded to 100 kPa (i.e., stress path *BC*) and dried to the suction of 250 kPa at the mean net stress of 100 kPa (i.e., stress path *CD*). During the subsequent loading (i.e., stress path *DE*) to 200 kPa, the test results showed an elastic behaviour in the sample, as predicted by the model (refer to phenomenological observation P8 in Chapter 3). The sample was then further wetted to the suction of 200 kPa in stress path *EF*. On this stress path, collapse was predicted (see phenomenological observation P10 in Chapter 3) by the simulations (see Figure 6.17(c)), although the experimental results did not exhibit much variation. Some of the initial deviations of v and S_r may be explained as being due to the elastic-plastic nature of the current model without allowing for material yield prior to the yield surface, as in a bounding surface plasticity model.

Table 6.1: Experimental validation A1

Stage			Net stress (p/kPa)	Suction (s/kPa)
A	B	Loading	10→250	150
B	C	Unloading	250→100	150
C	D	Drying (elastic)	100	150→250
D	E	Loading	100→200	250
E	F	Wetting (elastic)	200	250→200

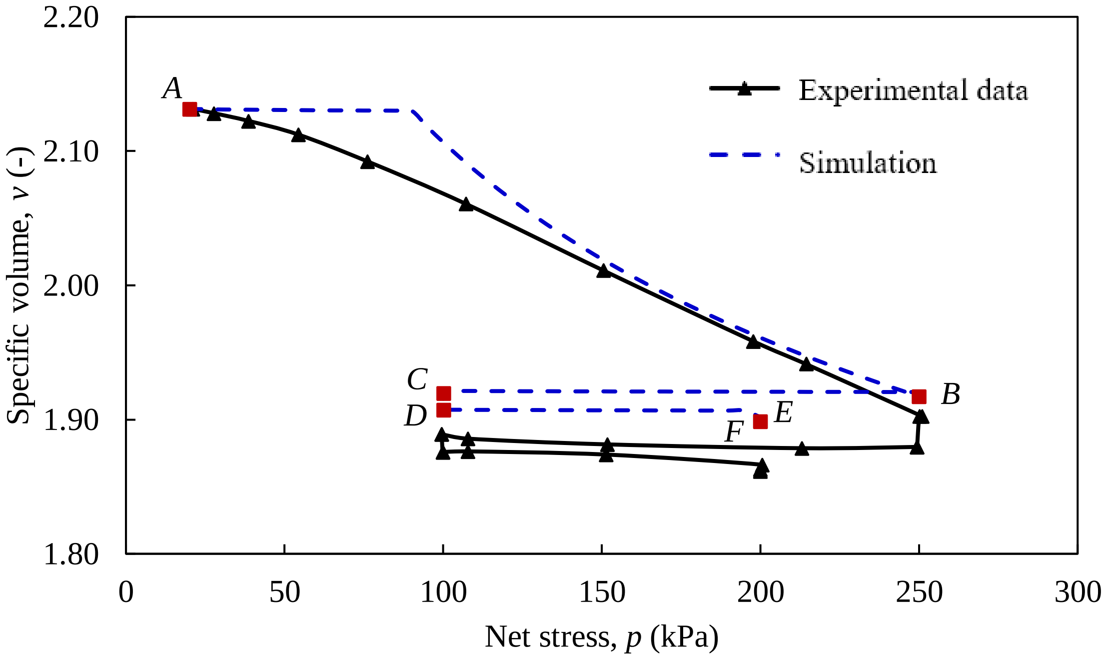
2.20
2.10
2.00
1.90
1.80
Specific volume, v (-)
0
50
100
150
200
250
300
Net stress, p (kPa)
A
B
C
D
E
F
Experimental data
Simulation

(a)

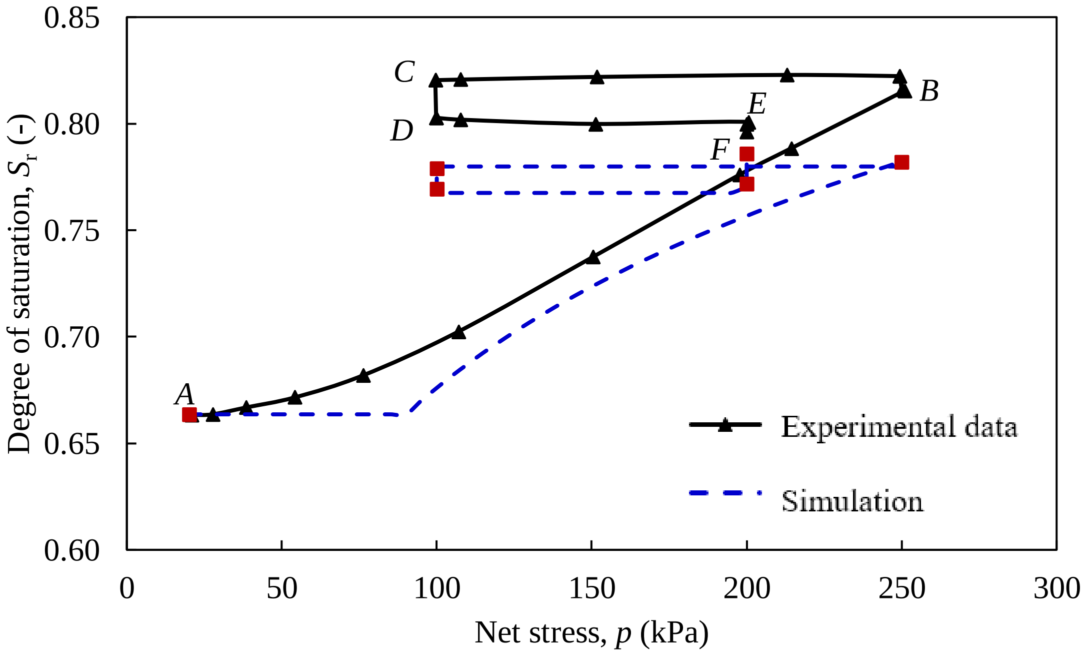
0.85
0.80
0.75
0.70
0.65
0.60
Degree of saturation, S_r (-)
0
50
100
150
200
250
300
Net stress, p (kPa)
A
B
C
D
E
F
Experimental data
Simulation

(b)

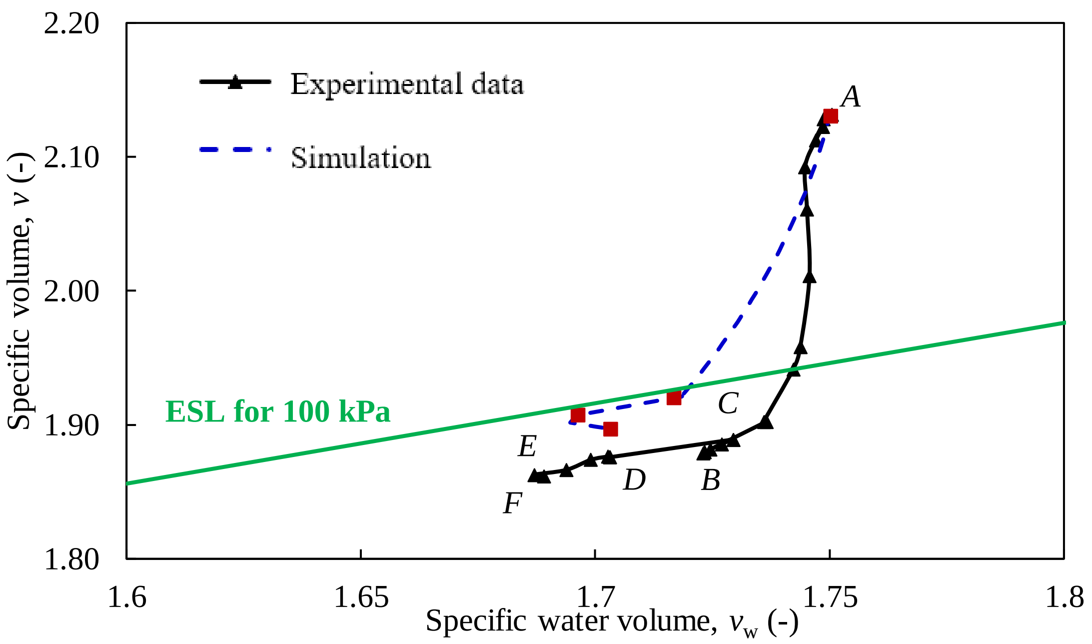

(c)

Figure 6.17: Comparison of simulated and experimental results on: (a)(v, p) plane; (b) (S_r, p) plane (c) (v, v_w) plane

6.4.2 Test A3: Loading→ Unloading and drying→ Wetting → Unloading and drying → Wetting –swelling collapse behaviour

The sample was equalised to the mean net stress of 20 kPa and suction of 350 kPa (State *A* in Figure 6.18) prior to the loading, unloading/drying, and wetting stress paths. The sample was loaded to the mean net stress of 325 kPa under suction of 350 kPa (i.e., stress path *AB*), whereas the model predicted yielding after 90 kPa. Then, similar to Test A4 (discussed in the next section), the sample was unloaded and simultaneously dried to the mean net stress of 250 kPa and suction of 365 kPa (i.e., stress path *BC*). During the subsequent constant net stress wetting (i.e., stress path *CD*), the test results showed some collapse in the sample, as predicted by the model. The sample was then further unloaded and simultaneously dried to the mean net stress of 175 kPa and suction of 185 kPa on stress path *DE*. During the next stress path *EF* of wetting, suction was reduced from 175 kPa to 50 kPa. Initially, on this stress path, swelling behaviour with eventual collapse was predicted by the simulations (see phenomenological observation P10 in Chapter 3). Figure 6.18(b) shows the corresponding variation in S_r during these stress paths.

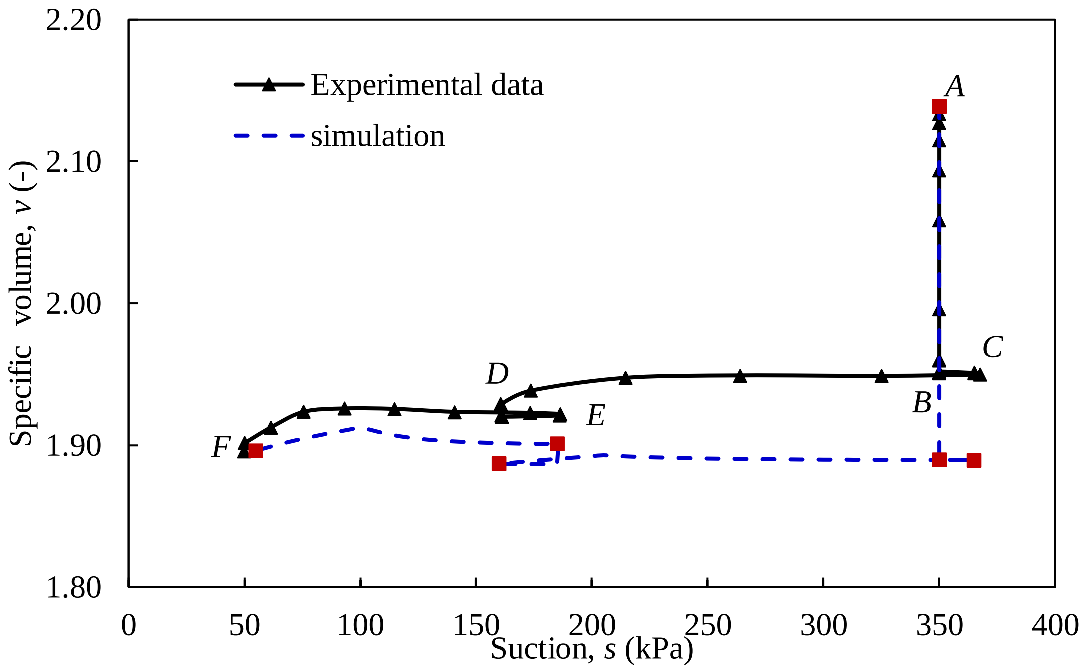

(a)

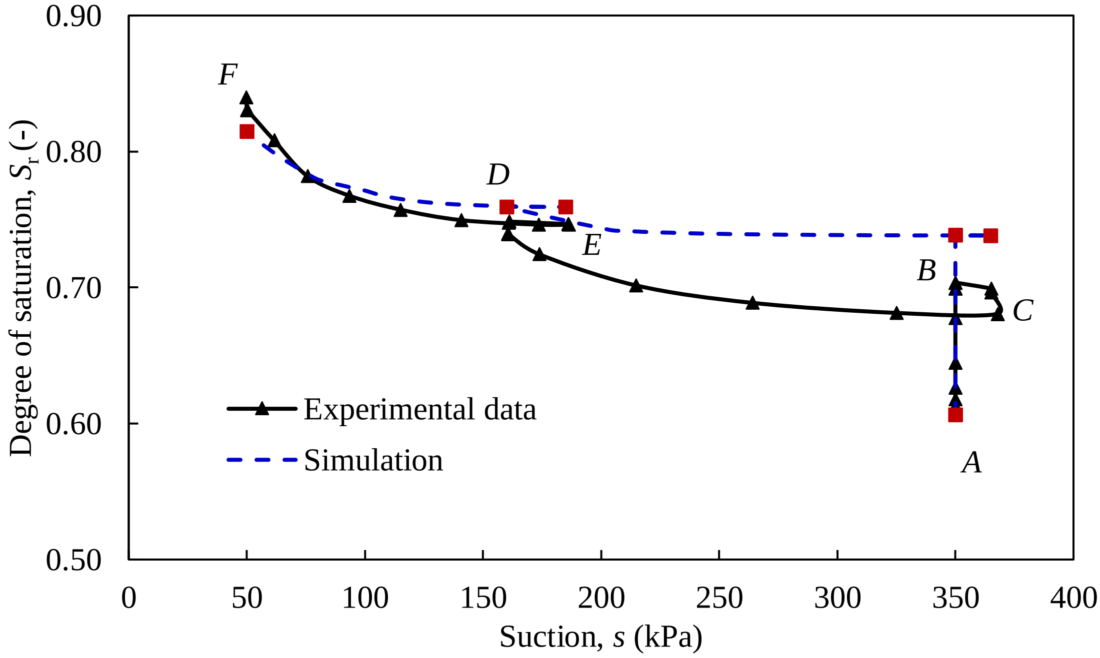

(b)

Figure 6.18: Comparison of simulated and experimental results on: (a) (v, s) plane (b) (S_r, s) plane

Table 6.2: Experimental validation A3

Stage			Net stress (p/kPa)	Suction (s/kPa)
A	B	Loading	20→325	350
B	C	Unloading & drying	325→250	350→365
C	D	Wetting	250	365→160
D	E	Unloading & drying	250→175	160→185
E	F	Wetting	175	185→50

6.4.3 Test A4: Loading→ Unloading and drying→ Loading→ Unloading and drying→ Loading

This test sample was equalised to the mean net stress of 20 kPa and suction of 150 kPa prior to the loading and unloading/drying cycles, as shown in Figure 6.19 and Table 6.3. The first stress path was loading to 150 kPa (i.e., stress path *AB*), where the model predicted yielding after 60 kPa, which is reasonably consistent with the test results. During stress path *BC*, the sample was simultaneously dried and unloaded to the suction of 200 kPa and net stress of 75 kPa. Generally, upon unloading the soil moves on the corresponding volumetric elastic plane (VEP) without changing the previously-attained yield stress. However, in this test, drying was also effected (with the increase of suction) with unloading. Hence, as far as drying is considered, the soil sample may have been on its first drying path where $\alpha_1 = 0.57$ ($< \alpha_{\mathrm{ES}}$) since $\bar{\eta} = -0.16 < 0$ (refer to phenomenological observation P8 in Chapter 3). Since the previous stress path AB was a loading path, the soil was on a wetting curve, and during path *BC*, it moved along the scanning curve first until it reached the corresponding drying curve, without apparent change in the plastic strain. Therefore, a slight reduction in both v and S_r was observed.

During the next loading (*CD*) stress path, the net stress was increased to 250 kPa under the suction of 200 kPa. Consistent with the experimental results, path *CD* featured two aspects: first, the yield stress increased slightly, and the yield curve shifted, both due to an increase in suction. The subsequent stress paths *DE* and *EF* were similar and displayed similar characteristics in both the experiment and the model. Figure 6.19(b) shows the variation of S_r during the test, where S_r continues to increase during the loading paths. However, the model predicts a slight initial reduction in S_r (prior to increasing substantially) during loading after drying (*CD* and *EF*), and this behaviour in the model is experimentally shown particularly clearly for path *EF*. A possible reason for this behaviour is that during loading at constant suction after drying, the state moves from a drying state (from a scanning curve position) towards the corresponding wetting curve (the same ε_v^p) with a small reduction in S_r and then moves on progressive wetting curves with further yielding. Using an effective stress model, Pasha et al. (2019) also predicted this observation.

Table 6.3: Experimental validation A4

Stage			Net stress (*p*/kPa)	Suction (*s*/kPa)
A	B	Loading	20→150	150
B	C	Unloading and drying	150→75	150→200
C	D	Loading	75→250	200
D	E	Unloading and drying	250→150	200→300
E	F	Loading	150→400	300

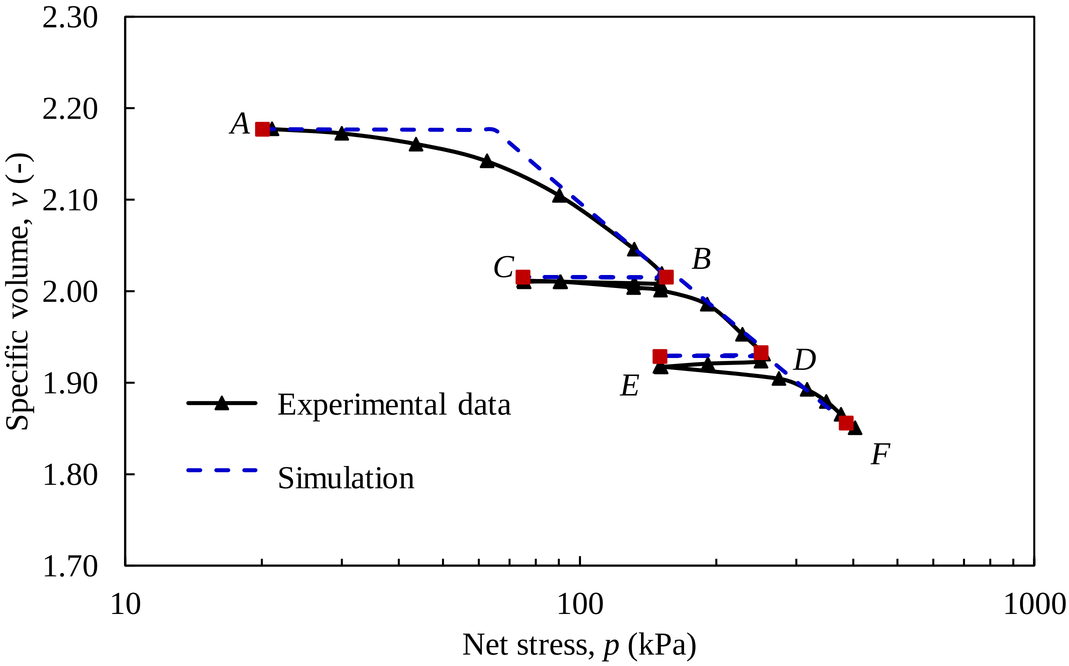

(a)

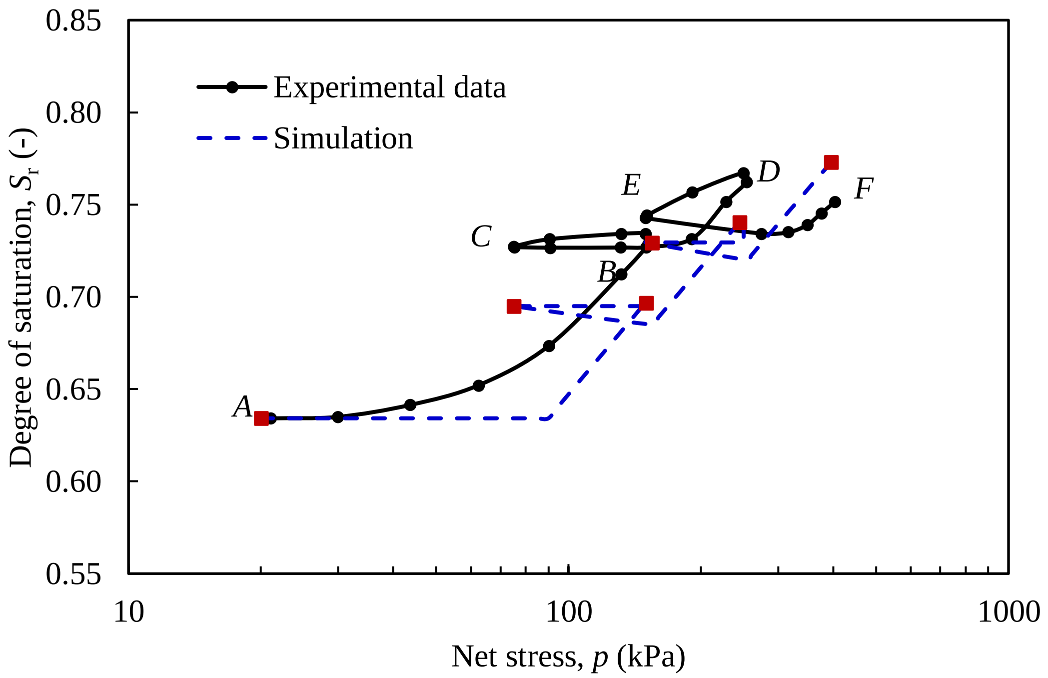

(b)

Figure 6.19: Comparison of simulated and experimental results on: (a) (v, p) *plane (b)* (S_r, p) *plane*

6.4.4 Test A5: Drying→ Wetting→ Drying→ Loading

Figure 6.20 shows a comparison of the computed and experimental results of stress paths comprising drying/wetting/drying/loading, as given in Table 6.4, and Figure 6.20(a) shows the experimental and model results both plotted on the (v, v_w) plane. Since the initial state of the soil (p =10 kPa and s =30 kPa) is reached by wetting, State A is on a wetting curve. Furthermore, A is above the ESL applicable to p =10 kPa, as shown. In this state, $\bar{\eta}$=0.039 > 0. For the first drying cycle (path AB to s = 300 kPa), α_1 of 0.63 was selected, where simulated and experimental paths coincide. Subsequently, the sample was wetted (first wetting) to the suction of 40 kPa (path BC) and α_2 = 0.57 (< α_{ES}= 0.6), $\bar{\eta}$=0.035>0, showing the path followed in Figure 6.20(a). Next, the sample was dried (second drying) to the suction of 200 kPa (path CD) and α_1 reduced to 0.6015 (new $\bar{\eta}$=0.034). It is apparent that the wet/dry cycles move the state downward slowly approaching ESL, as apparent from both experimental and simulated data. During these cycles, the sample underwent hardening (increase in yield stress considered at a particular v_w, S_r or s), since these states were above the ESL for p = 10 kPa. Finally, the sample was loaded from the mean net stress of 10 kPa to 275 kPa (path *DE*) at s = 200 kPa, as shown both experimentally and numerically. The model qualitatively follows the experimental results, although the amount of reduction in S_{r} during drying is somewhat under-estimated on the basis of the parameters estimated from the overall results presented by Sharma (1998).

Figure 6.20(b) and Figure 6.20(c) show comparisons of the experimental and model results on (v, s) and (S_{r}, s) planes. It is clear that the model is able to replicate the suction-based v and S_{r} variations reasonably accurately. One interesting observation to make from the experimental results is that suction-based modifications become more non-linear and significantly magnified than paths on the (v, v_{w}) plane. Note also that scanning curves are invoked when drying or wetting alternate, and this also adds to the non-linearity. Another associated inference is that when the soil is environmentally stabilised (on the ESL or close to it, as on path *ABCD*), the yield stress for a certain S_{r} (or v_{w}) is almost the same (on the (v, v_{w}) plane), but there are two different suctions for the wetting and drying paths, which means two different LC curves need to be invoked on the (s, p) plane for wetting and drying to represent the same yield stress due to subsequent loading. This need has been highlighted by several researchers ((Lloret-Cabot and Wheeler, 2018, Alonso et al., 2013)), and indirectly by Pasha et al. (2019), who advocated the requirement to consider hysteresis in the χ parameter for the effective stress. However, as explained in the current model, this feature naturally emerges, since uniqueness is discussed generally in (v, v_{w}, p) space (see phenomenological observation P9 in Chapter 3).

Table 6.4: Experimental validation A5

Stage			Net stress (p/kPa)	Suction (s/kPa)
A	B	Drying	10	30→300
B	C	Wetting	10	300→40
C	D	Drying	10	40→200
D	E	Loading	10→275	200

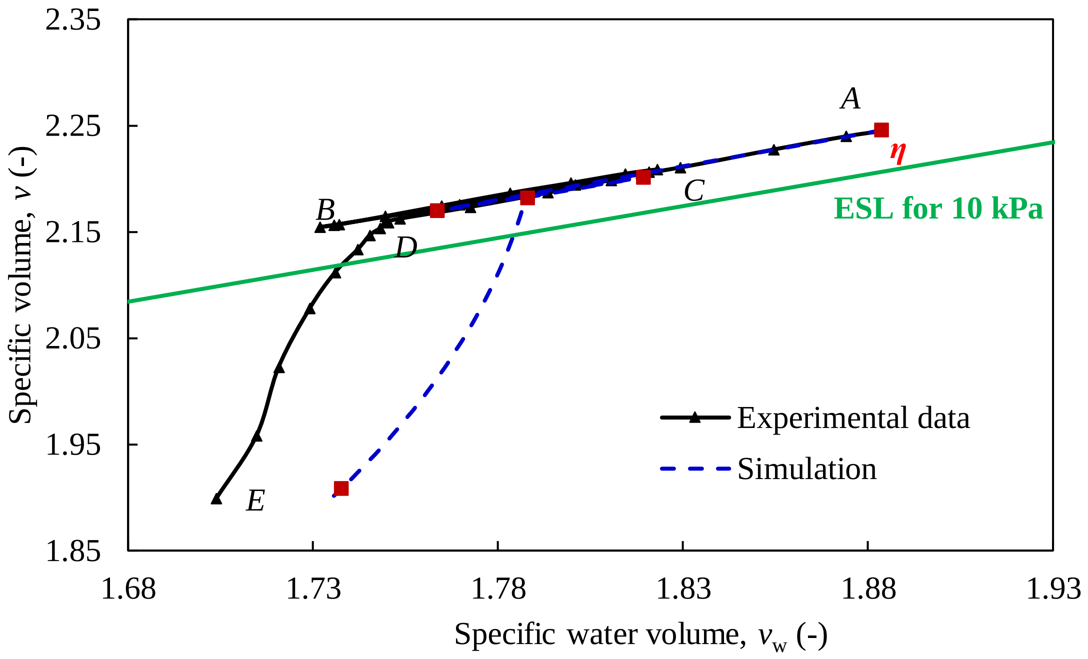

2.35
2.25
2.15
2.05
1.95
1.85
1.68
1.73
1.78
1.83
1.88
1.93
Specific volume, v (-)
Specific water volume, v_w (-)
A
B
C
D
E
η
ESL for 10 kPa
Experimental data
Simulation

(a)

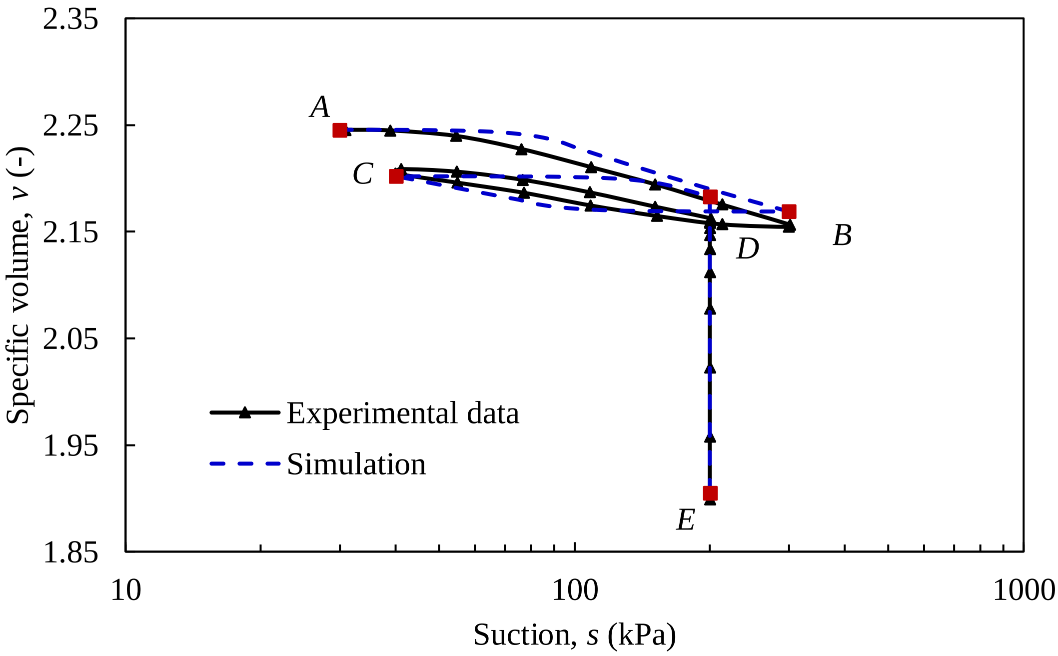

2.35
2.25
2.15
2.05
1.95
1.85
10
100
1000
Specific volume, v (-)
Suction, s (kPa)
A
B
C
D
E
Experimental data
Simulation

(b)

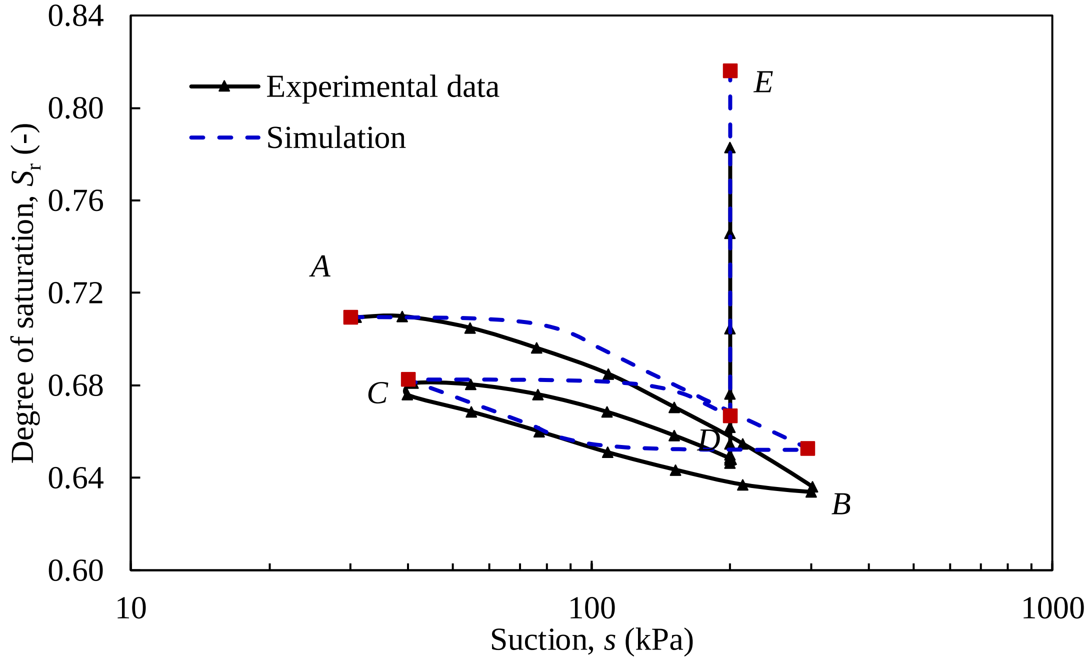

(c)

Figure 6.20: Comparison of simulated and experimental results on: (a) (v, v_w) plane (b) (v, s) plane (c) (S_r, s) plane

6.4.5 Test A9: Loading→ Unloading→ Wetting → Drying→ Loading

The sample was equalised to the mean net stress of 10 kPa and suction of 300 kPa (State *A* in Figure 6.21) prior to the loading, unloading, wetting, drying, and loading stress paths (see Table 6.5). The sample was loaded to the mean net stress of 200 kPa under the suction of 300 kPa (i.e., stress path *AB*), whereas the model predicted yielding after 120 kPa. Subsequently, the sample was unloaded to the mean net stress of 10 kPa at the suction of 300 kPa (i.e., stress path *BC*). As shown in Figure 6.21(a) and Figure 6.21(b), the simulation of v and S_r with p follows the experimental results and indicates a reasonable agreement (see phenomenological observation P5 in Chapter 3). At State C, $\bar{\eta}$=-0.083< 0. For the first wetting cycle, α_1 of 0.63 (> α_{ES}= 0.6) was selected, as shown in Figure 6.21(e), where the simulated and experimental paths coincide. During the subsequent constant net stress drying path (see phenomenological observation P8 in Chapter 3) (i.e., stress path *DE*), α_2 = 0.57 (< α_{ES}= 0.6), $\bar{\eta}$= -0.078 < 0, following the stress paths shown in Figure 6.21(c) and Figure 6.21(d). The sample was then further loaded simultaneously to a mean net stress of 375 kPa at the suction of 300 kPa in stress path *EF*.

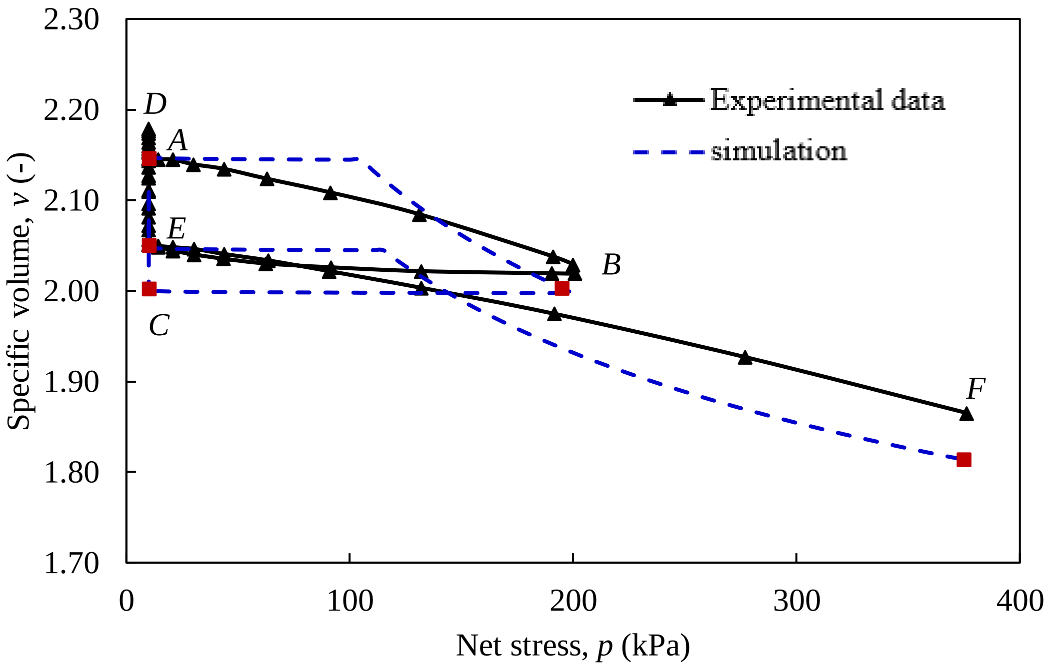

2.30
2.20
2.10
2.00
1.90
1.80
1.70
0
100
200
300
400
Specific volume, v (-)
Net stress, p (kPa)
Experimental data
simulation
D
A
E
B
C
F

(a)

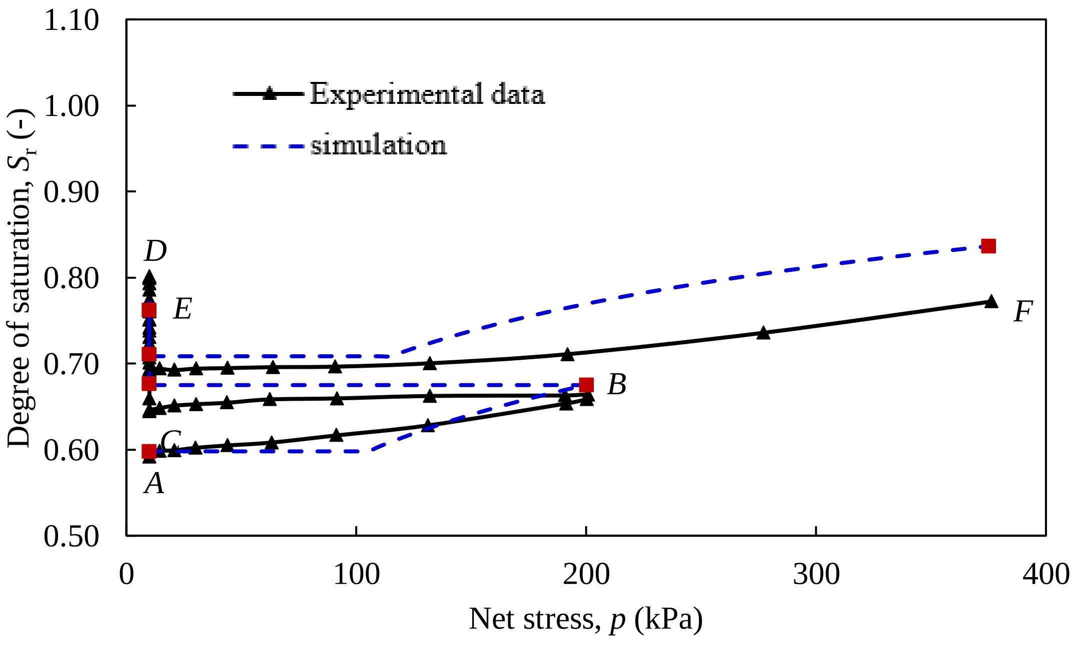

1.10
1.00
0.90
0.80
0.70
0.60
0.50
0
100
200
300
400
Degree of saturation, Sr (-)
Net stress, p (kPa)
Experimental data
simulation
D
E
B
C
A
F

(b)

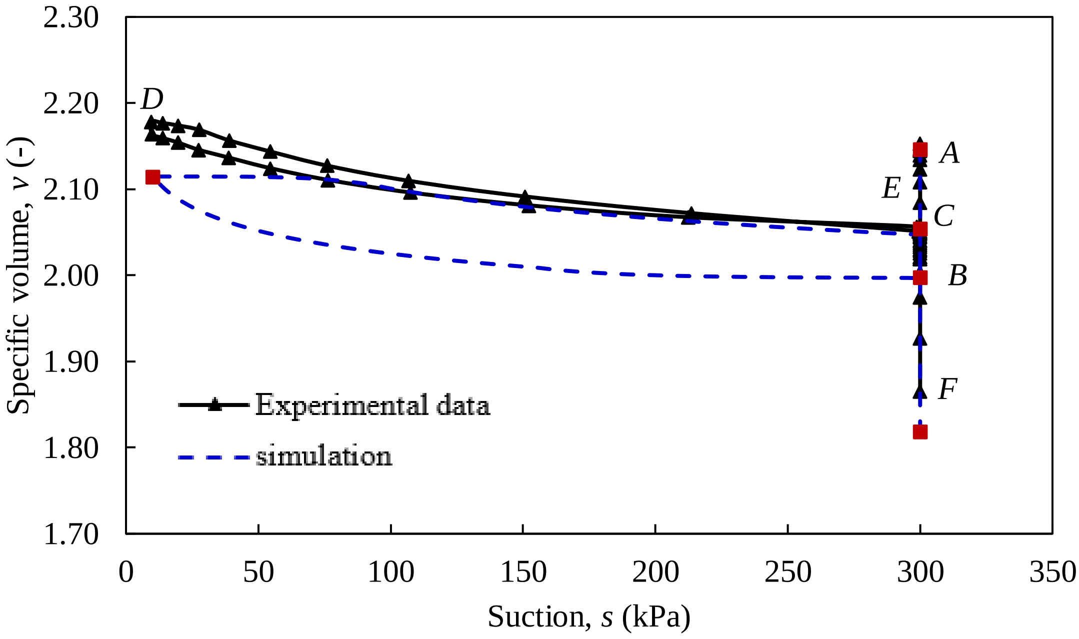
2.30
2.20
2.10
2.00
1.90
1.80
1.70
Specific volume, v (-)
0
50
100
150
200
250
300
350
Suction, s (kPa)
D
A
E
C
B
F
Experimental data
simulation

(c)

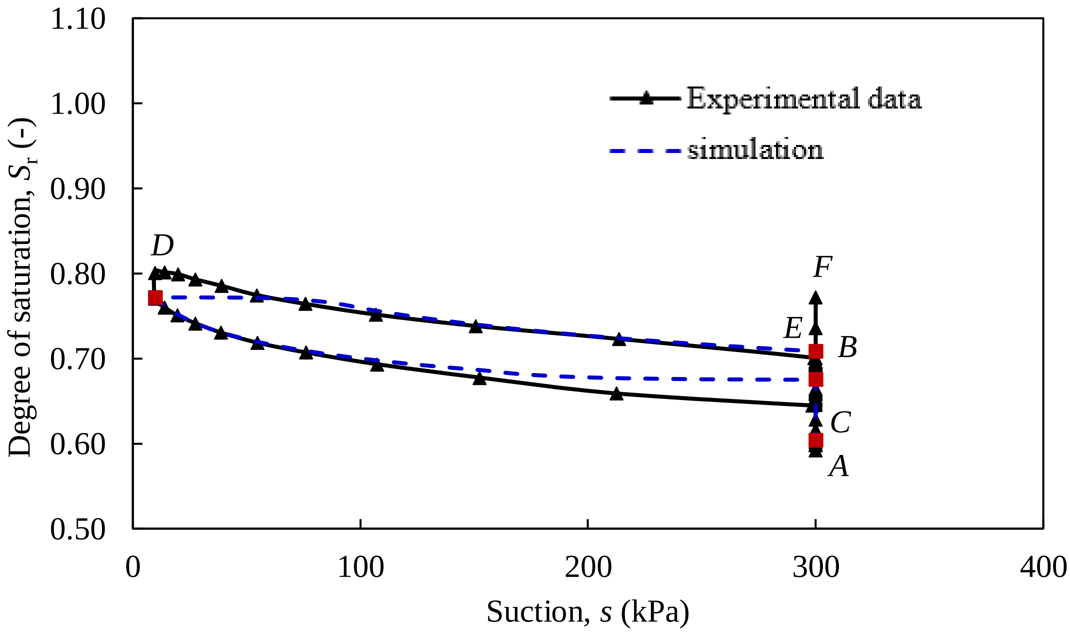
1.10
1.00
0.90
0.80
0.70
0.60
0.50
Degree of saturation, Sr (-)
0
100
200
300
400
Suction, s (kPa)
Experimental data
simulation
D
F
E
B
C
A

(d)

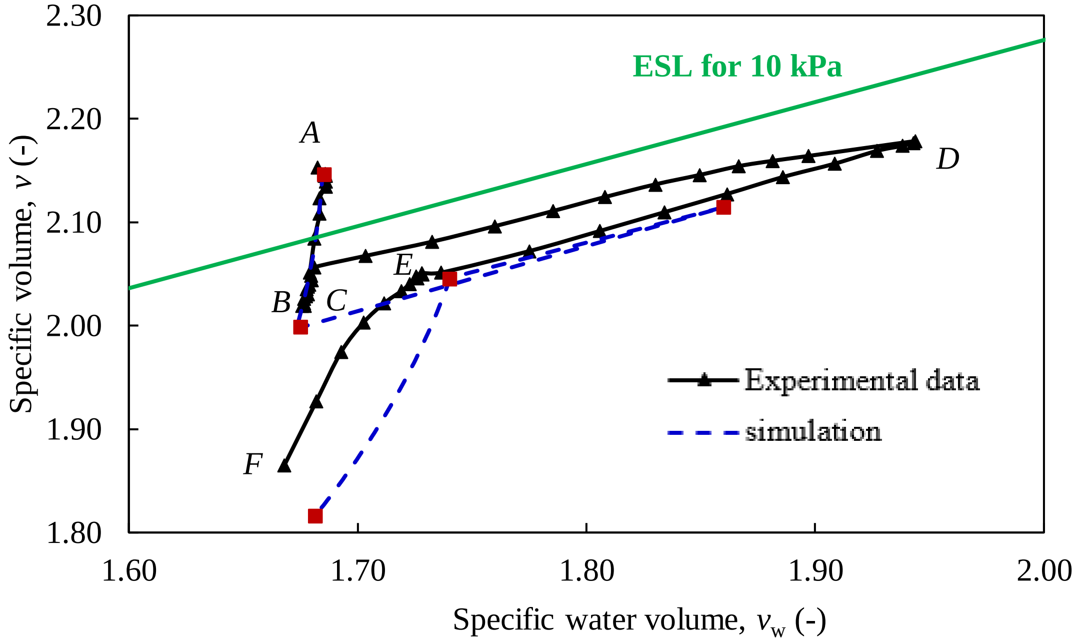

(e)

Figure 6.21: Comparison of simulated and experimental results on: (a) (v, p) plane (b) (S_r, p) plane; (c) (v, s) plane (d) (S_r, s) plane; (e) (v, v_w) plane

Table 6.5: Experimental validation A9

Stage			Net stress (*p*/kPa)	Suction (*s*/kPa)
A	B	Loading	10→200	300
B	C	Unloading	200→10	300
C	D	Wetting	10	300→10
D	E	Drying	10	10→300
E	F	Loading	10→375	300

6.4.6 Test A10: Drying → Wetting → Loading→ Unloading → Drying → Wetting → Loading→ Unloading→ Drying

Figure 6.22 shows a comparison of the computed and experimental results of stress paths comprising drying/ wetting/ loading/ unloading/ drying/ wetting/ loading/ unloading/ drying, as given in Table 6.6. Figure 6.22(a) shows the experimental and model results both plotted on (v, v_w) plane. Since the initial state of the soil (p =10 kPa and s = 40 kPa) is reached by wetting, State *A* is on a major wetting curve. Furthermore, *A* is below the ESL applicable to p =10 kPa, as shown. In this state, $\bar{\eta}$ = -0.1012 < 0. For the first drying cycle (path *AB* to s = 350 kPa), α_2 of 0.57 was selected, and the simulated and experimental paths exhibit reasonable agreement. Subsequently, the sample was wetted (first wetting) to the suction of 10 kPa (path *BC*) and α_1 = 0.63 (< α_{ES} = 0.6), $\bar{\eta}$ = -0.095 < 0, showing the path followed in Figure 6.22(b) on the (v, s) plane and Figure 6.22(c) on the (S_{r}, s) plane. The sample was loaded to the mean net stress of 60 kPa under the suction of 10 kPa (i.e., stress path *CD*), whereas the model predicted yielding after 40 kPa. Subsequently, the sample was unloaded to the mean net stress of 10 kPa at the suction of 10 kPa (i.e., stress path *DE*). As shown in Figure 6.22(d) and Figure 6.22(e), the simulation of v and S_{r} with p follows the experimental results, indicating reasonable agreement.

The sample was then dried (second drying) to the suction of 300 kPa (path *EF*) and α_2 reduced to 0.5827 (new $\bar{\eta}$ = -0.1818) prior to wetting to the suction of 10 kPa (path *FG*) and α_1 reduced to 0.6153 (new $\bar{\eta}$ = -0.1478). It is apparent that the wet/dry cycles move the state upward slowly approaching ESL, as evident from both the experimental and simulated data. During these cycles, the sample underwent softening (decrease in yield stress considered at a particular v_{w} , S_{r} or s), since these states were below the ESL for p = 10 kPa. Next, the sample was loaded from the mean net stress of 10 kPa to 85 kPa (path *GH*) at s = 10 kPa, as shown both experimentally and numerically. The model qualitatively follows the experimental results, where yielding occurs at 50 kPa, a stress lower than that for the previous loading path (i.e., 60 kPa) *CD* due to softening upon the second drying wetting cycle. Figure 6.22(b) and Figure 6.22(c) show comparisons of the experimental and model results on (v, s) and (S_{r}, s) planes. Finally, the sample was dried (third drying) to the suction of 330 kPa (path *IJ*) and α_2 reduced to 0.587 (new $\bar{\eta}$ = -0.2387). Overall, it is clear that the model is able to replicate the suction-based v and S_{r} variations reasonably accurately. The phenomenological observations P1, P4, P7, P9, P17, P19, P20 and P21 in Chapter 3 were captured during the simulation of test A10.

Table 6.6: Experimental validation A10

Stage	Net stress (p/kPa)	Suction (s/kPa)

A	B	Drying	10	40→350
B	C	Wetting	10	350→10
C	D	Loading	10→60	10
D	E	Unloading	60→10	10
E	F	Drying	10	10→300
F	G	Wetting	10	300→10
G	H	Loading	10→85	10
H	I	Unloading	85→10	10
I	J	Drying	10	10→330

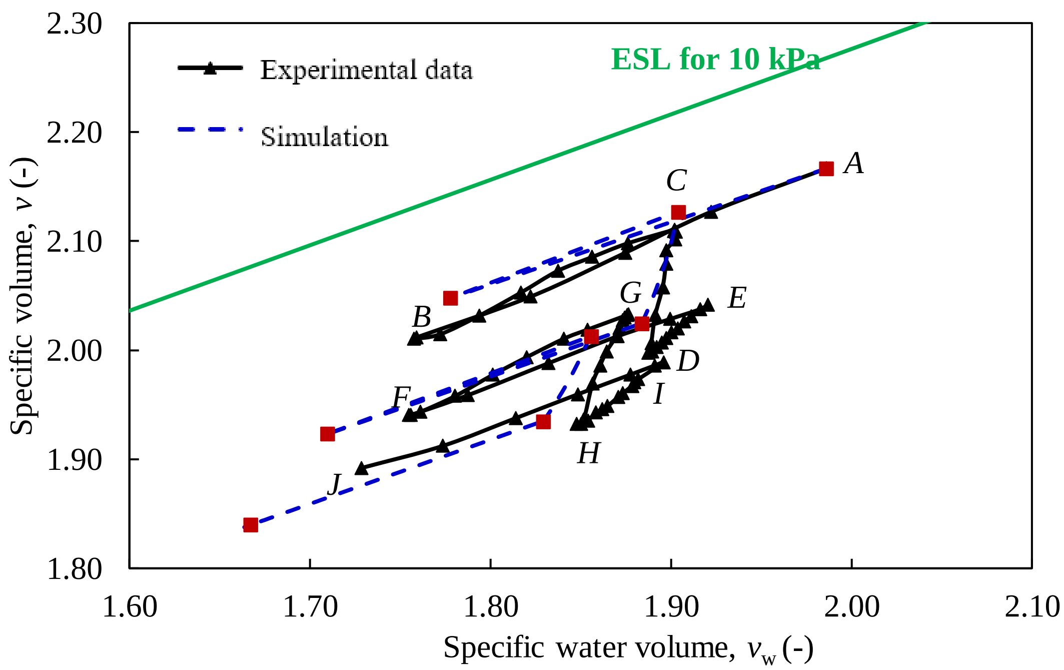

(a)

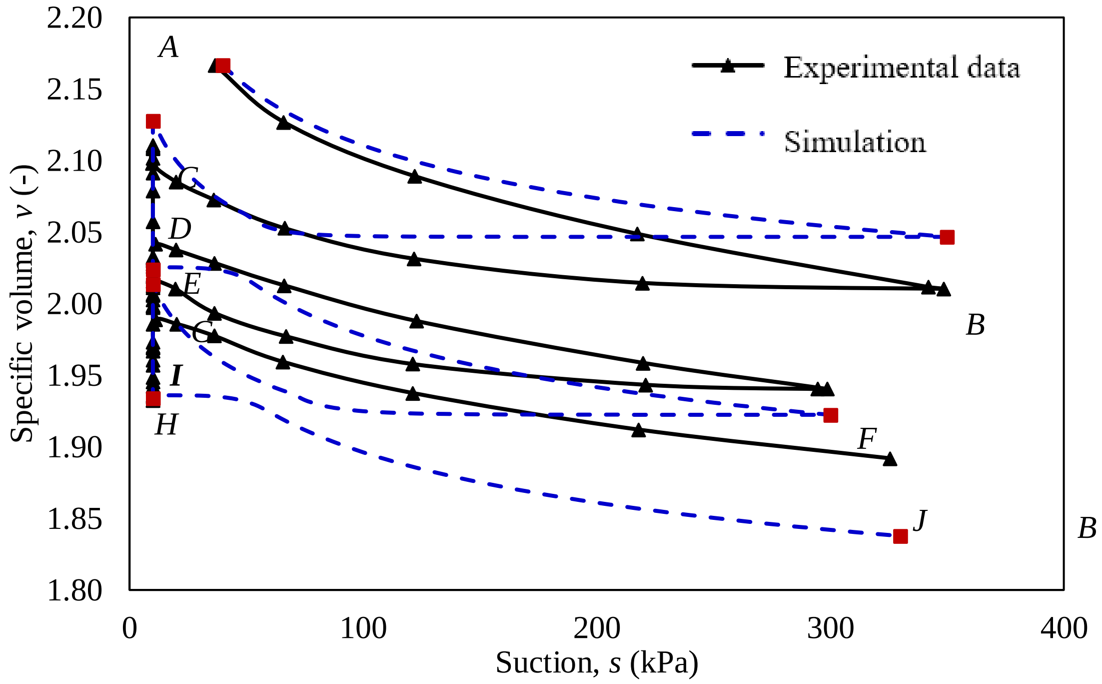
Experimental data
Simulation
Specific volume, v (-)
Suction, s (kPa)
A
B
C
D
E
F
G
H
I
J
B
2.20
2.15
2.10
2.05
2.00
1.95
1.90
1.85
1.80
0
100
200
300
400

(b)

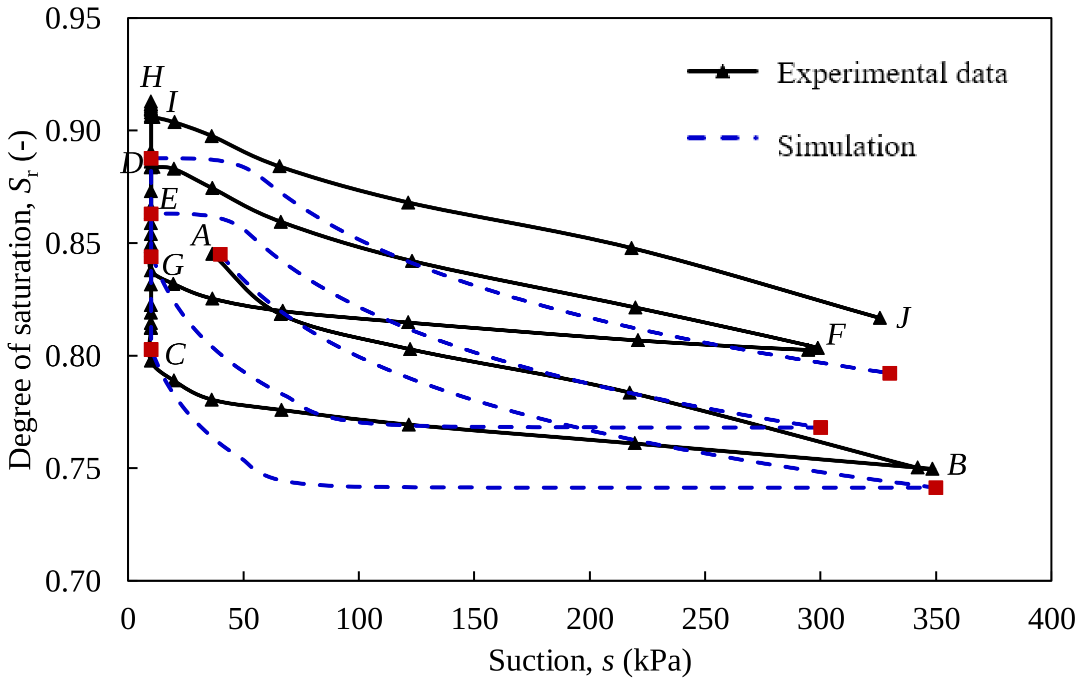
Experimental data
Simulation
Degree of saturation, Sr (-)
Suction, s (kPa)
H
I
D
E
A
G
C
J
F
B
0.95
0.90
0.85
0.80
0.75
0.70
0
50
100
150
200
250
300
350
400

(c)

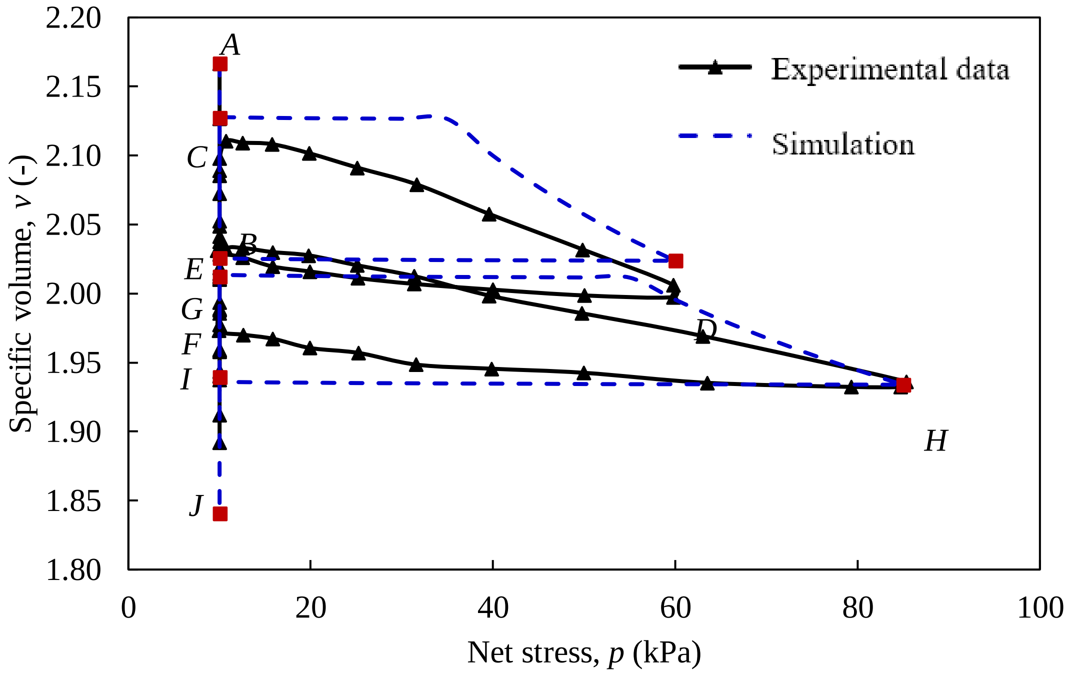

(d)

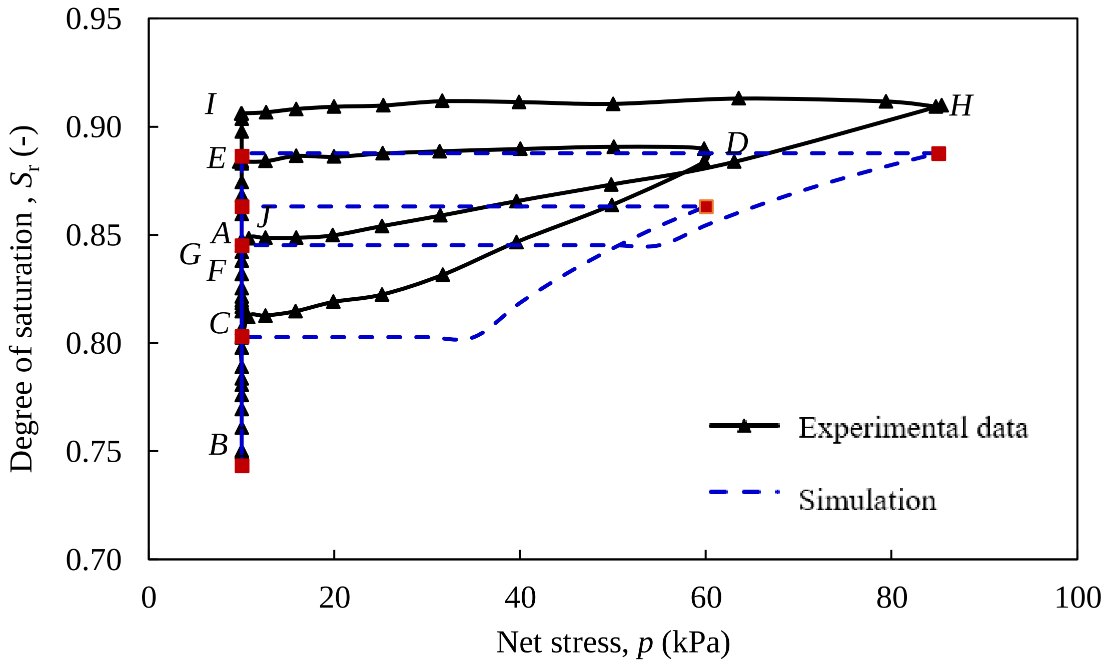

(e)

Figure 6.22: Comparison of simulated and experimental results on: (a) (v, v_w) plane; (b) (v, s) plane; (c) (S_r, s) plane; (d) (v, p) plane; (e) (S_r, p) plane

6.4.7 Test A11: Wetting → Drying → Loading

This test sample was equalised to the mean net stress of 10 kPa and suction of 300 kPa prior to wetting/drying and loading, as shown in Figure 6.23 and Table 6.7. At State A, $\bar{\eta}$=0.0837 >0. For the first wetting cycle, α_2 of 0.57 (> α_{ES} = 0.6) was selected, as shown in Figure 6.23(a), and the simulated and experimental paths exhibit reasonable agreement. During the subsequent constant net stress drying path (i.e., stress path *BC*) α_1 is 0.57 (< α_{ES} = 0.6), and $\bar{\eta}$ = 0.0778 > 0. The stress paths are shown in Figure 6.23Figure 6.(c) and Figure 6.23(d) on (v, s) plane and (S_r, s) plane respectively. The sample was then further loaded simultaneously to the mean net stress of 250 kPa at the suction of 300 kPa on stress path *CD*. Overall, the simulated and experimental paths exhibit reasonable agreement on all three stress paths (see phenomenological observations P7 and P10 in Chapter 3).

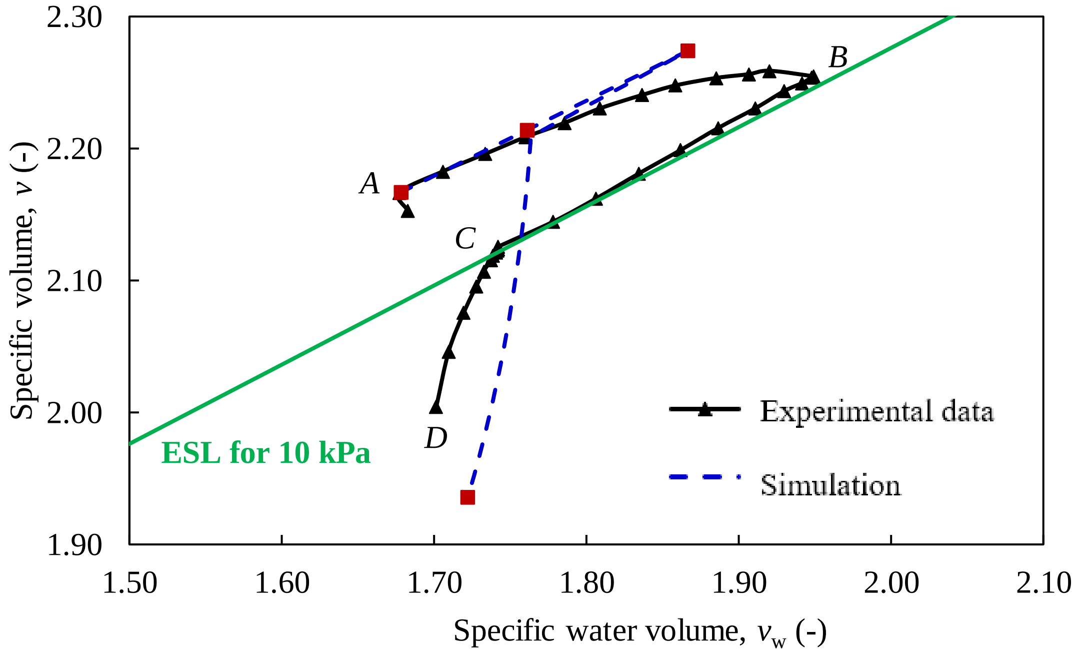

(a)

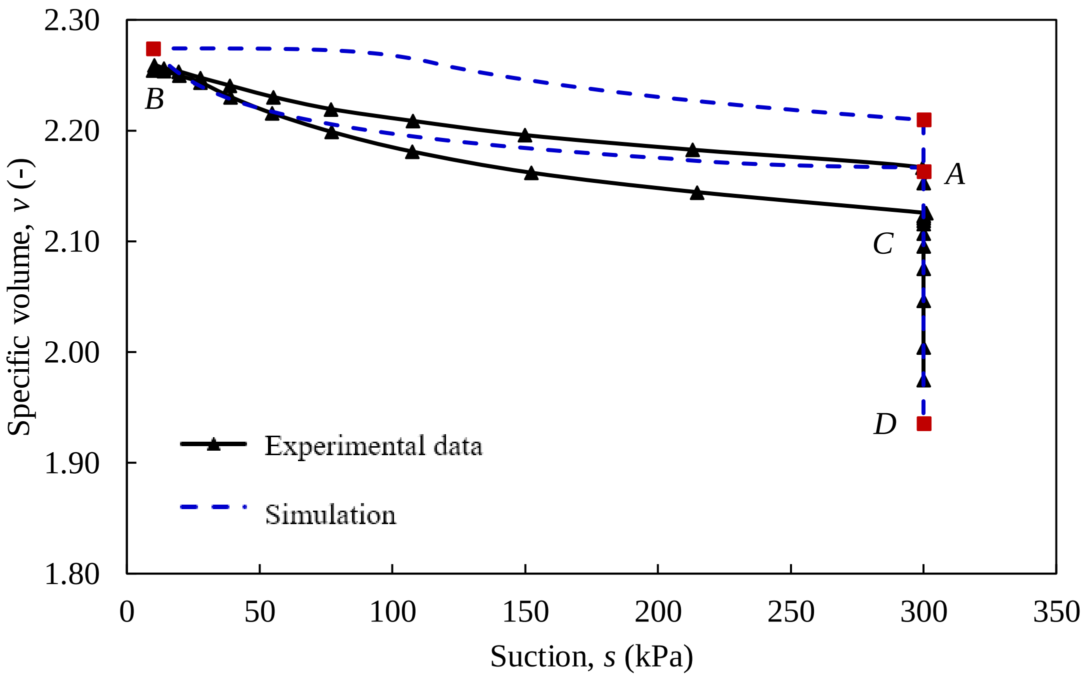

(b)

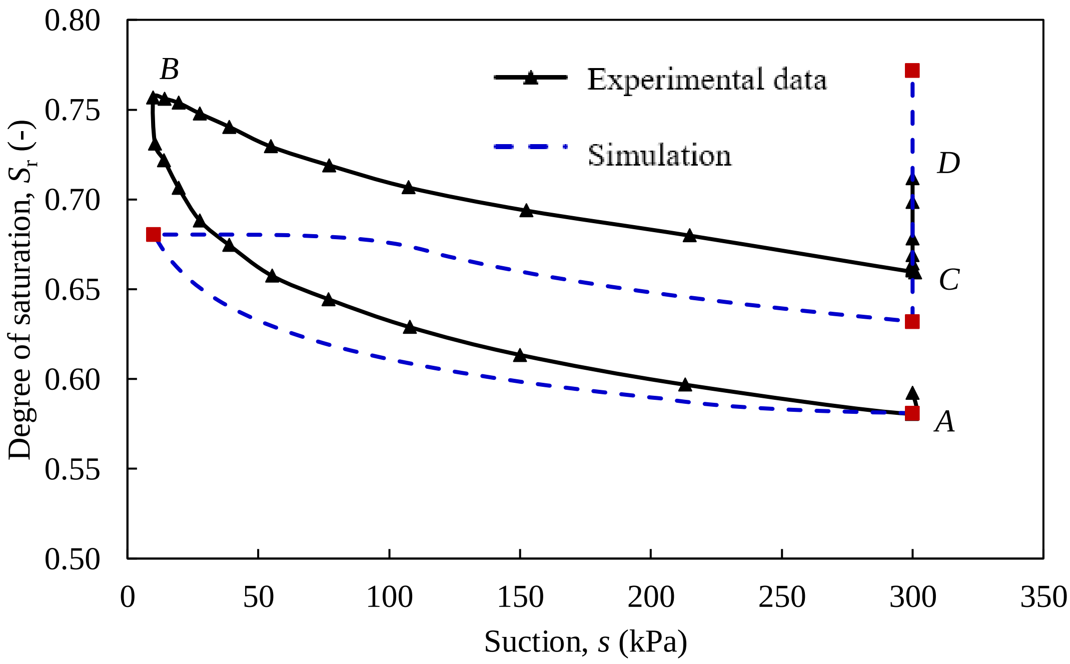

(c)

Figure 6.23: Comparison of simulated and experimental results on: (a) (v, v_w) plane (b) (v, s) plane (c) (S_r, s) plane

Table 6.7: Experimental validation A11

Stage			Net stress (p/kPa)	Suction (s/kPa)
A	B	Wetting	10	300→10
B	C	Drying	10	10→300
C	D	Loading	10→250	300

6.5 Tests reported by Sharma (1998)

Sharma (1998) conducted experiments on a mixture of compacted bentonite and kaolin to study the behaviour of expansive (or reactive) soils. On the basis of these test results, he argued that all compacted clayey soils feature similar phenomenological behaviour, but their degree of change depends on the severity of soil reactivity. In order to demonstrate the applicability of the MPK model to reactive soils, the following comparisons with his results were made. The samples were statistically compacted to stress levels of 400 kPa, 800 kPa and 1200 kPa. Therefore, Sharma's experiments included soils compacted to both loose and dense states with respect to the operational stresses used. All samples were compacted at a moisture content of 25%, and v and S_r immediately after compaction varied according to the compaction level. The tests were carried out after equalisation to target stress states.

6.5.1 Test T1: Drying → Wetting

The stress paths followed in Test T1 are summarised in Table 6.6, and the results are given in Figure 6.24. Since State *A* is placed above the ESL for 10 kPa (as shown in Figure 6.24(a)), the first drying (path *AB*) occurs at α_1 = 0.8 (> α_{ES}=0.7) since $\bar{\eta}$=0.067>0. As shown in Figure 6.24(a), the experimental and model paths agree reasonably well on the (v, v_w) plane for p=10 kPa. During the next stress path *BC* (first wetting), state *B* is also above the ESL; therefore, the first wetting occurs at α_2 = 0.6 (< α_{ES}) since $\bar{\eta}$=0.052>0. As with Test A5, the soil hardens at a certain S_r during these drying and wetting cycles, while approaching the relevant ESL. Figure 6.24(b) and 6.24(c) show comparisons of the experimental and model results on the (v, s) and (S_r, s) planes. It is clear that the model is capable of replicating suction-based v and S_r variations reasonably accurately (refer to phenomenological observations P7 and P10 in Chapter 3).

Table 6.8: Experimental validation T1

Stage			Net stress (p/kPa)	Suction (s/kPa)
A	B	Drying	10	50→400
B	C	Wetting	10	400→50

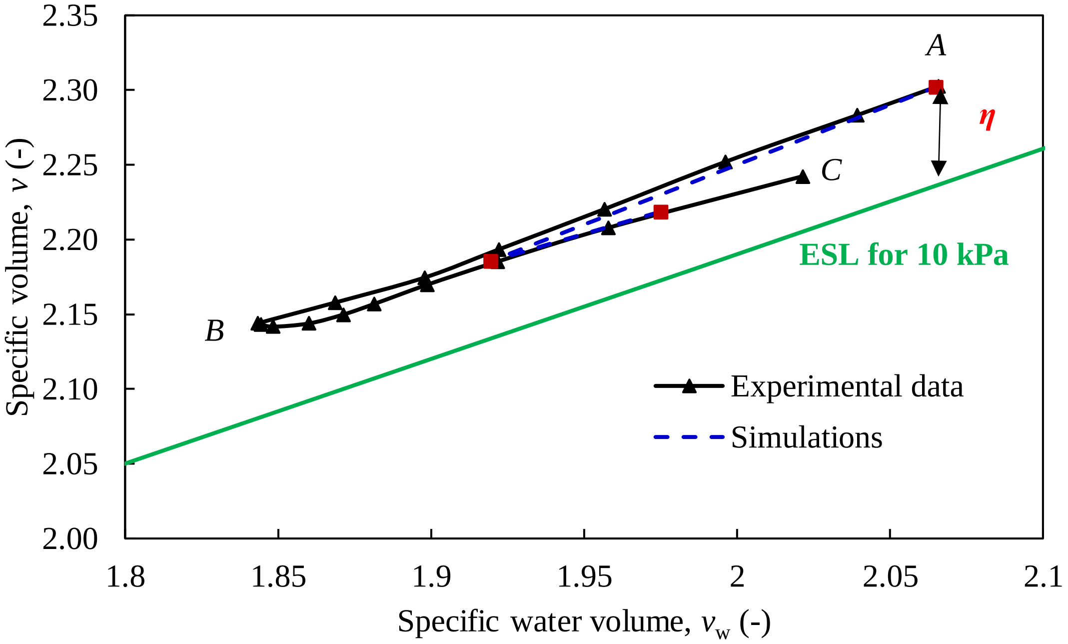

(a)

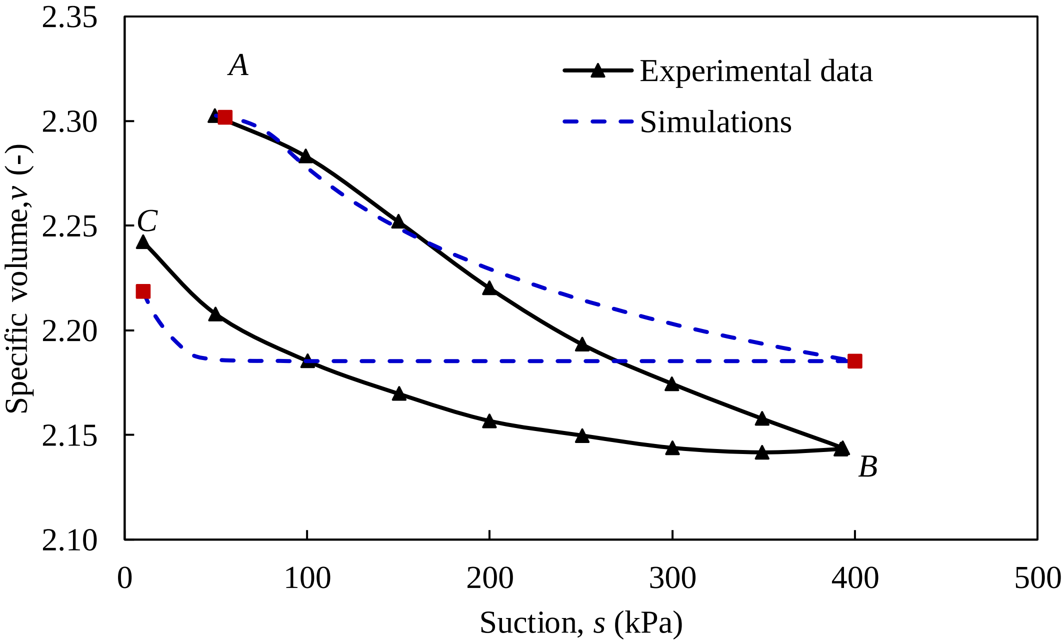

(b)

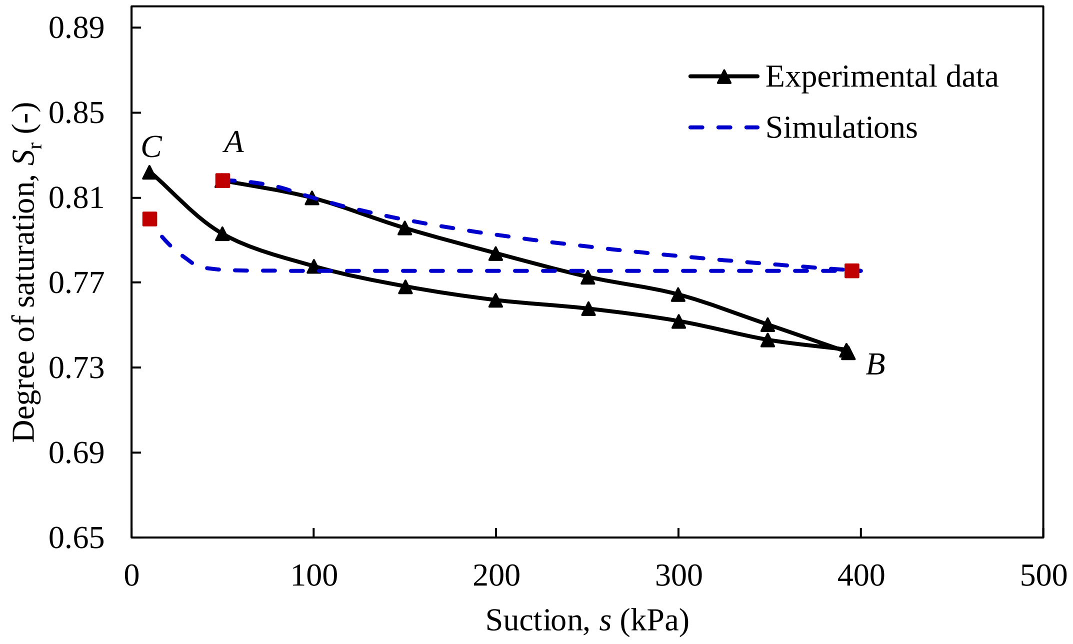

(c)

Figure 6.24: Comparison of simulated and experimental results on: (a) (v, v_w) plane (b) (v, s) plane (c) (S_r, s) plane

6.5.2 Test T2: Wetting (Collapse behaviour)→ Drying

Generally, upon wetting the soil at moderate net stress, swelling/collapse/swelling behaviour is observed. During Test 2 (see Figure 6.25), which involved wetting and drying paths at p = 50 kPa (Table 6.9), initial swelling and then collapse behaviour was observed (see phenomenological observations P10 and P11 in Chapter 3), and the corresponding stress paths are given in Table 6.9. In the model, State *A* is above the ESL, and the first wetting therefore occurs at α_2 = 0.6 (< α_{ES}) since $\bar{\eta}$=0.265>0. When v_w =1.75 (State *A*'), the soil starts to collapse, and hardening begins to occur. With further wetting, the soil starts to move on the constant 50 kPa net stress line on the volumetric yield surface (for example, as shown in Figure (4.8) according to Raveendiraraj (2009)), consistent with the experimental results. During the next stress path (*BC*, first drying), α_1 = 0.8 (> α_{ES}) since $\bar{\eta}$=0.209>0. Overall, hardening was observed during this wetting and drying cycle, and the simulation results were reasonably consistent with those of the experiments. The main reason for this deviation is the selection of the n parameter in SWRC as a constant (see phenomenological observation P21 in Chapter 3).

In future research, it will be possible to examine the possible evolution of the *n* parameter with the plastic volumetric strain.

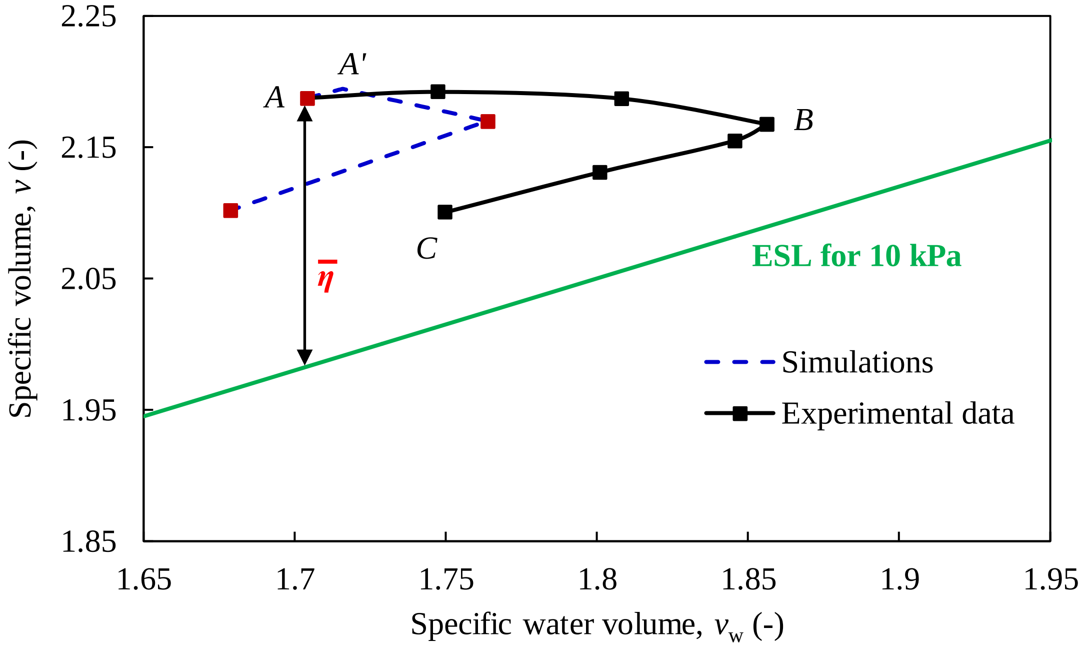

(a)

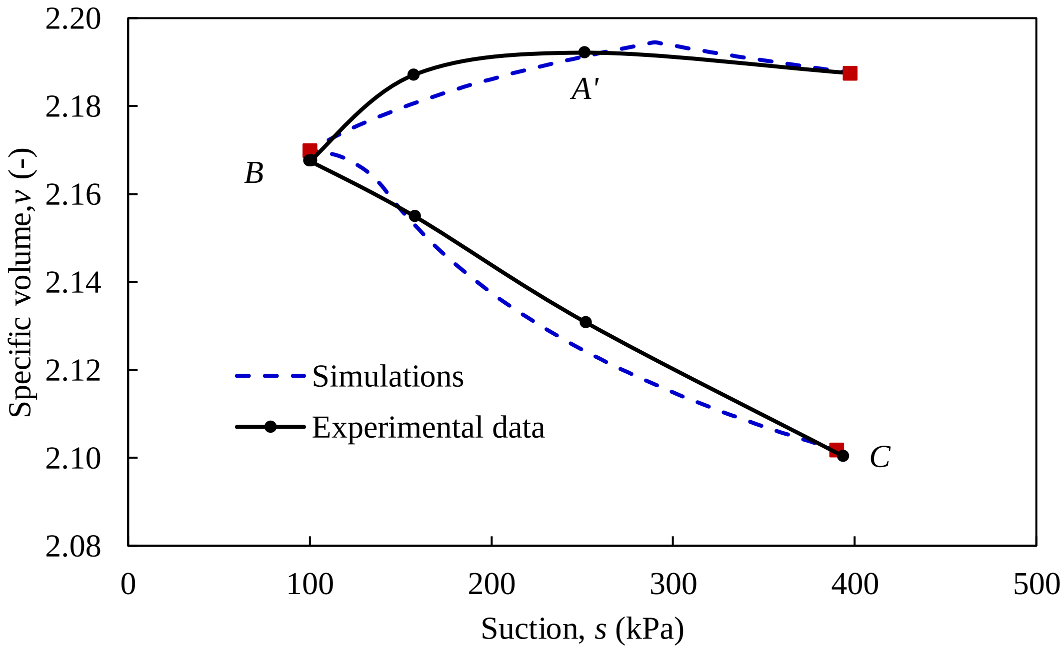

(b)

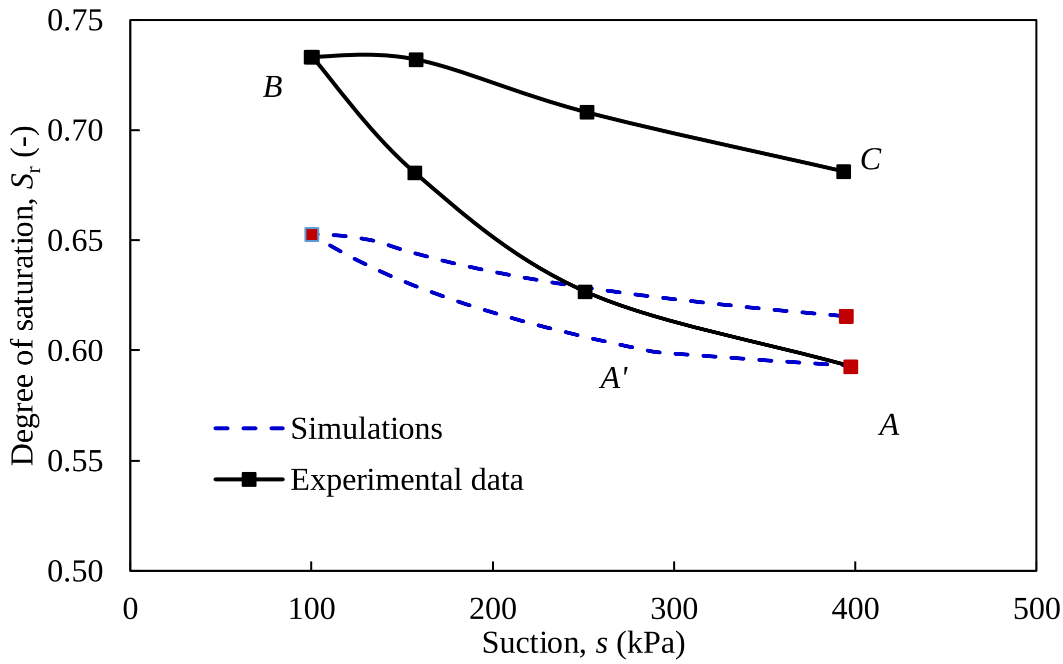

(c)

Figure 6.25: Comparison of simulated and experimental results on: (a) v, v_w plane (b) v, s (c) S_r, s plane

Table 6.9: Experimental validation T2

Stage			Net stress (*p*/kPa)	Suction (*s*/kPa)
A	B	Wetting	50	400→100
B	C	Drying	50	100→400

6.5.3 Test T5: Wetting→ Drying→ Wetting

Figure 6.26 shows a comparison of the computed and experimental results of stress paths comprising wetting/ drying/ wetting, as given in Table 6.10. The initial state of the soil is achieved at p =20 kPa and s = 400 kPa. Furthermore, State A is above the ESL applicable to p =20 kPa, as shown. In this state, $\bar{\eta}$ = 0.1981 > 0. For the first wetting cycle (path AB to s = 100 kPa), α_2 of 0.6 was selected, and the simulated and experimental paths do not exhibit reasonable agreement (refer to phenomenological observations P8 and P17 in Chapter 3). Subsequently, the sample was dried to the suction of 400 kPa (path BC) and α_1 = 0.8 (< α_{ES} =

0.6), $\bar{\eta}$ = 0.247 > 0, showing the path followed in Figure 6.26(a) on the (v, s) plane, Figure 6.26(b) (S_r, s) plane and Figure 6.26(c) on the (v, v_w) plane, respectively. Subsequently, the sample was wetted to the suction of 20 kPa under the net stress of 20 kPa (i.e., stress path *CD*). As shown in Figure 6.26(a) and Figure 6.26(b), the simulations of v and S_r with s are not consistent with the experimental results, primarily due to the selection of the constant n parameter during the shift of SWRC (see phenomenological observation P21 in Chapter 3).

Table 6.10: Experimental validation T5

Stage			Net stress (p/kPa)	Suction (s/kPa)
A	B	Wetting	20	400→100
B	C	Drying	20	100→400
C	D	Wetting	20	400→20

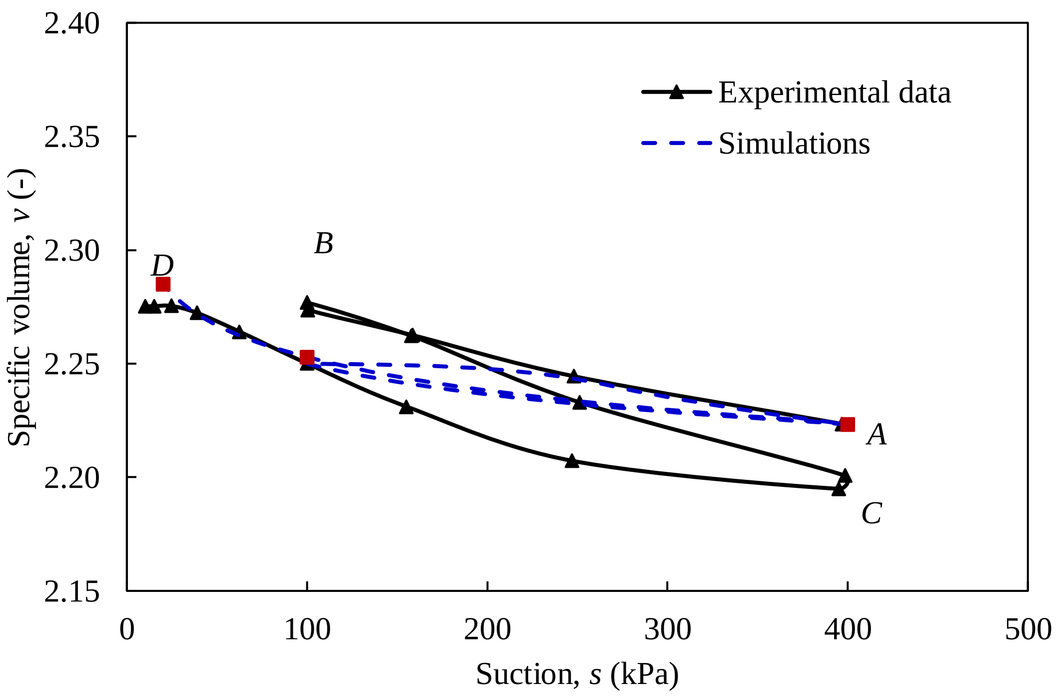

(a)

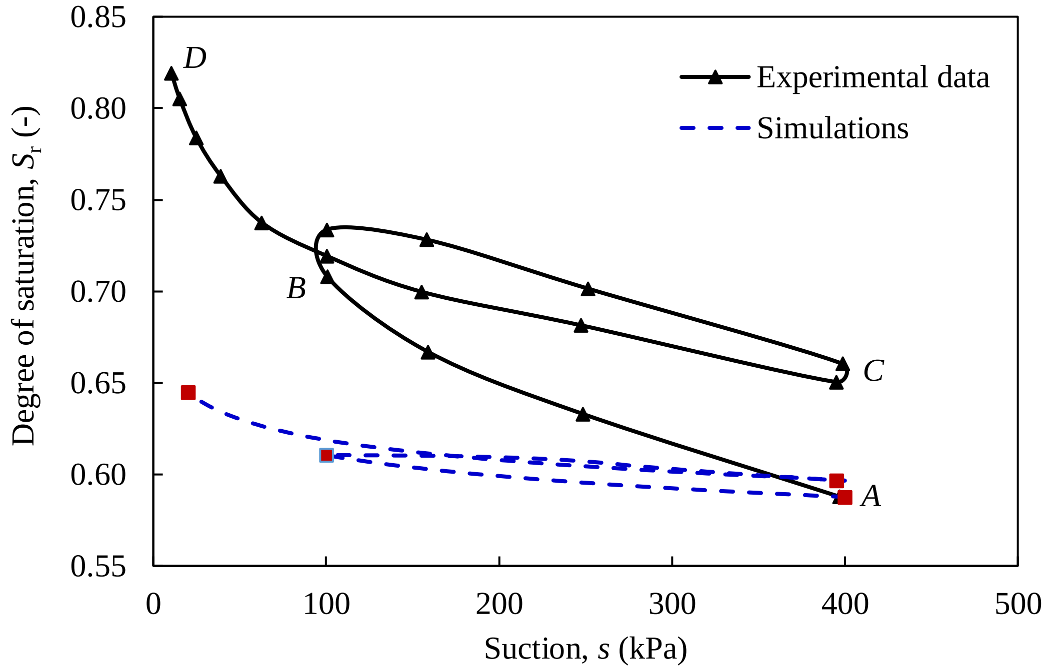

(b)

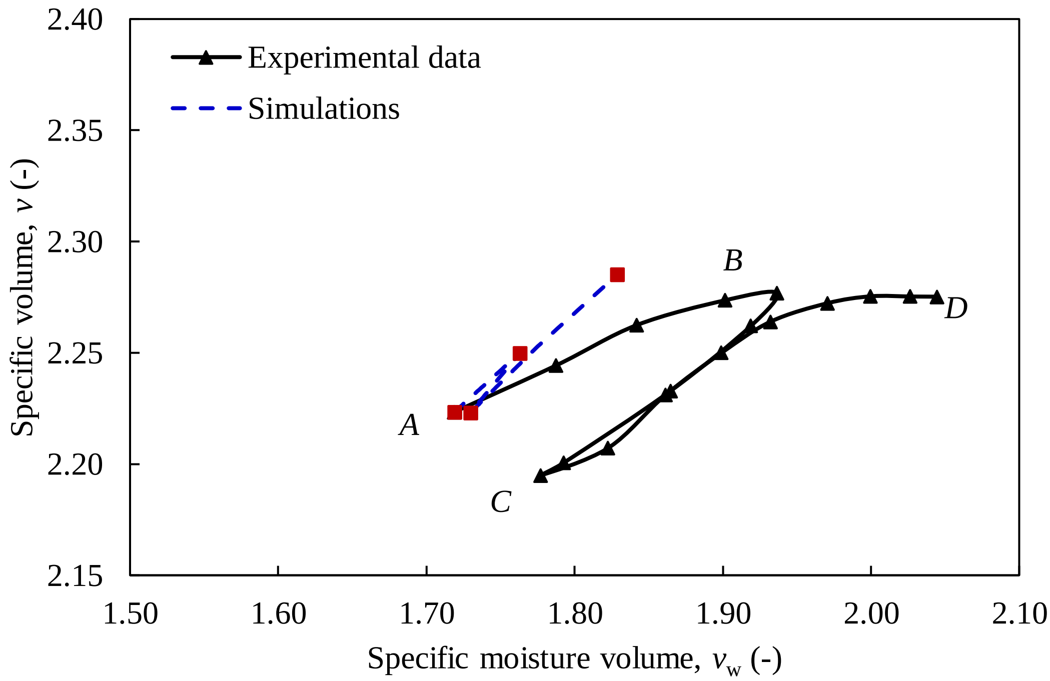

(c)

Figure 6.26: Comparison of simulated and experimental results on: (a) (v, s) plane; (b) (S_r, s) plane; (c) (v, v_w) plane

6.5.4 Test T6: Loading→ Unloading

The sample was equalised to the mean net stress of 10 kPa and suction of 300 kPa (State *A* in Figure 6.27) prior to the loading and unloading stress paths. The sample was loaded to the mean net stress of 90 kPa under the suction of 300 kPa (i.e., stress path *AB*), whereas the model predicted yielding after 70 kPa. The sample was subsequently unloaded to 10 kPa (i.e., stress path *BC*) at the suction of 300 kPa.). As shown in Figure 6.27(a) on the (v, p) plane, Figure 6.27(b) on the (S_r, p) plane, and Figure 6.27(c) on the (v, v_w) plane, the simulations of v, and S_r with p follow the experimental results reasonably well (see phenomenological observation P1 in Chapter 3).

Table 6.11: Experimental validation T6

Stage			Net stress (*p*/kPa)	Suction (*s*/kPa)
A	B	Loading	10→90	300
B	C	Unloading	90→10	300

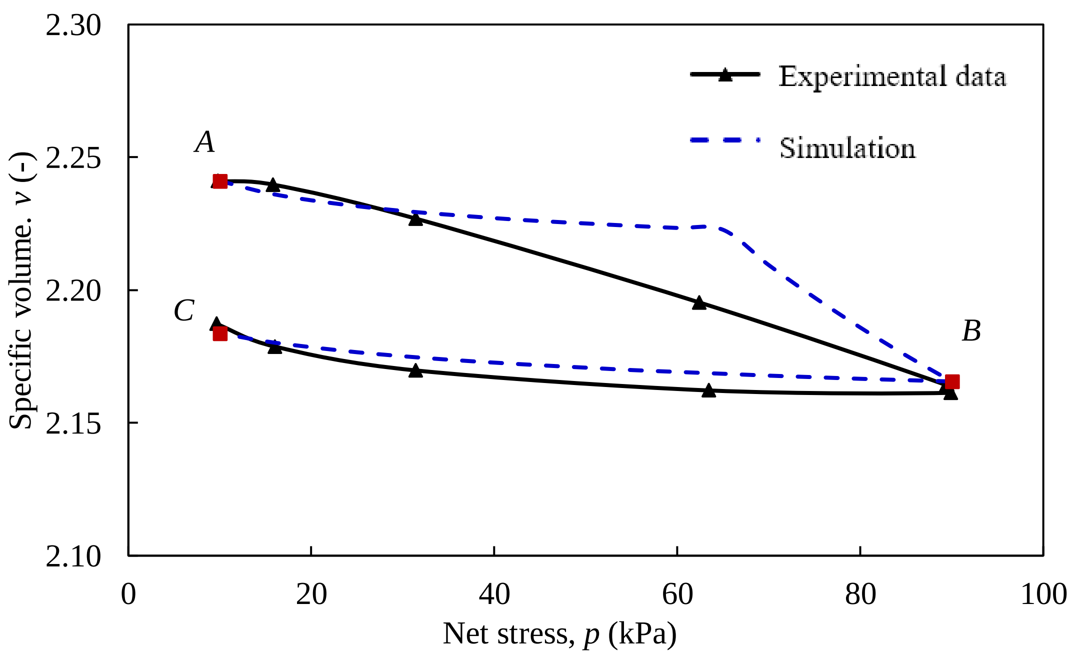

(a)

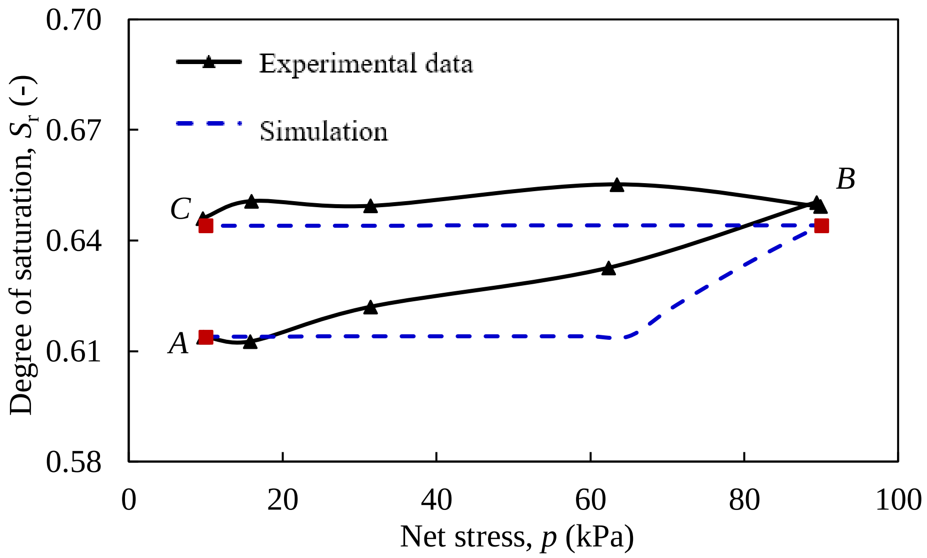

(b)

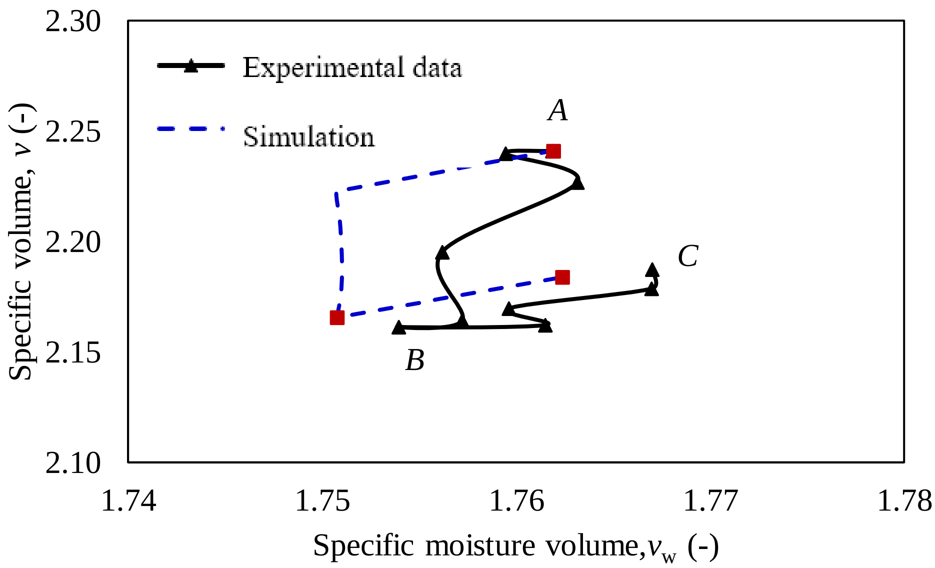

(c)

Figure 6.27: Comparison of simulated and experimental results on: (a) (v, p) plane (b) (S_r, p) plane (c) (v, v_w) plane

6.5.5 Test T7: Loading→ Unloading

This test sample was equalised to the mean net stress of 10 kPa and suction of 300 kPa prior to the loading and unloading cycle, as shown in Figure 6.28 and Table 6.12. The first stress path was loading to 170 kPa (i.e., stress path *AB*), whereas the model predicted yielding after 60 kPa, which agrees reasonably well with the test results. During stress path *BC*, the sample was simultaneously unloaded to the net stress of 10 kPa. Generally, upon unloading the soil moves on the corresponding volumetric elastic plane (VEP) without changing the previously-attained yield stress. Similar to test T6, as shown in Figure 6.28 (a) on the (v, p) plane, Figure 6.28(b) on the (S_r, p) plane, and Figure 6.28(c) on the (v, v_w) plane, the simulations of v, and S_r with p follow the experimental results reasonably well (refer to phenomenological observation P1 in Chapter 3).

Table 6.12: Experimental validation T7

Stage			Net stress (p/kPa)	Suction (s/kPa)
A	B	Loading	10→170	300
B	C	Unloading	170→10	300

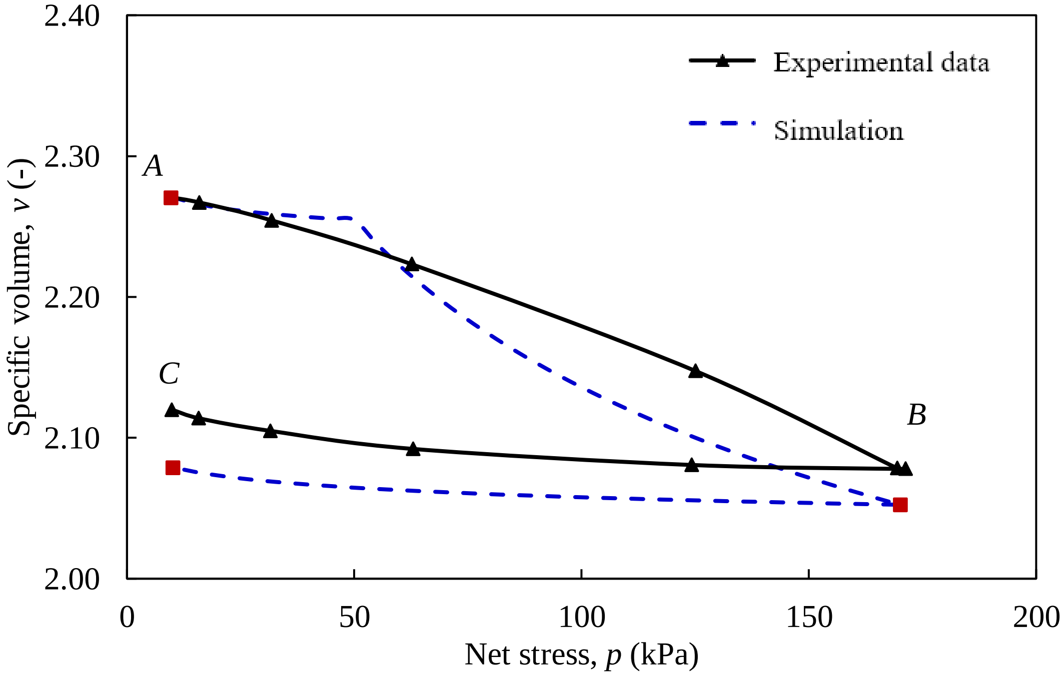

(a)

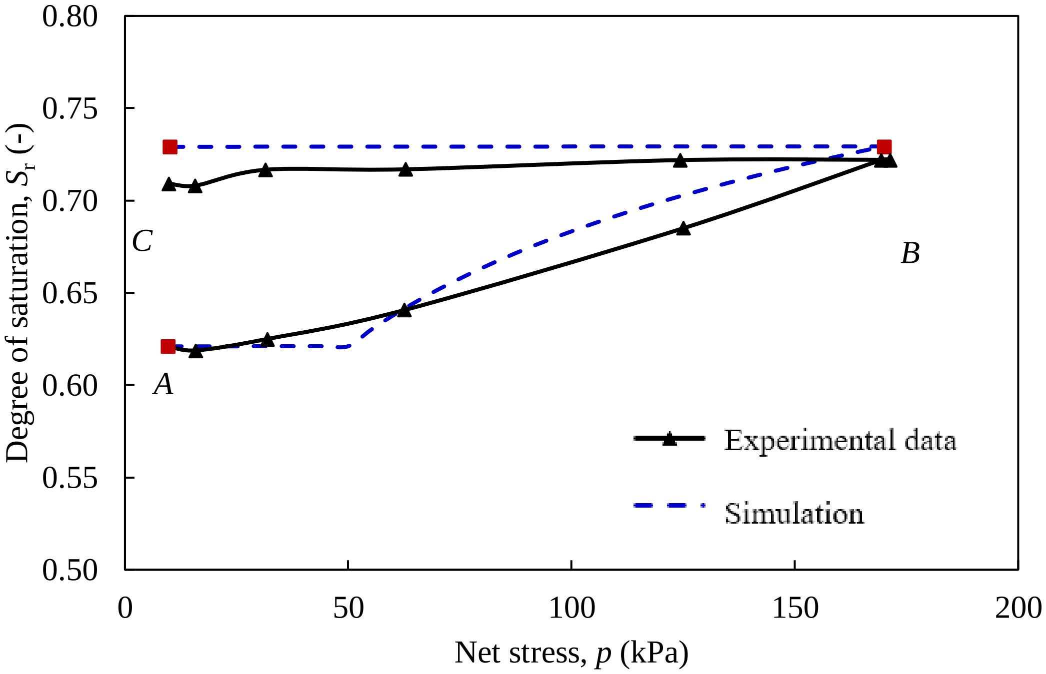

(b)

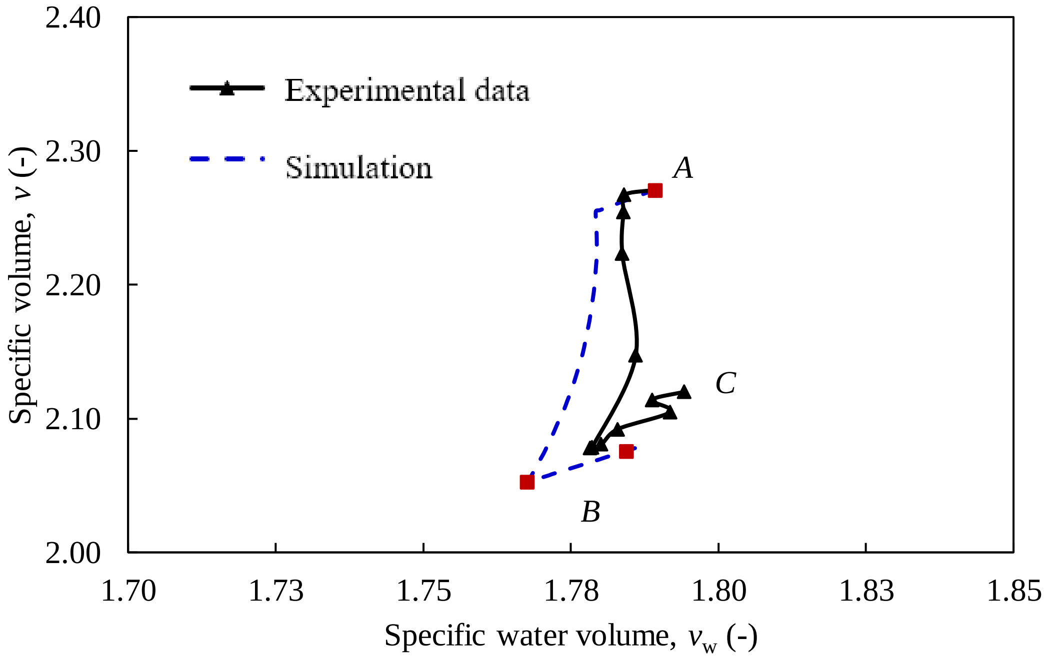

(c)

Figure 6.28: Comparison of simulated and experimental results on: (a) (v, p) plane (b) (S_r, p) plane (c) (v, v_w) plane

6.6 Conclusions

The generalised MPK constitutive model for unsaturated soils was developed in Chapter 4, with the main emphasis on the isotropic stress state. The mechanical behaviour of the model has nine parameters that can be determined through relatively simple testing. The evolution of the plastic-strain-based SWRCs involves 6 parameters, some of which require calibration through traditional SWRC testing under constant net stress. In Chapter 4, the parameter extraction was broadly discussed, and some typical features of the model were explained. The governing equations developed were programmed for the simulation of different stress paths at element level (e.g., loading, unloading, drying, wetting and their combinations). The application of this model to simulate volumetric behaviour with a combination of stress paths has been discussed in this chapter, with some examples from series of experiments on kaolin by Abeyrathne (2017), Raveendiraraj (2009) and an expansive kaolin bentonite mixture by Sharma (1998). First, the derived equations were validated against the test series conducted for the present study, and reasonable agreement was observed in all the 10 tests. Subsequently, the ability of the generalised MPK model to reproduce observed phenomenological behaviour was validated by other experiments.

6.7 References

ABEYRATHNE, A., SIVAKUMAR, V. & KODIKARA, J. 2019. Isotropic Volumetric Behaviour of Compacted Unsaturated Soils within (v, v w, p) Space. *Canadian Geotechnical Journal*.

ABEYRATHNE, W. K. A. P. 2017. *A new modelling approach for compacted clayey soils using specific water volume as a state variable*. Ph.D. thesis, Monash University, Melbourne, Australia.

ALONSO, E., PINYOL, N. & GENS, A. 2013. Compacted soil behaviour: initial state, structure and constitutive modelling. *Géotechnique,* 63**,** 463-478.

LLORET-CABOT, M. & WHEELER, S. J. 2018. The Mechanical Yield Stress in Unsaturated and Saturated Soils. *The 7th International Conference on Unsaturated Soils (UNSAT2018)*. Hong Kong, China.

PASHA, A. Y., KHOSHGHALB, A. & KHALILI, N. 2019. Can degree of saturation decrease during constant suction compression of an unsaturated soil? *Computers and Geotechnics,* 106**,** 199-204.

RAVEENDIRARAJ, A. 2009. *Coupling of mechanical behaviour and water retention behaviour in unsaturated soils.* Ph.D. thesis, University of Glasgow.

SHARMA, R. S. 1998. *Mechanical behaviour of unsaturated highly expansive clays.* Ph.D. thesis, University of Oxford.

CHAPTER 7

Theoretical development and validation of triaxial behaviour

7 Introduction

Catastrophic landslides usually occur due to extreme rainfall events. The maximum resisting force along the failure plane of the soil is controlled by the shear strength, which gradually reduces with an increase in the degree of saturation or decreases in suction (Fredlund et al., 1978; Wheeler and Sivakumar, 1995; Ng et al., 2008; Sheng et al., 2013). As a result, the potential for landslides with high failure consequences increases under anomalous climatic loading events. Therefore, a qualitative and quantitative assessment of the shear strength of unsaturated soils has been identified as essential over the last several decades.

With respect to the incorporation of shear behaviour, the formulation of the existing critical state elastoplastic constitutive models of unsaturated soils can be categorised according to the selection of the above state variables, which are explained by Houlsby (1997), as reported in Section 2.2.3 of Chapter 2. Alonso et al. (1990) (in the Barcelona Basic Model or BBM) and Wheeler and Sivakumar (1995) used the variables specific volume (v), net stress (p), shear stress (q), shear strain (ε_{s}) and suction (s), without directly coupling the specific moisture volume (v_{w}) or degree of saturation (S_{r}) (see working Equation (2.5)). In the model proposed by Abeyrathne et al. (2019), on the basis of the Monash–Peradeniya–Kodikara (MPK) framework (Kodikara, 2012), the researchers used p, q, v, ε_{s}, and v_{w} to describe the triaxial behaviour without incorporating suction directly (see working Equation (2.5)). In contrast, effective stress ($p+\chi s$) has been used (see working Equation (2.6)) without considering S_{r} as a separate variable (e.g., Loret and Khalili, 2002), and χ is proposed as a function of s (Khalili and Khabbaz, 1998). In addition, Bishop's effective stress ($p+S_{\mathrm{r}}s$) has been employed with S_{r} as a separate variable (e.g., Wheeler et al., 2003; Zhou, 2017).

This chapter extends the MPK model developed in Chapter 4 to shear behaviour, following the modified clay model for saturated soils.

7.1 Constitutive relationships in Monash-Peradeniya-Kodikara (MPK) critical state model

The critical state surface of the generalised MPK model is defined in the (p,q,S_{r}) space, where the model accepts the modified cam clay (MCC) model concepts when $S_{\mathrm{r}}=1$, as shown in

Figure 7.1. For simplicity, the critical stress ratio (q/p^*), M, is considered to be a constant, although M may vary with the degree of saturation, suction or water content (Sivakumar, 1993; Abeyrathne, 2017). The loading collapse (LC) yield curve shown below is adopted from the generalised MPK model and converted to the effective stress states.

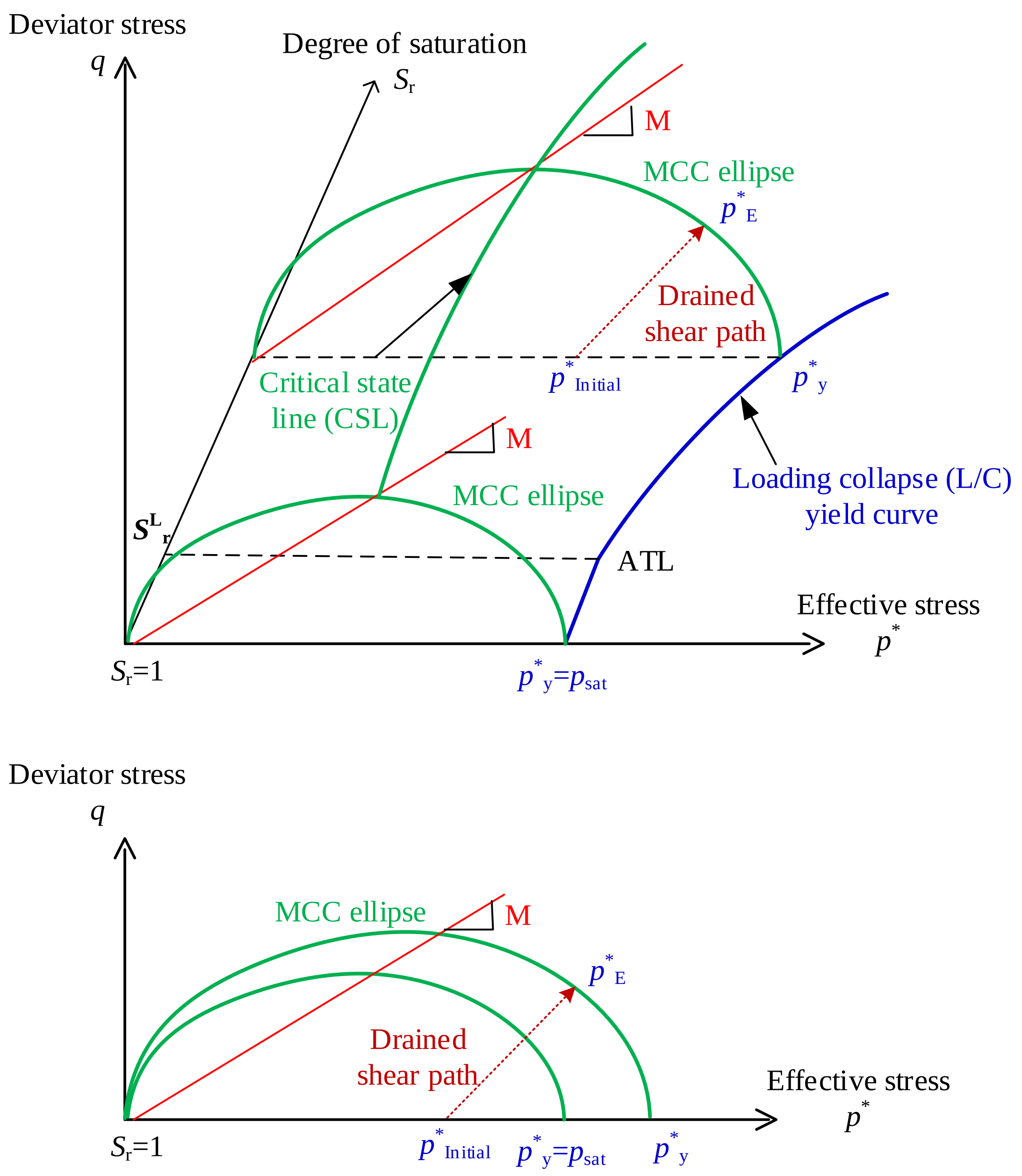

Figure 7.1: Yield surface for triaxial stress state

7.2 Formulation of MPK critical state model in triaxial stress space

Formulation of the generalised critical state model follows the following steps:

1. Yield condition, $f(p,q) \leq 0$

The final equations of the generalised MPK model for isotropic behaviour are based on the $p^{*}\mathrm{d}\varepsilon_{\mathrm{v}}$ and $s^{*}\mathrm{d}S_{\mathrm{r}}$ work conjugates enabling the easy capture of the triaxial response. Hence, similar to the MCC model, the yield function of the triaxial response is assumed as follows:

$$f = q^2 - M^2 p^{*}(p^{*}{}_{\mathrm{y}} - p^{*}) \equiv 0 \tag{7.1}$$

here, q is the deviator stress, p^{*} is the Bishop's effective stress, $p^{*}{}_{\mathrm{y}}$ is the intersection point between the MCC ellipse and the p^{*} axis and the M parameter denotes the slope of the critical state line on the (q,p^{*}) plane.

2. Elastic stress-strain relationship

In the generalised MPK model, the change in total strain ($\mathrm{d}\varepsilon$) is considered as the change in volumetric strain ($\mathrm{d}\varepsilon_{\mathrm{v}}$, + in compression) and the change in shear strain ($\mathrm{d}\varepsilon_{\mathrm{s}}$), which are further divided into their respective elastic and plastic strains. Therefore, the total volumetric strain can be written as the sum of the elastic volumetric strain ($\mathrm{d}\varepsilon_{\mathrm{v}}^{\mathrm{e}}$) and plastic volumetric strain ($\mathrm{d}\varepsilon_{\mathrm{v}}^{\mathrm{p}}$), as given in Equation (7.2). Similarly, the total shear strain ($\mathrm{d}\varepsilon_{\mathrm{s}}$) can be written as the sum of the elastic shear strain ($\mathrm{d}\varepsilon_{\mathrm{s}}^{\mathrm{e}}$) and plastic shear strain ($\mathrm{d}\varepsilon_{\mathrm{s}}^{\mathrm{p}}$), as given in Equation (7.3).

$$\mathrm{d}\varepsilon_{\mathrm{v}} = \mathrm{d}\varepsilon_{\mathrm{v}}^{\mathrm{e}} + \mathrm{d}\varepsilon_{\mathrm{v}}^{\mathrm{p}} \tag{7.2}$$

$$\mathrm{d}\varepsilon_{\mathrm{s}} = \mathrm{d}\varepsilon_{\mathrm{s}}^{\mathrm{e}} + \mathrm{d}\varepsilon_{\mathrm{s}}^{\mathrm{p}} \tag{7.3}$$

In Section 4.3.2 the elastic volumetric strain $\mathrm{d}\varepsilon_{\mathrm{v}}^{\mathrm{p}}$ was derived as follows:

$$\mathrm{d}\varepsilon_{\mathrm{v}}^{\mathrm{e}} = \frac{-\mathrm{d}v^{\mathrm{e}}}{v} = k(S_{\mathrm{r}})\frac{\mathrm{d}p}{vp} \tag{7.4}$$

where, the constant $k(S_{\mathrm{r}})\left(= \frac{k(v_{\mathrm{w}})}{1\text{-}S_{\mathrm{r}}\alpha_{\mathrm{ES}}}\right)$ is explicitly derived from material parameters (see Chapter 4 for the full derivation). The elastic shear strain $\mathrm{d}\varepsilon_{\mathrm{s}}^{\mathrm{e}}$ is given as:

$$\mathrm{d}\varepsilon_{\mathrm{s}}^{\mathrm{e}} = \frac{\mathrm{d}q}{3G} \tag{7.5}$$

where, the elastic shear modulus G is considered to be a constant.

3. Hardening rules and flow rule

As explained in Section 4.3.3.3, the hardening law of the proposed model is as follows:

$$\mathrm{d}\varepsilon_{\mathrm{v}}^{\mathrm{p}} = \left(\frac{\lambda_{\mathrm{sat}} - k_{\mathrm{sat}}}{v_{\mathrm{sat}}}\right)\frac{\mathrm{d}p_{\mathrm{sat}}}{p_{\mathrm{sat}}} \tag{7.6}$$

where, $\mathrm{d}\varepsilon_{\mathrm{v}}^{\mathrm{p}}$ is the change in plastic volumetric strain, v_{sat} is the specific volume at saturation for a particular net stress p_{sat} and λ_{sat} and k_{sat} are the saturation compressibility of the soil during yielding and elastic behaviour, respectively.

For simplicity, the associated flow rule is adopted for the current model, where the plastic potential function is assumed to be equal to the yield function. Therefore, with reference to Equation (7.1), flow rules were developed considering a single plastic multiplier (λ) for the plastic volumetric strain ($\mathrm{d}\varepsilon_{\mathrm{v}}^{\mathrm{p}}$) and plastic shearing strain ($\mathrm{d}\varepsilon_{\mathrm{q}}^{\mathrm{p}}$) as:

$$\mathrm{d}\varepsilon_{\mathrm{v}}^{\mathrm{p}} = \lambda \frac{\partial f}{\partial p^{*}} \tag{7.7}$$

$$\mathrm{d}\varepsilon_{\mathrm{s}}^{\mathrm{p}} = \lambda \frac{\partial f}{\partial q} \tag{7.8}$$

4. Kuhn-Trucker conditions

The Kuhn-Trucker conditions of the generalised MPK model include the loading/unloading criterion, where $\dot{\lambda} \geq 0$, $f(\sigma, q) \leq 0$ and $\dot{\lambda} . f(\sigma, q) = 0$.

5. Consistency condition $\dot{\lambda} . f(\sigma, q) = 0$

The consistency equation is depicted in Equation (7.9) considering four different independent variables, the Bishop's effective stress (p^{*}), the shear stress (q), the net stress at saturation (p_{sat}) and the degree of saturation (S_{r}).

$$\frac{\partial f}{\partial p^{*}}\mathrm{d}p^{*} + \frac{\partial f}{\partial q}\mathrm{d}q + \frac{\partial f}{\partial p_{\mathrm{sat}}}\mathrm{d}p_{\mathrm{sat}} + \frac{\partial f}{\partial S_{\mathrm{r}}}\mathrm{d}S_{\mathrm{r}} = 0 \tag{7.9}$$

The hydro-mechanical coupled behaviour of the proposed MPK model is given by

$$\mathrm{d}S_{\mathrm{r}} = C\mathrm{d}s^{*} + DH\mathrm{d}\varepsilon_{\mathrm{v}}^{\mathrm{p}} \tag{7.10}$$

where, C and D are two general functions (see Chapter 4) which can be represented using the hydraulic parameters (a_{w}, s^{*}) and the material parameters (m, n). In addition, H is another general function which has been defined in Section 7.2.1.

From Equations (7.6), (7.9) and (7.10), the change in volumetric plastic strain can be written as:

$$\frac{\partial f}{\partial p^{*}}\mathrm{d}p^{*} + \frac{\partial f}{\partial q}\mathrm{d}q + \frac{\partial f}{\partial p_{\mathrm{sat}}}\frac{v_{\mathrm{sat}}p_{\mathrm{sat}}}{\lambda_{\mathrm{sat}} - k_{\mathrm{sat}}}\mathrm{d}\varepsilon_{\mathrm{v}}^{\mathrm{p}} + \frac{\partial f}{\partial S_{\mathrm{r}}}\left(C\mathrm{d}s^{*} + DH\mathrm{d}\varepsilon_{\mathrm{v}}^{\mathrm{p}}\right) = 0 \tag{7.11}$$

$$\mathrm{d}\varepsilon_{\mathrm{v}}^{\mathrm{p}} = \frac{-\left(\dfrac{\partial f}{\partial p^{*}}\mathrm{d}p^{*} + \dfrac{\partial f}{\partial q}\mathrm{d}q + C\dfrac{\partial f}{\partial S_{\mathrm{r}}}\mathrm{d}s^{*}\right)}{\dfrac{\partial f}{\partial p_{\mathrm{sat}}}\left(\dfrac{v_{\mathrm{sat}}p_{\mathrm{sat}}}{\lambda_{\mathrm{sat}} - k_{\mathrm{sat}}}\right) + DH\dfrac{\partial f}{\partial S_{\mathrm{r}}}} \tag{7.12}$$

$$\mathrm{d}\varepsilon_{\mathrm{v}}^{\mathrm{p}} = -\left(\frac{1}{T}\right)\frac{\partial f}{\partial p^{*}}\mathrm{d}p^{*} - \left(\frac{1}{T}\right)\frac{\partial f}{\partial q}\mathrm{d}q - \left(\frac{C}{T}\right)\frac{\partial f}{\partial S_{\mathrm{r}}}\mathrm{d}s^{*} \tag{7.13}$$

where, $T = \dfrac{\partial f}{\partial p_{\mathrm{sat}}}\left(\dfrac{v_{\mathrm{sat}}p_{\mathrm{sat}}}{\lambda_{\mathrm{sat}} - k_{\mathrm{sat}}}\right) + DH\dfrac{\partial f}{\partial S_{\mathrm{r}}}$.

Hence, from Equation (7.10), $\mathrm{d}S_{\mathrm{r}}$ can be written as:

$$\mathrm{d}S_{\mathrm{r}} = -\left(\frac{DH}{T}\right)\frac{\partial f}{\partial p^{*}}\mathrm{d}p^{*} + \left\{C - \left(\frac{DHC}{T}\right)\frac{\partial f}{\partial S_{\mathrm{r}}}\right\}\mathrm{d}s^{*} - \left(\frac{DH}{T}\right)\frac{\partial f}{\partial q}\mathrm{d}q \tag{7.14}$$

Assuming that the associated flow rule is similar to the MCC model, $\mathrm{d}\varepsilon_{\mathrm{q}}^{\mathrm{p}}$ can be written as:

$$\mathrm{d}\varepsilon_{\mathrm{s}}^{\mathrm{p}} = \frac{2p^{*}q}{\left(M^{2}p^{*2} - q^{2}\right)}\left\{-\left(\frac{1}{T}\right)\frac{\partial f}{\partial p^{*}}\mathrm{d}p^{*} - \left(\frac{1}{T}\right)\frac{\partial f}{\partial q}\mathrm{d}q - \left(\frac{C}{T}\right)\frac{\partial f}{\partial S_{\mathrm{r}}}\mathrm{d}s^{*}\right\} \tag{7.15}$$

The change in elastic volumetric strain ($\mathrm{d}\varepsilon_{\mathrm{v}}^{\mathrm{e}}$) in Equation (7.4) is written in terms of the change in net stress ($\mathrm{d}p$) and the degree of change in saturation ($\mathrm{d}S_{\mathrm{r}}$). Equation (7.4) is required to change Bishop's effective stress (p^{*}) and modified suction (s^{*}) to capture the triaxial stress behaviour. The changes in Bishop's effective stress ($\mathrm{d}p^{*}$) and in modified suction ($\mathrm{d}s^{*}$) can be written as:

$$\mathrm{d}p^* = \mathrm{d}p + S_\mathrm{r}\mathrm{d}s + s\mathrm{d}S_\mathrm{r} \tag{7.16}$$

$$\mathrm{d}s^* = n\mathrm{d}s - \frac{s}{v}\mathrm{d}\varepsilon_\mathrm{v}^\mathrm{e} \tag{7.17}$$

where, n is the porosity of the soil. In addition, from Equation (7.10) the change in the degree of saturation ($\mathrm{d}S_\mathrm{r}$) upon elastic behaviour can be written as:

$$\mathrm{d}S_\mathrm{r} = C\mathrm{d}s^* \tag{7.18}$$

From Equations (7.16), (7.17), and (7.18) the change in elastic volumetric strain ($\mathrm{d}\varepsilon_\mathrm{v}^\mathrm{e}$) can be rewritten as:

$$\mathrm{d}s = \frac{1}{n}\left(\mathrm{d}s^* + \frac{s}{v}\mathrm{d}\varepsilon_\mathrm{v}^\mathrm{e}\right) \tag{7.19}$$

$$\mathrm{d}\varepsilon_\mathrm{v}^\mathrm{e} = \frac{-\mathrm{d}v^\mathrm{e}}{v} = k(S_\mathrm{r})\frac{\mathrm{d}p}{vp}$$

$$\mathrm{d}\varepsilon_\mathrm{v}^\mathrm{e} = \frac{-\mathrm{d}v^\mathrm{e}}{v} = k(S_\mathrm{r})\frac{\left(\mathrm{d}p^* - S_\mathrm{r}\mathrm{d}s - s\mathrm{d}S_\mathrm{r}\right)}{vp}$$

$$\mathrm{d}\varepsilon_\mathrm{v}^\mathrm{e} = \frac{-\mathrm{d}v^\mathrm{e}}{v} = k(S_\mathrm{r})\frac{\left(\mathrm{d}p^* - \frac{S_\mathrm{r}}{n}\left(\mathrm{d}s^* + \frac{s}{v}\mathrm{d}\varepsilon_\mathrm{v}^\mathrm{e}\right) - sC\mathrm{d}s^*\right)}{vp}$$

$$\mathrm{d}\varepsilon_\mathrm{v}^\mathrm{e} = \frac{\frac{k(S_\mathrm{r})}{vp}\mathrm{d}p^* - \left(k(S_\mathrm{r})\frac{\left(\frac{S_\mathrm{r}}{n} + sC\right)}{vp}\right)\mathrm{d}s^*}{\left(1 + k(S_\mathrm{r})\frac{sS_\mathrm{r}}{nv^2 p}\right)}$$

Therefore, the volumetric strain can be written as the sum of the elastic volumetric strain ($\mathrm{d}\varepsilon_\mathrm{v}^\mathrm{e}$) and plastic volumetric strain ($\mathrm{d}\varepsilon_\mathrm{v}^\mathrm{p}$), as given in Equation (7.20):

$$\mathrm{d}\varepsilon_{\mathrm{v}} = \left(\frac{k(S_{\mathrm{r}})}{vp\left(1 + k(S_{\mathrm{r}})\dfrac{sS_{\mathrm{r}}}{nv^2 p}\right)} - \left(\frac{1}{T}\right)\frac{\partial f}{\partial p^*} \right)\mathrm{d}p^* - \left(\frac{1}{T}\right)\frac{\partial f}{\partial q}\mathrm{d}q$$
$$+ \left\{ \frac{\left(-k(S_{\mathrm{r}})\dfrac{\left(\dfrac{S_{\mathrm{r}}}{n} + sC\right)}{vp} \right)}{\left(1 + k(S_{\mathrm{r}})\dfrac{sS_{\mathrm{r}}}{nv^2 p}\right)} - \left(\frac{C}{T}\right)\frac{\partial f}{\partial S_{\mathrm{r}}} \right\}\mathrm{d}s^* \tag{7.20}$$

Therefore, the change in total shear strain ($\mathrm{d}\varepsilon_{\mathrm{s}}$) can be written as the sum of the elastic shear strain ($\mathrm{d}\varepsilon_{\mathrm{s}}^{\mathrm{e}}$) (from Equation (7.5)) and plastic shear strain ($\mathrm{d}\varepsilon_{\mathrm{s}}^{\mathrm{p}}$) as given in Equation (7.15)):

$$\mathrm{d}\varepsilon_{\mathrm{s}} = \frac{2p^* q}{\left(M^2 p^{*2} - q^2\right)}\left\{ -\left(\frac{1}{T}\right)\frac{\partial f}{\partial p^*}\mathrm{d}p^* + \left\{\left(\frac{1}{3G}\right) - \left(\frac{1}{T}\right)\frac{\partial f}{\partial q}\right\}\mathrm{d}q - \left(\frac{C}{T}\right)\frac{\partial f}{\partial S_{\mathrm{r}}}\mathrm{d}s^* \right\} \tag{7.21}$$

Therefore, the variation of $\begin{Bmatrix} \mathrm{d}\varepsilon_{\mathrm{v}} \\ \mathrm{d}S_{\mathrm{r}} \\ \mathrm{d}\varepsilon_{\mathrm{q}} \end{Bmatrix}$ with $\begin{Bmatrix} \mathrm{d}p^* \\ \mathrm{d}s^* \\ \mathrm{d}q \end{Bmatrix}$ can be written as:

$$\begin{Bmatrix} \mathrm{d}\varepsilon_{\mathrm{v}} \\ \mathrm{d}S_{\mathrm{r}} \\ \mathrm{d}\varepsilon_{\mathrm{q}} \end{Bmatrix} = \begin{bmatrix} \left\{ \left(\dfrac{k(S_{\mathrm{r}})}{vp\left(1 + k(S_{\mathrm{r}})\dfrac{sS_{\mathrm{r}}}{nv^2 p}\right)} \right) - \left(\dfrac{1}{T}\right)\dfrac{\partial f}{\partial p^*} \right\} & \left(\left\{ \dfrac{\left(-k(S_{\mathrm{r}})\dfrac{\left(\dfrac{S_{\mathrm{r}}}{n} + sC\right)}{vp} \right)}{\left(1 + k(S_{\mathrm{r}})\dfrac{sS_{\mathrm{r}}}{nv^2 p}\right)} - \left(\dfrac{C}{T}\right)\dfrac{\partial f}{\partial S_{\mathrm{r}}} \right\} \right) & -\left(\dfrac{1}{T}\right)\dfrac{\partial f}{\partial q} \\ -\left(\dfrac{DH}{T}\right)\dfrac{\partial f}{\partial p^*} & \left\{ C - \left(\dfrac{DHC}{T}\right)\dfrac{\partial f}{\partial S_{\mathrm{r}}} \right\} & -\left(\dfrac{DH}{T}\right)\dfrac{\partial f}{\partial q} \\ -\left(\dfrac{1}{T}\right)\dfrac{\partial f}{\partial p^*}\dfrac{2p^* q}{\left(M^2 p^{*2} - q^2\right)} & -\left(\dfrac{C}{T}\right)\dfrac{\partial f}{\partial S_{\mathrm{r}}}\dfrac{2p^* q}{\left(M^2 p^{*2} - q^2\right)} & -\left(\dfrac{2p^* q}{\left(M^2 p^{*2} - q^2\right)}\left(\dfrac{1}{T}\right)\dfrac{\partial f}{\partial q} - \dfrac{1}{3G} \right) \end{bmatrix} \begin{Bmatrix} \mathrm{d}p^* \\ \mathrm{d}s^* \\ \mathrm{d}q \end{Bmatrix} \tag{7.22}$$

7.2.1 Derivation of $H = \left(\dfrac{\partial a_{\mathrm{w}}}{\partial \varepsilon_{\mathrm{v}}^{\mathrm{p}}}\right)$

The air entry value (a_{w}) was derived in Chapter 4 as:

$$a_{\mathrm{w}} = \left(\frac{v_{\mathrm{sat}}-1}{v_{\mathrm{sat}}}\right)\frac{p_{\mathrm{o}}}{S_{\mathrm{r}}^{\mathrm{L}}}\left[e^{\left(\frac{N_{\mathrm{sat}}-v_{\mathrm{sat}}}{\lambda_{\mathrm{sat}}}\right)} - e^{\left(\frac{v_{\mathrm{o}}^{\mathrm{L}}-v_{\mathrm{sat}}}{\lambda_{\mathrm{L}}}\right)}\right] \tag{7.23}$$

where, $v_{\mathrm{o}}^{\mathrm{L}}$ is the specific volume for the reference stress p_{o} on the LC yield stress surface for the ATL degree of saturation $S_{\mathrm{r}}^{\mathrm{L}}$, and λ_{L} is the stiffness parameter at the ATL for yielding behaviour, which is lower than λ_{sat} (the stiffness parameter at saturation). The partial derivative, $\frac{da_{\mathrm{w}}}{dv_{\mathrm{sat}}}$ can therefore be derived as:

$$\frac{da_{\mathrm{w}}}{dv_{\mathrm{sat}}} = \frac{p_{\mathrm{o}}}{S_{\mathrm{r}}^{\mathrm{L}}}\left(\frac{1}{v_{\mathrm{sat}}}\right)^2\left[e^{\left(\frac{N_{\mathrm{sat}}-v_{\mathrm{sat}}}{\lambda_{\mathrm{sat}}}\right)} - e^{\left(\frac{v_{\mathrm{o}}^{\mathrm{L}}-v_{\mathrm{sat}}}{\lambda_{\mathrm{L}}}\right)}\right] - \frac{p_{\mathrm{o}}}{S_{\mathrm{r}}^{\mathrm{L}}}\left(\frac{v_{\mathrm{sat}}-1}{v_{\mathrm{sat}}}\right)\left[\frac{1}{\lambda_{\mathrm{sat}}}e^{\left(\frac{N_{\mathrm{sat}}-v_{\mathrm{sat}}}{\lambda_{\mathrm{sat}}}\right)} - \frac{1}{\lambda_{\mathrm{L}}}e^{\left(\frac{v_{\mathrm{o}}^{\mathrm{L}}-v_{\mathrm{sat}}}{\lambda_{\mathrm{L}}}\right)}\right] \tag{7.24}$$

The change in specific volume along the saturation NCL can be written as:

$$\mathrm{d}v_{\mathrm{sat}} = -\lambda_{\mathrm{sat}}\frac{\mathrm{d}p_{\mathrm{sat}}}{p_{\mathrm{sat}}} \tag{7.25}$$

From Equations (7.6) and (7.25), $\frac{\mathrm{d}v_{\mathrm{sat}}}{\mathrm{d}\varepsilon_{\mathrm{v}}^{\mathrm{p}}}$ can be written as:

$$\frac{\mathrm{d}v_{\mathrm{sat}}}{\mathrm{d}\varepsilon_{\mathrm{v}}^{\mathrm{p}}} = -\frac{\lambda_{\mathrm{sat}}v_{\mathrm{sat}}}{\lambda_{\mathrm{sat}}-k_{\mathrm{sat}}} \tag{7.26}$$

Therefore, from the chain rule, $\frac{\mathrm{d}a_{\mathrm{w}}}{\mathrm{d}\varepsilon_{\mathrm{v}}^{\mathrm{p}}}\left(=\frac{\mathrm{d}a_{\mathrm{w}}}{\mathrm{d}v_{\mathrm{sat}}}\times\frac{\mathrm{d}v_{\mathrm{sat}}}{\mathrm{d}\varepsilon_{\mathrm{v}}^{\mathrm{p}}}\right)$ can be written as:

$$H = \frac{\mathrm{d}a_{\mathrm{w}}}{\mathrm{d}\varepsilon_{\mathrm{v}}^{\mathrm{p}}} = \frac{p_{\mathrm{o}}\lambda_{\mathrm{sat}}v_{\mathrm{sat}}}{S_{\mathrm{r}}^{\mathrm{L}}\left(\lambda_{\mathrm{sat}}-k_{\mathrm{sat}}\right)}\left\{\frac{p_{\mathrm{o}}}{S_{\mathrm{r}}^{\mathrm{L}}}\left(\frac{1}{v_{\mathrm{sat}}}\right)^2\left[e^{\left(\frac{N_{\mathrm{sat}}-v_{\mathrm{sat}}}{\lambda_{\mathrm{sat}}}\right)} - e^{\left(\frac{v_{\mathrm{o}}^{\mathrm{L}}-v_{\mathrm{sat}}}{\lambda_{\mathrm{L}}}\right)}\right] - \frac{p_{\mathrm{o}}}{S_{\mathrm{r}}^{\mathrm{L}}}\left(\frac{v_{\mathrm{sat}}-1}{v_{\mathrm{sat}}}\right)\left[\frac{1}{\lambda_{\mathrm{sat}}}e^{\left(\frac{N_{\mathrm{sat}}-v_{\mathrm{sat}}}{\lambda_{\mathrm{sat}}}\right)} - \frac{1}{\lambda_{\mathrm{L}}}e^{\left(\frac{v_{\mathrm{o}}^{\mathrm{L}}-v_{\mathrm{sat}}}{\lambda_{\mathrm{L}}}\right)}\right]\right\} \tag{7.27}$$

7.2.2 Derivation of partial derivatives

Equation (7.22) includes the partial derivatives of $\frac{\partial f}{\partial p^*}$, $\frac{\partial f}{\partial q}$, and, $\frac{\partial f}{\partial S_{\mathrm{r}}}$ and the general function T requires the $\frac{\partial f}{\partial p_{\mathrm{sat}}}$ derivative. Differentiating the yield function in Equation (7.1), the partial derivatives $\frac{\partial f}{\partial p^*}$ and $\frac{\partial f}{\partial q}$ can be found directly, as given below:

$$\frac{\partial f}{\partial p^*} = \frac{M^2 p^{*2} - q^2}{p^*} \tag{7.28}$$

$$\frac{\partial f}{\partial q} = 2q \tag{7.29}$$

From the chain rule, the other two derivatives can be written as:

$$\frac{\partial f}{\partial S_\mathrm{r}} = \frac{\partial f}{\partial p^*{}_\mathrm{y}} \frac{\partial p^*{}_\mathrm{y}}{\partial S_\mathrm{r}} \tag{7.30}$$

$$\frac{\partial f}{\partial p_\mathrm{sat}} = \frac{\partial f}{\partial p^*{}_\mathrm{y}} \frac{\partial p^*{}_\mathrm{y}}{\partial p_\mathrm{sat}} \tag{7.31}$$

The $\dfrac{\partial f}{\partial p^*{}_\mathrm{y}}$ can be found by differentiating the yield function in Equation (7.1) as:

$$\frac{\partial f}{\partial p^*{}_\mathrm{y}} = -M^2 p^* \tag{7.32}$$

7.2.2.1 Partial derivative, $\dfrac{\partial p^*{}_\mathrm{y}}{\partial S_\mathrm{r}}$

Since $p^*{}_\mathrm{y} = p_\mathrm{y} + S_\mathrm{r} s$ the $\dfrac{\partial p^*{}_\mathrm{y}}{\partial S_\mathrm{r}}$ can be found by differentiation with respect to the degree of saturation (S_r) as:

$$\frac{\partial p^*{}_\mathrm{y}}{\partial S_\mathrm{r}} = \frac{\partial p^*{}_\mathrm{y}}{\partial p_\mathrm{y}} \frac{\partial p_\mathrm{y}}{\partial S_\mathrm{r}} + \frac{\partial p^*{}_\mathrm{y}}{\partial s} \frac{\partial s}{\partial S_\mathrm{r}} \tag{7.33}$$

$$p^*{}_\mathrm{y} = p_\mathrm{y} + S_\mathrm{r} s$$

$$\frac{\partial p^*{}_\mathrm{y}}{\partial s} = S_\mathrm{r}$$

$$\frac{\partial p^*{}_\mathrm{y}}{\partial S_\mathrm{r}} = \frac{\partial p_\mathrm{y}}{\partial S_\mathrm{r}} + S_\mathrm{r} \frac{\partial s}{\partial S_\mathrm{r}}$$

7.2.2.1.1 Partial derivative, $\dfrac{\partial p_\mathrm{y}}{\partial S_\mathrm{r}}$

As derived in Section 4.3.3 of Chapter 4, the function of the LC curve for the proposed model is:

$$p_{\mathrm{y}} = p_{\mathrm{o}} e^{\left(\frac{v_{\mathrm{o}} - v_{\mathrm{o,UL}}}{\lambda(S_{\mathrm{r}}) - k(S_{\mathrm{r}})}\right)} \tag{7.34}$$

where, $\lambda(S_{\mathrm{r}})$, $k(S_{\mathrm{r}})$, v_{o} and $v_{\mathrm{o,UL}}$ are material parameters and degree of saturation (S_{r}) described in Section 4.3.3 of Chapter 4. Therefore, Equation (7.34) can be re-written as:

$$p_{\mathrm{y}} = p_{\mathrm{o}} e^{\left(\frac{v_{\mathrm{G}} - v_{\mathrm{E}}}{\lambda(S_{\mathrm{r}}) - k(S_{\mathrm{r}})}\right)} = p_{\mathrm{o}} e^{\left(\frac{\left[v_{\mathrm{o}}^{\mathrm{L}} - k_4(S_{\mathrm{r}} - S_{\mathrm{r}}^{\mathrm{L}})\right] - \frac{v_{\mathrm{C}}(1 - \alpha_{\mathrm{ES}} S_{\mathrm{r}}^{\mathrm{L}}) - \alpha_{\mathrm{ES}}(S_{\mathrm{r}} - S_{\mathrm{r}}^{\mathrm{L}})}{(1 - \alpha_{\mathrm{ES}} S_{\mathrm{r}})}}{\lambda(S_{\mathrm{r}}) - k(S_{\mathrm{r}})}\right)} \tag{7.35}$$

By differentiating Equation (7.35) by the degree of saturation, (S_{r}), Equation (7.36) can be obtained:

$$\frac{\partial p_y}{\partial S_{\mathrm{r}}} = p_{\mathrm{o}} e^{\left(\frac{\left[v_{\mathrm{o}}^{\mathrm{L}} - k_4(S_{\mathrm{r}} - S_{\mathrm{r}}^{\mathrm{L}})\right] - \frac{v_{\mathrm{C}}(1 - \alpha_{\mathrm{ES}} S_{\mathrm{r}}^{\mathrm{L}}) - \alpha_{\mathrm{ES}}(S_{\mathrm{r}} - S_{\mathrm{r}}^{\mathrm{L}})}{(1 - \alpha_{\mathrm{ES}} S_{\mathrm{r}})}}{\lambda(S_{\mathrm{r}}) - k(S_{\mathrm{r}})}\right)} * \left(\frac{(\lambda(S_{\mathrm{r}}) - k(S_{\mathrm{r}}))\mathrm{d}(v_{\mathrm{o}} - v_{\mathrm{o,UL}}) - (v_{\mathrm{o}} - v_{\mathrm{o,UL}})\mathrm{d}(\lambda(S_{\mathrm{r}}) - k(S_{\mathrm{r}}))}{(\lambda(S_{\mathrm{r}}) - k(S_{\mathrm{r}}))^2}\right) \tag{7.36}$$

7.2.2.1.2 Partial derivative $\frac{\partial s}{\partial S_{\mathrm{r}}}$

The hydro-mechanical coupling equation of the proposed model can also be written as follows (see Chapter 4 for full derivation):

$$\mathrm{d}S_{\mathrm{r}} = Cn\mathrm{d}s + \left(C\frac{s}{v^2} + Dhg\right)\mathrm{d}v \tag{7.37}$$

Therefore, $\frac{\partial s}{\partial S_{\mathrm{r}}}$ can be written as:

$$\frac{\partial s}{\partial S_{\mathrm{r}}} = \frac{1}{Cn} - \left(C\frac{s}{v^2} + Dhg\right)\frac{\mathrm{d}v}{\mathrm{d}S_{\mathrm{r}}} \tag{7.38}$$

where, C, D and h are three general functions defined in the previous section on volumetric behaviour.

$$v = v_{\mathrm{o}}^{\mathrm{L}} - k_4(S_{\mathrm{r}} - S_{\mathrm{r}}^{\mathrm{L}}) - \left(\lambda_{\mathrm{L}} - k_3(S_{\mathrm{r}} - S_{\mathrm{r}}^{\mathrm{L}})\right)\ln(p / p_{\mathrm{o}}) \tag{7.39}$$

$$\frac{\mathrm{d}v}{\mathrm{d}S_{\mathrm{r}}} = -k_4 + k_3 \ln(p / p_{\mathrm{o}})$$

7.2.2.2 Partial derivative, $\dfrac{\partial p^*{}_\mathrm{y}}{\partial p_\mathrm{sat}}$

Since $p^*{}_\mathrm{y} = p_\mathrm{y} + S_\mathrm{r} s$, $\dfrac{\partial p^*{}_\mathrm{y}}{\partial p_\mathrm{sat}}$ can be found by differentiation with respect to the net stress at saturation (p_sat) as:

$$\frac{\partial p^*{}_\mathrm{y}}{\partial p_\mathrm{sat}} = \frac{\partial p^*{}_\mathrm{y}}{\partial p_\mathrm{y}} \frac{\partial p_\mathrm{y}}{\partial p_\mathrm{sat}} \tag{7.40}$$

$$p^*{}_\mathrm{y} = p_\mathrm{y} + S_\mathrm{r} s$$

$$\frac{\partial p^*{}_\mathrm{y}}{\partial p_\mathrm{y}} = 1$$

$$\frac{\partial p^*{}_\mathrm{y}}{\partial p_\mathrm{sat}} = \frac{\partial p_\mathrm{y}}{\partial p_\mathrm{sat}}$$

7.2.2.3 Partial derivative, $\dfrac{\partial p_\mathrm{y}}{\partial p_\mathrm{sat}}$

Using the chain rule, $\dfrac{\partial p_\mathrm{y}}{\partial p_\mathrm{sat}}$ can be written as:

$$\mathrm{d}\varepsilon_\mathrm{v}^\mathrm{p} = (\lambda(S_\mathrm{r}) - k(S_\mathrm{r}))\frac{\mathrm{d}p_\mathrm{y}}{v p_\mathrm{y}} = \left(\frac{\lambda_\mathrm{sat} - k_\mathrm{sat}}{v_\mathrm{sat}}\right)\frac{\mathrm{d}p_\mathrm{sat}}{p_\mathrm{sat}} \tag{7.41}$$

$$\frac{\mathrm{d}p_\mathrm{y}}{\mathrm{d}p_\mathrm{sat}} = \left(\frac{\lambda_\mathrm{sat} - k_\mathrm{sat}}{\lambda(S_\mathrm{r}) - k(S_\mathrm{r})}\right)\left(\frac{v p_\mathrm{y}}{v_\mathrm{sat} p_\mathrm{sat}}\right)$$

7.3 Model parameters

The material parameters of the generalised MPK model can be identified considering both isotropic and triaxial behaviour: 15 material parameters were introduced for the isotropic response, namely 9 parameters ($\lambda_\mathrm{L}, k_3, v_\mathrm{o}^\mathrm{L}$, k_4 , k_w , v_sat^0 , λ_sat , k_sat and S_r^L) for mechanical behaviour and 6 parameters (n , X , b , α_ES , α_o and β) for water retention behaviour. In addition to these 15 parameters, only two additional material parameters (G and M) are introduced to consider the behaviour related to shearing. All 17 material parameters are included in Table 7.1, and a detailed description of the material parameters for isotropic behaviour can be found in

Kodikara et al. (2019). The parameter G corresponds to the elastic shear modulus and M is the stress ratio (q/p^*) at the critical state, which are assumed to be constants for a particular soil.

Table 7.1: Material parameters

Parameter	Raveendiraraj, 2009)	Abeyrathne (2017)	Casini (2008)
λ_{L}	0.175	0.167	0.14
k_3	0.23	0.242	0.1
$v_{\mathrm{o}}^{\mathrm{L}}$	2.38	2.714	2.12
k_4	1.3	1.522	0.7
k_{w}	0.0005	0.0005	0.005
v_{sat}^{0}	2.4	2.83	2.16
k_{sat}	0.0012	0.0012	0.012
λ_{sat}	0.181	0.17	0.145
$S_{\mathrm{r}}^{\mathrm{L}}$	0.85	0.85	0.7
n_{w} and n_{d}	1.45 and 1.35	0.9 and 0.8	0.35 and 0.32
X	0.5	0.5	0.4
b	5	5	3
α_{ES}	0.6	0.6	0.5
α_1 and α_2	0.63 and 0.57	0.63 and 0.57	0.52 and 0.48
β	0.1	0.1	0.2
G	5000	5000	5000
M	0.80	0.5	1.455

7.4 Experimental validation

The governing equations developed were used for the simulation of shearing stress paths at element level (constant suction or constant water content) to simulate the experiments by Raveendiraraj (2009) and Abeyrathne (2017) for compacted kaolin. In addition, the shear stress paths by Raveendiraraj (2009) were carried out with some intermittent isotropic stress paths (loading, unloading, wetting and drying) and the simulation of those stress paths is also reported in this chapter. A flow chart demonstrating how the simulation progressed is given in Figure 7.2.

$$p_{\mathrm{E}}^{*}=\frac{(18p_{\mathrm{Initial}}+M^{2}p_{\mathrm{y}}^{*})+\sqrt{(18p_{\mathrm{Initial}}+M^{2}p_{\mathrm{y}}^{*})^{2}-36\left(p_{\mathrm{Initial}}\right)^{2}(9-M^{2})}}{2(9-M^{2})} \tag{7.42}$$

$$\begin{Bmatrix} \mathrm{d}\varepsilon_{\mathrm{v}} \\ \mathrm{d}S_{\mathrm{r}} \\ \mathrm{d}\varepsilon_{\mathrm{q}} \end{Bmatrix} = \begin{bmatrix} \dfrac{k(S_{\mathrm{r}})}{vp\left(1+k(S_{\mathrm{r}})\dfrac{sS_{\mathrm{r}}}{\phi v^{2}p}\right)} & \dfrac{\left(-k(S_{\mathrm{r}})\dfrac{(\phi+s\mathrm{C})}{vp}\right)}{\left(1+k(S_{\mathrm{r}})\dfrac{sS_{\mathrm{r}}}{\phi v^{2}p}\right)} & 0 \\ 0 & \mathrm{C} & 0 \\ 0 & 0 & \dfrac{1}{3\mathrm{G}} \end{bmatrix} \begin{Bmatrix} \mathrm{d}p^{*} \\ \mathrm{d}s^{*} \\ \mathrm{d}q \end{Bmatrix} \tag{7.43}$$

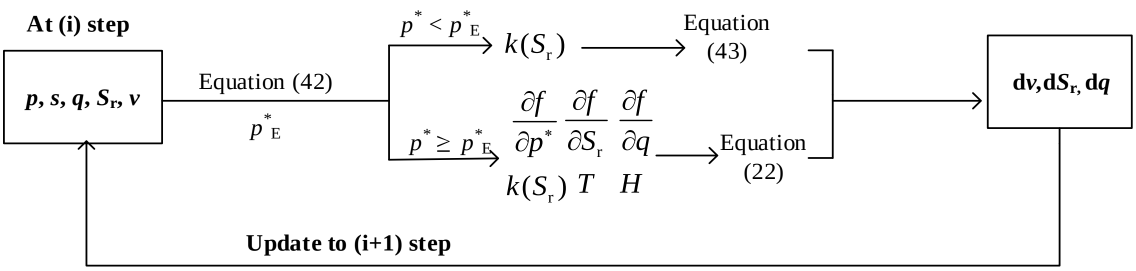

Figure 7.2: Computational flow chart for triaxial behaviour

As shown in Figure 7.1, the effective stress on the MCC ellipse for a particular drained path p_{E}^{*} was obtained from Equation (7.42). For the elastic behaviour, Equation (7.43) is used, whereas for elastoplastic behaviour Equation (7.22) is used. For Equation (7.22), the parameters, $k(S_{\mathrm{r}})$ (Equation7.4)), $\dfrac{\partial f}{\partial p^{*}}$ (Equation (7.28)), $\dfrac{\partial f}{\partial S_{\mathrm{r}}}$ (Equations (7.30), (7.32) and (7.33), $\dfrac{\partial f}{\partial q}$ (Equation (7.29)), T (Equation (7.13)) and H (Equation (7.27)) are used, and for Equation (7.43), only $k(S_{\mathrm{r}})$ (Equation (7.04) is required.

7.4.1 Constant water content shearing stress paths by Abeyrathne (2017)

Abeyrathne (2017) conducted constant moisture content isotropic shearing tests on compacted kaolin (LL=60.5%, PL=27.9%) with the commercial name Eckalite 1. These tests were used to demonstrate how the MPK generalised model performs upon constant water content shearing.

The dry kaolin was hand-mixed with distilled water for different moisture contents for the tests. The conditioned soil was statistically compacted in 1-D to the 50 kPa stress level, prior to placing it in the triaxial cell for isotropic loading. Suction was not measured during testing, which made the tests relatively easy. The predictions of the suction behaviour were not simulated due to to the unavailability of suction measurements. However, if the SWRC is measured by conventional experiments, the required coupled hydraulic parameters of the model can be captured, and the variation in suction can be simulated. However, this simulation is not reported here.

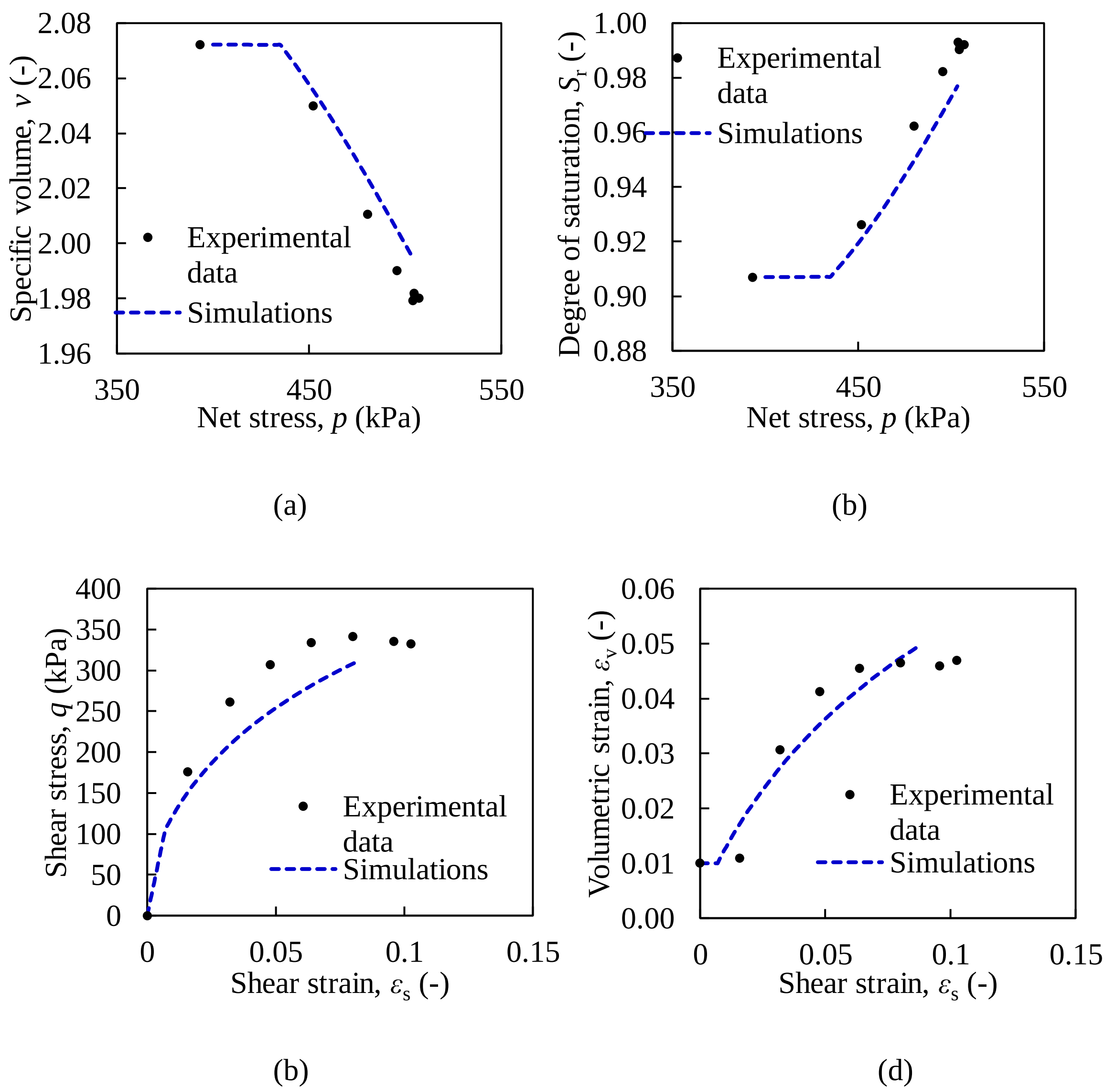

Figure 7.3: Comparison of constant water content shearing on: (a) (v, p) plane; (b) (S_r, p) plane; (c) (q, ε_s) plane; (d) $(\varepsilon_v, \varepsilon_s)$ plane for 36.7% and 30.1% water content

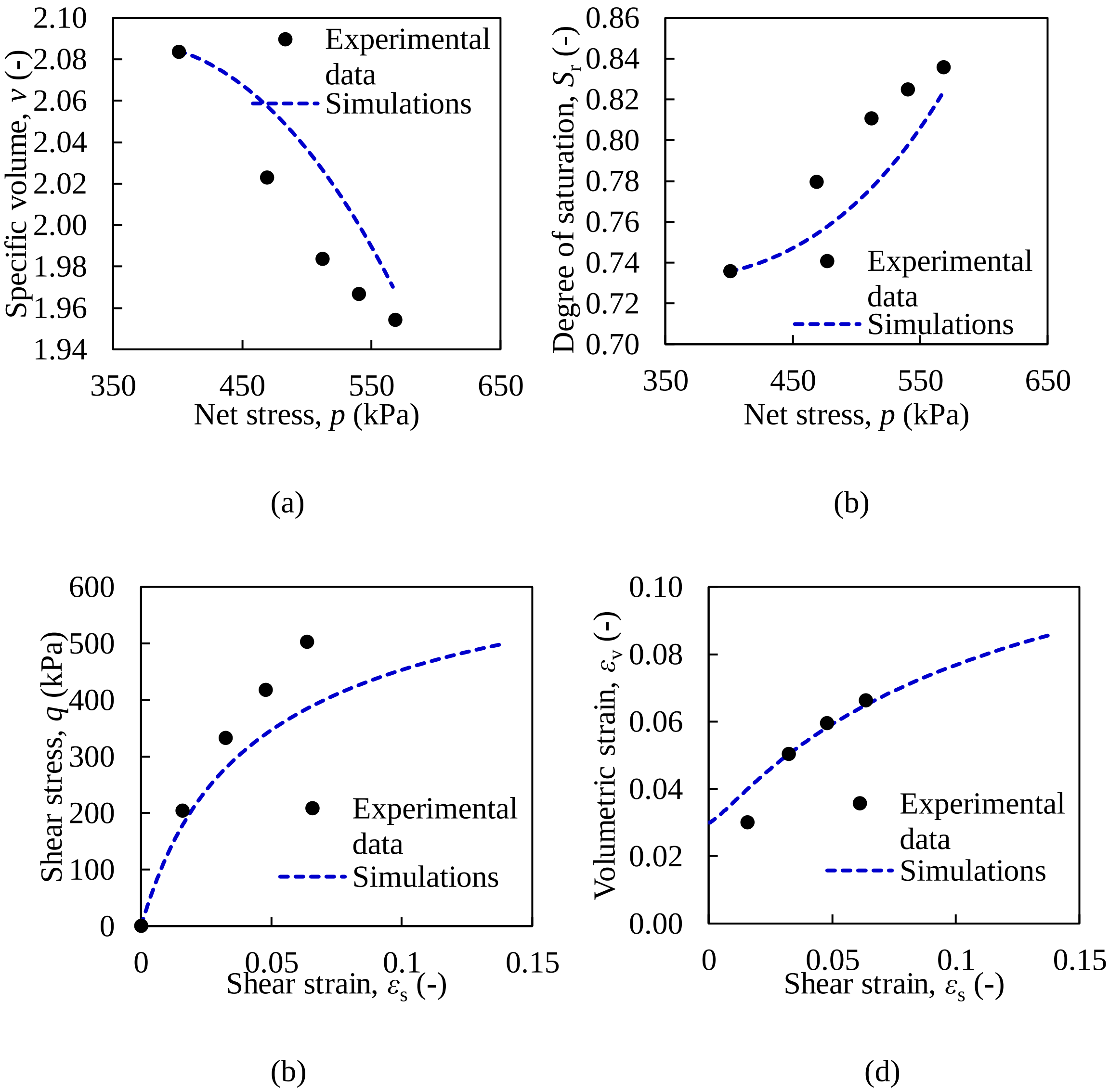

Figure 7.4: Comparison of constant water content shearing on: (a) (v, p) plane; (b) (S_r, p) plane; (c) (q, ε_s) plane; (d) $(\varepsilon_v, \varepsilon_s)$ plane for 30.1% water content

Figure 7.3 and Figure 7.4 show the constant water content shearing path of 36.7% and 30.1% on: (a) (v, p) plane; (b) (S_r, p) plane; (c) (q, ε_s) plane; (d) $(\varepsilon_v, \varepsilon_s)$ plane, respectively. Initially, the sample was statically compacted to 50 kPa at the respective moisture content prior to shearing. The simulations for both water contents followed the experiments reasonably well in all the planes.

7.4.2 Constant suction shearing stress paths by Raveendiraraj (2009)

Raveendiraraj (2009) reported a series of sophisticated experimental results for various combinations of triaxial and isotropic (loading, unloading, wetting and drying) stress paths performed on compacted kaolin. The samples 50 mm in diameter and 100mm in height were statically compacted at 25% moisture content. The initial v and S_r of the compacted samples were 2.14 ± 0.02 and 55.5 ± 2.5%. Initial equalisation was performed to reach the targeted initial mean net stress and suction values, and the test stress paths were completed after equalisation. In the following sections, MPK model predictions for the three tests, which include a combination of triaxial and isotropic stress paths, are compared with the respective experimental results.

7.4.2.1 B2 constant suction (200 kPa) shearing test with drying → loading → shearing stress paths

Figure 7.5 shows the constant suction shearing path on: (a) (v, p) plane; (b) (S_r, p) plane; (c) ($q, \varepsilon_\mathrm{s}$) plane; (d) ($\varepsilon_\mathrm{v}, \varepsilon_\mathrm{s}$) plane; (e) ($\left(q/p\right), \varepsilon_1$ or ε_3) plane, respectively. The sample sheared at a net stress of 75 kPa and a suction of 200 kPa, where an increase of shear stress, q, results in a decrease in v and an increase in S_r for both experimental results and model simulations, until it eventually reaches failure at a shear stress of 185 kPa, as shown in Figure 7.5(a) and Figure 7.5(b), respectively. During the model simulations, the behaviour of shear stress with the true shear strain (Figure 7.5(c)), volumetric strain with the true shear strain (Figure 7.5(d)) and $\left(q/p\right)$ with ε_1 or ε_3 (Figure 7.5(e)) were also simulated. Reasonable agreement between the experiments and model simulations was observed. It should be noted that for Test B2, after the initial equalisation stage, the soil sample was dried and loaded prior to shearing. Hence, the remaining two drying → loading stress paths were simulated, as shown in Table 7.2 and Figure 7.6.

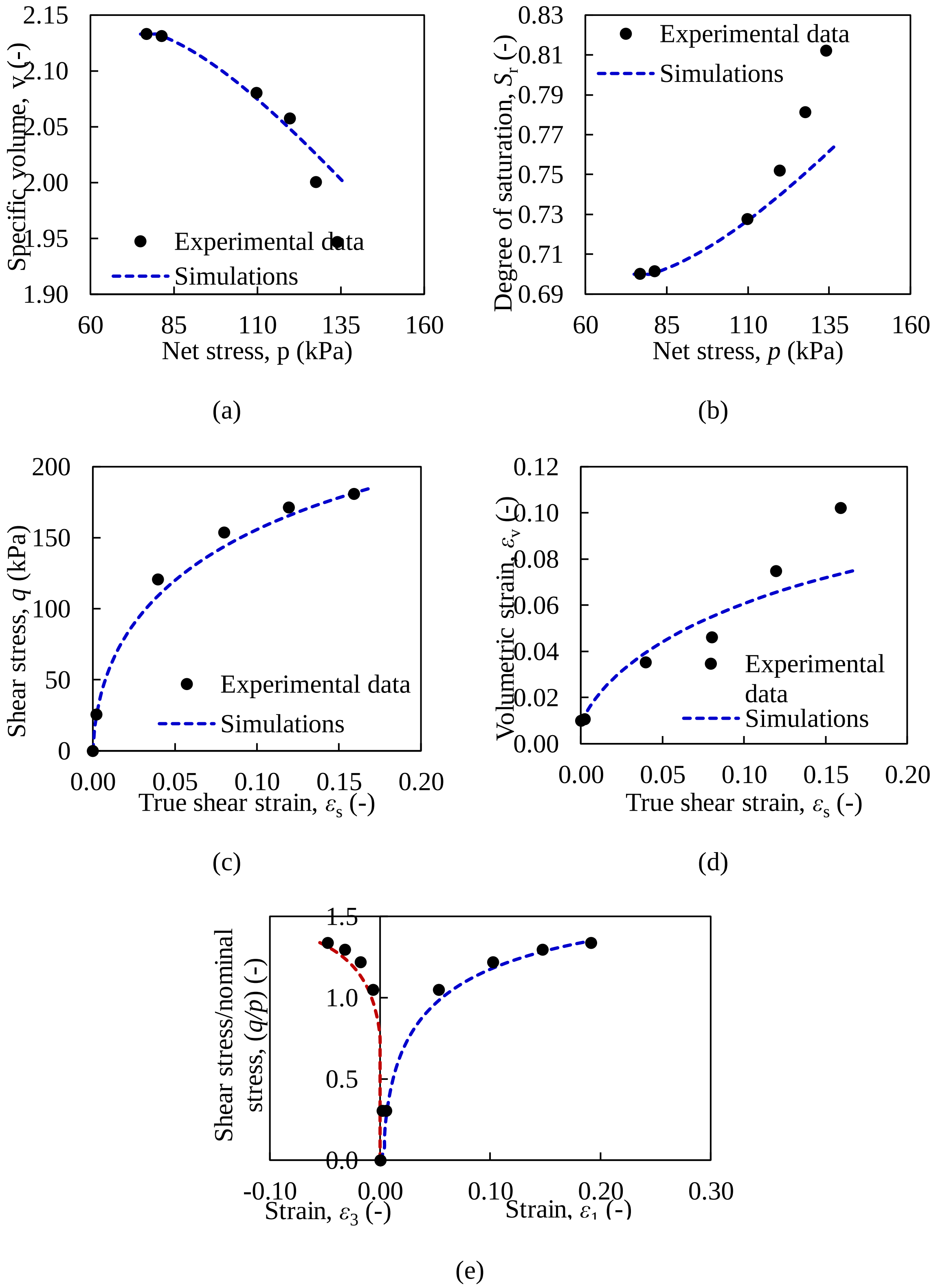

Figure 7.5: Comparison of constant suction shearing on: (a) (v, p) plane; (b)(S_r, p) plane; (c) (q, ε_s) plane; (d) $(\varepsilon_v, \varepsilon_s)$ plane; (e) $\left(\left(q/p\right), \varepsilon_1 \text{ or } \varepsilon_3\right)$ plane

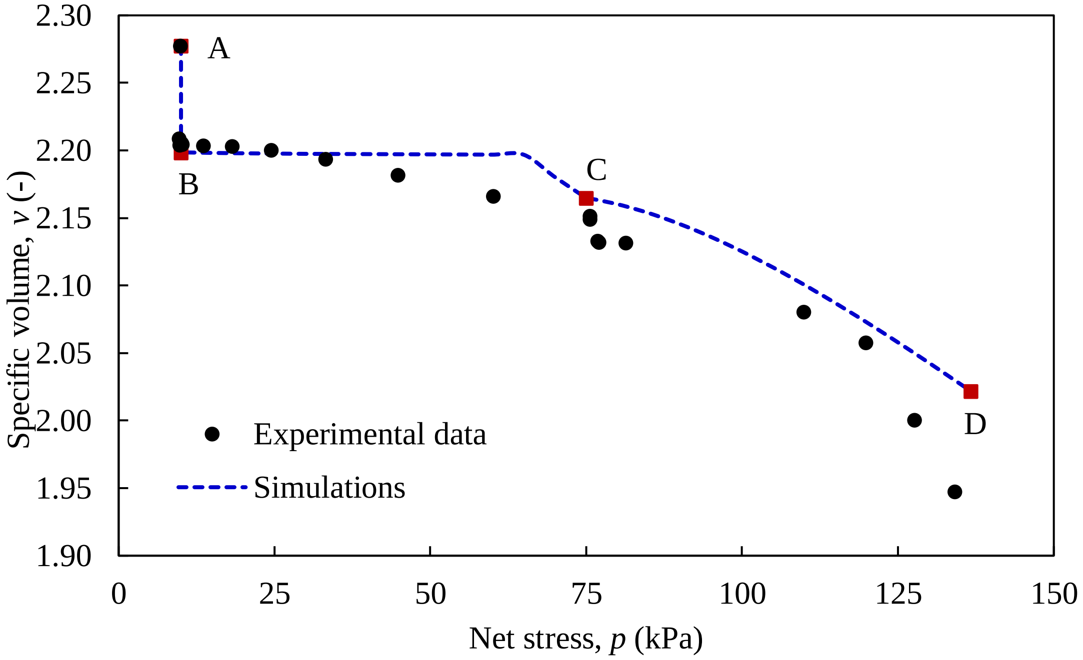

(a)

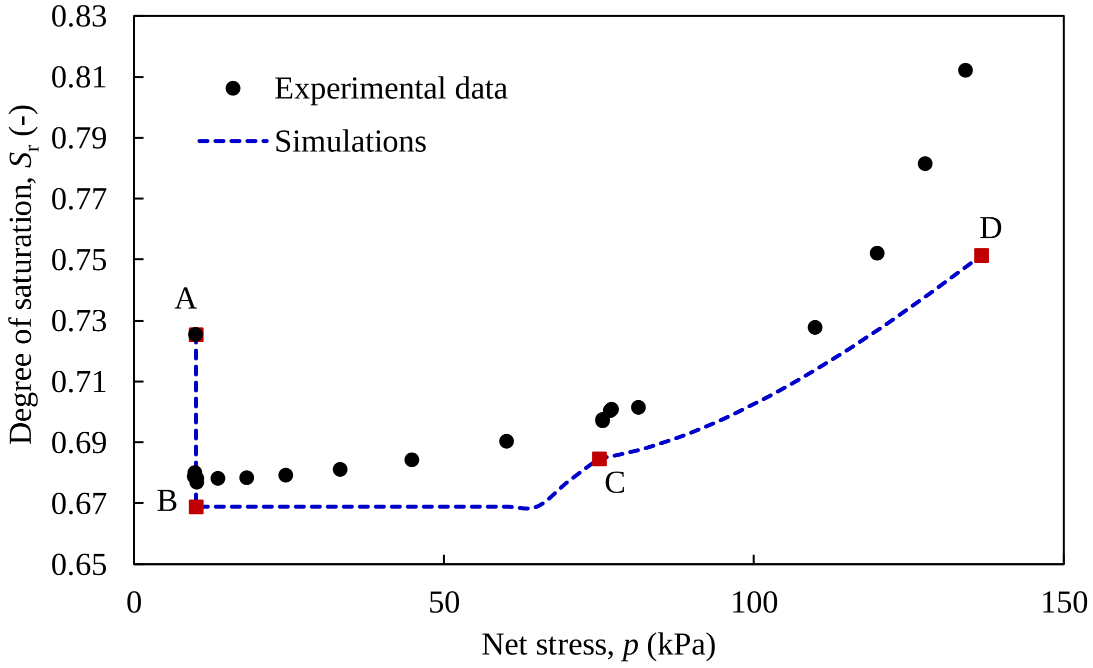

(b)

Figure 7.6: Comparison of stress paths on: (a)(v, p) plane; (b)(S_r, p) plane

Table 7.2: Experimental validation B2

Stage	Net stress (p/kPa)	Suction (s/kPa)	Shear stress (q/kPa)

A	B	Drying	10	30→200	0
B	C	Loading	10→75	200	0
C	D	Shearing	75 → 137	200	0 → 185

After the initial equalisation to the mean net stress of 10 kPa and suction of 30 kPa, the sample was dried to 200 kPa suction under the constant net stress of 10 kPa. During the drying path AB, since $\bar{\eta}$=0.045>0 (i.e. State A is above the environmentally-stabilised line), the drying gradient was α_2 = 0.63 (> α_{ES}). The sample started yielding on the drying SWRC paths at suction 40 kPa after moving along the scanning path. Then, upon loading path BC, the soil sample started to yield at 60 kPa during the simulations. Similar to shear stress path CD, both drying and loading model simulations showed acceptable agreement with the experimental results.

7.4.2.2 B3 constant suction (200 kPa) shearing test with loading → shearing stress paths

The constant suction shearing path of the 200 kPa suction is given Figure 7.7 on: (a) (v, p) plane; (b) (S_{r}, p) plane; (c) ($q, \varepsilon_{\mathrm{s}}$) plane; (d) ($\varepsilon_{\mathrm{v}}, \varepsilon_{\mathrm{s}}$) plane; (e) ($\left({q}/{p} \right), \varepsilon_1 \text{ or } \varepsilon_3$) plane, respectively. The sample was sheared at a net stress of 75 kPa and suction of 200 kPa, and an increase of shear stress, q, resulted in a decrease in v and an increase in S_{r} for both experimental results and model simulations, until it eventually reached failure at 185 kPa shear stress, as shown in Figure 7.7(a) and Figure 7.7(b), respectively. During the model simulations, the behaviour of shear stress with the true shear strain (Figure 7.7(c)), volumetric strain with the true shear strain (Figure 7.7(d)) and $\left({q}/{p} \right)$ with $\varepsilon_1 \text{ or } \varepsilon_3$ (Figure 7.7(e)) were also simulated. Reasonable agreement between experiments and model simulations was observed. It should be noted that for Test B3, after the initial equalisation stage, the soil sample was loaded prior to shearing. Hence, the loading stress path was also simulated, as shown in

Table 7.3 and Figure 7.8.

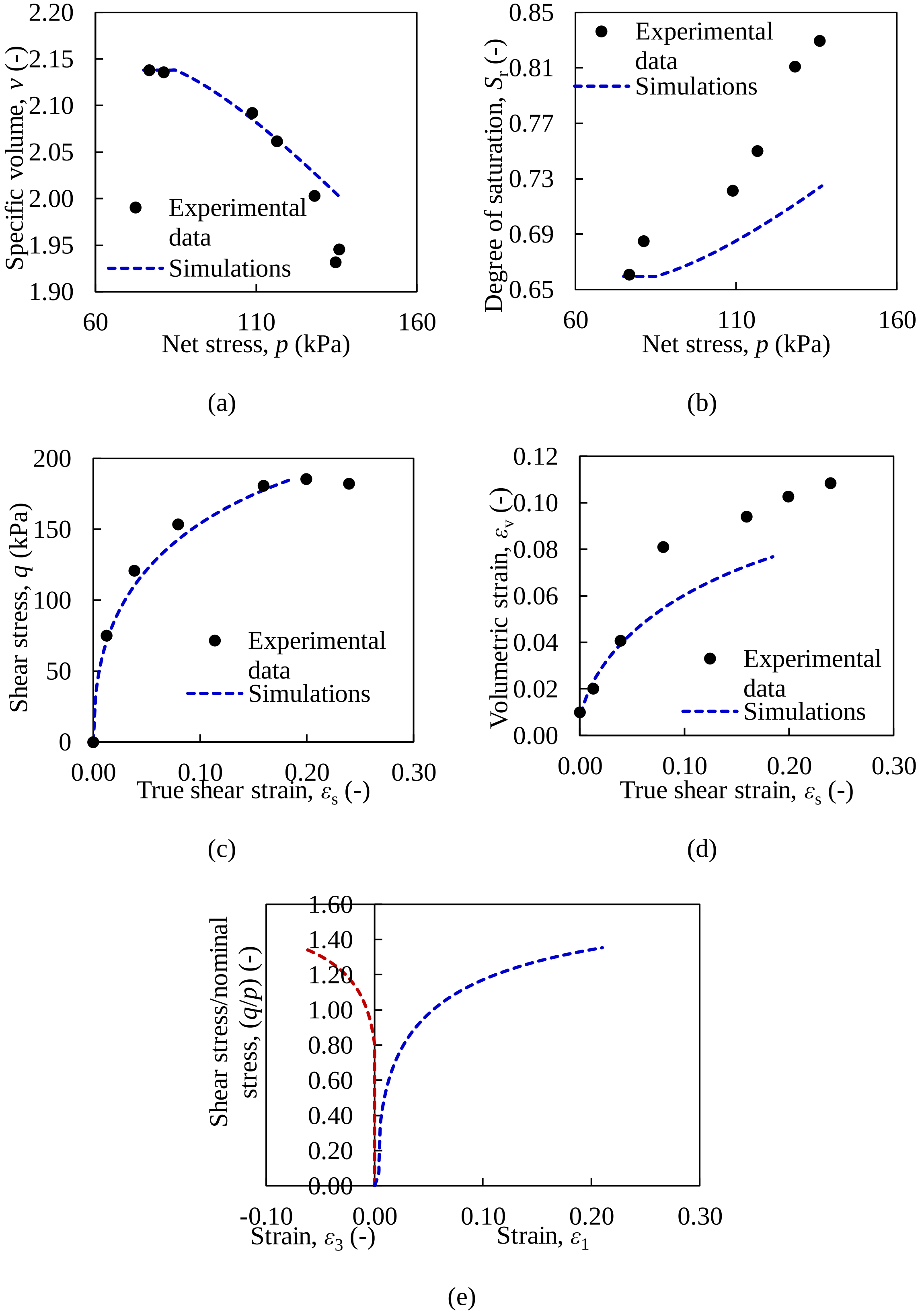

Figure 7.7: Comparison of constant suction shearing on: (a) (v, p) plane; (b)(S_r, p) plane; (c) (q, ε_s) plane; (d) $(\varepsilon_v, \varepsilon_s)$ plane; (e) $\left(\left(q/p\right), \varepsilon_1 \text{ or } \varepsilon_3\right)$ plane

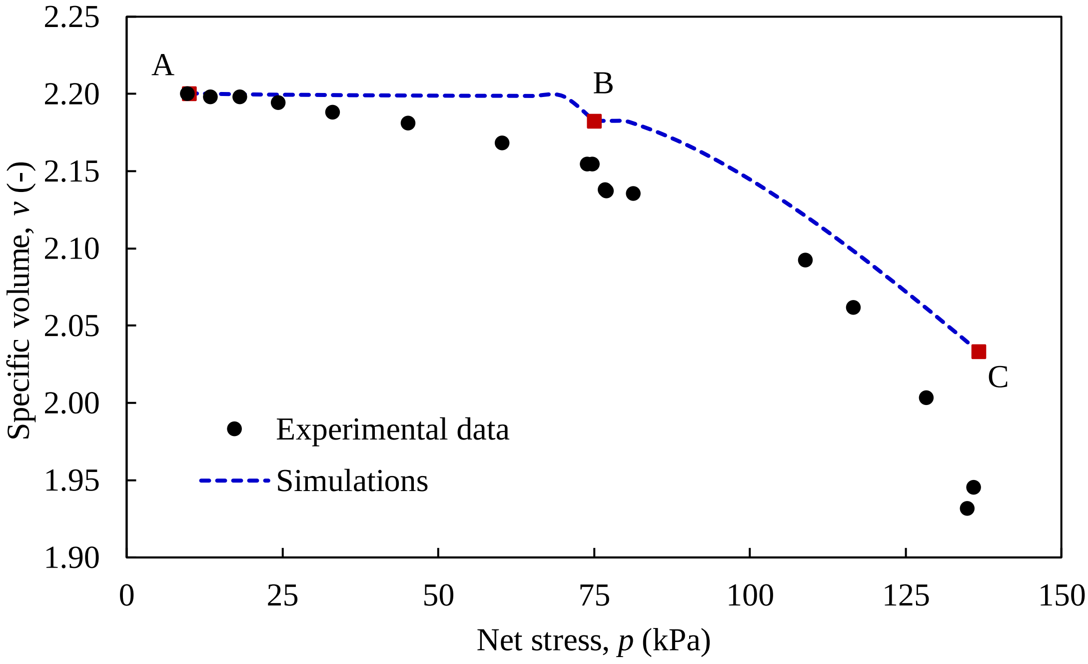

(a)

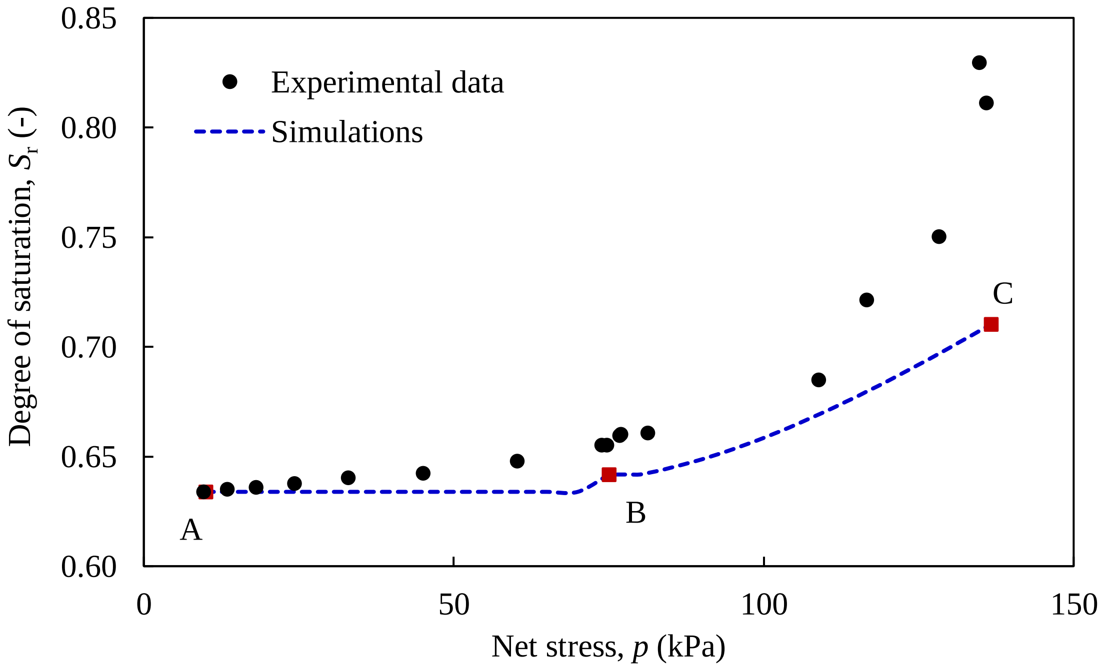

(b)

Figure 7.8: Comparison of stress paths on: (a) (v, p) plane; (b) (S_r, p) plane

Table 7.3: Experimental validation B3

Stage			Net stress (p/kPa)	Suction (s/kPa)	Shear stress (q/kPa)
A	B	Loading	10→75	200	0
B	C	Shearing	75 → 137	200	0 → 185

7.4.2.3 B4 constant suction (300 kPa) shearing test with loading → shearing stress paths

Figure 7.9 shows the constant suction shearing path on: (a) (v, p) plane; (b)(S_r, p) plane; (c) (q, ε_s) plane; (d) ($\varepsilon_v, \varepsilon_s$) plane; (e) ($\left(q/p\right), \varepsilon_1$ or ε_3) plane, respectively. The sample sheared at a net stress of 75 kPa and suction of 300 kPa, where an increase of shear stress, q, resulted in a decrease in v and an increase in S_r for both the experimental results and the model, until it eventually reached failure at 260 kPa shear stress simulations, as shown in Figure 7.9(a) and Figure 7.9(b. During the model simulations, the behaviour of shear stress with the true shear strain (Figure 7.9(c)), the volumetric strain with the true shear strain (Figure 7.9(d)) and $\left(q/p\right)$ with ε_1 or ε_3 (Figure 7.9(e)) were also simulated. It should be noted that for Test B4, after the initial equalisation stage, the soil sample was loaded prior to shearing. Hence, the remaining loading stress path was also simulated, as shown in Table 7.4 and Figure 7.10. Upon loading simulation, yielding was observed at a net stress of 60 kPa, resulting in yielding prior to shearing.

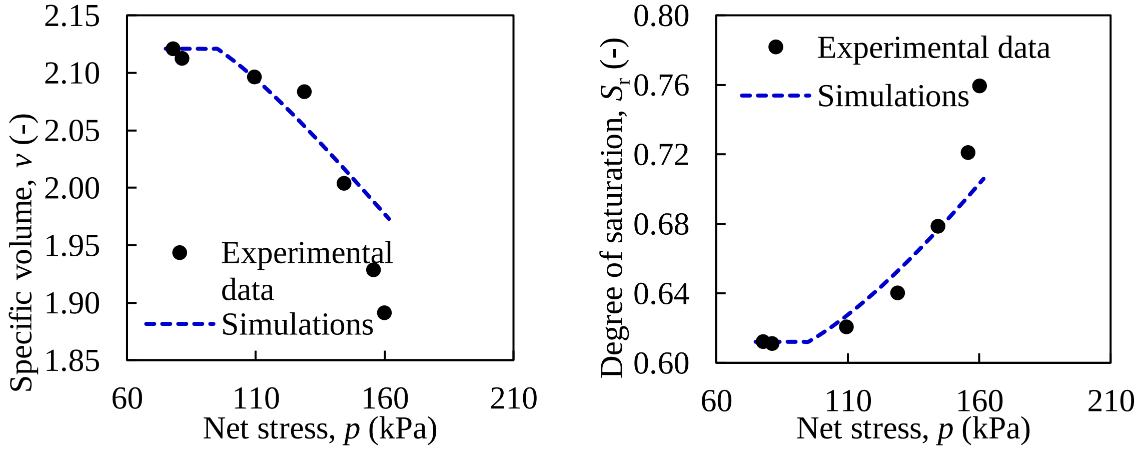

(a) (b)

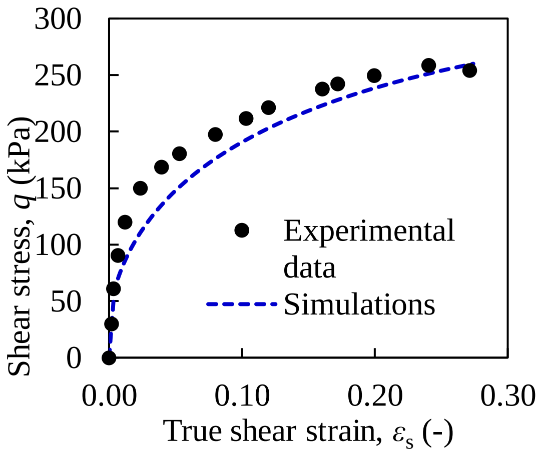

(c)

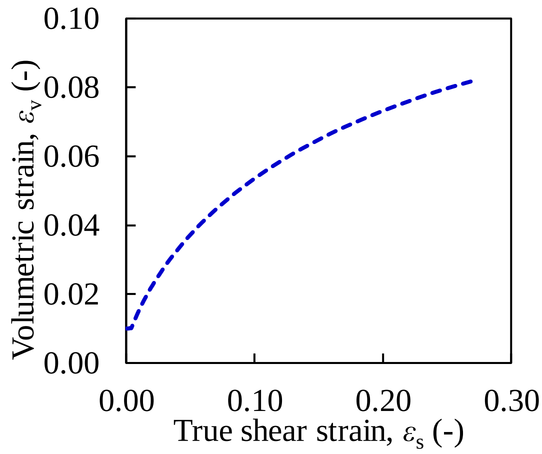

(d)

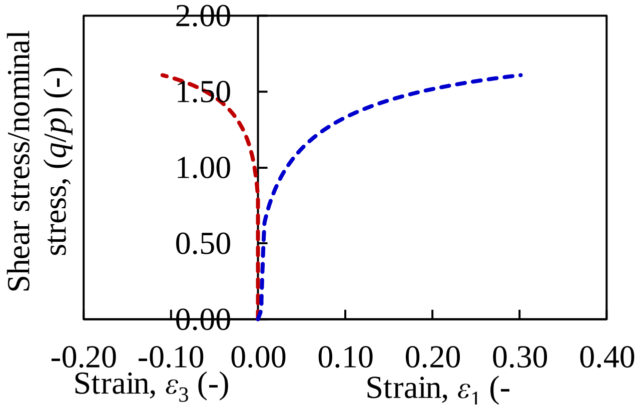

(e)

Figure 7.9: Comparison of constant suction shearing on: (a) (v, p) *plane; (b)*(S_r, p) *plane; (c)* (q, ε_s) *plane; (d)* $(\varepsilon_v, \varepsilon_s)$ *plane; (e)* $\left(\left(q/p\right), \varepsilon_1 \text{ or } \varepsilon_3\right)$ *plane*

Table 7.4: Experimental validation B4

Stage			Net stress (p/kPa)	Suction (s/kPa)	Shear stress (q/kPa)
A	B	Loading	10→75	300	0
B	C	Shearing	75 → 162	300	0 → 260

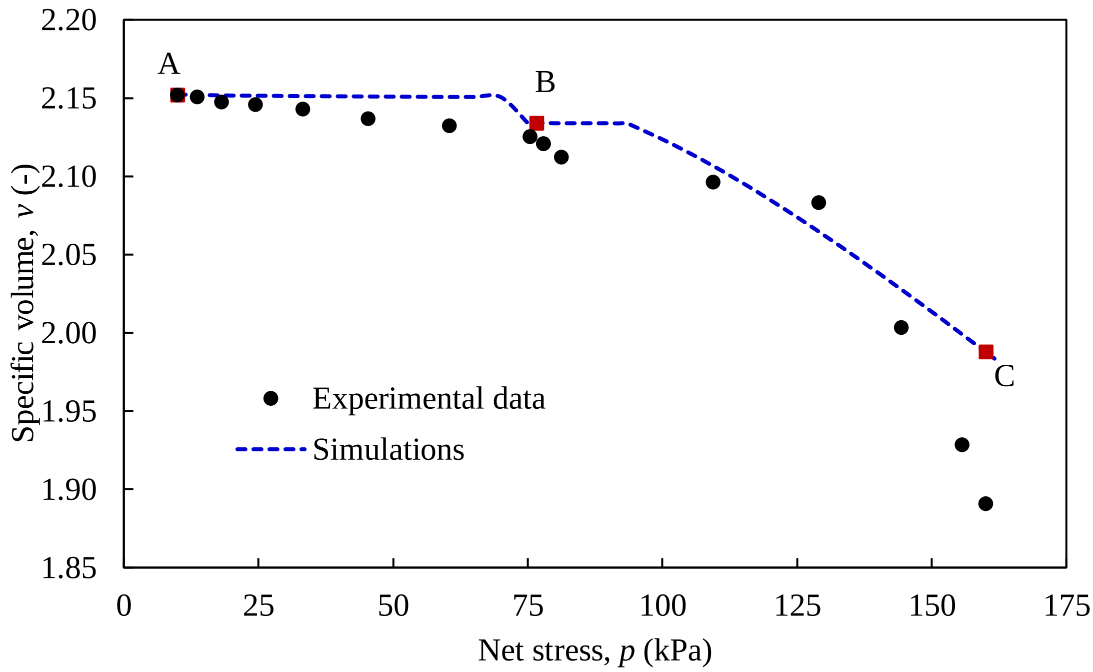

(a)

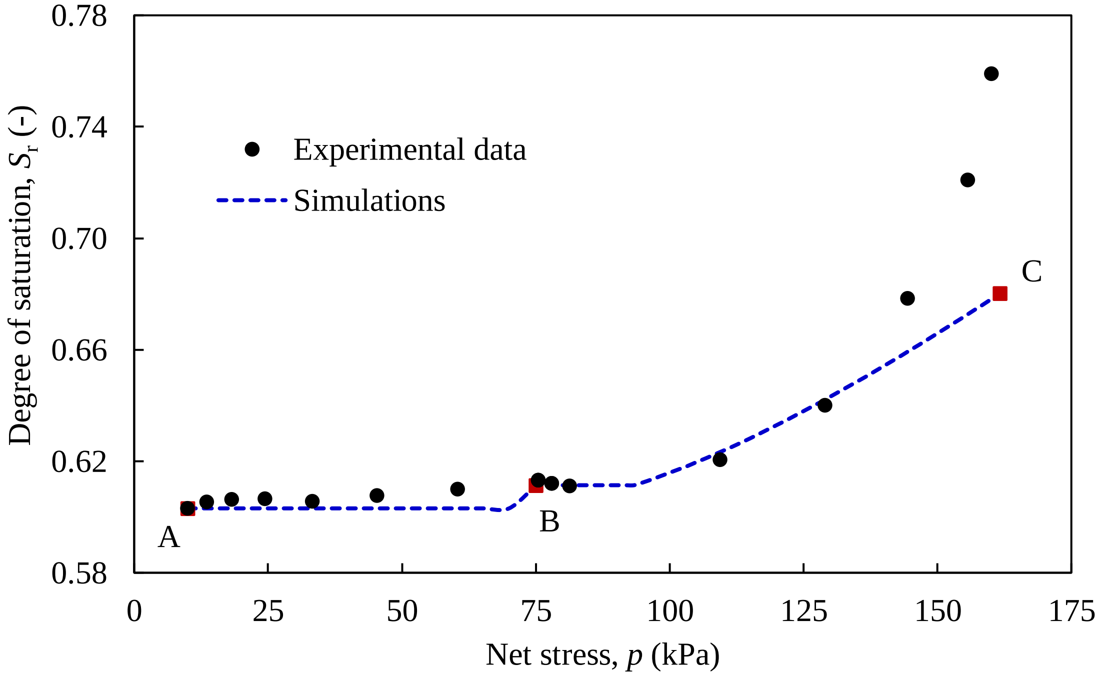

(b)

Figure 7.10: Comparison of stress paths on (a) (v, p) plane; (b) (S_r, p) plane

7.4.2.4 B5 constant suction (300 kPa) shearing test with drying → loading → shearing stress paths

Test B5 included constant net stress drying, constant suction loading and shearing stress paths with the suction of 300 kPa compared with the suction of 200 kPa for Test B2 (see Table 7.5). Comparisons of the simulations with experimental results are illustrated in Figure 7.11(a) on the (v, p) plane, and Figure 7.11(b) on the (S_r, p) plane, respectively. The sample was dried from net stress of 10 kPa and suction of 30 kPa, and both the v and S_r decreased with the increase of suction in simulations and experiments. During drying path AB, since $\bar{\eta}$ =0.0466>0 (i.e. State A is above the environmentally-stabilised line), the drying gradient was α_2 = 0.63 (> α_{ES}). Then, after reaching 300 kPa suction, the sample was loaded to 110 kPa and yielding started in model simulation at 75 kPa. The sample was then sheared under a constant suction of 300 kPa, exhibiting failure at 280 kPa shear stress. Reasonable agreement was obtained between the experimental results and model simulations.

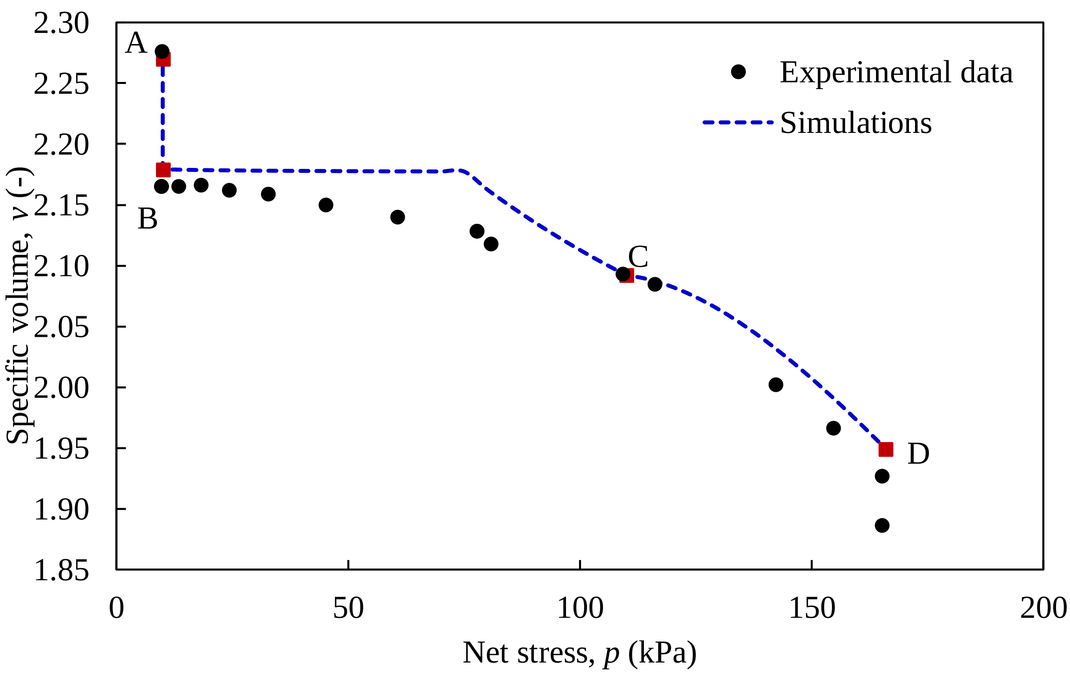

(a)

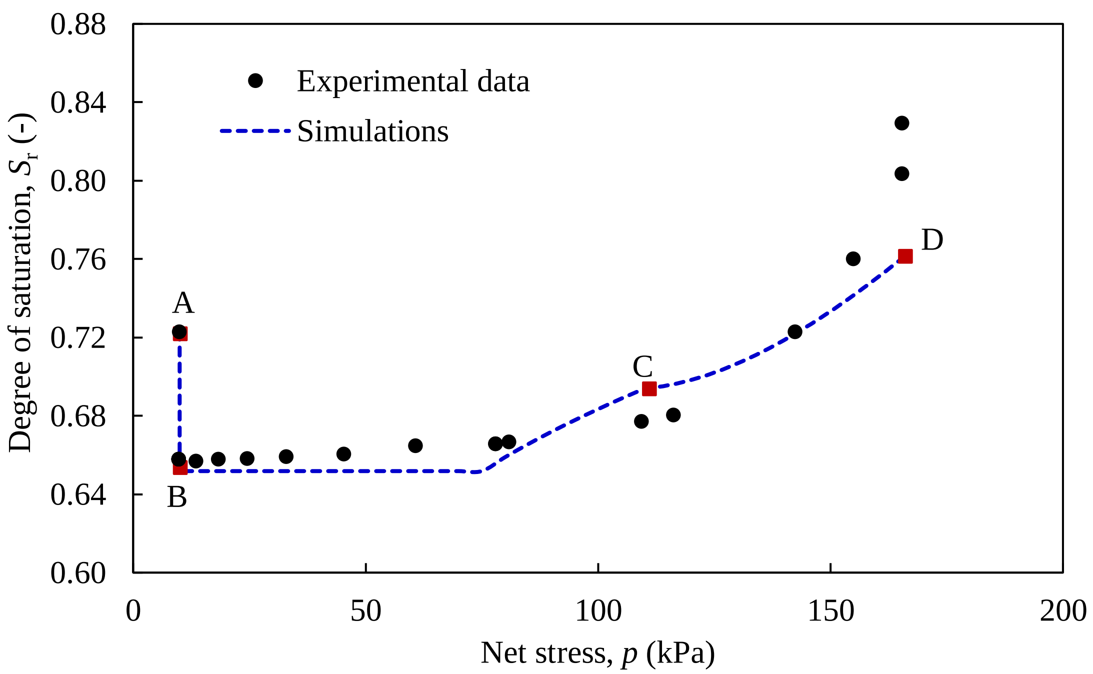

(b)

Figure 7.11: Comparison of stress paths on (a) (v, p) plane; (b) (S_r, p) plane

Table 7.5: Experimental validation B5

Stage			Net stress (p/kPa)	Suction (s/kPa)	Shear stress (q/kPa)
A	B	Drying	10	30→300	0
B	C	Loading	10→110	300	0
C	D	Shearing	110→ 166	300	0 → 280

7.4.2.5 B6 constant suction (300 kPa) shearing test with loading → shearing → wetting→ drying → wetting→ drying → shearing stress paths

Raveendiraraj (2009) conducted Test B6 to identify the influence of S_r on the shear behaviour of unsaturated soils with two wet/dry cycles before commencing shearing. Similar to Test B5, the sample was first equalised at a net stress of 10 kPa and a suction of 300 kPa before being volumetrically loaded and then sheared. In the simulation of stress path AB, the sample started yielding at 60 kPa, resulting in volumetric yielding behaviour, as shown in Figure 7.12(a) with respect to a specific volume and Figure 7.12(b) with respect to the degree of saturation. During the shearing stress path, the sample was already on the volumetric yield surface, and with the further increase of q, the sample started to intersect the critical state yield surfaces corresponding to a particular plastic volumetric strain. The next wetting stress path was induced at the mean net stress of 102 kPa, and both simulations and experiments showed collapse behaviour (see Figure 7.12(c)).

During drying path DE, since $\bar{\eta}$ =0.14>0 (i.e. State A is above the environmentally-stabilised line), the drying gradient was α_1 = 0.63 (> α_{ES}). After the collapse, during the equilibrium phase of the experiment, a slight drop in specific volume and an increase in the degree of saturation were observed. However, during the simulations, although the stress path followed a similar pattern, there was a slight deviation from the experiments. During the second wetting path EF, since $\bar{\eta}$ = 0.135 > 0 (i.e. State A is above the environmentally-stabilised line), the wetting gradient was α_2 = 0.5857 (> α_{ES}). Initially, swelling behaviour was observed in the simulations prior to collapse, as shown in Figure 7.12(c). During the second drying path FG, since $\bar{\eta}$ =0.095>0 (i.e. State A is above the environmentally-stabilised line), the drying gradient was α_1 = 0.61 (> α_{ES}). Wetting drying behaviour, with a scanning effect, is evident in Figure 7.12(d) on the (S_{r}, s) plane. Finally, the sample sheared under a constant suction of 300 kPa until it reached failure at a shear stress of 280 kPa. Overall, Figure 7.12 shows reasonable agreement between model simulations and experimental results for both isotropic and triaxial stress paths.

Table 7.6: Experimental validation B6

Stage			Net stress (p/kPa)	Suction (s/kPa)	Shear stress (q/kPa)
A	B	Loading	10→75	300	0
B	C	Shearing	75 → 102	300	0 → 80
C	D	Wetting	102	300 → 100	80
D	E	Drying	102	100 → 300	80
E	F	Wetting	102	300 → 100	80
F	G	Drying	102	100 → 300	80
G	H	Shearing	102 → 168	300	80 → 280

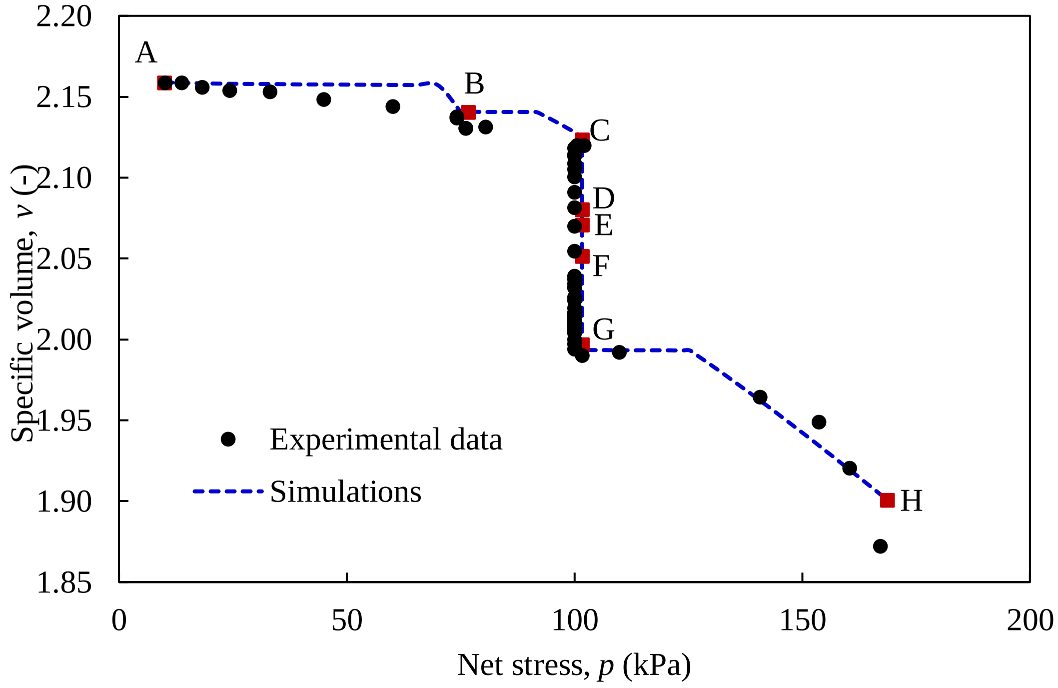
2.20
2.15
2.10
2.05
2.00
1.95
1.90
1.85
0
50
100
150
200
Specific volume, v (-)
Net stress, p (kPa)
A
B
C
D
E
F
G
H
Experimental data
Simulations

(a)

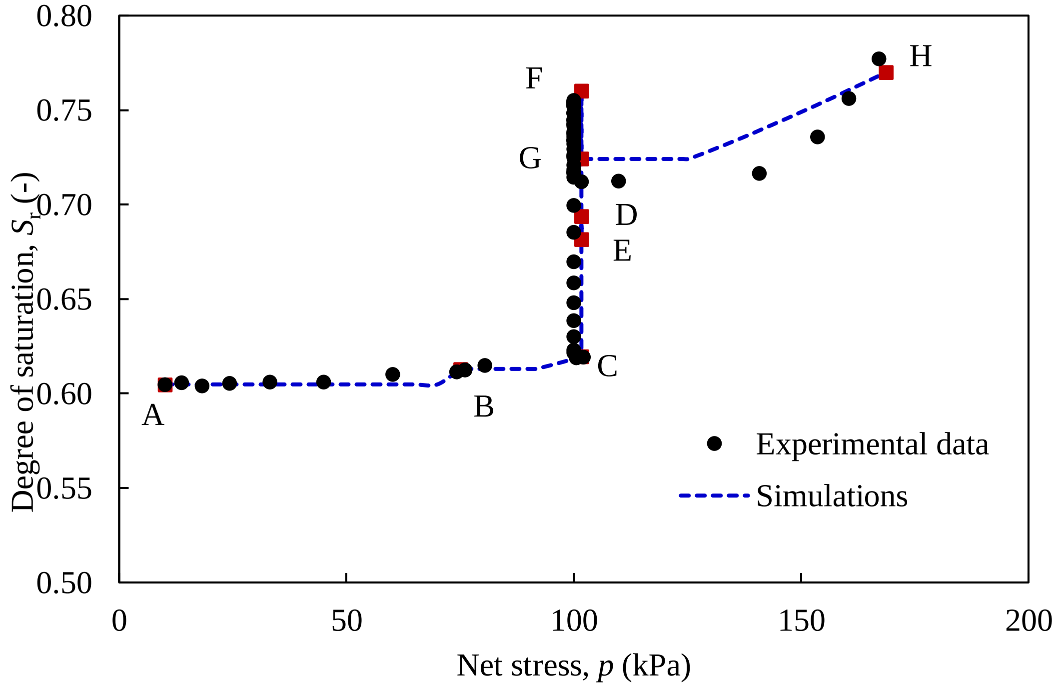
0.80
0.75
0.70
0.65
0.60
0.55
0.50
0
50
100
150
200
Degree of saturation, S_r (-)
Net stress, p (kPa)
A
B
C
D
E
F
G
H
Experimental data
Simulations

(b)

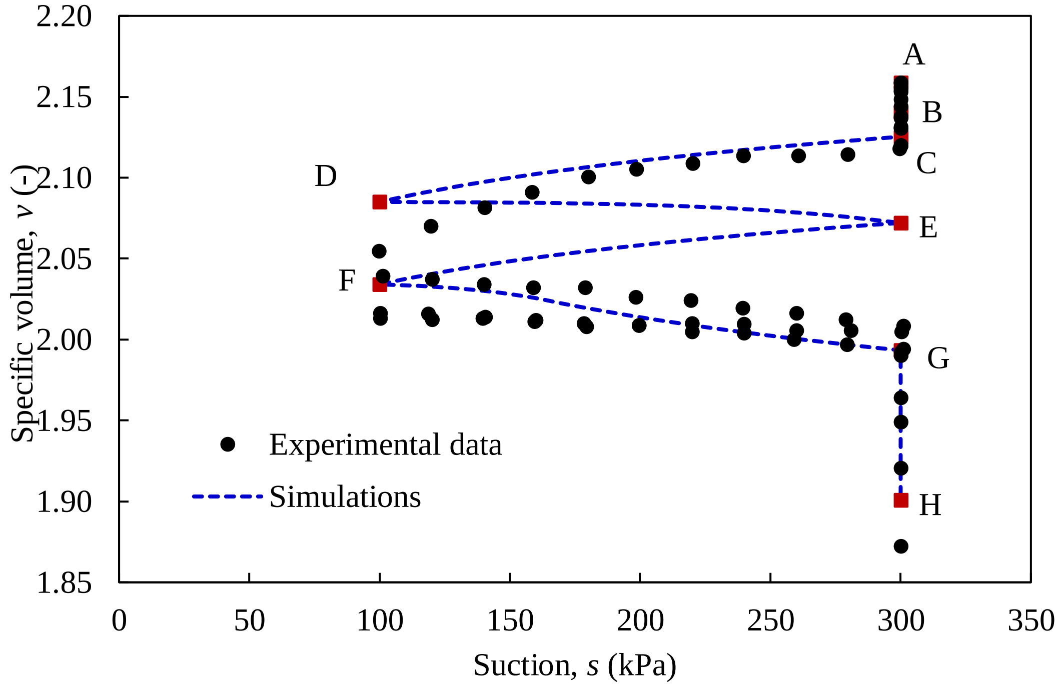

(c)

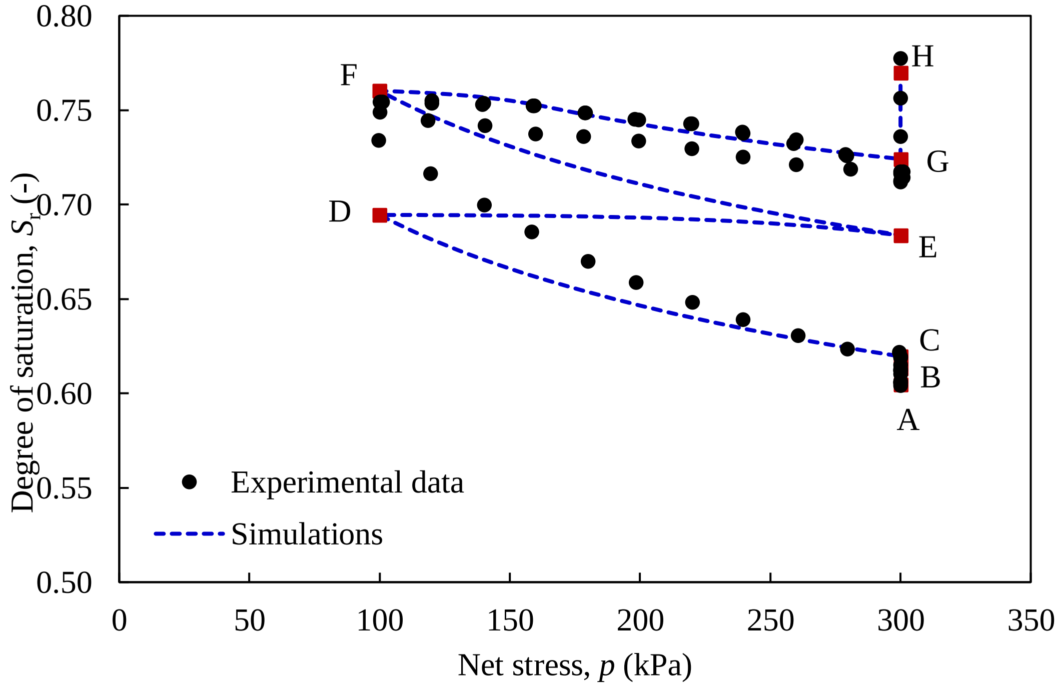

(d)

Figure 7.12: Comparison of stress paths on (a)(v, p) plane; (b)(S_r, p) plane; (c)(v, s) plane; (d)(S_r, s) plane

7.4.2.6 B7 constant suction (200 kPa and 300 kPa) shearing test with loading → shearing → drying → shearing → drying → shearing stress paths

Test B7 includes constant suction loading and shearing and constant net stress drying paths (see Table 7.7). A comparison of the simulations with experimental results is illustrated in Figure 7.13(a) on the (v, p) plane, Figure 7.13(b) on the (S_r, p) plane, Figure 7.13(c) on the (v, s) plane, and Figure 7.13(d) on the (S_r, s) plane, respectively. The sample was first equalised at a net stress of 10 kPa and suction of 100 kPa before commencing loading and shearing stress paths. The sample was loaded to a net stress of 75 kPa at the suction of 100 kPa. During the simulations, yielding was observed at 50 kPa, consistent with the experimental results. Subsequently, the sample sheared at a shear stress of 75 kPa prior to the drying stress path to achieve a suction of 200 kPa. The variables v and S_r both decreased with the increase of suction in the simulations; however, the experimental results of S_r increased prior to reducing later. Then, after reaching 200 kPa suction, the sample sheared at a shear stress of 175 kPa and yielding was observed at 100 kPa mean net stress. The sample then underwent drying under a constant net stress of 133 kPa, prior to the final shearing at the suction of 300 kPa. Reasonable agreement was obtained between the experimental results and model simulations.

Table 7.7: Experimental validation B7

Stage			Net stress (p/kPa)	Suction (s/kPa)	Shear stress (q/kPa)
A	B	Loading	10→75	100	0
B	C	Shearing	75 → 102	100	0 → 75
C	D	Drying	102	100 → 200	75
D	E	Shearing	102→ 133	200	75 → 175
E	F	Drying	133	200 → 300	175
F	G	Shearing	133→ 160	300	175 → 260

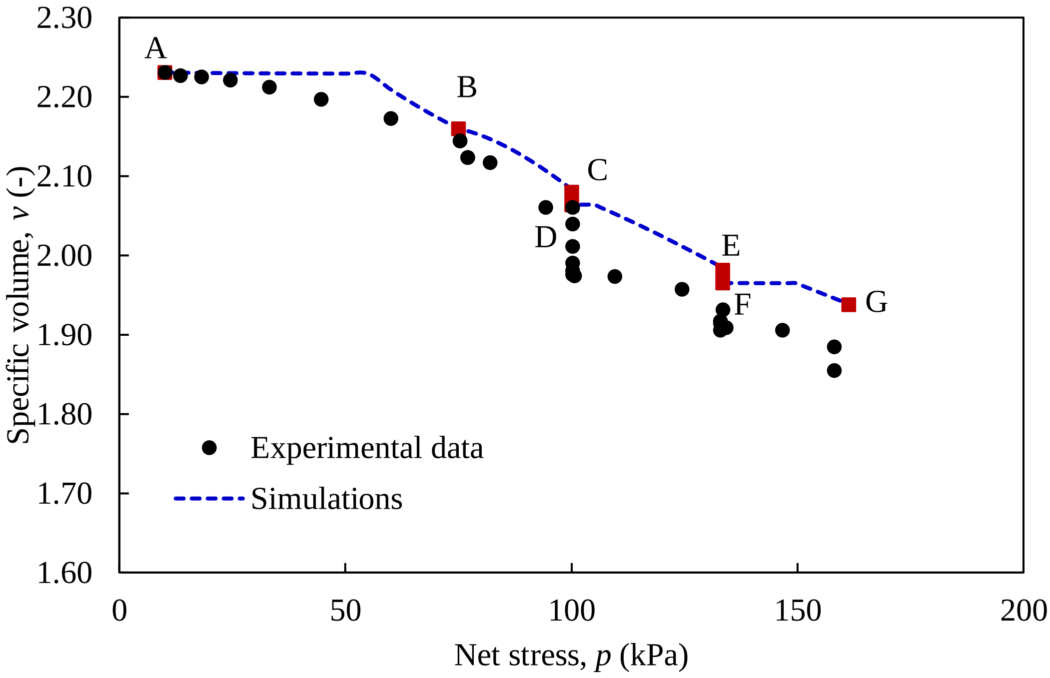
2.30
2.20
2.10
2.00
1.90
1.80
1.70
1.60
0
50
100
150
200
Specific volume, v (-)
Net stress, p (kPa)
A
B
C
D
E
F
G
Experimental data
Simulations

(a)

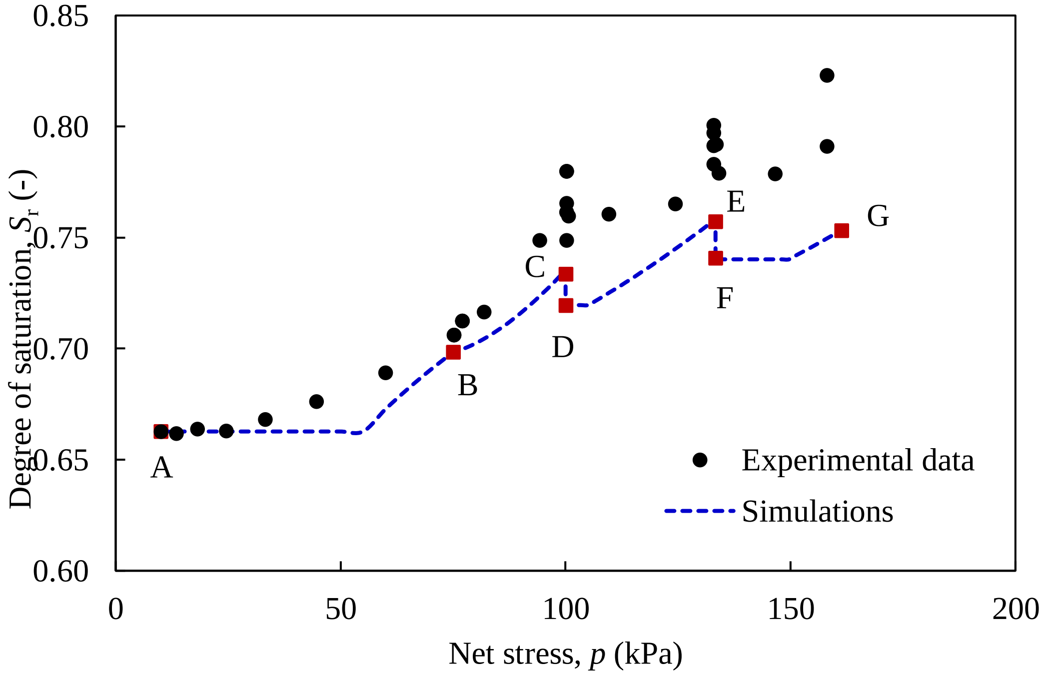
0.85
0.80
0.75
0.70
0.65
0.60
0
50
100
150
200
Degree of saturation, Sr (-)
Net stress, p (kPa)
A
B
C
D
E
F
G
Experimental data
Simulations

(b)

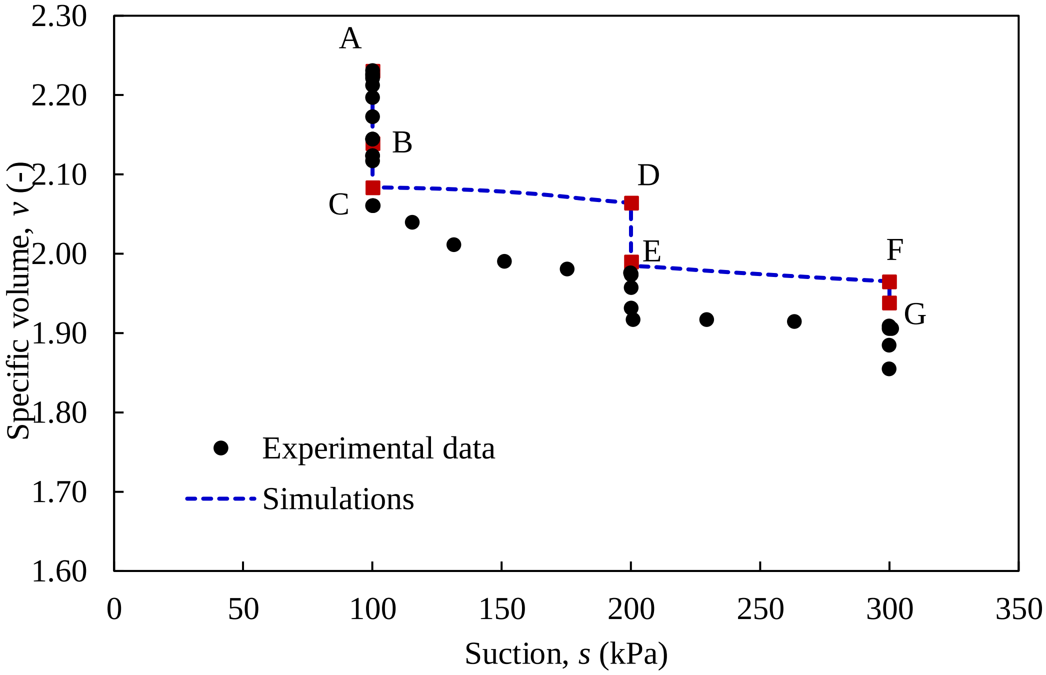

(c)

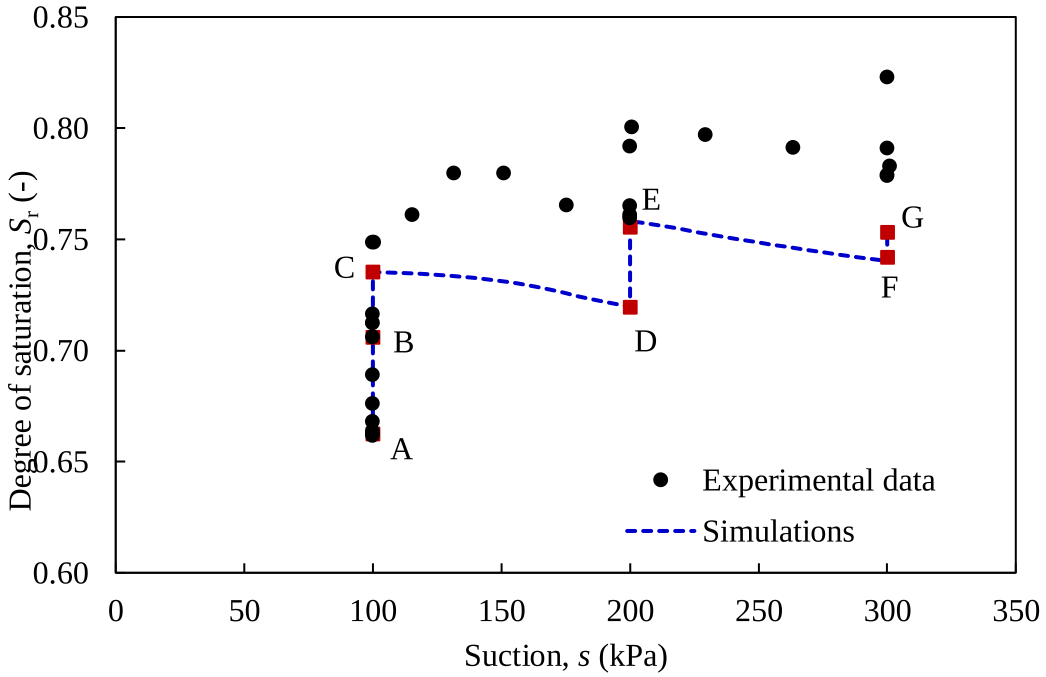

(d)

Figure 7.13: Comparison of stress paths on (a)(v, p) plane; (b) (S_r, p) plane; (c) (v, s) plane; (d) (S_r, s) plane

7.4.2.7 B9 constant suction (300 kPa) shearing test with drying → shearing → loading→ shearing stress paths

As Table 7.8 shows, the sample was first equalised at the suction of 5 kPa and the mean net stress of 10 kPa. A drying stress path, AB, was then performed on the sample to the suction of 300 kPa prior to shearing path BC. As stated by Raveendiraraj (2009), the original intention was to load the soil prior to shearing. On the BC shearing path, the model simulation exhibited a slight reduction in v and increase in S_r similar to the experimental results due to elastic behaviour, as shown in Figure 7.14. Then, while keeping the shear stress of 85 kPa, the sample was further loaded to 110 kPa. During the simulations, the sample started yielding at 90 kPa. Finally, shearing continued to a shear stress of 290 kPa. Simulations achieved a slightly higher value of v and a lower value in S_r than the experiments.

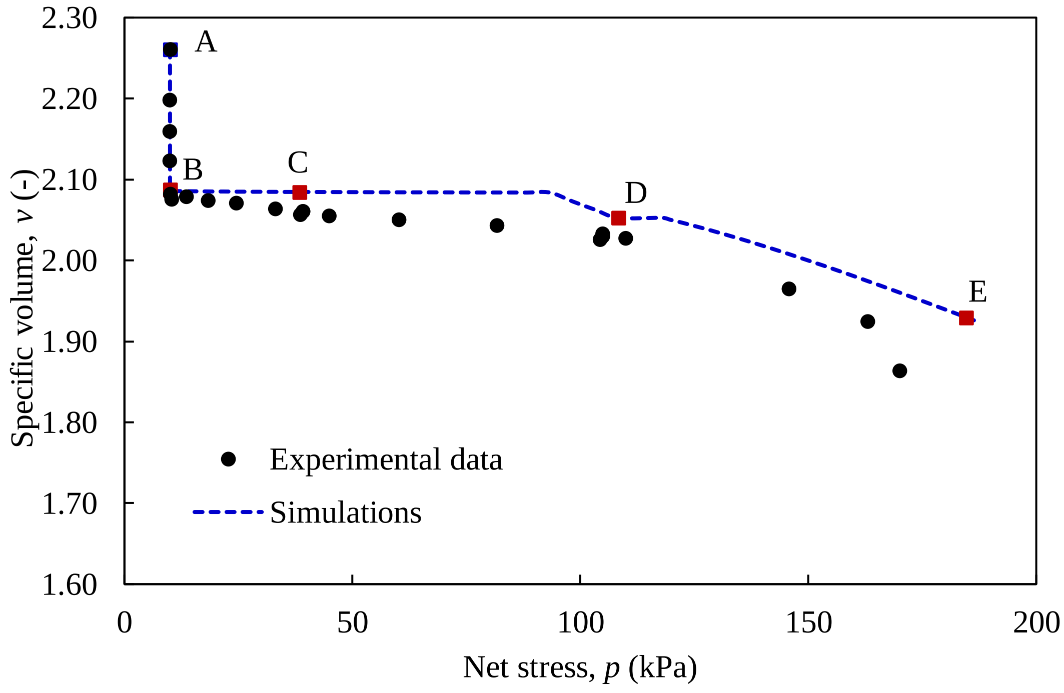

(a)

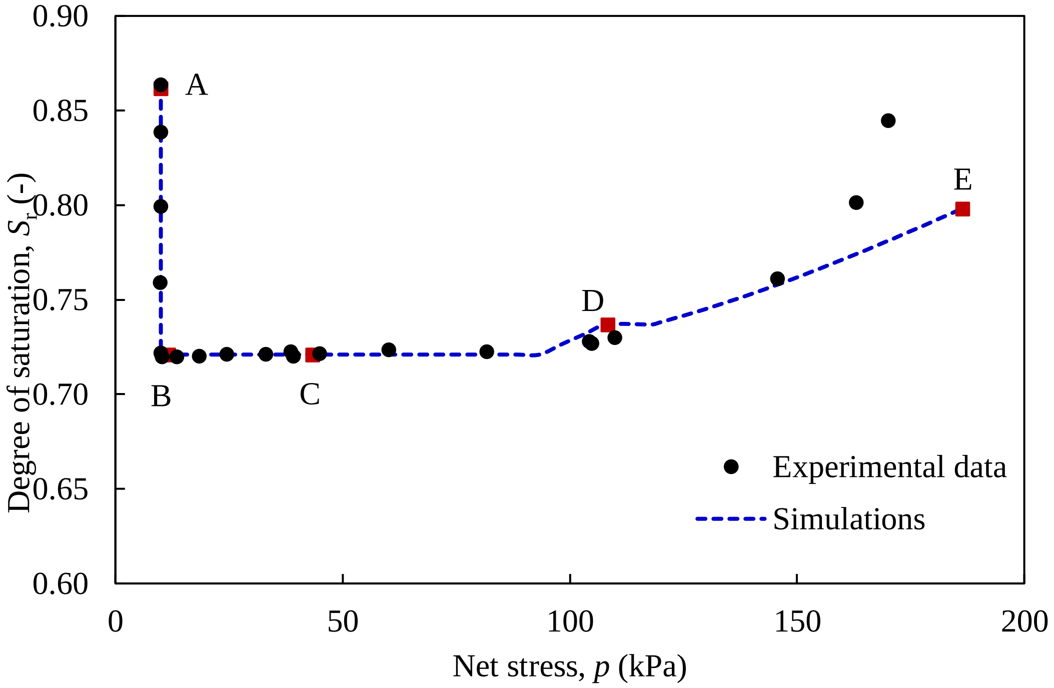

(b)

Figure 7.14: Comparison of stress paths on (a)(v, p) plane; (b)(S_r, p) plane

Table 7.8: Experimental validation B9

Stage			Net stress (p/kPa)	Suction (s/kPa)	Shear stress (q/kPa)
A	B	Drying	10	5→300	0
B	C	Shearing	10→ 40	300	0 → 85
A	B	Loading	40→110	300	85
B	C	Shearing	110 → 170	300	85 → 290

7.4.3 Stress paths by Casini (2008) and D'Onza et al. (2011)

The developed governing equations were used for the simulation of shearing stress paths at element level (constant suction) for the experiments by Casini (2008) for compacted Jossinny silt. A number of sophisticated experimental results were reported for various combinations of triaxial, isotropic, anisotropic and K_o loading (loading, unloading, wetting and drying) stress paths performed on compacted Jossingy silt (LL=32%, PL=16%). The samples were statically compacted at 23% moisture content, with pressures ranging from 150 kPa to 200 kPa. The targeted ρ of the compacted samples was 14.5kN/m^3. Initial equalisation was performed to reach the targeted initial stress values, and the test stress paths were completed after equalisation. In the following sections, MPK critical state model predictions for three tests are illustrated, including a combination of triaxial (constant suction, constant water content) and anisotropic stress paths with the respective experimental results. In addition, a blind test by D'Onza et al. (2011) was also simulated, and several unsaturated constitutive model behaviours were compared.

7.4.3.1 Suction-controlled anisotropically consolidated triaxial test

Casini (2008) performed four anisotropically-consolidated triaxial tests for four different η values, i.e. η = 1 (Tx03 in Figure 7.15), η = 0.375 (Tx04 in Figure 7.16), η = 0.75 (Tx08 in Figure 7.17) and η = 0.875 (Tx09 in Figure 7.18). Test Tx03 was a controlled isotropic compression (i.e. η = 1) test which started with an equalisation pressure of 200 kPa suction, and 20 kPa mean net stress. As shown in Figure 7.15, upon loading simulation, yielding was observed at 170 kPa net stress, which agrees reasonably well with the experiments. Test Tx04 was a controlled anisotropic compression test which started with equalisation pressures of s = 200 kPa, p = 20 kPa and q =10 kPa, as given in Figure 7.16. Upon anisotropic loading (η =0.375), yielding was observed at 80 kPa net stress in the simulations, although in the experiments yielding lagged. The next test Tx08 was an anisotropically-controlled compression test which started with s = 200 kPa suction, p = 30 kPa and q =20 kPa. Upon anisotropic loading (η =0.75), yielding was observed at 75 kPa net stress in the simulations. The simulations under-estimated the v and S_r as shown in Figure 7.17. The equalisation of Tx09 under anisotropic stress state (η =0.875) corresponds to p = 22 kPa and s = 200 kPa. As Figure 7.18, the sample was subsequently loaded anisotropically until the mean net stress reached 370 kPa. The simulation of v and S_r with p followed the experimental results and showed reasonable agreement with the experimental results.

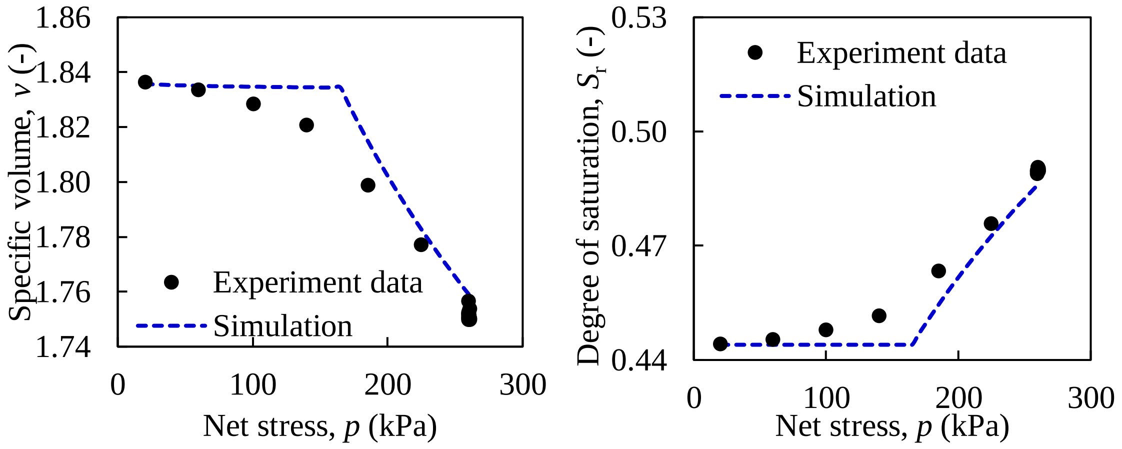

(a) (b)

Figure 7.15: Comparison of suction-controlled anisotropically (Tx03 - η =1, isotropic) consolidated triaxial test on: (a)(v, p) plane; (b)(S_r, p) plane

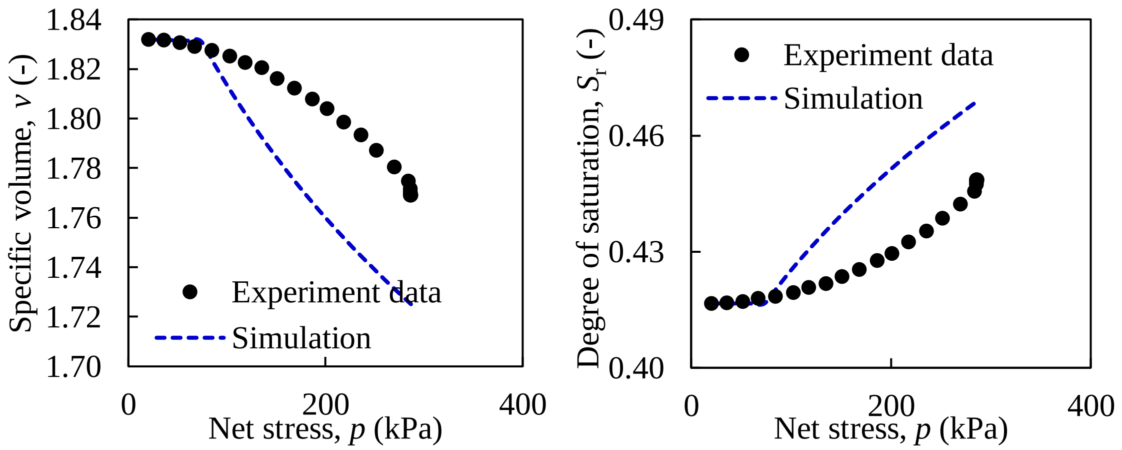

(a) (b)

Figure 7.16: Comparison of suction-controlled anisotropically (Tx04 - η =0.375) consolidated triaxial test on (a)(v, p) plane; (b)(S_r, p) plane

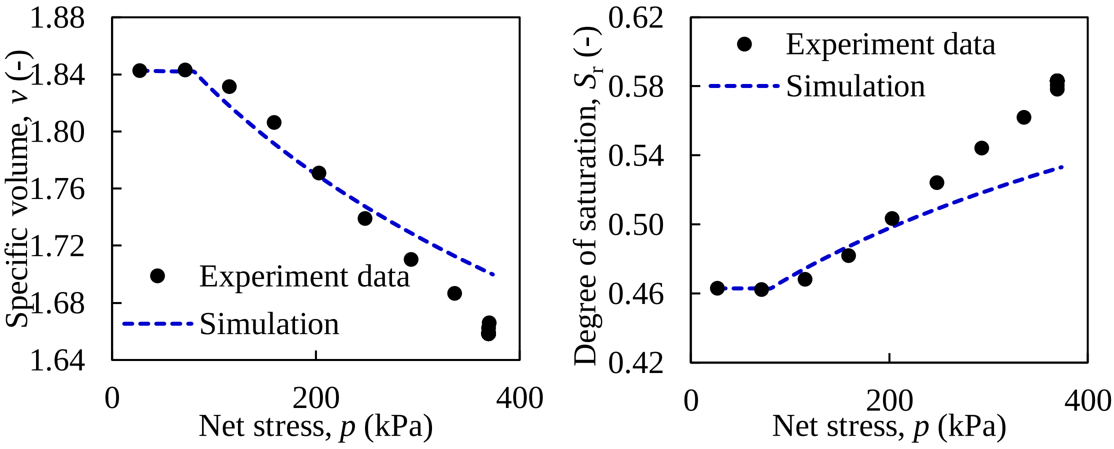

Figure 7.17: Comparison of suction-controlled anisotropically (Tx08 - η =0.75) consolidated triaxial test on (a)(v, p) plane; (b)(S_r, p) plane

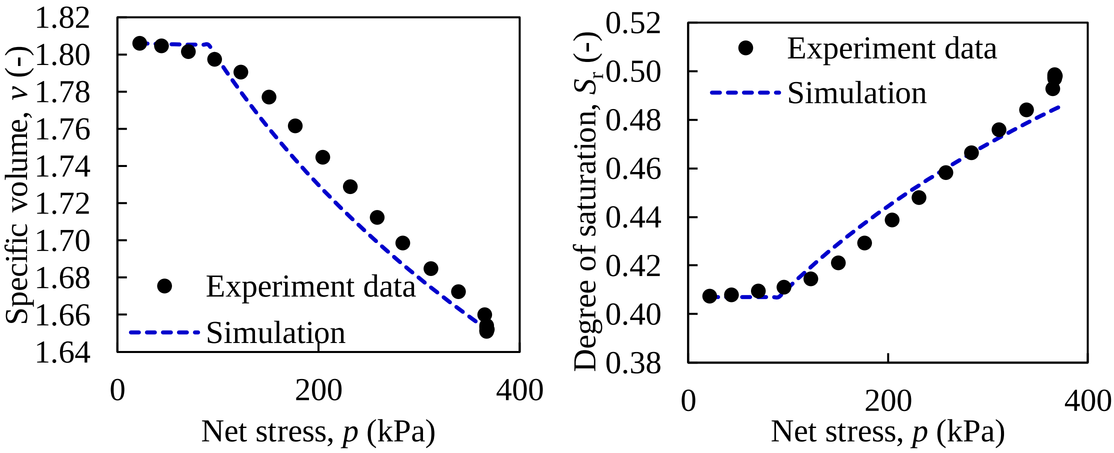

Figure 7.18: Comparison of suction-controlled anisotropically (Tx09 - η =0.875) consolidated triaxial test on (a) v, p plane; (b) S_r, p plane

7.4.3.2 Triaxial tests

7.4.3.2.1 Tx06 suction-controlled anisotropically-consolidated triaxial test

Test TX06 was initially equalised at a mean net stress of 20 kPa and suction of 200 kPa prior to anisotropic loading with η =0.75. The sample subsequently sheared (η =3) at a constant suction of 200 kPa. The experimental data, as well as the model simulations, are plotted in Figure 7.19, and the simulated and experimental paths exhibit reasonable agreement.

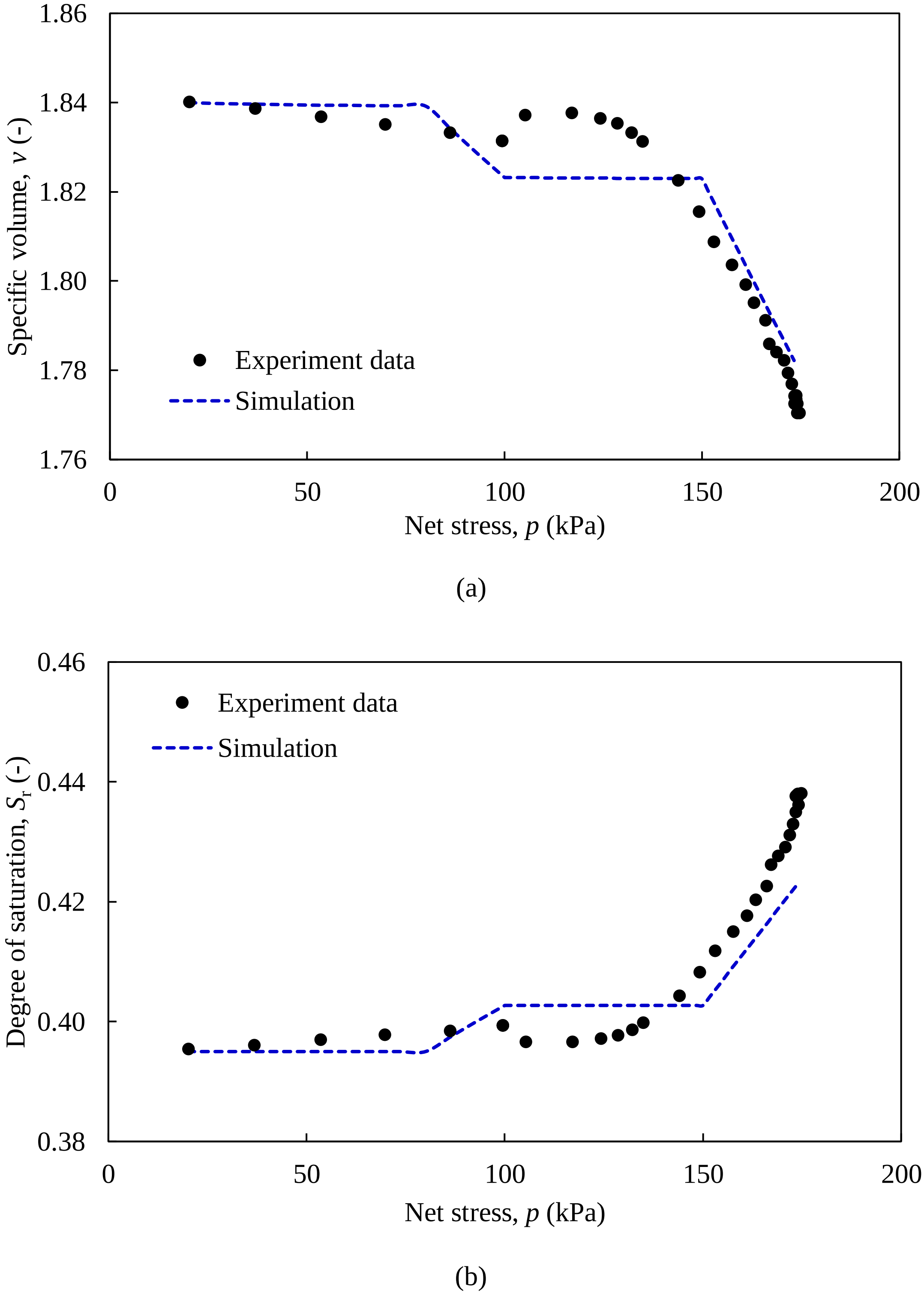

Figure 7.19: Comparison of suction-controlled anisotropically-consolidated triaxial test on (a) v, p plane; (b) S_r, p plane

7.4.3.2.2 Tx07 Suction-controlled anisotropically-consolidated triaxial test

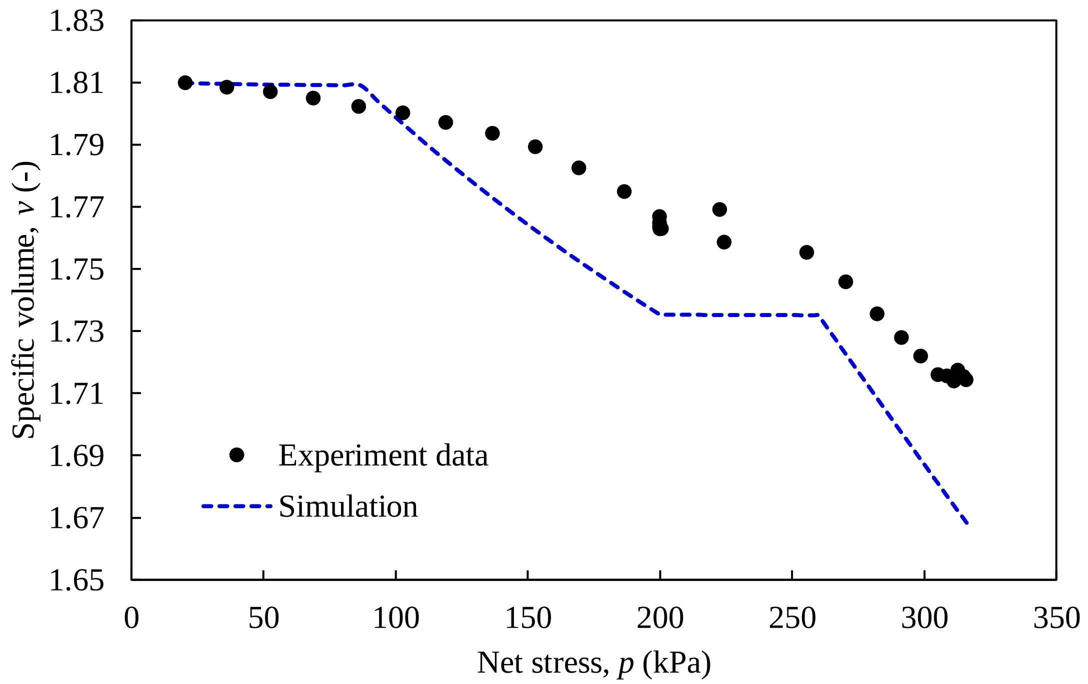

(a)

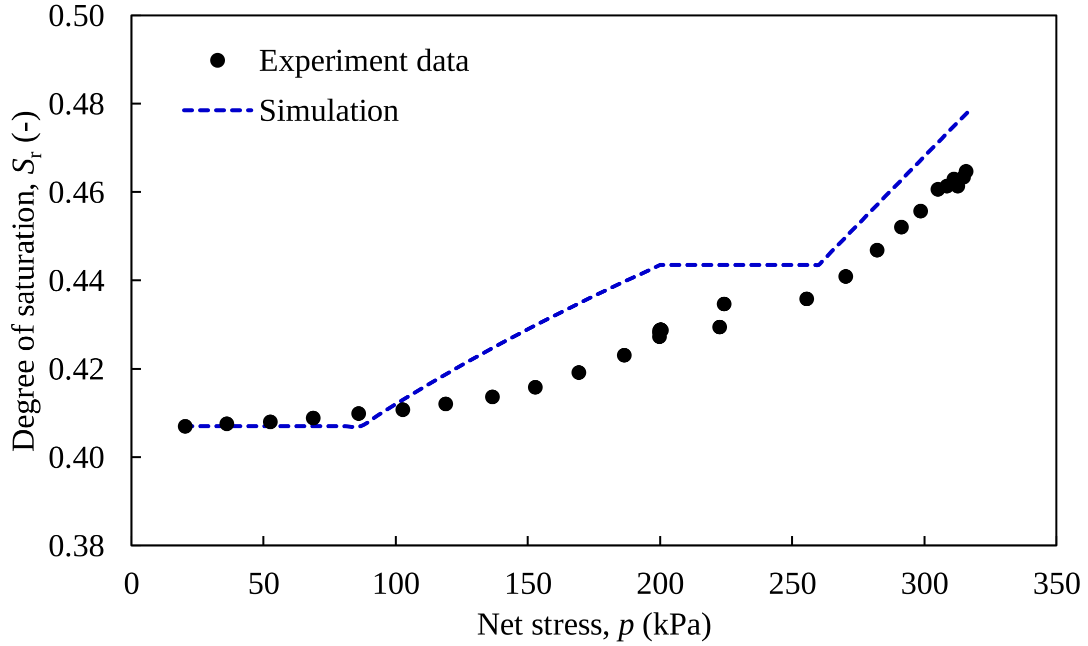

(b)

Figure 7.20: Comparison of suction-controlled anisotropically-consolidated triaxial test on (a) v, p *plane; (b)* S_r, p *plane*

Test Tx07 was an anisotropically-controlled consolidated triaxial test which started with equalisation pressures of s = 200 kPa and p = 20 kPa (see Figure 7.20). Upon anisotropic loading (η =0.75), yielding was observed at 75 kPa net stress in simulations. Then, upon shearing, initially in experiments, an increase in v and a decrease in S_r were observed. However, in this instance, the model simulations deviated slightly from the experiments, possibly due to the over-estimation of the compression index ($\lambda(S_r)$) or experimental errors.

7.4.3.3 Blind test (isotropic loading and constant water-content shearing)

After equalisation at q =0 kPa, p = 20 kPa and s =100 kPa, the sample was isotopically loaded prior to constant water-content shearing (Figure 7.21). The total experimental stress path and simulation for the blind test are compared in Figure 7.22. The simulated and experimental paths exhibit reasonable agreement up to 150 kPa and subsequent constant water content shearing.

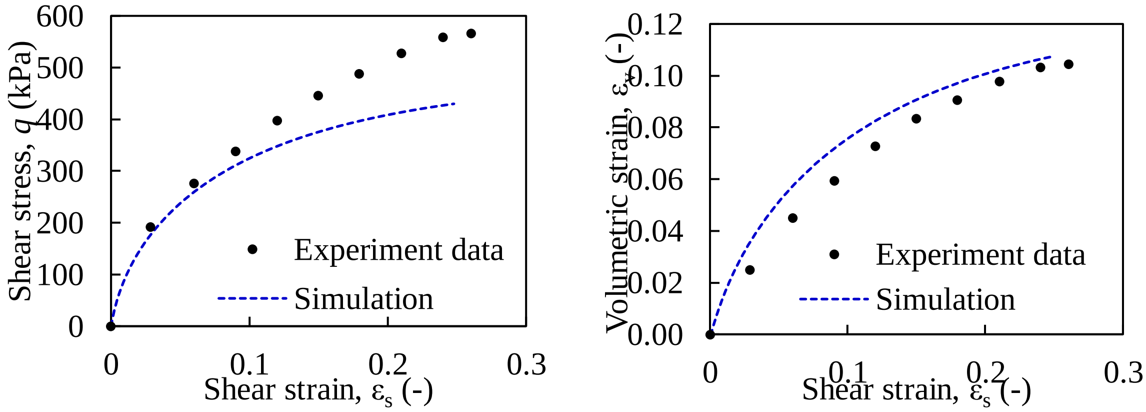

(a) (b)

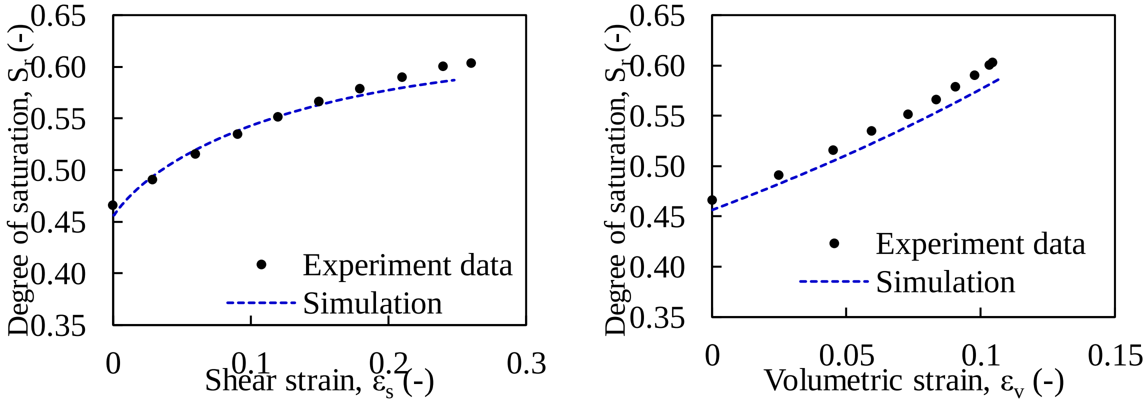

(c) (d)

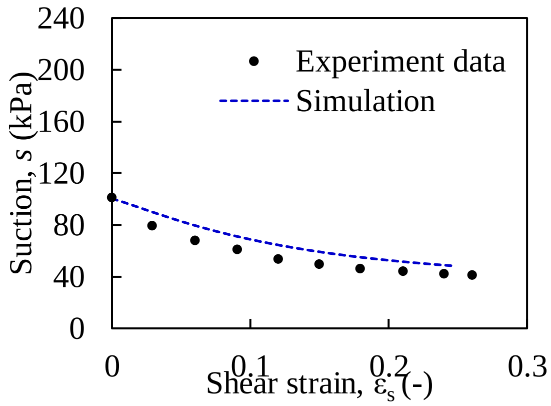

(e)

Figure 7.21: Comparison of blind test shearing path on (a) q, ε_s plane; (b) $\varepsilon_v, \varepsilon_s$ plane; (c) S_r, ε_s plane; (d) S_r, ε_v plane; (e) s, ε_s plane

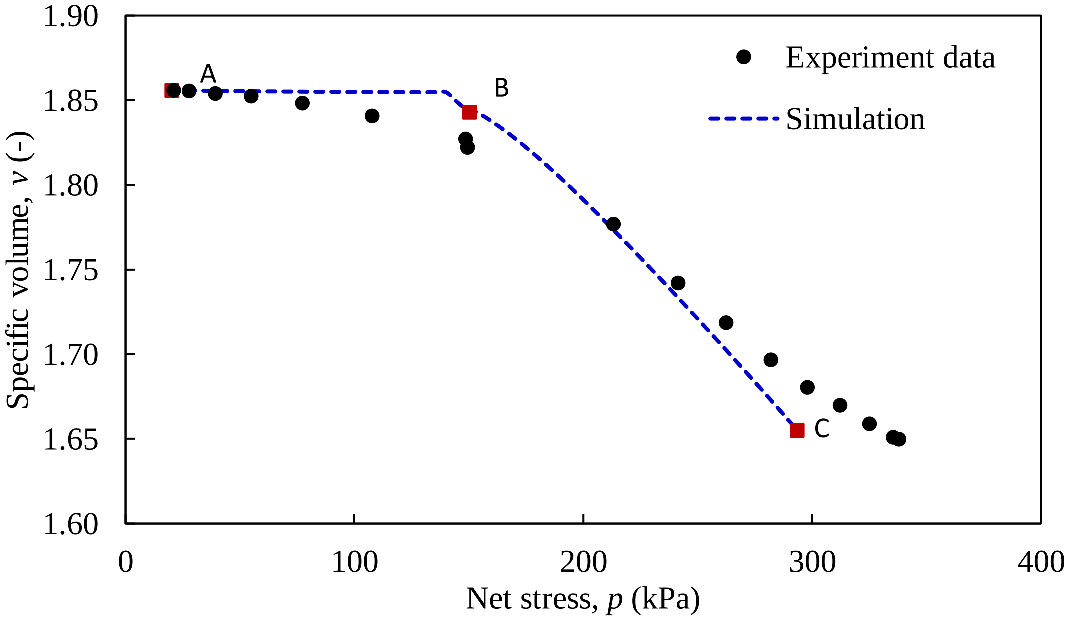

(a)

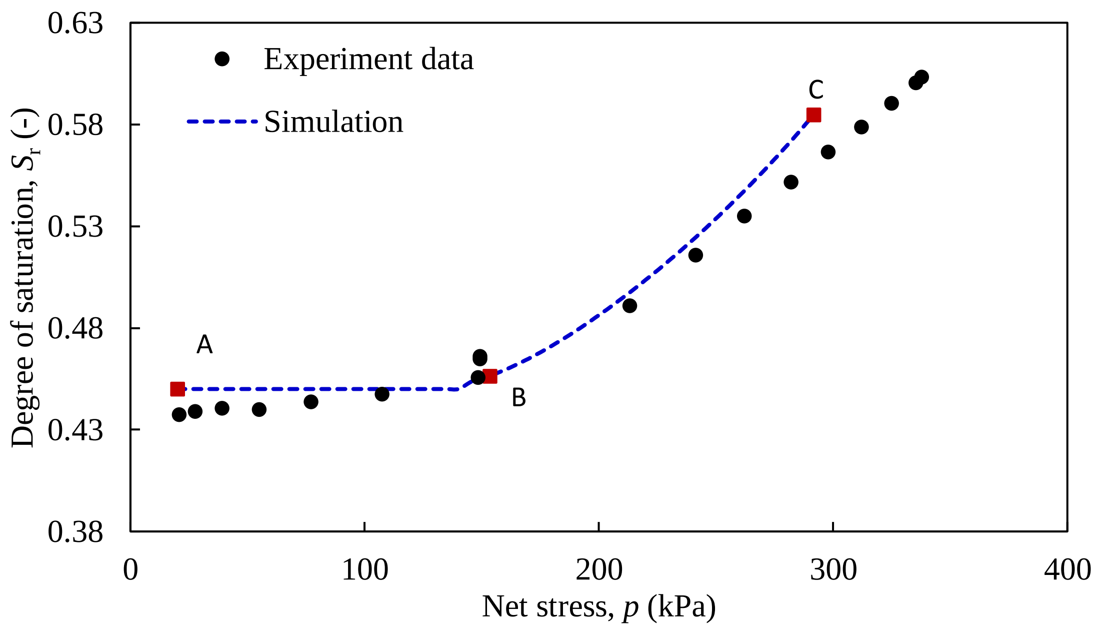

(b)

Figure 7.22: Comparison of constant water-content shearing on (a) v, p *plane; (b)* S_r, p *plane*

7.5 Conclusion

Kodikara et al. (2019) postulated a generalised Monash-Kodikara-Peradeniya (MPK) framework for the isotropic stress state by considering the accumulation of stress strains on wetting and drying cycles. The newly-developed critical state constitutive model becomes part of the MPK generalised model, making it applicable to both volumetric and shear simulations. The formulation of the critical state model was carried out assuming MCC principles. Due to its simplicity and the assumption of associative behaviour, only two parameters (G, M) are introduced. These two parameters can be found easily by experimentation. However, it has been found that the M parameter depends either on the suction or the degree of saturation. This has not been incorporated in the current model, and the future extensions need to consider this aspect.

A range of experiments on compacted kaolin experiments by Raveendiraraj (2009) and Abeyrathne (2017) on compacted Jossinny silt by Casini (2008) was analysed in this chapter, including some isotropic stress paths. Both constant suction and constant water content shearing stress path simulations showed reasonable agreement with the experimental results. However, experiment Tx06 by Casini (2008), includes an anisotropic compression stress path, which could not be simulated very successfully. As suggested by Stropeit et al. (2008), a modification to the yield surface may need to be considered to cater for anisotroipc loading in future studies. In addition, the prediction of high over-consolidation behaviour is not captured by the current proposed model. Such behaviour may be captured by implementing the theory proposed by Zhou and Sheng (2015).

7.6 References

Abeyrathne, A., Sivakumar, V. & Kodikara, J. 2019. Isotropic Volumetric Behaviour of Compacted Unsaturated Soils within (v, v w, p) Space. *Canadian Geotechnical Journal*.

Abeyrathne, W. K. a. P. 2017. *A new modelling approach for compacted clayey soils using specific water volume as a state variable.* Ph.D. thesis, Monash University, Melbourne, Australia.

Alonso , E. E., Gens , A. & Josa, A. 1990. A constitutive model for partially saturated soils. *Géotechnique,* 40(3)**,** pp.405-430.

Casini, F. 2008. Effetti del grado di saturazione sul comportamento meccanico di un limo. *Dottorato di Ricerca in Ingegneria Geotecnica."Sapienza" Universit'a degli Studi di Roma*.

Fredlund, D., Morgenstern, N. R. & Widger, R. 1978. The shear strength of unsaturated soils. *Canadian geotechnical journal,* 15**,** 313-321.

Houlsby, G. 1997. The work input to an unsaturated granular material. *Géotechnique,* 47**,** 193-196.

Khalili, N. & Khabbaz, M. 1998. A unique relationship of chi for the determination of the shear strength of unsaturated soils. *Geotechnique,* 48**,** 681-687.

Kodikara, J. 2012. New framework for volumetric constitutive behaviour of compacted unsaturated soils. *Canadian Geotechnical Journal,* 49**,** 1227-1243.

Kodikara, J., Jayasundara, C. & Zhou, A. 2019. A generalised constitutive model for unsaturated compacted soils considering wetting/drying cycles and environmentally stabilised line.

Loret, B. & Khalili, N. 2002. An effective stress elastic–plastic model for unsaturated porous media. *Mechanics of Materials,* 34**,** 97-116.

Ng, C. W., Springman, S. M. & Alonso, E. E. 2008. Monitoring the performance of unsaturated soil slopes. *Laboratory and Field Testing of Unsaturated Soils.* Springer.

Raveendiraraj, A. 2009. *Coupling of mechanical behaviour and water retention behaviour in unsaturated soils.* Ph.D. thesis, University of Glasgow.

Sheng, D., Zhang, S. & Yu, Z. 2013. Unanswered questions in unsaturated soil mechanics. *Science China Technological Sciences,* 56**,** 1257-1272.

Sivakumar, V. 1993. *A critical state framework for unsaturated soil.* Ph.D. thesis, University of Sheffield.

Stropeit, K., Wheeler, S. & Cui, Y. 2008. An anisotropic elasto-plastic model for unsaturated soils.

Wheeler, S., Sharma, R. & Buisson, M. 2003. Coupling of hydraulic hysteresis and stress–strain behaviour in unsaturated soils. *Géotechnique,* 53**,** 41-54.

Wheeler, S. & Sivakumar, V. 1995. An elasto-plastic critical state framework for unsaturated soil. *Géotechnique,* 45**,** 35-53.

Zhou, A. 2017. Modelling hydro-mechanical behavior for unsaturated soils. *Japanese Geotechnical Society Special Publication,* 5**,** 79-94.

Zhou, A. & Sheng, D. 2015. An advanced hydro-mechanical constitutive model for unsaturated soils with different initial densities. *Computers and Geotechnics,* 63**,** 46-66.

CHAPTER 8

Conclusions and recommendations for future studies

8 Summary of the research

The Monash-Peradeniya-Kodikara (MPK) framework is based on traditional compaction curves, where suction is treated as a dependent variable in the (v, v_w, p) space. Considering Houlsby (1997) unsaturated soil working equation, the selected variables of the MPK framework are the specific volume (v), mean net stress (p) and specific water volume (v_w), without the linked consideration of the degree of saturation (S_r) or suction (s). The MPK framework has been validated against a large number of experiments for the 1-D stress state (Islam, 2015; Islam and Kodikara, 2015; Kodikara et al., 2015) and the isotropic stress state (Abeyrathne, 2017; Abeyrathne et al., 2019). The framework has also been extended to the triaxial stress state and validated for compacted kaolin (Abeyrathne (2017). The parameters of the MPK framework for volumetric and triaxial behaviour can be obtained by simple water content tests.

The original MPK framework is considered to be a partial theory since it does not couple the soil water retention curve (SWRC). Because of the simplicity and practical application of the MPK framework, the main aim of the present research was to develop a generalised model for unsaturated compacted soils by coupling hydraulic and mechanical behaviour incorporating the effects of environmental stabilisation and strain accumulation on wet-dry cycles and extending it to model shear behaviour. The research had six main objectives to accomplish the main aim. These were:

a) to identify the phenomenological observations of unsaturated soils in the isotropic stress state and triaxial stress state and to determine the interpretation of these features in the MPK framework;
b) to develop a generalised model incorporating environmental stabilisation in the MPK framework to capture the accumulation of plastic strain and the structural stabilisation of wet/dry cycles;
c) to formulate a set of theoretical equations to represent general constitutive isotropic behaviour, guided by the past phenomenological observations and theory and validation based on existing data available in the research literature;
d) to conduct an experimental program for fthe urther verification and refinement of the proposed model at the element level; and

e) to formulate a set of theoretical equations to represent triaxial behaviour, guided by past phenomenological observations and theory and validation based on existing data available in the research literature.

As identified in the literature review, phenomenological observations of the volumetric and triaxial responses of unsaturated soils have not been considered fully in most recent constitutive models. Hence, motivated by the MPK framework proposed by Kodikara (2012), a generalised constitutive model was proposed, on the basis of constant water-content testing. The main features of the model are an environmentally-stabilised line representing the states achieved after a large number of wetting/drying cycles, a constant plastic volumetric strain-based LC yield curve and a soil water retention curve. The MPK generalised model has fifteen parameters, including nine parameters for mechanical behaviour. These nine mechanical parameters can be determined by relatively simple constant water-content tests, which are a significant advantage of the model. The evolution of the plastic-strain-based SWRCs involves six parameters, some of which require calibration through traditional SWRC testing under constant net stress. The equations for coupled hydro-mechanical behaviour were developed considering Bishop's effective stress for the wet side of the air transition line and independent stress for the dry side of the air transition line, and the stress/strain conjugates were finally transformed to Bishop's effective stress approach for the overall behaviour. The derived equations for the isotropic stress state were validated by reproducing a range of phenomenological observations, and the generalised MPK model is capable of reproducing most observed phenomenological behaviour, at least qualitatively.

A series of loading/unloading experiments was carried out in the isotropic stress state to establish the uniqueness of LWSBS upon drying. It has been observed that the LWSBS is unique, not only for major wetting but also states after major drying. In addition, several other experiments were carried out to capture the strain accumulation through a minimum of four wet-dry cycles, and these were successfully simulated by the proposed model.

The MPK generalised model was then extended to the triaxial stress state based on critical stress state concepts. Although isotropic stress state equations were proposed in the net stress space, the final constitutive equations of triaxial stress state were formed in the Bishop's effective stress space. The corresponding yield surface of the loading collapse curve was generalised to the deviatoric stress state by incorporating the modified cam clay model. Only two material parameters were introduced for the extension of the model to the triaxial stress state. The performance of the postulated critical state model was then evaluated through a series of experiments, including constant suction, constant water content shearing and shearing in anisotropically-loaded shearing tests. The constant suction shearing experiments included isotropic stress paths (loading, unloading, wetting and drying), and the model simulations agreed reasonably well with the experiments, some of which were very complex.

8.1 Summary of thesis

8.1.1 Chapter 1 – Introduction

The current understanding of and knowledge gaps in the constitutive modelling of unsaturated soil were outlined in Chapter 1. In addition, the aim and objectives of the thesis were introduced.

8.1.2 Chapter 2 - Literature review

Chapter 2 provided a brief overview of unsaturated soil mechanics in relation to the constitutive modelling of the hydro-mechanical behaviour of unsaturated soils. The comprehensive literature review identified the gaps in the current state-of-the-art of constitutive modelling of unsaturated soils based on phenomenological observations.

8.1.3 Chapter 3 – Review of the MPK framework and related phenomenological observations

Phenomenological observations of unsaturated soils are scattered and sometimes not highlighted in the constitutive modelling of unsaturated soils. Hence, in Chapter 3, phenomenological observations of volumetric and triaxial responses and associated behaviours were compiled, taking into consideration the soil type and initial state. A total of 25 phenomenological observations were identified for isotropic responses, whereas 11 phenomenological observations were identified for triaxial behaviour. These observations were taken into consideration for future advancements in unsaturated soil constitutive modelling.

8.1.4 Chapter 4 - Development of the MPK generalised model: isotropic stress state

Motivated by the MPK framework, a generalised constitutive model was postulated for the isotropic stress state considering stress-strain accumulation through wet-dry cycles and environmental stabilisation. The proposed model has numerous attractive features, including, in particular, a constant-moisture-content-testing-based yield surface or volumetric yield surface, a plastic strain-based LC curve and SWRC, the air transition line (ATL) to demarcate the continuity of the air and water phases, the environmentally-stabilised line (ESL) to represent states achieved after wetting/drying cycles, and the use of Bishop's effective stress and conjugate strains to serve the hydro-mechanical energetics allowing for the transition from unsaturated to saturated behaviour. The mechanical behaviour of the model has 9 parameters which can be determined by relatively simple testing. The evolution of the plastic-strain-based SWRCs involves 6 parameters, some of which require calibration by traditional SWRC testing under constant net stress. The generalised MPK model is capable of capturing the general characteristics of unsaturated behaviour, and typical features of the model were explained .

8.1.5 Chapter 5 - Materials, methods, and experimental results

The uniqueness of the yield surface through drying loading stress paths was validated, as previous research on the MPK framework was based only on loading/unloading and wetting stress paths. Based on experiments performed (1) an increase in yield stress during loading after drying in comparison to loading prior to drying was observed; (2) during yielding, a similar pattern of stress paths was found with or without drying. The second aim was to identify the possibility of an environmentally-stabilised state through several wet-dry cycles. However, it was possible to complete only one test during this study, and further experiments are proposed.

8.1.6 Chapter 6 – Validation of the isotropic stress state

The application of the generalised MPK constitutive model for unsaturated soils to simulate volumetric behaviour with a combination of stress paths was discussed in Chapter 6. First, the derived equations were validated against test series performed in this study, and reasonable agreement was observed in all ten tests. Next, the ability of the generalised MPK model to reproduce observed phenomenological behaviour was validated against several experiments on kaolin by Raveendiraraj (2009); Abeyrathne (2017) and on an expansive kaolin bentonite mixture by Sharma (1998).

8.1.7 Chapter 7 – Theoretical development and validation of triaxial behaviour

A critical state extension of the MPK generalised model was developed considering the modified cam clay principles and introducing only two extra parameters, G and M. The G

and M parameters can easily be found by triaxial experiments. The validation of the proposed critical state model was performed on tests by Raveendiraraj (2009) and Abeyrathne (2017) for compacted kaolin. A range of stress paths was successfully analysed, including some isotropic stress paths.

8.2 Suggestions for future research

The following section provides some recommendations for future research, based on the research undertaken to date.

- The main focus of this research is compacted kaolin, a compacted kaolin-bentonite mixture and compacted Jossingy silt. Further research can be undertaken to validate the model for various soil types, including in particular, sands, silts and expansive clays. Since the compaction curve is common to all soil types, it is considered that the concepts developed are valid with some modifications.
- Due to its simplicity and the assumption of associative behaviour, only two parameters (G, M) are introduced. These two parameters can easily be found by experimentation. However, it has been found that the M parameter depends available on the suction or the degree of saturation. This has not been incorporated in the current model, and future extensions will consider this aspect.
- The dependency of the hydric coefficient on net stress is highlighted by Kodikara (2012), although the current model does not incorporate this effect. Hence, in the future, it would be appropriate if the change in mean net stress can take the hydric coefficient into consideration
- In future research, the possible evolution of the n parameter with plastic volumetric strain should be further analysed.
- A series of laboratory experiments are recommended to validate the volumetric and triaxial behaviour of unsaturated soil upon wet-dry cycling with a lesser sample height as single drainage set up requires a longer time for equilibrium. Besides, it is recommended to use silty soil as equilibrium reach sooner compared to the kaolin used in this thesis.
- Further refinement of the calibration of SWRC should also be carried out for a better understanding of the associated behaviour of coupling behaviour through constant plastic dependent strain.

- As suggested by Stropeit et al. (2008), a modification to the current yield surface should be adopted in order to capture anisotropic behaviour, and sub-loading concepts should be incorporated in constitutive modelling to capture high over-consolidation behaviour. The MPK generalised critical state model can be modified utilising the theory proposed by Zhou and Sheng (2015), incorporating sub-loading concepts and a unified hardening parameter.
- The ability of the bound surface plasticity theory to capture unsaturated soil behaviour to tackle cyclic external loading should also be studied for the future refinement of the model. This extension would allow the application of the MPK model to field processes such as intelligent compaction and pavement design.
- Finite element implementation of the MPK generalised model is required to model general geotechnical field problems.
- As discussed in Appendix D, proximal soil sensing techniques can be integrated with the proposed model to envision a finite element model in the future to study the behaviour of geo-infrastructures.

8.3 References

Abeyrathne, A., Sivakumar, V. & Kodikara, J. 2019. Isotropic Volumetric Behaviour of Compacted Unsaturated Soils within (v, v w, p) Space. *Canadian Geotechnical Journal*.

Abeyrathne, W. K. a. P. 2017. *A new modelling approach for compacted clayey soils using specific water volume as a state variable.* Ph.D. thesis, Monash University, Melbourne, Australia.

Houlsby, G. 1997. The work input to an unsaturated granular material. *Géotechnique,* 47**,** 193-196.

Islam, M. 2015. *A study of volumetric behaviour of compacted clayey soils in the void ratio, moisture ratio and net stress space.* Monash University. Faculty of Engineering. Department of Civil Engineering.

Islam, T. & Kodikara, J. 2015. Interpretation of the loading–wetting behaviour of compacted soils within the “MPK” framework. Part I: Static compaction 1. *Canadian Geotechnical Journal,* 53**,** 783-805.

Kodikara, J. 2012. New framework for volumetric constitutive behaviour of compacted unsaturated soils. *Canadian Geotechnical Journal,* 49**,** 1227-1243.

Kodikara, J., Islam, T. & Rajeev, P. 2015. Interpretation of the loading–wetting behaviour of compacted soils within the “MPK” framework. Part II: Dynamic compaction 1. *Canadian Geotechnical Journal,* 53**,** 806-827.

Raveendiraraj, A. 2009. *Coupling of mechanical behaviour and water retention behaviour in unsaturated soils.* Ph.D. thesis, University of Glasgow.

Sharma, R. S. 1998. *Mechanical behaviour of unsaturated highly expansive clays.* Ph.D. thesis, University of Oxford.

Stropeit, K., Wheeler, S. & Cui, Y. 2008. An anisotropic elasto-plastic model for unsaturated soils.

Zhou, A. & Sheng, D. 2015. An advanced hydro-mechanical constitutive model for unsaturated soils with different initial densities. *Computers and Geotechnics,* 63**,** 46-66.

Appendix

1 Appendix A: Derivation of the elastic surface

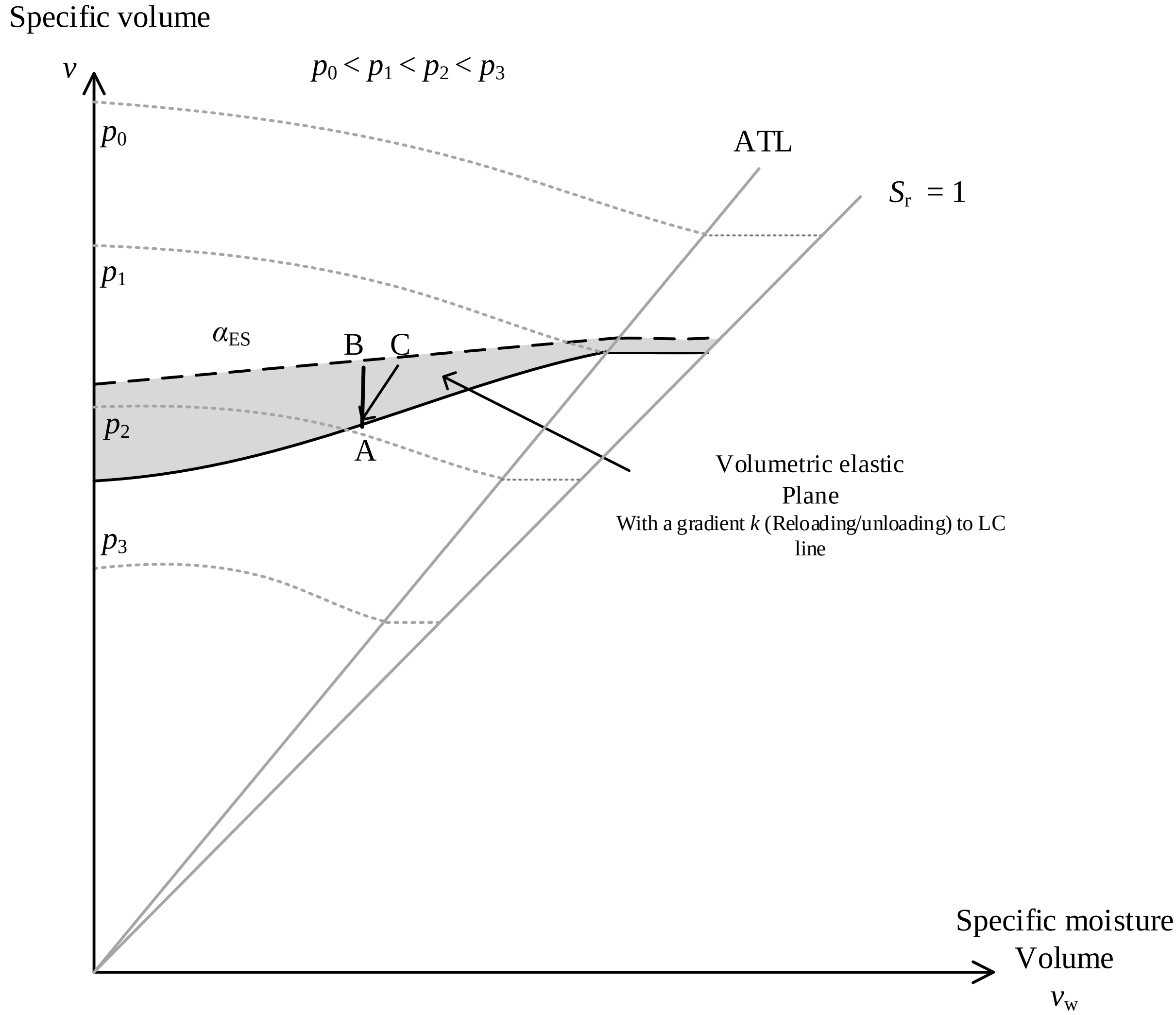

Figure A1: volumetric elastic plane in the (v, v_{w}, p) space

Considering *A*, *B* and *C* point coordinates,

$$A = \begin{bmatrix} v_{\mathrm{w}}^{1} \\ v^{1} \\ \ln(p_{\mathrm{y}}) \end{bmatrix}, B = \begin{bmatrix} v_{\mathrm{w}}^{1} \\ v_{0,\mathrm{uL}}^{1} \\ \ln(p_{\mathrm{o}}) \end{bmatrix} \text{ and } C = \begin{bmatrix} v_{\mathrm{w}}^{2} \\ v_{0,\mathrm{uL}}^{2} \\ \ln(p_{\mathrm{o}}) \end{bmatrix}$$

Considering constant specific moisture volume unloading and reloading,

$$v = v_{\mathrm{o,uL}} - \kappa(v_{\mathrm{w}})\ln(p / p_{\mathrm{o}}) \tag{A 1}$$

Equation (A 1) for *A* and *B*,

$$v^1 = v^1_{\mathrm{o,uL}} - \kappa(v_{\mathrm{w}})\ln(p_{\mathrm{y}} / p_{\mathrm{o}}) \tag{A 2}$$

Considering the gradient of the environmentally-stabilised line,

$$\alpha_{\mathrm{ES}} = \frac{v^{\mathrm{L}}_{\mathrm{o,uL}} - v_{\mathrm{o,uL}}}{v^{\mathrm{L}}_{\mathrm{w}} - v_{\mathrm{w}}} \tag{A 3}$$

Equation (A 3) for *B* and *C*,

$$\alpha_{\mathrm{ES}} = \frac{v^2_{\mathrm{o,uL}} - v^1_{\mathrm{o,uL}}}{v^2_{\mathrm{w}} - v^1_{\mathrm{w}}} \tag{A 4}$$

Vector $\overrightarrow{BA}$ and $\overrightarrow{BC}$,

$$\overrightarrow{BA} = \vec{A} - \vec{B} = \begin{bmatrix} 0 \\ v^1 - v^1_{0,\mathrm{uL}} \\ \ln(p_{\mathrm{y}} / p_{\mathrm{o}}) \end{bmatrix} = \begin{bmatrix} 0 \\ -\kappa(v_{\mathrm{w}})\ln(p_{\mathrm{y}} / p_{\mathrm{o}}) \\ \ln(p_{\mathrm{y}} / p_{\mathrm{o}}) \end{bmatrix} \tag{A 5}$$

$$\overrightarrow{BC} = \vec{C} - \vec{B} = \begin{bmatrix} v^2_{\mathrm{w}} - v^1_{\mathrm{w}} \\ v^2_{0,\mathrm{uL}} - v^1_{0,\mathrm{uL}} \\ 0 \end{bmatrix} = \begin{bmatrix} v^2_{\mathrm{w}} - v^1_{\mathrm{w}} \\ \alpha_{\mathrm{ES}}\left(v^2_{\mathrm{w}} - v^1_{\mathrm{w}}\right) \\ 0 \end{bmatrix}$$

Normal vector, $\vec{n} = \overrightarrow{BC} \times \overrightarrow{AB}$,

$$\vec{n} = \begin{bmatrix} 0 \\ -\kappa(v_{\mathrm{w}})\ln(p_{\mathrm{y}} / p_{\mathrm{o}}) \\ \ln(p_{\mathrm{y}} / p_{\mathrm{o}}) \end{bmatrix} \times \begin{bmatrix} v^2_{\mathrm{w}} - v^1_{\mathrm{w}} \\ \alpha_{\mathrm{ES}}\left(v^2_{\mathrm{w}} - v^1_{\mathrm{w}}\right) \\ 0 \end{bmatrix} = \left[\alpha_{\mathrm{ES}} i - j + \kappa(v_{\mathrm{w}})k\right]\left(v^2_{\mathrm{w}} - v^1_{\mathrm{w}}\right)\ln(p_{\mathrm{y}} / p_{\mathrm{o}})$$

The equation of a plane can be written as follows:

$$a(x - x_0) + b(y - y_0) + c(z - z_0) = 0$$

Therefore, the equation of the plane considering normal vector and point *A* can be written as:

$$\alpha_{\mathrm{ES}}(v_{\mathrm{w}} - v^1_{\mathrm{w}}) - (v - v_1) + \kappa(v_{\mathrm{w}})\ln(p / p_{\mathrm{y}}) = 0 \tag{A 6}$$

The equation of the S_{r} constant plane can be written as:

$$v = \frac{v_{\mathrm{w}} - 1}{S_{\mathrm{r}}} + 1 \tag{A 7}$$

Solving Equations (B 8) and (B 9) gives the constant S_{r} unloading reloading line,

$$\alpha_{\mathrm{ES}}(v_{\mathrm{w}} - v_{\mathrm{w}}^{1}) - (\frac{v_{\mathrm{w}} - 1}{S_{\mathrm{r}}} + 1 - v_{1}) + \kappa(v_{\mathrm{w}})\ln(p / p_{\mathrm{y}}) = 0 \quad \text{(B 8)}$$

$$\left(\alpha_{\mathrm{ES}} - \frac{1}{S_{\mathrm{r}}}\right)v_{\mathrm{w}} - \alpha_{\mathrm{ES}}v_{\mathrm{w}}^{1} - (-\frac{1}{S_{\mathrm{r}}} + 1 - v_{1}) + \kappa(v_{\mathrm{w}})\ln(p / p_{\mathrm{y}}) = 0 \quad \text{(B 9)}$$

Considering the $v_{\mathrm{w}} = S_{\mathrm{r}}(v-1)+1$ relationship,

$$\left(\alpha_{\mathrm{ES}} - \frac{1}{S_{\mathrm{r}}}\right)\left(vS_{\mathrm{r}} - S_{\mathrm{r}} + 1\right) - \alpha_{\mathrm{ES}}v_{\mathrm{w}}^{1} - \left(1 - \frac{1}{S_{\mathrm{r}}} - v_{1}\right) + \kappa(v_{\mathrm{w}})\ln(p / p_{\mathrm{y}}) = 0 \quad \text{(B 10)}$$

Differentiating Equation (A 11) with respect to $\ln(p / p_{\mathrm{y}})$,

$$v = f(S_{\mathrm{r}}, p)$$

$$\frac{\partial v}{\partial(\ln(p / p_{\mathrm{y}}))} = -\kappa(S_{\mathrm{r}})$$

$$\frac{\partial v}{\partial(\ln(p / p_{\mathrm{y}}))} = \kappa(S_{\mathrm{r}}) = \frac{\kappa(v_{\mathrm{w}})}{1 - \alpha_{ES}S_{r}} \quad \text{(A 11)}$$

2 Appendix B: Transformation matrixes

Considering the relationship between $\mathrm{d}s^*$ and $\mathrm{d}s$, $\mathrm{d}s^* = \phi \mathrm{d}s - \frac{s}{v}\mathrm{d}\varepsilon_\mathrm{v}$:

$$\mathrm{d}S_\mathrm{r} = C_\mathrm{w}\left(\phi \mathrm{d}s - \frac{s}{v}\mathrm{d}\varepsilon_\mathrm{v}\right) + D_\mathrm{w} h \,\mathrm{d}v_\mathrm{sat} \tag{B 1}$$

Assuming v_sat is a function of v, where $\mathrm{d}v_\mathrm{sat} = g\,\mathrm{d}v$, as a result $g = \frac{\partial v_\mathrm{sat}}{\partial v}$ can be derived as follows:

Considering the constant degree of saturation hyper lines,

$$\begin{aligned}
&v = v_\mathrm{o} - \lambda(S_\mathrm{r})\ln(p/p_\mathrm{o}) \\
&\frac{\partial v}{\partial p} = -\lambda(S_\mathrm{r})\frac{1}{p} \\
&v_\mathrm{ul} = v + \kappa(S_\mathrm{r})\ln(p/p_\mathrm{o}) \\
&v_\mathrm{ul} = v_\mathrm{o} - \lambda(S_\mathrm{r})\ln(p/p_\mathrm{o}) + \kappa(S_\mathrm{r})\ln(p/p_\mathrm{o}) \\
&\frac{\partial v_\mathrm{ul}}{\partial p} = -\left(\lambda(S_\mathrm{r}) - \kappa(S_\mathrm{r})\right)\frac{1}{p} \\
&\mathrm{d}v_\mathrm{ul} = -\left(\lambda(S_\mathrm{r}) - \kappa(S_\mathrm{r})\right)\frac{1}{p}\frac{1}{-\lambda(S_\mathrm{r})\frac{1}{p}}\mathrm{d}v \\
&\mathrm{d}v_\mathrm{ul} = \frac{\left(\lambda(S_\mathrm{r}) - \kappa(S_\mathrm{r})\right)}{\lambda(S_\mathrm{r})}\mathrm{d}v
\end{aligned} \tag{B 2}$$

Considering the environmentally-stabilised gradient,

$$\begin{aligned}
&v_\mathrm{L,ul} = \frac{v_\mathrm{ul}(1-\alpha_\mathrm{ES}S_\mathrm{r}) + \alpha_\mathrm{ES}(S_\mathrm{r} - S_\mathrm{r}^\mathrm{L})}{(1-\alpha_\mathrm{ES}S_\mathrm{r}^\mathrm{L})} \\
&\mathrm{d}v_\mathrm{L,ul} = \frac{(1-\alpha_\mathrm{ES}S_\mathrm{r})}{(1-\alpha_\mathrm{ES}S_\mathrm{r}^\mathrm{L})}\mathrm{d}v_\mathrm{ul}
\end{aligned} \tag{B 3}$$

Therefore,

$$\mathrm{d}v_\mathrm{L,ul} = \frac{(1-\alpha_\mathrm{ES}S_\mathrm{r})}{(1-\alpha_\mathrm{ES}S_\mathrm{r}^\mathrm{L})}\frac{\left(\lambda(S_\mathrm{r}) - \kappa(S_\mathrm{r})\right)}{\lambda(S_\mathrm{r})}\mathrm{d}v \tag{B 4}$$

Considering the wet side of the ATL,

$$v_\mathrm{L} = v_\mathrm{L,ul} - \kappa_\mathrm{sat}\ln(p_\mathrm{L}/p_\mathrm{o}) \tag{B 5}$$

For the same LC curve, $v_{\mathrm{L}} = v_{\mathrm{sat}}$

$$
\begin{aligned}
v_{\mathrm{sat}} &= v_{\mathrm{L,ul}} - \kappa_{\mathrm{sat}} \ln(p_{\mathrm{L}} / p_{\mathrm{o}}) \\
v_{\mathrm{L,ul}} &= v_{\mathrm{sat}} + \kappa_{\mathrm{sat}} \ln(p_{\mathrm{L}} / p_{\mathrm{o}}) \\
\frac{\mathrm{d}\,v_{\mathrm{L,ul}}}{\mathrm{d}\,v_{\mathrm{sat}}} &= 1 + \frac{\mathrm{d}(\kappa_{\mathrm{sat}} \ln(p_{\mathrm{L}} / p_{\mathrm{o}}))}{\mathrm{d}\,v_{\mathrm{sat}}} \\
\frac{\mathrm{d}\,v_{\mathrm{L,ul}}}{\mathrm{d}\,v_{\mathrm{sat}}} &= 1 + \frac{\kappa_{\mathrm{sat}}}{p_{\mathrm{L}}} \frac{\mathrm{d}\,p_{\mathrm{L}}}{\mathrm{d}\,v_{\mathrm{sat}}}
\end{aligned}
\tag{B 6}
$$

Considering the yield hyper line along the ATL,

$$
\begin{aligned}
v_{\mathrm{L}} &= C_2 - \lambda_{\mathrm{L}} \ln(p_{\mathrm{L}} / p_{\mathrm{o}}) \\
\frac{\partial v_{\mathrm{L}}}{\partial p_{\mathrm{L}}} &= -\lambda_{\mathrm{L}} \frac{1}{p_{\mathrm{L}}}
\end{aligned}
\tag{B 7}
$$

Therefore,

$$
\begin{aligned}
\frac{\mathrm{d}\,v_{\mathrm{L,ul}}}{\mathrm{d}\,v_{\mathrm{sat}}} &= 1 + \left(\frac{\kappa_{\mathrm{sat}}}{p_{\mathrm{L}}}\right) / \left(-\lambda_{\mathrm{L}} \frac{1}{p_{\mathrm{L}}}\right) \\
\frac{\mathrm{d}\,v_{\mathrm{L,ul}}}{\mathrm{d}\,v_{\mathrm{sat}}} &= \frac{\lambda_{\mathrm{L}} - \kappa_{\mathrm{sat}}}{\lambda_{\mathrm{L}}}
\end{aligned}
\tag{B 8}
$$

Hence,

$$
\begin{aligned}
\frac{\lambda_{\mathrm{L}} - \kappa_{\mathrm{sat}}}{\lambda_{\mathrm{L}}} \mathrm{d}\,v_{\mathrm{Sat}} &= \frac{(1-\alpha_{\mathrm{ES}} S_{\mathrm{r}})}{(1-\alpha_{\mathrm{ES}} S_{\mathrm{r}}^{\mathrm{L}})} \frac{\left(\lambda(S_{\mathrm{r}}) - \kappa(S_{\mathrm{r}})\right)}{\lambda(S_{\mathrm{r}})} \mathrm{d}\,v \\
\mathrm{d}\,v_{\mathrm{Sat}} &= \frac{(1-\alpha_{\mathrm{ES}} S_{\mathrm{r}})}{(1-\alpha_{\mathrm{ES}} S_{\mathrm{r}}^{\mathrm{L}})} \frac{\left(\lambda(S_{\mathrm{r}}) - \kappa(S_{\mathrm{r}})\right)}{\lambda(S_{\mathrm{r}})} \frac{\lambda_{\mathrm{L}}}{\left(\lambda_{\mathrm{L}} - \kappa_{\mathrm{sat}}\right)} \mathrm{d}\,v \\
g &= \frac{(1-\alpha_{\mathrm{ES}} S_{\mathrm{r}})}{(1-\alpha_{\mathrm{ES}} S_{\mathrm{r}}^{\mathrm{L}})} \frac{\left(\lambda(S_{\mathrm{r}}) - \kappa(S_{\mathrm{r}})\right)}{\lambda(S_{\mathrm{r}})} \frac{\lambda_{\mathrm{L}}}{\left(\lambda_{\mathrm{L}} - \kappa_{\mathrm{sat}}\right)}
\end{aligned}
\tag{B 9}
$$

Therefore, Equation (B 5)

$$
\begin{aligned}
\mathrm{d}S_{\mathrm{r}} &= C_{\mathrm{w}} \left(\phi \mathrm{d}s - \frac{s}{v} \mathrm{d}\varepsilon_{\mathrm{v}}\right) + D_{\mathrm{w}} h\, \mathrm{d}\,v_{\mathrm{sat}} \\
\mathrm{d}S_{\mathrm{r}} &= C_{\mathrm{w}} \phi \mathrm{d}s + C_{\mathrm{w}} \frac{s}{v^2} \mathrm{d}v + D_{\mathrm{w}} hg \mathrm{d}v \\
\mathrm{d}S_{\mathrm{r}} &= C_{\mathrm{w}} \phi \mathrm{d}s + \left(C_{\mathrm{w}} \frac{s}{v^2} + D_{\mathrm{w}} hg\right) \mathrm{d}v
\end{aligned}
\tag{B 10}
$$

Considering Bishop's effective stress ($p^* = p + S_{\mathrm{r}} s$), the incremental of Bishop's effective stress can be written as:

$$\mathrm{d}p^* = \mathrm{d}p + S_\mathrm{r}\mathrm{d}s + s\mathrm{d}S_\mathrm{r} \tag{B 11}$$

On the other hand, $\mathrm{d}s^* = \phi\mathrm{d}s - \frac{s}{v}\mathrm{d}\varepsilon_\mathrm{v}$ and hence,

$$\mathrm{d}p^* = \mathrm{d}p + \frac{S_\mathrm{r}}{\phi}\left(\mathrm{d}s^* + \frac{s}{v}\mathrm{d}\varepsilon_\mathrm{v}\right) + s\mathrm{d}S_\mathrm{r} \tag{B 12}$$

In addition, $\mathrm{d}p$ can be written from Equation (B 13):

$$\mathrm{d}p = \frac{p}{\lambda(S_\mathrm{r})}\mathrm{v}\mathrm{d}\varepsilon_\mathrm{v} \tag{B 13}$$

Considering Equation (B 2) and the relationship $\mathrm{d}\,v_\mathrm{sat} = g\,\mathrm{d}\,v$:

$$\mathrm{d}s^* = \frac{1}{C_\mathrm{w}}\mathrm{d}S_\mathrm{r} + \frac{D_\mathrm{w}hgv}{C_\mathrm{w}}\mathrm{d}\varepsilon_\mathrm{v} \tag{B 14}$$

Hence, for the dry side Bishop's effective stress can be written as (Equation (B 12), Equation (B 15) and Equation (B 16)):

$$\mathrm{d}p^* = \left(\frac{pv}{\lambda(S_\mathrm{r})} + \frac{S_\mathrm{r}D_\mathrm{w}hgv}{\phi C_\mathrm{w}} + \frac{sS_\mathrm{r}}{v\phi}\right)\mathrm{d}\varepsilon_\mathrm{v} + \left\{\left(\frac{S_\mathrm{r}}{C_\mathrm{w}\phi}\right) + s\right\}\mathrm{d}S_\mathrm{r} \tag{B 15}$$

Therefore, D_HM for the dry side can be written as:

$$\begin{Bmatrix} \mathrm{d}p^* \\ \mathrm{d}s^* \end{Bmatrix} = \begin{bmatrix} \left(\frac{pv}{\lambda(S_\mathrm{r})} + \frac{S_\mathrm{r}D_\mathrm{w}hgv}{\phi C_\mathrm{w}} + \frac{sS_\mathrm{r}}{v\phi}\right) & \left\{\left(\frac{S_\mathrm{r}}{C_\mathrm{w}\phi}\right) + s\right\} \\ \frac{D_\mathrm{w}hgv}{C_\mathrm{w}} & \frac{1}{C_\mathrm{w}} \end{bmatrix} \begin{Bmatrix} \mathrm{d}\varepsilon_\mathrm{v} \\ -\mathrm{d}S_\mathrm{r} \end{Bmatrix} \tag{B 16}$$

Considering the yielding behaviour on the wet side:

$$\mathrm{d}v = -\lambda_\mathrm{sat}\frac{\mathrm{d}p^*}{p^*} \tag{B 17}$$

Therefore, D_{HM} for the wet side can be written as:

$$\begin{Bmatrix} \mathrm{d}p^* \\ \mathrm{d}s^* \end{Bmatrix} = \begin{bmatrix} \dfrac{vp^*}{\lambda_{\mathrm{sat}}} & 0 \\ \dfrac{D_{\mathrm{w}}hgv}{C_{\mathrm{w}}} & \dfrac{1}{C_{\mathrm{w}}} \end{bmatrix} \begin{Bmatrix} \mathrm{d}\varepsilon_{\mathrm{v}} \\ -\mathrm{d}S_{\mathrm{r}} \end{Bmatrix} \tag{B 18}$$

3 Appendix C:

3.1 Loading behaviour

```
clc;
clear;
close all;

%parameters
C3 =0.175;
k3 =0.23;
C4 =2.38;
voL=2.38;
k4 =1.25;
kw =0.0005;
alphaes = 0.6;
SrL =0.85;
vwL=SrL*(voL-1)+1;
po=10;
m=0.055;
n=1.45;
lamda=0.181;
k=0.0012;
vosat=(((C4-1)*lamda)/C3)+1
md=0.055;
nd=1.35;
lamdasrL=C3;

%ESS
b=5;
alphao =0.63;
alphawu =0.57;
beta=0.1;
N=1;
X=0.5;

%initial conditions
pin=20;
pfinal =250;
sin=150;
lamdasrL=C3;

%defining vectors
dp=0.0001;
column=ceil((pfinal-pin)/dp);
v= zeros(column+1,1);
sr=zeros(column+1,1);
aw=zeros(column+1,1);
```

```
p=zeros(column+1,1);
vw=zeros(column+1,1);
pstr=zeros(column+1,1);
p=zeros(column+1,1);
%defining initial values
p(1)=pin;
v(1)=2.1314;
sr(1)=0.6636;
vw(1)=sr(1)*(v(1)-1)+1;
s(1)=sin;

lamdasr=C3-k3*(sr(1)-SrL);
ksr=(kw)/(1-alphaes*sr(1));
vo=C4-k4*(sr(1)-SrL);
py=po*exp(((vo-v(1))/((lamdasr-ksr))))%assuming that sr change is neglegible in the elastic
loading
vy=vo-lamdasr*log(py/po);
nn(1)=(vy-1)/vy;

for r=2:column+1;
   p(r) = p(r-1)+dp;
   if  p(r) <py && p(r) < pfinal; %Elastic condition
      lamdasr=C3-k3*(sr(1)-SrL);
      ksr=(kw)/(1-alphaes*sr(r-1));
      Vul= v(r-1)+ksr*log(p(r-1)/po);
      VLooUl=((Vul*(1-(alphaes*sr(r-1))))+(alphaes*(sr(r-1)-SrL)))/(1-(alphaes*SrL));

      %Defining aw,psat and vsat
      if VLooUl > C4
         psat=po;
         vsat=VLooUl;
         VLoo=C4;
         aw(r-1)=((vsat-1)/vsat)*(po/SrL)*((exp((vosat-vsat)/lamda))-(exp((C4-
vsat)/lamdasrL)));

      else
         pbLoo=po*exp((C4-VLooUl)/(lamdasrL-k));
         VLoo=C4-lamdasrL*log(pbLoo/po);
         psat= pbLoo;
         vsat=VLoo;
         aw(r-1)=((vsat-1)/vsat)*(po/SrL)*((exp((vosat-vsat)/lamda))-(exp((C4-
vsat)/lamdasrL)));

      end

      nn(r-1)=((v(r-1)-1)/v(r-1));
      ss(r-1)=nn(r-1)*s(r-1);
      C=-n*(1/ss(r-1))*((ss(r-1)/aw(r-1))^n)*((1+((ss(r-1)/aw(r-1))^n)*(1/m))^(-m-1));
```

```
        syms x y
        S = vpasolve(x==-(ksr*((p(r)-p(r-1))/p(r-1))) ,  y==((ss(r-1)*C)/(v(r-1)*v(r-1)))*x,[x,y]) ;
        dv=S.x;
        dsr=S.y;

        v(r)=v(r-1)+dv;
        sr(r)=sr(r-1)+dsr;
        vw(r)=sr(r)*(v(r)-1)+1;
        s(r)=s(r-1);


    else p(r)>= py ; %yielding behaviour
        lamdasr=C3-k3*(sr(r-1)-SrL);
        ksr=(kw)/(1-alphaes*sr(r-1));
        Vul= v(r-1)+ksr*log(p(r-1)/po);
        VLooUl=((Vul*(1-(alphaes*sr(r-1))))+(alphaes*(sr(r-1)-SrL)))/(1-(alphaes*SrL));

         if VLooUl > C4
            psat=po;
            vsat=VLooUl;
            VLoo=C4;
            aw(r-1)=((vsat-1)/vsat)*(po/SrL)*((exp((vosat-vsat)/lamda))-(exp((C4-
vsat)/lamdasrL)));

        else
            pLoo=po*exp((C4-VLooUl)/(lamdasrL-k)); %on the Loo line
            VLoo=C4-lamdasrL*log(pLoo/po);
            psat= pLoo;
            vsat=VLoo;
            aw(r-1)=((vsat-1)/vsat)*(po/SrL)*((exp((vosat-vsat)/lamda))-(exp((C4-
vsat)/lamdasrL)));

        end

        x=(1/lamda)*(vosat-vsat);
        y=(1/lamdasrL)*(C4-vsat);
        h=-(po/SrL)*(((exp(x))/lamda)-((exp(y))/lamdasrL))+(po/SrL)*(1/(vsat*vsat))*(exp(x)-
exp(y));
        g=((1-(alphaes*sr(r-1)))/(1-(alphaes*SrL)))*((lamdasr-
ksr)/lamdasr)*(lamdasrL/(lamdasrL-k));


        nn(r-1)=((v(r-1)-1)/v(r-1));
        ss(r-1)=nn(r-1)*s(r-1);
        C=-n*(1/ss(r-1))*((ss(r-1)/aw(r-1))^n)*((1+((ss(r-1)/aw(r-1))^n)*(1/m))^(-m-1));
        D=n*((ss(r-1))^(n))*((aw(r-1))^(-n-1))*((1+((ss(r-1)/aw(r-1))^n)*(1/m))^(-m-1));

        syms x y z
        S        =        vpasolve(x==-(lamdasr*((p(r)-p(r-1))/p(r-1))),y==((s(r-1)*C)/(v(r-1)*v(r-
1)))*x+D*z, z==h*g*x,[x,y,z]) ;
```

```
        dv=S.x;
        daw=S.z;
        dsr=S.y;

        v(r)=v(r-1)+dv;
        sr(r)=sr(r-1)+dsr;
        vw(r)=sr(r)*(v(r)-1)+1;
        s(r)=s(r-1);


    end
end
```

3.2 Unloading behaviour

```
clc;
clear;
close all;

%parameters
%parameters
C3 =0.175;
k3 =0.23;
C4 =2.38;
voL=2.38;
k4 =1.25;
kw =0.0005;
alphaes = 0.6;
SrL =0.85;
vwL=SrL*(voL-1)+1;
po=10;
m=0.055;
n=1.45;
lamda=0.181;
k=0.0012;
vosat=(((C4-1)*lamda)/C3)+1
md=0.055;
nd=1.35;
lamdasrL=C3;

%ESS
b=5;
alphao =0.63;
alphawu =0.57;
beta=0.1;
N=1;
X=0.5;


%initial conditions
```

```
pin=250;
pfinal =100;
sin=150;


%defining vectors
dp=-0.0001;
column=ceil((pfinal-pin)/dp);
v= zeros(column+1,1);
sr=zeros(column+1,1);
aw=zeros(column+1,1);
vw=zeros(column+1,1);
pstr=zeros(column+1,1);
p=zeros(column+1,1);
%defining initial values
p(1)=pin;
v(1)=1.9205;
sr(1)=0.7799;
vw(1)=sr(1)*(v(1)-1)+1;
s(1)=sin;

lamdasr=C3-k3*(sr(1)-SrL);
ksr=(kw)/(1-alphaes*sr(1));
vo=C4-k4*(sr(1)-SrL);
py=po*exp(((vo-v(1))/((lamdasr-ksr))))%assuming that sr change is neglegible in the elastic
loading
vy=vo-lamdasr*log(py/po);
nn(1)=(vy-1)/vy;
for r=2:column+1;
    p(r) = p(r-1)+dp;
    lamdasr=C3-k3*(sr(1)-SrL);
    ksr=(kw)/(1-alphaes*sr(r-1));
    Vul= v(r-1)+ksr*log(p(r-1)/po);
    VLooUl=((Vul*(1-(alphaes*sr(r-1))))+(alphaes*(sr(r-1)-SrL)))/(1-(alphaes*SrL));

        %Defining aw,psat and vsat
        if VLooUl > C4
            psat=po;
            vsat=VLooUl;
            VLoo=C4;
            aw(r-1)=((vsat-1)/vsat)*(po/SrL)*((exp((vosat-vsat)/lamda))-(exp((C4-
vsat)/lamdasrL)));

        else
            pLoo=po*exp((C4-VLooUl)/(lamdasrL-k));
            VLoo=C4-lamdasrL*log(pLoo/po);
            psat= pLoo;
            vsat=VLoo;
            aw(r-1)=((vsat-1)/vsat)*(po/SrL)*((exp((vosat-vsat)/lamda))-(exp((C4-
vsat)/lamdasrL)));
```

```
    end

    nn(r-1)=((v(r-1)-1)/v(r-1));
    ss(r-1)=nn(r-1)*s(r-1);
    C=-n*(1/ss(r-1))*((ss(r-1)/aw(r-1))^n)*((1+((ss(r-1)/aw(r-1))^n)*(1/m))^(-m-1));

    syms x y
    S = vpasolve(x==-(ksr*((p(r)-p(r-1))/p(r-1))) ,  y==((ss(r-1)*C)/(v(r-1)*v(r-1)))*x,[x,y]) ;
    dv=S.x;
    dsr=S.y;

    v(r)=v(r-1)+dv;
    sr(r)=sr(r-1)+dsr;
    vw(r)=sr(r)*(v(r)-1)+1;
    s(r)=s(r-1);



end
```

3.3 Wetting behaviour

```
clc;
clear;
close all;

%parameters
C3 =0.175;
k3 =0.23;
C4 =2.38;
voL=2.38;
k4 =1.25;
kw =0.0005;
alphaes = 0.6;
SrL =0.85;
vwL=SrL*(voL-1)+1;
po=10;
m=0.055;
n=1.45;
lamda=0.181;
k=0.0012;
vosat=(((C4-1)*lamda)/C3)+1
md=0.055;
nd=1.35;
lamdasrL=C3;

%ESS
```

```
b=5;
alphao =0.63;
alphawu =0.57;
beta=0.1;
N=1;
X=0.5;

%ESS
b=5;
alphao =0.63;
alphawu =0.57;
beta=0.1;
N=1;
X=0.5;

%initial conditions
sin=250;
sfinal=200;
pin=200;

%defining vectors
column=ceil((sin-sfinal)/0.0001);
v= zeros(column+1,1);
sr=zeros(column+1,1);
s=zeros(column+1,1);
p=zeros(column+1,1);
vw=zeros(column+1,1);
py=zeros(column+1,1);

%defining initial values
v(1)=1.9017;
sr(1)=0.7704;
vw(1)=sr(1)*(v(1)-1)+1;
s(1)=sin;
ds=-0.0001;
lamdasr=C3-k3*(sr(1)-SrL);
ksr=(kw)/(1-alphaes*sr(1));
vo=C4-k4*(sr(1)-SrL);
py=po*exp(((vo-v(1))/((lamdasr-ksr))));%assuming that sr change is neglegible in the elastic
loading
vy=vo-lamdasr*log(py/po);
nn(1)=(vy-1)/vy;

for r=2:column+1;
   s(r) = s(r-1)+ ds;
   p(r-1)=pin;
   ksrL=(kw)/(1-alphaes*SrL);
   %Finding Vw loo
   vloo=C4-(C3*log(pin/po))
   vwl=(SrL*(vloo-1))+1
```

```
   Vlooul=vloo+ksrL*log(pin/po)
   vv = Vlooul-(alphaes*(vwl-vw(1)))
   neta=v(1)-vv
   if neta > 0
      alphao=alphawu;
   else
      alphao;
   end
   alpha = alphaes+((alphao-alphaes)*exp((-beta*(N-1))/abs(neta)))
   %Finding  VwF
   vwF=(C4-v(1)+(k4*vwl)+(alpha*vw(1))-(C3*log(pin/po))-(k3*vwl*(log(pin/po))))/(k4-
(k3*(log(pin/po)))+alpha)%vwl is changing
   vF=v(1)-(alpha*(vw(1)-vwF));
   %V=(C2-(k2*(vwF-vwl)))-((C1-(k1*(vwF-vwl)))*log(pin/po))

   if vw(r-1)< vwF && vw(r-1)< vwl;%swelling condition
      VLooUl=((v(r-1)*(1-(alphaes*sr(r-1))))+(alphaes*(sr(r-1)-SrL)))/(1-(alphaes*SrL));
      nn(r-1)=((v(r-1)-1)/v(r-1));
      ss(r-1)=nn(r-1)*s(r-1);
         %if last path is unloading
      if VLooUl > C4;
               psat=po;
               VLoo=C4;
               vsat=VLooUl;
               aw(r-1)=((vsat-1)/vsat)*(po/SrL)*((exp((vosat-vsat)/lamda))-(exp((C4-
vsat)/lamdasrL)));
               ad(r-1)=10^(X+log10(aw(r-1)));
               S=(m^(1/n))*aw(1)*((((sr(1))^(-1/m))-1)^(1/n))

               %if last stress path is wetting or unloading
%                 ad=(nn(1)*s(1))/((((sr(1))^(-1/md))-1)^(1/n))
%                 S=ss(r-1)-5
       else
               pbLoo=po*exp((C4-VLooUl)/(lamda-k));
               VLoo=C4-C3*log(pbLoo/po);
               psat= pbLoo;
               vsat=VLoo;
               aw(r-1)=((vsat-1)/vsat)*(po/SrL)*((exp((vosat-vsat)/lamda))-(exp((C4-
vsat)/lamdasrL)));
               ad(r-1)=10^(X+log10(aw(r-1)));
               S=(m^(1/n))*aw(1)*((((sr(1))^(-1/m))-1)^(1/n))
               %if last stress path is wetting or unloading
%                 ad=(nn(1)*s(1))/((((sr(1))^(-1/md))-1)^(1/n))
%                 S=ss(r-1)-5
      end
      S
      ss(r-1)


      if ss(r-1) > S %elastic wetting %ns condition
```

```
        EE=(S/ss(r-1))^(b);%ns given here
        aw(r-1)=10^(log10(ad(r-1))-X);
        x=(1/lamda)*(vosat-vsat);
        y=(1/lamdasrL)*(C4-vsat);
        h=-(po/SrL)*(((exp(x))/lamda)-
((exp(y))/lamdasrL))+(po/SrL)*(1/(vsat*vsat))*(exp(x)-exp(y));
        C=-n*(1/ss(r-1))*((ss(r-1)/aw(r-1))^n)*((1+((ss(r-1)/aw(r-1))^n)*(1/m))^(-m-1));

        syms x y
        S = vpasolve(x==((alpha*(v(r-1)-1))/(1-(alpha*sr(r-1))))*y,y==EE*((C*nn(r-
1)*ds)+(((s(r-1)*C)/(v(r-1)*v(r-1)))*x)),[x,y,]) ;
        dv=S.x;
        dsr=S.y;

        v(r)=v(r-1)+dv;
        sr(r)=sr(r-1)+dsr;
        vw(r)=sr(r)*(v(r)-1)+1;

      else %swelling
        aw(r-1)=10^(log10(ad(r-1))-X);
        lamdasr=C3-k3*(sr(1)-SrL);
        ksr=(kw)/(1-alphaes*sr(r-1));
        x=(1/lamda)*(vosat-vsat);
        y=(1/lamdasrL)*(C4-vsat);
        h=-(po/SrL)*(((exp(x))/lamda)-
((exp(y))/lamdasrL))+(po/SrL)*(1/(vsat*vsat))*(exp(x)-exp(y));
        g=((1-(alphaes*sr(r-1)))/(1-(alphaes*SrL)))*((lamdasr-
ksr)/lamdasr)*(lamdasrL/(lamdasrL-k));

        C=-n*(1/ss(r-1))*((ss(r-1)/aw(r-1))^n)*((1+((ss(r-1)/aw(r-1))^n)*(1/m))^(-m-1));
        D=n*((ss(r-1))^(n))*((aw(r-1))^(-n-1))*((1+((ss(r-1)/aw(r-1))^n)*(1/m))^(-m-1));

        syms x y z
        S = vpasolve(x==((alpha*(v(r-1)-1))/(1-(alpha*sr(r-1))))*y,y==(C*nn(r-1)*ds)+(((s(r-
1)*C)/(v(r-1)*v(r-1)))*x)+(D*z), z==h*g*x,[x,y,z]) ;
        dv=S.x;
        daw=S.z;
        dsr=S.y;

        sr(r)=sr(r-1)+dsr;
        v(r)=v(r-1)+dv;
        vw(r)=sr(r)*(v(r)-1)+1;
      end
    elseif vwF < vw(r-1)&& vw(r-1)< vwl;
      lamdasr=C3-k3*(sr(1)-SrL);
      ksr=(kw)/(1-alphaes*sr(r-1));
      Vul= v(r-1)+ksr*log(pin/po);
      VLooUl=((Vul*(1-(alphaes*sr(r-1))))+(alphaes*(sr(r-1)-SrL)))/(1-(alphaes*SrL));
      %Defining aw,psat and vsat
      if VLooUl > C4
```

```
          psat=po;
          vsat=VLooUl;
          nn(r-1)=(v(r-1)-1)/v(r-1);
          VLoo=C4;
          aw(r-1)=((vsat-1)/vsat)*(po/SrL)*((exp((vosat-vsat)/lamda))-(exp((C4-
vsat)/lamdasrL)));

       else
          pLoo=po*exp((C4-VLooUl)/(lamda-k));
          nn(r-1)=(v(r-1)-1)/v(r-1);
          VLoo=C4-C3*log(pLoo/po);
          vsat=VLoo
          aw(r-1)=((vsat-1)/vsat)*(po/SrL)*((exp((vosat-vsat)/lamda))-(exp((C4-
vsat)/lamdasrL)));
          psat= pLoo+(aw(r-1)*SrL);
          vsat=vosat-(lamda*(log(psat/po)));


       end

       x=(1/lamda)*(vosat-vsat);
       y=(1/lamdasrL)*(C4-vsat);
       h=-(po/SrL)*(((exp(x))/lamda)-((exp(y))/lamdasrL))+(po/SrL)*(1/(vsat*vsat))*(exp(x)-
exp(y));
       g=((1-(alphaes*sr(r-1)))/(1-(alphaes*SrL)))*((lamdasr-
ksr)/lamdasr)*(lamdasrL/(lamdasrL-k));

       nn(r-1)=((v(r-1)-1)/v(r-1));
       ss(r-1)=nn(r-1)*s(r-1);
       C=-n*(1/ss(r-1))*((ss(r-1)/aw(r-1))^n)*((1+((ss(r-1)/aw(r-1))^n)*(1/m))^(-m-1));
       D=n*((ss(r-1))^(n))*((aw(r-1))^(-n-1))*((1+((ss(r-1)/aw(r-1))^n)*(1/m))^(-m-1));

       syms x y z
       S     =     vpasolve(     x==((((k3*log(pin/po))-k4)*(v(r-1)-1))/(1+(sr(r-1)*((-
k3*log(pin/po))+k4))))*y,y==(C*nn(r-1)*ds)+(((s(r-1)*C)/(v(r-1)*v(r-1)))*x)+(D*z),
z==h*g*x,[x,y,z]) ;
       dv=S.x;
       daw=S.z;
       dsr=S.y;

       sr(r)=sr(r-1)+dsr;
       v(r)=v(r-1)+dv;
       vw(r)=sr(r)*(v(r)-1)+1;
    else
       lamdasr=C3-k3*(sr(1)-SrL);
       ksr=(kw)/(1-alphaes*sr(r-1));
       pLoo=pin;
       nn(r-1)=(v(r-1)-1)/v(r-1);
       VLoo=C4-C3*log(pLoo/po);
```

```
        vsat=2.5
        aw(r-1)=((vsat-1)/vsat)*(po/SrL)*((exp((vosat-vsat)/lamda))-(exp((C4-vsat)/lamdasrL)));
        psat= pin+(aw(r-1)*SrL);%ploo=pin
        vsat=vosat-(lamda*(log(psat/po)));

        x=(1/lamda)*(vosat-vsat);
        y=(1/lamdasrL)*(C4-vsat);
        h=-(po/SrL)*(((exp(x))/lamda)-((exp(y))/lamdasrL))+(po/SrL)*(1/(vsat*vsat))*(exp(x)-
exp(y));


        A=((lamdasr-ksr)/(v(r-1)*p(r)));


        nn(r-1)=((v(r-1)-1)/v(r-1));
        ss(r-1)=nn(r-1)*s(r-1);
        C=-n*(1/ss(r-1))*((ss(r-1)/aw(r-1))^n)*((1+((ss(r-1)/aw(r-1))^n)*(1/m))^(-m-1));
        D=n*((ss(r-1))^(n))*((aw(r-1))^(-n-1))*((1+((ss(r-1)/aw(r-1))^n)*(1/m))^(-m-1));

        dsr =(((C*nn(r-1))))*(s(r)-s(r-1));
        sr(r)=sr(r-1)+dsr;
        v(r)=v(r-1)+(k*log((pin+(s(r)*sr(r)))/pin));
        vw(r)=sr(r)*(v(r)-1)+1;
        end
end
```

3.4 Drying behaviour

```
clc;
clear;
close all;

%parameters
C3 =0.175;
k3 =0.23;
C4 =2.38;
voL=2.38;
k4 =1.25;
kw =0.0005;
alphaes = 0.6;
SrL =0.85;
vwL=SrL*(voL-1)+1;
po=10;
m=0.055;
n=1.45;
lamda=0.181;
k=0.0012;
vosat=(((C4-1)*lamda)/C3)+1
md=0.055;
```

```
nd=1.35;
lamdasrL=C3;

%ESS
b=5;
alphao =0.63;
alphawu =0.57;
beta=0.1;
N=2;
X=0.5;

%initial conditions
sin=40;
sfinal=200;
pin=10;

%defining vectors
column=ceil((sfinal-sin)/0.0001);
v= zeros(column+1,1);
sr=zeros(column+1,1);
s=zeros(column+1,1);
p=zeros(column+1,1);
vw=zeros(column+1,1);
aw=zeros(column+1,1);

%defining initial values
v(1)=2.2019;
sr(1)=0.6825;
vw(1)=sr(1)*(v(1)-1)+1;
s(1)=sin;
ds=0.0001;
lamdasr=C3-k3*(sr(1)-SrL);
ksr=(kw)/(1-alphaes*sr(1));
vo=C4-k4*(sr(1)-SrL);
py=po* exp(((vo-v(1))/(( lamdasr-ksr))));%assuming that sr change is neglegible in the elastic
loading
vy=vo-lamdasr*log(py/po);
nn(1)=(vy-1)/vy;

for r=2:column+1;
    s(r) = s(r-1)+ ds;
    p(r-1)=pin;
    lamdasr=C3-k3*(sr(1)-SrL);
    ksrL=(kw)/(1-alphaes*SrL);
    vloo=C4-(lamda*log(pin/po));
    vwl=(SrL*(vloo-1))+1;
    Vlooul=vloo+ksrL*log(pin/po);
    VLooUl=((v(r-1)*(1-(alphaes*sr(r-1))))+(alphaes*(sr(r-1)-SrL)))/(1-(alphaes*SrL));
    vv = Vlooul-(alphaes*(vwl-vw(1)));
```

```
    neta=v(1)-vv
    if neta < 0
       alphao=alphawu;
    else
       alphao;
    end
    alpha = alphaes+((alphao-alphaes)*exp((-beta*(N-1))/abs(neta)))
    ss(r-1)=nn(r-1)*s(r-1)  ;

    if VLooUl > C4;
          psat=po;
          vsat=VLooUl;
          VLoo=C4;
          %if last path is wetting or unloading po
          aw(r-1)=((vsat-1)/vsat)*(po/SrL)*((exp((vosat-vsat)/lamda))-(exp((C4-
vsat)/lamdasrL)));
          ad(r-1)=10^(X+log10(aw(r-1)));
          S=(md^(1/nd))*ad(1)*((((sr(1))^(-1/md))-1)^(1/nd))
       else
          pLoo=po*exp((C4-VLooUl)/(lamda-k));
          VLoo=C4-lamda*log(pLoo/po);
          psat= pLoo;
          vsat=VLoo;
          aw(r-1)=((vsat-1)/vsat)*(po/SrL)*((exp((vosat-vsat)/lamda))-(exp((C4-
vsat)/lamdasrL)));
          ad(r-1)=10^(X+log10(aw(r-1)));
          S=(md^(1/nd))*ad(1)*((((sr(1))^(-1/md))-1)^(1/nd))
       end

    ss(r-1)=nn(r-1)*s(r-1);


    if ss(r-1) < S %elastic drying
       EE=(S/ss(r-1)).^(-b);
       C=-nd*(1/ss(r-1))*((ss(r-1)/ad(r-1))^nd)*((1+((ss(r-1)/ad(r-1))^nd)*(1/md))^(-md-
1));%S used

       syms x y
       S=vpasolve(x==((alpha*(v(r-1)-1))/(1-(alpha*sr(r-1))))*y,y==EE*((C*nn(r-
1)*ds)+(((s(r-1)*C)/(v(r-1)*v(r-1)))*x)),[x,y,]);
       dv=S.x;
       dsr=S.y;

       v(r)=v(r-1)+dv;
       sr(r)=sr(r-1)+dsr;
       vw(r)=sr(r)*(v(r)-1)+1;
       nn(r)=((v(r)-1)/v(r));

    else %drying
       ad(r-1);
```

```
        x=(1/lamda)*(vosat-vsat);
        y=(1/lamdasrL)*(C4-vsat);
        h=-(po/SrL)*(((exp(x))/lamda)-((exp(y))/lamdasrL))+(po/SrL)*(1/(vsat*vsat))*(exp(x)-
exp(y));
        g=((1-(alphaes*sr(r-1)))/(1-(alphaes*SrL)))*((lamdasr-
ksr)/lamdasr)*(lamdasrL/(lamdasrL-k));
        lamdasr=C3-k3*(sr(1)-SrL);
        ksr=(kw)/(1-alphaes*sr(r-1));
        C=-nd*(1/ss(r-1))*((ss(r-1)/ad(r-1))^nd)*((1+((ss(r-1)/ad(r-1))^nd)*(1/md))^(-md-1));
        D=nd*((ss(r-1))^(nd))*((ad(r-1))^(-nd-1))*((1+((ss(r-1)/ad(r-1))^nd)*(1/md))^(-md-1));

        syms x y z
        S = vpasolve(x==((alpha*(v(r-1)-1))/(1-(alpha*sr(r-1))))*y,y==(C*nn(r-1)*ds)+(((s(r-
1)*C)/(v(r-1)*v(r-1)))*x)+(D*z), z==h*g*x,[x,y,z]) ;
        dv=S.x;
        daw=S.z;
        dsr=S.y;

        v(r)=v(r-1)+dv;
        sr(r)=sr(r-1)+dsr;
        vw(r)=sr(r)*(v(r)-1)+1;
        nn(r)=((v(r)-1)/v(r));
    end
end

v
sr
```

4 **Appendix D:** An integrated conceptual approach for the monitoring and modelling of geo-structures subjected to climatic loading

4.1 Introduction

Civil engineering structures involve interaction within the soil/atmosphere continuum, whereby some of the critical structures are made of geological materials, *e.g.*, embankments, rock fill/earth dams, cut slopes, *etc*., as schematised in Fig. 1. In addition, there are natural geo-structures such as slopes, which apart from providing aesthetics are usually utilised for a range of societal activities. These anthropogenic and natural geo-infrastructures are vulnerable to failure due to climatic loading (Brideau et al., 2012). Monitoring and failure prediction of geo-infrastructures depends upon the risk due to soil behaviour and associated economic considerations. For example, shallow foundations of lightweight structures may not have high risk, and therefore its monitoring may not be economical. On the other hand, heavy and complex foundations, and similar critical geotechnical infrastructure, where the consequence of failure and the risk is high, demand advanced analysis of the subsurface soil behaviour in order to implement failure mitigation strategies. Engineering design of these types of structures is mainly based on the mechanics of saturated soil, whereby the real soil behaviour is clearly well unaccounted. Many geo-infrastructures may be placed on unsaturated soil subjected to atmospheric interaction. Monitoring of these structures may provide a general idea on the behaviour of the underneath soil. With regards to risk and the economic value, all the aforementioned situations may or may not demand structural monitoring. However, the presence of vast natural slopes in the vicinity of populated and developed areas (see Fig. 1) need special attention and, in this regard, failure predictions due to potential landslides are important.

4.1.1 Deformation state analysis

Geohazards such as landslides usually occur under conditions of intense rainfall. Failure occurs due to the outward or downward movement of the soil masses along the line of maximum stress. The maximum resisting force of the soil movement is controlled by the shear strength, which gradually reduces with increase in the degree of saturation (Fredlund et al., 1978; Wheeler and Sivakumar, 1995; Ng et al., 2008; Sheng et al., 2013). Consequently, soil can suffer strength reduction under anomalous climatic loading, leading to potential landslides with high failure consequences (Fig. 1). Therefore, monitoring and periodic assessments of geostructures, such as slopes, are important for generating accurate early warnings (Gallipoli et al., 2000; Hu, 2013; Scaioni et al., 2014; Dong et al., 2018; Tohari, 2018). The major issues affecting the predictive response analysis of geo-infrastructure are the dynamic properties of the ground surface and subsurface. Although localised sampling methods, such as borehole measurements, penetration tests or laboratory testing, can be utilised to estimate the relevant parameters, dependence on discrete measurements is usually time-consuming and may provide information only within a small elemental region. Consequently, deformation state analysis of the large regions of surface/subsurface soil can become inaccurate. Deformation state analysis of soil refers to the analysis of the non-material variables required for strain characterisation upon climatic loading events (Fredlund and Rahardjo, 1993). There is a need to identify a systematic process that can assist in acquiring the highly dynamic soil surface/surface parameters in a quasi-continuous manner and therefore lead to improvements in existing geo-infrastructure deformation state analysis. Although this has been attempted in several scattered studies in literature, the integration of several available geophysical and optical sensing methods for geo-infrastructure rehabilitation and management purposes remains an active area of research. Accuracies in the prediction of field behaviour for geotechnical structures depends on the ability of the constitutive model to capture the real soil behaviour. Therefore, the selection of an appropriate constitutive model amenable to integration with proximal soil sensing techniques is also important. In other words, an assemblage of relevant methodologies for parameter estimation and an appropriate constitutive model is still elusive.

The objective of the present study is to integrate advances from scattered disciplines and provide a systematic workflow for modelling deformation state analysis of natural and anthropogenic geo-infrastructures. It incorporates geophysical and proximal optical sensing methods into a suite a proximal soil sensing (PSS) techniques that can be used seamlessly as part of deformation state modelling. The paper is organised as follows. Section 2 presents an overview of the proximal soil sensing techniques that can be useful for the work advocated in this paper. Section 3 provides a discussion on the constitutive model that is needed for accurate and realistic deformation state modelling. Construction of the model geometry with the incorporation of important geological and petrophysical properties are discussed in Section 4. Features of a numerical model leading to critical analysis and future implementation of the proposed conceptual approach is discussed in Section 5. In this manner, the present work provides an integrated conceptual approach for efficient management of critical geo-infrastructures.

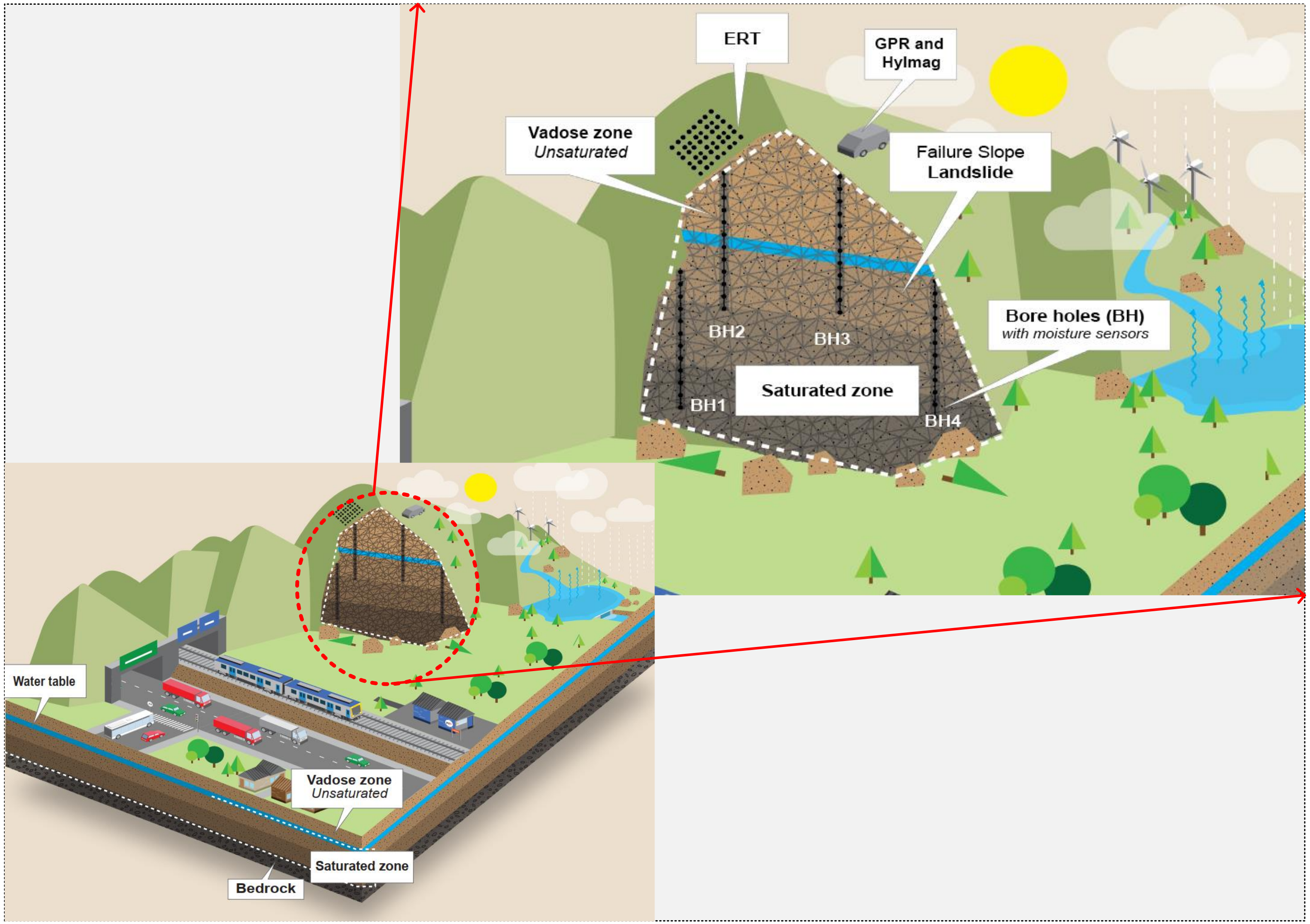

Fig. 1*: Geo-infrastructures are an integral part of modern society and their proper management is important for sustainable development.*

4.2 Proximal soil sensing techniques

When considering landslides risks in complex geological environments, it is essential to consider the surface geomorphological and subsurface geological features. Geognostic knowledge, such as the elevation, surface lithology, ground stratigraphy and petrophysical properties, the location of the bedrock, *etc.*, are essential in this regard and information on these attributes can be acquired through a mixture of ground-based, and air-borne (Perrone et al., 2014), or near-ground-based techniques. The suite of ground-based and near ground-based methods can generally be classified as PSS techniques and involves the acquisition of data from sensors that are either in direct contact or very close to the ground (Viscarra Rossel et al., 2011).

The use of ground-based geophysical methods for subsurface characterisation is common. Its ability to retrieve subsurface soil information (*e.g.*, Zieher et al., 2017; Klotzsche et al., 2018; Riese and Keller, 2018) and simultaneously elucidate hydrogeological processes (Klotzsche et al., 2018) is a significant attribute for its integration in environmental and engineering related investigations. Electrical resistivity tomography (ERT) and ground penetrating radar (GPR) techniques are well suited for the type of information generally expected from subsurface site characterisations (Perrone et al., 2014; Klotzsche et al., 2018) for engineering applications. These techniques extend beyond the point-scale characterisation, which is a norm in traditional geotechnical measurements using small discrete probes (Rahardjo and Leong, 2006; Tarantino et al., 2008; Mendes et al., 2018). On the other hand, proximal hyperspectral imaging (HyImag) methods have emerged as useful techniques for retrieval of surface information and are attractive for providing solutions currently needed for most geotechnical problems. In order to provide completeness in this paper, a brief background on the three techniques, *viz.*, ERT, GPR, and HyImag, are presented in the subsections that follow. Applications of these techniques in achieving the objectives of model construction will be discussed later in the paper (Section 4).

4.2.1 Electrical resistivity tomography

Electrical resistivity tomography involves acquiring the 2D or 3D subsurface resistivity distributions. It is an active direct-current (DC) technique and involves injecting a known amount of current (I) through two outer (AB) steel electrodes and measuring the induced potentials (ΔU) using two inner (MN) non-polarisable potential electrodes (Deo et al., 2017) as schematised in Fig. 2.

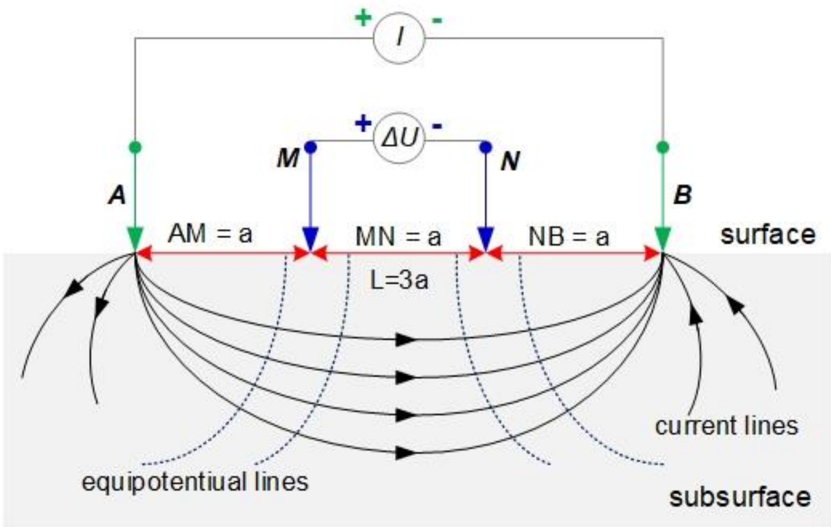

Fig. 2*: Electrical resistivity tomography (ERT) is an active technique for acquiring information on subsurface resistivity distributions.*

In some cases, stainless steel electrodes are used as potential electrodes in order to improve data collection efficiencies. The use of steel electrodes necessitates some consideration to be given to signal processing procedures (*e.g*., Dahlin et al., 2002; Deo and Cull, 2016) in order to remove baseline wandering and improve accuracy. To conform to the DC-regime requirement for a current source, switched square waves usually between frequencies of 0.5 – 2 Hz (Binley and Kemna, 2005) are utilised. An important aspect of resistivity measurements is the separation distance amongst the four collinear electrodes, and several arrangements are possible resulting in different array configurations Szalai et al., 2009. The Wenner array is a common configuration, whereby the electrodes are located equi-distant (*a*) from each other (Fig. 2).

The subsurface apparent resistivity, ρ_a (Ω m) measured with any array configuration is related to its geometrical factor, G (m), through Eq. 1.

(1) $$\rho_a = \frac{\Delta U}{I} G$$

For a Wenner array, $G = 2\pi a$. Another important parameter in resistivity measurement is the depth of investigation (DOI), which is defined as the depth at which a thin horizontal layer parallel to the ground surface contributes the maximum amount of signal measured at the ground surface (Evjen, 1938; Edwards, 1977; Barker, 1989). For the Wenner array, the DOI is ~0.519a (Roy and Apparao, 1971). The term apparent resistivity in Eq. 1 implies that the measured resistivity is not the true resistivity at the particular depth of DOI, but instead will depend on the subsurface inhomogeneity and the type of array used. For an ideal homogeneous half-space, the measured apparent resistivity will correspond to the true resistivity (ρ), i.e., $\rho_a = \rho$. If the measurements are conducted systematically for different a-spacing values along a transect, then the apparent resistivity at different depths (vertical location $\rightarrow$ DOI(a)) can be ascertained, whereby the horizontal location will coincide with the array midpoint (Telford et al., 1990). In this manner, the distribution of subsurface apparent resistivities along the transect, within a 2D plane known as pseudo-section, can be obtained. If the data acquisition is repeated along several closely spaced transects, then a 3D distribution of the apparent resistivity, collection of different pseudo-sections, can be constructed. Through an inversion of the pseudo-section(s) (Loke et al., 2013), the subsurface electrical resistivity tomography is obtained and can be used for further qualitative or quantitative assessment. In the context of the work proposed in this paper, the inverted 3D resistivity distribution can be used for quantitative assessment of 3D porosity and suction distributions, and will be discussed later (Section 4.3.2).

4.2.2 Ground penetrating radar

Ground penetrating radar is an imaging technique that utilises information on the transmitted and received electromagnetic (EM) waves to determine subsurface characteristics and properties. It is similar to seismic reflections methods, which are based on the propagation of elastic waves. The underlying basis of GPR is the set of constitutive equations (see Annan, 2009) that associate the material properties with the stimuli/response of the subsurface media upon interaction with the EM waves. The reader is referred to Cassidy, 2009 and the references therein for a formal treatment on the subject. An important parameter that is important in GPR applications is the velocity, v_{GPR} (m s^{-1}), of the EM waves in the direction of propagation (Reynolds, 2011) and is given by Eq. 2.

(2) $$v_{\mathrm{GPR}} = \frac{c}{\left(\frac{\varepsilon_r \mu_r}{2}\left[\left(1+\left(\frac{\sigma}{\omega\varepsilon}\right)^2\right)+1\right]\right)^{\frac{1}{2}}},$$

where, $\varepsilon = \varepsilon_r \varepsilon_o$, ε_r is the relative permittivity or the dielectric constant (dimensionless), ε_o is the permittivity of free space (8.854×10^{-12} F m^{-1}), μ_r is the relative magnetic permeability (dimensionless), σ is the soil conductivity (Ω m), ω is the angular frequency (rad s^{-1}), and the quantity $\sigma/\omega\varepsilon$ is known as the loss factor. Note that for free space, $\varepsilon_r = \mu_r = 1$, leading to the speed of EM waves in free space, $v_{\mathrm{GPR}} = c \approx 3 \times 10^8$ ms^{-1}. For soils the μ_r is usually unity, and provided the $\sigma << \omega\varepsilon$ (low-loss subsurface material), the velocity expression can be reduced to Eq. 3.

(3) $$v_{\mathrm{GPR}} = \frac{c}{\sqrt{\varepsilon_r}} ,$$

Single transmitter (Tx)/ and receiver (Rx) GPR system using common offset (CO) reflection survey methods are typical in most engineering subsurface assessments. The method involves acquiring the reflected EM signals along a transect with a fixed separation distance between the Tx/Rx unit as shown in Fig. 3. A propagating EM wave encountering an interface between two materials of different electrical properties (ε_r) undergoes two processes. Part of the energy is reflected as shown in Fig. 3, and the remainder is transmitted through the second medium. An essential parameter for the reflected signal is its arrival time, *t*, which is related to the depth of the reflector, *d*, by Eq. 4.

(4) $$t = \frac{2d}{v_{\mathrm{GPR}}} ,$$

For low-loss soils, the velocity can easily be estimated (Eq. 3) provided the dielectric constant of the medium is reasonably known. Consequently, the depth of the reflector can be determined through a measurement of the arrival time. The reflected component, measured as a time-domain signal at the Rx, provides the information that is used to discern subsurface characteristics. If data is collected along a single transect, then the subsurface information is retrieved below the single line. If multiple transects are scanned within a grid format, then a 3D subsurface image can be constructed. In any case, GPR techniques can greatly assist in determining subsurface stratigraphy and identification of bedrock location, which are of importance to the present study.

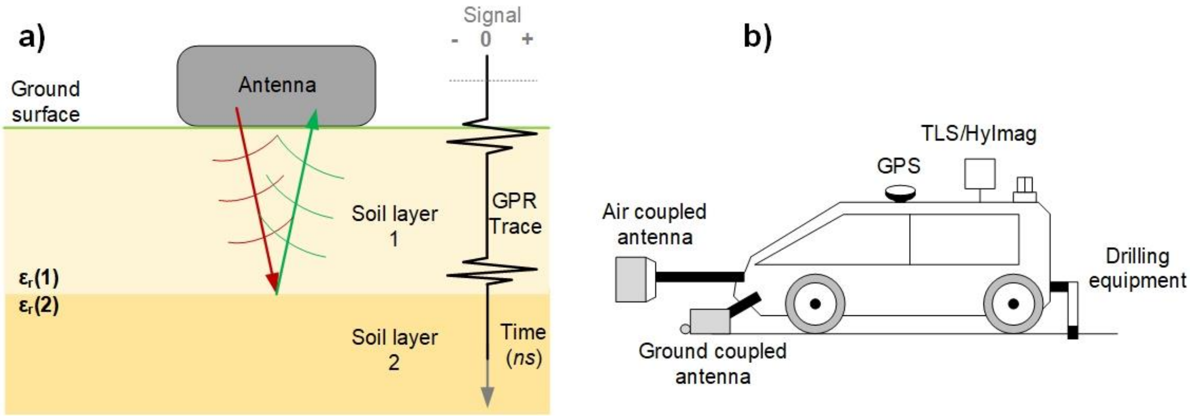

***Fig. 3**: GPR techniques **a**) utilise EM theory to provide assessment of subsurface structure and **b**) can be deployed on a moving vehicle for efficient data acquisition.*

4.2.3 Hyperspectral imaging

Hyperspectral imaging (HyImag) originally started as a remote sensing technique and now has widespread applications across different disciplines (Amigo et al., 2015). Although HyImag is generally an air-borne technique, the availability of portable cameras permits it to be utilised within the PSS suite of methods (*e.g.*, Jung et al., 2015). HyImag differs from traditional photogrammetry techniques as it acquires spectral data within narrow bandwidths over a contiguous wavelength band for every pixel within a complete image. For this reason, HyImag is also referred to as imaging spectrometry. The typical range for HyImag is the visible to short wave infra-red region in the EM spectrum, which generally corresponds to wavelengths of 0.4 μm to 2.5 μm (Fig. 4). Data from HyImag is presented as a 3D stack of 2D spatial images at different wavelengths and is referred to as a hypercube. The basis for the hyperspectral technique is reflectance spectroscopy, which is concerned with the ratio of reflected to incident energies as schematised in Fig. 4. Different materials, *e.g.*, vegetation, soil, rocks, reflect, absorb, and emit EM waves in a manner which depends on their physical and chemical nature. Consequently, materials exhibit characteristic fingerprint spectral signatures and an analysis of the reflection spectra for each pixel in an acquired image can identify the material type. For identification purposes, spectral libraries (Nidamanuri and Ramiya, 2014) are important since they provide the reference for comparison and subsequent segmentation of images.

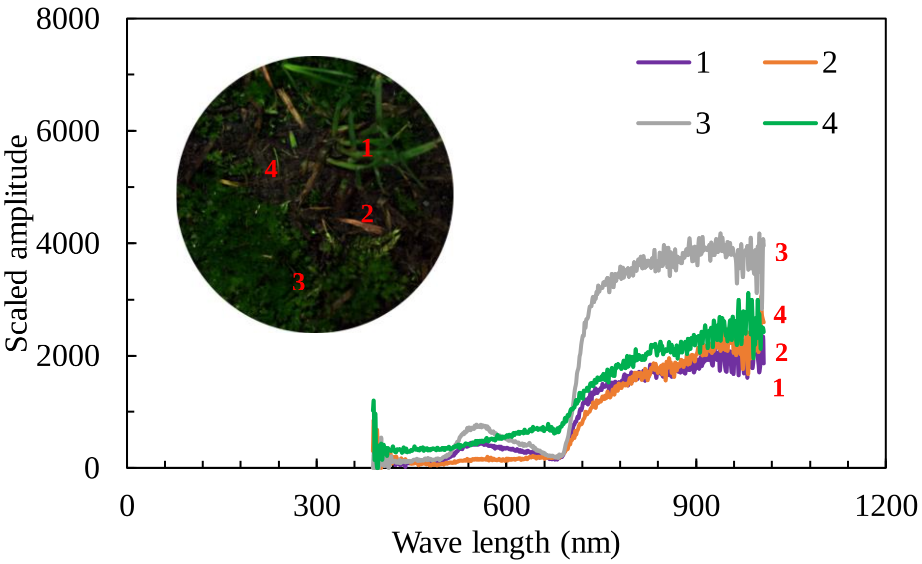

Fig. 4*: Reflectance spectra using hyperspectral techniques can be used to distinguish different materials. Note, different earth materials (1-4) shown in the inset figure displays distinct reflectance spectra.*

The techniques discussed in this section will be necessary for providing different levels of detail for a physical 3D model required for numerical modelling. However, the foundation for numerical modelling is the set of governing equations, which are based on firm constitutive equations. These are addressed in next section.

4.3 Selection of a numerical model

In most geotechnical engineering design, the service condition considered is mostly linear elasticity and the limit equilibrium on the perfectly plastic condition. However, real soil behaviour cannot be captured by linear elasticity or perfectly plastic conditions (Potts, 2002). Hence, an appropriate constitutive model needs to be selected on the basis of the following conditions, whereby it is capable of capturing basic phenomenological features of unsaturated soils.

4.3.1 Constitutive model requirements

C1*: The unsaturated constitutive model should comply with the parameters that can be readily acquired with proximal soil sensing techniques.*

The constitutive models have developed significantly over the last few decades with considerable improvement in the numerical modelling (Alonso et al., 1990; Jommi, 2000;

Gallipoli et al., 2003; Tarantino and Tombolato, 2005; Romero et al., 2011; Azizi et al., 2017). However, the application of unsaturated soil mechanics to geotechnical practice is limited due to the inability of state parameters to be estimated reliably in the field. Generally, a finite element model requires the soil state variables (degree of saturation, suction, specific volume or porosity), the 3D geometry (ground surface, subsurface profile), and boundary conditions (precipitation, relative humidity, wind speed, short-wave and long-wave radiation exchanges). With regards to the surface and subsurface profiles, the PSS techniques can be utilised efficiently. Consequently, the constitutive model should be compatible with the suite of parameters obtainable from PSS techniques.

C2*:* *The unsaturated constitutive model should be able to smoothly transit and explain saturated soil behaviour.*

The most commonly used saturated constitutive models are the Mohr-Coulomb and Modified Cam Clay models, which are based on the effective stress state approach (Coulomb, 1776; Roscoe and Burland, 1968). Although the near-surface soil is assumed to be saturated for simplicity, it is not generally true and applicable. For practical implementation, Krahn et al., 1989 highlighted the importance of the behaviour of unsaturated soils in the Notch Hill slope, whereby the required soil parameters were determined experimentally for failure analysis. In addition, most of the soil near the ground surface, soils in compacted fills, embankments and dams are unsaturated soils with an induced complexity of the air phase. Hence, the selected model should be simple and capable of handling a smooth transition from a saturated state to the unsaturated state without any loss of accuracy.

C3: *All coefficients in the unsaturated constitutive model should be easily obtainable through less sophisticated and less time-consuming experiments.*

The constitutive relationships are the set of the stress-strain relationship of a material, stress volumetric strain relationship, and the soil water retention behaviour, which all provide the correspondences amongst different state variables. For example, BBM model requires nine material parameters including four critical state parameters which are constants for a particular soil where the suction-based testing is required for estimation of these parameters. It is commonly accepted (Sivakumar, 1993; Raveendiraraj, 2009) that suction based testing is time-consuming and may provide constraints to be incorporated into time-limited field programs. In this regard, a practical yet reasonable satisfying rigorous approach may be required. It is noted that testing using constant water content loading is less time consuming and can be an alternative.

C4: *The selected model should capture significant phenomenological observations of unsaturated soils.*

The selected constitutive model should be capable of capturing the significant phenomenological observations of unsaturated soils. Some of these observations, relevant to climatic loading, are noted as follows. Tripathy et al. (2002) studied the behaviour of expansive soils under wet-dry cycles and observed that it exhibits reversible strains, when subjected to a sufficient number of wet-dry cycles. In the literature, these type of soils has been referred to as "ripened soil" (Kodikara et al., 2002) or "environmentally stabilised soil" (Gould et al., 2011). The existence of environmentally stabilised soil is also highlighted in Kodikara (2012), while Gens and Alonso (1992) used the same concept in terms of the accumulation of plastic strains with wet/dry cycles to formulate the Barcelona Expansive Model (BExM). Therefore, utilising the environmentally stabilised soil is a promising approach for capturing the soil behaviour subjected to climatic loading and its long-term performance.

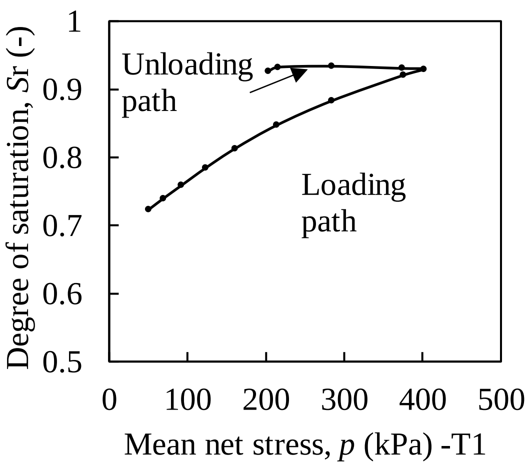

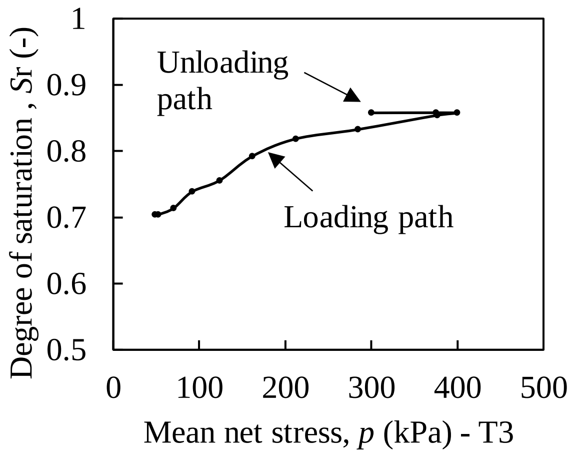

Fig. 5*: Isotropic loading-unloading test at constant suction on compacted Speswhite kaolin (data from Zakaria (1994)).*

Another important feature is that most of the experimental evidence shows that the change in the degree of saturation upon loading is most significant, whereas during unloading/reloading change in the degree of saturation is minimum, as shown in Fig. 5 (Zakaria (1994)). In other words, the hydraulic behaviour as captured by the degree of saturation can be represented by two aspects: a) the hysteresis behaviour during wetting and drying with the suction, and b) the shift in the wetting-drying curves with an increase in the plastic volumetric strain. The dependency of the plastic volumetric stain on the soil water retention curve (SWRC) has been utilised in a few constitutive models (*e.g.*, Tamagnini (2004)). Furthermore, Lloret-Cabot et al. (2017) used this approach to modify the model developed by Wheeler et al. (2003). Some of the other significant phenomenological features of unsaturated soil include: a) the smooth transition from saturated to unsaturated state, (Cunningham et al., 2003; Fredlund et al., 2013; Khalili, 2018) b) under constant net stress wetting, swelling/collapse/swelling behaviour has been observed with the decrease in suction (Sharma, 1998; Raveendiraraj, 2009), c) the collapse behaviour shows that the collapse potential (at constant net stress wetting) increases with net stress and then decrease after preconsolidation stress (Sun et al., 2007; Delage et al., 2015; Das and Thyagaraj, 2018), d) the associated shear behaviour (Raveendiraraj, 2009), and e) the general applicability to natural, slurry and compacted soils (Tarantino, 2010) . Hence, the constitutive model should attest to most of these additional phenomenological observations. In addition, it may be important to consider other lesser-known phenomena such as creep and pore pressure generation due to heat associated with plastic work (Pinyol et al., 2018).

4.3.2 The MPK framework

The MPK (Monash-Peradeniya-Kodikara) framework (Fig. 6) is based on the traditional compaction curves, whereby the suction is treated as a dependent variable in the v, v_{w}, p space. By considering the Houlsby (1997) unsaturated soil equation given by Eq. 5, the selected variables of the MPK framework are the specific volume (v), mean net stress (p_{net}) and specific water volume (v_{w}) without coupled consideration of the degree of saturation (S_{r}) or suction (s).

(5) $$\mathrm{d}W = p\mathrm{d}\varepsilon_{\mathrm{v}} + \frac{s}{1+e}\mathrm{d}e_{\mathrm{w}} \ ,$$

Where the $\mathrm{d}W$ is the rate of work for unit volume, p is the mean net stress, S_{r} is the degree of saturation, s is the suction, e is the void ratio, $\mathrm{d}\varepsilon_{\mathrm{v}}$ is the change in the volumetric strain and $\mathrm{d}e_{\mathrm{w}}$ is the change in moisture ratio. The MPK framework has been validated against a comprehensive number of experiments for I-D stress state (Islam and Kodikara, 2015; Kodikara et al., 2015) and isotropic stress state (Abeyrathne, 2017). The framework also has been extended to triaxial stress state and validated for compacted kaolin (Abeyrathne (2017). The parameters of the MPK framework for volumetric and triaxial behaviour can be obtained through simple water content testings.

The MPK framework is considered a partial theory since it does not couple the soil water retention curve (SWRC). Considering the simplicity and practical application of the MPK framework, it is recommended that a generalised constitutive model incorporating hydro coupling with plasticity based SWRC can be derived satisfying the requirements in Section 3.1. Foremost, this will provide the compatibility being sought as required by **C1**. Furthermore, the said model will naturally satisfy the other requirements and phenomenological observations. The generalised hydro mechanical coupled model is currently under development and is based on the environmentally stabilised concept and the accumulation of plastic strains upon wet-dry cycles.

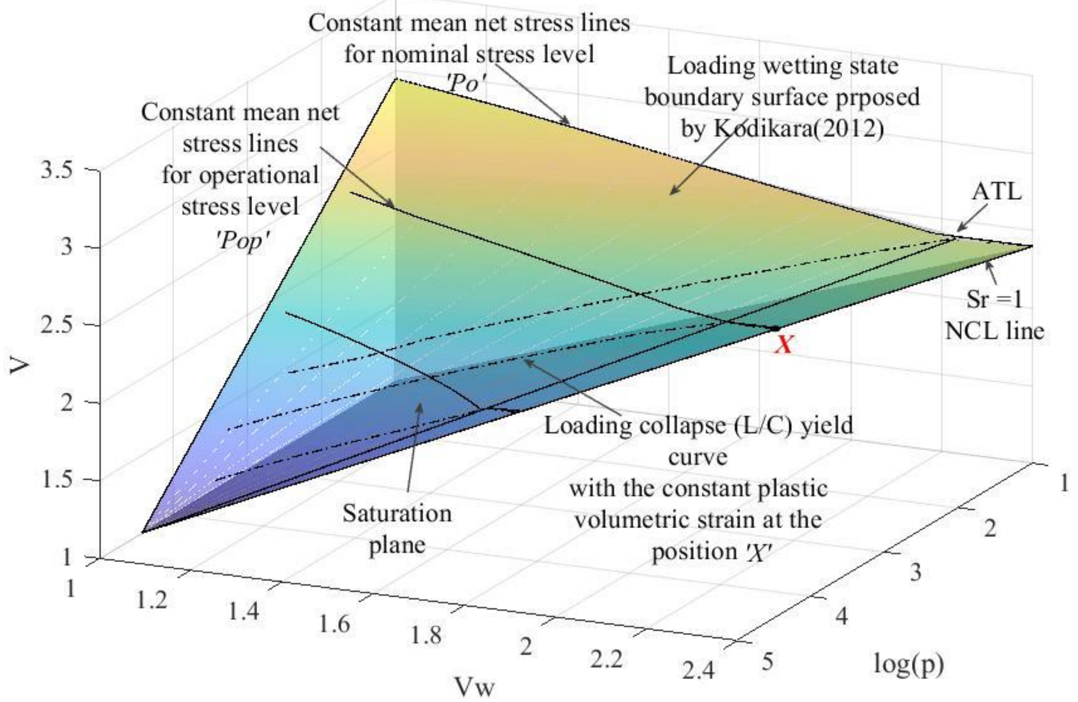

Fig. 6: The Monash-Peradeniya-Kodikara framework.

4.4 Developing the ground surface/subsurface model

Forecasting potential landslide events through accurate numerical modelling is an important and economical risk mitigating method and require information at various levels of detail. This section provides a discussion on the manner a 3D geological, and petrophysical model (3DGPM) (see also Hu et al., 2012) can be developed that will be of importance to the numerical modelling being proposed in this paper. Generally, the attributes of the 3DGPM can be subsumed into either surface or subsurface features. Although the latter is of high significance and forms the essential component of numerical modelling of landslides, the surface features are seldom discussed in detail. In the following sections, the surface and subsurface features are both categorically discussed, and the techniques for implementing their relevant properties within the 3DGPM are presented.

4.4.1 Model geometry and surface refinements

For efficient forecasting of landslides using numerical modelling tools, a 3D model geometry (3DMG) is needed that accurately represents the site characteristics. This geometry needs to include the relevant properties, which are important for accurate landslide analysis. The use of

LiDAR (light detection and ranging) based techniques in constructing topography models for use numerical modelling is now becoming common (see Hu et al., 2012; Jaboyedoff et al., 2012). Acquisition of 3D point-clouds using terrestrial laser scanning (TLS, Shan and Toth, 2018) for deriving high-resolution digital elevation models (HRDEM) provides the required level of detail necessary for accurate analysis of landslides and slope instability issues, amongst other geomatic applications. Since the HRDEM is concerned only with the soil surface of relevance to landslide analysis, the presence of trees and vegetation are viewed as noises (*e.g.*, Hu et al., 2012). Therefore, some post-processing procedures are necessary for noise filtering. Although automatic procedures for filtering noises from TLS are available, they are not always efficient, and some manual editing is necessary for complete elimination of noises and as well as non-intended targets. Once the HRDEM is constructed using LiDAR-derived techniques, the next step is to implement surface lithological variabilities. The significant lithological variabilities will be bare soil; small vegetation covered soil, and the presence of relatively large rock structures. For this purpose, the HyImag techniques can be very useful. Surface variabilities can be identified with their characteristic reflectance spectra from HyImag and comparison with existing spectral libraries (*e.g.*, Nidamanuri and Ramiya, 2014). In this manner, data fusion from LiDAR and HyImag techniques can be utilised effectively for developing the 3DMG. Apart from assigning appropriate boundary conditions at the 3DMG surface, the HyImag can also be used for elevating noise reduction from the TLS through identification of large vegetation. We believe that the joint use of LiDAR and HyImag in creating model geometries for use in numerical modelling of landslide analysis is relatively new. Consequently, it serves as a good basis for future research.

4.4.2 Subsurface stratigraphy implementation

Transforming the 3DMG into a 3D geological model (3DGM) requires knowledge on the underlying geology at the region of interest. The use of LiDAR and HyImag from the previous section (Section 4.1) are highly apposite for developing the surface topography and features. However, for a true 3D model, the appropriate depth of the model needs to be established, *i.e.*, the depth below ground surface that needs to be considered. Realistic numerical modelling of landslides requires that inter-alia, the location of the bedrock/topsoil interface is accurately known. It is common in numerical modelling to assume a parallel interface between the topsoil layer and the underlying bedrock. A reasonable estimate of the water table location is also then implemented, which may or may not be validated, through localised borehole sampling, with actual site geology. It needs to be emphasised that 3D numerical modelling requires information in 3D space and the aforementioned landslide parameter constitutes the baseline feature for the 3DGM. Apart from the bedrock/topsoil interface, identification and implementation of other stratigraphic information are also advantageous. For example, the presence of clay layer between the bedrock and topsoil can be problematic since it acts as a catalyst for shallow landslides (Carpentier et al., 2012).

The bedrock/topsoil interface and soil stratigraphy can be constrained effectively using GPR methods as demonstrated in numerous studies available in the literature (Davis and Annan, 1989; Weerasinghe, 2018). A detailed 3D GPR survey at the region of interest will assist in developing the soil stratigraphy model that can transform the 3DMG to 3DGM. For deep evaluations, GPR systems with low frequencies (≤100 MHz) will be suitable that can be blended with measurements conducted with high frequencies (>100 MHz) to provide a reasonable structural assessment. Of course, the choice of antenna frequencies will highly depend upon local soil conditions that can be estimated with archived geological information or pilot measurements at the site. Once the 3DGM is developed the petrophysical properties will be required to transform the 3DGM into the desired 3DGPM further. This can be achieved through the series of workflows described in the next section.

4.4.3 Model geometry parameter estimations

The transition from a 3D model geometry to 3D geological model attained in preceding sections (Sections 4.1 and 4.2) needs further refinements. Petrophysical properties correspond to the features of the soil pore network and the fluid that partially/completely occupies it. For efficient numerical modelling, the petrophysical properties are needed. This information can be obtained readily with the proximal sensing techniques discussed in Section 2. In this section, the manner in which important petrophysical parameters, required as inputs or secondary information for numerical modelling of landslides, can measure using PSS techniques is described. It is worthy to note here that the major petrophysical properties in the context of this paper are the porosity and moisture content distribution within the near-surface scale. Therefore, a systematic workflow is discussed that can be used to provide reasonably accurate information on these parameters.

4.4.3.1 Soil sampling, analysis, and pedophysical transfer functions

Prior to conducting PSS techniques for measurement of various subsurface soil properties, it is necessary to obtain the electropetrophysical relationships (*e.g.*, Merritt et al., 2016) that exist at the region of interest and simultaneously validate measurements of soil stratigraphy and bedrock depth assessments conducted using GPR. These tasks can be completed with undisturbed discrete core samples acquired systematically along several boreholes as follows. A widely used pedophysical transfer function relating soil resistivity to water content and porosity is the Waxman-Smits equation, which is given by Eq. 6 (Ackerson et al., 2017).

$$\frac{1}{\rho} = \sigma = \frac{1}{\phi^{-\mathbf{m}}}\left[\sigma_{\mathrm{w}}\left(\frac{\theta}{\phi}\right)^{\mathbf{n}} + \left(1-\phi^{-\mathbf{m}}\right)\sigma_{\mathrm{s}}\right] \tag{6}$$

where, σ is the soil conductivity (S m^{-1}), ϕ is the porosity (dimensionless), σ_w is the conductivity of the pore fluid (S m^{-1}), θ is the volumetric water content (dimensionless), σ_s is the surface conductivity (S m^{-1}), and m and n are the cementation factor and Archie's exponent respectively. The acquired soil samples should be analysed in a laboratory for their volumetric moisture contents, porosities, suction, surface conductivities, and resistivities. A large number of samples, from different depths and different boreholes, will need to be analysed. Following this, the applicability of Eq. 6 to the soil samples should be determined, especially the values of the cementation factor and Archie's exponent. It is noted here that an average value of surface conductivity will need to be established at the region of interest. Any corrective terms required for Eq. 6 at the site should also be identified. Apart from these, analysis of the soil type with depth and identification of the bedrock location from coring exercise will assist in validation of the GPR measurements and hence, the 3DGM. Measurement of suction on acquired soil samples at their field moisture contents will be needed to establish an empirical relationship between suction and resistivity at the region of interest. The use of this functional relationship will be discussed in next section (Section 4.3.2). Nevertheless, it will provide the initial suction values for the 3DGPM. Consequently, initial assessments from borehole samples are very important to the work being proposed in this paper.

4.4.3.2 Estimation of spatial water content, porosity, and suction distributions

Revisiting Eq. 6 again, it is noted that the soil resistivity can be considered mainly as a function of the water content and porosity. Consequently, both can not be estimated simultaneously from ERT measurements. Fortunately, data for in-situ volumetric water contents can be acquired readily using wireless moisture sensors that are small and economical. Therefore, it is proposed that columns of moisture sensors be embedded into the ground at different depths and covering a large spatial extent at the region of interest. These sensors should be capable of providing real-time variations in water contents over a network and can be part of the Internet of Things (IoT). Acquisition of water content data in this manner will need to be interpolated at unsampled locations using kriging or random forests methods (*e.g.*, Gasch et al., 2015) in order to provide an indication of 3D continuous distributions. Since the water contents will be estimated independently, the porosity variations within the region of interest can be readily estimated from 3D ERT measurements. The ERT measurements can be conducted either with deployment of surface electrode array at the time of measurement, or with permanently installed surface electrode array in the field. The latter is attractive since it will avoid manual presence at the site and the data stream generated from the measurements can be transmitted wirelessly to a cloud computing platform as part of the IoT architecture. Following measurements and 3D ERT inversion, the inverted electrical resistivity can be transformed into the region's 3D porosity distributions with the use of Eq. 6 and the 3D soil water content distribution. A reasonable similarity between the elemental sizes in the inverted 3D resistivity and 3D water content distributions will be essential for accurate porosity estimations.

It is strongly suggested that a ground-truthing of the estimated 3D porosity, inverted 3D resistivity, and 3D water content distributions are conducted through additional boreholes. This will provide confidence to the estimated and measured parameters. Once the ground-truthing is completed, the subsurface soil parameters can be implemented within the 3DGM to establish the 3DGPM.

Apart from the 3D moisture content and porosity distributions, the 3D suction distributions are also essential. The suction distributions can be measured either directly or indirectly (Tarantino et al., 2008). Direct measurements can be conducted through spot measurements using tensiometers or miniature tensiometers with maximum measuring capacities of 100 kPa (Tarantino et al., 2008) and 200 kPa (Cui et al., 2007; Ng et al., 2008) respectively. However, in-situ field suction values can get >200 kPa. For relatively large suction measurements, Mendes et al. (2018) have developed ultra-high capacity tensiometers capable of measuring up to 7 MPa. On the other hand, indirect measurements of suction can be conducted using thermocouple psychrometers, filter papers, and *etc*. (see Bulut and Leong, 2008). The aforementioned direct and indirect methodologies provide discrete measurements of suction. If the sensors based on direct methods are wireless, installed permanently, and connected over a network, then they can also be part of the IoT, similar to the moisture sensors. Alternatively, Piegari and Di Maio (2013) demonstrated that it is possible to acquire subsurface suction distributions through ERT measurements. They achieved this by developing analytical models for resistivity-suction based on van Genuchten model and experimental data. Similar to 3D porosity and water content distributions, the suction profiles can also be developed through the analytical concepts demonstrated by Piegari and Di Maio (2013).

4.5 Data fusion approach

Data fusion is termed as an improved version of raw data obtained through sensors with the help of other sources of information. Data fusion classifications are based on the relations between data sources, input/output data types and their nature, the abstraction levels, and type of architecture. In this paper, one of the categories of Dasarathy's classification (data in-feature out (DAI-FEO)) is utilized Dasarathy, 1997. This approach is predicting environmental features from raw data. In this paper, the raw data is from the ERT measurements, which are transformed through various processing stages in order to retrieve the QCSP at the site of interest. The overall measurement and processing architecture of the proposed concept is shown in Fig. 2. There are 3 important phases involved in acquiring the computed suction field as shown in Fig. 2. Phase A consists of laboratory measurements in order to develop an initial petro geophysical transfer function for retrieving suction from soil resistivity. Phase B involves field measurement, whereby the subsurface apparent resistivity profiles are acquired from ERT and inverted to provide the true subsurface resistivity variations, and the point scale suction measurements are acquired using discrete sensors. Phase C stage involves the major processing stage, whereby the true resistivity variations are transformed to the QCSP using the initial mode, which is subsequently updated based on the level of error and within a selective correction approach (SCA) framework. The individual phases are explained in detail as follows.

4.5.1 Phase A: Laboratory testing and the formulation of the initial petro geophysical transfer function

The Waxman-Smits (WS) model Ackerson et al., 2017 defines the relationship between soil resistivity (reciprocal of conductivity), porosity, and volumetric water content as given in Eq. 1.

$$\frac{1}{\rho}=\sigma=\frac{1}{\phi^{-\mathbf{m}}}\left[\sigma_{\mathrm{w}}\left(\frac{\theta}{\phi}\right)^{\mathbf{n}}+\left(1-\phi^{-\mathbf{m}}\right)\sigma_{\mathrm{s}}\right] \tag{5}$$

where, σ is the soil conductivity (S m^{-1}), ϕ is the porosity (dimensionless), σ_w is the conductivity of the pore fluid (S m^{-1}), θ is the volumetric water content (dimensionless), σ_S is the surface conductivity (S m^{-1}) and can be reasonably assumed for predominant clay types at a given field site, and m and n are the cementation factor and Archie's exponent respectively. On the other hand, the Van Genuchten (1980) equation, which describes the soil water retention curves (SWRC), can be written in terms of the volumetric water content for a range of suction values (s) as shown in Eq. 2.

$$\theta=\frac{1}{\left(1+\left(\frac{s}{a}\right)^{\mathrm{n}^*}\right)^{\mathrm{m}^*}} \tag{6}$$

where, a (kPa), m^* (dimensionless), and n^* (dimensionless), are the parameters related to air entry value, asymmetric shape of the curve and the rate of change of the slope of the curve respectively. The parameter a does not define any specific point in the SWRC. Therefore, to incorporate the inflection point properties, Eq. 2 needs to be modified. In other words, the point with maximum slope, which plays a critical role where air phase and water phase becomes discontinuous and continuous, can be incorporated in constitutive modelling of unsaturated soils as it lies on the Line of optimum (LOO) of the compaction curve. Hence, the point of inflection can be obtained by as per Eq. 3.

$$\frac{\mathrm{d}^2\theta}{\mathrm{d}(\ln s)^2}=\frac{-m^*n^*s^{\mathrm{n}^*-1}}{a^{\mathrm{n}^*}}\left(1+\left(\frac{s}{a}\right)^{\mathrm{n}^*}\right)^{-\mathrm{m}^*-2}\left\{n^*\left(1+\left(\frac{s}{a}\right)^{\mathrm{n}^*}\right)-\frac{(m^*+1)n^*s^{\mathrm{n}^*}}{a^{\mathrm{n}^*}}\right\} \tag{7}$$

Consequently, at the inflection point, the volumetric water content and suction are $\theta^{\mathrm{L}}=\left(\frac{m}{1+m}\right)^{\mathrm{m}}$ and $a_{\mathrm{w}}=am^{-1/\mathrm{n}}$ respectively. Following these arguments, Eq. 2 can be rewritten as:

$$\theta=\frac{1}{\left(1+\frac{1}{m^*}\left(\frac{s}{a_{\mathrm{w}}}\right)^{\mathrm{n}^*}\right)^{\mathrm{m}^*}} \tag{8}$$

Following Eqs. 1 and 4, the relationship between suction and electrical resistivity can be explicitly stated as per Eq. 5. The petro geophysical transfer function given by Eq. 5 can be used to determine the suction from ERT measurements, provided the other parameters are known.

$$\frac{1}{\rho}=\sigma=\frac{1}{\phi^{-\mathbf{m}}}\left[\sigma_{\mathrm{w}}\left(\frac{\left(1+\frac{1}{m^*}\left(\frac{s}{a_{\mathrm{w}}}\right)^{\mathrm{n}^*}\right)^{\text{-m}^*}}{\phi}\right)^{\mathbf{n}}+\left(1-\phi^{-\mathbf{m}}\right)\sigma_{\mathrm{s}}\right] \tag{9}$$

It is noted that there are 7 material parameters (m, m^*, n , n^*, a_{w} , σ_{s} and σ_{w}) in Eq. 5 along with the porosity parameter. A pre-assessment of porosity is needed before the petro geophysical transfer function in Eq. 5 can be calibrated for the material parameters. A similar petro geophysical transfer function was obtained by Piegari and Di Maio (2013) for predicting the suction distribution at field-scale through ERT measurements.

The initial laboratory testing involves suction and electrical resistivity measurements on a suite of soil samples acquired from the field of interest. The laboratory suction measurements can be conducted using the HYPROP test equipment and WP4C dew-point potentiometer for low (up to 150 kPa) and high suction (>150 kPa) ranges respectively to obtain the SWRC. The electrical resistivity measurements can be conducted at different soil moisture contents using the Wenner 4-point method. The suite of suction and electrical resistivity measurements at different moisture contents can then be used to ascertain the feasibility of Eq. 5 and simultaneously provide initial estimates of the 7 material parameters. As mentioned previously, a porosity value will need to be ascertained, which is representative of the soil samples and is also applicable generally to the field. The generalisation of a single porosity estimation at field level may not be highly accurate and can be refined. However, it is not the intent of this work to provide the manner in which porosity estimation refinements can be conducted. Rather, the aim of this paper is to provide an indication of how suction profiles can be generated using ERT.

4.5.2 Phase B: ERT and suction measurements and processing

Electrical resistivity tomography is an advanced geophysical technique, which is used to characterize the subsurface material characteristics remotely from the ground surface. A complete description of the ERT method is not required here and can be found in Binley and Kemna, 2005. However, it is noted that there are two ways ERT measurements can be acquired for the purpose of work discussed in this paper. Permanently installed electrodes can be placed strategically within the field of interest, and the measurements can be transmitted wirelessly to a data cloud. Alternatively, the measurements can be acquired using an autonomous vehicle retrofitted with drag-along electrodes, that can acquire ERT measurements and also transmit the data stream to a cloud network. Either approach is suitable and can be decided based on the frequency of measurements required, measurement refinement needs, consequence of failure, and economical feasibility. Data from the ERT measurements can be retrieved from the cloud and processed to obtain apparent resistivity distributions in the subsurface. The apparent resistivity distributions will need to be transformed into true resistivity distributions through inversion processes Loke et al., 2013. Integrating knowledge on known local geological conditions to improve the inversion process can also be seen as an added layer of data fusion problem. The ERT can be used to acquire either 2D or true 3D resistivity distributions and for the purpose of estimating suction profiles, the latter is preferred.

Field suction distributions can be measured directly using tensiometers with a maximum measuring capacity of 100 kPa Tarantino et al., 2008 or up to 200 kPa Cui et al., 2007; Ng et al., 2008. Since in the field suction can be > 200 kPa, the ultra-high capacity tensiometer with a maximum capacity of 7 MPa developed by Mendes et al. (2018) can also be utilised. The finite point-scale measurements of suction can be conducted using a suite and a mixture of the various tensiometers mentioned. Here again, measurements from the tensiometers can be configured to be transmitted wirelessly to the data cloud. In this manner both the ERT and suction data streams can be accessed via data cloud for processing, avoiding the need for manual site visitations for data collection.

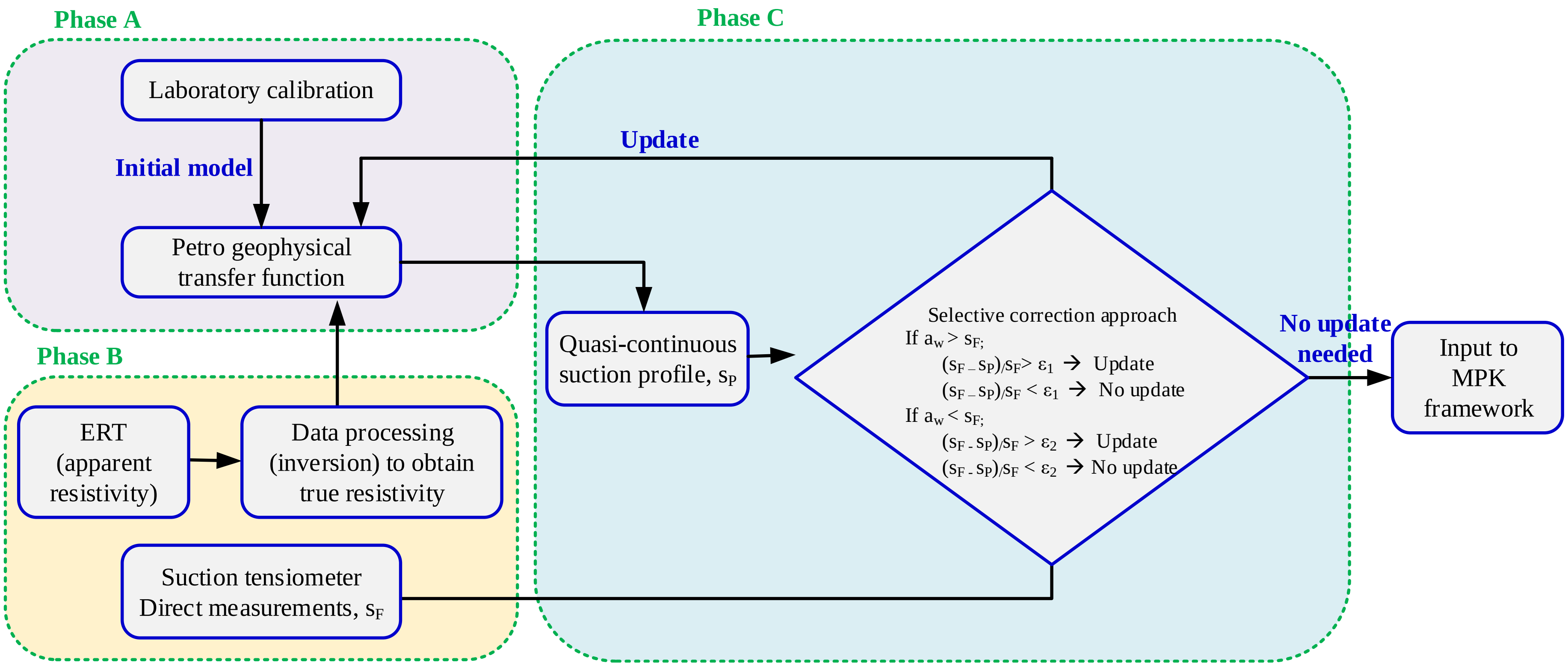

Fig. 2: Estimation of the quasi-continuous suction profile via electrical resistivity tomography involving the selective correction approach for petro geophysical transfer function updating.

4.5.3 Phase C: Suction profiles from ERT and Selective Correction Approach

In the first execution of the model predictions, the QCSP is obtained with the initial petro geophysical transfer function from Phase A. A comparison of the QCSP at selected locations with the actual suction measurements from the tensiometers will indicate the level of error in the estimated QCSP. Note, the selected locations refer to the locations where the tensiometers are located. Since the QCSP at field scale can be a computationally demanding feature to improve in every execution step, alternate correction approaches need to be considered. These alternative approaches should weigh the benefit of improvising the complete QCSP against the improvements in deformation stress state modelling using the MPK framework. In this paper, we suggest the selective correction approach (SCA), which can be seen as an optimised model updating procedure based on the errors involved in the computed and measured suction values as follows.

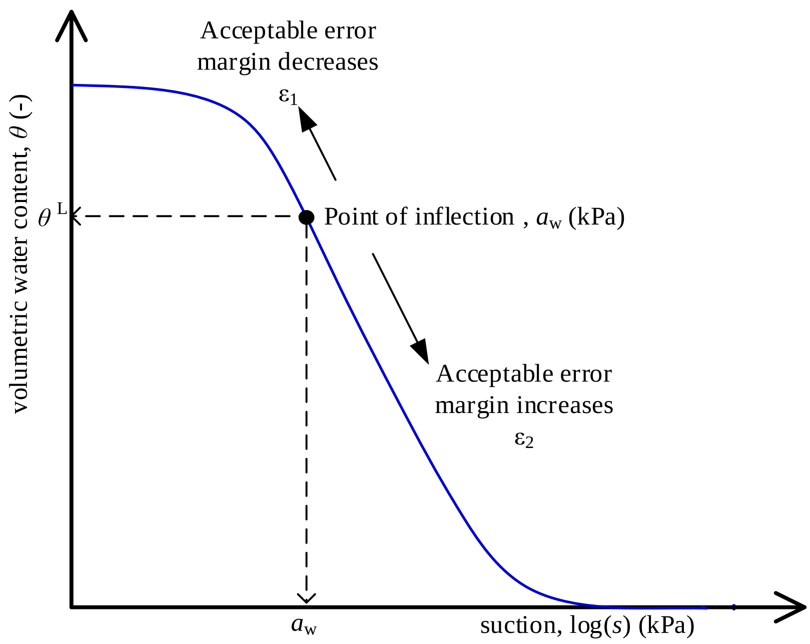

Fig. 3: A typical soil water retention curve showing the point of inflection. Relatively high accuracies in suction values are needed for $s_F < a_w$ to ensure accurate constitutive unsaturated soil modelling. The acceptable error margins in suction generally increases beyond a_w. This basis forms the concept of selective correction approach.

The hydraulic behaviour of unsaturated soils is well captured by the SWRC, where the change in the volumetric water content follows a '*S*' shaped pattern with the log-scaled suction as shown in Fig. 3. As the initial suction variation is low up to the air transition, high accuracy (error margin, ε_1, of 0.05) is needed for efficient modelling using the MPK framework.

Furthermore, hence the Bishop's effective stress is applicable in this region, the need of accuracy of suction is further emphasised. However, the same error margin is not necessarily needed at relatively higher suction values, *i.e.*, a relatively larger ε_2 can suffice at higher suction, and hence lower volumetric water content, values. The SCA will be a programmed software routine within the data analysis, which will investigate the relative deviations between the suction values from direct measurements and the estimations within the QCSP derived using the petro geophysical transfer function. If for a given low suction range the difference is higher than 0.05, the petro geophysical transfer function will be updated accordingly by varying the material parameters to minimise the error. Similarly, different error margins can be associated with different suction ranges and the relative differences between estimated and measured suction determined during each execution in order to decide if the petro geophysical transfer function needs to be updated. Apart from saving computational time, the SCA approach will ensure that resources are more focussed in improving the estimations that will directly improve the deformation stress state modelling with the MPK framework. Furthermore, this approach will minimise unnecessary petro geophysical transfer function updates for the complete suction range in every model iteration, which itself can exist as a difficult optimisation problem.

4.6 Proposed conceptual approach, validations, and forecasting

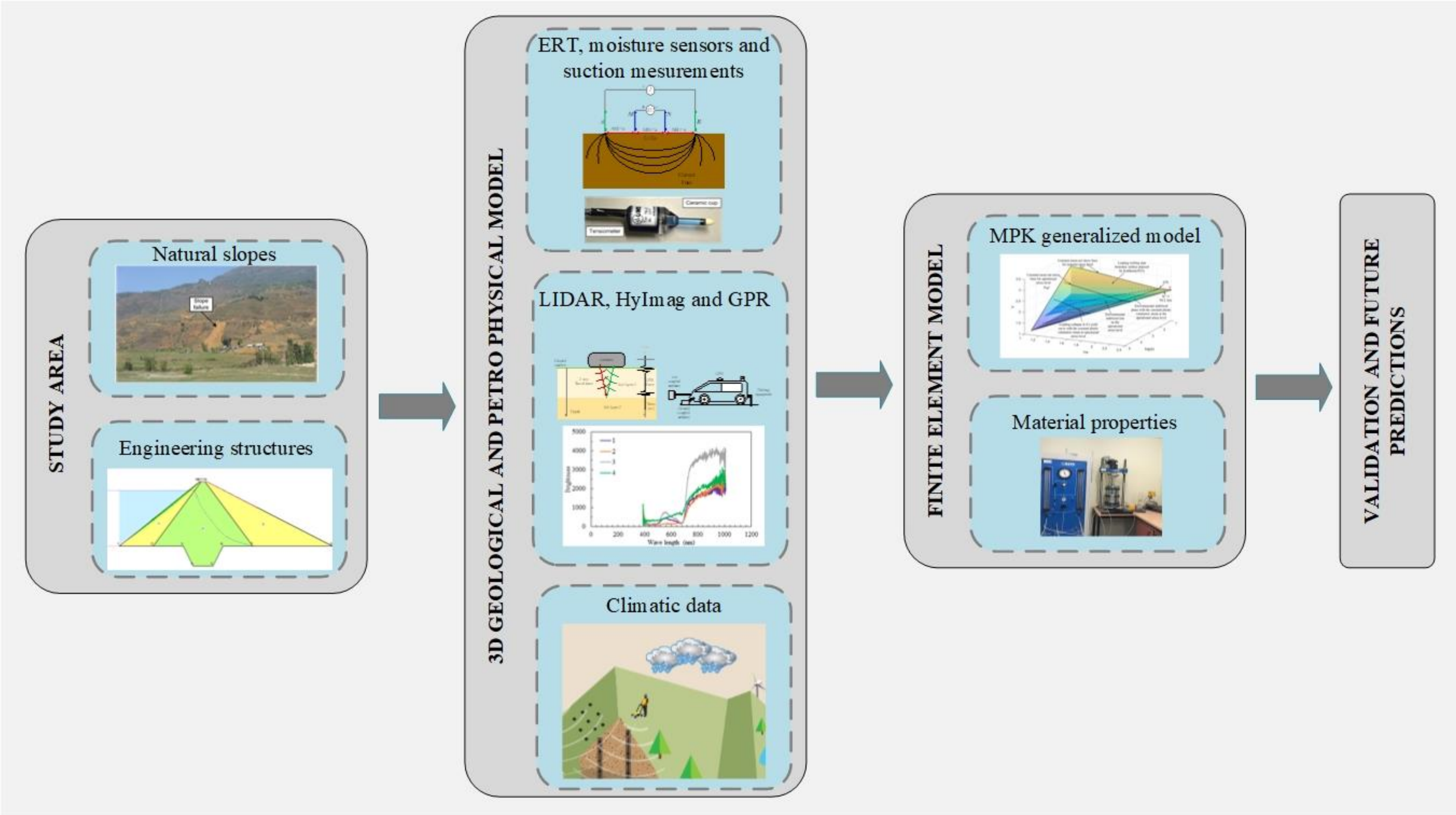

Fig. 7: Summary of the proposed conceptual approach.

The conceptual framework for numerical modelling of landslide events advocated in this paper is focused on natural slope failure analysis, albeit it is duly noted that the same concepts are equally applicable to engineered structures. The workflow for the conceptual approach is summarised in Fig. 7. Initially, a three-dimensional topography data for the region of interest is needed. The LiDAR and HyImag techniques are considered the primary methodologies for creating the 3D geometry. The subsurface structural and petrophysical details can be determined from GPR and ERT methods as discussed in Section 4. The boundary conditions for the 3DGPM will mainly be based on local precipitation trends since other ambient and micro-meteorological conditions can be safely ignored (Tarantino et al., 2008). The surface of the 3DGPM representing the air/ground interface will need to be imposed with time-dependent rainfall trends. These trends can be ascertained from archived meteorological data (*e.g.*, Wang et al., 2017) and complimented with permanently installed rain gauges at the study area. The other internal interfaces of the 3DGPM will need to be imposed with accurate permeability information, which can be evaluated in-situ with double ring infiltrometer tests (Ng et al., 2008) or under laboratory conditions using core samples from boreholes.

In the finite element modelling phase (Fig. 7), a material model will be required, which is capable of capturing significant unsaturated soil phenomenological behaviours. Generally, the application of unsaturated soil mechanics in geotechnical practice is limited. This is mainly because the estimation of relevant state parameters in the field are viewed as time-consuming. In this study, we show that there are several proximal sensing techniques, which can be tailored to suit the parameter requirements of unsaturated soil mechanics and as well as provide high turn-over in the field. Validation of the finite element model will need to be conducted using the mixture of PSS techniques and as well as with discrete measurements. Ground settlement can be captured through LiDAR measurements (*e.g.*, Hu, 2013) and utilised for validating the deformation state predicted from the finite element modelling exercise. Additionally, it is worthwhile to consider a smart feedback finite element modelling approach. Here, the smart feedback should provide an indication whether the modelling results can be improved with local refinements in elemental subsurface properties (*e.g.*, stratigraphy, petrophysical properties *etc*) of the 3DGPM. This feature will ensure that the finite element modelling is tuneable to dynamic site conditions. Moreover, any discrepancies in the data stream from moisture and suction sensors, and ERT measurements will also be easily identifiable. Discrete suction measurements using appropriate tensiometers (Section 4.3.2) with the numerical modelling results are also proposed for stringent validation. Once the finite element model and modelling results are confidently validated, it can then be used for predicting soil deformation states.

The preceding methods for estimating the initial values of the 3DGPM will provide the starting conditions for the numerical modelling of soil deformation. Measurements or estimations of suction in the unsaturated zone will also be important. The analytical modelling work of Piegari and Di Maio, 2013 is promising for this application. Discrete suction measurements should also be conducted to validate the 3D suction distributions estimated via ERT. It is duly noted that research in developing pedophysical transfer functions amongst resistivity and suction needs to be advanced further and will provide strong solutions to current challenges in geotechnical engineering. Nevertheless, in this study, the porosity and water content distributions are considered as baseline measurements, while suction is utilised as supplementary information, for model calibration and ground truthing. Furthermore, in this study we have suggested the use of a generalised MPK model. However, any model based on unsaturated soil mechanics satisfying the conditions presented in Section 3.1 can be utilised for numerical modelling.

The conceptual approach proposed in this paper provides means to address several geohazards and includes early warning and monitoring of hazardous areas, monitoring existing engineered structures (*e.g.*, embankments and dams), forecasting critical-level event scenarios (*e.g.*, intense rainfall), and *etc*. The complete analysis and forecasting system can be based on cloud computing, with data streams from different sensors and measurements processed centrally and results broadcasted over the internet to geo-infrastructure management teams. It is noted that data streams from the TLS, HyImag, and GPR using a mobile vehicle (Fig. 3b) can all be transmitted wirelessly to the cloud based data processing. Accuracy of the proposed conceptual approach can be hindered with errors resulting from initial 3DGPM development. However, this should be addressable if a smart feedback modelling approach is implemented as discussed elsewhere. Nonetheless, a practical implementation of the conceptual work proposed in this paper should also cater for significant uncertanities of state and material parameters at different stages of model development, execution, and validation.

4.7 Discussion

Accurate constitutive modelling of unsaturated soil behaviour within the MPK framework relies on accurate input of relevant constitutive variables. In regards to suction, the expensive tensiometers and point-scale nature of measurements necessitate the use of alternative techniques that can assist in high-density estimations of subsurface suction profiles. In this work we presented a methodology that can be utilised for efficient monitoring of subsurface quasi-continuous suction profiles via electrical resistivity tomography and data fusion approaches, for validation and calibration, that can be implemented within a data cloud architecture.

Retrieval of suction from soil electrical resistivity was based on a petro geophysical transfer function, which needs to be initially developed with laboratory soil samples. Updates and recalibration of the petro geophysical transfer function using field measurements can then be conducted using a selective correction approach, which is based on the error margins acceptable within the MPK framework. Developments in the refinement of the selective correction approach discussed in the paper will be highly beneficial to achieving this aim. Moreover, the methodology discussed can be extended to the estimation of the other constitutive variables necessary in the MPK framework, thereby enabling the constitutive modelling of unsaturated soil to be implementable within the context of IOT. This should be pursued further.

4.8 Conclusion

In this paper, a conceptual framework has been presented, where proximal soil sensing techniques were integrated with unsaturated soil mechanics concepts to envision a finite element model capable of studying the behaviour of geo-infrastructures. The proximal soil sensing methods for spatial and temporal analysis has advanced rapidly over the years with improvements in analytical, statistical and computational methods, which is capable of providing accurate, qualitative, and quantitative surface/subsurface soil properties information with relatively high resolution. A systematic workflow was presented, which would provide a strong framework within which soil deformation state analysis can be conducted efficiently. Important stages of the workflow are summarised as follows:

- identification of the study area,
- development of the 3D geological and petrophysical model,
- application of boundary conditions to the model using past and recent climatic data,
- development of a constitutive finite element model with smart feedback capabilities,
- material parameter estimation and implementation of the initial stress state variables and,
- validation of the envisioned finite element model and its application in forecasting.

Furthermore, the possibility of integrating data streams from all sensors and measurements onto a cloud based processing architecture was highlighted. The ideas expressed in this paper are capable of providing timely advances in geohazard mitigation. The scope for further research discussed will be very beneficial in this aspect. In particular, development of accurate and robust pedophysical transfer functions will greatly benefit geotechnical practitioners for incorporating modern benefits of proximal soil sensing techniques in geohazard management. In future studies, we aim to implement the proposed conceptual approach in a case study, which will provide indications on its practical limitations and advantages.

4.9 REFERENCES

Abeyrathne, W. K. a. P. 2017. *A new modelling approach for compacted clayey soils using specific water volume as a state variable.* Ph.D. thesis, Monash University, Melbourne, Australia.

Ackerson, J. P., Mcinnes, K. J., Morgan, C. L. S. & Everett, M. E. 2017. Measuring Crack Porosity using Three-Dimensional Electrical Resistivity Tomography. *Soil Science Society of America Journal,* 81**,** 1025-1035.

Alonso , E. E., Gens , A. & Josa, A. 1990. A constitutive model for partially saturated soils. *Géotechnique,* 40(3)**,** pp.405-430.

Amigo, J. M., Babamoradi, H. & Elcoroaristizabal, S. 2015. Hyperspectral image analysis. A tutorial. *Analytica chimica acta,* 896**,** 34-51.

Annan, A. P. 2009. Chapter 1 - Electromagnetic Principles of Ground Penetrating Radar. *In:* JOL, H. M. (ed.) *Ground Penetrating Radar Theory and Applications.* Amsterdam: Elsevier.

Azizi, A., Jommi, C. & Musso, G. 2017. A water retention model accounting for the hysteresis induced by hydraulic and mechanical wetting-drying cycles. *Computers and Geotechnics,* 87**,** 86-98.

Barker, R. D. 1989. Depth of investigation of collinear symmetrical four-electrode arrays. *Geophysics,* 54**,** 1031-1037.

Binley, A. & Kemna, A. 2005. DC Resistivity and Induced Polarization Methods. *In:* RUBIN, Y. & HUBBARD, S. S. (eds.) *Hydrogeophysics.* Dordrecht: Springer Netherlands.

Brideau, M.-A., Sturzenegger, M., Stead, D., Jaboyedoff, M., Lawrence, M., Roberts, N. J., Ward, B. C., Millard, T. H. & Clague, J. J. 2012. Stability analysis of the 2007 Chehalis lake landslide based on long-range terrestrial photogrammetry and airborne LiDAR data. *Landslides,* 9**,** 75-91.

Bulut, R. & Leong, E. C. 2008. Indirect measurement of suction. *Laboratory and Field Testing of Unsaturated Soils.* Springer.

Carpentier, S., Konz, M., Fischer, R., Anagnostopoulos, G., Meusburger, K. & Schoeck, K. 2012. Geophysical imaging of shallow subsurface topography and its implication for shallow landslide susceptibility in the Urseren Valley, Switzerland. *Journal of Applied Geophysics,* 83**,** 46-56.

Cassidy, N. J. 2009. Chapter 2 - Electrical and Magnetic Properties of Rocks, Soils and Fluids. *In:* JOL, H. M. (ed.) *Ground Penetrating Radar Theory and Applications.* Amsterdam: Elsevier.

Coulomb, C. A. 1776. Essai sur une application des règles de maximis & minimis à quelques problèmes de statique, relatifs à l'architecture. *Mémoires de Mathématique de l'Académie Royale des Sciences,* 7**,** 343-383.

Cui, Y.-J., Tang, A.-M., Mantho, A. T. & De Laure, E. 2007. Monitoring field soil suction using a miniature tensiometer. *Geotechnical Testing Journal,* 31**,** 95-100.

Cunningham, M., Ridley, A., Dineen, K. & Burland, J. 2003. The mechanical behaviour of a reconstituted unsaturated silty clay. *Géotechnique,* 53**,** 183-194.

Dahlin, T., Leroux, V. & Nissen, J. 2002. Measuring techniques in induced polarisation imaging. *Journal of Applied Geophysics,* 50**,** 279-298.

Das, A. P. & Thyagaraj, T. 2018. Collapse behaviour of compacted red soil. *International Journal of Geotechnical Engineering,* 12**,** 20-27.

Dasarathy, B. V. 1997. Sensor fusion potential exploitation-innovative architectures and illustrative applications. *Proceedings of the IEEE,* 85**,** 24-38.

Davis, J. L. & Annan, A. P. 1989. Ground-penetrating radar for high-resolution mapping of soil and rocks stratigraphy. *Geophysical Prospecting,* 37**,** 531-551.

Delage, P., Pereira, J. & Cui, Y. 2015. Collapse behaviour of a natural loess from Northern France. *Bioinspired Photonics: Optical Structures and Systems Inspired by Nature***,** 315.

Deo, R. N., Azoor, R. M., Zhang, C. & Kodikara, J. K. 2017. Decoupling pipeline influences in soil resistivity measurements with finite element techniques. *Journal of Applied Geophysics,* 150**,** 304-313.

Deo, R. N. & Cull, J. P. 2016. Denoising time-domain induced polarisation data using wavelet techniques. *Exploration Geophysics,* 47**,** 108-114.

Dong, M., Hu, H. & Song, J. 2018. Combined methodology for three-dimensional slope stability analysis coupled with time effect: a case study in Germany. *Environmental Earth Sciences,* 77**,** 311.

Edwards, L. S. 1977. A modified pseudosection for resistivity and IP. *Geophysics,* 42**,** 1020-1036.

Evjen, H. M. 1938. Depth factor and resolving power of electrical measurements. *Geophysics,* 3**,** 78-95.

Fredlund, D., Houston, S. & Caicedo, B. 2013. Interpretation of soil-water characteristic curves when volume change occurs as soil suction is changed. *Advances in unsaturated soils,* 1**,** 15.

Fredlund, D., Morgenstern, N. R. & Widger, R. 1978. The shear strength of unsaturated soils. *Canadian geotechnical journal,* 15**,** 313-321.

Fredlund, D. G. & Rahardjo, H. 1993. *Soil mechanics for unsaturated soils,* New York, USA, John Wiley & Sons Inc.

Gallipoli, D., Gens, A., Sharma, R. & Vaunat, J. 2003. An elasto-plastic model for unsaturated soil incorporating the effects of suction and degree of saturation on mechanical behaviour. *Géotechnique.,* 53**,** 123-136.

Gallipoli, M., Lapenna, V., Lorenzo, P., Mucciarelli, M., Perrone, A., Piscitelli, S. & Sdao, F. 2000. Comparison of geological and geophysical prospecting techniques in the study of a landslide in southern Italy. *European Journal of Environmental and Engineering Geophysics,* 4**,** 117-128.

Gasch, C. K., Hengl, T., Gräler, B., Meyer, H., Magney, T. S. & Brown, D. J. 2015. Spatio-temporal interpolation of soil water, temperature, and electrical conductivity in 3D + T: The Cook Agronomy Farm data set. *Spatial Statistics,* 14**,** 70-90.

Gens, A. & Alonso, E. 1992. A framework for the behaviour of unsaturated expansive clays. *Canadian Geotechnical Journal,* 29**,** 1013-1032.

Gould, S. J., Kodikara, J., Rajeev, P., Zhao, X.-L. & Burn, S. 2011. A void ratio–water content–net stress model for environmentally stabilized expansive soils. *Canadian Geotechnical Journal,* 48**,** 867-877.

Houlsby, G. 1997. The work input to an unsaturated granular material. *Géotechnique,* 47**,** 193-196.

Hu, H. 2013. *Deformation monitoring and modeling based on LiDAR data for slope stability assessment.* Ph.D. thesis, RWTH Aachen University.

Hu, H., Fernandez-Steeger, T. M., Dong, M. & Azzam, R. 2012. Numerical modeling of LiDAR-based geological model for landslide analysis. *Automation in Construction,* 24**,** 184-193.

Islam, T. & Kodikara, J. 2015. Interpretation of the loading–wetting behaviour of compacted soils within the "MPK" framework. Part I: Static compaction 1. *Canadian Geotechnical Journal,* 53**,** 783-805.

Jaboyedoff, M., Oppikofer, T., Abellán, A., Derron, M.-H., Loye, A., Metzger, R. & Pedrazzini, A. 2012. Use of LIDAR in landslide investigations: a review. *Natural hazards,* 61**,** 5-28.

Jommi, C. 2000. Remarks on the constitutive modelling of unsaturated soils. *Experimental evidence and theoretical approaches in unsaturated soils***,** 139-153.

Jung, A., Vohland, M. & Thiele-Bruhn, S. 2015. Use of A Portable Camera for Proximal Soil Sensing with Hyperspectral Image Data. *Remote Sensing,* 7**,** 11434.

Khalili, N. 2018. Guidelines for the application of the effective stress principle to shear strength and volume change determination of unsaturated soils. *AGS VICTORIA 2018 Symposium.* Melbourne.

Klotzsche, A., Jonard, F., Looms, M., Van Der Kruk, J. & Huisman, J. 2018. Measuring Soil Water Content with Ground Penetrating Radar: A Decade of Progress. *Vadose Zone Journal,* 17.

Kodikara, J. 2012. New framework for volumetric constitutive behaviour of compacted unsaturated soils. *Canadian Geotechnical Journal,* 49**,** 1227-1243.

Kodikara, J., Barbour, S. & Fredlund, D. G. 2002. Structure development in surficial heavy clay soils: a synthesis of mechanisms. *Australian Geomechanics: Journal and News of the Australian Geomechanics Society,* 37**,** 25.

Kodikara, J., Islam, T. & Rajeev, P. 2015. Interpretation of the loading–wetting behaviour of compacted soils within the "MPK" framework. Part II: Dynamic compaction 1. *Canadian Geotechnical Journal,* 53**,** 806-827.

Krahn, J., Fredlund, D. & Klassen, M. 1989. Effect of soil suction on slope stability at Notch Hill. *Canadian Geotechnical Journal,* 26**,** 269-278.

Lloret-Cabot, M., Wheeler, S. J., Pineda, J. A., Romero, E. & Sheng, D. 2017. From saturated to unsaturated conditions and vice versa. *Acta Geotechnica***,** 1-23.

Loke, M. H., Chambers, J. E., Rucker, D. F., Kuras, O. & Wilkinson, P. B. 2013. Recent developments in the direct-current geoelectrical imaging method. *Journal of Applied Geophysics*, 95**,** 135-156.

Mendes, J., Gallipoli, D., Tarantino, A. & Toll, D. 2018. On the development of an Ultra-High Capacity Tensiometer capable of measuring water tensions to 7 MPa. *Géotechnique***,** 1-5.

Merritt, A. J., Chambers, J. E., Wilkinson, P. B., West, L. J., Murphy, W., Gunn, D. & Uhlemann, S. 2016. Measurement and modelling of moisture—electrical resistivity relationship of fine-grained unsaturated soils and electrical anisotropy. *Journal of Applied Geophysics,* 124**,** 155-165.

Ng, C. W., Springman, S. M. & Alonso, E. E. 2008. Monitoring the performance of unsaturated soil slopes. *Laboratory and Field Testing of Unsaturated Soils.* Springer.

Nidamanuri, R. R. & Ramiya, A. M. 2014. Spectral identification of materials by reflectance spectral library search. *Geocarto International,* 29**,** 609-624.

Perrone, A., Lapenna, V. & Piscitelli, S. 2014. Electrical resistivity tomography technique for landslide investigation: A review. *Earth-Science Reviews,* 135**,** 65-82.

Piegari, E. & Di Maio, R. 2013. Estimating soil suction from electrical resistivity. *Natural Hazards and Earth System Sciences,* 13**,** 2369-2379.

Pinyol, N. M., Alvarado, M., Alonso, E. E. & Zabala, F. 2018. Thermal effects in landslide mobility. *Géotechnique,* 68**,** 528-545.

Potts, D. 2002. *Guidelines for the use of advanced numerical analysis,* Thomas Telford.

Rahardjo, H. & Leong, E. 2006. Suction measurements. *Unsaturated Soils 2006***,** 81-104.

Raveendiraraj, A. 2009. *Coupling of mechanical behaviour and water retention behaviour in unsaturated soils.* Ph.D. thesis, University of Glasgow.

Reynolds, J. M. 2011. *An Introduction to Applied and Environmental Geophysics,* New York, UNITED KINGDOM, John Wiley & Sons, Incorporated.

Riese, F. M. & Keller, S. Fusion of hyperspectral and ground penetrating radar to estimate soil moisture. IEEE WHISPERS 2018 conference, 2018.

Romero, E., Della Vecchia, G. & Jommi, C. 2011. An insight into the water retention properties of compacted clayey soils. *Géotechnique,* 61**,** 313-328.

Roscoe, K. H. & Burland, J. 1968. On the generalized stress-strain behaviour of wet clay. *Enginnering plasticity.* London, England: , J. Heyman and F. A. Lekie, eds., Cambridge University Press.

Roy, A. & Apparao, A. 1971. Depth of investigation in direct current methods. *Geophysics,* 36**,** 943-959.

Scaioni, M., Longoni, L., Melillo, V. & Papini, M. 2014. Remote sensing for landslide investigations: An overview of recent achievements and perspectives. *Remote Sensing,* 6**,** 9600-9652.

Shan, J. & Toth, C. K. 2018. *Topographic Laser Ranging and Scanning: Principles and Processing, Second Edition,* Taylor & Francis.

Sharma, R. S. 1998. *Mechanical behaviour of unsaturated highly expansive clays.* Ph.D. thesis, University of Oxford.

Sheng, D., Zhang, S. & Yu, Z. 2013. Unanswered questions in unsaturated soil mechanics. *Science China Technological Sciences,* 56**,** 1257-1272.

Sivakumar, V. 1993. *A critical state framework for unsaturated soil.* Ph.D. thesis, University of Sheffield.

Sun, D. A., Sheng, D. & Xu, Y. 2007. Collapse behaviour of unsaturated compacted soil with different initial densities. *Canadian Geotechnical Journal,* 44**,** 673-686.

Szalai, S., Novak, A. & Szarka, L. 2009. Depth of investigation and vertical resolution of surface geoelectric arrays. *Journal of Environmental and Engineering Geophysics,* 14**,** 15-23.

Tamagnini, R. 2004. An extended Cam-clay model for unsaturated soils with hydraulic hysteresis. *Géotechnique,* 54**,** 223-228.

Tarantino, A. Unsaturated soils: compacted versus reconstituted states. 5th International Conference on Unsaturated Soil, 2010. 113-136.

Tarantino, A., Ridley, A. M. & Toll, D. G. 2008. Field measurement of suction, water content, and water permeability. *Geotechnical and Geological Engineering,* 26**,** 751-782.

Tarantino, A. & Tombolato, S. 2005. Coupling of hydraulic and mechanical behaviour in unsaturated compacted clay. *Géotechnique,* 55**,** 307-317.

Telford, W. M., Geldart, L. P. & Sheriff, R. E. 1990. *Applied geophysics,* UK, Cambridge University Press.

Tohari, A. Study of rainfall-induced landslide: a review. IOP Conference Series: Earth and Environmental Science, 2018. IOP Publishing, 012036.

Tripathy, S., Rao, K. S. & Fredlund, D. 2002. Water content-void ratio swell-shrink paths of compacted expansive soils. *Canadian geotechnical journal,* 39**,** 938-959.

Van Genuchten, M. T. 1980. A closed-form equation for predicting the hydraulic conductivity of unsaturated soils. *Soil science society of America journal,* 44**,** 892-898.

Viscarra Rossel, R. A., Adamchuk, V. I., Sudduth, K. A., Mckenzie, N. J. & Lobsey, C. 2011. Chapter Five - Proximal Soil Sensing: An Effective Approach for Soil Measurements in Space and Time. *In:* SPARKS, D. L. (ed.) *Advances in Agronomy.* Academic Press.

Wang, M., Liu, K., Yang, G. & Xie, J. 2017. Three-dimensional slope stability analysis using laser scanning and numerical simulation. *Geomatics, Natural Hazards and Risk,* 8**,** 997-1011.

Weerasinghe, D. 2018. *A failure analysis of small diameter cast iron pipes in reactive soil zones of Melbourne.* PhD, Monash University.

Wheeler, S., Sharma, R. & Buisson, M. 2003. Coupling of hydraulic hysteresis and stress–strain behaviour in unsaturated soils. *Géotechnique,* 53**,** 41-54.

Wheeler, S. & Sivakumar, V. 1995. An elasto-plastic critical state framework for unsaturated soil. *Géotechnique,* 45**,** 35-53.

Zakaria, I. 1994. *Yielding of unsaturated soil.* Ph.D. thesis, University of Sheffield.

Zieher, T., Markart, G., Ottowitz, D., Römer, A., Rutzinger, M., Meißl, G. & Geitner, C. 2017. Water content dynamics at plot scale–comparison of time-lapse electrical resistivity tomography monitoring and pore pressure modelling. *Journal of Hydrology,* 544**,** 195-209.

4.10 NOMENCLATURE

ω	angular frequency (rad s^{-1})
ρ_a	apparent resistivity (Ω m)
n	Archie's exponent (dimensionless)
m	cementation factor (dimensionless)
$d\varepsilon_v$	change in the volumetric strain (dimensionless)
de_w	change in moisture ratio (dimensionless)
σ_w	conductivity of the pore fluid (S m^{-1})
I	current (A)
S_r	degree of saturation (dimensionless)
G	geometrical factor (dimensionless)
v_{GPR}	GPR wave velocity (m s^{-1})
P	loss factor (dimensionless)
ρ_d	maximum dry density (g cm^{-3})
p	mean net stress (kPa)
ε_0	permittivity of free space (F m^{-1})
n	Porosity (dimensionless)
ΔU	potential (V)
dW	rate of work for unit volume (kg m^{-1} s^{-3})
ε_r	relative permittivity or the dielectric constant (dimensionless)
μ_r	relative magnetic permeability (dimensionless)
ρ	true resistivity (Ω m)
σ	soil conductivity (S m^{-1})
G_s	specific gravity (kg m^{-3})
v	specific volume (dimensionless)
v_w	specific water volume (dimensionless)
s	Suction (kPa)
σ_s	surface conductivity (S m^{-1})
e	void ratio (dimensionless)
θ	volumetric water content (dimensionless)

4.11 ABBREVIATIONS

ATL	Air transition line
BExM	Barcelona expansive model
CO	Common offset
DOI	Depth of investigation
DC	Direct current
ERT	Electrical resistivity tomography
EM	Electromagnetic
GPR	Ground penetrating radar
HRDEM	High-resolution digital elevation models
HyImag	Hyperspectral imaging
LiDAR	Light detection and ranging
LOO	Line of optimum
LL	Liquid limit
LWSBS	Loading Wetting State Boundary Surface
MPK	Monash-Peradeniya-Kodikara
PSD	Particle size distribution
PL	Plastic limit
PSS	Proximal soil sensing
SL	Shrinkage limit
SWRC	Soil water retention curve
TLS	Terrestrial laser scanning
3DGPM	3D geological and petrophysical model
3DGM	3D geological model
3DMG	3D model geometry

End of thesis